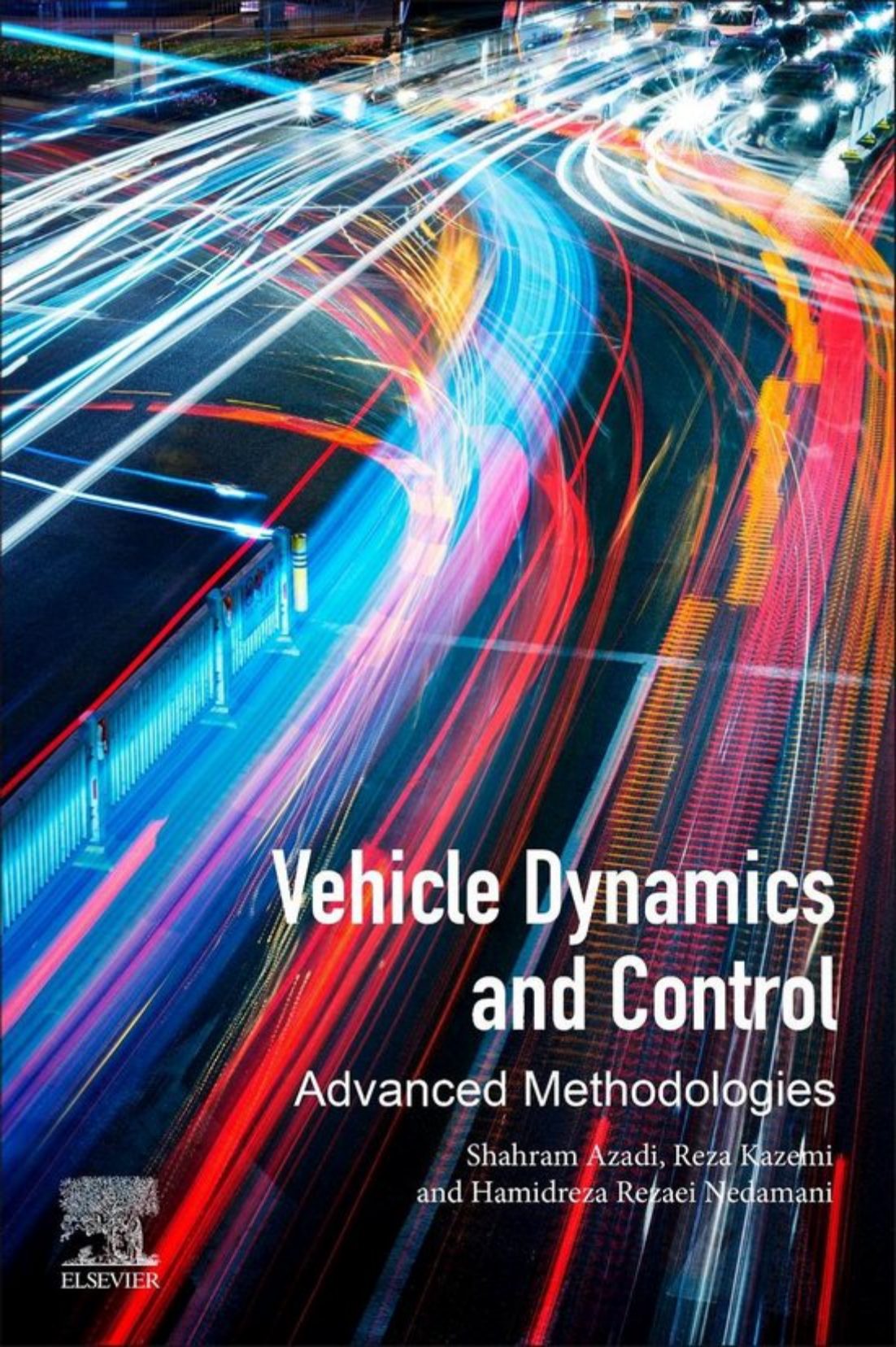
Vehicle Dynamics and Control
Advanced Methodologies
Shahram Azadi, Reza Kazemi and Hamidreza Rezaei Nedamani
ELSEVIER

VEHICLE DYNAMICS AND CONTROL

VEHICLE DYNAMICS AND CONTROL

Advanced Methodologies

SHAHRAM AZADI
Associate Professor, Faculty of Mechanical Engineering, K.N. Toosi University of Technology, and Vehicle Advanced Technologies Deputy Manager, Automotive Industries Research and Innovation Center, Tehran, Iran

REZA KAZEMI
Professor, Faculty of Mechanical Engineering, K.N. Toosi University of Technology, Tehran, Iran

HAMIDREZA REZAEI NEDAMANI
Active Safety System Engineer and ADAS (Advanced Driver Assistance System) Project Manager, Automotive Industries Research and Innovation Center, Tehran, Iran

ELSEVIER

Elsevier
Radarweg 29, PO Box 211, 1000 AE Amsterdam, Netherlands
The Boulevard, Langford Lane, Kidlington, Oxford OX5 1GB, United Kingdom
50 Hampshire Street, 5th Floor, Cambridge, MA 02139, United States

Notices
Knowledge and best practice in this field are constantly changing. As new research and experience broaden our understanding, changes in research methods, professional practices, or medical treatment may become necessary.

Practitioners and researchers must always rely on their own experience and knowledge in evaluating and using any information, methods, compounds, or experiments described herein. In using such information or methods they should be mindful of their own safety and the safety of others, including parties for whom they have a professional responsibility.

To the fullest extent of the law, neither the Publisher nor the authors, contributors, or editors, assume any liability for any injury and/or damage to persons or property as a matter of products liability, negligence or otherwise, or from any use or operation of any methods, products, instructions, or ideas contained in the material herein.

Library of Congress Cataloging-in-Publication Data
A catalog record for this book is available from the Library of Congress

British Library Cataloguing-in-Publication Data
A catalogue record for this book is available from the British Library

ISBN: 978-0-323-85659-1

Publisher: Matthew Deans
Acquisitions Editor: Carrie Bolger
Editorial Project Manager: Chiara Giglio
Production Project Manager: Prem Kumar Kaliamoorthi
Cover Designer: Christian Bilbow

Typeset by SPi Global, India

Dedication

I dedicate this book to my dear wife, Vida, who has always encouraged me in this way.

Shahram Azadi

This book is dedicated to my dearest wife, Atousa, and my two children, Kimia and Kiana, who have all been the source of my perseverance.

Reza Kazemi

In honor of my dear wife, Behnaz.
This book is due to her patience and support.

Hamidreza Rezaei Nedamani

Acknowledgments

Writing a book is more problematic than we thought and more rewarding than we could have ever imagined. In this regard, we owe several people. We thank those who have personally helped us develop the main content, and we thank them for their inspiration and help with this project. Without their continuous assistance during this project, we could not have prepared this book for publication. The names mentioned below have helped us in one or more chapters. We would like to thank Dr. Majid Shabani, Dr. Masoud Vaziri, Dr. Abbas Soltani, Dr. Hadi Sazgar, Dr. Ali Ghasemi Goorji, Dr. Masoud Samadian Zakaria, Dr. Mohammad Amin Saeedi, Dr. Hamed Tabatabaei Oreh, Dr. Saeed Shojaei, and Mohsen Gholipoor.

A significant part of our technical and academic experiences results from research and industrial projects at K.N. Toosi University of Technology and Automotive Industries Research and Innovation Center (AIRIC) of SAIPA. It is necessary to give special thanks to them because the opportunity to write this book would not have been possible without their support and cooperation. Finally, we thank Professor Reza N. Jazar and Dr. Sina A. Milani for their sincere support.

Foreword

I have had the honor to be a friend, classmate, and colleague of Professor Shahram Azadi since 1995. Shahram was a great classmate who studied every subject far more than what was required and far deeper than normal texts provided. That gave Shahram an excellent capability to be a teacher and researcher later when he became an academic. As a colleague, I enjoyed working with Shahram on some projects on vehicle vibrations, vehicle dynamics, vehicle stability, vehicle chassis systems, and vehicle control. In all of them, Shahram has been the supervisor manager of scientific aspects. Shahram has devoted his career to vehicle control, and he is one of the best in the world at it.

I have personally learned very much from Shahram, who always had a clear and correct feeling on engineering aspects of vehicles. Such a vision is crucial when your limited time needs a hint to move in the right research directions.

Professor Azadi is a great teacher who explains everything in the simplest way to his class. Shahram's students and colleagues always appreciate the simplicity of his explanations. Such an ability is the thing that makes a gifted instructor a teacher. Readers of this book will quickly realize how complicated concepts are simply and logically explained.

Shahram is a warm, welcoming, and kind person with a positive outlook on life and a fundamental faith in engineering. He could always put his students at ease with his stories on applied engineering projects. Some of those stories I have heard several times, but I never tire of hearing them again.

Shahram's rich analytic and experimental knowledge and experience on applied vehicle projects make him the best person to write this book. Researchers, instructors, and students will learn from this book to the edge of knowledge in vehicle dynamics and control. The information in the book is excellent for a researcher interested in mathematical modeling of vehicles and those looking for the future of transportation such as control of autonomous vehicles.

This book covers the material straightforwardly and directly to create a shortcut in reviewing the concepts and techniques to prepare readers for their future research. The aim is to provide readers with recent novel control methods and the biggest challenges facing researchers. The authors distribute that knowledge by taking the readers through important aspects of the

advanced approach of vehicle dynamics and control. The contents of the book have been organized into 10 chapters, as follows:

Chapter 1. This chapter reviews the advantages of the simplified vehicle model and shows its shortcoming due to ignoring some variables. In this chapter, an advanced control strategy called "the optimal adaptive self-tuning control" has been used for vehicle dynamic control. The simplified vehicle model is a two-track model for which we will be using an advanced control strategy to compensate for the inaccuracies in the model.

Chapter 2. Modern software tools have enhanced modeling, analysis, and simulation capabilities regarding the control of dynamic systems. In this chapter, a full vehicle model is designed with a flexible body that is exposed to MSC ADAMS and MSC NASTRAN. A vehicle dynamic control system has been implemented to improve the vehicle lateral and yaw motions in critical maneuvers. The readers will appreciate the differences between models' control efforts due to the differences in dynamic behaviors of rigid and flexible vehicle dynamic models.

Chapter 3. During extreme maneuvers, the probability of vehicle roll-over increases, and the stability of lateral and yaw motions deteriorates because of the saturation of tire forces. This chapter presents an integrated control of yaw, roll, and vertical dynamics based on a semiactive suspension and electronic stability control with an active differential braking system.

Chapter 4. The purpose of this chapter is to develop an advanced driver assistance system for integrated longitudinal and lateral guidance of vehicles in high-speed lane-change maneuvers. As the first step, several feasible and collision-free trajectories are generated at different accelerations by considering the position of a target vehicle, the road's speed limit, and the host vehicle's available longitudinal acceleration range.

Chapter 5. In this chapter, the problem of controlling a string of vehicles moving in one dimension is considered. A hierarchical platoon controller design framework is established. The stability criterion is examined using a partial differential equation approximation for a limited number of vehicles subjected to unequal asymmetry in position and velocity feedback. For disturbance attenuation, string stability analysis is examined.

Chapter 6. In terms of articulated vehicles and fluid carriers, the directional response and roll stability characteristics of a partly filled tractor semitrailer vehicle with a cylindrical tank shape are investigated in various maneuvers. In this chapter, the liquid's dynamic interaction with the tractor semitrailer vehicle is evaluated by integrating liquid sloshing dynamics in a partly filled tank with a tractor semitrailer's multibody dynamics.

Chapter 7. This chapter is dedicated to improving maneuverability and preventing jackknifing as well as the rollover stability of an articulated vehicle carrying liquid. A new active roll control system and an active steering control system are designed to control such vehicles.
Chapter 8. In this chapter, the desired articulation angle is considered for directional control of the articulated vehicles. The significant effect on improving the articulated vehicle's directional stability behavior is proven through high-speed lane change maneuver simulations on slippery roads.
Chapter 9. This chapter reviews the problem that articulated vehicle parking is much more complicated than a passenger car. In other words, due to many factors such as control theory, vehicle and environmental nonholonomic constraint, nonlinearities, and time-varying kinematic equations of motion, the articulated vehicle requires a sophisticated control method. In this chapter, the autonomous parking of articulated vehicles is presented using a supervised training technique.
Chapter 10. This chapter's main goal is to extract an algorithm for truck-semitrailer lane change maneuver decision-making in a real dynamic environment. The chosen feasible trajectory is collision-free. It will be shown that because trajectory planning is carried out algebraically, its computational cost will be low, which is very valuable in the experimental implementation.

Reza N. Jazar

Preface

It is hoped that this book will provide a unified and balanced treatment and a useful perspective on the enterprise of an advanced approach to vehicle dynamics and control as well as emphasize the common links and connections that exist between layers of vehicle dynamics and control problems. The first five chapters are related to passenger car topics, and the other chapters deal with articulated vehicles.

The main contents are excerpts from many postgraduate theses, books, and articles that have been compiled from various sources; at the end of each chapter, a list of references is provided to inform and refer the readers. We hope the reader enjoys this book and, more importantly, finds this work educational.

We hope that the sincere efforts of all those involved in preparing this book will be noticed. Because there is no perfect work, we ask all experts to help us with their feedback to correct any defects and improve the book's quality in future editions. Please feel free to inform us if you spot a typo or other error. Our email addresses are listed below:

Shahram Azadi azadi@kntu.ac.ir
Reza Kazemi kazemi@kntu.ac.ir
Hamidreza Rezaei Nedamani rezaei.h@airic-ir.com

CHAPTER 1

Integrated vehicle dynamics and suspension control

1.1 Introduction

Modern vehicles include several control systems responsible for a wide variety of control tasks. A review of past control systems reveals that the controller was individually designed and implemented on the vehicle. However, with modern advancements in electronic systems, remarkable progress has been made in analyzing, transferring, and transmitting data in the digital field. Therefore, this industry is witnessing the emergence of novel techniques and ideas in integrating control systems to improve the overall vehicle performance and optimize costs. Currently, vehicles are equipped with many control systems, which increases their complexity.

The most commonly presented solution is the use of hierarchical control structures, in the sense that all control commands are computed using a single central algorithm, and the key to control integration is the coordination of subsystem performance. According to the definition presented in [1], the integrated vehicle dynamics control can be considered responsible for combining and coordinating all the control subsystems affecting the vehicle's dynamics behavior to improve performance, safety, and comfort while reducing costs.

Chassis control systems follow two main objectives: handling and ride comfort. These systems are divided into active and passive classes. Seat belts and airbags are common passive systems. Passive systems usually reduce the damage from accidents, whereas active systems prevent the occurrence of accidents. On the other hand, active systems primarily avoid some of the vehicle's unwanted events, such as wheel locking, traction dissipation, or excessive changes in the roll and yaw angles, which can result in the loss of vehicle control by the driver. In other words, in the case of incorrect vehicle behavior, these systems either fully take control of the vehicle or participate with the driver in the vehicle's control until the vehicle behavior is corrected [2].

Vehicle Dynamics and Control
https://doi.org/10.1016/B978-0-323-85659-1.00007-0

In summary, the reasons for the tendency toward integration are the following:

- Diversity of control systems
- Diversity in the technology and requirements of each system
- Independent performance of these systems
- Undesired effects of these systems on each other.

Handling and ride comfort have an inverse relationship, such that an improvement in one leads to a loss in the other. For example, to improve vehicle handling, it is preferable to increase the damping ratio and stiffness of the dampers, which decreases the ride comfort [3]. According to these discussions and the fact that control systems usually improve only one of these two parameters, a significant role integration can combine the systems related to these parameters. Several techniques have been developed to reach integrated control of the chassis. These techniques can be divided into the following two groups:

- Multivariable control
- Hierarchical control.

In this chapter, we used a hierarchical control system. The advantages of hierarchical control include the following:

- Facilitation of designing control subsystems
- Control of the complexities by taking them into account in the lower control layers
- Preference for more tasks and workload.

1.2 Control system design

Fig. 1.1 shows an integrated control system with a hierarchical strategy that has combined ABS (antilock braking system) and ASS (active suspension system). The lower controller layer consists of the individual ABS and ASS, whereas the upper layer contains an algorithm for combining the two systems. Indeed, such a process is more straightforward and more understandable than a complicated model with a single control layer for reaching the desired state [4].

One of the most important factors in achieving the main objectives is a suitable integration algorithm. This is the most important goal in the current chapter. In the algorithm used during the vehicle maneuver, contact between the tire and the road may be eliminated due to the existing

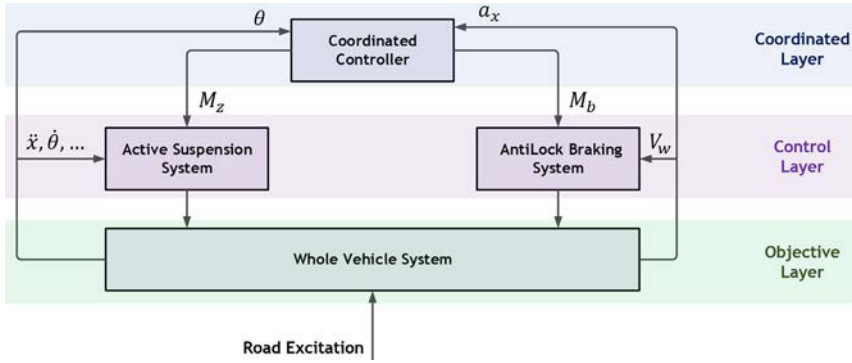

Fig. 1.1 Sample of an integrated control system with a hierarchical strategy.

conditions, especially road input. It is worth mentioning that the ride comfort is important under normal conditions, and the system must act in such a way that the passenger does not become tired under normal driving conditions.

In this chapter, self-tuning regulator (STR) adaptive optimal control is selected to explain the control structure by introducing the optimal control strategy and the recursive least squares (RLS) error estimator. The self-tuning regulator adaptive control strategy is used to design the ESP (electronic stability program). The algorithm used to design the ABS is simple and consists of several logical conditions. Moreover, an optimal control strategy has been used to design the ASS. Finally, the integration algorithm utilized will be introduced.

Adaptive control is defined as a control scheme with adjustable parameters and a mechanism for adapting the parameters. The reasons for using this strategy include the following:

- Changes in the process dynamics
- Changes in the properties of the system disturbance
- Engineering efficiency and simplicity of use
- Various adaptive control ideas
- Gain scheduling.

In the STR structure, the controller is updated by estimating the parameters. The self-tuning in this controller means that the controller parameters are tuned automatically to attain the desired state; see Fig. 1.2 [5].

In the STR method, we update the structure of the controller, but we also update the desired state in the design of the ESP. The STR method will

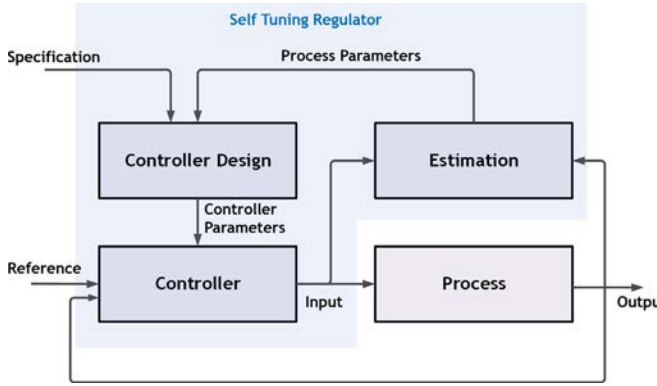

Fig. 1.2 STR schematic.

assist the optimal control method in the proposed algorithm. The RLS method has been employed to estimate the system parameters. The combination of these two methods will provide us with a self-tuning adaptive controller that updates in each step with changes in the system parameters. As will be discussed, significant and wide changes in the lateral stiffness of the tires make it impossible to obtain the desired results using only optimal control. Because changes in the parameters affecting the system vibrations are slight, the LQR control strategy is used alone in the design of the ASS.

1.2.1 Design of the ESP

1.2.1.1 Lateral force estimator

The self-tuning adaptive control strategy has been employed to design the ESP. For this purpose, an estimator suitable for this system must be developed first. It is worth mentioning that the parameters with the most changes in the ESP control system's design are the lateral stiffness of the front and rear wheels. The variation ranges of these parameters change with a change in the road surface material or even in the tire load. The estimator is responsible for determining the values of these two parameters at each instant. In this section, we use the equations of the bicycle model, as shown in Fig. 1.3. These equations are presented in Eqs. (1.1)–(1.3);

$$\dot{X} = AX + BU_c + EU \tag{1.1}$$

$$X = \begin{Bmatrix} v_y \\ r \end{Bmatrix}, U_c = M_z, U = \delta \tag{1.2}$$

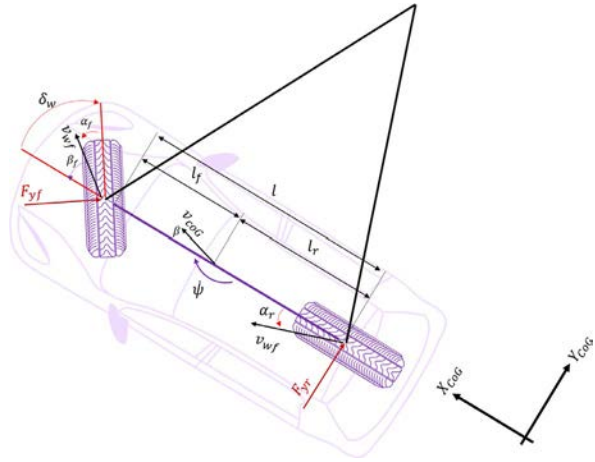

Fig. 1.3 Vehicle bicycle model.

$$A=\begin{bmatrix} -\dfrac{C_{\alpha r}+C_{\alpha f}}{m_t\,v_x} & \dfrac{C_{\alpha r}\,l_r+C_{\alpha f}\,l_f}{m_t\,v_x}-v_x \\ \dfrac{C_{\alpha r}\,l_r+C_{\alpha f}\,l_f}{I_{zz}\,v_x} & \dfrac{C_{\alpha r}\,l_r{}^2+C_{\alpha f}\,l_f{}^2}{I_{zz}\,v_x} \end{bmatrix}, B=\begin{bmatrix} 0 \\ \dfrac{1}{I_{zz}} \end{bmatrix}, E=\begin{bmatrix} \dfrac{C_{\alpha f}}{m_t} \\ \dfrac{C_{\alpha f}\,l_f}{I_{zz}} \end{bmatrix} \tag{1.3}$$

where $C_{\alpha f}$ and $C_{\alpha r}$ are the turning constants of the front and rear tires, respectively. To this end, we use the bicycle model in the form of Eq. (1.4);

$$\begin{cases} a_y=\dfrac{1}{m_t}\left(F_{y_f}+F_{y_r}\right) \\ \dot{r}=\dfrac{1}{I_{zz}}\left(F_{y_f}\,l_f-F_{y_r}\,l_r+M_z\right) \end{cases} \tag{1.4}$$

In Eq. (1.4), the values of a_y and $\dot{r}$ are readily determined using the existing sensors. Moreover, M_z is the output of this system. As mentioned before, F_{y_f} and F_{y_r} are the parameters that must be estimated. The last equation can be written in the form of Eqs. (1.5) and (1.6) to use the RLS method.

$$y(t)=\begin{bmatrix} a_y \\ \dot{r}-\dfrac{M_z}{I_{zz}} \end{bmatrix} \tag{1.5}$$

$$\theta(t)=\begin{bmatrix} F_{y_f} \\ F_{y_r} \end{bmatrix} \tag{1.6}$$

After determining the lateral forces and obtaining the slip angle values from the above relationships, the lateral stiffness values can be determined.

It is worth mentioning that the technique of tuning the forgetting factor is used to design the estimator.

1.2.1.2 Longitudinal velocity estimation

Longitudinal velocity is another parameter that can have a wide range of variations. This parameter plays an important role both in determining the control gain and in determining the desired state. Because deciding the longitudinal velocity using a sensor is not economical, it must be specified in another way. One method is employing an observer. However, because the sensors for the longitudinal and lateral velocity and the yaw rate of the vehicle are both economic and accurate, one can use the simple method introduced in Eq. (1.7) to compute the longitudinal and the lateral velocity:

$$\frac{d}{dt}\begin{bmatrix} v_x \\ v_y \end{bmatrix} = \begin{bmatrix} 0 & r \\ -r & 0 \end{bmatrix}\begin{bmatrix} v_x \\ v_y \end{bmatrix} + \begin{bmatrix} a_x \\ a_y \end{bmatrix} \tag{1.7}$$

where a_x, a_y, and r are obtained from the sensor. This recursive relationship is derived from the equations of vehicle acceleration in the 3-DOF model [6].

1.2.1.3 Determination of the yaw moment

The LQR (linear–quadratic regulator) strategy has been used to determine the yaw moment. It must be noted that systems discussed in these types of problems are either linear themselves or the linearized part of a nonlinear system. The cost function is selected as a square of the system's state variables and the control function. This feedback system's significant advantage is that the design is performed based on minimizing the cost function instead of determining the closed-loop poles. As such, the closed-loop system's eigenvalues are automatically selected, and the designer must only determine the specific parameters of the cost function. By choosing these parameters, the physical constraints of the system and state variables are determined. The system configuration is selected in the form of (1.8).

$$\dot{x}(t) = A(t)x(t) + B(t)u_c(t) + E(t)u(t) \tag{1.8}$$

In Eq. (1.8), u_c is the control input, and u is the noncontrol input. The cost function is defined as follows:

$$\begin{aligned} J = {} & \frac{1}{2}\Big(x\Big(t_f\Big) - r\Big(t_f\Big)\Big)^T G\Big(x\Big(t_f\Big) - r\Big(t_f\Big)\Big) \\ & + \frac{1}{2}\int_{t_r}^{t_f} \Big((x(t) - r(t))^T Q(t)(x(t) - r(t))^T + u^T(t)R(t)u(t)\Big)dt \triangleq \frac{1}{2}\Big\|x\Big(t_f\Big) - r\Big(t_f\Big)\Big\|_H^2 \\ & + \frac{1}{2}\int_{t_r}^{t_f} \Big(\|(x(t) - r(t))\|_{Q(t)}^2 - \|u(t)\|_{R(t)}^2\Big)dt \end{aligned} \tag{1.9}$$

In Eq. (1.9), the matrices G and Q are real, positive semidefinite, and symmetric, whereas the matrix R is real, positive definite, and symmetric. $r(t)$ is the desired state. Existing relationships have been used for the bicycle model, and Eq. (1.10) has been employed to determine the desired state:

$$r_d(t) = \frac{v_x}{\rho} = \frac{v_x}{l_f + l_r + \dfrac{m_t v_x^2 \left(l_r C_{\alpha r} - l_f C_{\alpha f}\right)}{2 C_{\alpha r} C_{\alpha f} \left(l_f + l_r\right)}} \delta \tag{1.10}$$

In Eq. (1.10), ρ is the radius of the curvature of the vehicle path. However, this relationship is limited by the friction capacity of the road surface. The range of validity of this relationship is determined as Eq. (1.11). In this equation, μ is the friction coefficient between the road surface and the tire, and g is the gravitational acceleration.

$$r_{up.\lim.}(t) = 0.85 \frac{\mu g}{v_x} \tag{1.11}$$

Eventually, Eqs. (1.10) and (1.11) lead to the following conclusion;

$$\begin{cases} r_{f.d}(t) = r_d(t), & |r_d(t)| \le r_{up.\lim.}(t) \\ r_{f.d}(t) = r_{up.\lim.}(t) \times \operatorname{sign}(r_d(t)), & |r_d(t)| > r_{up.\lim.}(t) \end{cases} \tag{1.12}$$

To implement optimal control in this section, $Q = \begin{bmatrix} 0 & 0 \\ 0 & q \end{bmatrix}$ and $R = \xi$ are assumed, where the values of ξ and q have been optimized via trial and error. As such, the matrix $r(t)$ will be as follows (1.13):

$$r(t) = \begin{bmatrix} 0 \\ r_{f.d}(t) \end{bmatrix} \tag{1.13}$$

1.2.1.4 Braking strategy in the ESP system

After the adequate yaw moment is determined, it must be applied to the vehicle, which is done in the ESP system via braking. Hence, a proper braking strategy must be established. Before the establishment of this strategy, its concepts must be well understood.

Understeer: This is when the slippage of the front wheels is larger than that of the rear wheels during a turn, leading the vehicle outward and forcing the driver to steer more than usual to return the vehicle to the intended path.

Oversteer: This is when the slippage of the front wheels is smaller than that of the rear wheels during a turn, leading the vehicle inward and forcing the driver to steer less than usual to return the vehicle to the intended path.

When none of the above conditions were presented, *neutral* steering is said to exist. Given the bicycle model presented in the previous sections, a parameter called the understeering gradient is defined as in (1.14).

$$K_v = \frac{m_t}{(l_f + l_r)}\left(\frac{l_r}{C_{\alpha f}} + \frac{l_f}{C_{\alpha r}}\right) \tag{1.14}$$

Considering Eq. (1.14), the concepts of understeering, oversteering, and neutral steering can also be expressed via Eq. (1.15) [7].

$$\begin{cases} \dfrac{l_r}{C_{\alpha f}} = \dfrac{l_f}{C_{\alpha r}} \Rightarrow K_v = 0 \Rightarrow \text{Nuetral} \\ \dfrac{l_r}{C_{\alpha f}} > \dfrac{l_f}{C_{\alpha r}} \Rightarrow K_v > 0 \Rightarrow \text{Understeer} \\ \dfrac{l_r}{C_{\alpha f}} < \dfrac{l_f}{C_{\alpha r}} \Rightarrow K_v < 0 \Rightarrow \text{Oversteer} \end{cases} \tag{1.15}$$

In the design process, the vehicle should be understeered because, in this case, its control is more comfortable and far from instability. On the other hand, when an understeered vehicle veers out of the road turn, the radius of curvature of its path increases, leading to a decrease in the lateral acceleration and slipping, and therefore a decrease in understeering. On the opposite, in an oversteered vehicle, the oversteering increases, and the vehicle's condition becomes more critical (Fig. 1.4).

Because applying braking on the wheels increases their slipping and given the above discussion, it is better to use the braking on the front wheels for oversteered vehicles and the rear wheels for understeered vehicles. Here, the yaw moment is provided only by applying a brake on one wheel. The process of selecting that wheel is shown in Table 1.1.

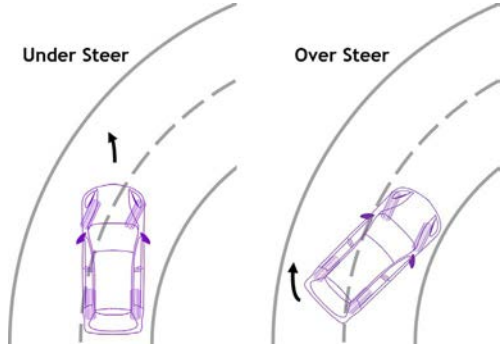

Fig. 1.4 Handling comparison between oversteered and understeered vehicles.

Table 1.1 Strategy for determining the brake wheel in ESP design.

Steering angle	Desired yaw rate	Applied yaw moment	Handling state	Braking force and corresponding wheel
$\delta > 0$	$r > 0$	$M_z < 0$	Oversteer	$F_{b_{fr}} = 2\frac{M_z}{T_f}$
	$r > 0$	$M_z > 0$	Understeer	$F_{b_{rl}} = 2\frac{M_z}{T_r}$
$\delta < 0$	$r < 0$	$M_z < 0$	Understeer	$F_{b_{rr}} = 2\frac{M_z}{T_r}$
	$r < 0$	$M_z > 0$	Oversteer	$F_{b_{fl}} = 2\frac{M_z}{T_f}$

After the brake force and the suitable wheel for applying this force are determined, one must determine the brake torque, which is easily distinguished from (1.16).

$$T_{b_i} = F_{b_i} \times R_{\mathit{eff}.}, \ (i = fr, fl, rr, rl) \tag{1.16}$$

1.2.2 Design of the ABS

The aim of designing the ABS is to maintain the wheels' longitudinal slip in the range from 0.1 to 0.15. The braking efficiency is highest in this range. Fig. 1.5 displays the optimal range of braking performance [3]. In this region, the performances of longitudinal and lateral forces are simultaneously at their best.

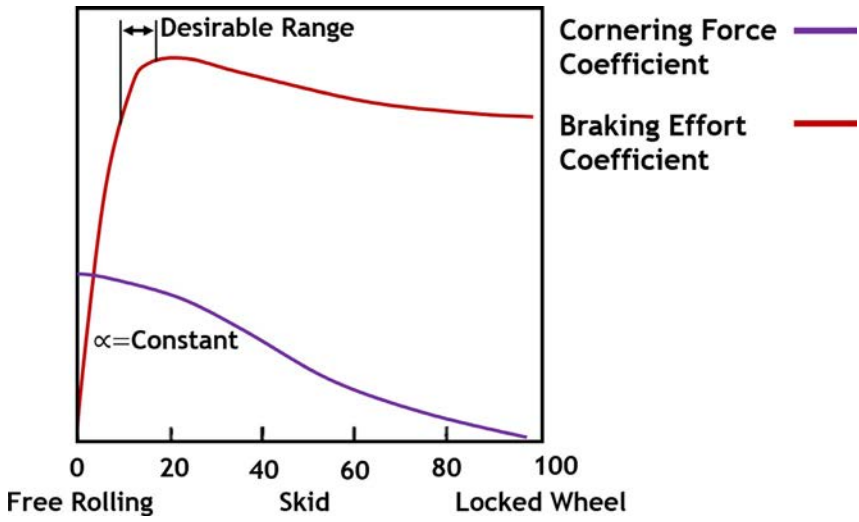

Fig. 1.5 Desired region for optimal performance of the brakes [8].

Table 1.2 Longitudinal slip limitation in the ABS.

Longitudinal slip	$0.15 < \lambda$	$0.125 < \lambda < 0.15$	$0 < \lambda < 0.125$
ABS reaction	$T_{ABS} = 0.9\ T_{b_{prev.}}$	$T_{ABS} = T_{b_{prev.}}$	$T_{ABS} = T_b$

Table 1.2 is recommended to reach the above goal. In this table, $T_{b_{Prev}}$ refers to the brake torque applied in the previous step. In fact, by increasing the longitudinal slip ratio beyond 0.125, the ABS will not increase the brake torque even if needed. Under more critical conditions where the longitudinal slip exceeds 0.15, the ABS will even act to reduce the brake torque [6].

1.2.3 Active suspension system design

The LQR optimal control strategy has been used in the design of the active suspension system. Because the parameters do not change much here, and the variable intensity of the lateral stiffness coefficient is not observed in parameters of the 7-DOF and 2-DOF vibration models, there is no need for adaptive control. Besides, the linear property of the models makes the use of this strategy possible.

In the active suspension system design, the matrix Q in Eq. (1.8) plays a significant role in obtaining satisfactory results. During the active suspension system design, four 2-DOF vibration models are used on the four sides of the body. Depending on which state variable must be optimized, the corresponding element on the matrix Q's main diagonal must be given a nonzero value, and the other elements of the matrix must be set to zero. When the aim is to improve ride comfort, the matrix Q will be different from when the objective is to improve handling. When using the 7-DOF model, this matrix is 14×14, and if we would like to improve ride comfort, only the main diagonal elements on rows 1 to 6 must be nonzero. In this case, the matrix R will be 4×4, and the matrix $r(t)$ in Eq. (1.9) will be a 1×4 zero matrix. However, when using the one-fourth vibration model, the matrix Q is 4×4, and if we would like to improve ride comfort, only the main diagonal elements on the first and third rows are nonzero. Besides, the matrix R will be 1×1, and the matrix $r(t)$ will be a 1×1 zero matrix. However, if we would like to use the one-fourth vibration model to improve the road-holding of the tires, the matrix $r(t)$ will be in the form $\begin{bmatrix} z_{r_i} & 0 & z_{u_i} & 0 \end{bmatrix}^T$, where z_{r_i} is the road input from the ith wheel, and z_{u_i} is the bounce of the ith wheel [9].

1.3 Integration strategy

The lower control layer consists of the ABS, ESP, and ASS systems, and the upper layer consists of an integration algorithm. According to this integration algorithm, the ESP is always active, and its output is applied to the vehicle. However, the ASS will have two types of inputs. One is $F_{Handling}$, which is determined with the aim of minimizing tire compression and improving handling. The other is F_{Ride}, which is determined with the aim of improving ride comfort. The upper layer plays an important role here. In this layer, each of these outputs is given a weighting factor based on which outcome is determined. The lateral acceleration is the indicator that determines the weight given to each of these outputs. The integration algorithm is proposed in the form of Eq. (1.17):

$$\begin{cases} F = F_{Ride} & ,|a_y| < 0.2g \\ F = e^{(0.2g-|a_y|)} \times F_{Ride} + e^{(|a_y|-0.4g)} \times F_{Handling} & ,0.2 < |a_y| < 0.4g \\ F = F_{Handling} & ,0.4g < |a_y| \end{cases} \quad (1.17)$$

1.4 Simulation of the proposed strategies

First, the outputs resulting from controlling the vehicle using the ESP have been shown. Then, the ASS is implemented on the model, and the results have been delivered. In this part, the controller designed based on a 7-DOF vibration model has been compared to one created based on a four 2-DOF vibration model. Moreover, we have improved the tires' road-holding using four 2-DOF vibration models, and the related graphs are displayed. Ultimately, the obtained results for the integrated system have been plotted. The parameters used in the design are shown in Table 1.3.

1.4.1 Handling control of the vehicle

In this case, the only input is the steering angle, and the results are as follows; see Figs. 1.6–1.9.

1.4.2 Suspension system control

In this section, the only input is the road surface roughness. First, the goal is to improve the ride comfort using the 7-DOF [8] vibration model and the one-fourth ride model. Subsequently, the results will be compared. As seen in Fig. 1.10, we have applied this input so that all the ride comfort DOFs, namely the vertical displacement of the body and wheels and the pitch and

Table 1.3 Quantities used in the models.

Quantity	Value
Moment of inertia about the Z-axis (I_{ZZ})	1350 kg m^2
Moment of inertia about the X-axis (I_{XX})	350 kg m^2
Moment of inertia about the Y-axis (I_{YY})	1288 kg m^2
Rotational inertia of the wheel I_W	1.2544 kg m^2
Mass of the body (m_s)	1300 kg
Mass of each wheel (m_u)	31.9 kg
Spring constant of the front suspension (k_{s_f})	14200 N/m
Spring constant of the rear suspension (k_{s_r})	18500 N/m
The equivalent spring constant of the front tire (k_{t_f})	180000 N/m
The equivalent spring constant of the rear tire (k_{t_r})	180000 N/m
The damping ratio of the front suspension (c_{s_f})	1085 N s/m
The damping ratio of the rear suspension (c_{s_r})	5850 N s/m
Rolling resistance coefficient (f_{roll})	0.015
Lateral stiffness coefficient of the tire (C_α)	44248 N/rad
Lateral stiffness coefficient of the tire (C_λ)	50000 N
Friction coefficient for full slipping (μ_{min})	0.7
Friction coefficient for zero slipping (μ_{max})	0.9
Longitudinal distance between the mass center and the front wheels (l_f)	1224.7 mm
Longitudinal distance between the mass center and the front wheels (l_r)	1437.3 mm
Lateral distance between the front wheels (t_f)	1408 mm
Lateral distance between the rear wheels (t_r)	1388 mm
Effective radius of the tire ($R_{eff.}$)	283 mm
Height of the vehicle mass center (h)	307 mm
Tire width (*Width*)	235 mm

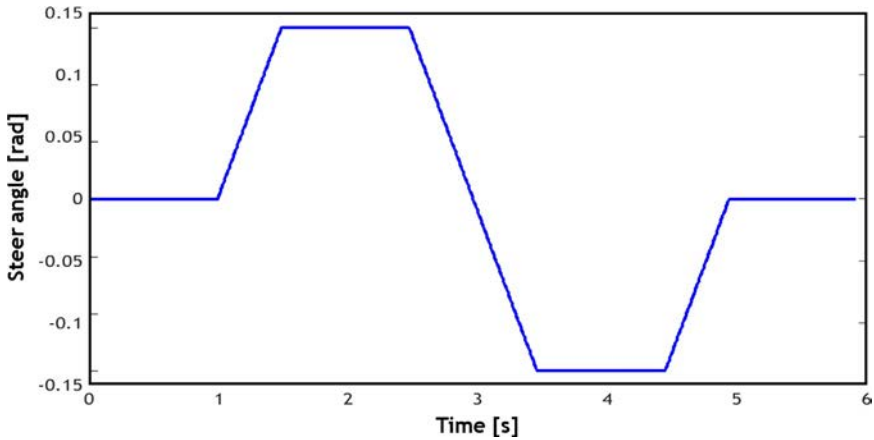

Fig. 1.6 The steering input used in the handling test of the vehicle.

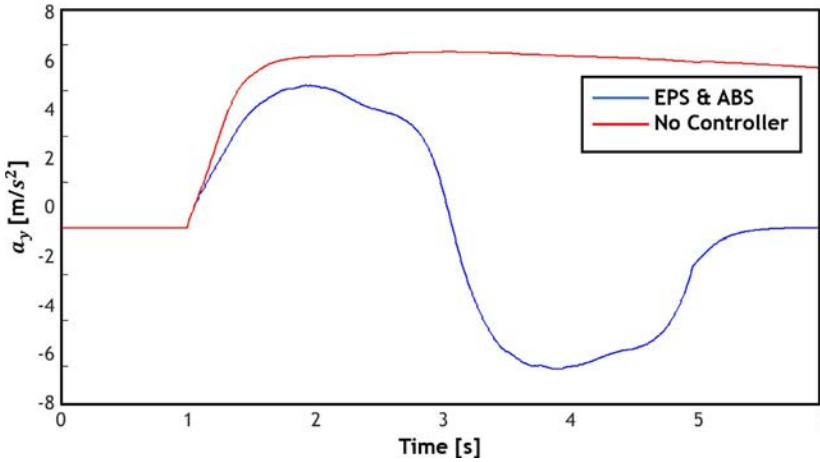

Fig. 1.7 The lateral acceleration of the vehicle with and without ABS and ESP.

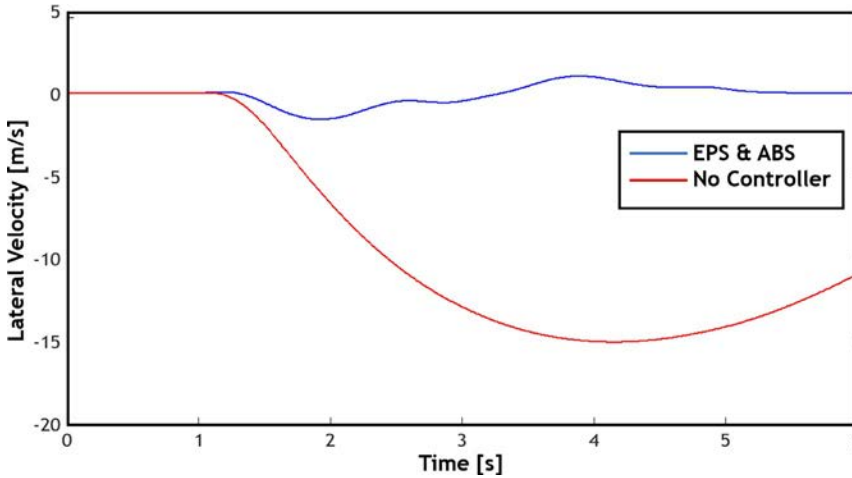

Fig. 1.8 The lateral velocity of the vehicle with and without ABS and ESP.

roll angles, are activated. Although the active suspension systems used have improved the ride comfort, the graphs in Figs. 1.11–1.16 clearly show the advantage of using the 7-DOF vibration model instead of four one-fourth vibration models at four sides of the vehicle body. This is because the dynamics used to design the controller via the 7-DOF vibration model consider the four vehicle sides' interaction.

The following presents the results of another test. Also, in this case, the steering input is zero, and the initial velocity of the velocity is 120 km/s.

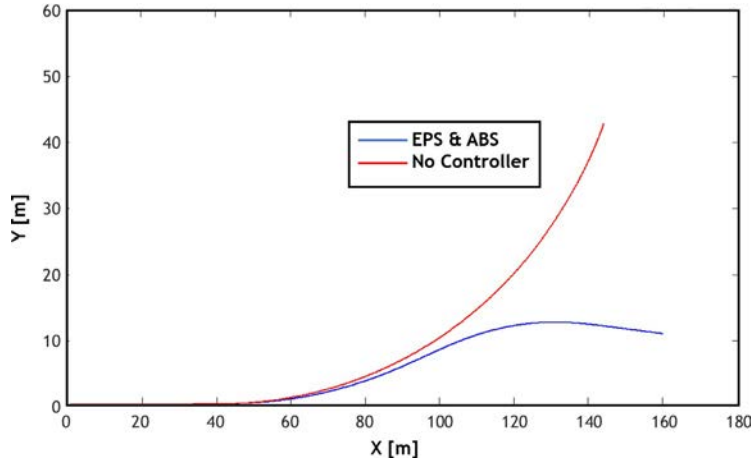

Fig. 1.9 Motion path of the vehicle with and without ABS and ESP.

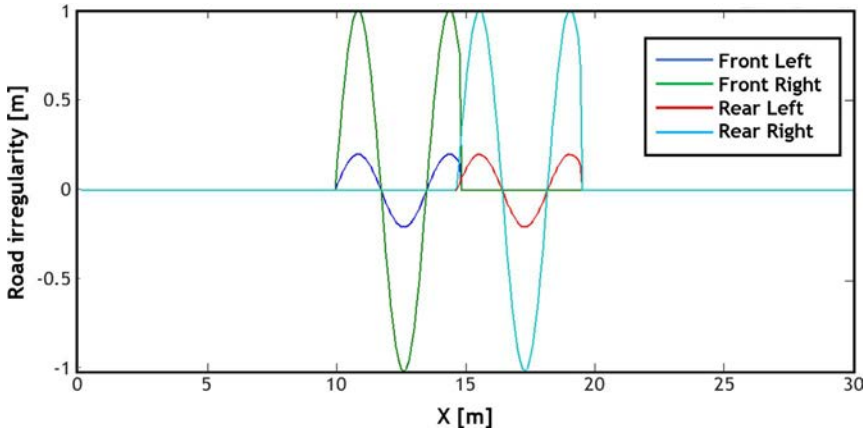

Fig. 1.10 Road irregularity in the ride test.

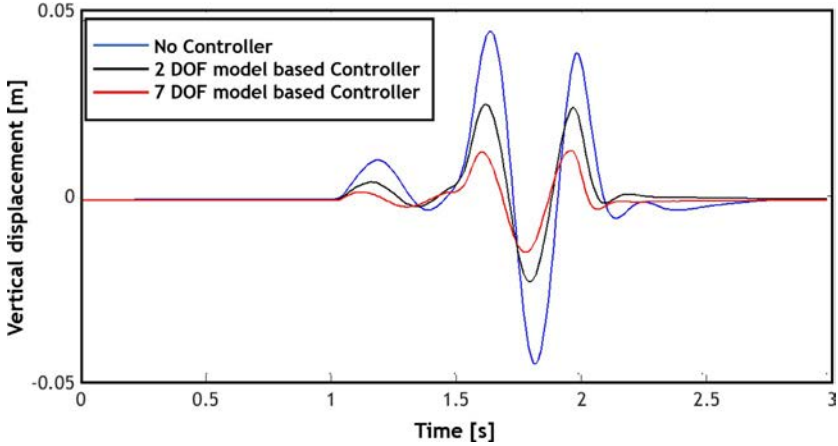

Fig. 1.11 Vertical displacement of the body in the ride test.

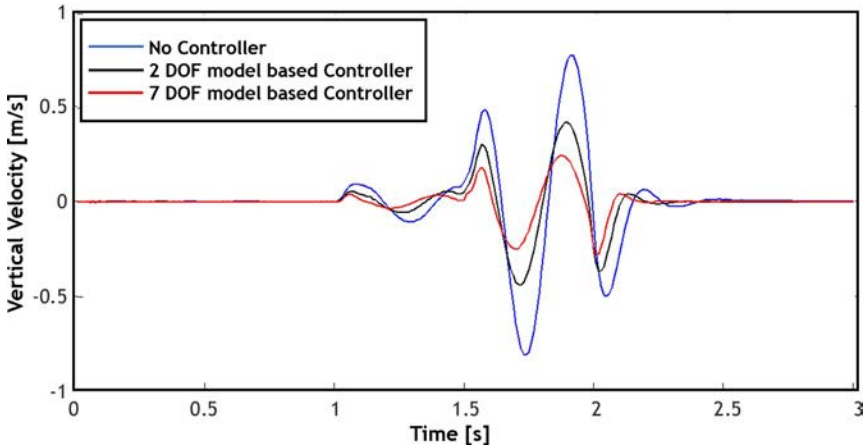

Fig. 1.12 Body vertical velocity in the ride test.

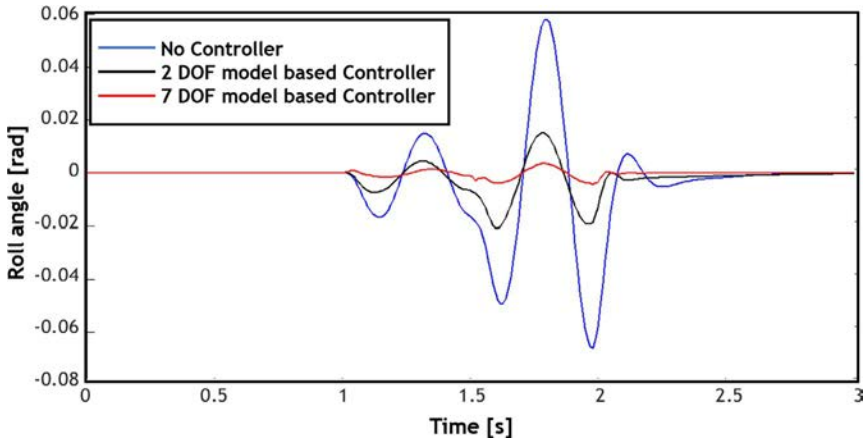

Fig. 1.13 Roll angle in the ride test.

Besides, a constant brake torque has been considered on the rear wheels. We have applied the road input so that the contact between the tire and the road is removed; see Fig. 1.17.

Given that the positive in downward in the coordinate system used, negative values in Fig. 1.18 mean that the downward movement of the wheel mass center is more, compared to the road input and the tire is compressed. Positive values indicate that the road input is lower than the displacement of the wheel mass center and the tire is separated from the road. Using the

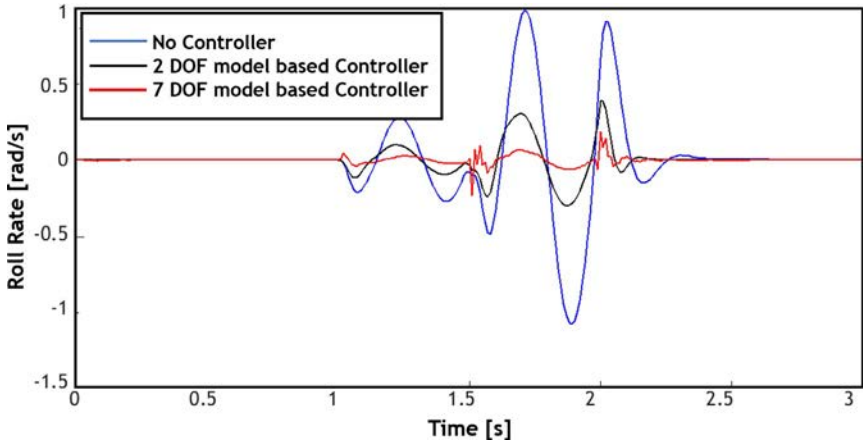

Fig. 1.14 Roll rate in the ride test.

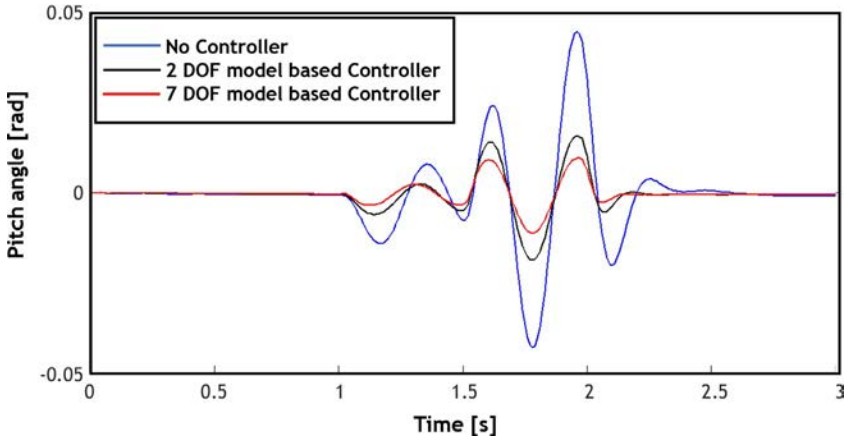

Fig. 1.15 Pitch angle in the ride test.

controller has reduced the absolute value of the difference between the road input and the displacement of the wheel center.

One result of keeping contact between the tires and the road is reducing the longitudinal slip ratio. A comparison of Figs. 1.19 and 1.20 indicates this reduction. The separation of the tire from the road surface causes the wheel to rotate idly, and the absolute value of the longitudinal slip ratio increases. Here, because a brake torque has been applied on the rear wheels, the longitudinal slip ratio's absolute value is larger for these wheels. Moreover, the longitudinal slip ratio's negative values in these two graphs indicate

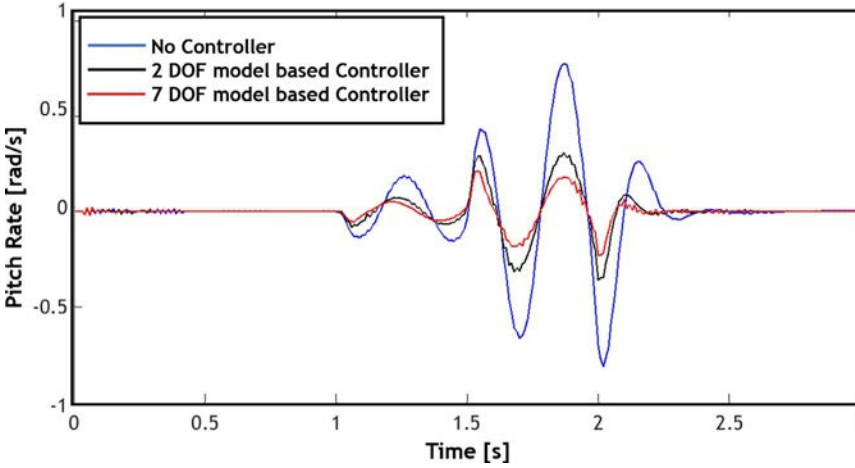

Fig. 1.16 Pitch velocity in the ride test.

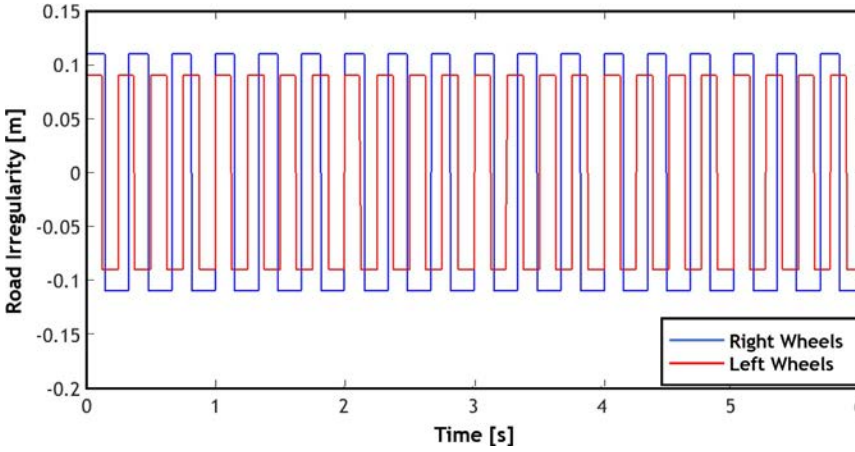

Fig. 1.17 Road irregularities for removing contact between the tire and the road.

the smaller wheel rotation equivalent velocity compared to the velocity of the point of contact of the wheel and the ground.

In the following, we consider the initial velocity to be $50[^{km}/_{h}]$ with the same road input and steering input. In this case, we apply a constant traction torque to the rear wheels instead of brake torque. As will be seen later, the road-holding of the tire has improved significantly, and, hence, the absolute value of the longitudinal slip ratio has decreased. Here also, the longitudinal slip ratio's absolute values are larger in the rear wheels due to the application

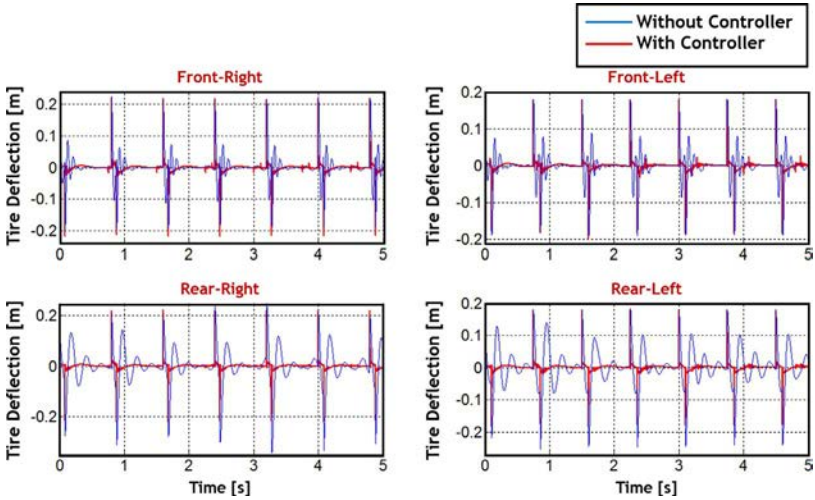

Fig. 1.18 Difference between the road input and the displacement of the wheel center in the active suspension system test with an applied brake torque.

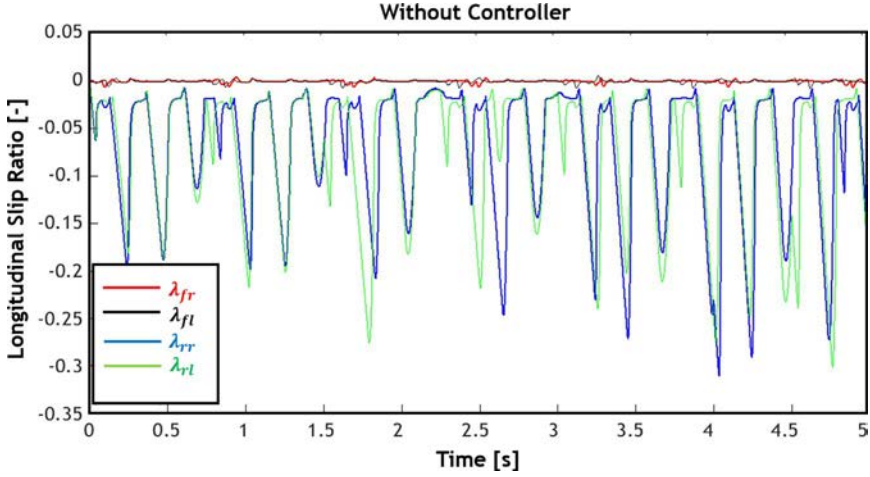

Fig. 1.19 Longitudinal slip ratio of the wheels without the controller in the active suspension system test with an applied brake torque.

of the traction torque on them. Moreover, the longitudinal slip ratio's positive values in these two graphs indicate the larger wheel rotation equivalent velocity compared to the velocity of the point of contact of the wheel and the ground. Finally, as expected, the increase in the vehicle velocity will be larger in the controller's presence due to the reduction of the longitudinal slip ratio in the rear wheels; see Figs. 1.21–1.24.

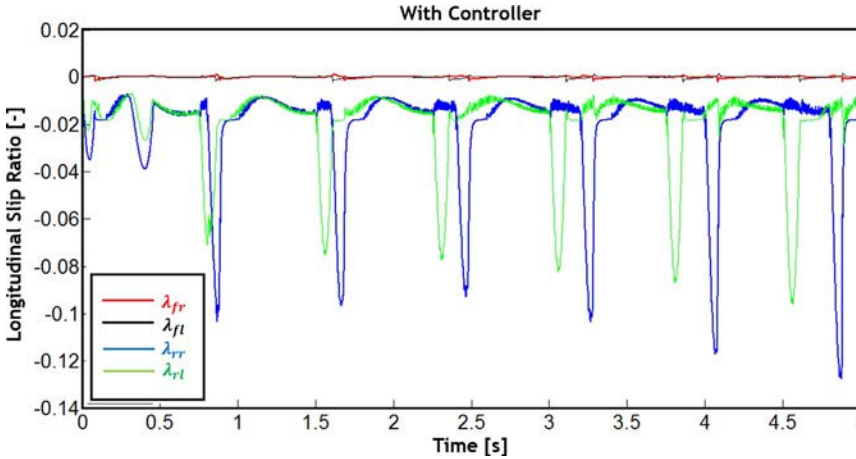

Fig. 1.20 Longitudinal slip ratio of the wheels in the presence of the controller in the active suspension system test with an applied brake torque.

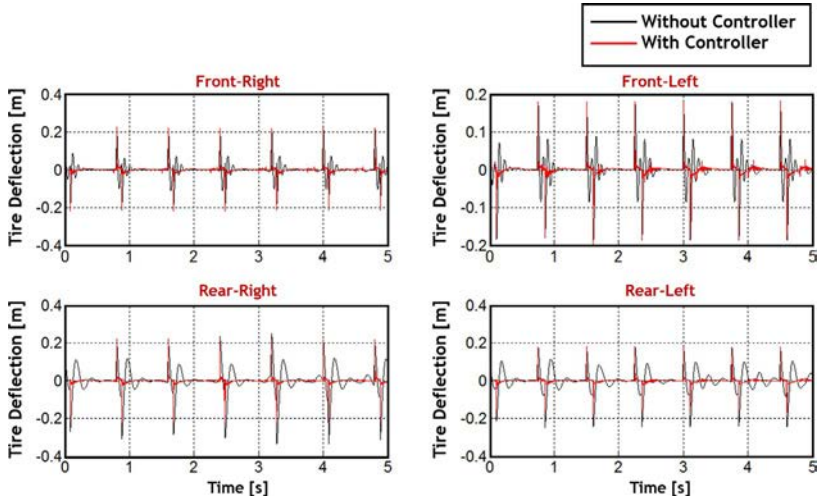

Fig. 1.21 Difference between the road input and the displacement of the wheel center in the active suspension system test with an applied traction torque.

1.4.3 Integrated control of suspension system and vehicle dynamics

It must be noted that, in this section, the active suspension system contributes to stability improvement only in the integrated control state, and only when the lateral acceleration of the vehicle exceeds 0.2 g. In other control

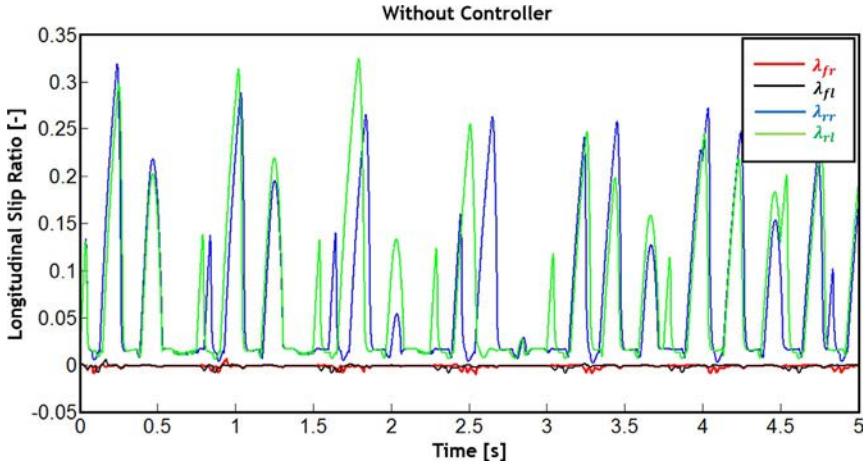

Fig. 1.22 Longitudinal slip ratio of the wheels without the controller in the active suspension system test with an applied traction torque.

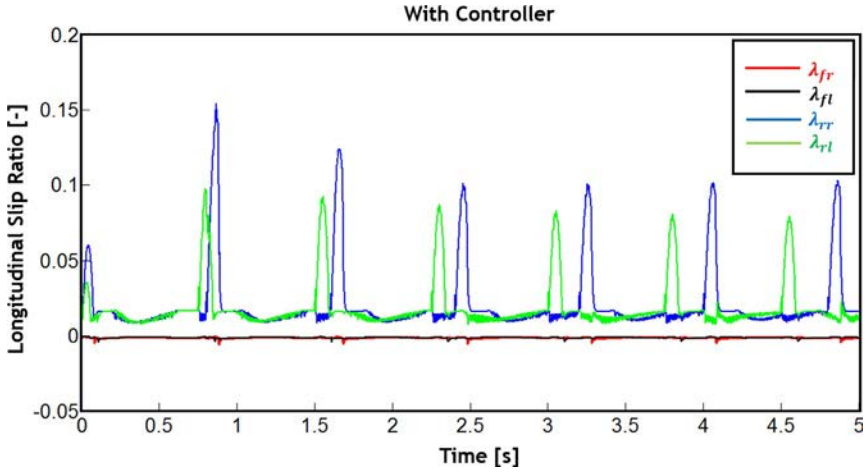

Fig. 1.23 Longitudinal slip ratio of the wheels in the presence of the controller in the active suspension system test with an applied traction torque.

states, its only goal is to improve the ride comfort. It is seen in Fig. 1.25 that the lateral acceleration is at its worst in the ride improvement mode. The best state is using integrated control. Although this improvement is not remarkable compared to stability control and individual control states, it still considerably improves the lateral velocity, yaw rate, lateral slip angle, and vehicle path.

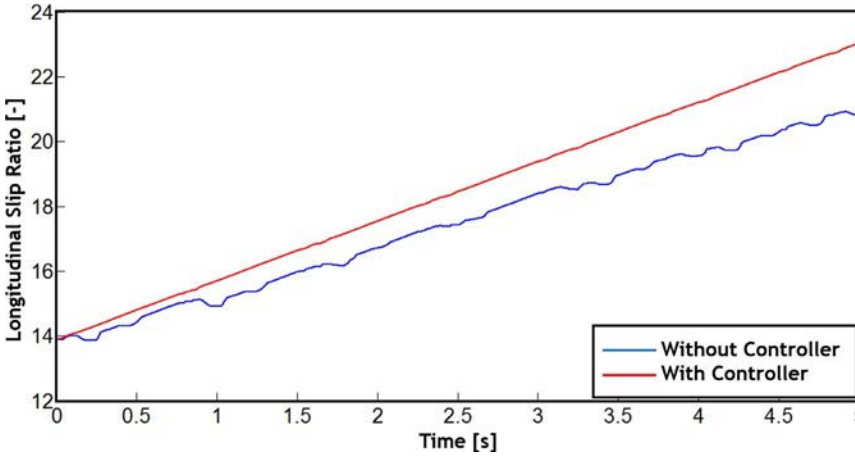

Fig. 1.24 The longitudinal velocity of the vehicle in the active suspension system test with an applied traction torque.

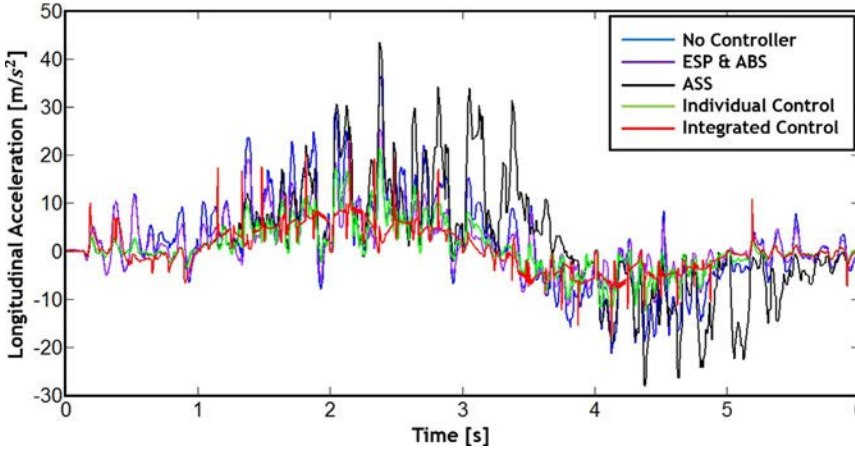

Fig. 1.25 The lateral acceleration of the vehicle in the integration test.

As seen in Figs. 1.26–1.28, the integration strategy used has led to reductions in the lateral slip angle and lateral velocity of the vehicle and an improvement in the vehicle's yaw rate. This strategy has especially been effective in areas where the lateral acceleration exceeds 0.2 *g*.

We see in Fig. 1.29 that the results in the ride comfort improvement and individual control states overlap. However, the use of the integration strategy has led to a drop in ride comfort. As mentioned previously, under critical

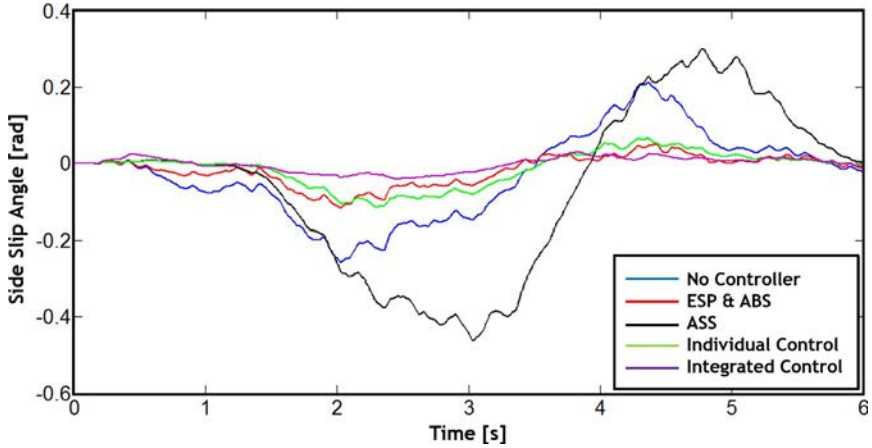

Fig. 1.26 Lateral slip angle of the vehicle in the integration test.

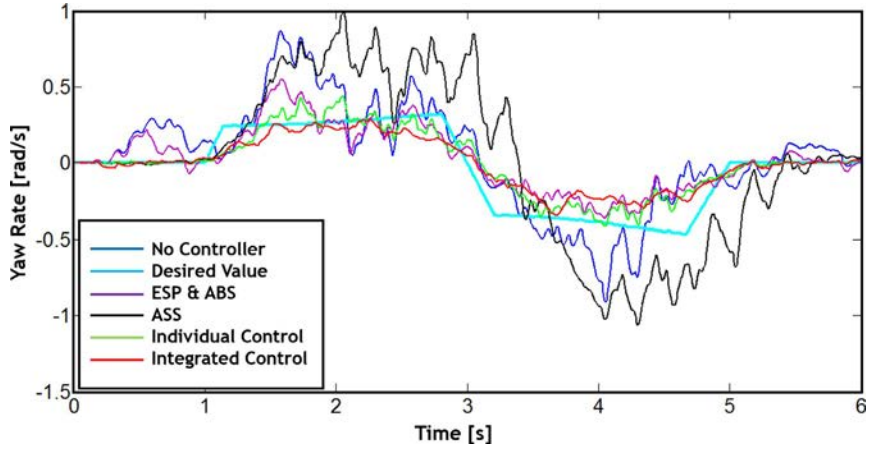

Fig. 1.27 Yaw rate of the vehicle in the integration test.

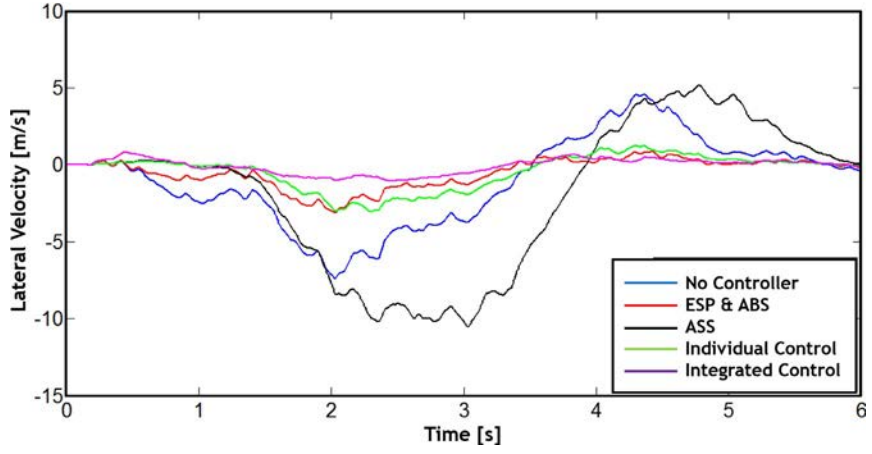

Fig. 1.28 The lateral velocity of the vehicle in the integration test.

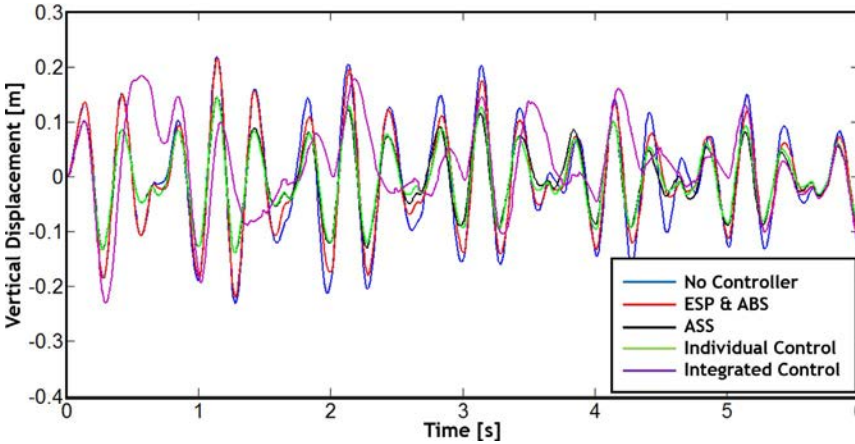

Fig. 1.29 Vertical displacement of the vehicle body in the integration test.

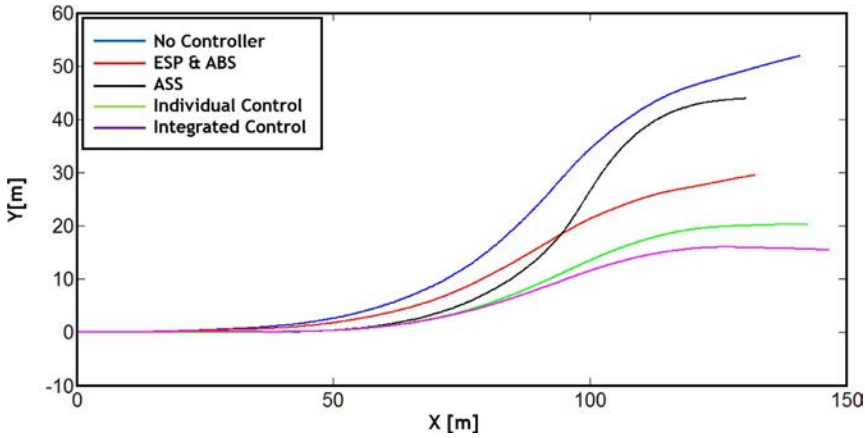

Fig. 1.30 The path traveled by the vehicle in the integration test.

conditions, the emphasis is on handling; hence, the quality of ride comfort decreases.

Given the quantities used, the tested vehicle is understeered. Fig. 1.30 shows the understeer characteristic of the vehicle, especially under critical test conditions. The uncontrolled vehicle and the understeered vehicle with the ASS controller show the most understeered states. Even using ESP and ABS alone could not improve vehicle understeer. Using individual controllers has improved conditions because the vertical wheel forces change when the ride comfort is improved. Finally, using integrated control has led to the

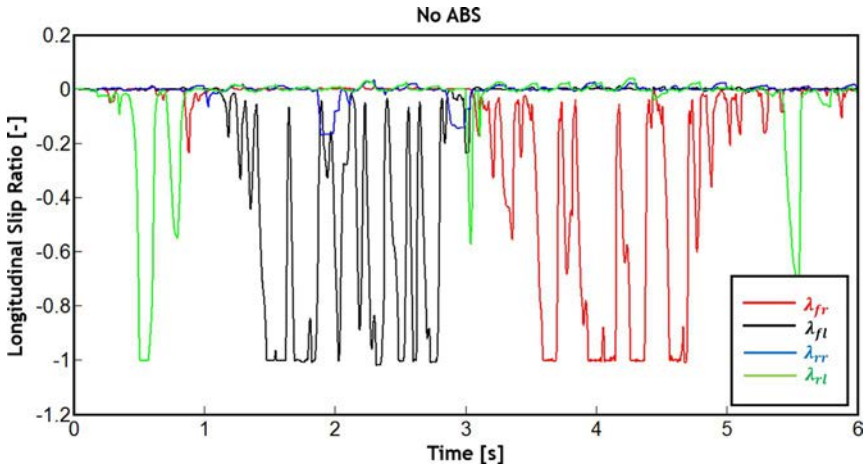

Fig. 1.31 Longitudinal slip ratio of the vehicle in the handling test without ABS.

best handling state. In the following, the slip ratio of the wheels has been drawn versus time. As mentioned before, the tested vehicle is understeered; thus, the EPS system will apply the braking force on the front wheels. For this purpose, the left or right wheel will be selected according to the input steering angle. The graphs obtained for the longitudinal slip ratio confirm this fact.

Fig. 1.31 displays the wheels' slip ratio for when the ESP is active, but the ABS does not control the slip ratio. It is seen that the longitudinal slip ratio of the front wheels repeatedly becomes equal to -1, which is a 100% slip. This can oversteer the vehicle up to critical limits. In other words, the ESP system can make conditions more critical if it does not consider the longitudinal slip ratio. In Fig. 1.32, the handling control system consists of the active ESP and ABS systems. As seen in the figure, the ABS control system has control of the longitudinal slip ratio to an adequate extent. Two points can be mentioned in this figure. First, the slip in wheels without braking is still uncontrollable. Second, despite ABS's presence, the longitudinal slip ratio even exceeds the desired limit at some points. Finally, as shown in Fig. 1.32, the systems' integrated control provides the best conditions for the longitudinal slip ratio, such that the longitudinal slip ratio has decreased even in wheels without braking. In Fig. 1.33, integrated control provides the best conditions for the longitudinal slip ratio; even in wheels without braking, the longitudinal slip ratio is reduced.

Figs. 1.34 and 1.35 display the lateral forces' real and estimated values for the front and rear wheels. Because the estimator has been designed based on

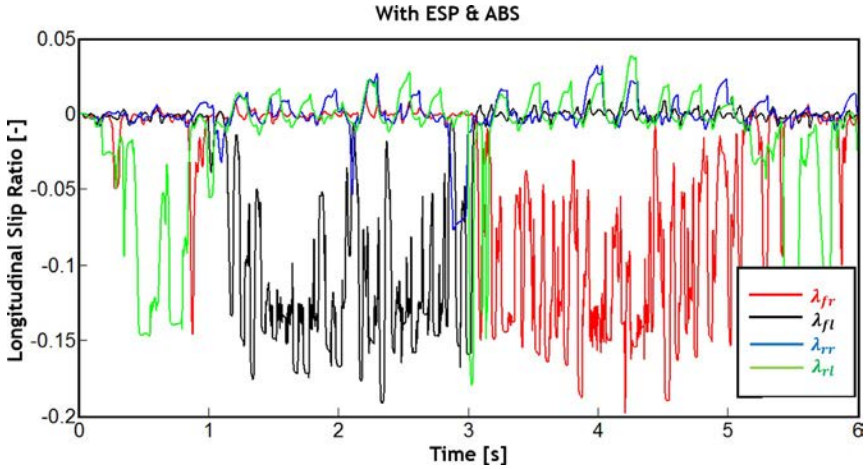

Fig. 1.32 Longitudinal slip ratio of the vehicle in the presence of ESP and ABS alone.

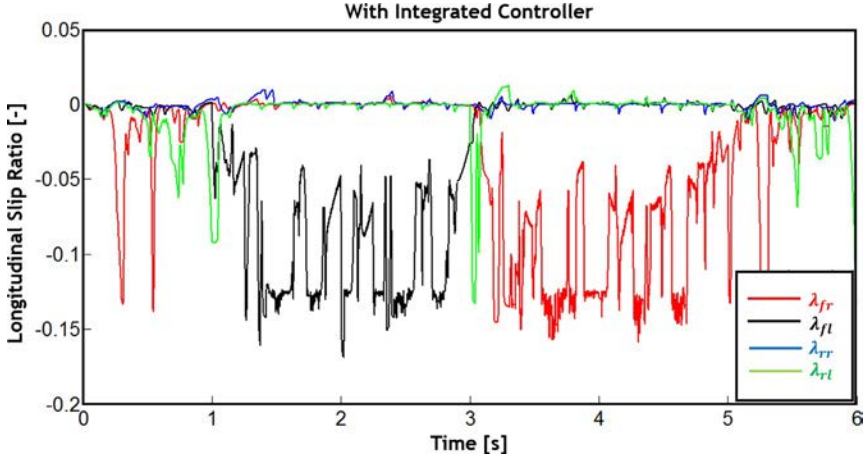

Fig. 1.33 Longitudinal slip ratio of the vehicle in the integration test.

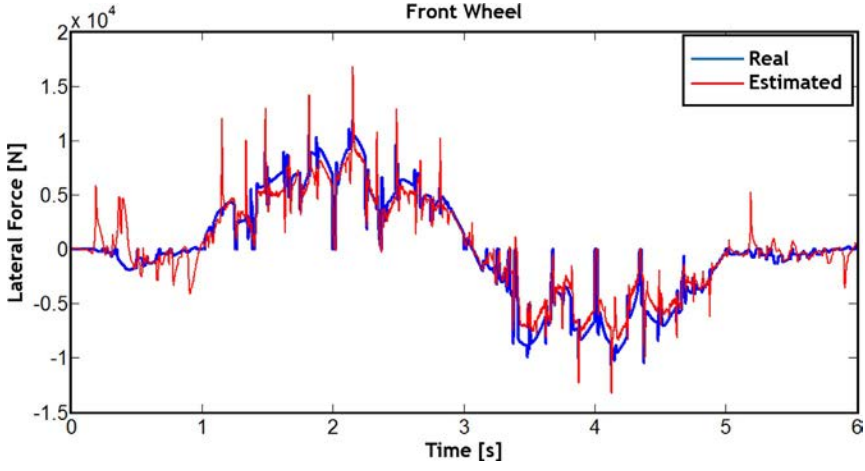

Fig. 1.34 Sum of the lateral forces exerted on the front wheels in the integration test.

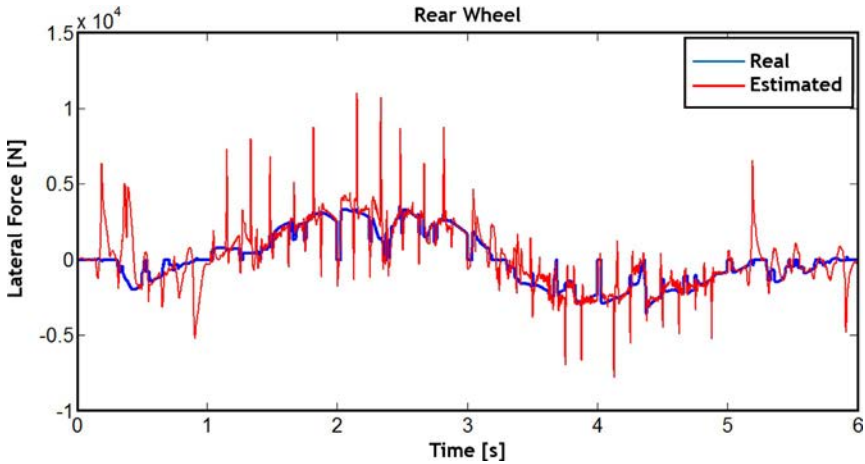

Fig. 1.35 Sum of the lateral forces exerted on the rear wheels in the integration test.

the bicycle model, its output is the sum of the front wheels' lateral forces and the lateral forces of the rear wheels.

1.5 Conclusion

It can be seen from the results that, given that the tested vehicle was understeered, using the ESP system has increased its handling and has improved its lateral velocity and yaw rate. The active suspension system was designed to enhance ride comfort. In the end, the controlled systems used were compared in individual and integrated forms. An improvement in lateral acceleration was observed, which has a desirable effect on the vehicle's other outputs, including the lateral slip angle, lateral velocity, and yaw rate of the vehicle.

References

[1] Aloysius J. (Alois) Seewald," Integrated vehicle control system technology steering, braking, suspension, and powertrain systems", Technol. Rev. J. — Millennium Issue Fall/Winter (2000) 79–88.

[2] E.S. Öztürk, L. Güvenç, T. Yiğit, B.A. Güvenç, Application of combined steering and individual wheel braking actuated yaw stability control to a realistic vehicle model, in: Intelligent Vehicles Symposium, 2003, pp. 288–293.

[3] T.D. Gillespie, Fundamentals of Vehicle Dynamics, Society of Automotive Engineers, 1992.

[4] C. Changbao, W. Chen, Integrated design of vehicle suspension and braking systems based on layered coordinated control (LCC) strategy, in: SAE International World Congress, Detroit, no. 2008-01-1152, Apr. 2008.
[5] K.J. Astrom, B. Wittenmark, Adaptive Control, second ed., Addison-Wesley, Canada, 1995.
[6] M. Bayani, R. Kazemi, S. Azadi, n.d."Vehicle stabilization via a self-tuning optimal controller", Amirkabir J. Sci. Technol. (2011) 33–41.
[7] R. Rajamani, Vehicle Dynamics and Control, Springer, New York, NY, 2006.
[8] J.Y. Wong, Theory of Ground Vehicles, John Wiley & Sons, 2008.
[9] M. Shabani, Integrated Vehicle Dynamic & Suspension Control Systems for a Passenger Car, Master Thesis in Mechanical engineering, K.N.Toosi University of technology, 2011 (In Persian).

CHAPTER 2

Vehicle dynamics control using a flexible body model

2.1 Introduction

The dynamics responses of a vehicle are defined based on the forces applied to the vehicle. These responses are studied in the dynamics of vehicles and their components to determine what forces are generated by each of these sources in a given maneuver or how the vehicle responds to these forces. For this reason, it is necessary to develop an accurate and suitable model for simulating the systems and principles used in describing the motion. The collection of all vehicle motions; the relationship between these motions and accelerating, braking, aerodynamic effects, and steering angle; and the influence of forces and moments on the vehicle responses make up the kinematics and dynamics of vehicles. In vehicle dynamics, some of the vehicle's motions and degrees of freedom (DOFs) become more important based on the desired response parameters and the type and accuracy of the analysis. After the significant motions and DOFs are determined, the vehicle is modeled accordingly, and the vehicle equations are derived according to the considered model.

There are various vehicle models, including 1-DOF one-fourth vehicle models (used to analyze ride comfort), 2-DOF bicycle vehicle models (used to analyze handling), and several-hundred-DOF models created in vehicle analysis software. In full vehicle dynamics models generated in software such as MSC ADAMS, the vehicle body is conventionally assumed to be rigid. For the vehicle model to replicate real-world behavior more accurately, one can model the vehicle body as flexible. In this case, the vehicle body's flexibility effects will be added as DOFs to the dynamics model.

2.2 Vehicle dynamics control

Vehicle stability control systems are usually equipped with the following sensors:

- Longitudinal acceleration sensor.
- Lateral acceleration sensor.

Vehicle Dynamics and Control
https://doi.org/10.1016/B978-0-323-85659-1.00005-7

- Yaw rate sensor.
- Steering wheel angle sensor.
- Wheel speed sensor.

The vehicle dynamics control system automatically maintains vehicle equilibrium within the physical and motion ranges of the vehicle. However, when the boundaries of these ranges are reached, when the control system cannot maintain the vehicle stability under existing conditions, the driver is warned via blinkers that the vehicle dynamics control system has been deactivated or is no longer able to keep the vehicle equilibrium.

Generally, using vehicle stability control systems has the following advantages [1]:

- Vehicle motion correction according to the path desired by the driver.
- Reduction of lateral and longitudinal slip hazards.
- Increase in vehicle stability during severe maneuvers and motion on slippery roads.
- Possibility of readily converting the antilock brake system (ABS) to a dynamic control system.
- Improvement in handling during critical conditions.
- Better performance during braking in turns and on slippery roads compared to ABS.

During recent years, models with higher DOFs have seen wider use due to advances in software and modeling capability [2]. To design more efficient controllers, one must use dynamics models that mimic actual vehicle behavior. Therefore, nonlinear models with high DOFs must be used to improve accuracy. For this purpose, the ADAMS/CAR module within MSC ADAMS software can be used for modeling.

2.2.1 Full vehicle dynamics model

In this chapter, an attempt has been made to present a full vehicle dynamics model in ADAMS software to investigate vehicle dynamics, given the importance of modeling and simulation. In addition to a large number of DOFs, the model must include a flexible body.

To this end, first, the finite element (FE) model of the vehicle body is created in HYPER-MESH software, and then this model is used in ADAMS software (ADAMS/CAR module) via the NASTRAN solver and the ADAMS/FLEX module. A linearized 2-DOF dynamics vehicle model has been utilized to design the controller.

2.2.1.1 Full vehicle dynamics model in ADAMS software

Virtual models of the SEDAN vehicle have been used in ADAMS/CAR software to examine their dynamics behavior. The performances of these two virtual models, which are created by combining accurate mathematical models of chassis subsystems, engine transmission train subsystems, steering subsystems, controllers, and bodies, can be simulated on a virtual test road or a virtual laboratory. Various analytical models are used to study vehicle dynamics performance. Numerous simplifying assumptions have been used in these analytical models, resulting in a lack of ability to represent the vehicle's actual behavior and its significant parameters. The major shortcomings of these models include ignoring the suspension, steering, transmission, and engine subsystems.

Here, we will understand the necessity of using ADAMS/CAR software for accurately modeling the vehicle. Various elements, such as springs and dampers, tire stiffness, bushing, joint stiffness, positions of the components, and the type of suspension system, affect the vehicle's vibration behavior. Therefore, to better understand the vehicle dynamics behavior, a better and more sophisticated model in which springs, dampers, bushings, and joint positions have been considered must be employed. ADAMS software has become a powerful tool for modeling vehicle behavior due to its capability of creating nonlinear models for springs, dampers, bushings, and tires. Besides, this software can represent the effect of the type of suspension mechanism, which is a function of the joint locations and suspension joints in the vehicle's behavior. In addition to the mentioned capabilities, this software can communicate with other software to employ their abilities to improve model behavior. For example, by connecting FE software such as IDEAS, NASTRAN, and ANSYS to this software, one can create a flexible model and import it into ADAMS. Another capability of this software is its ability to connect with control software such as MATLAB.

First, the sample vehicle is selected as the reference vehicle. The full model is then built using the reference vehicle data in ADAMS/CAR software, which is the most powerful software in this field. Because debugging and evaluating a large model is very difficult, the vehicle is first divided into several subsystems built in ADAMS/CAR software. Then, each of these subsystems is checked using the analyses in ADAMS software. After these steps and validation of the subsystems, they must be connected. This is performed by defining connectors. Connectors are, in fact, the interactions

between two secondary systems. After completing the sample vehicle's full model, several special analyses are performed on the model, and the analysis results are compared to the effects of actual tests performed on the sample vehicle. If the results are not in agreement, some secondary system parameters are modified to produce an agreement. If the process of creating this agreement is successful, the model is validated. Otherwise, the model is incorrect and requires general modifications.

The overall modeling procedure is as follows:

- Dividing the vehicle into subsystems (front suspension system, rear suspension system, steering system, brake system, tire, and body).
- Accessing subsystem data (component geometry, bushings, tire, dampers, masses, and moments of inertia).
- Subsystem modeling.
- Validating the subsystems via analysis.
- Building the full model by combining the subsystems.
- Comparing the model with the vehicle test.
- Performing necessary modifications to improve model accuracy.
- Confirming the model.

In order to model the vehicle in ADAMS/CAR software, the vehicle must first be divided into its constituent subsystems. Then, these subsystems are modeled in various modules of ADAMS and carefully examined. The subsystems and the modules used for modeling them are shown in Table 2.1.

It must be noted that other than the modules mentioned above, there are other modules and software used in the modeling process. For example, because ADAMS/CAR cannot create flexible objects, MSC NASTRAN software and the ADAMS/Flex module are used instead for this purpose.

Table 2.1 Modules used in the modeling.

Subsystem	Module used in the modeling
Front suspension system set	ADAMS/CAR
Rear suspension system set	ADAMS/CAR
Brake system set	ADAMS/CAR-ADAMS/VIEW
Steering system set	ADAMS/CAR
Transmission system set	ADAMS/CAR-ADAMS/VIEW
Body set	ADAMS/CAR
Tire set	ADAMS/CAR-ADAMS/VIEW

To create the sets, their TEMPLATE must be built first. Each TEMPLATE is a parametric expression of a subset in which the parameters are editable inside the subset. Hence, the modeling procedure can be divided into TEMPLATE creation, subset creation, and subset assembly.

2.2.1.2 Full SEDAN vehicle model

The vehicle used in this section is a medium-sized SEDAN weighing approximately 1000 kg. This vehicle has a MacPherson suspension system in the front and a torsion beam suspension system in the back. The steering system used in this car is the rack and pinion type. The vehicle engine has four cylinders and produces 68 hp. The vehicle is a front-wheel-drive type and uses a five-gear transmission. The body in the vehicle model has been created in rigid and flexible modes, as explained subsequently.

Full SEDAN vehicle model with rigid a body

According to Table 2.1, the subsystems used in the full vehicle model are the following:

Front suspension system set: The front suspension of the SEDAN vehicle is of the MacPherson type with its schematic model shown in Fig. 2.1.

The front spring in the vehicle is linear, with its stiffness characteristic curve shown in Fig. 2.2.

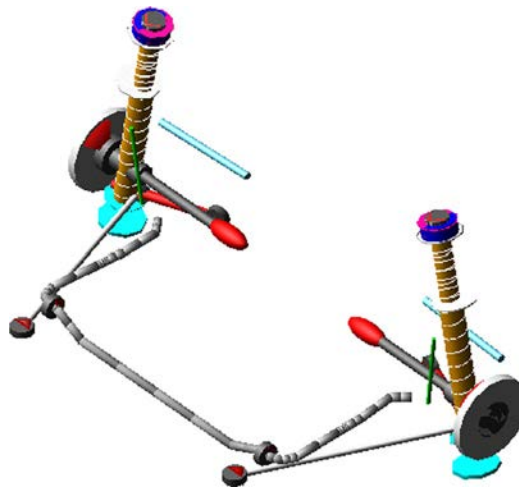

Fig. 2.1 Front suspension set of the SEDAN vehicle.

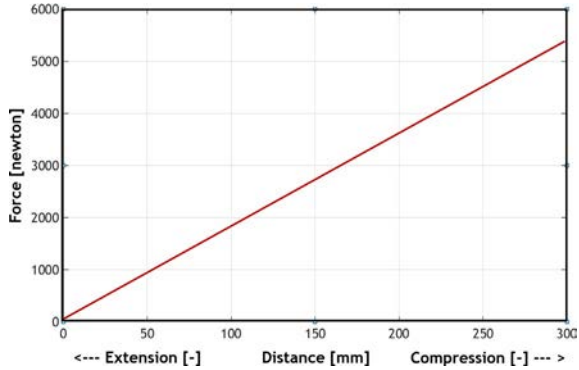

Fig. 2.2 Stiffness coefficient of the front spring of the SEDAN vehicle.

Hardpoints, construction frames, bushings, springs, dampers, shock absorbers, various parts, communicators, etc., have been used to create this TEMPLATE. The vehicle's front dampers are nonlinear, and the corresponding stiffness characteristic curve is shown in Fig. 2.3.

Besides, flexible components in the form of nonlinear rods have been used to model the antiroll bar.

Rear suspension system set: The SEDAN vehicle's rear suspension is a torsion beam suspension system with its schematic model shown in Fig. 2.4.

The rear spring in the vehicle is nonlinear with its stiffness characteristic curve shown in Fig. 2.5. The elements used in this TEMPLATE are almost similar to those used in the front suspension system model. In order to model the flexible torsion beam, first, the geometry was meshed in the I-DEAS finite element software, and the material properties and element type of the beam were defined. Then, this model was converted to the model-neutral

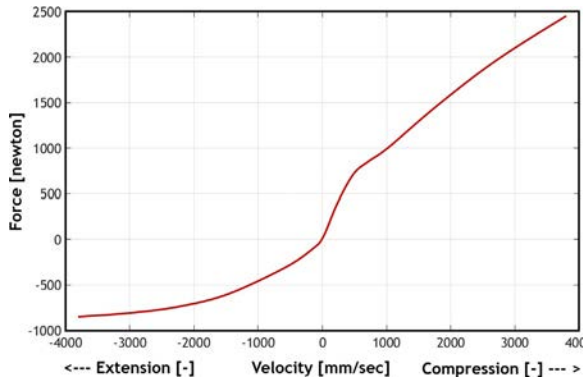

Fig. 2.3 The characteristic curve of the front damper of the SEDAN vehicle.

Fig. 2.4 Rear suspension set of the SEDAN vehicle.

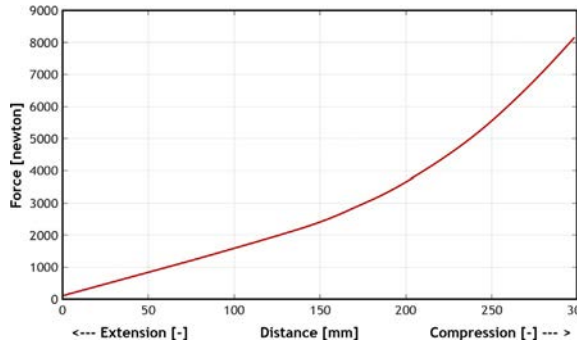

Fig. 2.5 The characteristic curve of the rear spring of the SEDAN vehicle.

format (MNF) using the options in I-DEAS software because the finite element model of a flexible object must be converted to this format so that it can be modeled in ADAMS software.

The vehicle's rear dampers are nonlinear, and the corresponding stiffness characteristic curve is shown in Fig. 2.6.

Brake system set: The brake system has been modeled as a disc brake for each of the four wheels. The brake torque, the control input of the vehicle dynamics control system, is applied to the wheel disc via a caliper.

Steering system set: The steering system is the rack and pinion type with the schematic displayed in Fig. 2.7. In this TEMPLATE, hardpoints, construction frames, bushings, communicators, etc., have been used. In this model, too, splines have been used to model the bushings' characteristic curve accurately.

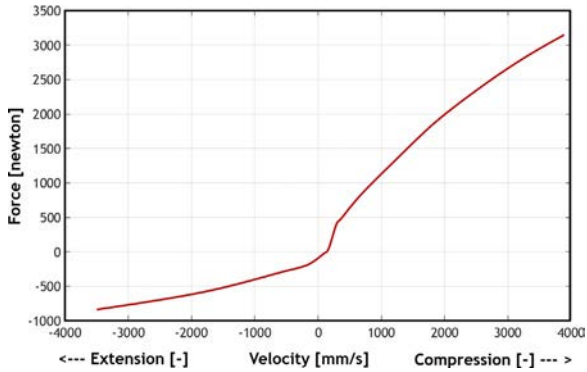

Fig. 2.6 The characteristic curve of the rear damper of the SEDAN vehicle.

Fig. 2.7 Steering system set of the SEDAN vehicle.

Transmission system set: The transmission set was modeled in the ADAMS/DRIVELINE module and was then transferred to the ADAMS/CAR environment where it was connected to the body at three points via communicators and bushings.

Body: In order to model the body in the rigid mode, concentrated masses have been used, and the body has been attached to them in the form of a shell. This is the standard method of modeling the body in ADAMS/CAR software. The schematic of the body model is shown in Fig. 2.8.

Tires: It is possible to create tires using different mathematical models in the ADAMS/TIRE module. In this model, the *Fiala* [3] tire model has been utilized to model the tire. This model has then been finalized in the ADAMS/CAR environment to be connected to the front and rear suspension via communicators.

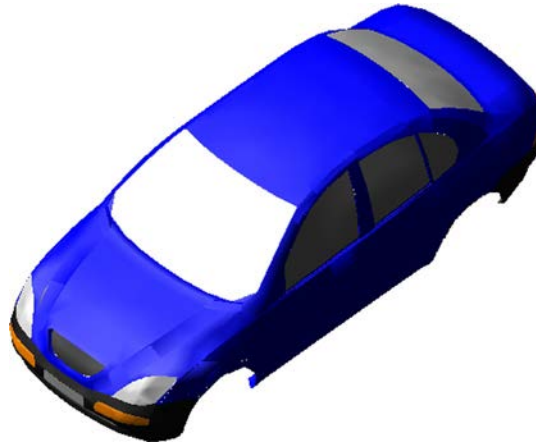

Fig. 2.8 The rigid body of the SEDAN vehicle.

The full model of the SEDAN vehicle with a flexible body

The full vehicle model has been created in this mode with a flexible body. The body in white (BIW) model converted into MNF has been used to model the vehicle body. ADAMS software is unable to create a flexible object capable of vibrating. In other words, only rigid bodies can be made in ADAMS software. However, it is possible to create flexible items with simple geometries in ADAMS software using its tools. For example, one can directly create a flexible beam with a circular or rectangular cross-section inside the ADAMS environment. However, to create a flexible object with complex geometry such as a vehicle body, the torsion beam of the rear suspension, or other vehicle components, they must be first modeled in a finite element software package such as ALTAIR HYPER MESH. Then, specific actions must be taken to convert the model data into the MNF format, after which the MNF finite element model can be imported to the ADAMS software.

The MNF file includes the following data:

- Model geometry (node locations and connections).
- Masses and moments of inertia of the nodes and elements.
- Natural frequencies and mode shapes of the finite element model.
- General mass and stiffness matrices for each mode shape.

However, it must be noted that the MNF file not only contains data relating to the mode shape and natural frequency but also can contain data relating to the stress and strain computed from the static analysis or fatigue analysis performed in the finite element software. The latter MNF-converted file is used

in the ADAMS/DURABILITY environment. The BIW finite element model comprises 128 separate parts meshed using shell elements and connected using rigid connection elements. This model consists of 149,076 quadrilateral and triangular shell elements and 3879 rigid connection elements of the RBE2 type, with a total BIW mass of 228 kg.

After the finite element model is converted to MNF and analyzed using MSC.NASTRAN, a *.out file is generated, which is converted to MNF using ADAMS/FLEX to be used in the ADAMS/CAR environment. Eventually, the vehicle body model is generated as a combination of flexible BIW and the sum of the vehicle body components' masses. The vehicle body model is shown in the flexible form in Fig. 2.9.

It is worth mentioning that the first 36 frequency modes of the body, up to 51 Hz, are selected given the type of dynamics analysis performed on the vehicle, which is the handling analysis; see Table 2.2 (Figs. 2.10 and 2.11). Fig. 2.12 represents the normal modes of the body and the corresponding natural frequency. It must be noted that the first six modes correspond to the free movement of the body with zero frequencies.

2.2.1.3 Fully assembled model of the SEDAN vehicle

After the vehicle subsystems are created in the ADAMS/CAR environment, they are combined to generate the vehicle's fully assembled model (Fig. 2.13). Based on the obtained final model, one can perform the handling analyses of the vehicle.

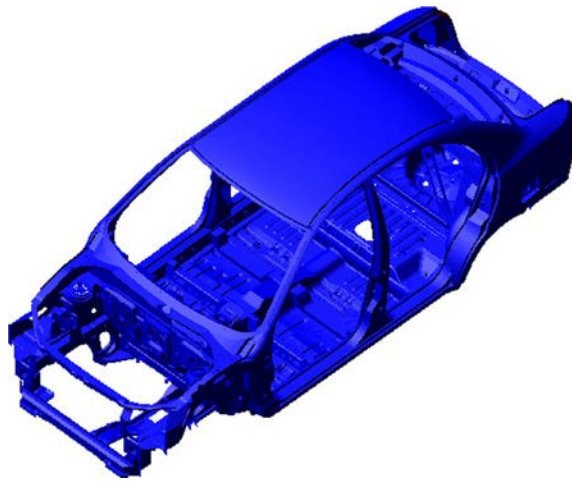

Fig. 2.9 The flexible body of the SEDAN vehicle.

Table 2.2 Vehicle body's flexible natural modes.

Mode	Shape mode	Frequency (Hz)
7	Spare tire mount local bending	14.1
8	First body global torsion	18.1
9	Floor local torsion	18.2
10	Floor local bending	18.7
11	First body global bending	20.7
12	Body front half torsion	21.1
13	Body rear half torsion	23.5
14	First rear-end bending	24.4
15	First front-end bending	28.0
16	Second body global bending	31.9
17	Second body global bending	33.8
18	First front-end local bending	34.3
19	First rear-seat support bending	34.4
20	Third body global torsion	36.5
21	Second rear-end bending	37.7
22	Second front-end bending	40.2
23	Second rear-seat support bending	41.5
24	Third rear-seat support bending	42.9
25	Third body local bending	43.6
26	Front end local torsion	44.7
27	Second front-end local bending	45.1
28	First rear-end local torsion	46.1
29	Second rear-end local torsion	47.0
30	Third rear-end local torsion	47.2
31	First rear right quarter panel bending	48.4
32	Second rear right quarter panel bending	49.1
33	Third rear right quarter panel bending	49.2
34	Fourth rear right quarter panel bending	49.6
35	Rear left lamp support bending	49.8
36	Roof local bending	51.9

The values determined for the primary vehicle parameters are shown in Table 2.3.

2.2.2 Vehicle dynamics control using the ADAMS/CONTROL module

One of the MSC ADAMS software modules is the ADAMS/CONTROL module, which can be used to apply a control variable to the dynamics model in the software and provide to the controller the state variable from the dynamics model. In fact, after creating a full dynamics model as the plant

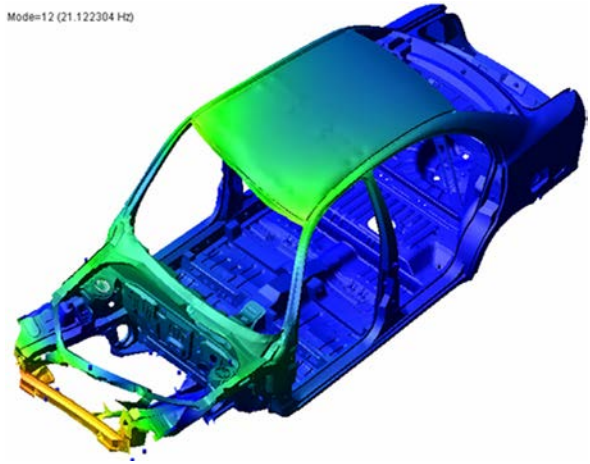

Fig. 2.10 The sixth vehicle body's flexible natural frequency at body front half torsion mode.

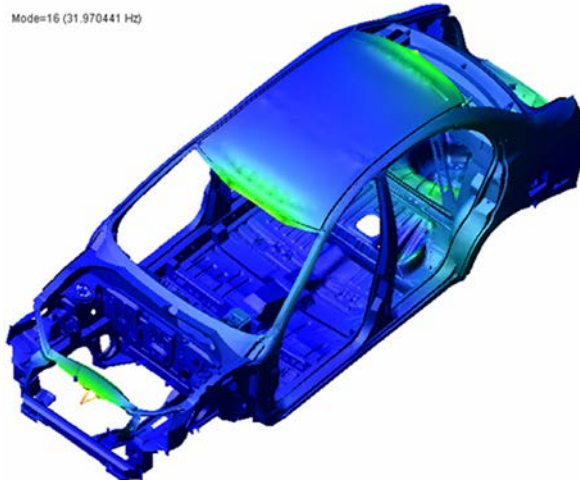

Fig. 2.11 The 10th vehicle body's flexible natural frequency at second body global bending mode.

in the ADAMS/CAR or ADAMS/VIEW environment using the corresponding module, one can apply the designed controller to the model in an online manner, as shown in Fig. 2.14.

The ADAMS/CONTROL module provides online communication between ADAMS as the dynamics modeling software and software packages such as MATLAB, MATRIX X, and MSC EASY5 as the control software.

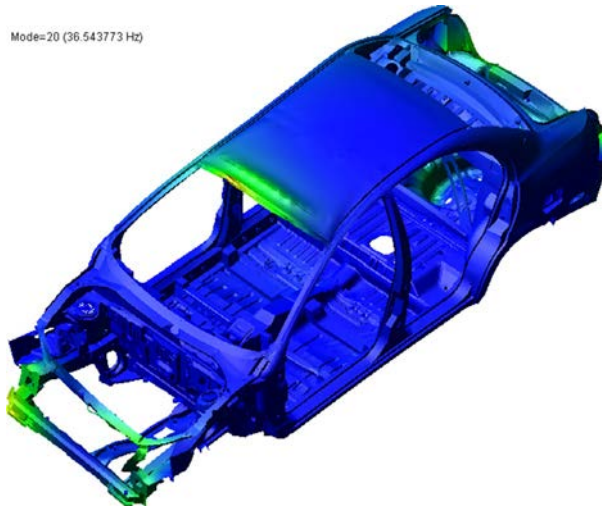

Fig. 2.12 The 14th vehicle body's flexible natural frequency at third body global torsion mode.

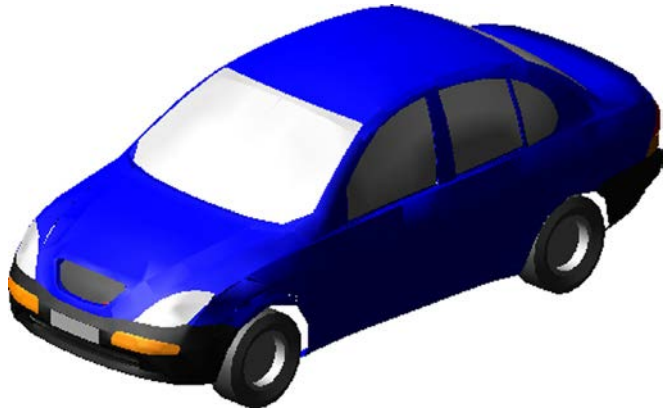

Fig. 2.13 The full model of the SEDAN vehicle in the ADAMS/CAR environment.

Table 2.3 Main vehicle parameters.

Parameter	SEDAN vehicle dynamics model	Unit
m	1000	kg
I_z	$1.5e^9$	kg mm^2
J_w	$4.8e^5$	kg mm^2
l_1	1007	mm
l_2	1403	mm
h	496.6	mm
b_F	1408	mm
b_R	1410	mm

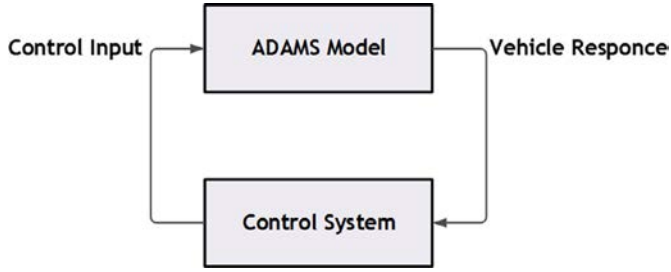

Fig. 2.14 Online communication between the dynamics model and the control system.

Using such a method has the following advantages [4]:

- Use of the dynamics model created in MSC ADAMS software for the control system.
- Application of the control system, no matter how simple or complex, to the dynamics model.
- Possibility of simulating the created set (model and controller) and analyzing the results in the ADAMS environment or the control software environment.

In this chapter, because the vehicle dynamics model has been created in the ADAMS/CAR software and the designed controller has been implemented in the MATLAB software, this section presents the online communication between ADAMS/CAR and MATLAB software.

2.2.2.1 Preparation of the mechanical model

To create a link between the dynamics model and the control system, one needs to provide the controller with the required signals as the output state variables and apply the signal created by the controller as the input state variable to the dynamics model. Thus, it is required to generate the input and output state variables in the dynamics model. The steps are fully explained in the following.

Creating the input state variables

The input state variables must be created according to the number of inputs we would like to apply to the dynamics model, as shown in Fig. 2.15.

As seen in this figure, *F*(time) equals zero. This means that the created state variable takes its value from the controller. Hence, an initial value of zero is recorded for the corresponding variable at each time step so that it is updated via the value determined by the controller. In this chapter,

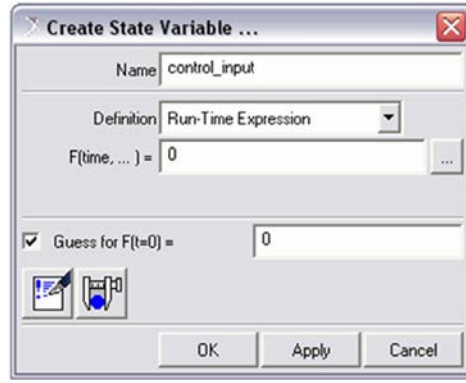

Fig. 2.15 Creating the input state variable.

two control modifications have occurred, namely the direct torque input to the vehicle and the brake torque input to each of the wheels.

Creating the input functions

The created input state variables must be defined at the appropriate locations, mostly in force or displacement. VARVAL-type input functions have been employed for this purpose, as shown in Fig. 2.16.

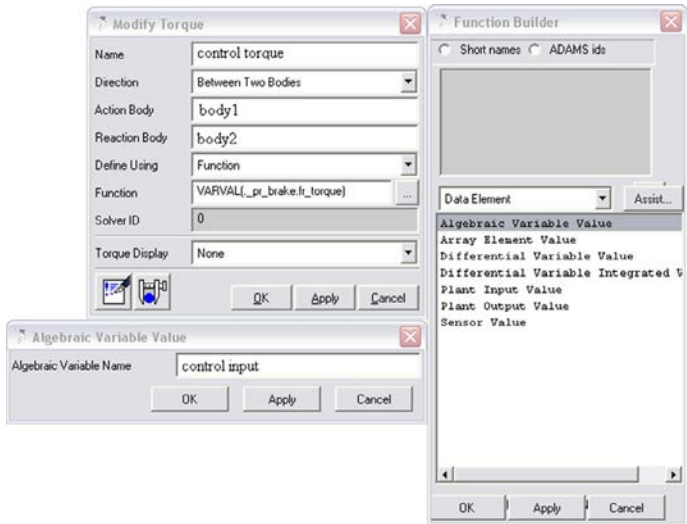

Fig. 2.16 Creating the input functions.

Creating the output state variables and functions

Given the controller's number of outputs, the output state variables must be created in the dynamics model. Accordingly, the outlet variables can be made, as shown in Fig. 2.17.

As seen in Fig. 2.17, the value of *F*(*time*) is no longer zero and is determined by the output function. In other words, the output state variables obtain their values from functions, as shown in Fig. 2.18. With these

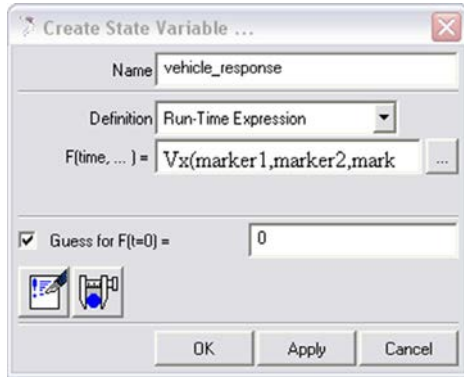

Fig. 2.17 Creating the outlet state variable.

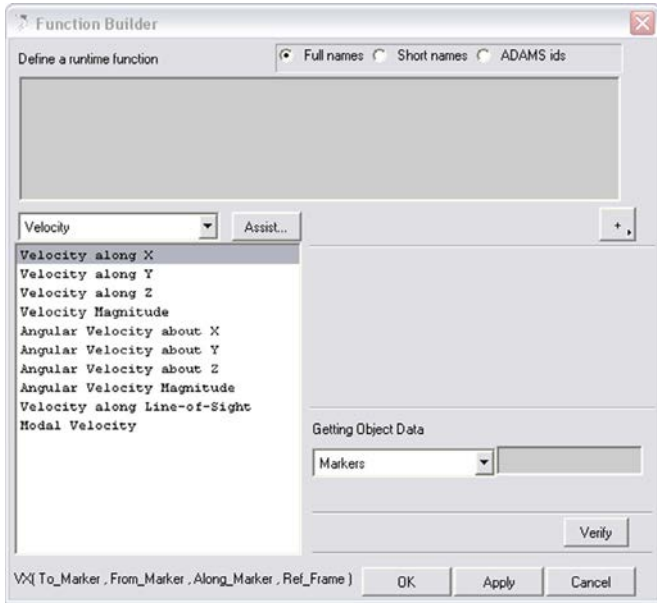

Fig. 2.18 Functions in the function generator.

functions' help, one may assign the displacement, velocity, acceleration, etc., of the model's point to the corresponding state variable. In the present chapter, given the vehicle dynamics control system's performance and the ABS, the longitudinal, lateral, and rotational velocities of the vehicle mass center, the steering angle, and the wheels' angular velocity have been considered the output state variables.

Defining the model inputs and outputs

After the input and output state variables are created, we must define the created variables as model inputs and outputs in another step, as shown in Fig. 2.19.

As seen in Fig. 2.19, plant input and plant output have been defined for the input and output state variables.

2.2.2.2 Creating a link between the dynamics model and the controller

In this section, the ADAMS/CONTROL module will be used to describe how to create a link between the ADAMS and MATLAB software.

Loading the ADAMS/CONTROL module

The first step is loading the ADAMS/CONTROL module in the work environment, namely ADAMS/CAR, as shown in Fig. 2.20.

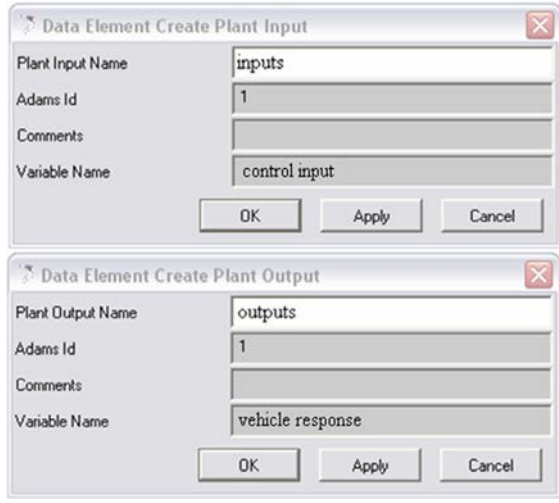

Fig. 2.19 Creating the plant input and plant output.

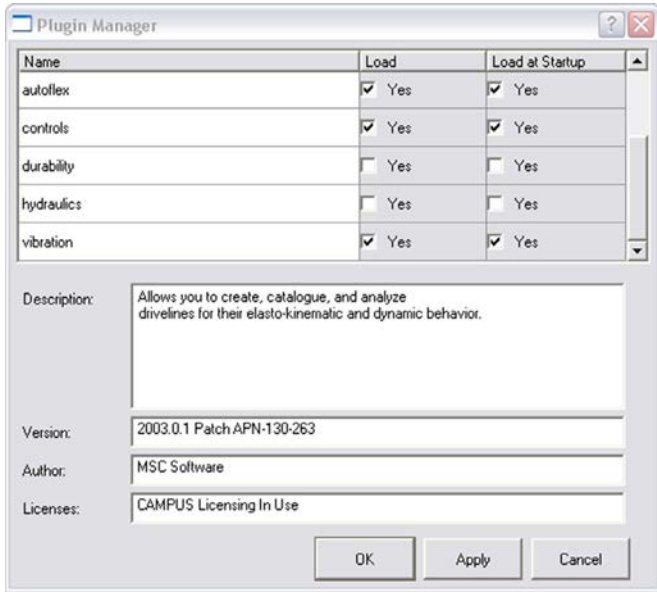

Fig. 2.20 Loading the ADAMS/CONTROL module.

Plant export process

After the loading, the ADAMS/CONTROL module is added to the work environment. By entering this module in the control section, as shown in Fig. 2.21, the following results:

As shown in this figure, in this section, one first applies the Plant Vars defined as inputs and outputs and then determines the control software (MATLAB here). Eventually, one can determine whether the dynamics model provided to the controller is linear or nonlinear.

Importing the model to the control software

After the above steps are completed, one may import the laden dynamics model to MATLAB software to apply control inputs. Depending on the selected analysis type and by choosing the simulation type as Files Only, files with (*.adm), (*.acf), etc., extensions are generated that contain information about the model and analysis type and provide the user with the dynamics model in MATLAB software inside the SIMULINK environment, as shown in Fig. 2.22.

In Fig. 2.22, three types of blocks are generated, which represent the dynamics model created in ADAMS.

- The S-Function block contains the model of the nonlinear dynamics.

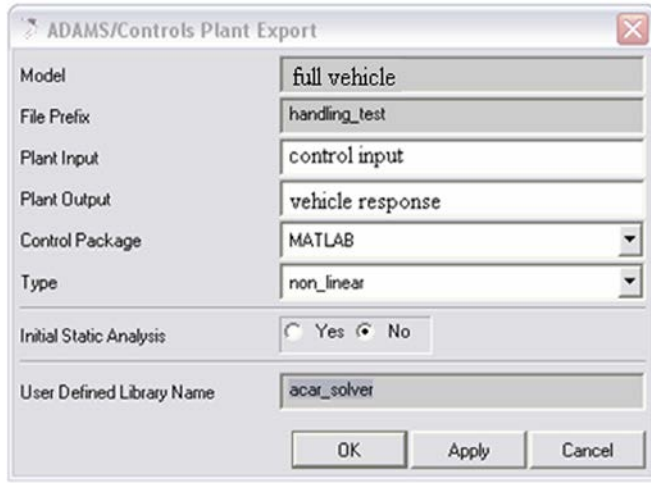

Fig. 2.21 Plant export process.

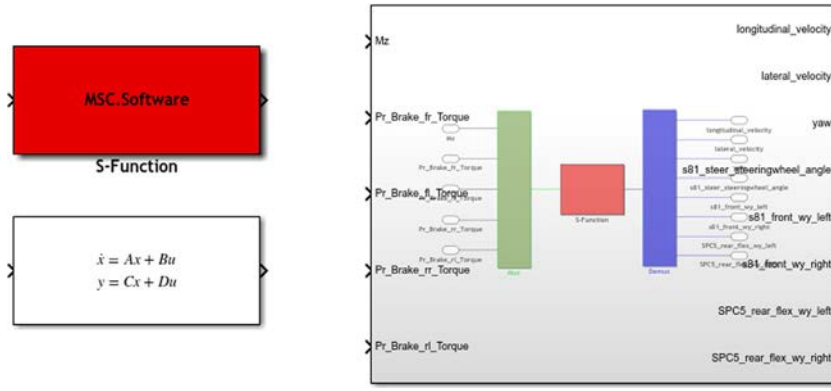

Fig. 2.22 A dynamics model in the SIMULINK environment.

- The ADAMS subblock provides direct access to input and output state variables in addition to containing the S-Function block.
- The State-Space block contains the linear dynamics model.

The second block diagram, namely ADAMS-sub, has been used in this project. After the controller was designed and implemented in the SIMULINK environment, the simulation variables such as the final time, time step, etc., were tuned. Then, by performing analyses in MATLAB's SIMULINK environment using the ADAMS solver at each time step, a control input has been applied to the ADAMS model, and the corresponding effect has been made available online to the controller, as shown in Fig. 2.23.

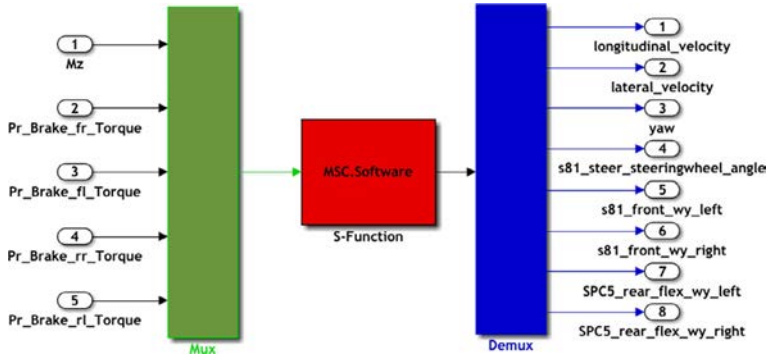

Fig. 2.23 ADAMS-sub block diagram.

As shown in this figure, the control input has been applied to the dynamics model in two forms: a direct moment M_Z about the vertical axis of the vehicle and brake torques exerted on each of the four wheels, which can be activated or deactivated based on the type of controller performance.

- Direct torque around the vertical axis of the vehicle.
- Brake torques on each of the four wheels.

Moreover, the outputs of the dynamics model, namely the longitudinal, lateral, and rotational velocities of the vehicle mass center, steering angle, and rotational velocity of each of the four wheels, are made available to the controller in the form of state variables to be used by the control system.

- The longitudinal velocity of the vehicle center of mass.
- The lateral velocity of the vehicle center of mass.
- The rotational velocity of the vehicle center of mass.
- The steering wheel angle.
- The rotational speed of each of the four wheels.

It should be noted that the next step after completing the full vehicle model in ADAMS software is to ensure the correct behavior of the model; detailed validation results can be provided in [5, 6].

2.3 Optimal control of vehicle dynamics

A vehicle may veer off course when turning. This occurs when the forces created in the tires have reached the adhesion threshold. Although the ABS system can prevent wheel locking during braking and the traction control system prevents wheel-spinning during acceleration, these systems cannot actively control the vehicle's directional behavior.

With an increase in safety requirements, a new type of control system was proposed for controlling vehicle directional behavior. These systems were used to improve the vehicle's stability and its ability to maintain course under different operational conditions. These systems are known as vehicle dynamics control systems or stability control systems.

Different vehicle manufacturers use other names for these systems, and their respective designs might be different. However, the operation principles of these systems are identical: the desired vehicle path is determined from the driver input (steering angle, gas pedal position, braking pressure, etc.) and vehicle behavior (e.g., the angular velocity of the wheels), and the actual vehicle path is specified from the measured variables such as yaw rate, lateral acceleration, longitudinal acceleration, etc., of the vehicle. Then, the desired vehicle path is compared to the actual vehicle path. If a considerable difference exists between them, the vehicle dynamics control system creates a yaw moment by adjusting the brake pressure on the wheels or reducing the traction torque on one of the wheels. As a result, the difference between the desired and actual vehicle paths decreases. Fig. 2.24 displays the operational principles of the vehicle dynamics control system.

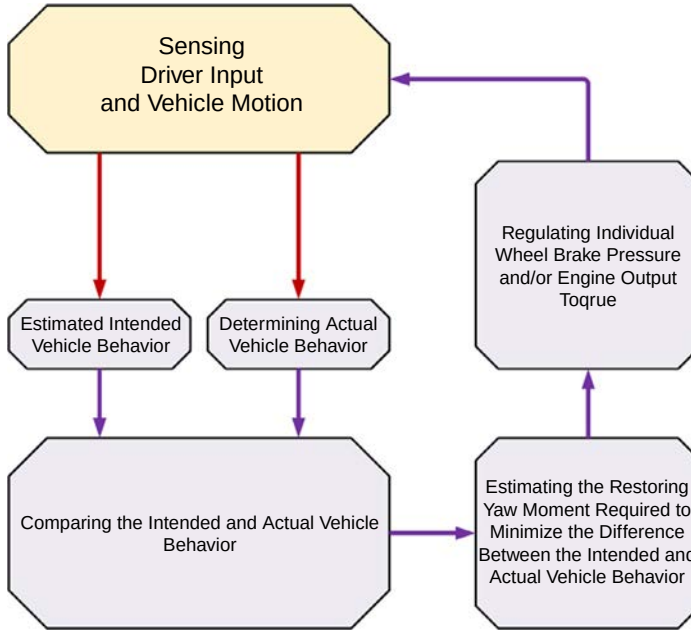

Fig. 2.24 Operational principles of the vehicle dynamics control system.

In many control systems, the vehicle's yaw rate and slip angle are used as the main parameters for determining the vehicle path. Therefore, the control system is designed to control these two parameters. The control system controlling the vehicle's yaw rate can maintain the vehicle's yaw rate and direction within the desired range. Nonetheless, merely controlling the yaw rate does not seem sufficient for keeping the vehicle in the desired path. For example, on slippery roads, controlling the yaw rate and correcting the steering angle can only improve the rotational vehicle behavior about the z-axis; however, the slip angle might vastly increase and veer the vehicle off the desired path, as shown in Fig. 2.25.

1. Steep input at steering wheel.
2. On high friction road.
3. On slippery road with steering correction and yaw rate control.
4. On slippery road with body yaw rate and side slip angle control.

This issue highlights the necessity of simultaneously controlling the yaw rate and the slip angle. Based on these discussions, it has been attempted to define the desired path by specifying variables such as the longitudinal and lateral velocities of the vehicle, yaw rate, angular velocity of each wheel, and steering angle and to design a controller based on this desired path that can bring the vehicle yaw rate close to the desired value and simultaneously reduce the slip angle by consuming optimal energy. The optimal control method has been utilized to design the controller, given the problem's tracking and

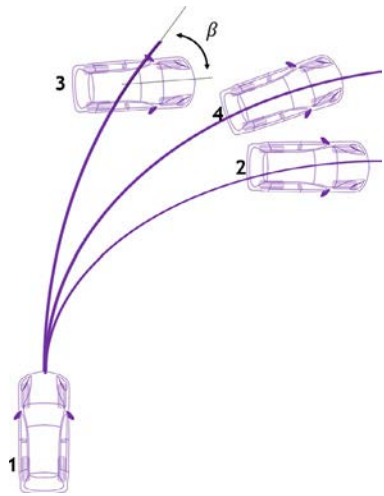

Fig. 2.25 Comparison between the handling behavior of the vehicle in the presence of the yaw rate controller and the presence of yaw rate and slip angle controller.

optimization nature. It must be noted that the effect of the vehicle traction forces has been ignored, and therefore no traction control system has been created. The control torque is created through differential braking, and, hence, only ABS systems are designed for the wheels.

2.3.1 Designing the ABS

The ABS aims to minimize the braking distance while keeping the steerability of the vehicle during braking. The shortest braking distance is obtained when the wheel slip is within the maximum friction coefficient range. In other words, the braking distance decreases when the maximum braking force is applied to the wheels. The control torque M_Z is created in the designed vehicle dynamics control system. This control torque results from brake forces generated in the tires.

In order to apply the control torque accurately to the vehicle, it is required to have a correct understanding of tire dynamics. Moreover, the brake torque exerted on the tire must be such that the tire brake force's full capacity is used. If we call the vehicle stability control and the determined control torque the upper controller layer, the lower layer will adjust the longitudinal tire slip to exert the tire's largest longitudinal brake force. According to the free-body diagram of the wheel presented in Fig. 2.26, one can write (2.1);

$$J_\omega \dot{\omega} = T_{Drive} - T_{Brake} - T_{Roll} + r_{eff} F_X \tag{2.1}$$

where

J_ω: wheel moment of inertia
$\dot{\omega}$: angular acceleration
T_{Brake}: braking torque
T_{Roll}: rolling resistance torque

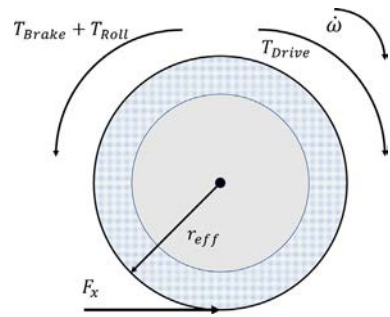

Fig. 2.26 Wheel free-body diagram.

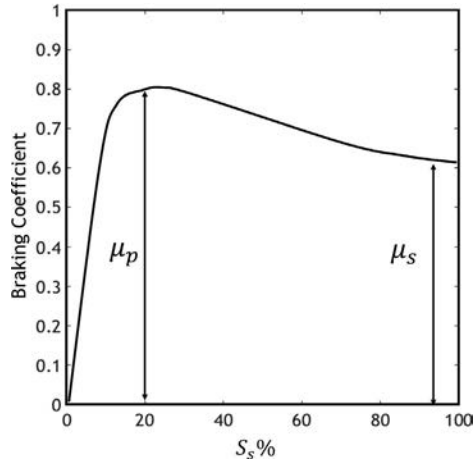

Fig. 2.27 Changes in the braking coefficient with slip [7].

r_{eff}: effective wheel radius

F_X: longitudinal force.

Given the above relationship, the brake torque required for each wheel is determined. This braking torque must be corrected by the ABS regulator to be exerted on the wheel in the next step. The friction coefficient (braking coefficient) is proportional to the wheel slip, as shown in Fig. 2.27. In the presented figure, the coefficients μ_s and μ_p, respectively, represent the brake force coefficient corresponding to the full slip of the wheel and the brake force coefficients corresponding to a 20% slip for a dry road. Therefore, the ideal state for exerting the highest braking coefficient is keeping the wheel slip in the range μ_p. The slip corresponding to this coefficient is very unstable because the value of μ reduces strongly with a slight increase in the slip.

On the other hand, other factors affect the changes in μ [7]:

Road surface: The effect of the road surface on the braking coefficient is shown in Fig. 2.28. As seen in this figure, the higher the slip percentage (from a dry road to a wet road), the lower the braking coefficient.

Velocity: The effect of velocity on the braking coefficient on an asphalt road is shown in Fig. 2.29. As seen in the figure, the braking coefficient drops with an increase in the velocity.

Tire pressure and normal tire load: The effect of the normal tire load on the braking coefficient on an asphalt road is shown in Fig. 2.30. According to this figure, a higher braking coefficient results from an increase in the normal tire load.

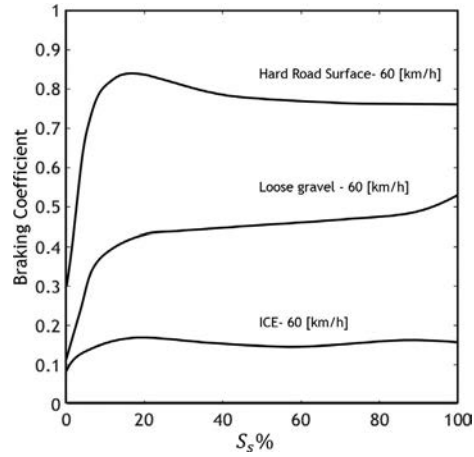

Fig. 2.28 Effect of the road surface on the braking coefficient [8].

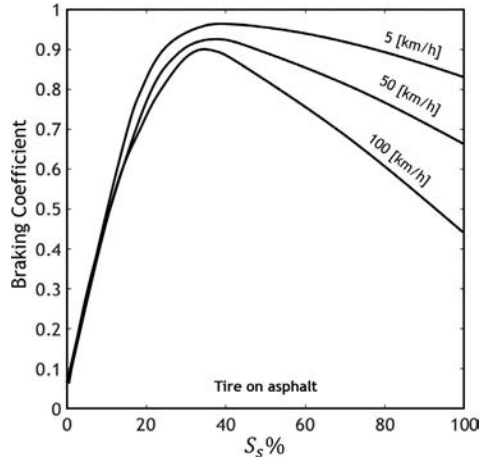

Fig. 2.29 Effect of velocity on the braking coefficient [8].

Given the above factors, a slip of 12% is selected as the desired wheel slip. The ABS works as follows: the longitudinal slip of the wheel is computed at every instant based on the longitudinal slip estimation methods presented in the modeling section. If the slip is smaller than the desired slip, the brake torque determined by the dynamics control system is exerted on the wheel. However, if the slip exceeds the desired value, the regulator designed for the ABS controls the wheel slip by removing the brake torque from the current wheel and exerting it on the wheel, which creates a torque in the same direction as the required control torque.

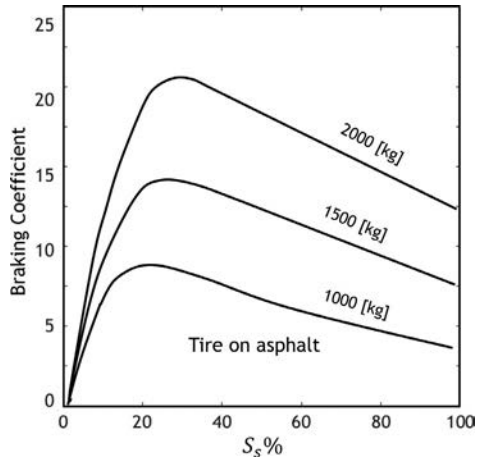

Fig. 2.30 Effect of normal tire load on the braking force [8].

It must be noted that the lateral slip of the tire is also essential, given the friction circle and the limitation on the total friction coefficient, which is divided into lateral and longitudinal directions. Fig. 2.31 displays the changes in the friction coefficient versus longitudinal and lateral slips. Because the vehicle dynamics control system has controlled the lateral slip of the vehicle and maintained its value at about 5 degrees, one can claim that adjusting the tire's longitudinal slip within the mentioned range will provide the wheel's braking coefficient.

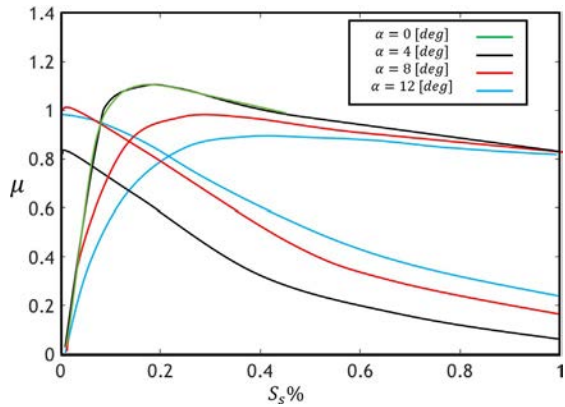

Fig. 2.31 Changes in the longitudinal and lateral friction coefficients versus longitudinal and lateral slip [8].

The optimal control method is designed based on the linearized 2-DOF dynamics model of the vehicle, and the method of linear quadratic regulators has been employed to implement this controller.

2.3.2 Designing the vehicle dynamics control system using brake torque

The governing equations of the 2-DOF model according to Fig. 2.32, considering M_Z in the state-space, are as (2.2):

$$\dot{X} = AX + BU + E\delta_W \tag{2.2}$$

The state vector based on the degrees of freedom of the system ($v \equiv$ lateral velocity and $r \equiv$ yaw rate) is as (2.3):

$$X = [v \; r]^T \tag{2.3}$$

The control input is the torque M_z, which is exerted about the vertical axis of the vehicle (2.4):

$$U = M_z \tag{2.4}$$

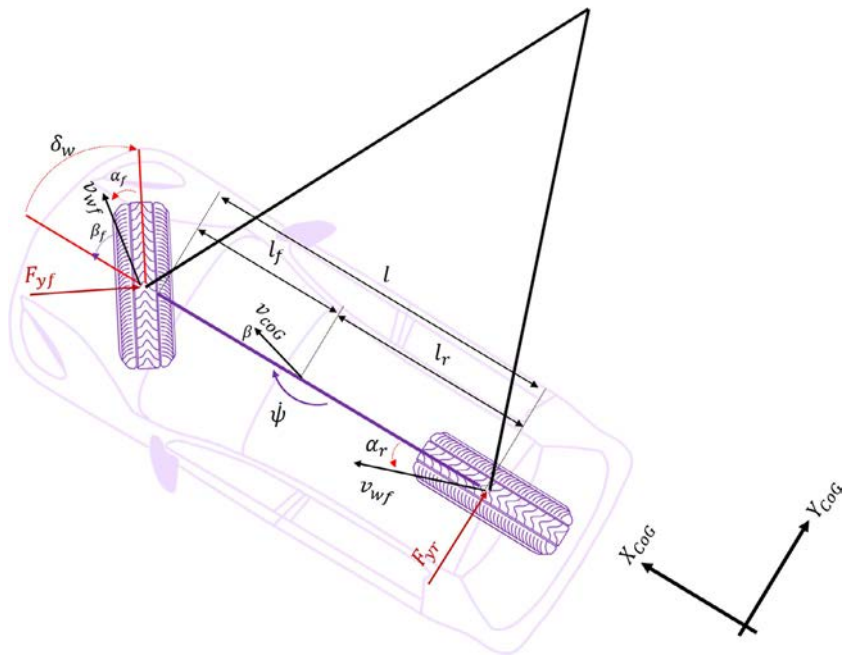

Fig. 2.32 Vehicle 2 DOF schematic.

Moreover, the front steering angle δ_W acts on the system as external excitation. Based on the equations governing the 2-DOF model, which were presented in Fig. 2.32, the matrices A, B, and E are as (2.5)–(2.7):

$$A = \begin{bmatrix} -2\dfrac{C_{\alpha r} + C_{\alpha f}}{mV_x} & +2\dfrac{l_2 C_{\alpha r} - l_1 C_{\alpha f}}{mV_x} \\ -2\dfrac{l_2 C_{\alpha r} - l_1 C_{\alpha f}}{I_z V_x} & -2\dfrac{{l_2}^2 C_{\alpha r} + {l_1}^2 C_{\alpha f}}{mV_x} \end{bmatrix} \tag{2.5}$$

$$B = \begin{bmatrix} 0 & \dfrac{1}{I_z} \end{bmatrix}^T \tag{2.6}$$

$$E = \begin{bmatrix} 2\dfrac{C_{\alpha r}}{m} & 2\dfrac{l_1 C_{\alpha r}}{I_z} \end{bmatrix} \tag{2.7}$$

where $C_{\alpha f}$ and $C_{\alpha r}$ are the turning constants of the front and rear tires, respectively.

In this optimal control problem, the objective is to optimize the following performance criterion, in which X_d is the desired state vector or path, (2.8):

$$\begin{cases} e = X - X_d \\ J = \dfrac{1}{2}\displaystyle\int_{t_0}^{t} f\left[e^T Q e + U^T R U\right] dt \end{cases} \tag{2.8}$$

The matrices Q and R are selected as the positive semi-definite and positive definite, respectively, [9] as (2.9) and (2.10). Hence:

$$R = [W_3] \tag{2.9}$$

$$Q = \begin{bmatrix} W_1 & 0 \\ 0 & W_2 \end{bmatrix} \tag{2.10}$$

The desired vehicle path is determined based on a zero lateral slip and the desired yaw rate r_d, and the basis for its choice is presented in the following. The Hamiltonian relationship is written as (2.11):

$$\begin{cases} e = X - X_d \\ H(X, U, P, t) = \dfrac{1}{2} e^T Q e + \dfrac{1}{2} U^T R U + P^T \dot{X} \end{cases} \tag{2.11}$$

The matrix P is defined as in (2.12):

$$P = \begin{bmatrix} P_1 & P_2 \end{bmatrix}^T \tag{2.12}$$

According to the relationships in the tracking problem, (2.13):

$$\begin{cases} \dot{X} = \dfrac{\partial H}{\partial P} = AX + BU + E\delta_W \\ \dot{P} = -\dfrac{\partial H}{\partial X} = -Q(X - X_d) - A^T P \\ 0 = \dfrac{\partial H}{\partial U} = RU + B^T P \end{cases} \tag{2.13}$$

On the other hand, P is equal to (2.14):

$$P = KX + S \tag{2.14}$$

And the control input is equal to (2.15):

$$U = -R^{-1}B^T(KX + S) \tag{2.15}$$

The algebraic Riccati equations are written according to (2.16):

$$\begin{cases} KA + A^T K + Q - KBR^{-1}B^T K = 0 \\ [A^T - KBR^{-1}B^T]S - Qr + KE\delta_W = 0 \end{cases} \tag{2.16}$$

Accordingly, the matrix K is determined to be a 2×2 matrix, and its value is obtained according to $K = X_2 {X_1}^{-1}$. The matrix S, which is a 2×1 matrix, is also determined.

$$K = \begin{bmatrix} K_{11} & K_{12} \\ K_{21} & K_{22} \end{bmatrix} \tag{2.17}$$

$$S = \begin{bmatrix} S_1 & S_1 \end{bmatrix}^T \tag{2.18}$$

With the determination of the matrices K and S, one can write the control input such as (2.19):

$$U = \frac{1}{w_3}[B_{12}(K_{11}v + K_{12}r + S_1) + B_{22}(K_{21}v + K_{22}r + S_2)] \tag{2.19}$$

As shown in the previous relationships, the matrix S is itself a function of the steering angle; therefore, the control law can be presented as (2.20):

$$M_z = K_{\delta_W}\delta_W + K_v v + K_r r \tag{2.20}$$

where K_{δ_W}, K_v, and K_r are the control gains of the front wheel steering angle, the lateral vehicle velocity, and the vehicle yaw rate signals, respectively.

The values of the matrices R and Q, or the weighting factors, are significant in determining the control gains. The *Bryson* method can be used for an initial guess of the weighting factors, according to (2.21) [9]:

$$\begin{cases} w_1 = \dfrac{1}{|v(\max)|} \\ w_2 = \dfrac{1}{|r(\max)|} \\ w_3 = \dfrac{1}{|M_z(\max)|} \end{cases} \tag{2.21}$$

The process of determining the weighting factors consists of regulating the controller. In this section, the weighting factors' suitable values have been determined according to the dynamics model.

2.3.3 Determination of the desired vehicle path

The designed controller is of the tracking type; hence, the desired path must be defined, as mentioned before. According to the dynamics control system introduced by the Ford Motor Company, the determination of the desired vehicle path is based on determining the desired yaw rate of the vehicle [1]. Based on this assumption, the desired path is defined as (2.22):

$$X_d = [0 \quad r_d]^T \tag{2.22}$$

In other words, the controller aims to make the lateral velocity of the vehicle zero and to track the vehicle yaw rate based on the desired yaw rate r_d. To determine the desired vehicle yaw rate, one can write based on Ackermann's formula:

$$\delta_W = \frac{l}{R} + K_{us}\frac{{V_X}^2}{gR} \tag{2.23}$$

where l is the distance between the two-vehicle axles, V_X denotes the longitudinal velocity of the vehicle, R is the turning radius of the vehicle, and K_{us} represents the understeer coefficient with a static value equal to (2.24):

$$K_{us} = \frac{W_f}{C_{\alpha f}} - \frac{W_r}{C_{\alpha r}} \tag{2.24}$$

where W_f and W_r are the weights of the front and rear axles, respectively. Given the centripetal behavior of the vehicle during turning, one can write

the desired yaw rate of the vehicle in terms of its longitudinal velocity in the form of (2.25):

$$V_X = Rr_d \tag{2.25}$$

According to the obtained equations, the desired yaw rate of the vehicle is defined as in (2.26):

$$r_d = \frac{\delta_W V_X}{l + K_{us}\dfrac{{V_X}^2}{g}} \tag{2.26}$$

Given the equations governing the directional stability of the vehicle in the 2-DOF bicycle model of the vehicle, it is proven that the vehicle will be stable if $K_{us} > 0$. Therefore, one attempts to select an appropriate value for the understeer coefficient during the controller's design to guarantee vehicle stability under different driving conditions.

2.3.4 Distribution of braking forces

During handling maneuvers, the steering angle applied by the driver is used as input to the vehicle. When the vehicle's slip angle reaches an undesirable value, the driver tries to correct the vehicle's behavior by modifying the steering angle. Under critical driving conditions, the driver becomes overloaded. The braking force inputs can correct the lateral and rotational behavior of the vehicle. Depending on the conditions, even a small braking force exerted on the wheel can stabilize the vehicle. Fig. 2.33 shows cases where braking forces have been used to correct the vehicle's rotational and lateral behavior, depending on the desired vehicle path.

By looking at the naming of tires according to Fig. 2.34, when the vehicle is understeered, the braking force F_{rr} is exerted on the rear-right wheel so that the torque M_Z is generated about the vertical axis of the vehicle. This torque can correct the understeer of the vehicle. For oversteer conditions, this correction is performed by applying a braking force on the front-left wheel F_{fl}. The control torque is determined according to the system dynamics and the designed control system. The application of the control torque has been evaluated in two parts. First, the provided control torque is applied to the vehicle mass center, and, in another part, the control torque is generated by differential braking in the front wheels.

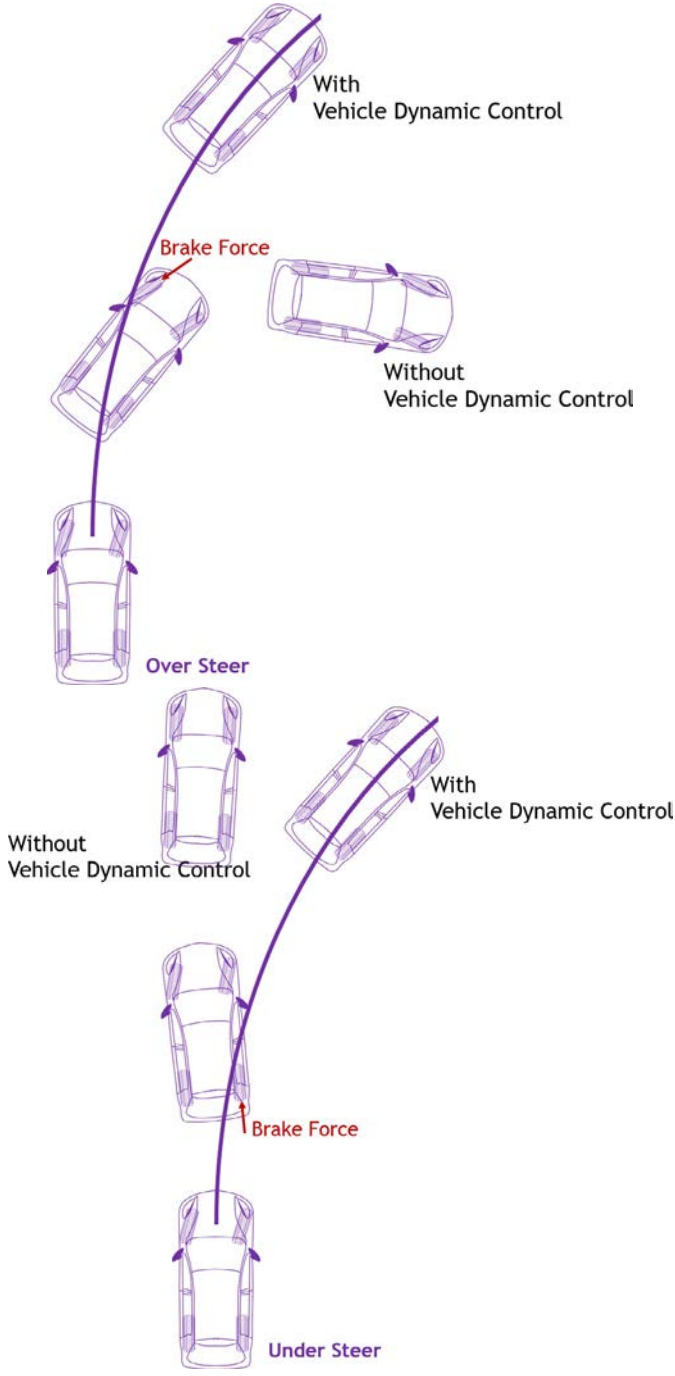

Fig. 2.33 Application of the braking force by the controller under oversteer and understeer conditions.

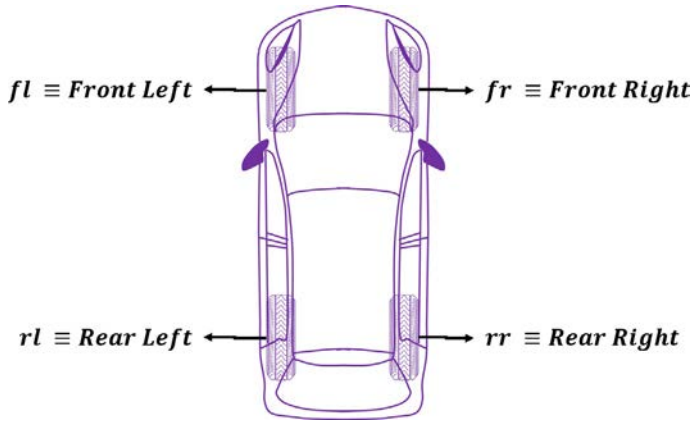

Fig. 2.34 Tire naming for braking strategy.

The braking forces' distribution has been explained using the following algorithm, according to the steering angle and the detection of understeer or oversteer in the vehicle.

- Oversteered vehicle; $\delta_w > 0$, $r_d > 0$, $M_z < 0$

$$F_{fr} = 2\frac{M_z}{b_f}$$

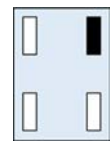

- Understeered vehicle, $\delta_w > 0$, $r_d > 0$, $M_z > 0$

$$F_{rl} = 2\frac{M_z}{b_r}$$

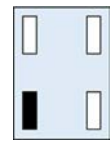

- Understeered vehicle $\delta_w < 0,\ r_d < 0,\ M_z < 0$

$$F_{rr} = 2\frac{M_z}{b_r}$$

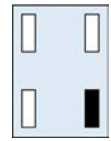

- Oversteered vehicle $\delta_w < 0,\ r_d < 0,\ M_z > 0$

$$F_{fl} = 2\frac{M_z}{b_f}$$

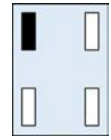

After determining the brake forces F_{ij}, the brake torque is computed. The ABS regulator then corrects the brake torque, and the corrected brake torque is exerted on the wheels. One can now present an algorithm describing the modeling and controller design as well as their interaction in the form of a vehicle dynamics control system; see Fig. 2.35.

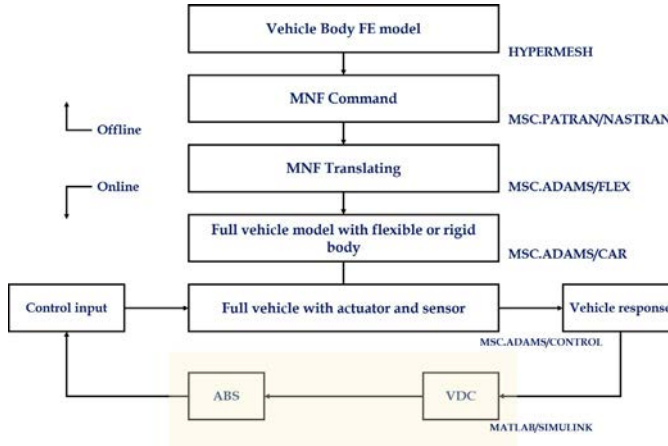

Fig. 2.35 The vehicle dynamics control system set.

2.3.5 Dynamics analysis of vehicle handling in the presence of an optimal controller

In order to simulate the handling behavior of the vehicle, standard dynamics analyses can be performed in ADAMS software on the full vehicle model. The analyses selected for studying vehicle behavior have been performed under transient conditions.

The performance of vehicle dynamics control systems is basically evaluated under critical conditions. Consequently, the analyses performed were such that they strongly destabilized the vehicle and veered it off course. These analyses were performed on the full dynamics model of the vehicle (SEDAN with a rigid and flexible body), and the difference in the vehicle response has been shown. Then, the performances of the vehicle dynamics control (VDC) and direct torque control systems have been evaluated under the above conditions by creating a link between the control software (MATLAB) and the dynamics software (ADAMS/CAR).

It must be noted that in the conducted analyses, the driver inputs applied to the vehicle are the steering angle and initial speed. The studies performed on the full vehicle dynamics model are the following:

- Single lane change analysis.
- Step steer input analysis.
- Single lane change on wet road analysis.

In this chapter, only the dry road has been examined, and other cases should be referred to Refs. [5] and [6] for further study. The analyses were performed under dry (friction coefficient of 0.9) road conditions (Table 2.4). A significant factor in dynamics analyses is the vehicle's loading condition, which significantly affects vehicle behavior. Fig. 2.35 shows the approximate loading changes of the SEDAN vehicle.

Table 2.4 Approximate changes in the SEDAN vehicle parameters under different loading conditions.

	SEDAN vehicle dynamics model	
Parameter	**Unladen condition**	**Laden condition**
m	1000 kg	1300 kg
I_z	1.54 e^9 kg mm^2	1.79 e^9 kg mm^2
l_1	1007 mm	1167.3 mm
l_2	1403 mm	1242.7 mm
h	496.6 mm	452.6 mm

Accordingly, the single lane change analysis at a speed of 120 km/h and with steering angle input has been performed with laden and unladen SEDAN velocity models under dry road conditions, as shown in Fig. 2.36.

Figs. 2.37–2.40 show the performance results of the VDC system. According to these figures, the controller has maintained the vehicle's

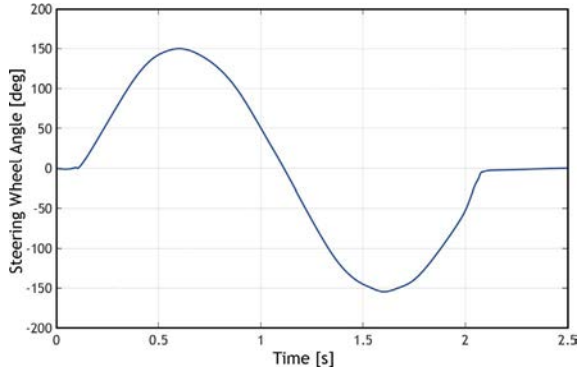

Fig. 2.36 Steering wheel angle.

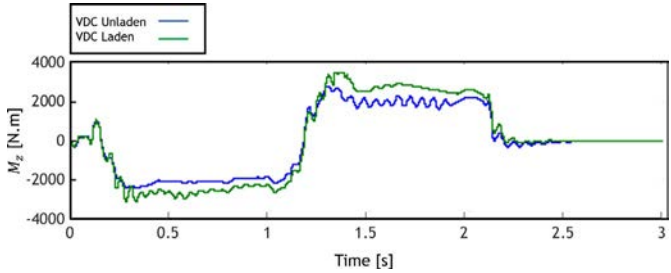

Fig. 2.37 Control torque of the SEDAN vehicle under different loading conditions.

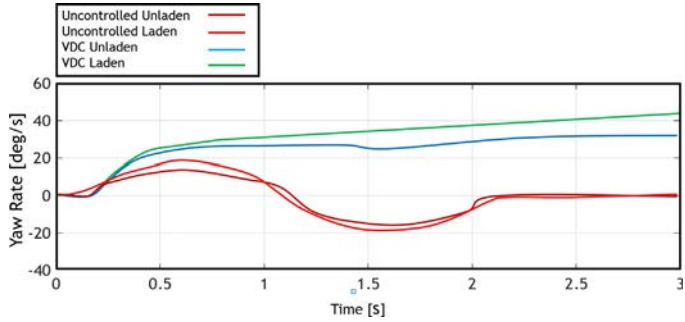

Fig. 2.38 Yaw rate of the SEDAN vehicle under different loading conditions.

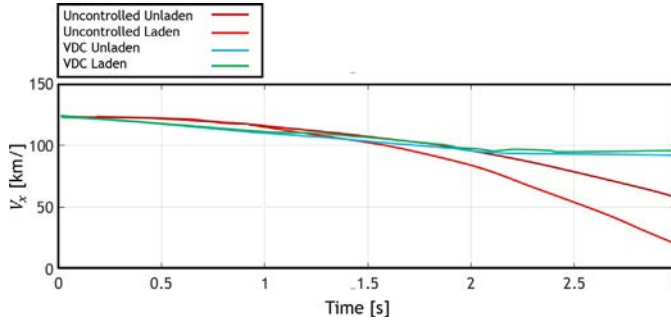

Fig. 2.39 The longitudinal velocity of the SEDAN vehicle under different loading conditions.

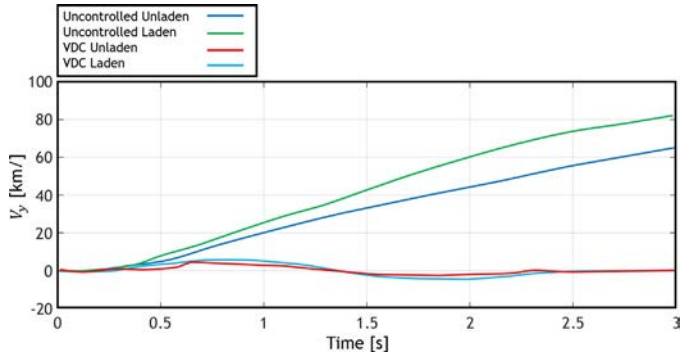

Fig. 2.40 The lateral velocity of the SEDAN vehicle under different loading conditions.

stability in each state by applying different control inputs. Given the obtained results, we can conclude that the laden vehicle's conditions are more critical than those of the unladen vehicle. Hence, it is better to perform the analyses under loaded conditions; however, given the limitation in the availability of the full vehicle model in the flexible state, the performed dynamics analyses presented in the following correspond to the unladen state.

2.4 Dynamics handling analyses of the SEDAN vehicle

2.4.1 Single lane change analysis on a dry road

In this analysis, the vehicle moves at an initial velocity of 120 km/h, and the steering input has been applied to it, as shown in Fig. 2.36. In Figs. 2.41–2.44, changes in the rigid-body vehicle's behavior in the presence

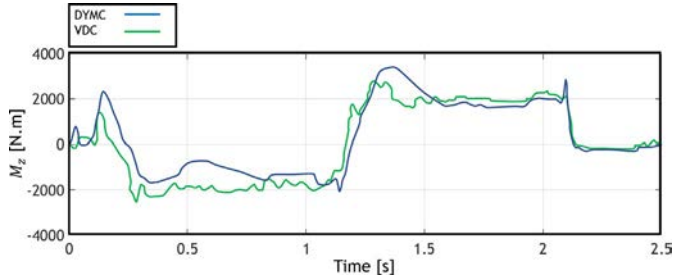

Fig. 2.41 Control torque of the SEDAN vehicle with a rigid body.

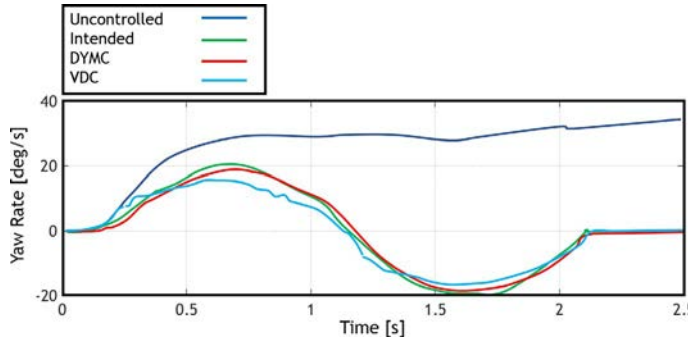

Fig. 2.42 Yaw rate of the SEDAN vehicle with a rigid body.

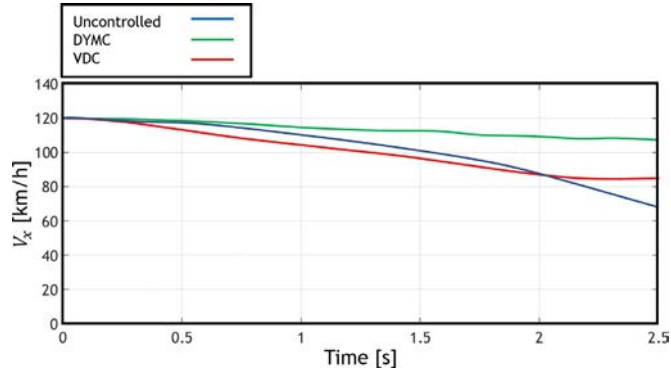

Fig. 2.43 Longitudinal velocity of the SEDAN vehicle with a rigid body.

of direct yaw moment control (DYMC) and vehicle dynamics control (VDC) are shown. The yaw rate and lateral velocity of the vehicle have been acceptably controlled in both states, and the changes in the yaw rate have followed the intended yaw rate. In the DYMC state, the yaw rate has

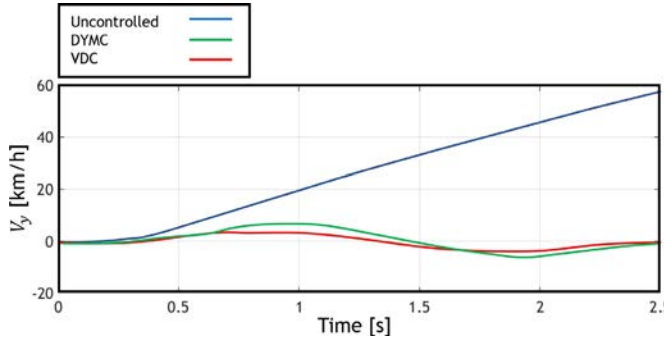

Fig. 2.44 The lateral velocity of the SEDAN vehicle with a rigid body.

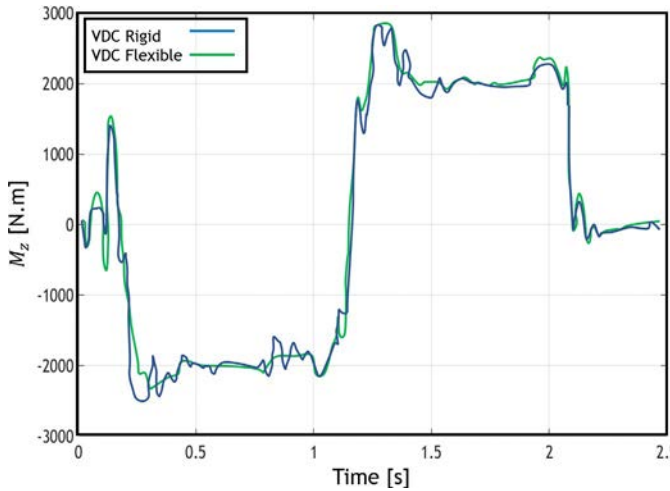

Fig. 2.45 Control torque of the SEDAN vehicle in rigid-body and flexible-body states.

accurately tracked the intended yaw rate, and the lateral velocity has increased compared to VDC. In the VDC state, the vehicle's lateral velocity has decreased with a slight deviation from the intended yaw rate, indicating the VDC system's acceptable performance.

Figs. 2.45–2.51 display the vehicle's behavior in rigid-body and flexible-body states in the presence of the VDC system. As shown in the figures, there is a significant difference between the vehicle's behaviors in rigid-body and flexible-body states in the uncontrolled mode. Via determining the desired path for rigid-body and flexible-body states (due to the identical initial velocity and steering inputs), the controller has been able to control both vehicles by consuming different amounts of energy to take the same path.

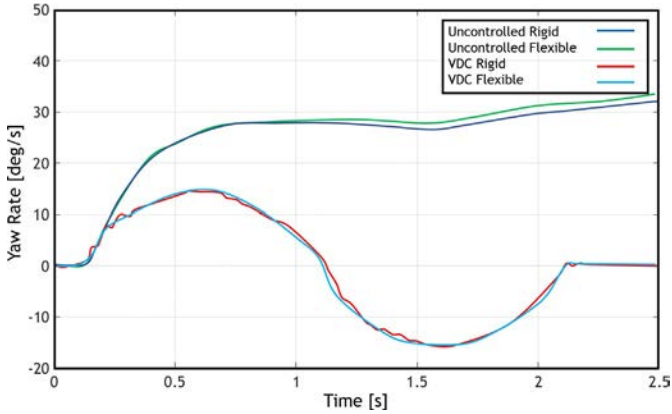

Fig. 2.46 Yaw rate of the SEDAN vehicle in rigid-body and flexible-body states.

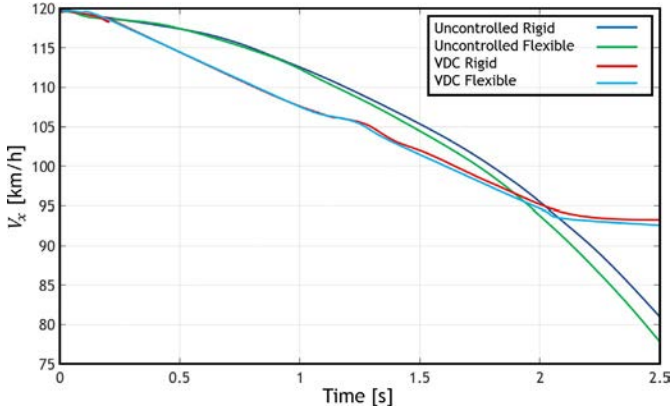

Fig. 2.47 The longitudinal velocity of the SEDAN vehicle in rigid-body and flexible-body states.

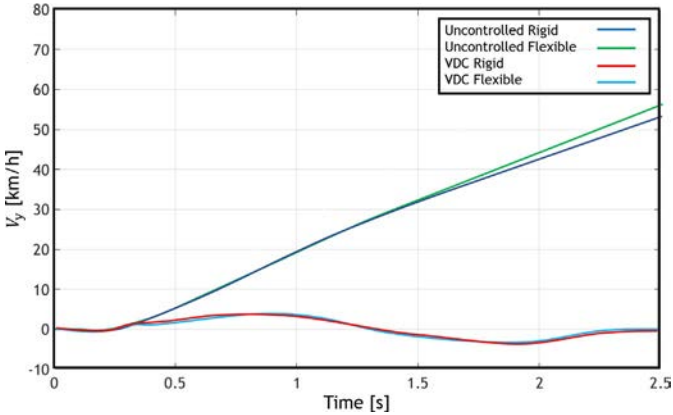

Fig. 2.48 The lateral velocity of the SEDAN vehicle in rigid-body and flexible-body states.

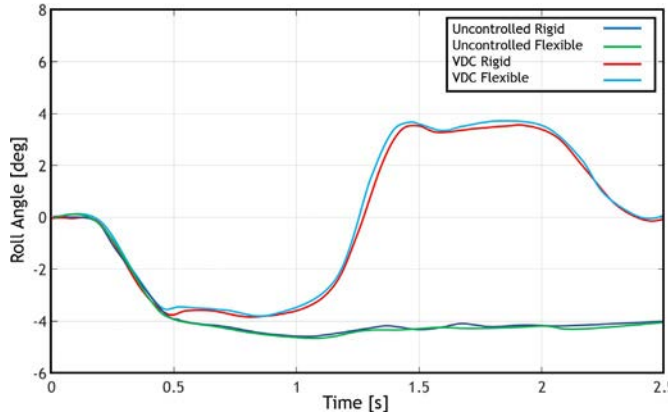

Fig. 2.49 Roll angle of the SEDAN vehicle in rigid-body and flexible-body states.

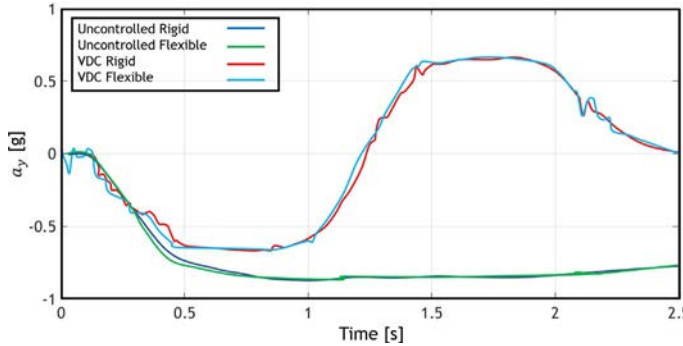

Fig. 2.50 Lateral acceleration of the SEDAN vehicle in rigid-body and flexible-body states.

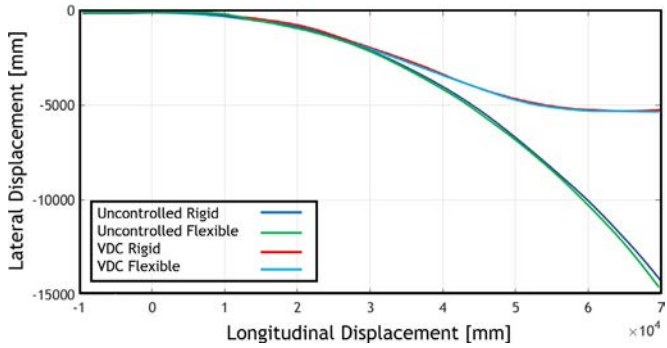

Fig. 2.51 Path of the SEDAN vehicle in rigid-body and flexible-body states.

2.4.2 Step steer analysis on a dry road

In this analysis, the vehicle moves at an initial velocity of 120 km/h, and the steering input has been applied to it, as shown in Fig. 2.52.

In Figs. 2.53–2.56, changes in the rigid-body vehicle's behavior in the presence of direct yaw moment control (DYMC) and vehicle dynamics control (VDC) are shown. The yaw rate and lateral velocity of the vehicle have been acceptably controlled in both states, and the changes in the yaw rate have followed the intended yaw rate. In the DYMC state, the yaw rate has accurately tracked the intended yaw rate, and the lateral velocity has increased compared to VDC. In the VDC state, the vehicle's lateral velocity has decreased with a slight deviation from the intended yaw rate, indicating the VDC system's acceptable performance.

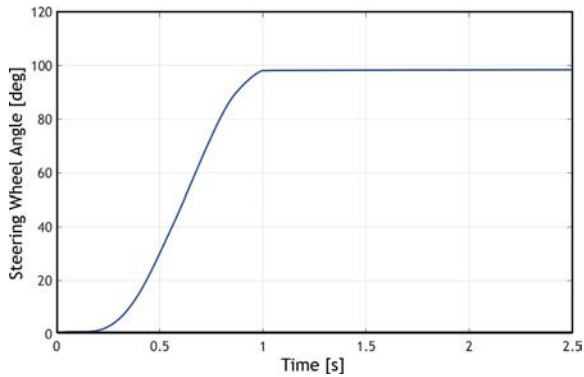

Fig. 2.52 The steering angle of the SEDAN vehicle.

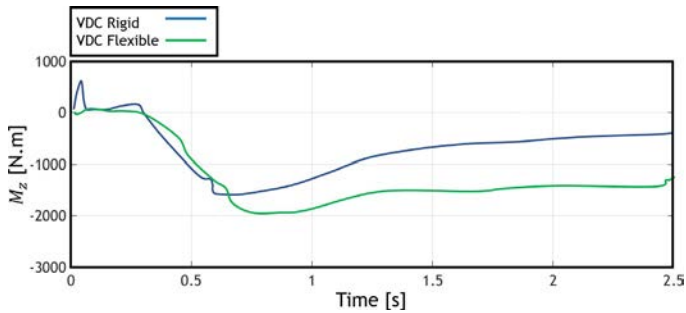

Fig. 2.53 Control torque of the SEDAN vehicle with a rigid body.

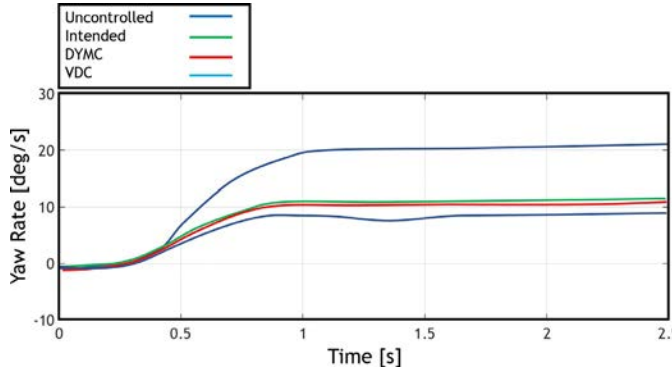

Fig. 2.54 Yaw rate of the SEDAN vehicle with a rigid body.

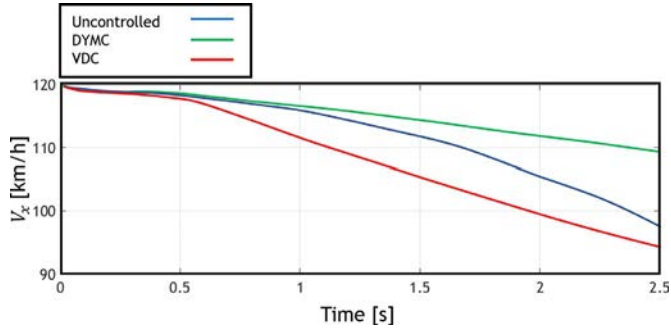

Fig. 2.55 The longitudinal velocity of the SEDAN vehicle with a rigid body.

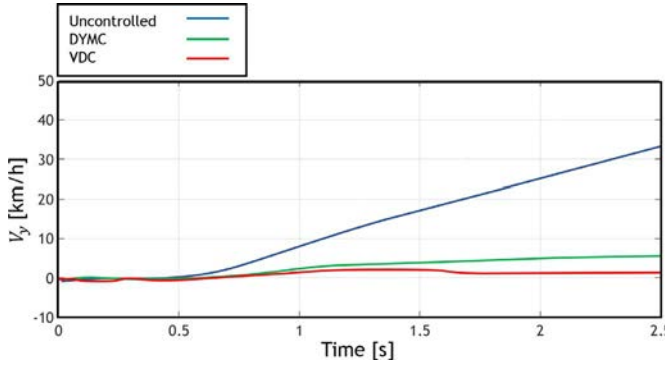

Fig. 2.56 The lateral velocity of the SEDAN vehicle with a rigid body.

Figs. 2.57–2.63 display the vehicle's behavior in rigid-body and flexible-body states in the presence of the VDC system. As shown in the figures, there is a significant difference between the vehicle's behaviors in rigid-body and flexible-body states in the uncontrolled mode. Via determining the desired path for rigid-body and flexible-body states (due to the identical initial velocity and steering inputs), the controller has been able to control both vehicles by consuming different amounts of energy to take the same path.

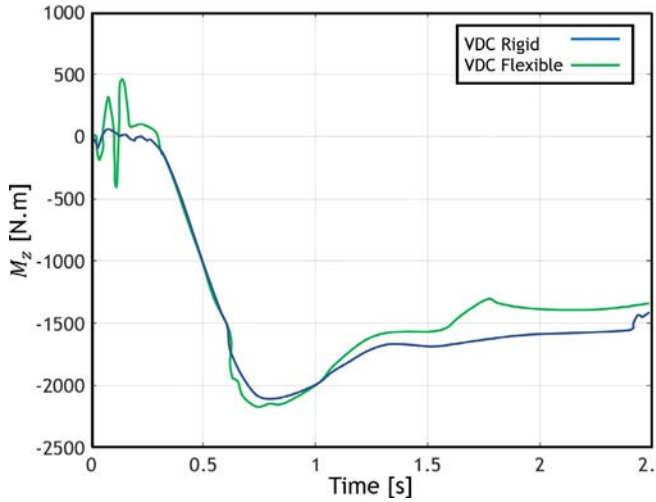

Fig. 2.57 Control torque of the SEDAN vehicle in rigid-body and flexible-body states.

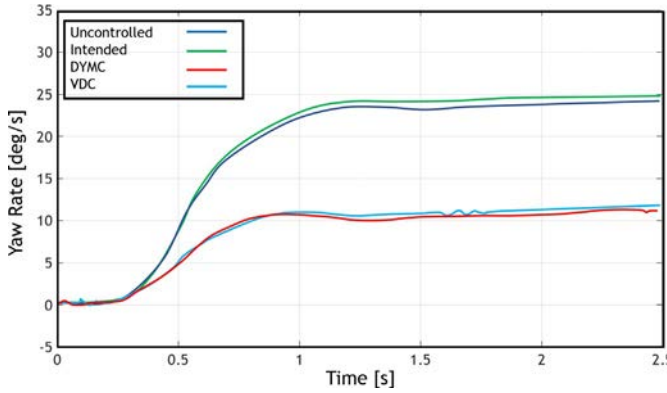

Fig. 2.58 Yaw rate of the SEDAN vehicle in rigid-body and flexible-body states.

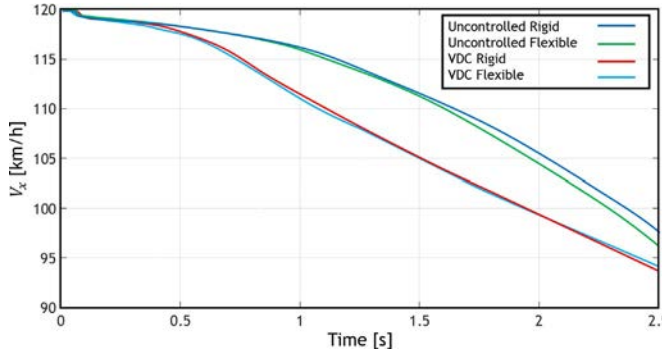

Fig. 2.59 The longitudinal velocity of the SEDAN vehicle in rigid-body and flexible-body states.

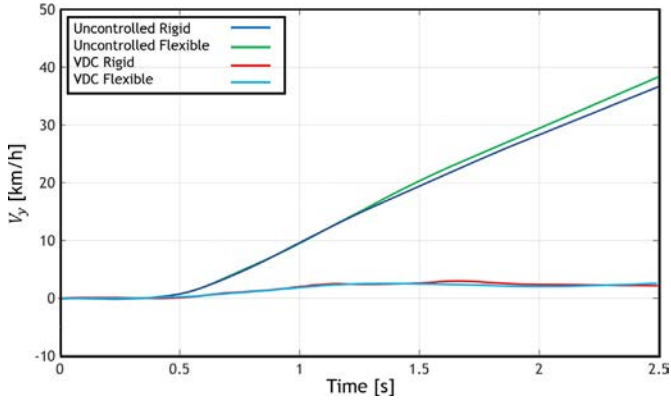

Fig. 2.60 The lateral velocity of the SEDAN vehicle in rigid-body and flexible-body states.

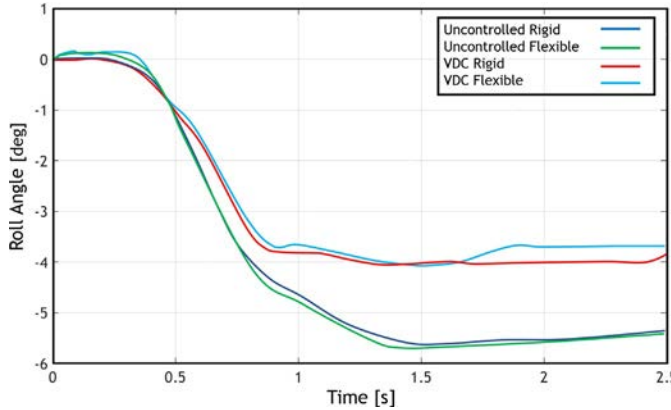

Fig. 2.61 Roll angle of the SEDAN vehicle in rigid-body and flexible-body states.

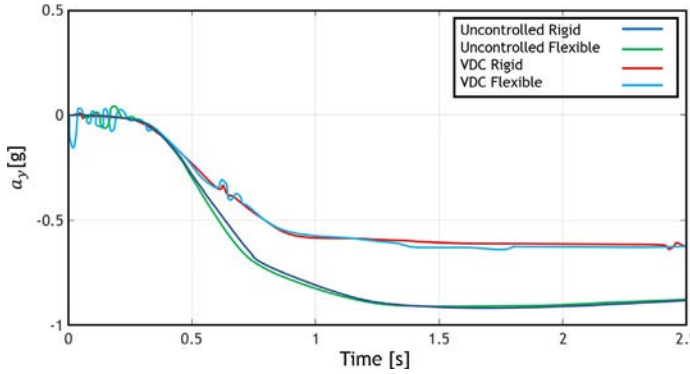

Fig. 2.62 The lateral acceleration of the SEDAN vehicle in rigid-body and flexible-body states.

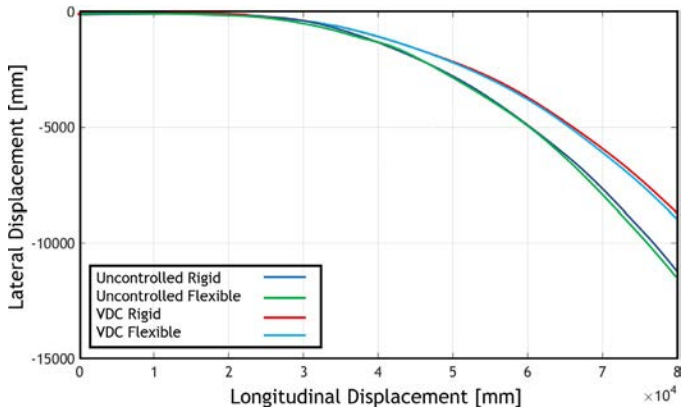

Fig. 2.63 Path of the SEDAN vehicle in rigid-body and flexible-body states.

2.5 Conclusion

In this chapter, a vehicle dynamics control system was designed for a passenger vehicle considering the vehicle body's flexibility. The following summarizes this chapter:

- Creating a link between finite element, dynamics, and control software.
- Presenting a dynamic model for a full vehicle with a flexible body, which can communicate with control software.
- Suggesting a suitable control method for designing dynamics control systems for vehicles, including vehicle dynamics control and four-wheel steering.

To reach a comprehensive dynamics control system, one must create its subsystems, namely the ABS and traction control system. One can succeed in this task by considering the traction forces' effects and designing a traction control system.

References

[1] R.K.M. Ali, Design of YMC Control System for Passenger Car, Master Thesis in Mechanical Engineering, Islamic Azad University, South Tehran Branch, September 2007.
[2] Mando R&D Center – Hyundai Motor Co. – SeoMoon Technology Inc, Handling Analysis of Height Control and ECS, 2001. Korea ADAMS User Conference.
[3] MSC.ADAMS/TIRE Help, 2003.
[4] T.D. Gillespie, Fundamentals of Vehicle Dynamics, vol. 400, Society of Automotive Engineers, Warrendale, PA, 1992.
[5] S. Azadi, M. Vaziri, M. Hoseini, Vehicle dynamic control of a passenger car applying flexible body model, Veh. Syst. Dyn. 48 (5) (2010) 587–617.
[6] M. vaziri, Dynamic Control of a Passenger Car by Considering Body Flexibility, Master Thesis in Mechanical Engineering, K.N.toosi University of Technology, 2007 (In Persian).
[7] H. Heisler, Advanced Vehicle Technology, Elsevier, 2002.
[8] S. Zheng, H. Tang, Z. Han, Y. Zhang, Controller Design for Vehicle Stability Enhancement, Elsevier, 2005.
[9] A.E. Bryson, Applied Optimal Control: Optimization, Estimation, and Control, CRC Press, 1975.

CHAPTER 3

Integrated vehicle dynamics control using active braking and semiactive suspension systems

3.1 Introduction

Nowadays, vehicle safety is a significant competitive factor in the global vehicle market. The top vehicle manufacturers always attempt to equip their vehicles with the best safety systems. With an increase in vehicle speeds over time, stability has become a significant issue in automotive engineering. The focus has shifted toward research and development in control systems that improve vehicle stability, resulting in a considerable increase in vehicle safety.

Research on factors causing severe damage and injuries in accidents has introduced strong and uncontrolled yaw and roll motions as well as slippage in lateral motion as the most significant factors causing stability and severe accidents. In the first type of instability, the yaw rate (angular speed about a vertical axis) of the vehicle increases beyond limits and causes the vehicle to gyrate. This turning also causes a lateral motion, which results in lateral instability. The turning is due to the moments resulting from longitudinal and lateral forces of the tires about the vertical axis of the vehicle. In a normal situation (linear motion on a smooth road with no steering input), this moment is zero, and hence no turning occurs. On the other hand, the turning appears under conditions such as steering input, a difference in the friction coefficient for different wheels, and asymmetric traction and braking force moments exerted on the wheels.

In addition to yaw and lateral instability, vehicle rollover is another major factor threatening vehicles, especially sport utility vehicles (SUVs). Vehicle rollovers are either tripped or untripped. Tripped rollovers happen due to the lateral impact of the vehicle with an obstacle such as a curb or a hole in the ground. These types of rollovers can sometimes be prevented using

Vehicle Dynamics and Control
https://doi.org/10.1016/B978-0-323-85659-1.00003-3

an electronic stability program (ESP) system. Untripped rollovers occur during critical maneuvers when the lateral acceleration increases. In this situation, the lateral tire forces increase, causing a large roll moment about the roll axis of the vehicle. Untripped rollovers do not happen on low-friction roads, at low vehicle speeds, or in general when the lateral acceleration is small.

With advancements in control engineering, extensive research has been conducted on the application of vehicle active safety systems, and they are increasingly used in modern vehicles. These systems have replaced older mechanical systems in order to improve handling, stability, and ride comfort. Among the most important such systems are the antilock brake system (ABS), active braking (AB), active front steering (AFS), electric power steering (EPS), active roll control (ARC), active suspension (AS), and semiactive suspension (SAS).

Each of these active control systems is designed for a specific purpose in the vehicle and acts independently; therefore, they have a parallel control structure. These structures have two fundamental problems:

- The system will be physically complex because it has numerous hardware and software items.
- Interference and coupling will be inevitable in the performance of the control systems because vertical, lateral, and longitudinal motions are inherently coupled, and an improvement in one can lead to a deterioration in another.

Vehicle researchers and engineers have introduced an approach called integrated vehicle dynamics control (IVDC) in recent decades to deal with this issue. IVDC is a high-technology system that is tasked with coordination between all the control systems and their components to improve the overall dynamic performance of the vehicle in terms of safety, comfort, and economy. This coordination and cooperation happen between the sensors, hardware, and control strategies. Hierarchical control methods are most often used in IVDC systems. In this strategy, each layer in the hierarchy takes control of the motion of one element or one subsystem of the chassis. IVDC systems have certain advantages, as mentioned in the following [1]:

- Overcoming interference and coupling in the performance of independent control systems in the chassis.
- Reducing costs and complexities by sharing sensor data among control subsystems in the chassis.
- Reducing the limitations usually encountered by the actuators while attempting to achieve specific control objectives.

Numerous studies have been carried out in recent years on the development of these types of systems. Researchers investigated the integrated control of SAS and four-wheel drive (FWD) systems in [1]. Two types of simulations were performed for this purpose. In the first part, an 11-DOF (3 DOFs for the yaw body movements, 1 DOF for each of the bounce and lateral movements of the mass center, 4 DOFs for the rotations of the wheels, and 2 DOFs for the steering angle of the front and rear wheels) full vehicle model was used. Because the velocity of the vehicle had been considered as constant throughout the research, the equation of longitudinal motion of the vehicle was eliminated, and only the lateral tire forces were modeled. The integrated control of the system was performed using H_∞ robust optimal control, which led to an improvement in the overall dynamics of the vehicle that was moving with a constant velocity on a random road with step steering input. In [2], researchers introduced a method for integrating the FWD and traction/braking distribution systems using online nonlinear optimization. This algorithm was used to minimize the load density of each tire by estimating the properties and the friction circle of that tire. Among these properties is the fact that the self-aligning torque (SAT) of the tire is saturated more than the lateral force in turning movements with smaller lateral acceleration. In this research, a hierarchical control structure was designed. In the first layer, the force and torque required for the desired movement of the vehicle, which was under the effect of the gas pedal and steering inputs, were determined. In the second layer, the determined force and torque were distributed among the four wheels based on the friction circle of each tire. In the last layer, the movement of each wheel was controlled to create the required forces. A nonlinear optimal control method was used in this research. Finally, the results of simulating a lane-change maneuver on a dry road indicated the adequate performance of the integrated control of these systems in improving the lateral stability and the handling of the vehicle.

A novel idea for integrating the control of the suspension system and the ARC system was presented in [3]. A 9-DOF (3 DOFs for the rotation of the body, 1 DOF for each of the bounce and lateral movements of the mass center, and 4 DOFs for the rotation of the wheels) full vehicle model and a linear tire model were used in the modeling section. This research was conducted with the aim of improving ride comfort and preventing rollover, and the system was controlled using the H_∞ robust control method. The method proposed in this research led to an overall improvement in ride comfort and roll angle control and a reduction in the lateral acceleration and the probability of rollover.

Karbalaei et al. [4] designed an IVDC system with a hierarchical structure in which the AFS system was combined with direct yaw moment control (DYC). A 7-DOF nonlinear model was used for the vehicle. The modified Pacejka tire model, in which the longitudinal and lateral forces are a combination of the vertical wheel forces, road friction coefficient, longitudinal slip, and lateral slip angle, was used for the tire. The high-level controller adjusted the yaw rate of the vehicle based on fuzzy logic to achieve adequate value. The yaw rate error and the rate of its changes were the inputs to this control level, and the yaw-moment control signal and the modified front-wheel steering angle were the outputs. Meanwhile, the low-level controller, which was designed separately for each wheel, maintained the lateral forces and slip of the tires within the acceptable range. Fuzzy logic was also used in the design of this control system.

In [5], a structure based on two control logics was designed to integrate the control of the AFS and ESP systems. The first logic monitored the control laws of each of the AFS and ESP systems, and the second logic used the root locus method along with a multivariable control strategy in the frequency domain. A 27-DOF full vehicle model and a nonlinear tire model were used in the simulation in CarSim software. Sliding mode control and LQR optimal control were used in the design of the AFS and ESP systems, respectively.

An integrated control structure for the AS and AB systems for improving vehicle safety and a diagnostic filter for the suspension actuators were designed in [6]. The linear parameter varying (LPV) strategy was utilized as the control method to guarantee stability, and a 9-DOF (3 DOFs for body rotations, 2 DOFs for the bounce and lateral motions of the mass center, and 4 DOFs for the vertical displacement of the unsprung masses) full vehicle model was used. The results showed that the integrated control of the chassis systems using the LPV control method was able to activate the AB system and reduce the rollover probability, despite the failure of one of the AS actuators, by taking advantage of the diagnostic system.

Lu et al. [7] proposes a hierarchical control strategy for the integrated control of the AS, AB, and active steering subsystems to improve ride comfort and stability. A 10-DOF full vehicle model was used for the vehicle and the modified Pacejka tire model. The control structure in this research had two layers, with the upper layer monitoring the system to identify the state variables of the vehicle and making logical decisions under various driving conditions and the lower layer containing the suspension, braking, and AFS actuators. Fuzzy and sliding-mode control methods were used in the suspension system, and the active braking and active steering systems, respectively,

and a design was made for switching the control subsystems. For instance, the adopted active shock absorbers not only improve ride comfort but also can reinforce safety during braking and stability during turnings by aiding the active braking and front steering systems via an increase in the vertical tire force.

In another study, IVDC was addressed in three parts. The first part involved the integrated control of the EPS and AS systems using stochastic optimal control. A nonlinear full vehicle model consisting of 14 ride and handling DOFs (6 DOFs for the translational and yaw motions of the body, 4 DOFs for the vertical displacement of the unsprung masses, and 4 DOFs for the rotation of the wheels) and a steering wheel model were employed. The nonlinear Pacejka tire model was used for modeling the tire forces, and random roads were used independently for each wheel in the ride analysis section. A 2-DOF linear handling model was used as the reference model for designing the controllers and computing the acceptable responses to steering inputs. In the second section, the authors designed a two-layer control structure for the integrated control of the ESP and ASS systems. The upper-layer controller monitored the driver inputs and the vehicle state variables, namely the front steering angle, slip angle, yaw rate, and lateral acceleration of the vehicle, and calculated the adequate yaw moments to be applied to the lower layer of the control system to achieve the desired behavior of the vehicle. The lower layer consisted of ESP and AS, and linear quadratic Gaussian (LQG) and adaptive fuzzy controllers were used in the design of the AS and ESP controllers, respectively. In the third part, the experimental tests were compared to the simulation results [8].

The integrated control of active braking and active steering systems and SAS using MR dampers was investigated in a single lane-change maneuver in [9]. In [10], a multilayer control structure was used to improve the yaw stability and integrated chassis control in fully electric vehicles. Sliding mode control was adopted to seek the desired outputs better, and the behavior of the driver was also modeled for a more realistic study. Another study [11] presented a coordination scheme for yaw moment control and active front steering systems for improving vehicle handling characteristics. To this end, the optimal yaw moment was computed by solving an adaptive optimization problem, and then the optimal braking torque and active front steering angle were calculated. In [12], optimization methods were proposed for improving the dynamic stability of the vehicle and overcoming the issues and limitations associated with modeling the vehicle and the nonlinear tire dynamics.

Each active control system is designed for a specific purpose in the vehicle and acts independently; therefore, they have a parallel control structure. These structures have two fundamental problems. The first problem is the physical complexity of the system due to its multitude of software and hardware. The second problem is the inevitable interference and coupling in the performance of the control systems. This is inevitable because the vertical, lateral, and longitudinal motions are inherently coupled, and an improvement in one can lead to a deterioration in another.

An IVDC approach has been used in this research in order to deal with these issues. The integrated control of lateral, vertical, yaw, and roll motions of the vehicle using active braking and semiactive suspension systems is investigated. Sliding mode control has been selected for the stability control system of the vehicle so as to make it accurate and robust against external disturbance, sensor noise, and system uncertainties. The adaptive rule method has been used to tune the controller gains. Furthermore, the unscented Kalman filter is used to estimate the state variables because it is uneconomical to measure some of the dynamic variables of the vehicle, such as the longitudinal and lateral velocities of the vehicle body and the longitudinal tire slip. The aim of using the semiactive suspension system in the present chapter is to improve ride comfort in addition to increasing yaw stability and lateral stability and reducing the probability of vehicle rollover.

3.2 The dynamic model of the system

3.2.1 The full model of the vehicle with 14 DOFs

In this section, a nonlinear full vehicle model with 14 ride and handling DOFs (6 DOFs for translational and yaw motion of the vehicle body, 4 DOFs for the vertical displacement of the unsprung masses, and 4 DOFs for the rotation of the wheels) is presented [8]. Fig. 3.1A, B, and C respectively display the yaw motion, pitch motion, and roll motion.

The equation of motion for the yaw motion shown in Fig. 3.1A is as follows:

$$I_z\dot{\omega}_z = M_z + M_{zc} + M_{zd} \tag{3.1}$$

where M_{zc} is the corrective yaw moment generated by the ESP, and M_{zd} is the disruptive yaw moment. M_z is expressed using the following relationship:

$$M_z = a\left(F_{y1} + F_{y2}\right) - b\left(F_{y3} + F_{y4}\right) + d\left(F_{x1} + F_{x3} - F_{x2} - F_{x4}\right) \tag{3.2}$$

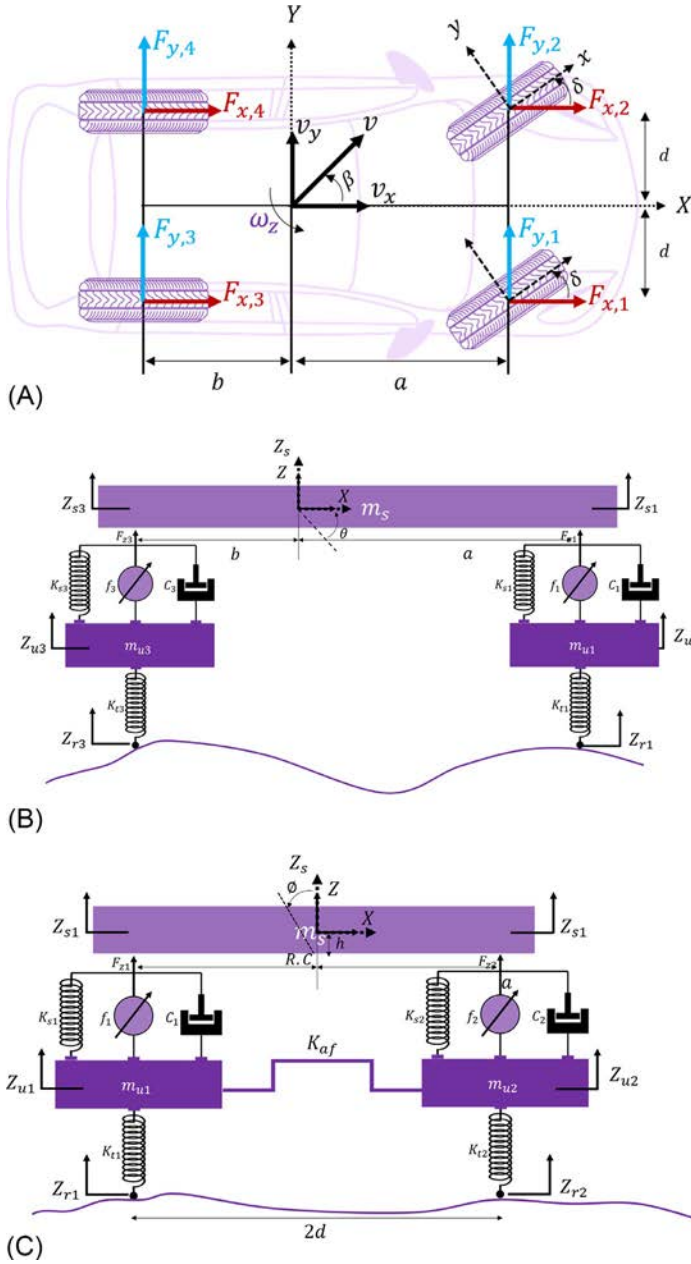

Fig. 3.1 Full vehicle model (A) Yaw motion, (B) Pitch motion, (C) Roll motion.

The equations of motion for longitudinal and lateral motion are as follows, respectively:

$$m\left(\dot{v}_x - v_y\omega_z\right) - m_s h\dot{\omega}_z\varphi = F_{x1} + F_{x2} + F_{x3} + F_{x4} \tag{3.3}$$

$$m\left(\dot{v}_y + v_x w_z\right) + m_s h\ddot{\phi} = F_{y1} + F_{y2} + F_{y3} + F_{y4} \tag{3.4}$$

The equations of motion for the pitch and roll motions shown respectively in Fig. 3.1B and C are as follows, respectively:

$$I_y\ddot{\theta} = b(F_{z3} + F_{z4}) - a(F_{z1} + F_{z2}) \tag{3.5}$$

$$I_x\ddot{\varphi} + m_s\left(\dot{v}_y + v_x\omega_z\right)h = m_s g h\varphi + (F_{z2} + F_{z4} - F_{z1} - F_{z3})d \tag{3.6}$$

The equations of motion for vertical and lateral motions of the sprung and unsprung masses are as follows, respectively:

$$m_s\ddot{z}_s = F_{z1} + F_{z2} + F_{z3} + F_{z4} \tag{3.7}$$

$$m_{ui}\ddot{z}_{ui} = k_{ti}(z_{ri} - z_{ui}) - F_{zi}, \qquad i = 1,2,3,4 \tag{3.8}$$

The values of the counter i for the front-right, front-left, rear-right, and rear-left wheels are 1, 2, 3, and 4, respectively. Moreover, the force F_{zi} is obtained from the following relationships:

$$F_{z1} = k_{s1}(z_{u1} - z_{s1}) + c_1(\dot{z}_{u1} - \dot{z}_{s1}) - \frac{k_{af}}{2d}\left[\varphi - \frac{(z_{u2} - z_{u1})}{2d}\right] + f_1 \tag{3.9}$$

$$F_{z2} = k_{s2}(z_{u2} - z_{s2}) + c_2(\dot{z}_{u2} - \dot{z}_{s2}) + \frac{k_{af}}{2d}\left[\varphi - \frac{(z_{u2} - z_{u1})}{2d}\right] + f_2 \tag{3.10}$$

$$F_{z3} = k_{s3}(z_{u3} - z_{s3}) + c_3(\dot{z}_{u3} - \dot{z}_{s3}) + \frac{k_{ar}}{2d}\left[\varphi - \frac{(z_{u3} - z_{u4})}{2d}\right] + f_3 \tag{3.11}$$

$$F_{z4} = k_{s4}(z_{u4} - z_{s4}) + c_4(\dot{z}_{u4} - \dot{z}_{s4}) - \frac{k_{ar}}{2d}\left[\varphi - \frac{(z_{u3} - z_{u4})}{2d}\right] + f_4 \tag{3.12}$$

where f_i represents the control force of the semiactive suspension system and is generated by the MR damper. The following approximations can be used if the angles θ and φ are small:

$$z_{s1} = z_s - a\theta - d\varphi \tag{3.13}$$

$$z_{s2} = z_s - a\theta + d\varphi \tag{3.14}$$

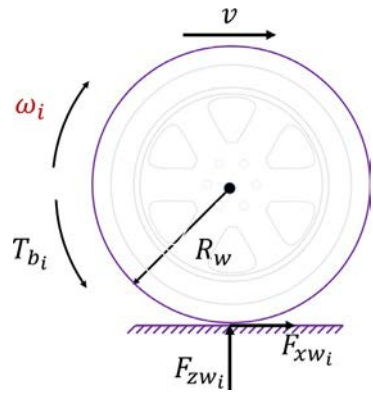

Fig. 3.2 Wheel dynamic model.

$$z_{s3} = z_s + b\theta - d\varphi \tag{3.15}$$

$$z_{s4} = z_s + b\theta + d\varphi \tag{3.16}$$

Considering the yaw dynamics of the wheel shown in Fig. 3.2, the corresponding equation of motion can be written as below:

$$I_w\dot{\omega}_i = -F_{xwi}R_w - T_{bi} \quad (i = 1, \ldots 4) \tag{3.17}$$

It must also be noted that due to the angle between the coordinate system attached to the ith wheel, $(x-y)_w$, and the coordinate system attached to the body along the longitudinal axis, $(x-y)$, which is the steering angle δ_i, there is a relationship between the longitudinal and lateral tire forces in the reference frame attached to the wheel (F_{xwi}, F_{ywi}) and the vehicle body coordinate system (F_{xi}, F_{yi}), expressed as follows for the ith wheel:

$$F_{xi} = (F_{xwi} - F_{zwi}\mu_{roll})\cos\ \delta_i - F_{ywi}\sin\ \delta_i + F_{xd} \tag{3.18}$$

$$F_{yi} = (F_{xwi} - F_{zwi}\mu_{roll})\sin\ \delta_i + F_{ywi}\cos\ \delta_i + F_{yd} \tag{3.19}$$

The vertical force exerted on the ith wheel is obtained from the following relationships:

$$F_{zwi} = k_{ti}(z_{gi} - z_{ui}) + \frac{0.5mgb}{L} \quad (i = 1, 2) \tag{3.20}$$

$$F_{zwi} = k_{ti}(z_{gi} - z_{ui}) + \frac{0.5mga}{L} \quad (i = 3, 4) \tag{3.21}$$

The longitudinal and lateral aerodynamic resistance forces (F_{dx}, F_{dy}) are determined using Eqs. (3.22) and (3.23), respectively:

$$F_{xd} = F_{air,x} = -\frac{1}{2}\rho C_{dx} A_f v_x{}^2 \tag{3.22}$$

$$F_{yd} = F_{air,y} = -\frac{1}{2}\rho C_{dy} A_s v_w{}^2 \tag{3.23}$$

In the above relationships, ω_z is the yaw rate, v_x and v_y respectively represent the longitudinal and lateral velocity of the vehicle, z_s and z_u respectively denote the vertical displacement of the mass center and the unsprung mass, and z_{si} is the velocity displacement of the body above the ith wheel. Furthermore, z_r represents the road profile roughness, k_s and k_t respectively are the stiffness coefficients of the suspension spring and the tire, k_{af} and k_{ar} respectively denote the stiffness coefficients of the front and rear antiroll bars, c is the damping coefficient of the suspension system, and ρ represents the density of air. Moreover, C_{dx} and C_{dy} are aerodynamic drag coefficients, A_f and A_s respectively denote the front and side surface areas of the vehicle, and v_w represents the lateral component of the wind velocity (the longitudinal component has been ignored). In addition, m, m_s, and m_u respectively represent the total mass, sprung mass, and unsprung mass of the vehicle; I_x, I_y, and I_z respectively denote the moment of inertia of the vehicle about its longitudinal, lateral, and velocity axes; I_w and R_ω are the moment of inertia and radius of the wheel, respectively; and T_{bi} and ω_i respectively represent the brake torque and angular velocity of the ith wheel. Finally, μ_{roll} is the rolling friction coefficient of the tire while d denotes the lateral distance between the mass center and the right or left wheels. a and b respectively represent the longitudinal distances between the mass center and the front and rear wheels, h is the height of the vehicle mass center as measured from the ground, and L is the length of the vehicle, which is the sum of a and b.

3.2.2 Tire modeling

The Pacejka magic tire formula has been used for modeling the longitudinal and lateral tire forces, which are functions of the vertical force exerted on the wheels (F_{zw}), the longitudinal slip ratio (λ), the lateral slip angle of the wheel (α), the friction coefficient of the road (μ), and the camber angle of the wheels. The self-aligning moment has been ignored. First, the longitudinal

tire force, Fx0, is expressed in a way such that it is only a function of the slip ratio and not the slip angle of the wheel [13]:

$$F_{x0} = D.\text{Sin}\overleftrightarrow{}[C_x.\arctan(B_x.\varphi_x)] \tag{3.24}$$

$$\varphi_x = (1-E).s_x + \frac{E}{B_x}.\arctan(B_x\lambda) \tag{3.25}$$

$$D = \mu.\left(a_1F_z^2 + a_2F_z\right) \tag{3.25a}$$

$$C_x = 1.65 \tag{3.25b}$$

$$B_x = (2-\mu).\left(\frac{a_3F_z^2 + a_4F_z}{C_x.D.e^{a_5F_z}}\right) \tag{3.25c}$$

$$E = a_6F_z^2 + a_7F_z + a_8 \tag{3.25d}$$

where B, C, D, and E represent the stiffness factor, shape factor, maximum factor, and curvature factor of the tire, respectively. Because the factors C and B used to determine the longitudinal forces are different from those used to calculate lateral forces, they are distinguished using x and y subscripts. The lateral tire force, such that it is only dependent on the slip angle of the wheel and not the slip ratio, is determined as follows:

$$F_{y0} = D.\text{Sin}\overleftrightarrow{}\left[C_y.\arctan\left(B_y.\varphi_y\right)\right] + \Delta S_v \tag{3.26}$$

$$\varphi_y = (1-E).(\alpha + \Delta S_h) + \frac{E}{B_y}.\arctan\left[\left(B_y.(\alpha + \Delta S_h)\right)\right] \tag{3.27}$$

$$C_y = 1.3 \tag{3.27a}$$

$$B_y = (2-\mu).\frac{a_3.\text{Sin}\left[a_4.\arctan\left(a_5F_z\right)\right]}{C_y.D}.(1 - a_{12}.|\gamma|) \tag{3.27b}$$

$$\Delta S_h = a_9.\gamma \tag{3.27c}$$

$$\Delta S_v = \left(a_{10}F_z^2 + a_{11}F_z\right).\gamma \tag{3.27d}$$

S_v and S_h are the transmission factors, which are dependent on the wheel camber angle. Under combined conditions, the longitudinal and lateral tire forces are each a function of both the slip ratio and slip angle of the wheel and are determined as follows:

$$F_x = \frac{\delta_x}{\delta_t}.F_{xo} \tag{3.28}$$

$$F_y = \frac{\delta_y}{\delta_t}.F_{yo} \tag{3.29}$$

where $\delta_x = \frac{\lambda}{1+\lambda}$, $\delta_y = \frac{\tan\alpha}{1+\lambda}$, and $\delta_t = \sqrt{\delta_x^2 + \delta_y^2}$. Moreover, the longitudinal slip ratio and slip angle of the ith wheel are expressed as follows:

$$\lambda = \rightleftarrows \frac{R_w\omega_i - v_{xwi}}{\max\left(R_w\omega_i, v_{xwi}\right)} \tag{3.30}$$

$$\alpha_i = \delta_i - \arctan\rightleftarrows\left(\frac{v_{ywi}}{v_{xwi}}\right) \tag{3.31}$$

v_{xwi} and v_{ywi} are the longitudinal and lateral velocities of the ith wheel, respectively. Because only the front wheels are steered by the driver in this research, $\delta_1 = \delta_2 = \delta$ and $\delta_3 = \delta_4 = 0$. The steering angle must be small during high velocities and critical maneuvers in order to prevent lateral slippage and vehicle rollover. With this assumption, the longitudinal and lateral velocities of the ith wheel are obtained from the following relationships:

$$v_{xw1} = v_{xw3} = v_x + d\omega_z \tag{3.32}$$

$$v_{xw2} = v_{xw4} = v_x - d\omega_z \tag{3.33}$$

$$v_{yw1} = v_{yw2} = v_y + a\omega_z \tag{3.34}$$

$$v_{yw3} = v_{yw4} = v_y - b\omega_z \tag{3.35}$$

The lateral slip angle of the vehicle body is calculated as follows:

$$\beta = \arctan\rightleftarrows\left(\frac{v_y}{v_x}\right) \tag{3.36}$$

The parameters a_{12}, …, a_1 are mentioned in Table 3.1 [13]. The grip between the tire and the road, which is expressed by the road friction coefficient, is a very important factor in the longitudinal and lateral tire forces. Hence, there will be large variations in these forces on dry, rainy, and snowy roads, as shown in Fig. 3.3, assuming $F_z = 3$ KN and a zero-camber angle.

3.2.3 Random road input modeling

This section presents the determination of the roughness of a random road using the inverse of its power spectral density (PSD). The PSD function of a road with a length L_r is expressed by $S_g(\Omega)$, where $\Omega = \frac{2\pi}{\lambda_r}$ represents the

Table 3.1 Pacejka tire model parameters.

Coefficient	Value (F_x)	Value (F_y)
a_1	−213	−22.1
a_2	1144	1011
a_3	49.6	1078
a_4	226	1.82
a_5	0.069	0.208
a_6	−0.006	0
a_7	0.056	−0.354
a_8	0.486	0.707
a_9	_	0.028
a_{10}	_	0
a_{11}	_	14.8
a_{12}	_	0.022

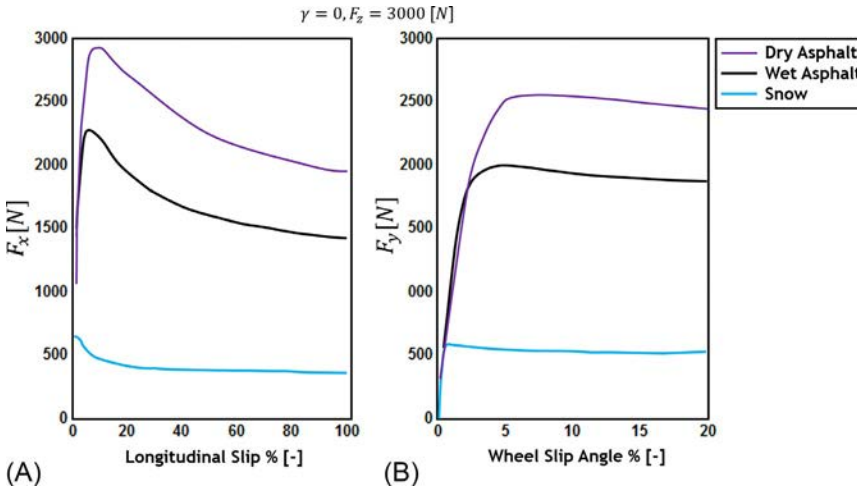

Fig. 3.3 The effect of the road friction coefficient on the tire forces: (A) lateral force, (B) longitudinal force.

wavenumber or spatial frequency with a unit of $\frac{\text{cycle}}{\text{m}}$.$\lambda_r$ is the wavelength of the road. Assuming N sampling points along the road, one can obtain the roughness amplitude of the road in terms of time, $z_r(t)$, as follows [14]:

$$z_r(t) = \sum_{n=1}^{N} s_n.\text{Sin}\left(n\omega_0 t + \phi_n\right) \tag{3.37}$$

where $s_n = \sqrt{2S_g(n\Delta\Omega).\Delta\Omega}$, $\omega_0 = \frac{2\pi}{L_r}v_x$, $\Delta\Omega = \frac{2\pi}{L_r}$, and v_x is the longitudinal velocity of the vehicle, which is assumed to be constant. Also, ϕ_n is the

random phase angle, which is uniformly distributed throughout the interval $[0, 2\pi)$. ISO 8606 has classified roads in terms of surface roughness. This classification ranges from very smooth to very rough (classes A–E) in terms of surface quality based on the PSD of the roads. The relationship between the road profile PSD and the spatial frequency for various roads is approximated as follows:

$$S_g(\Omega) = S_g(\Omega_0)\left(\frac{\Omega}{\Omega_0}\right)^{-\omega} \tag{3.38}$$

where Ω_0 represents the spatial reference frequency and is equal to 1 rad/m. Also, ω has a constant value of 2. The variation range of $S_g(\Omega_0)$ for various roads according to ISO 8606 is presented in Table 3.2 [15].

The profile of the E-type rough road and its PSD are plotted in Fig. 3.4 and compared to the PSD of the type-E road obtained from Table 3.2.

3.2.4 MR damper modeling

The use of MR dampers in semiactive suspension systems of vehicles has increased considerably due to the high reaction speed of magnetic fields, their insensitivity to temperature, and their simple structure. The force in these types of dampers is controllable via an electric current or voltage. Two approaches are often presented in the modeling of these dampers: Parametric and nonparametric. A common parametric model is the modified Bouc-Wen model, which is fairly complex and contains numerous parameters. Because the present study aims to use MR dampers in a semiactive suspension to improve lateral stability and to prevent vehicle rollover, a simpler model (the modified LuGre model, Fig. 3.5) has been used. The nonlinear dynamic equations of this model are expressed using Eqs. (3.38)–(3.40) [16].

Table 3.2 The variation range of roughness value for various roads, $S_g(\Omega_0)$.

	Degree of roughness $\Phi(\Omega_0)$ (10^{-6} m^3) where $\Omega_0 = 1$ rad/m		
Road class	**Lower limit**	**Geometric mean**	**Upper limit**
A (very good)	–	1	2
B (good)	2	4	8
C (average)	8	16	32
D (poor)	32	64	128
E (very poor)	128	256	512

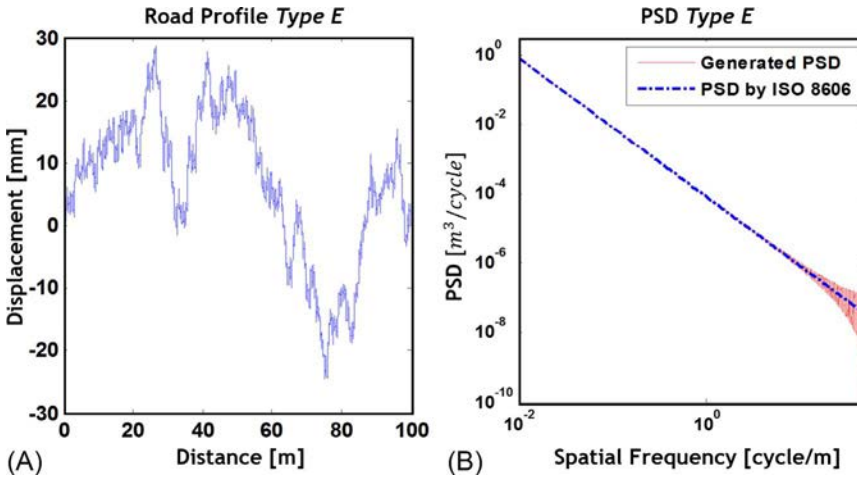

Fig. 3.4 (A) Road PSD function, (B) road roughness profile in the spatial domain.

$$F_{MR} = (\alpha_a + \alpha_b \nu)z + (c_{0a} + c_{0b}\nu)\dot{x} + c_1\dot{z} \tag{3.39}$$

$$\dot{z} = \dot{x} - a_0|\dot{x}|z \tag{3.40}$$

$$x = x_s - x_u \tag{3.41}$$

where F_{MR} is the damper force, α is a parameter for scaling the hysteresis loop, z is an auxiliary variable for keeping a data record, x is the relative displacement of the damper ends, $\boldsymbol{a_0}$ is a parameter for generating the hysteresis properties, $\boldsymbol{c_{0a}}$,$\boldsymbol{c_{0b}}$ respectively represent the viscous damping coefficient and the voltage-dependent viscous damping coefficient, $\boldsymbol{\alpha_b}$,$\boldsymbol{\alpha_a}$ respectively denote the stiffness coefficient z and the voltage-dependent stiffness coefficient, and ν is the applied voltage. The values of these parameters are mentioned in Table 3.3 [16]. The force-velocity graph has been plotted in

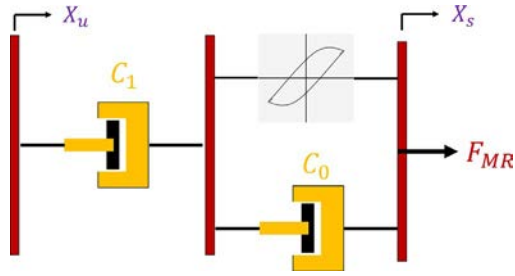

Fig. 3.5 Modified LuGre model in MR dampers.

Table 3.3 Values of the parameters used in the LuGre model of the MR damper.

Value	Parameter	Value	Parameter
15,000 N/m	α_a	100 N s/m	c_{0a}
40,000 N/mv	α_b	2500 N s/mv	c_{0b}
190 m^{-1}	a_0	200 N s/m	c_1

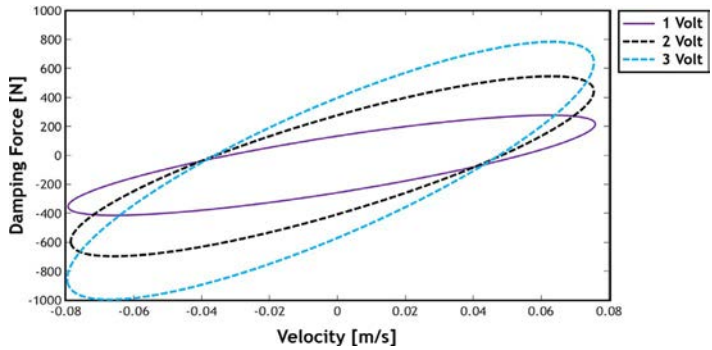

Fig. 3.6 Force versus velocity in the MR damper.

Fig. 3.6 for voltages of 1 V, 2 V, and 3 V under sinusoidal excitation with an amplitude of 5 mm and a frequency of 2.5 Hz.

3.3 Estimator design using unscented Kalman filter

In recent decades, identifying the state variables and the parameters of a dynamic model using incomplete and noisy measurement data has drawn the attention of researchers. The Kalman filter is a well-known model identification and noisy data refinement method. The Kalman filter provides adequate performance in case sufficient data are present about the process noise, such that it can minimize the root mean square of the estimation error. Using measurement data recorded by a noisy or inaccurate observer, this filter can estimate the state variables of the system as close as possible to the process noise-free values of the variables. This filter uses a series of recursive calculations based on minimizing the root mean square of the estimation error for optimal estimation of the variables and parameters of the system. Estimation using the Kalman filter requires accurate data about the covariance of the process noise and the observer. The dynamic equations for a discrete-time nonlinear system are expressed as follows:

$$x_{k+1} = f(x_k, u_k, t_k) + w_k \tag{3.42}$$

$$y_k = h(x_k, t_k) + v_k \tag{3.43}$$

where x_k represents the unknown state variables of the system at the time of sampling k, u_k denotes the known external input, and y_k indicates the noise-corrupted measurable signal, which is a function (h) of the state variables and the time. The system dynamics are expressed using the nonlinear function f. Both functions f and h are assumed to be known in the estimation process. The process noise w_k is due to the system dynamics, and the measurement noise v_k is due to the uncertainty of the recorded data. The process noise and measurement noise are both white Gaussian noise with mean values of zero and covariances of Q_k and R_k, respectively. The performance algorithm of the Kalman filter consists of the following three steps:

(a) The initial values of the system state variables ($\hat{x}_0^+$) and error covariances (P_0^+) are applied:

$$\hat{x}_0^+ = E(x_0) \tag{3.44}$$

$$P_0^+ = E\left[\left(x_0 - \hat{x}_0^+\right)\left(x_0 - \hat{x}_0^+\right)^T\right] \tag{3.45}$$

(b) The update equations based on the estimated values of the state variables and their covariances consist of the following four steps:

(b1) 2n sigma points ($\hat{x}_{k-1}^{(i)}$) are selected based on the mean and covariance of the random variable x, where n is the number of system state variables:

$$\hat{x}_{k-1}^{(i)} = \hat{x}_{k-1}^+ + \tilde{x}^{(i)} \; i = 1, \ldots, 2n \tag{3.46}$$

$$\tilde{x}^{(i)} = \left(\sqrt{n\,P_{k-1}^+}\right)_i^T \; i = 1, \ldots, n \tag{3.47}$$

$$\tilde{x}^{(n+i)} = -\left(\sqrt{n\,P_{k-1}^+}\right)_i^T \; i = 1, \ldots, n \tag{3.48}$$

(b2) The nonlinear dynamic equations of the system are used to convert the sigma points to $\hat{x}_k^{(i)}$. In this step, the sigma points move from the time $k-1$ to the time k:

$$\hat{x}_k^{(i)} = f\left(\hat{x}_{k-1}^{(i)}, u_k, t_k\right) \tag{3.49}$$

(b3) The $\hat{x}_k^{(i)}$ values obtained in the previous step are used to determine $\hat{x}_k^-$:

$$\hat{x}_k^- = \frac{1}{2n}\sum_{i=1}^{2n} \hat{x}_k^{(i)} \tag{3.50}$$

(b4) The error covariance is computed using the values obtained in this step (b):

$$P_k^- = \frac{1}{2n}\sum_{i=1}^{2n}\left(\hat{x}_k^{(i)} - \hat{x}_k^-\right)\left(\hat{x}_k^{(i)} - \hat{x}_k^-\right)^T + Q_{k-1} \tag{3.51}$$

(c) The update equations based on the measured values consist of the following six steps:

(c1) 2n sigma points ($\hat{x}_k^{(i)}$) are selected as follows:

$$\hat{x}_k^{(i)} = \hat{x}_k^- + \tilde{x}^{(i)}\ i = 1, \ldots, 2n \tag{3.52}$$

$$\tilde{x}^{(i)} = \left(\sqrt{n\,P_k^-}\right)_i^T\ i = 1, \ldots, n \tag{3.53}$$

$$\tilde{x}^{(n+i)} = -\left(\sqrt{n\,P_k^-}\right)_i^T\ i = 1, \ldots, n \tag{3.54}$$

(c2) The nonlinear measurement equations are used to convert the sigma points to $\hat{y}_k^{(i)}$:

$$\hat{y}_k^{(i)} = h\left(\hat{x}_k^{(i)}, t_k\right) \tag{3.55}$$

(c3) The $\hat{y}_k^{(i)}$ values obtained in the previous step are used to determine $\hat{y}_k$:

$$\hat{y}_k = \frac{1}{2n}\sum_{i=1}^{2n}\hat{y}_k^{(i)} \tag{3.56}$$

(c4) The error covariance is computed using the values obtained in this step (c):

$$P_y = \frac{1}{2n}\sum_{i=1}^{2n}\left(\hat{y}_k^{(i)} - \hat{y}_k\right)\left(\hat{y}_k^{(i)} - \hat{y}_k\right)^T + R_k \tag{3.57}$$

(c5) The cross-covariance between $\hat{x}_k^-$ and $\hat{y}_k$ is determined:

$$P_{xy} = \frac{1}{2n}\sum_{i=1}^{2n}\left(\hat{x}_k^{(i)} - \hat{x}_k^-\right)\left(\hat{y}_k^{(i)} - \hat{y}_k\right)^T \tag{3.58}$$

(c6) The measurement update equations are complemented using the following equations:

$$K_k = P_{xy}P_y^{-1} \tag{3.59}$$

$$\hat{x}_k^+ = \hat{x}_k^- + K_k(y_k - \hat{y}_k) \tag{3.60}$$

$$P_k^+ = P_k^- - K_k P_y K_k^T \tag{3.61}$$

The Kalman filter can provide an adequate estimate of the system state variables if accurate statistical data about the covariances of the process noise and observer noise, Q_k and R_k, are available, and the system dynamic equations are known.

In this chapter, all the state variables of a full vehicle model with 14 DOFs (introduced in Section 3.2) are estimated using the unscented Kalman filter. The measurement variables are the steering angle, the longitudinal and lateral acceleration of the vehicle, the angular velocity of the wheels, and the wheel travel.

3.4 Design of the active subsystems of the chassis

3.4.1 Design of the active braking system of the vehicle

In this section, an active braking system is designed using ASMC. The yaw motion of a vehicle is generally controlled using either of two methods. The first method is directly applying a control yaw moment by controlling the longitudinal wheel forces at the sides of the vehicle; this is the most effective method in providing vehicle stability. The second method is indirectly applying a yaw moment to the vehicle by controlling the lateral forces of the front or rear wheels. The yaw moment generation capability in this method is limited to the linear region due to the saturation of the lateral wheel forces. On the other hand, the first method also includes the nonlinear region of the tire (the region beyond the saturation region of the longitudinal forces).

Controlling the yaw rate of the vehicle to trace the desired value obtained from the driver inputs causes the vehicle trajectory to approach that intended by the driver. However, if the road is slippery, the lateral slip angle of the vehicle increases rapidly, leading to vehicle instability. Therefore, both the yaw rate and the lateral slip angle along with the vehicle trajectory must be limited proportionally to the road friction coefficient. Due to this reason, the simultaneous control of both yaw rate and side slip angle has been considered in recent studies on vehicle dynamics control.

In practical applications of vehicle dynamics control, it is difficult to accurately determine the road friction coefficient and the mass, the center of mass, and the moments of inertia of the vehicle given different driving

conditions during long trips and the variation in the vehicle mass. It is essential to have sufficient information about the conditions and friction coefficient of the road because all the forces required for lateral and yaw stability of the vehicle are related to the friction between the tire and the road.

Researchers have proposed adaptive and robust controllers in order to overcome these challenges. Adaptive control can compensate for parametric uncertainties; however, robust control methods such as sliding mode control perform well not only in compensating for structural uncertainties but also in dealing with external disturbance and nonstructural uncertainties or unmodeled dynamics. A disadvantage of sliding mode control is the determination of bounds for the uncertainties. Moreover, the control law includes switching, which causes control signal fluctuation, an undesirable phenomenon. As a result, smoothing methods such as boundary layer and adaptive approaches have been proposed for reducing control signal fluctuation. The combination of adaptive and robust controllers benefits from the advantages of both.

For this reason, an adaptive sliding mode controller has been designed in this section to improve the yaw stability of a vehicle using an active braking system. Because vehicle parameters such as the road friction coefficient changes during long drives and because braking forces are independent of this coefficient, an adaptive robust control method is necessary to guarantee stability. Accordingly, a two-layer control system has been designed. The upper layer determines the corrective yaw moment for tracing the desired yaw rate of the vehicle obtained from a reference model, whereas the lower layer, which has been designed individually for each wheel, adjusts the longitudinal slip of the wheels to its desired value in such a way that the braking force required for generating the corrective yaw moment is applied. ASMC has been used within each layer.

Furthermore, the unscented Kalman filter is employed to estimate the state variables because it is uneconomical to measure some of the dynamic variables of the vehicle, such as the longitudinal, lateral, and yaw velocities of the vehicle body and the longitudinal tire slip.

3.4.1.1 Active braking system strategy

The aim in designing the active braking system is to create adequate vehicle stability and handling under all motion conditions such that the vehicle is robust against changes in parameters and disturbances and maintains the yaw rate and lateral slip angle at the respective desired values. The desired value of the yaw rate is computed from the linear 2-DOF bicycle model [8]:

$$\omega_{zd} = \frac{v_x \delta}{L\left(1 + K_{us} v_x^2\right)} \tag{3.62}$$

In Eq. (3.62), K_{us} represents the understeer coefficient, which is obtained as follows:

$$K_{us} = m\left(\frac{b}{\mu C_f} - \frac{a}{\mu C_r}\right) L^2 \tag{3.63}$$

where C_f and C_r represent the lateral stiffness of the front and rear tires, respectively. However, ω_{zd} is limited in the form of $\omega_{zd} \leq \frac{\mu g}{v_x}$. Moreover, the desired lateral slip angle has been considered to be zero ($\beta_d = 0$) [17].

The controller acts by calculating the error of tracing the lateral slip angle and yaw rate of the vehicle, and then the corrective yaw moment M_{zc} is generated by applying braking force on one of the wheels using a differential braking mechanism. The forces generated by the tire depend on the longitudinal slip of the wheel; therefore, it is possible to produce the required braking force and, hence, corrective yaw-moment by adjusting the slip of each wheel to its desired value.

Given these explanations, the control system designed consists of two control layers. In the upper or supervisory layer of the controller, the torque required to stabilize the vehicle is determined. The lower layer, which acts as the system actuator, decides on the appropriate wheel for adjusting the longitudinal slip based on the sign of the corrective moment and generates the required yaw moment by applying braking force on this wheel. The ASMC method has been employed in both control layers. To this end, it is more appropriate to apply braking force only on the internal rear-wheel or the external front wheel to reduce the unwanted lateral force that generates an undesirable yaw moment. This is because an increase in the braking force of the tires generally reduces their lateral force, and these different changes in forces create opposing yaw moments in a tire. The corresponding results are shown in Table 3.4 for each wheel. In addition, the direction of the steering

Table 3.4 Effect of a change in the tire forces on a change in the direction of the corrective yaw moment [7].

Tire force	Inside front	Outside front	Inside rear	Outside rear
F_x increase	$+\Delta M$	$-\Delta M$	$+\Delta M$	$-\Delta M$
F_y increase	$-\Delta M$	$-\Delta M$	$+\Delta M$	$+\Delta M$

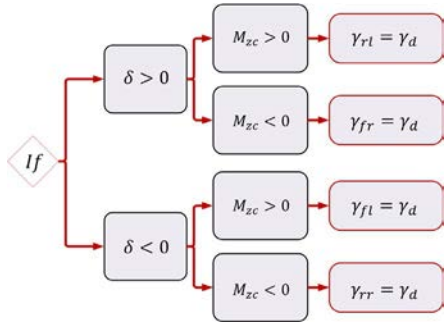

Fig. 3.7 Control logic in the active braking system.

angle also affects the decision-making process for selecting the appropriate wheel in controlling the longitudinal slip of the tire. The method shown in Fig. 3.7 has been used for this purpose.

As mentioned before, the stability control system of the vehicle in this research is made up of a two-layer structure. In the upper layer, the corrective yaw moment is computed for tracing the desired yaw rate of the vehicle. In the lower layer, first, the wheel on which the braking force must be applied is determined via decision-making logic, and then the brake torque required to produce the desired longitudinal slip of the tire of that wheel is obtained.

3.4.1.2 Upper layer control

In this layer, first, a common siding mode controller (SMC) is designed to trace the desired yaw rate and slip angle. Then, the controller gains are considered variable to counter changes in the vehicle parameters and the model uncertainties, resulting in an ASMC system. To this end, first, a hybrid error function is defined as follows [18]:

$$e_\gamma = k_{\gamma 1}(\omega_z - \omega_{zd}) + (\beta - \beta_d) \tag{3.64}$$

In the above equation, $k_{\gamma 1} > 0$ and β_d are zero based on the previous discussions. Then, a sliding surface consisting of the error function and its integral is selected as follows [7]: The integral term increases the rate of convergence of the error to zero.

$$s_\gamma = e_\gamma + k_{\gamma 2}\int_0^t e_\gamma dt \tag{3.65}$$

$k_{\gamma 2}$, is a positive parameter. The derivative of Eq. (3.65) will be as follows:

$$\dot{s}_\gamma = k_{\gamma 1}(\dot{\omega}_z - \dot{\omega}_{zd}) + \dot{\beta} + k_{\gamma 2} e_\gamma \tag{3.66}$$

In the above relationship, $\dot{\omega}_z$ is substituted from the vehicle dynamic equations (3.1):

$$\dot{s}_\gamma = k_{\gamma 1}\left(\frac{M_z + M_{zc} + M_{zd}}{I_z} - \dot{\omega}_{zd}\right) + \dot{\beta} + k_{\gamma 2} e_\gamma \tag{3.67}$$

$\dot{\omega}_{zd}$ is obtained from differentiating Eq. (3.62), and $\dot{\beta}$ is calculated by differentiating Eq. (3.36), as follows:

$$\dot{\beta} = k_\beta\left(\frac{\dot{v}_\gamma}{v_x} - \frac{\dot{v}_x}{v_x}\tan(\beta)\right) \tag{3.68}$$

where $k_\beta = (1 + \tan^2(\beta))^{-1}$. For the sliding condition to be satisfied, the following must hold:

$$\dot{s}_\gamma = -\eta_\gamma \operatorname{sgn}(s_\gamma); \left(\eta_\gamma > 0\right) \tag{3.69}$$

In which case:

$$\frac{1}{2}\left(\frac{d}{dt}\right)s_\gamma^2 = \dot{s}_\gamma s_\gamma = -\eta_\gamma \operatorname{sgn}(s_\gamma)\, s_\gamma < 0 \tag{3.70}$$

where 'sgn' is the sign function. The corrective yaw moment M_{zc} is obtained via a sliding mode control method by equating Eqs. (3.67) and (3.69). M_{zc} is considered as a control input in the upper control layer.

An issue present in the designed sliding mode controller is selecting the gain, η_γ, in Eq. (3.69), which strongly depends on the upper uncertainty bounds in the vehicle dynamics, including those for the mass and moment of inertia of the vehicle. In practice, these uncertainties and disturbances are due to the nonlinear dynamics of the vehicle and the tire, which are not fully specified, and their exact value cannot be determined. Trial-and-error methods are often used in tuning the gains of these types of controllers. Hence, they have a conservative performance and may not carry out the tracing well or may cause undesired fluctuations in the control signal.

To overcome this issue, researchers have begun considering the SMC gains as adaptive, such that they can be tuned online and updated. Accordingly, Eq. (3.69) is modified as follows:

$$\dot{s}_y = -\left(\hat{\eta}_{y1} + \hat{\eta}_{y2}|e_y|\right) \operatorname{sgn}(s_y) \tag{3.71}$$

where the variable gains $\hat{\eta}_{y1}$ and $\hat{\eta}_{y2}$ are determined instantaneously and updated by solving the below differential equations (3.8):

$$\dot{\hat{\eta}}_{y1} = \gamma_{y1}|s_y|; \qquad \left(\gamma_{y1} > 0\right) \tag{3.72}$$

$$\dot{\hat{\eta}}_{y2} = \gamma_{y2}|e_y||s_y|; \quad \left(\gamma_{y2} > 0\right) \tag{3.73}$$

The corrective yaw moment M_{zc} is obtained via the ASMC method by equating Eqs. (3.67) and (3.71).

$$M_{zc} = \hat{I}_z\left(\frac{k_{y1}\dot{\omega}_{zd} - \dot{\beta} - k_{y2}e_y}{k_{y1}}\right) - M_z - \left(\hat{\eta}_{y1} + \hat{\eta}_{y2}|e_y|\right) \operatorname{sgn}(s_y) \tag{3.74}$$

In the above control law, $\hat{I}_z$ is the approximate value of I_z. Moreover, $\dot{\omega}_{zd}$ is determined by differentiating Eq. (3.62), $\dot{\beta}$ is substituted from Eq. (3.68), and M_z is substituted from Eq. (3.2). It must be noted that $\dot{v}_x$ and $\dot{v}_y$ must be substituted into Eq. (3.10), respectively, from Eqs. (3.3) and (3.4).

We assume that there are constant and positive values η_{y1}^d and η_{y2}^d such that:

$$\eta_{y1}^d > |d(t)| \tag{3.75}$$

$$\eta_{y2}^d > \frac{k_{y2}}{k_{y1}}\left|\tilde{I}_z\right| \tag{3.76}$$

In Eq. (3.75), $d(t)$ is the disturbance moment of the system in the yaw dynamics. It is caused by all the uncertainties in modeling the longitudinal and lateral tire forces due to the unknown and variable road friction coefficient and is determined as follows:

$$d(t) = M_{zd} + \tilde{I}_z\dot{\omega}_{zd} - \frac{\tilde{I}_z\dot{\beta}}{k_{y1}} \tag{3.77}$$

$\tilde{I}_z$ represents the difference between the estimated value $\hat{I}_z$ and the actual value I_z. Thus, $\tilde{I}_z = \hat{I}_z - I_z$. One can conclude from the assumptions in Eqs. (3.75) and (3.76) that the parametric uncertainties of the system have limited values. In the following, the stability of the control system designed via ASMC is proven. To this end, first, a Lyapunov function is defined as follows:

$$V = \frac{1}{2} I_z s_\gamma^2 + \frac{k_{\gamma 1}}{2\gamma_{\gamma 1}} \tilde{\eta}_{\gamma 1}^2 + \frac{k_{\gamma 2}}{2\gamma_{\gamma 2}} \tilde{\eta}_{\gamma 2}^2 \tag{3.78}$$

where

$$\tilde{\eta}_{\gamma 1} = \hat{\eta}_{\gamma 1} - \eta_{\gamma 1}^d ; \tilde{\eta}_{\gamma 2} = \hat{\eta}_{\gamma 2} - \eta_{\gamma 2}^d \tag{3.79}$$

The following is obtained by differentiating Eq. (3.78):

$$\dot{\mathrm{V}} = I_z s_\gamma \dot{s}_\gamma + \frac{k_{\gamma 1}}{\gamma_{\gamma 1}} \tilde{\eta}_{\gamma 1} \dot{\tilde{\eta}}_{\gamma 1} + \frac{k_{\gamma 2}}{\gamma_{\gamma 2}} \tilde{\eta}_{\gamma 2} \dot{\tilde{\eta}}_{\gamma 2} \tag{3.80}$$

Now, the two sides of Eq. (3.67) are multiplied by I_z, and M_{zc} is substituted from Eq. (3.74) in the resulting equation:

$$\begin{aligned} I_z \dot{s}_\gamma = k_{\gamma 1} \Bigg[& \hat{I}_z \left(\frac{k_{\gamma 1} \dot{\omega}_{zd} - \dot{\beta} - k_{\gamma 2} e_\gamma}{k_{\gamma 1}} \right) + M_{zd} - \left(\hat{\eta}_{\gamma 1} + \hat{\eta}_{\gamma 2} |e_\gamma| \right) \operatorname{sgn}(s_\gamma) \Bigg] \\ & - k_{\gamma 1} I_z \dot{\omega}_{zd} + I_z \dot{\beta} + k_{\gamma 2} I_z e_\gamma \mathrm{l} \end{aligned} \tag{3.81}$$

By using Eq. (3.79), substituting Eqs. (3.80) in Eq. (3.81), and noting that $s_\gamma \, sgn\,(s_\gamma) = |s_\gamma|$, the derivative of the Lyapunov function is simplified as follows:

$$\dot{\mathrm{V}} = s_\gamma \left(k_{\gamma 1} M_{zd} + k_{\gamma 1} \tilde{I}_z \dot{\omega}_{zd} - \tilde{I}_z \dot{\beta} - k_{\gamma 2} \tilde{I}_z e_\gamma \right) - k_{\gamma 1} |s_\gamma| \eta_{\gamma 1}^d - k_{\gamma 1} |s_\gamma| |e_\gamma| \eta_{\gamma 2}^d \tag{3.82}$$

Given the term $d(t)$ in Eq. (3.77), which expresses the system uncertainties, Eq. (3.82) is written in the following form:

$$\begin{aligned} \dot{V} &= k_{\gamma 1} s_\gamma \left(d(t) - \frac{k_{\gamma 2} \tilde{I}_z e_\gamma}{k_{\gamma 1}} \right) - k_{\gamma 1} |s_\gamma| \eta_{\gamma 1}^d - k_{\gamma 1} |s_\gamma| |e_\gamma| \eta_{\gamma 2}^d \\ &\le k_{\gamma 1} |s_\gamma| \left(|d(t)| + \frac{k_{\gamma 2} \left| \tilde{I}_z \right| |e_\gamma|}{k_{\gamma 1}} \right) - k_{\gamma 1} |s_\gamma| \eta_{\gamma 1}^d - k_{\gamma 1} |s_\gamma| |e_\gamma| \eta_{\gamma 2}^d \\ &\le k_{\gamma 1} |s_\gamma| \left(|d(t)| - \eta_{\gamma 1}^d \right) + |e_\gamma| |s_\gamma| \left(k_{\gamma 2} \left| \tilde{I}_z \right| - k_{\gamma 1} \eta_{\gamma 2}^d \right) \end{aligned} \tag{3.83}$$

The following results from Eqs. (3.75), (3.76), and (3.83):

$$\dot{V} < 0 \tag{3.84}$$

Because the Lyapunov function defined in Eq. (3.78) is a positive definite function and its derivative, $\dot{V}$, is a definite negative function, it can be concluded from Lyapunov's direct method that the controller designed using ASMC is stable.

Due to the discontinuity of the function *sgn* in Eq. (3.74), certain fluctuations usually appear in the control law, M_{zc}. To omit these fluctuations, it is better to replace the function 'sgn' with the saturation function 'sat'. The saturation function is defined as follows:

$$\mathrm{sat}(s_\gamma) = \begin{cases} 1 & (s_\gamma > \varphi) \\ \dfrac{s_\gamma}{\varphi} & (|s_\gamma| \le \varphi) \\ -1 & (s_\gamma < -\varphi) \end{cases} \tag{3.85}$$

where φ represents the thickness of the boundary layer.

3.4.1.3 Lower layer control

After the corrective yaw moment M_{zc} is determined in the upper layer, the braking torque required to produce the moment M_{zc} and the wheel that must be subjected to braking must be determined in the lower control layer. To this end, the wheel to which active braking must be applied is selected first using the signs of the steering angle and M_{zc}, as shown in Fig. 3.7. Then, the required braking force, F_{xb}, must be computed according to Eq. (3.86). For example, if the brake torque must be applied to the front right wheel:

$$F_{xb} = \frac{M_{zc}}{d} \tag{3.86}$$

In the next step, the desired longitudinal slip of the tire, λ_d, is obtained using interpolation methods. Finally, the brake torque, T_b, required to trace λ_d is determined using an adaptive sliding mode controller. Therefore, another error function and sliding surface are defined [7]:

$$e_b = \lambda - \lambda_d \tag{3.87}$$

$$s_b = e_b + k_b \int_0^t e_b dt; \quad (k_b > 0) \tag{3.88}$$

The following relationship is defined to satisfy the sliding condition:

$$\dot{s}_b = -(\hat{\eta}_{b1} + \hat{\eta}_{b2}|e_b|)\,\mathrm{sat}(s_b) \tag{3.89}$$

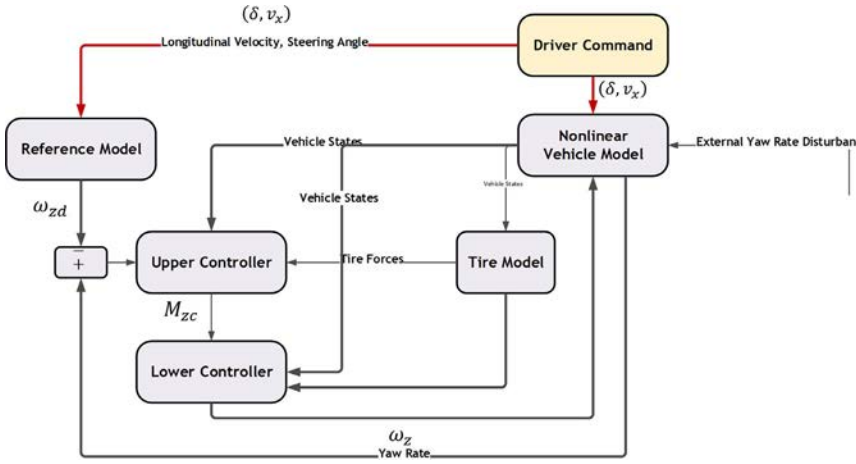

Fig. 3.8 Block diagram of the controller structure.

where the adaptive gains $\hat{\eta}_{b1}$ and $\hat{\eta}_{b2}$ are determined by solving the following differential equations (3.8):

$$\dot{\hat{\eta}}_{b1} = \gamma_{b1}|s_b|; \qquad (\gamma_{b1} > 0) \tag{3.90}$$

$$\dot{\hat{\eta}}_{b2} = \gamma_{b2}|e_b||s_b|; \quad (\gamma_{b2} > 0) \tag{3.91}$$

In the end, the brake torque required for the ith wheel, which is the control input, is calculated by combining Eqs. (3.87)–(3.91) and using Eq. (3.17) according to Eq. (3.92), where a_x is the longitudinal acceleration of the vehicle.

$$T_{bi} = -R_\omega F_{xwi} - \frac{I_\omega a_x \omega_i}{v_x} + \frac{I_\omega v_x k_b e_b}{R_\omega} + \frac{I_\omega v_x}{R_\omega}(\hat{\eta}_{b1} + \hat{\eta}_{b2}|e_b|)\,\mathrm{sat}(s_b) \tag{3.92}$$

The block diagram of the controller structure is displayed in Fig. 3.8.

3.4.2 Design of the semiactive suspension system of the vehicle

For increased ride comfort and safety in vehicles, vehicle designers attempt to reduce the vibrations of the vehicle body, and various suspension systems have been developed for this purpose. Suspension systems so far built to reduce and control vehicle vibrations can be divided into three groups, namely passive suspension, semiactive suspension (SAS), and active suspension. The first group consists of systems commonly used in most vehicles.

The characteristics of their components, including the stiffness coefficient of the springs and the damping ratio of the dampers, are constant and change only due to wear, reducing their quality. On the other end of the spectrum are active suspension systems, which provide high quality and comfort compared to passive suspension systems due to their actuators. However, they are less commonly used due to their high price, high energy and power consumption, and relatively complex components such as actuators, sensors, control valves, and high-pressure vessels for controlling the fluid. In these systems, there are no passive components such as springs or dampers, and an actuator adjusts the mutual reaction between the vehicle body and wheel. Nowadays, semiactive suspension systems, which benefit from the advantages of both previous groups, have drawn the attention of researchers. In these suspension systems, changes occur in the damping ratio of the damper with small amounts of energy under different road conditions, leading to better ride comfort and road holding.

In this research, the SAS uses an MR damper, which changes the damping ratio by varying the viscosity of the fluid inside it. Features of this damper include fast response to the control signal and low energy consumption. Two fuzzy strategies have been employed in the design of the SAS: the first is to improve ride comfort (SAS1), and the other is to improve stability and handling (SAS2) by increasing the damping force. The SAS1 system is addressed first.

3.4.2.1 Design of the SAS1 system

When the vehicle is on a straight course or is turning with a small lateral acceleration, ride comfort is the priority of the SAS system control actions. Accordingly, a fuzzy controller has been designed for reducing vertical vibrations of the sprung mass. The inputs to this controller are the velocity of the sprung mass and the relative velocity of the sprung and unsprung masses, and the output of the fuzzy network is the control force of the SAS system, which is considered the input of the control system. Seven triangular membership functions and seven linguistic variables–NB, NM, NS, ZE, PS, PM, and PB, respectively denoting negative big, negative medium, negative small, zero, positive small, positive medium, and positive big–have been defined for each input and output. The max-min inference method in the Mamdani fuzzy inference system and the centroid defuzzifier have been used. The fuzzy rules can be seen in Table 3.5. An important ride comfort

Table 3.5 Fuzzy rules for the SAS1 system.

	Relative velocity $\dot{z}_{su}$						
$\dot{z}_s$	NB	NM	NS	ZE	PS	PM	PM
NB	PB	PB	PM	PS	ZE	ZE	ZE
NM	PB	PM	PM	PS	ZE	ZE	ZE
NS	PM	PM	PS	ZE	ZE	ZE	ZE
ZE	PS	PS	ZE	ZE	ZE	NS	NS
PS	ZE	ZE	ZE	ZE	NS	NM	NM
PM	ZE	ZE	ZE	NS	NM	NM	NB
PB	ZE	ZE	ZE	NS	NM	NB	NB

indicator is the RMS of the vertical acceleration of the vehicle mass center, Eq. (3.93), which has been utilized in this section to assess the performance of the suspension system [19].

$$RMS(\ddot{z}_s) = \sqrt{\frac{1}{T}\int_0^T \ddot{z}_s^2\, dt} \tag{3.93}$$

3.4.2.2 Design of the SAS2 system

When the vehicle undergoes critical maneuvers, stability and handling become the main goals of the control system. In this situation, the active braking system is the most effective chassis subsystem in improving handling and stability. This is because this subsystem has a significant influence on the longitudinal tire forces and the lateral tire forces during turning. However, because these forces depend on the vertical force exerted on the wheel, controlling the vertical force of the tires can also be addressed in the discussion on the stability and handling of a vehicle. A criterion used for evaluating the performance of the suspension system in improving handling and road holding of the vehicle is the reduction in the RMS or the standard deviation of the tire deflection [19]. The RMS indicator has been used in this section. MR dampers can take on this responsibility by increasing the damping ratio of the system if necessary. Accordingly, a fuzzy controller has been designed in the SAS2 system that can reduce the tire deflection well. The inputs, membership functions, fuzzy inference method, and defuzzification of this network are similar to those for the network presented for SAS1 in the previous section. The only differences are that its input is the voltage input to the MR damper instead of the damper force and that its fuzzy rules are

Table 3.6 Fuzzy rules for the SAS2 system.

	Relative velocity $\dot{z}_{su}$						
$\dot{z}_s$	**NB**	**NM**	**NS**	**ZE**	**PS**	**PM**	**PM**
NB	B	B	B	B	ZE	ZE	ZE
NM	B	B	M	M	ZE	ZE	ZE
ZE	B	M	M	S	ZE	S	S
PS	M	S	S	S	S	S	M
PM	S	S	S	ZE	S	S	B
PB	ZE	ZE	ZE	ZE	S	M	B

different, as shown in Table 3.6. The RMS value of the tire deflection can be computed from Eq. (3.94):

$$RMS(\textit{Tire deflection}) = \sqrt{\frac{1}{T}\int_0^T (z_u - z_r)^2\, dt} \tag{3.94}$$

3.5 Integrated vehicle dynamics control

In this section, the integrated control of lateral, vertical, yaw, and roll dynamics of the vehicle using active braking and semiactive suspension systems is investigated. The vehicle stability control structure is the active braking system defined in the previous section. The aim of using the semiactive suspension system is to improve ride comfort in addition to increasing yaw stability and lateral stability and reducing the probability of vehicle rollover. The simulation of the IVDC system has been performed for a nonlinear full vehicle model with 14 DOFs in MATLAB software.

In severe maneuvers, the lateral and yaw stabilities of the vehicle are undermined, and the probability of rollover increases due to the saturation of tire forces. In addition, if the road excitation frequencies coincide with the natural frequencies of the wheel bounce, resonance occurs, causing fluctuations in the lateral and yaw dynamic responses of the vehicle. In this condition, the active braking system cannot improve handling and stability by itself. To deal with this problem, a structure has been designed for coordinating the semiactive suspension and active braking systems.

3.5.1 Integrated vehicle dynamics control structure

As mentioned previously, the coordination between active braking and semiactive suspension systems to improve ride comfort and stability is

addressed in this section. The active systems are those described in the previous sections. In other words, two strategies have been used in the design of the suspension system, one for improving ride comfort (SAS1) and one for improving stability and handling (SAS2). The SAS2 system can have a significant effect on the roll angle and the vertical force exerted on the wheels. The lateral acceleration of the vehicle is in the range of 0.3–0.5 g in common noncritical maneuvers. In this range, SAS2 can improve the lateral dynamics and reduce the possibility of vehicle rollover via decreasing the vertical tire forces and the roll angle. When the lateral acceleration reaches a specific value (0.3 g in this study), the operational task of the semiactive suspension switches from SAS1 to SAS2. Using a supervisory layer, three driving states, namely direct, mild turning, and sharp turning, are identified using the lateral acceleration and steering angle, as shown in Table 3.7.

The vehicle rollover threshold is defined using the Rollover Index (RI) In this research, the lateral-load transfer ratio (LTR) has been considered as the RI. This ratio is equal to the absolute value of the ratio of the difference in the vertical loads of the left and right wheels to the total vertical load of the four wheels and is obtained from Eq. (3.95).

$$LTR = \frac{|F_{ZR} - F_{ZL}|}{F_{ZR} + F_{ZL}} \tag{3.95}$$

Moreover, the use of an estimator seems necessary because measuring some of the dynamic variables of the vehicle, including the longitudinal and lateral velocities and the yaw rate of the vehicle body, the vertical velocity of the sprung and unsprung masses, and the longitudinal slip of the tires, is not economical. For this reason, the UKF has been used in this section to estimate the state variables of the system and the road profile.

In the process of estimation using the Kalman filter, the dynamic equations of the system are solved at every step, and the road roughness inputs are considered as external system disturbances. It is incorrect to assume these disturbances as low-amplitude noise in the estimation algorithm due to their

Table 3.7 Identification of the operational task of the active chassis subsystem based on various driving conditions [16].

Driving situation detection	Task assignment
$\delta = 0$	SAS1
$\delta > 0 \wedge a_y < -0.3g$ cornering	SAS1 + AB
$\delta > 0 \wedge a_y > +0.3g$ cornering	SAS2 + AB

considerable intensity compared to other vehicle vibrational signals. Therefore, they must be considered as measurable inputs. However, because it is almost impossible to measure the road profile online in practical vehicle dynamic control applications, the road profile is estimated in this section using the vertical acceleration of the wheels, their dynamic equations, and the estimated state variables. The 14-DOF full vehicle model introduced in the previous sections is also used in this section. All the state variables of the full model are estimated via the UKF. The measurement variables are the steering angle, the longitudinal and lateral acceleration of the vehicle, the angular velocity of the wheels, the vertical acceleration of the wheels, and the wheel travel.

As an example, the estimated road roughness under the first wheel, $\widetilde{Z}_{r1}$, is obtained using the following relationship:

$$\widetilde{z}_{r1} = \widetilde{z}_{u1} + m_{u1}\ddot{\widetilde{z}}_{u1} + \widetilde{F}_{z1} \over k_{t1} \tag{3.96}$$

where

$$\widetilde{F}_{z1} = -k_{s1}z_{su1} - c_1\dot{\widetilde{z}}_{su1} - \frac{k_{af}}{2d}\left[\widetilde{\varphi} - \frac{\left(\widetilde{z}_{u2} - \widetilde{z}_{u1}\right)}{2d}\right] + f_1 \tag{3.97}$$

3.5.2 Integrated vehicle dynamics control simulation

The 14-DOF nonlinear model introduced in the previous sections has be[8] en used for the simulation, with the parameters in, as shown in Table 3.8. In this section, the performance of the semiactive suspension is evaluated and simulated in two states:

(A) Evaluation of the performance of the SAS1 system in ride comfort improvement.

(B) Evaluation of the performance of the SAS2 system in handling and stability improvement.

3.5.2.1 Ride comfort analysis

This section analyzes the ride comfort improvement of the SAS1 system. The road input has been considered as random of type C, the simulation has been performed in 5 s, and the vehicle velocity has been assumed to be 25 m/s. The vertical acceleration of the vehicle mass center has been plotted in Fig. 3.9, and RMS value of the acceleration has been used for the quantitative analysis. A remarkable drop in the acceleration amplitude in

Table 3.8 Parameters of the 14-DOF vehicle model.

Parameter	Value	Parameter	Value
m (kg)	1030	b (m)	1.39
m_s (kg)	810	I_w (kg m^2)	2.1
m_{u1}/m_{u2} (kg)	31	R_w (m)	0.3
m_{u3}/m_{u4} (kg)	24	μ_{roll}	0.015
I_x (kg m^2)	300	L (m)	2.36
I_y (kg m^2)	1058	h (m)	0.5
I_z (kg m^2)	1088	c_f/c_r (N/rad)	40,000
k_{s1}/k_{s2} (N/m)	18.600	ρ (kg/m^3)	1.2
k_{s3}/k_{s4} (N/m)	19.600	C_{dx}	0.35
k_t (N/m)	132,000	C_{dy}	0.8
k_{af}/k_{ar} (N m/rad)	6695	A_f (m^2)	2.5
c_{s1}/c_{s2} (N s/m)	1300	A_s (m^2)	4.5
c_{s3}/c_{s4} (N s/m)	1400	V_w (m/s)	18
d (m)	0.64	μ	0.9
a (m)	0.97		

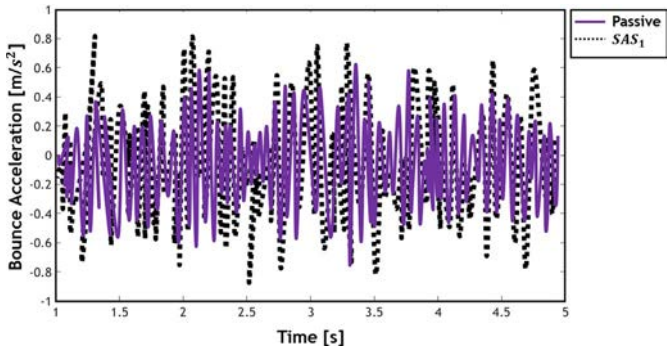

Fig. 3.9 Vertical acceleration of the vehicle mass center.

the active system is observed in this graph. The RMS of the acceleration in SAS1 has decreased by 29% compared to the passive mode.

3.5.2.2 Handling and stability analyses

The computer simulation of the double lane-change maneuver on a dry road ($\mu = 0.9$) has been performed to evaluate the designed control system. The steering angle input is sinusoidal with an amplitude of 4 degrees (0.07 rad) and a frequency of 0.43 Hz, as shown in Fig. 3.10.

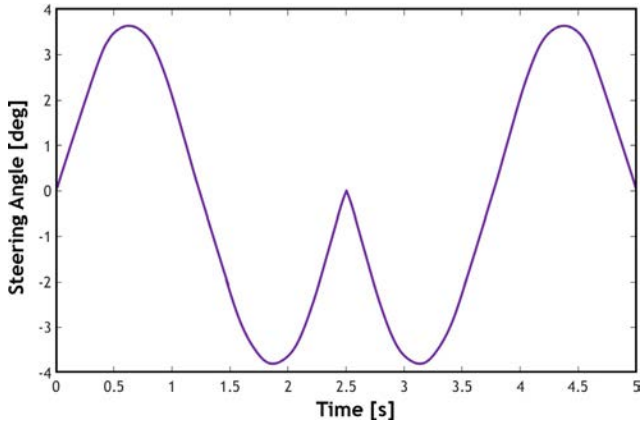

Fig. 3.10 Steering angle input in the double lane-change maneuver.

The road input has been considered as random of type C, the simulation has been performed in 5 s, and the vehicle velocity has been assumed to be 25 m/s. A sinusoidal wave with an amplitude of 10 mm and a wavelength of 2 m has been added to the road input. The simulation results of passive, AB only, and AB with SAS2 integrated control systems and the estimated values are displayed in Figs. 3.11–3.16. The yaw rate plot of the vehicle in various modes is shown in Fig. 3.11.

As shown in Fig. 3.11, the AB with the SAS2 integrated control system has been able to trace the desired vehicle yaw with better accuracy than the AB-only system. Furthermore, some fluctuations due to resonance are

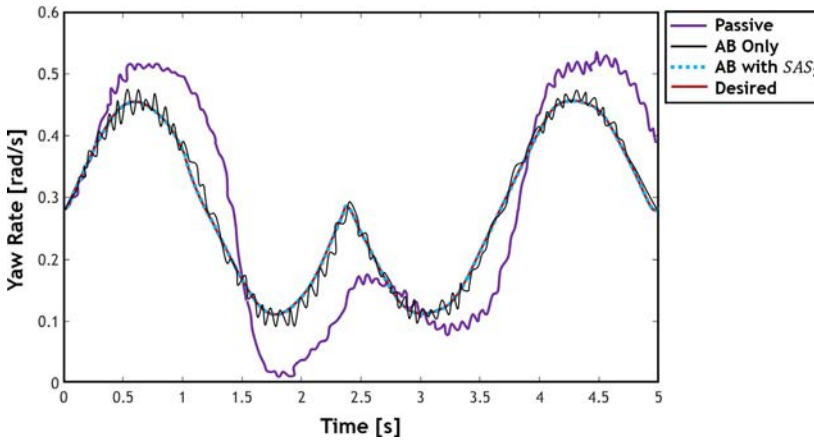

Fig. 3.11 Graph of the vehicle yaw rate in the double lane-change maneuver.

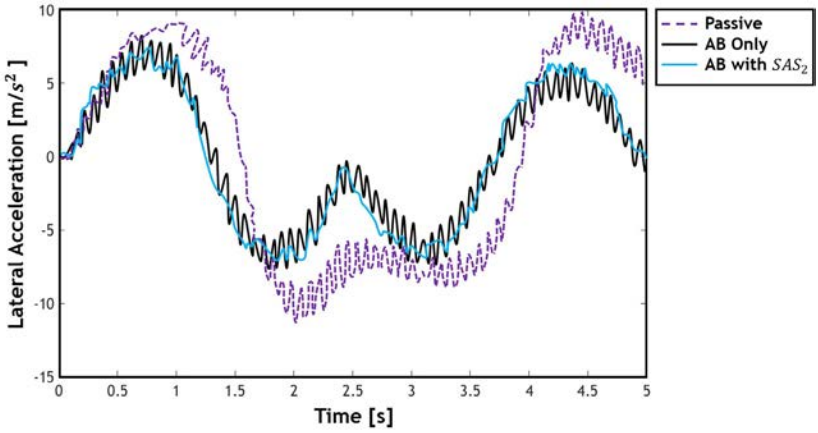

Fig. 3.12 Graph of the vehicle lateral acceleration in the double lane-change maneuver.

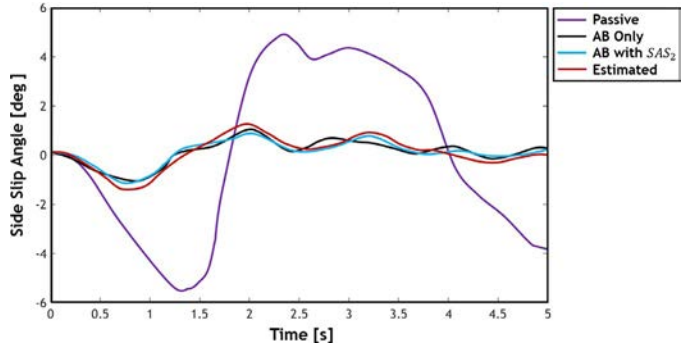

Fig. 3.13 Graph of the vehicle lateral slip angle in the double lane-change maneuver.

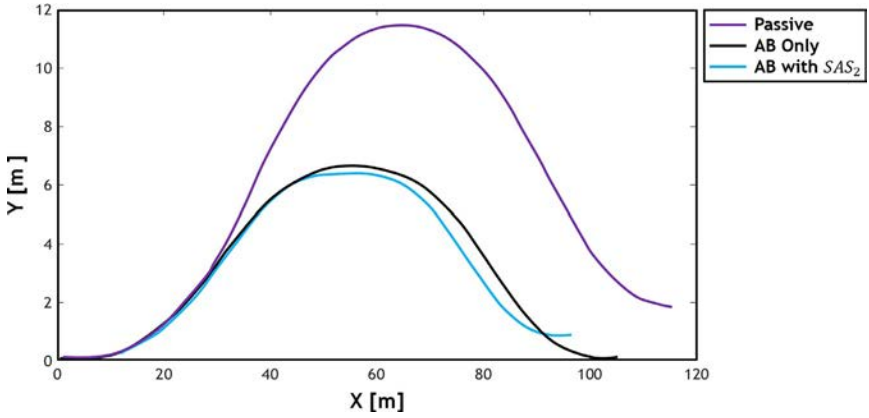

Fig. 3.14 Graph of the vehicle path in the double lane-change maneuver.

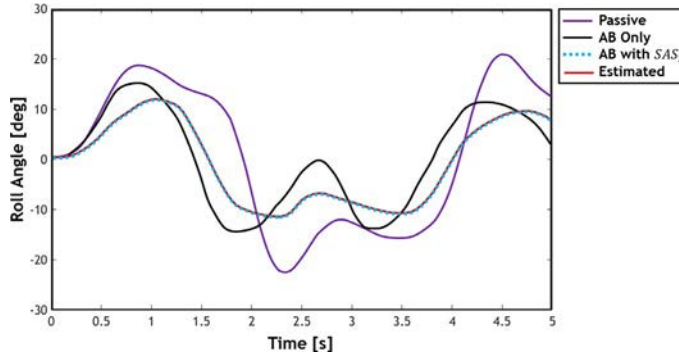

Fig. 3.15 Vehicle roll angle in the double lane-change maneuver.

observed in the vertical vibrations of the wheels on the curve for the passive system, which the AB system has not been able to omit. However, the integrated control system has smoothed the curve well. The road excitation frequency is obtained by dividing the vehicle velocity by the road wavelength. Given the assumed velocity and road wavelength values, the road excitation frequency has been obtained as 12.5 Hz, which lies in the natural frequency range of unsprung masses. The same conclusion can be drawn from Fig. 3.12, which displays the lateral acceleration. This means that the

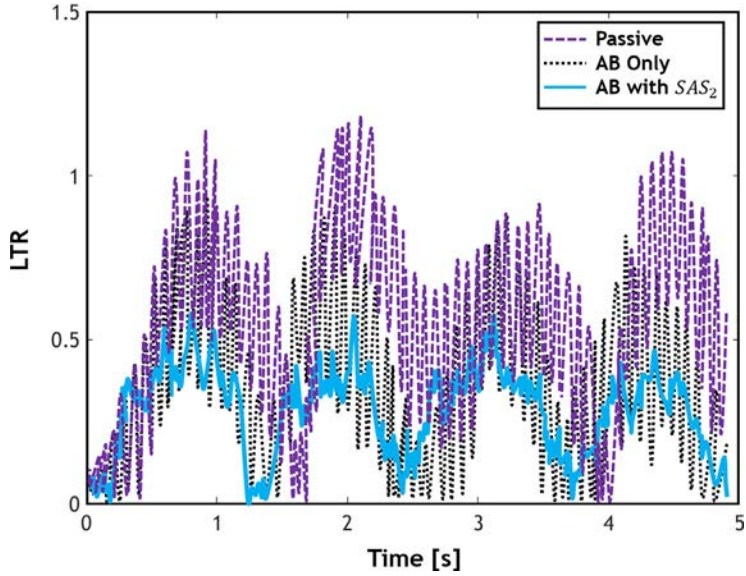

Fig. 3.16 Graph of lateral-load transfer ratio of the vehicle.

reduction in the lateral acceleration and the relevant fluctuations are clearly visible for the integrated control system, such that the maximum lateral acceleration has fallen by 35%.

The lateral slip angle of the vehicle can be seen in Fig. 3.13. It is clear in this graph that both the AB-only and AB with SAS2 systems perform well in reducing the lateral slip angle and that the estimator has performed its task with little error.

The vehicle path during the double lane-change maneuver is displayed in Fig. 3.14. As seen in the figure, both controllers have significantly affected the vehicle path and have been able to stabilize the initially uncontrolled vehicle that had not moved in the desired path. Moreover, the AB with SAS2 system has performed better than the AB only system in returning the vehicle to its initial direct path.

Changes in the roll angle are displayed in Fig. 3.15. The reduction in this angle is observed to be larger in the AB with SAS2 system than the AB-only system. This is desirable because a reduction in the roll angle in severe maneuvers prevents vehicle rollover.

The vertical tire forces have a large effect on the longitudinal and lateral tire forces. The road-holding of the tire and, consequently, handling and stability improve with the minimization of changes in the vertical tire forces. Standard deviation is a suitable index for evaluating changes in this quantity. For this reason, the standard deviation of the vertical forces of the four wheels has been computed and is shown in Table 3.9. As shown in the figure, there is a considerable decrease in the standard deviation in the integrated control system compared to the AB-only system.

The LTR as the vehicle rollover index is displayed in Fig. 3.16. As seen in the figure, the maximum value of this quantity is lower in the AB-only system than in the passive system by 22.8% while this reduction is almost 49% for the integrated control system. As an example, the control voltage of SAS2 actuators and the graph of the input voltage of the MR damper belonging to the front-right wheel are displayed in Fig. 3.17.

Table 3.9 The standard deviation of the vertical forces of the four wheels.

	Passive	AB only	AB with SAS2
FR wheel	2730.9	2475.2	1326.9
FL wheel	2682.3	2425.1	1302.3
RR wheel	2603.8	2315.2	1344.1
RL wheel	2625.3	2290.2	1353.9

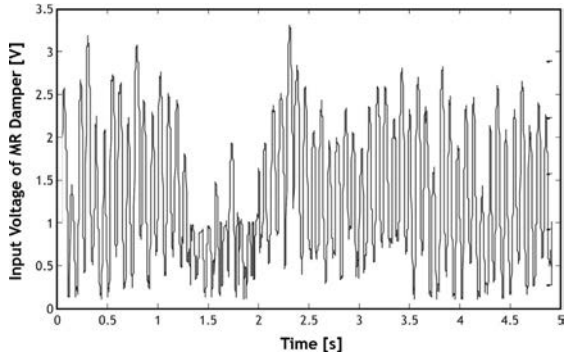

Fig. 3.17 Graph of the input voltage of the MR damper belonging to the front-right wheel.

3.6 Conclusion

In the present study, the integrated control of the vertical, roll, and yaw dynamics of a vehicle via semiactive suspension and active braking was implemented on a 14-DOF full vehicle model. In severe maneuvers, the lateral and yaw stabilities of the vehicle are undermined, and the probability of rollover increases due to the saturation of tire forces. Also, if the road excitation frequencies coincide with the natural frequencies of the wheel bounce, resonance occurs, causing fluctuations in the lateral and yaw dynamic responses of the vehicle. In this condition, the active braking system cannot improve handling and stability by itself. To deal with this problem, a structure was proposed for coordinating the semiactive suspension and active braking systems.

An adaptive sliding mode controller was presented to improve the yaw stability of the vehicle using the active braking system. The adaptive rule method was used for tuning the gains of the sliding mode controller. Furthermore, a semiactive suspension system with MR dampers was designed for changing the vertical forces exerted on the body and the tires. Two fuzzy strategies were used in its design, one of which was to improve ride comfort and the other was to improve stability and handling. Because the longitudinal and lateral tire forces depend on the vertical force exerted on the wheel, controlling the vertical force of the tires can also be addressed in the discussion on stability and handling of a vehicle. Accordingly, a semiactive suspension system was designed in the second strategy.

The analysis results show that the integrated control of the semiactive suspension and active braking systems improves the lateral and yaw stabilities

of the vehicle more than the active braking system does alone. This is more significant when the vertical vibration of the wheels results in resonance. Furthermore, the desired yaw rate was traced more accurately compared to the active braking system. It must be noted that all the state variables required by the controller to produce the control law and the road profile were estimated online with little error using the unscented Kalman filter and the measured outputs.

References

[1] X. Shen, F. Yu, Investigation on integrated vehicle chassis control based on vertical and lateral tire behavior correlativity, Veh. Syst. Dyn. J. 44 (2006) 506–519.
[2] E. Ono, Y. Hattori, Y. Muragishi, K. Koibuchi, Vehicle dynamic integrated control for four-wheel-distributed steering and four-wheel-distributed traction/braking systems, Veh. Syst. Dyn. J. 44 (2) (2006) 139–151.
[3] J. Wang, S. Shen, Integrated vehicle ride and roll control via active suspensions, Veh. Syst. Dyn. J. 46 (2008) 495–508.
[4] R. Karbalaei, A. Ghaffari, R. Kazemi, H. Tabatabaei, A new intelligent strategy to integrated control of AFS/DYC based on fuzzy logic, Int. J. Math. Phys. Eng. Sci. 1 (1) (2008) 47–52.
[5] T. Hwang, K. Park, S. Heo, S. Lee, J. Lee, Design of integrated chassis control logics for AFS and ESP, Int. J. Automot. Technol. 9 (1) (2008) 17–27.
[6] P. Gaspar, Z. Szabo, J. Bokor, "Switched systems", chapter 5, in: Active Suspension in Integrated Vehicle Control, In Tech, 2009, pp. 83–104.
[7] S.B. Lu, Y.N. Li, S.B. Choi, J.-S. Han, M.S. Seong, Global integrated control of vehicle suspension and chassis key subsystems, Proc. IMechE, Part. D, J. Automob. Eng. 224 (2010) 423–441.
[8] H. Xiao, W. Chen, H. Zhou, W.Z. Jean, Integrated control of active suspension system and electronic stability programme using hierarchical control strategy: theory and experiment, Veh. Syst. Dyn. J. 49 (2011) 381–397.
[9] S.B. Lu, Y.N. Li, S.B. Choi, L. Zheng, M.S. Seong, Integrated control on MR vehicle suspension system associated with braking and steering control, Veh. Syst. Dyn. J. 49 (2011) 361–380.
[10] P. Song, M. Tomizuka, C. Zong, A novel integrated chassis controller for full drive-by-wire vehicles, Veh. Syst. Dyn. J. 53 (2) (2015) 215–236.
[11] Y. Seongjin, K. Seungjun, Y. Heesung, Coordinated control with electronic stability control and active front steering using the optimum yaw moment distribution under a lateral force constraint on the active front steering, IMechE J., Part D 230 (5) (2016) 581–592.
[12] H. Hyundong, J. Eunhyek, Y. Kyongsu, K. Kilsoo, Integrated chassis control for optimized Tyre force coordination to enhance the limit handling performance, IMechE J., Part D 230 (8) (2016) 1011–1026.
[13] A. Bagheri, S. Azadi, A. Soltani, A combined use of adaptive sliding mode control and unscented Kalman filter estimator to improve vehicle yaw stability, Proc. IMechE, Part K, J. Multi-body Dyn. 231 (2017) 388–401.
[14] G. Verros, S. Natsiavas, C. Papadimitriou, Design optimization of quarter-car models with passive and semi-active suspensions under random road excitation, J. Vib. Control. 11 (2005) 581–606.

[15] F. Tyan, Y.F. Hong, S.H. Tu, W.S. Jeng, Generation of random road profiles, J. Chin. Soc. Mech. Eng. 4 (2) (2006) 1373–1378.
[16] A. Soltani, A. Bagheri, S. Azadi, Integrated vehicle dynamics control using semi-active suspension and active braking systems, Proc. IMechE, Part K: J. Multi-body Dyn. 232 (3) (2018) 314–329.
[17] J. Song, Development and comparison of integrated dynamics control systems with fuzzy logic control and sliding mode control, J. Mech. Sci. Technol. 27 (6) (2013) 1853–1861.
[18] R. Tchamna, I. Youn, Yaw rate and side-slip control considering vehicle longitudinal dynamics, Int. J. Automot. Eng. 14 (1) (2013) 53–60.
[19] M.A. Eltantawie, Decentralized neuro-fuzzy control for half car with semi-active suspension system, Int. J. Automot. Eng. 13 (3) (2012) 423–431.

CHAPTER 4

Trajectory planning and integrated control for high-speed autonomous lane change

4.1 Introduction

Nowadays, the applications and capabilities of the advanced driver assistance system (ADAS) are increasing dramatically. These systems play a crucial role in reducing accidents, along with providing ride comfort, reducing traffic, optimizing fuel consumption, and reducing pollution. According to the World Health Organization (WHO), more than 3400 people die each day in accidents, and tens of millions are injured each year around the world. The WHO reports also state that the expenses of accidents are more than 3% of the gross domestic products of countries [1]. Previous studies also show that about 80% of road accidents and fatalities have been caused by human error [2, 3]. Automated driving is one of the proposed solutions to reduce human error. A driverless vehicle or fully automated driving is ideal for an engineer or a car manufacturer. However, automated driving has proven to be a complex undertaking with many challenging aspects. It requires proficiency in a variety of fields such as computer vision, trajectory planning, modeling, and automated control. ADAS is one of the main solutions for reducing human error. In recent decades, many driver assistance systems have been developed to minimize driver error and avoid risky situations [4, 5]. Many of these studies have been implemented in practice, and some have attained mass production. Some of the most important ones are antilock braking systems (ABS), electronic stability control (ESC) systems, collision avoidance system (CAS), adaptive cruise control (ACC) systems, lane departure warning systems (LDWS), lane-keeping assistant (LKA) systems, lane-change assistant (LCA) systems, and automated parking systems (APS). By examining the available systems, it can be inferred that most of these

https://doi.org/10.1016/B978-0-323-85659-1.00002-1

systems either take care of the longitudinal dynamics or deal with the lateral dynamics. A few driver assistance systems can perform integrated longitudinal-lateral guidance. Even these systems have limitations and are only effective for simple maneuvers. However, in critical maneuvers, there are substantial couplings between longitudinal and lateral dynamics at different levels of dynamics, kinematics, and tire forces. Therefore, a driver assistance system that can guide the vehicle in these maneuvers is highly required.

The layout of this chapter is as follows. The longitudinal-lateral integrated guidance system is briefly introduced in the subsequent section. The vehicle and tire dynamics are presented in detail in the fourth section. The fifth section is dedicated to the introduction of utilized rules of applications and hypotheses. Details of the trajectory planning and integrated control design are explained in the sixth and seventh sections, respectively. The eighth section is dedicated to the results of the simulation and performance evaluation of the proposed integrated guidance algorithm. In the ninth section, conclusions and suggestions for future investigations are stated. Stability conditions are also provided in the appendix. References are listed in the last section.

4.2 Summary of the integrated longitudinal-lateral guidance system

The integrated longitudinal-lateral guidance system is a driver assistance system that generates an optimal trajectory primarily by considering the highway speed limit, the position of the target vehicle, the vehicle dynamics, and the tire dynamics. This system computes the proper control inputs subsequently by an integrated longitudinal-lateral controller and transmits them to brake/throttle and steering actuators. As shown in Fig. 4.1, the integrated longitudinal-lateral guidance system consists of multiple subsections. However, this chapter focuses only on trajectory planning and longitudinal-lateral control of the vehicle. In other words, it is assumed that the required information from the other subsections is entirely available.

The critical collision avoidance system is an example of the application of this algorithm. Consider a host vehicle (HV) moving at high speed on a highway (Fig. 4.2).

The target vehicle is also moving in its current lane. In an instant, the target vehicle decelerates so severely that collision is inevitable if the host vehicle only uses its brake system. In this situation, the only possible approach for the host vehicle to avoid a collision is to slow down and move

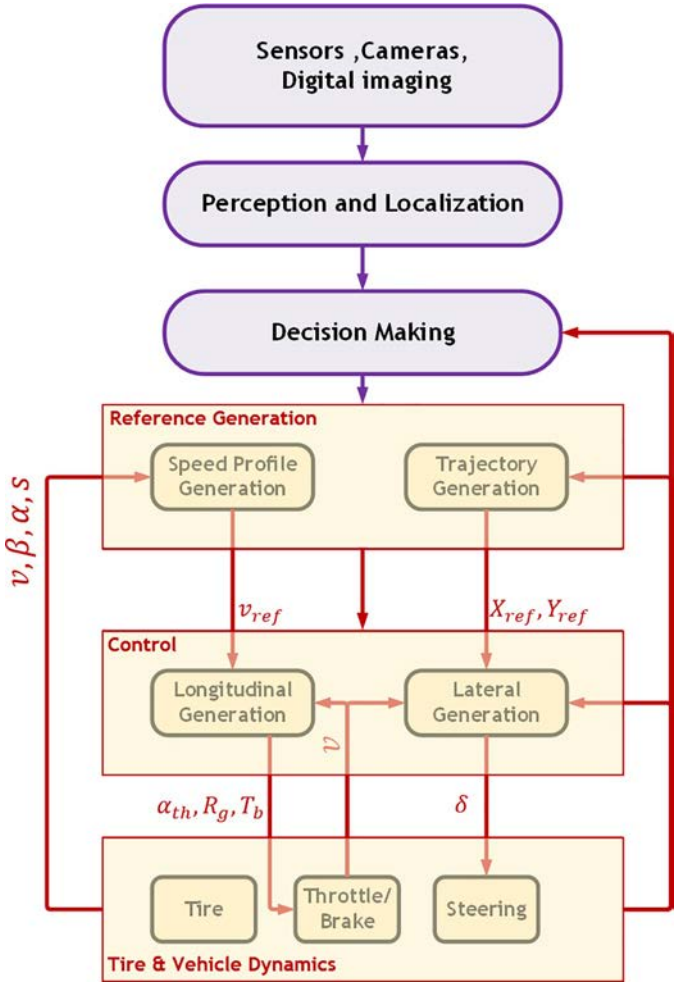

Fig. 4.1 The integrated longitudinal-lateral guidance system of the vehicle.

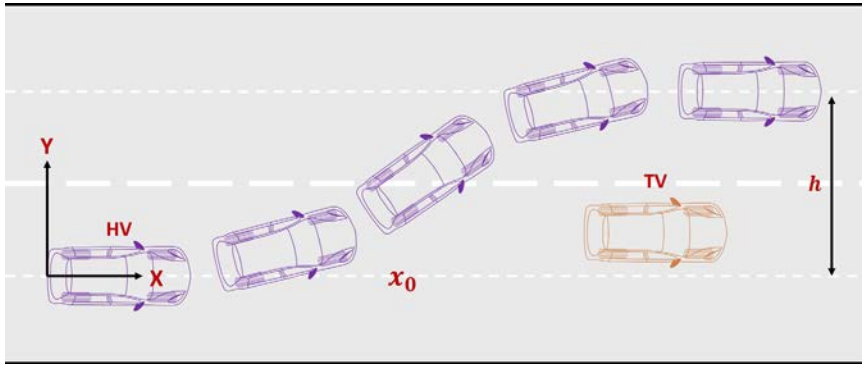

Fig. 4.2 The lane-change maneuver.

to the adjacent lane. It is assumed that the initial speed and distance between the two vehicles allow for such a maneuver. At the end of this section, an overview of the most important challenges is provided in integrated vehicle guidance. Selecting an appropriate dynamic model for the vehicle and tire is the first challenge. The behavior of the vehicle and tire in the maneuver must be carefully analyzed to select an appropriate model. In the following, the applied hypotheses and rules are extracted according to these analyses. Undoubtedly, these rules will be useful in various steps of trajectory planning and integrated control design. Another important challenge is that the proposed algorithm must have an acceptable computational cost. In addition, the required data must be measurable or identifiable using the existing equipment. Eventually, the stability of the control algorithm is a concern that must be addressed.

4.3 Dynamic model

The vehicle dynamics model used in this research is the bicycle model [6]. However, a few considerations, such as longitudinal load transfer and a nonlinear tire model, are taken into account to improve the accuracy of the model. The dynamic model can be divided into three sections, including equations of motion for the vehicle, equations of motion for the wheel, and tire dynamics. Each of these sections will be discussed thoroughly in the following.

4.3.1 Equations of motion for the vehicle

The bicycle model of the vehicle is depicted in Fig. 4.3. This model includes three degrees of freedom, namely x, y, and ψ, which indicate the longitudinal position, lateral position, and direction angle of the vehicle, respectively. The velocity of the vehicle's center of mass is v, which is decomposed to v_x and v_y in the local coordinate system of the vehicle. The steering and the sideslip angles are indicated by δ and β, respectively. Besides, it is assumed that the vehicle can only steer by its front wheels.

It should be noted that tire forces are also expressed in terms of local tire coordinates. The force collinear with the tire axis is indicated by the y index, and the forces perpendicular to it are denoted by the x index. The distance between the center of mass and the front and rear axles is represented by l_f and l_r, respectively. The height of the aerodynamic center and the height of the center of mass of the vehicle are h_{cg} and h_{aero}, respectively. In addition, the vehicle mass is shown by m, and its moment of inertia is

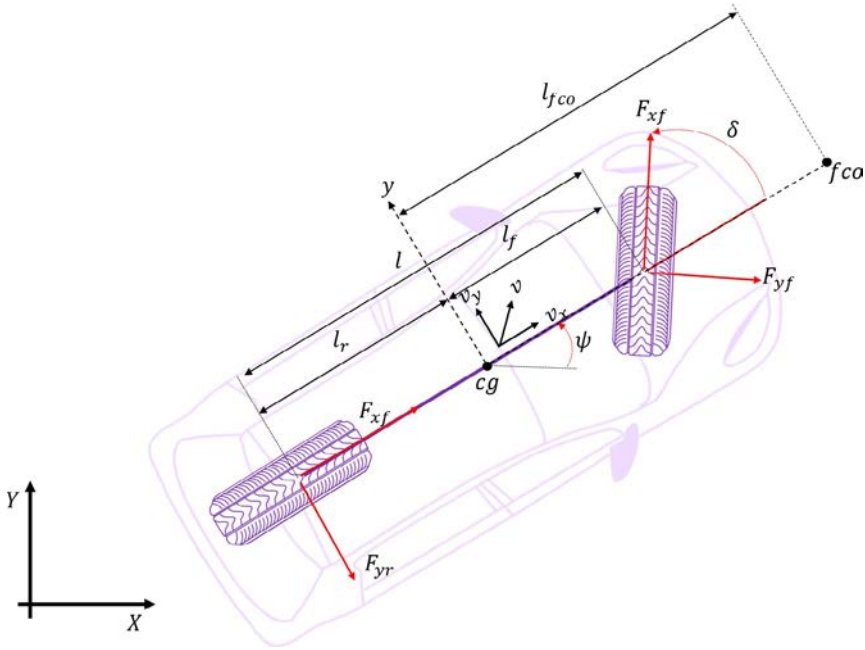

Fig. 4.3 The bicycle model.

demonstrated by I_z. According to Fig. 4.3 and by applying Newton's second law, vehicle motion can be described by (4.1)

$$ma_{x_{cg}} = F_{x_f}\cos\delta - F_{y_f}\sin\delta + F_{x_r} - F_{aero} \tag{4.1a}$$

$$ma_{y_{cg}} = F_{x_f}\sin\delta + F_{y_f}\cos\delta + F_{y_r} \tag{4.1b}$$

$$I_z\ddot{\psi} = l_f\left(F_{x_f}\sin\delta + F_{y_f}\cos\delta\right) - l_rF_{y_r} \tag{4.1c}$$

In the equations of motion, *f* and *r* indicate the front and rear wheels, respectively. The symbol *Faero* means the aerodynamic force, which is defined by Eq. (4.6).

$$F_{aero} = \frac{1}{2}\rho C_dA_F(v_x + v_{wind})^2 \tag{4.2}$$

where ρ, C_d, and v_{wind} indicate the air density, aerodynamic drag coefficient, and wind velocity, respectively. The symbol A_F is the frontal projected area of the vehicle, which can be estimated by $1.6 + 0.00056(m - 765)$ for passenger cars with a mass of 800–2000 kg [6]. Also, the longitudinal and lateral accelerations of the mass center are defined by Eqs. (4.3a) and (4.3b), respectively.

$$a_{x\mathrm{cg}} = \dot{v}_x - v_y\dot{\psi} \tag{4.3a}$$

$$a_{y\mathrm{cg}} = \dot{v}_y + v_x\dot{\psi} \tag{4.3b}$$

At the end of this section, it is necessary to mention a crucial and practical concept called the center of oscillation. In some cases, trajectory planning and controller design are performed much more accessible by this concept, which indicates the importance of the center of oscillation [7]. Front/rear centers of oscillation are the points at which the lateral forces of the rear/front tires do not affect the lateral acceleration of these points, respectively. These points are located on the longitudinal axis of the car. Also, the front and rear centers of oscillation are adjacent to the front and the rear axles, respectively. In this study, the concept of the center of oscillation will be used in trajectory planning and integrated longitudinal-lateral controller design. The front center of oscillation is shown by *fco* in Fig. 4.3, and its distance from the vehicle's center of mass is l_{fco}. The value of l_{fco} can be determined by the concept of the front center of oscillation in addition to writing the longitudinal and lateral dynamics equations of the fco point. This value is equal to $I_z/(ml_{\mathrm{r}})$ [8]. By using the concept of front oscillation center, the lateral dynamics of the vehicle can be expressed by Eq. (4.4)

$$ma_{y\mathrm{fco}} = \frac{l}{l_{\mathrm{r}}}\left[F_{x_{\mathrm{f}}}\sin\delta + F_{y_{\mathrm{f}}}\cos\delta\right] \tag{4.4}$$

where $a_{y\mathrm{fco}}$ is the lateral acceleration of the front center of oscillation in the local coordinate system and can be determined easily by the concept of relative acceleration (4.5).

$$a_{y\mathrm{fco}} = a_{y\mathrm{cg}} + l_{\mathrm{fco}}\ddot{\psi} = \dot{v}_y + v_x\dot{\psi} + l_{\mathrm{fco}}\ddot{\psi} \tag{4.5}$$

It can be inferred from Eq. (4.4) that the lateral acceleration of the front center of oscillation is independent of the force of the rear tires. As can be observed in the trajectory of the integrated controller design section, using Eq. (4.4) instead of Eq. (4.1b) would be very effective.

4.3.2 Equation of motion for the wheel

The wheel is one of the most important subsystems in the study of the dynamic behavior of the vehicle within acceleration and deceleration. The free-body diagram of a wheel is shown in Fig. 4.4.

Assuming $T = T_{\mathrm{e}} - T_{\mathrm{b}}$ in Fig. 4.4, the equation of motion of the wheel can be expressed by Eq. (4.6) using Newton's second law.

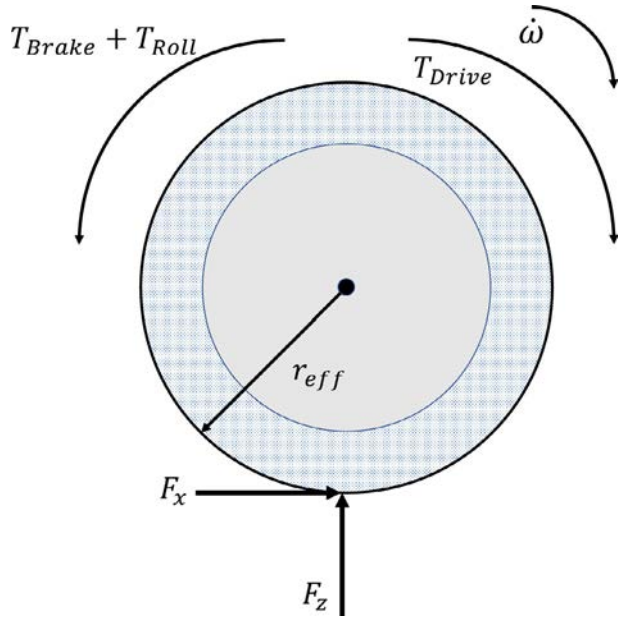

Fig. 4.4 The free-body diagram of a wheel during acceleration.

$$I_{\mathrm{w}}\dot{\omega} = T - F_x R_{\mathrm{w}} - T_{\mathrm{Roll}} \tag{4.6}$$

where I_w represents the mass moment of inertia of the wheel, F_x is the longitudinal force of the tire, R_{w} is the effective radius of the wheel, T_{e} is the engine torque transmitted to the wheel, T_{b} is the braking torque, and T_{Roll} is the torque caused by rolling resistance, which can be calculated by Eq. (4.7). The (→) direction shown in Fig. 4.4 for F_x is related to the acceleration state.

$$T_{\mathrm{Roll}} = f_{\mathrm{r}} F_z R_{\mathrm{w}} \tag{4.7}$$

where f_{r} and F_z indicate the rolling resistance coefficient and the normal force of the tire, respectively.

4.3.3 Tire dynamics

Assuming that the friction force of the tires is linearly dependent on the vertical force of each tire, the longitudinal or lateral friction force of the tire can be expressed by Eq. (4.8)

$$F_{\gamma_\tau} = \mu_{\gamma_\tau} F_{z_\tau}, \quad \gamma \in \{x, y\}, \quad \tau \in \{\mathrm{f}, \mathrm{r}\} \tag{4.8}$$

where F_{z_τ} indicates the vertical load of each front and rear tire and μ_{γ_τ} represents the longitudinal or lateral friction coefficient of the corresponding tire. Although the accurate calculation of the vertical force of the tire can be easily performed by considering the dynamics of the suspension system, it will increase the order of the dynamic model. To avoid this problem, the dynamics of the suspension system are not considered in this study. In addition, the vertical force of the tires is calculated approximately by considering the longitudinal acceleration of the vehicle.

$$F_{z_\mathrm{f}} = \frac{m}{2l}\left(gl_\mathrm{r} - a_{x_\mathrm{cg}}h_\mathrm{cg} - \frac{F_\mathrm{aero}h_\mathrm{aero}}{m}\right) \tag{4.9a}$$

$$F_{z_\mathrm{r}} = \frac{m}{2l}\left(gl_\mathrm{f} + a_{x_\mathrm{cg}}h_\mathrm{cg} + \frac{F_\mathrm{aero}h_\mathrm{aero}}{m}\right) \tag{4.9b}$$

Given the relationships of Eqs. (4.9a) and (4.9b), it is clear that the sum of the vertical forces of the tires is equal to the force of the vehicle weight (mg). The $\mu_{\gamma_\tau,\,\varepsilon}$ coefficient can also be calculated using the Pacejka/Magic Formula (MF) [9].

$$\mu_{\gamma_\tau} = \frac{s_{\gamma_\tau}}{s_\tau}\mu_\tau, \quad \gamma\in\{x,y\}, \quad \tau\in\{\mathrm{f},\mathrm{r}\} \tag{4.10a}$$

$$\mu_\tau = D\sin\left[C\arctan\left(Bs_\tau\right)\right], \quad \tau\in\{\mathrm{f},\mathrm{r}\} \tag{4.10b}$$

$$s_\tau = \sqrt{{s_{x_\tau}}^2 + {s_{y_\tau}}^2}, \quad \tau\in\{\mathrm{f},\mathrm{r}\} \tag{4.10c}$$

B, C, and D are constant coefficients that are determined based on the tire and road conditions. This study assumes that these constants are available and identical for all tires. μ_τ indicates the total friction coefficient, which is a function of the total slip (s_τ). The total slip of the tire is a function of longitudinal slip (s_{x_τ}) and lateral slip (s_{y_τ}). The longitudinal slip of the front or rear tires is a function of the longitudinal velocity of the contact point of the tire with the road surface ($v_{\mathrm{cw}_{\tau,\varepsilon}}$), and the equivalent longitudinal of the wheel rotation ($v_{\mathrm{rw}_{\tau,\varepsilon}}$), which is defined by Eq. (4.11)

$$s_{x_\tau} = \frac{v_{\mathrm{rw}_\tau} - v_{\mathrm{cw}_\tau}}{\max\left(v_{\mathrm{rw}_\tau}, v_{\mathrm{cw}_\tau}\right)}, \quad \tau\in\{\mathrm{f},\mathrm{r}\} \tag{4.11}$$

The longitudinal velocity of the contact point of the tire with the road surface for front and rear tires is also calculated by Eqs. (4.12a) and (4.12b), respectively.

$$v_{\mathrm{cw}_\mathrm{f}} = v + \dot{\psi}\beta l_\mathrm{f} \tag{4.12a}$$

$$v_{cw_r} = v - \dot{\psi}\beta l_r \tag{4.12b}$$

If the angular velocity of the wheel is indicated by ω_τ, the equivalent longitudinal velocity of the wheel rotation (v_{rw_τ}) is obtained from Eq. (4.13)

$$v_{rw_\tau} = R_{w_\tau}\omega_\tau, \quad \tau \in \{f, r\} \tag{4.13}$$

The slip angle of the tire must be determined first to calculate the lateral slip. The slip angles of the front tire (α_f) and rear tire (α_r) can be determined by Eqs. (4.14a) and (4.14b), respectively.

$$\alpha_f = \delta - \tan^{-1}\left(\frac{v_y + \dot{\psi} l_f}{v_x}\right) \tag{4.14a}$$

$$\alpha_r = -\tan^{-1}\left(\frac{v_y - \dot{\psi} l_r}{v_x}\right) \tag{4.14b}$$

After determining the slip angle, the lateral slip can be calculated by Eqs. (4.15a) and (4.15b) [10].

First case ($s_{x_\tau} \leq 0$):

$$s_{y_\tau} = \frac{v_{rw_\tau}\sin(\alpha_\tau)}{v_{cw_\tau}}, \quad \tau \in \{f, r\} \tag{4.15a}$$

$$s_{y_\tau} = \tan(\alpha_\tau), \quad \tau \in \{f, r\} \tag{4.15b}$$

The parameters of the dynamic model of the vehicle are presented in Table 4.1.

4.4 Applied rules and important assumptions

As stated before, the proposed algorithm can be used for high speeds on highways. By careful study of the vehicle motion in these situations, crucial practical rules can be extracted, which will be very helpful in the trajectory planning and integrated controller design. These rules are summarized as follows.

Rule 1: Due to the vehicle's high speed, the direction angle (ψ) and steering angle (δ) must be small to maintain vehicle stability.

Rule 2: Braking proportionality: According to this rule, the distribution of braking torque between the front and rear wheels is proportional to the normal force of the front and rear tires.

Table 4.1 The vehicle parameters [9].

Value	Unit	Symbol
1450	kg	m
2740	kg m^2	I_z
1.1	m	l_f
1.6	m	l_r
0.4	m	h_{cg}
0.4	m	h_{aero}
0	m/s	v_{wind}
0.85	m	w_{HV}
2	m	b_f
0.3	m	R_w
0.9	kg m^2	I_w
0.015	–	f_r
7	–	B
1.6	–	C
0.52	–	D

Rule 3: Traction torque is applied to the front wheels only; therefore, the longitudinal slip of the rear tires (compared to the front tires) is negligible in these conditions. Thus, the longitudinal force of these tires can be ignored in comparison with the front tires.
Rule 4: The slip angle of the tires is small in the mentioned maneuver. Thus, $\sin(\alpha_{\tau,\varepsilon}) \approx \alpha_{\tau,\varepsilon}$ and $\tan(\alpha_{\tau,\varepsilon}) \approx \alpha_{\tau,\varepsilon}$ approximations are valid, and Eqs. (4.15a) and (4.15b) turn to Eq. (4.16)

$$s_{y_\tau} = K_{\alpha_\tau}\alpha_\tau, \quad \tau \in \{f, r\} \tag{4.16}$$

where $K_{\alpha_\tau} = v_{rw_\tau}/v_{cw_\tau}$ for $s_{x_\tau} \leq 0$, and $K_{\alpha_\tau} = 1$ for $s_{x_\tau} > 0$.

4.5 Trajectory planning

Two objectives of collision avoidance and feasibility must be met in trajectory planning. Regarding the previous studies, it can be concluded that the topic of trajectory in a dynamic environment has been studied extensively. In a recent study, researchers performed a detailed survey of various proposed methods in the field of real-time trajectory planning of vehicles [11]. According to the mentioned study and other references, it can be stated that considering the dynamic limitations of the vehicle and tire is among the neglected topics in trajectory planning. Some of the most important limitations of trajectory planning methods are mentioned in the following. A few

of the investigations assumed that vehicle speed is constant [12]. Many researchers, such as [11], have only considered the kinematic constraints of the vehicle in trajectory planning. Some have approximated the behavior of the vehicle with a linear dynamic model [13]. Also, several studies have assumed that the maximum longitudinal or lateral acceleration is constant [14]. However, the assumptions made in recent studies are not consistent with real situations because the tire enters its saturation zone in critical maneuvers. In such maneuvers, the tire dynamics and, consequently, the behavior of the vehicle will be completely nonlinear. In addition, a tire can provide a certain amount of output force. This implies that the maximum lateral/longitudinal force that the tire can supply decreases if the longitudinal/lateral force of the tire increases. Hence, a constant maximum longitudinal/lateral acceleration cannot be considered in critical maneuvers for the entire trajectory planning process. Valid maximum longitudinal or lateral acceleration is different at each moment. Jeon et al. has conducted research that considered the nonlinear dynamics of the vehicle and tire in trajectory planning. Their proposed method is general, which can be used for all driving conditions. However, the computational cost of their proposed method is high and may also be stuck with the local minimum. On the other hand, trajectory planning for high-speed lane-change maneuvers is relatively simple, and it appears that the appropriate trajectory can be computed by more straightforward methods such as the use of polynomials [7]. The studies carried out by Jafarian [15] and Shojaei [16] are among the studies that used polynomials for trajectory planning of cars and semitrailers, respectively. Similar methods are used in the mentioned studies, and a suitable trajectory is planned based on collision avoidance and the dynamic capacity of the vehicle. The ability to assess the possibility of maneuvering as well as the ability for utilization in a variety of traffic conditions are among the capabilities of Ref. [15]. Ref. [16] is also of great importance due to its application for trailers. However, these studies have fundamental limitations. The most critical limitation is assuming the host vehicle speed as a constant value. The algorithms presented in these two studies are not useful for critical collision avoidance maneuvers because braking/acceleration is also required in addition to changing the lanes. Another limitation is that it is necessary to solve several nonlinear equations simultaneously to find the final maneuver time. Because trajectory planning is an online procedure, these equations may not be solved in a short time; therefore, problems may occur in the process of guidance of the vehicle.

Based on the above explanations, it can be concluded that trajectory planning in critical maneuvers and dynamic environments requires further research.

In the present study, different trajectories are computed for different accelerations according to the collision avoidance criteria, and valid trajectories are determined by considering the highway speed limit. Subsequently, the maximum required friction is determined in each trajectory by considering the vehicle and tire dynamics. On the other hand, the maximum available friction is also given; therefore, trajectories at which the maximum friction is greater than the maximum permissible friction are unacceptable. Eventually, the trajectory with the minimum required friction is selected as the optimal trajectory. In the following section, details of the collision avoidance strategy are provided at first, and then, an evaluation of the feasibility of the trajectory will be discussed.

4.5.1 Collision avoidance

Collision avoidance aims to design a trajectory in which the host vehicle passes the target vehicle at a safe distance and moves to the adjacent line. An infinite number of trajectories exist to accomplish this end. However, some of these trajectories are not feasible in terms of vehicle and tire dynamics. These trajectories will be examined in the next section. This section focuses on trajectories that meet the requirements of safe distance and the speed limit of the highway. The lateral position of the two vehicles at the moment of arrival is shown in Fig. 4.5.

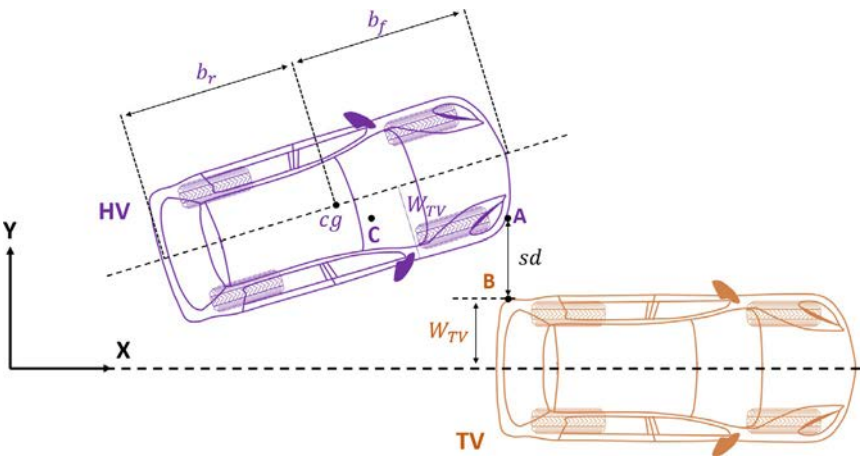

Fig. 4.5 The lateral distance between the host vehicle and the target vehicle at the moment of arrival.

In Fig. 4.5, the distance from the center of mass of the host and target vehicles to the farthest points of the front and rear bumper are indicated with b_f and b_r, respectively. The width of the vehicle is also considered to be $2w_{HV}$. The coordinates of the right rear corner of the target vehicle in terms of time (t) are ($X_B(t)$, $Y_B(t)$), which is expressed in the $X-Y$ inertial frame. The lateral position of the target vehicle at the arrival moment is also assumed to be equal to w_{TV}. In addition, it is assumed that the $X_B(t)$ and $Y_B(t)$ functions are specified at the beginning of the maneuver. The optimal motion of the mass center of the host vehicle in the lateral direction $Y_R(t)$ is considered as a fifth-degree polynomial of time. The reason for using a fifth-degree polynomial is that the trajectories of the fifth degree are smooth for being twice differentiable. Besides, a fewer number of points are required to determine the trajectory. The fifth-degree trajectory can be defined by knowing the values of the variables at two points [11]. According to the above, the optimal lateral position of the center of mass of the host vehicle in the inertial coordinate system can be expressed by Eq. (4.17)

$$Y_R(t) = b_1 t^5 + b_2 t^4 + b_3 t^3 + b_4 t^2 + b_5 t + b_6 \tag{4.17}$$

In the above equation, b_1 to b_6 are constant coefficients used to define a trajectory, and index R represents the desired condition. It is also assumed that at the beginning of the maneuver, the mass center of the host vehicle is located at the origin of the coordinate system. Also, lateral velocity and acceleration are zero both at the beginning and at the end of the maneuver. Furthermore, lateral displacement of the center of mass of the vehicle in the entire maneuver is denoted by h. The total time of the maneuver is assumed to be t_f, which is unknown. By applying these considerations to Eq. (4.17), the optimal lateral position of the center of mass can be determined by Eq. (4.18)

$$Y_R(t) = \left(\frac{6h}{{t_f}^5}\right) t^5 - \left(\frac{15h}{{t_f}^4}\right) t^4 + \left(\frac{10h}{{t_f}^3}\right) \tag{4.18}$$

This study assumes that the vehicle moves with constant acceleration in the longitudinal direction during the study. However, according to the dynamics of the brake/throttle system, it cannot be assumed that the desired acceleration is available since the beginning of the maneuver. Hence, the desired longitudinal acceleration (a_{xR}) is suggested to be calculated by Eq. (4.19)

$$\frac{A_{x_R}(s)}{A_x(s)} = \frac{K}{s+K} \tag{4.19}$$

where k is the time constant of the brake/throttle system. Assuming that the final acceleration of the host vehicle is a_{HV}(constant), by applying inverse Laplace transformation on Eq. (4.19), the desired acceleration will be in the form of Eq. (4.20)

$$a_{x_R}(t) = a_{HV}\left(1 - e^{-Kt}\right) \tag{4.20}$$

Because the vehicle is in the direction of the highway at the beginning of the movement, it can be stated that its initial longitudinal velocity is $v_R(0) = v_0$. Assuming that the center of the vehicle mass is located on the origin of the inertial reference frame ($X_R(0) = 0$), and the heading angle is small, the desired longitudinal position of the vehicle can be calculated as a function of time Eq. (4.21) by integrating the acceleration equation twice (Eq. 4.20).

$$X_R(t) = a_{HV}\left[\frac{1}{K^2}\left(1 - e^{-Kt}\right) - \frac{t}{K} + \frac{t^2}{2}\right] + v_0 t \tag{4.21}$$

According to rule number 1 and by observing Fig. 4.5, the longitudinal position of point A can be expressed by Eq. (4.22)

$$X_A(t) = X_R(t) + b_f \tag{4.22}$$

As for the target vehicle, $X_B(t)$ and $Y_B(t)$ can be any arbitrary functions. However, to complete the formulation, it is assumed that the target vehicle moves at a constant acceleration of a_{TV}. Assuming that the initial longitudinal velocity and position of the vehicle are v_0 and x_0, the longitudinal position of the target vehicle can be described as (4.23)

$$X_B(t) = \frac{1}{2}a_{TV}t^2 + v_0 t + x_0 \tag{4.23}$$

After determining the position of points A and B as functions of time, the final time of the maneuver t_f can be obtained by applying the safe pass condition. According to Fig. 4.5, it is evident that $X_A(t)$ and $X_B(t)$ are equal at the arrival time t_r. Therefore, the value of t_r is determined by equating the right side of Eqs. (4.22) and (4.23). After determining t_r, the value of $Y_B(t_r)$ can easily be calculated. For the sake of simplicity, the value of $Y_B(t_r)$ will be indicated by w_{TV}. Based on Fig. 4.5, Eq. (4.24) relates the lateral position of points A and B at time t_r.

$$Y_A(t_r) = Y_B(t_r) + sd \tag{4.24}$$

where $Y_A(t_r)$ is calculated by Eq. (4.25)

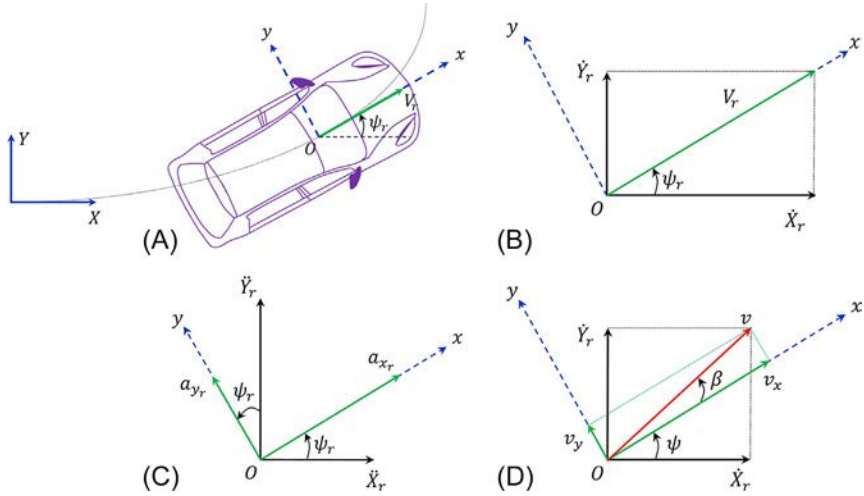

Fig. 4.6 Inertial and local coordinate systems.

$$Y_{\mathrm{A}}(t_{\mathrm{r}}) = Y_{\mathrm{R}}(t_{\mathrm{r}}) - w_{\mathrm{HW}}\cos\psi_{\mathrm{R}} + b_{\mathrm{f}}\sin\psi_{\mathrm{R}} \tag{4.25}$$

By the determination of $\dot{Y}_{\mathrm{R}}(t_{\mathrm{r}})$ and $v_{\mathrm{R}}(t_{\mathrm{r}})$, the value of $\psi_{\mathrm{R}}(t_{\mathrm{r}})$ can be calculated (Fig. 4.6). Eventually, according to rule number 1, Eq. (4.25) can be expressed in a simplified form of Eq. (4.26)

$$Y_{\mathrm{A}}(t_{\mathrm{r}}) = Y_{\mathrm{R}}(t_{\mathrm{r}}) - w_{\mathrm{HV}} + b_{\mathrm{f}}\frac{\dot{Y}_{\mathrm{R}}(t_{\mathrm{r}})}{v_{\mathrm{R}}(t_{\mathrm{r}})} \tag{4.26}$$

By substituting $Y_{\mathrm{A}}(t_{\mathrm{r}})$ in Eq. (4.24) and simplifying the results, a quantic equation will be obtained.

$$t_{\mathrm{f}}{}^5 - 10ht_{\mathrm{r}}{}^2\left(t_{\mathrm{c1}} + \frac{3b_{\mathrm{f}}}{v_{\mathrm{R}}(t_{\mathrm{r}})}\right)t_{\mathrm{f}}{}^2 + 15ht_{\mathrm{r}}{}^3\left(t_{\mathrm{c1}} + \frac{4b_{\mathrm{f}}}{v_{\mathrm{R}}(t_{\mathrm{r}})}\right)t_{\mathrm{f}} \tag{4.27}$$

$$- 6ht_{\mathrm{r}}{}^4\left(t_{\mathrm{c1}} + \frac{5b_{\mathrm{f}}}{v_{\mathrm{R}}(t_{\mathrm{r}})}\right) = 0$$

By solving Eq. (4.27), the value of t_{f} is determined; therefore, the trajectory is completely determined.

In this step, different trajectories will be achieved for different values of a_{HV} in trajectory planning. Although the range and step size of a_{HV} are arbitrary, this study assumes that the a_{HV} is selected from maximum possible braking deceleration (a_{bmax}) to maximum possible thrust acceleration (a_{tmax}) with the step size of 1 m/s^2. A trajectory will be obtained for each

acceleration. However, the trajectories in which the vehicle's final speed fall off the speed limits of the highway ($[V_{\min}\ V_{\max}]$) will not be accepted.

4.5.2 Feasibility analysis of trajectories

In general, the feasibility analysis of trajectories is a complicated problem because both vehicles and tire dynamics must be taken into account. If the trajectory is planned without considering the properties of vehicle and tire dynamics, the vehicle motion may become unstable despite a decent control system. For example, suppose that a sharp steering angle is applied during longitudinal speed reduction. In such conditions, the tire may not be able to provide the required longitudinal and lateral forces at the same time (the total capacity of the tire force is limited); therefore, the vehicle will become unstable. This section aims to provide a novel approach in which the feasibility analysis of the trajectory for high-speed maneuvers can be done by only solving a set of simple algebraic equations, without solving differential equations (including wheel dynamics, vehicle motion equations, and controller). This analysis is based on the frictional capacity of the tire and road. The trajectory will not be feasible if the tire and road fail to provide the required friction for it. Otherwise, the trajectory will be feasible. The closer the required coefficient of friction is to the maximum available coefficient of friction, the more critical the proposed trajectory will be. Hence, the criticality of the proposed feasible trajectories is also determined in this section.

It should be noted that the suggested trajectories were completely determined at the end of the collision avoidance section. Therefore, the values of the longitudinal and lateral acceleration of the center of mass, along with the lateral angle of the vehicle, are available in terms of time for each trajectory. These values can be used for the feasibility analysis of the trajectory. Details of the proposed method will be summarized as follows.

According to rule number 1 and by observing Eq. (4.1a), it can be assumed that the value of $F_{y_f}\sin\delta$ is negligible compared to $F_{x_f}\cos\delta + F_{x_r}$. Similarly, in Eq. (4.4), it can be assumed that the value of $F_{x_f}\sin\delta$ is negligible compared to $F_{y_f}\cos\delta + F_{y_r}$. Hence, Eqs. (4.1a) and (4.4) can be rewritten in the form of Eqs. (4.28a) and (4.28b), respectively.

$$a_{x\mathrm{cg}} = \frac{1}{m}\left(F_{x_f} + F_{x_r} - F_{\mathrm{aero}}\right) \tag{4.28a}$$

$$a_{y\mathrm{fco}} = \frac{l}{ml_r}F_{y_f} \tag{4.28b}$$

Given that the lateral acceleration of the center of mass is known, the lateral acceleration of the center of oscillation is determined using Eq. (4.5). Subsequently, the lateral force of the front tires can be determined by Eq. (4.28b). The value of F_{y_r} can also be calculated by substituting F_{y_f} in Eq. (4.1b). Assuming that the vehicle is moving tangent to the desired trajectory, a_{xcg} is equal to the desired longitudinal acceleration of the center of mass. On the other hand, by knowing the desired speed and using Eq. (4.2), the value of F_{aero} at each time is also available. Now, Eq. (4.28a) can be used to determine the value $(F_{x_f} + F_{x_r})$ at any given time in the trajectory. In addition, the second and third rules (braking mode of Eq. (4.29) and traction mode of Eq. (4.30)) can be used to determine the values of F_{x_f} and F_{x_r}.

$$F_{x_\tau} = \frac{F_{z_\tau}}{mg}\left(ma_{x\text{r}} + F_{\text{aero}}\right), \quad \tau \in \{\text{f}, \text{r}\} \tag{4.29}$$

$$F_{x_\text{f}} = \left(ma_{x\text{r}} + F_{\text{aero}}\right), \quad F_{x_\text{r}} = 0 \tag{4.30}$$

Therefore, it is possible to calculate the coefficient of friction between the front and rear tires within the motion by considering the bicycle vehicle model. In addition, the maximum required coefficient of friction $\mu_{\text{req,max}}$ can be determined (4.31)

$$\mu_{\text{req, max}} = \max\left(\frac{\sqrt{{F_{x_\text{f}}}^2 + {F_{y_\text{f}}}^2}}{F_{z_\text{f}}}, \frac{\sqrt{{F_{x_\text{r}}}^2 + {F_{y_\text{r}}}^2}}{F_{z_\text{r}}}\right) \tag{4.31}$$

The trajectory would be infeasible if the maximum required coefficient of friction ($\mu_{\text{req,max}}$) is greater than the maximum available coefficient of friction ($\mu_{\text{ro,max}}$) at least at one point throughout the trajectory. It is necessary to calculate $\mu_{\text{req, max}}$ for each of the suggested trajectories in the collision avoidance section and compare it with $\mu_{\text{ro,max}}$ to select the optimal trajectory. Eventually, the trajectory that meets the condition $\mu_{\text{req,max}} < \mu_{\text{ro,max}}$ with the lowest $\mu_{\text{req, max}}$, is selected as the optimal trajectory.

The question that may arise here is whether the criterion of the required maximum coefficient of friction is sufficient for selecting the trajectory. Fundamentally, various criteria such as collision avoidance, stability, ride comfort, and fuel consumption can be considered in choosing the trajectory. All criteria would be important if the maneuver was a normal lane change. However, the situation is different for critical maneuvers. In such maneuvers, collision avoidance and vehicle stability are of very high priority, and other criteria are insignificant. Because the collision avoidance condition is assumed identical for all the suggested trajectories in this study, all routes are similar. Hence,

it can be stated that the trajectory that provides more stability for the vehicle will be optimal. According to Eq. (4.10b), increasing the coefficient of friction decreases the total slip of the tire, and consequently increases the lateral slip angle of the vehicle. Increasing the lateral slip angle also means that the vehicle is getting closer to instability. Based on the above explanations, it can be concluded that the criterion of the maximum required coefficient of friction is an appropriate criterion for the critical maneuver in hand.

4.6 Integrated longitudinal-lateral control

The integrated longitudinal and lateral dynamic control is inevitable while guiding the vehicle in critical maneuvers. Various control methods were proposed to solve this interesting problem in the literature. Some of the most important limitations of these investigations are as follows. Many studies are done based on the kinematic model of the vehicle [17, 18]. The majority of the studies in this area utilize a linear dynamic model in controller design [19]. A number of references have considered integrated longitudinal and lateral control only for collision avoidance analysis [20, 21]. However, the methods introduced in these references do not consider longitudinal accelerations; hence, they cannot be applied for all types of maneuvers. One of the studies that considered nonlinear vehicle dynamics in the subject of integrated control design was published by Attia et al. [22]. They used the idea of the Lyapunov function in longitudinal control and assumed that vehicle mass, tire inertia, and resistant rolling torque have uncertainties. In the mentioned research, a single-wheel model of the vehicle was used for longitudinal control, and the longitudinal slip of the tire was not considered. In addition, the model predictive control approach was used for lateral control. High computational cost as well as the possibility of being stuck in the local minimum during the optimization are the main disadvantages of the mentioned approach. Hence, it can be concluded that the problem of integrated vehicle control in critical maneuvers has received less attention.

In this section, an integrated controller will be proposed for longitudinal speed control as well as lateral position control using a sliding mode control approach of reference [23]. The torques applied to the wheels (throttle/brake) are the control input of the longitudinal control, and the steering angle is the control input of lateral control.

4.6.1 Longitudinal control

In this study, longitudinal control aims to make sure the longitudinal speed of the vehicle's center of mass (v_x) follows the desired longitudinal speed (v_R). To use the sliding mode approach [23], a relation between the longitudinal speed (or one of its derivatives) and the applied torques to the wheels must be derived. This relation can be established by combining the longitudinal dynamics and the equation of motion of the wheel. For this purpose, it is enough to replace the longitudinal force of each tire in Eq. (4.1a) with the equivalent value from Eq. (4.6). It may be inferred that this method is not useful because the steering angle and lateral forces of the front tires are also unknown in Eq. (4.1a).

But it should be noted that the effect of the lateral force of tires is insignificant on longitudinal dynamics, and it is neglected in several references [6]. However, this study suggests the use of the steering angle and lateral forces in the previous step to improve accuracy. The equations of computing the control inputs are briefly stated in the following.

First, the slip surface is defined according to Eq. (4.32)

$$s_x = (v_x - v_R) \tag{4.32}$$

Now, we can differentiate the slip surface s_x, and assume it to be zero. Then, instead of $\dot{v}_x$, its equivalent term from Eq. (4.1a) is substituted to obtain Eq. (4.33)

$$\frac{F_{x_f}\cos\overline{\delta} - F_{y_f}\sin\overline{\delta} + F_{x_r} - F_{aero}}{m} + v_y\dot{\psi} - \dot{v}_R = 0 \tag{4.33}$$

The $\overline{\delta}$ symbol that appears in Eq. (4.41) is the steering angle of the previous step, which is known. For each tire, the longitudinal force is replaced by its equivalent in Eq. (4.6). Eq. (4.34) is obtained after simplifying the relations.

$$\begin{aligned} T_{t_{eq}} = {} & R_w\left(f_r F_{z_f}\cos\overline{\delta} + f_r F_{z_r} + F_{y_f}\sin\overline{\delta} + F_{aero} - mv_y\dot{\psi} + m\dot{v}_R\right) \\ & + 2I_w\left(\dot{\omega}_f\cos\overline{\delta} + \dot{\omega}_r\right) \end{aligned} \tag{4.34}$$

It is assumed that $T_{t_{eq}} = \left(T_f\cos\overline{\delta}\right)_{eq} + T_{req}$. A sign input term must be added to the equivalent input (T_{teq}) to handle probable uncertainties. Therefore, the total required torque is defined by Eq. (4.35).

$$T_t = T_{teq} - K_x\,\mathrm{sat}(s_x, \varnothing_x) \tag{4.35}$$

In Eq. (4.35), 'sat' is a saturation function. The constant K_x is also determined considering the level of uncertainties. The thickness of the boundary

layer ($\varnothing_x$) should be selected in such a way that the control accuracy is guaranteed while avoiding the chattering. Subsequently, the applied torque to the front and rear wheels should also be determined. According to the second rule, for braking mode, the torque applied to the front (T_f) and rear (T_r) wheels can be calculated by Eq. (4.36).

$$T_f = \frac{F_{zf}}{F_z} T_t \quad \text{and} \quad T_r = \frac{F_{zr}}{F_z} T_t \tag{4.36}$$

According to the second rule, the torque applied to the front and rear wheels for the acceleration mode can be determined by Eq. (4.37).

$$T_f = T_t \quad \text{and} \quad T_r = 0 \tag{4.37}$$

4.6.2 Lateral control

The purpose of the lateral controller is to move the vehicle's center of mass in the desired direction while ensuring vehicle stability. Similar to the longitudinal control, for using the control approach of reference [23], a relationship must be derived between the desired lateral position (or one of its derivatives) and the steering angle. Although the control inputs do not appear directly in the equations, this relation can be established according to the following method. By assuming that Y and Y_R represent the current and desired lateral positions, respectively, error (e) is defined as $Y - Y_R$. Also, the slip surface is defined by Eq. (4.38)

$$ss_y = \left(\frac{d}{dt} + \lambda_y\right) e, \ \lambda_y > 0 \tag{4.38}$$

The value of $\dot{v}_y$ can be calculated by differentiating the slip surface ss_y and setting it to be zero.

$$\dot{v}_y = \frac{v_y \dot{\psi} \sin\psi - \dot{v}_x \sin\psi + \ddot{Y}_R - \lambda_y \left(v_x \sin\psi - \dot{Y}_R\right)}{\cos\psi} - v_x \dot{\psi} - \lambda_y v_y \tag{4.39}$$

The value of $\dot{v}_y$ can also be determined using the lateral dynamics of the center of oscillation (Eqs. 4.4 and 4.5).

$$\dot{v}_y = \frac{l}{m l_r} \left[F_{x_f} \sin\overline{\delta} + F_{y_f} \cos\overline{\delta}\right] - v_x \dot{\psi} - l_{fco} \ddot{\psi} \tag{4.40}$$

By eliminating $\dot{v}_y$ from Eqs. (4.39) and (4.40), the summation of the lateral force of the front tires is determined (4.41).

$$\left(F_{y_f}\right)_{eq} = \frac{ml_r\left[v_y\dot{\psi}\sin\psi - \dot{v}_x\sin\psi + \ddot{Y}_R - \lambda_y\left(v_x\sin\psi - \dot{Y}_R\right)\right]}{l\cos\bar{\delta}\cos\psi} + \frac{ml_r\left(l_{fco}\ddot{\psi} - \lambda_y v_y\right)}{l\cos\bar{\delta}} + \frac{ml_r\left(l_{fco}\ddot{\psi} - \lambda_y v_y\right)}{l\cos\bar{\delta}} - F_{x_f}\tan\bar{\delta} \tag{4.41}$$

Now, using Eqs. (4.14a), (4.16), (4.10a), and (4.8), the equivalent steering angle can be extracted in terms of $(F_{y_f})_{eq}$ (4.42).

$$\delta_{eq} = \frac{s_f}{K_{\alpha_f}\mu_f F_{z_f}}\left(F_{y_f}\right)_{eq} + \tan^{-1}\left(\frac{v_y + \dot{\psi}l_f}{v_x}\right) \tag{4.42}$$

A sign input term must be added to the equivalent input δ_{eq} to take care of existing uncertainties. Hence, the required steering angle can be calculated by Eq. (4.43)

$$\delta = \delta_{eq} - k_y \text{sat}\left(s_y, \varnothing_y\right) \tag{4.43}$$

Similar to longitudinal control, the constant K_y in Eq. (4.43) is determined considering the level of uncertainties. In addition, the thickness of the boundary layer ($\varnothing_y$) should be selected in such a way that chattering doesn't occur while maintaining control accuracy.

4.7 Simulation of integrated longitudinal and lateral vehicle guidance algorithm

In this *sec*tion, the results of the simulations are provided in two areas of trajectory planning as well as the implementation of integrated control for critical collision maneuvers. Because the maneuver scenario is introduced briefly at the end of the introduction, here only the parameters of the maneuver are summarized in Table 4.2. In this maneuver, it is assumed that the braking deceleration of the target vehicle and the lateral position of point B (w_{TV}) are constant over time.

4.7.1 Simulation results of trajectory planning

The summary of the simulation results of trajectory planning for the maneuver is presented in Table 4.3. The resulting trajectories indicate that the rear and front tires are critical in braking and acceleration conditions, respectively. By examining the acceleration of the vehicle and the final speed of the maneuver in trajectory number 1 (longitudinal acceleration of 3 m/s^2),

Table 4.2 Description of maneuver assumptions.

Value	Unit	Symbol
110	km/h	v_0
6	m	x_0
3	m	h
−8	m/s^2	a_{bmax}
5	m/s^2	a_{tmax}
125	km/h	$V_{\max}$
70	km/h	$V_{\min}$
0.85	m	w_{TV}
−8	m/s^2	a_{TV}
0.6	m	sd
0.52	–	$\mu_{\mathrm{ro,max}}$
20	–	K

Table 4.3 Overview and evaluation of the trajectories.

Maximum required friction coefficient					
Rear tires	**Front tires**	**Maneuver time (s)**	**Final speed (km/h)**	**Acceleration (m/s^2)**	**Trajectory number**
0.573	0.928	1.69	128	3	1
0.54	0.741	1.77	122	2	2
0.504	0.584	1.85	116	1	3
0.466	0.47	1.95	110	0	4
0.438	0.417	2.08	103	−1	5
0.433	0.396	2.23	94	−2	6
0.452	0.41	2.42	84	−3	7
0.492	0.455	2.67	72	−4	8
0.551	0.524	3.05	56	−5	9

it is observed that the speed of the host vehicle is equal to 128 km/h at the end of this trajectory, which is more than the maximum speed limit (125 km/h). Hence, it can be concluded that this trajectory is invalid. All trajectories with an acceleration of more than 3 m/s^2 will also be unacceptable. Similarly, by examining trajectory number 9 (braking deceleration of −5 m/s^2), it is concluded that the vehicle speed at the end of this trajectory is 56 km/h, which is less than the minimum speed limit of 70 km/h. Hence, all trajectories with a braking deceleration value greater than 5 m/s^2 will be invalid. Other suggested trajectories having final speed in disagreement with

the highway speed limits are not listed in Table 4.3 for the sake of conciseness. According to Table 4.3, it is observed that the maximum coefficient of friction required in trajectories 2 and 3 is higher than the maximum available friction (0.52); therefore, these trajectories are also infeasible.

An accurate observation of Table 4.3 yields interesting results. Each of the feasible trajectories is examined in detail as follows. Longitudinal slips are almost zero in trajectory number 4; as a result, the required longitudinal forces are negligible. In trajectory No. 4, the longitudinal slips are approximately zero, so the required longitudinal forces will be negligible. In this trajectory, the lateral acceleration imposed on the vehicle is also high due to the short maneuvering time (compared to other acceptable routes), and as a result, the required lateral forces will increase. Eventually, the sum of the required tire forces is such that the maximum required coefficient of friction is equal to 0.47 in the front tires. The condition is improved by applying a braking acceleration of -1 m/s^2 in trajectory number 5. In this trajectory, the required longitudinal force by the tire is increased compared to trajectory number 4 due to braking. On the other hand, the maximum lateral acceleration decreases as maneuver time increases (from 1.95 s to 2.08 s); therefore, the required lateral force decreases. The result of these changes eventually decreases the maximum required forces of the tire, and consequently, decreases the required maximum coefficient of friction (from 0.47 to 0.438). It is interesting to observe what happens when braking deceleration decreases to -2 m/s^2 in trajectory number 6. In fact, the maximum required coefficient of friction remains almost constant (0.433) by further decreasing the braking deceleration compared to trajectory number 5. The latter is because, compared to trajectory number 5, the increase in the longitudinal force is approximately equal to the decrease in the lateral forces in the tire; therefore, the maximum required friction has not changed. As a result, it can be expected that the maximum required friction will increase by a further decrease in deceleration. The accuracy of this point is well proved by examining the results of trajectory 7 and 8. Based on the above explanations, if the minimum required friction is the criterion of optimality, it can be concluded that trajectory number 6, with the maximum coefficient of friction needed of 0.433, is the optimal trajectory among the feasible trajectories. It should be noted that trajectory number 6 is selected for the simulation of integrated control. At the end of this *sec*tion, the changes in the longitudinal and lateral positions of points A and B over time are shown in Figs. 4.7 and 4.8, respectively, to assure that the vehicles do not collide.

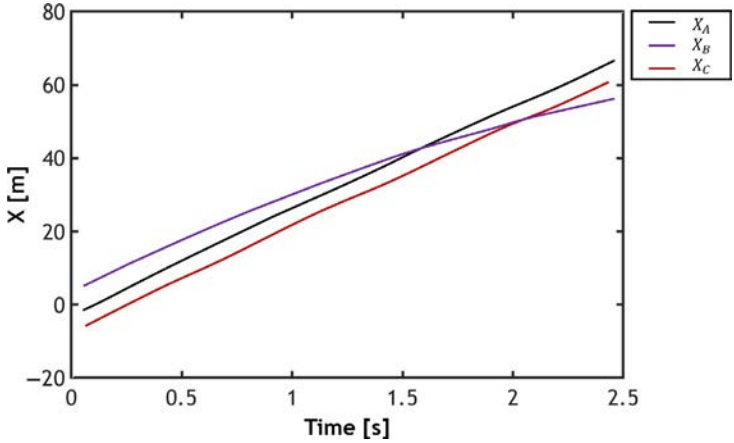

Fig. 4.7 Longitudinal position of three points of A, B, and C by assuming the safe passage of points A and B.

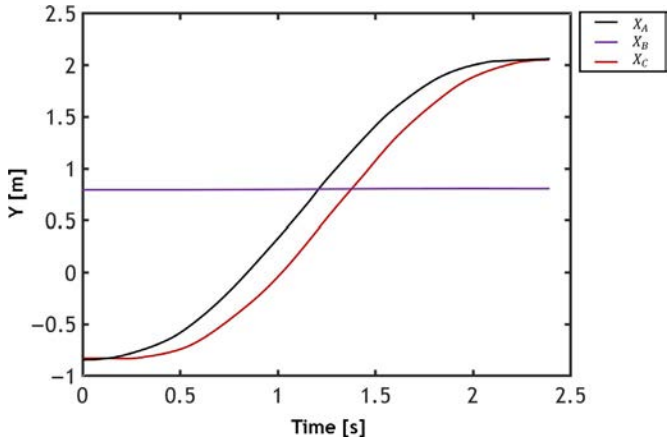

Fig. 4.8 Lateral position of three points of A, B, and C by assuming the safe passage of points A and B.

According to Fig. 4.7, the two vehicles will meet after traveling a longitudinal distance of 43 m in 1.4 s (points A and B). In addition, Fig. 4.8 indicates that at this time, the lateral positions of points A and B are equal to 1.45 m and 0.85 m, respectively. In fact, the distance between the two vehicles is 0.6 m at the time of arrival. In this section, it is necessary to validate the accuracy of an important assumption. In the trajectory planning section, it was assumed that the right front corner of the host vehicle (point A) had a safe vertical distance with the left rear corner of the target vehicle (point B) at the time of arrival. (Fig. 4.5).

The following questions may arise:

- Despite the safe passage of points A and B, how can the safe passage of points C and B be ensured?
- In the trajectory planning section and the calculation of final maneuvering time, is it possible to use the safe distance between points C and B instead of the distance between points A and B?

To answer the first question, trajectory number 6 with the acceleration of −2 m/s is considered. According to Fig. 4.7, it can be observed that points B and C reach each other in 1.8 s, which is equivalent to the longitudinal position of 55 m. In addition, Fig. 4.8 indicates that in 1.8 s, the vertical distance between points B and C is 1.1 m. Hence, in trajectory planning, it can be ensured that points B and C also pass each other at an acceptable vertical distance if the assumption of safe passage of points A and B is used. To answer the second question, it is assumed that the trajectory is planned with an acceleration of −2 m/s, along with the assumption of the safe passage of points B and C. Based on these assumptions, the final maneuver time will be 2.7 s. The longitudinal and lateral positions of the three points of A, B, and C are displayed in Figs. 4.9 and 4.10, respectively. Fig. 4.9 indicates that points A and B reach each other in 1.4 s (position 38 m), and points B and C reach each other in 1.8 s (position 50 m). In addition, Fig. 4.10 shows that although, at 1.8 s, the vertical distance between points B and C is 0.6 m, at 1.4 s, the lateral position of point A is less than the lateral position of point B, which leads to a collision. Hence, it can be concluded that in

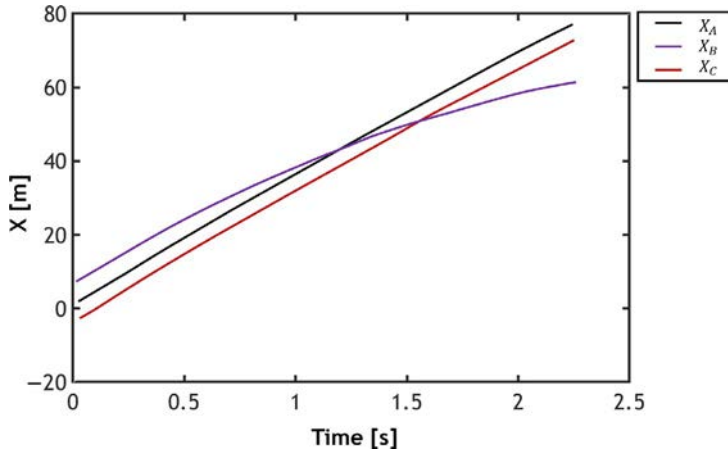

Fig. 4.9 Longitudinal position of three points A, B, and C with the assumption of safe passage of points B and C.

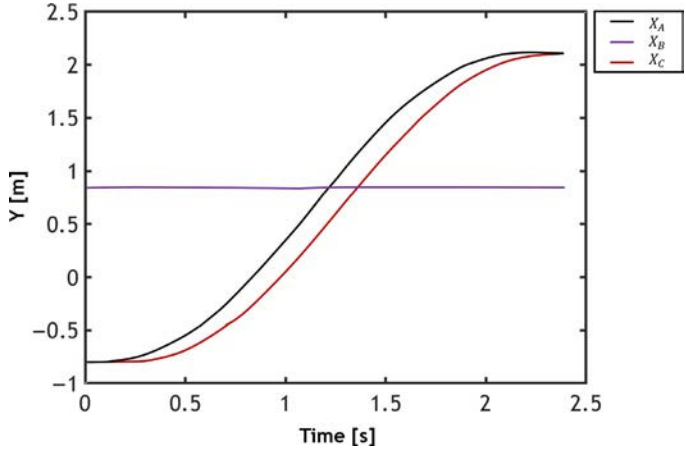

Fig. 4.10 Lateral position of three points A, B, and C with the assumption of safe passage of points B and C.

trajectory planning, points A and B may collide with each other if the assumption of safe passage of points C and B is used.

At the end of this section, it is necessary to evaluate the accuracy of an important hypothesis. In trajectory planning, selecting an appropriate trajectory was performed based on the maximum required friction. The coefficients of friction of the front and rear tires are calculated approximately based on a set of hypotheses and a few simple algebraic operations. Subsequently, the trajectory with the minimum required friction is selected as the optimal trajectory. This section aims to check the accuracy of the approximate coefficient of friction. Hence, the friction coefficients of the front and rear tires for trajectory number 6 are shown in Figs. 4.11 and 4.12, respectively. The real coefficients of friction are the result of applying integrated control.

By comparing the real and approximate coefficients of friction, it can be concluded that the changes are almost similar in both curves. Because only the maximum coefficient of friction is important in the proposed method, it is unimportant how accurately these two curves coincide. In terms of quantity, the approximate coefficients of friction are 15% lower than the real coefficients of friction. This is due to the difference between the magnitude of real and approximate accelerations. Considering that the vehicle was assumed tangent to the trajectory in the trajectory planning section, the value of v_y was considered zero. Therefore, according to Eq. (4.3a), it can be concluded that the approximate longitudinal acceleration will be less than the real acceleration. In this case, the longitudinal force of the tire, and consequently the total friction, will be less than the real value.

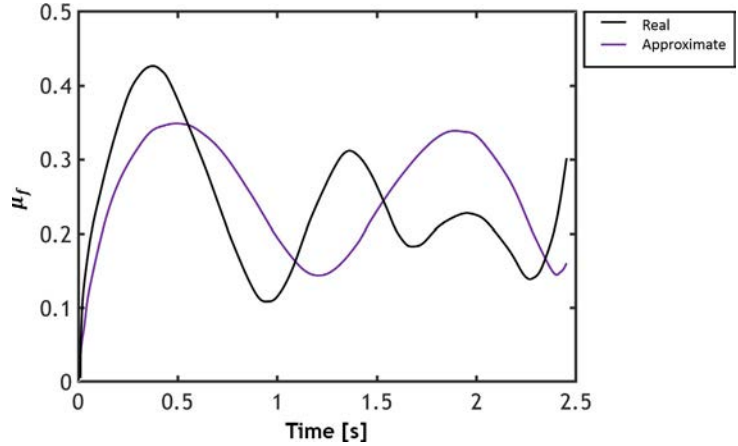

Fig. 4.11 The approximate and real coefficient of friction of front tires.

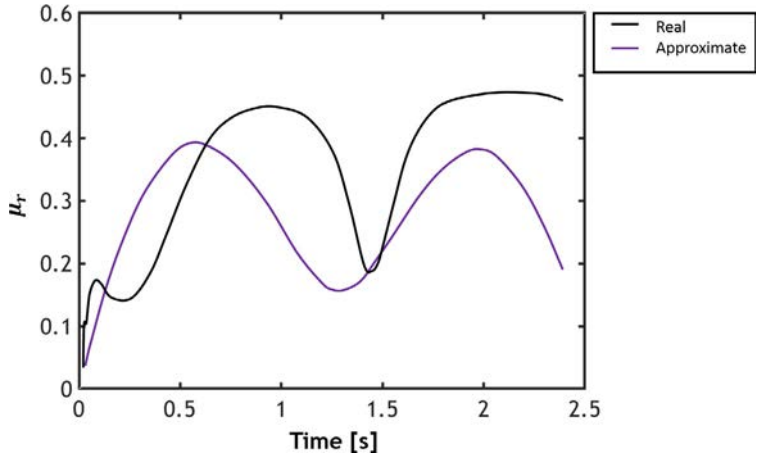

Fig. 4.12 The approximate and real coefficient of friction of rear tires.

4.7.2 Simulation results of integrated control

Fig. 4.13 displays the overall performance of the integrated controller. This figure indicates that the real trajectory coincides with the desired trajectory very accurately

The longitudinal and lateral components of the vehicle motion will be evaluated in the following. The longitudinal performance of the vehicle is shown in Figs. 4.14–4.17.

Figs. 4.14 and 4.15 indicate that the longitudinal controller succeeded in tracking the desired speed, as the maximum value of the tracking error is less

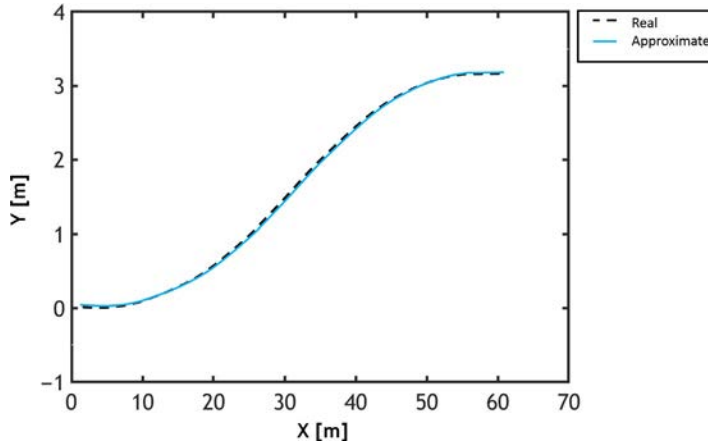

Fig. 4.13 Changing a lane in a lane-changing maneuver.

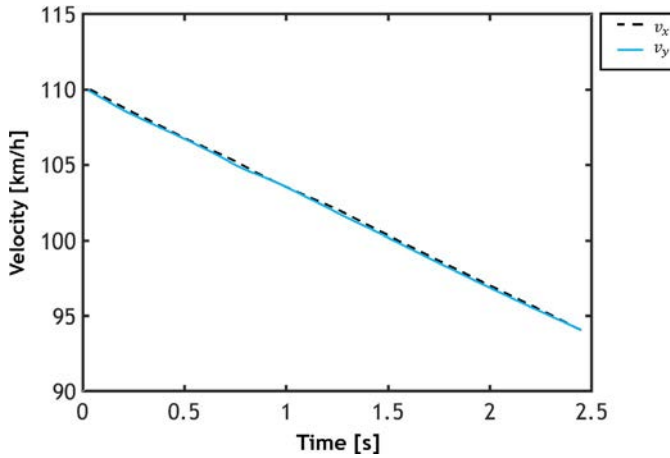

Fig. 4.14 Tracking of longitudinal velocity.

than 0.1 km/h. Concerning the control inputs, the changes of applied torques to the wheels are also continuous and smooth (Fig. 4.16). Because the normal force of the front tires is more than the normal force of the rear tires in braking mode, the torque applied to these tires is also higher.

The longitudinal position error of point A belonging to the host vehicle is a very important subject. If the speed control is not performed correctly, the difference between the desired and the real longitudinal positions will increase, which may lead to a collision. The longitudinal position error curve over time is shown in Fig. 4.17. By comprehensive observation of this

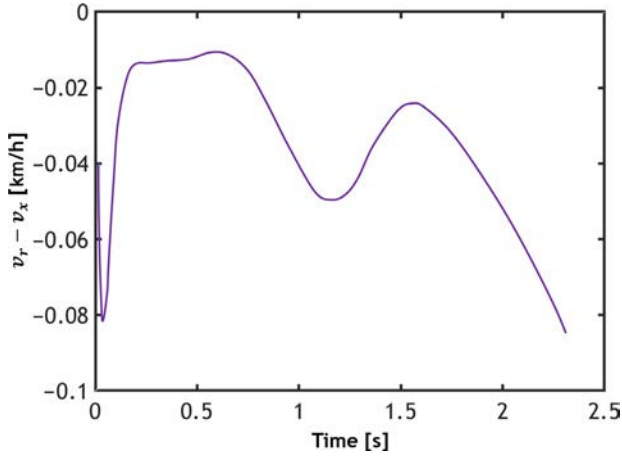

Fig. 4.15 Tracking error of longitudinal velocity.

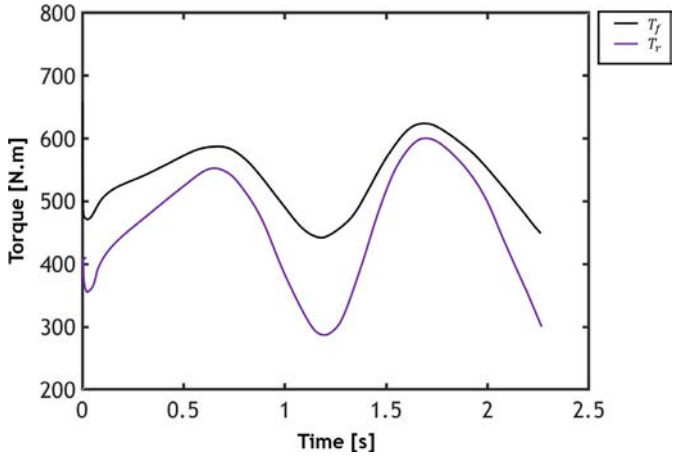

Fig. 4.16 Applied torque to the front and rear wheels.

figure, it can be inferred that the longitudinal position error is small and approximately equal to 15 cm at the arrival time of the two vehicles (1.4 s). As mentioned at the end of the previous section, the safe distance criterion is met for the two vehicles at the arrival time. The performance of tracking the lateral position of the vehicle is shown in Figs. 4.18–4.21.

Figs. 4.18 and 4.19 indicate that the task of the lateral control is appropriately performed with a maximum lateral position error of less than 0.2 cm. In addition, Fig. 4.20 shows that the changes in the steering angle inputs are

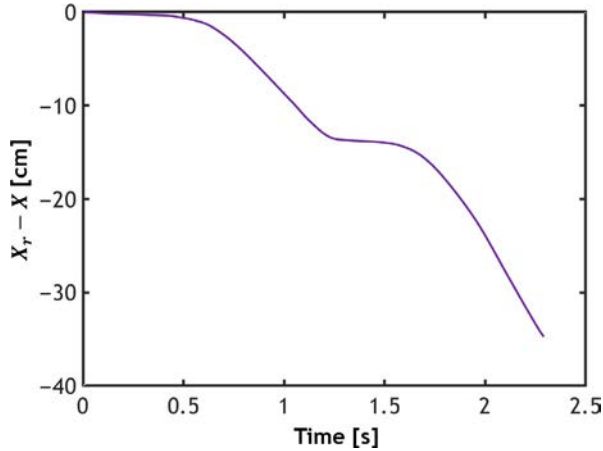

Fig. 4.17 Tracking of the longitudinal position of point A.

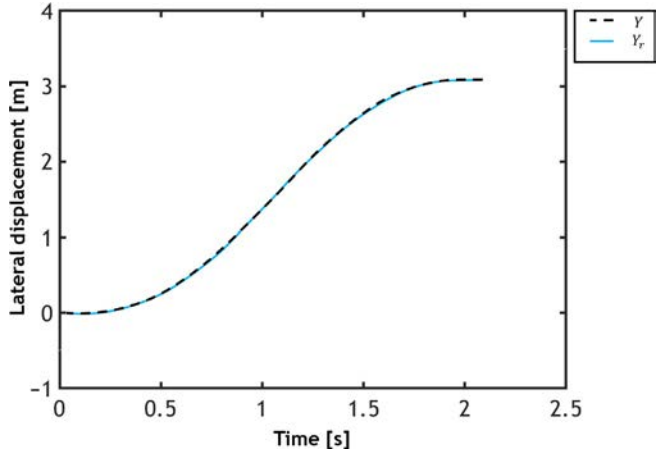

Fig. 4.18 Tracking of the lateral position.

perfectly continuous and smooth. Note that the steering angle is still increasing at the end of the maneuver (2.25 s). This is because the vehicle is not yet tangential to the optimal trajectory due to the high slip angle at the end of the maneuver; therefore, the steering angle will not be zero. However, the steering angle will gradually tend to zero if the vehicle keeps moving in a straight line. This is well illustrated in Fig. 4.21.

For a further illustration of the integrated control performance, the lateral acceleration curve, along with the changes of lateral direction angle and lateral slip angle, is shown in Figs. 4.22 and 4.23, respectively.

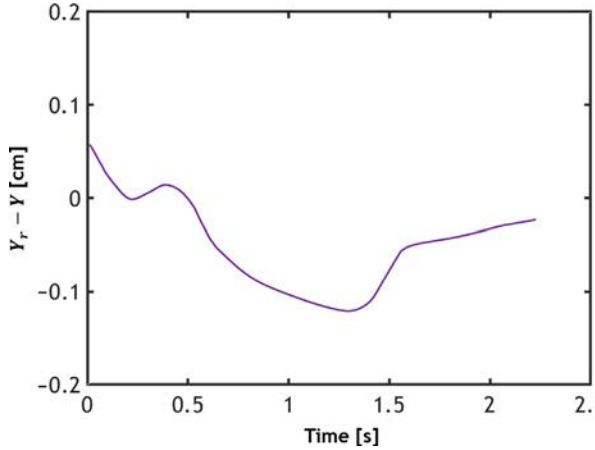

Fig. 4.19 Tracking error of the lateral position.

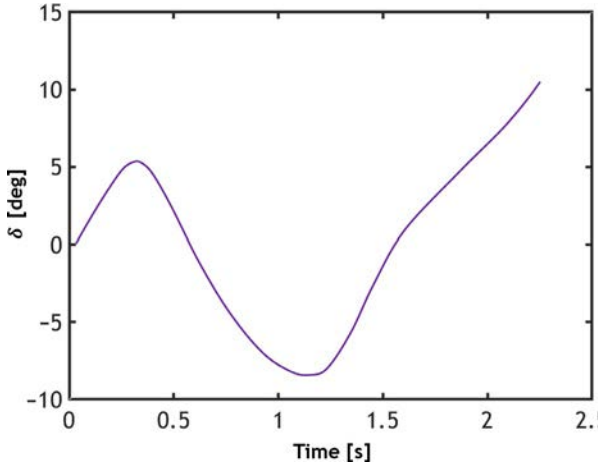

Fig. 4.20 Steering angle input in the lane-changing maneuver.

Fig. 4.22 indicates that the maximum lateral acceleration is approximately 4 m/s^2. By comparing the curves of the lateral acceleration and the optimal trajectory (Fig. 4.13), it is inferred that the maximum lateral acceleration occurred approximately at points where the trajectory has the highest curvature. In addition, the lateral acceleration value is approximately zero when the center of mass of the host vehicle reaches half of the desired lateral position (1.5 m) (Figs. 4.18 and 4.22). It should be noted that the curvature is zero at this point in the trajectory; therefore, the radius of curvature is infinite. A comprehensive observation of lateral direction and

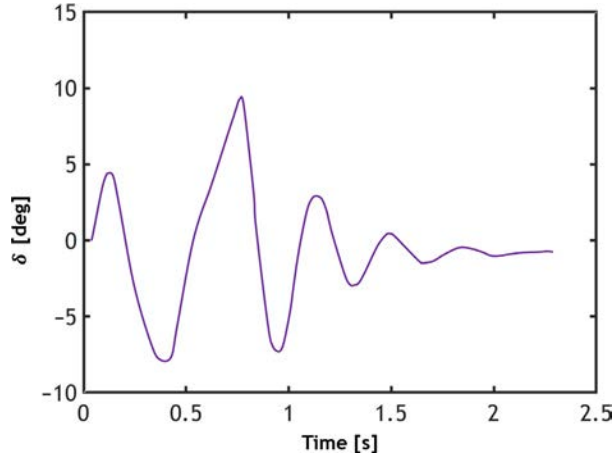

Fig. 4.21 Steering angle during the lane-changing maneuver and a few seconds later.

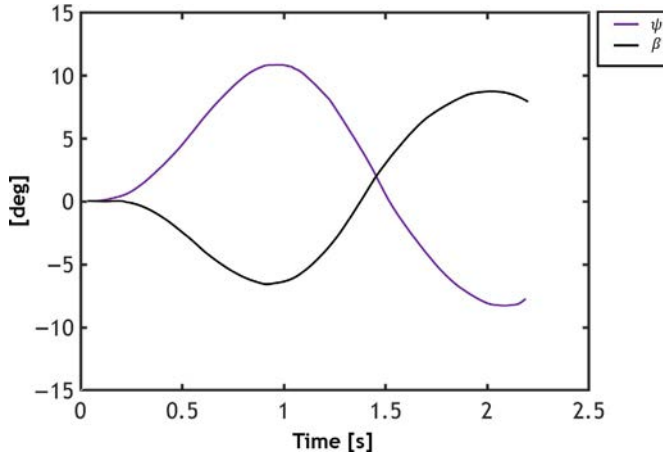

Fig. 4.22 The lateral acceleration of the vehicle relative to the local coordinate system.

lateral slip angles (Fig. 4.23) indicates that the maximum lateral slip angle occurs at the end of the maneuver and is equal to 10 degrees. However, this value will gradually decrease and become zero.

At the end of this section, the integrated controller performance is presented for an infeasible trajectory to evaluate the accuracy of the trajectory planning method. Trajectory number 3, with the maximum required coefficient of friction of 0.584, is selected for this purpose. The overall performance of the integrated control for this trajectory is shown in Fig. 4.24.

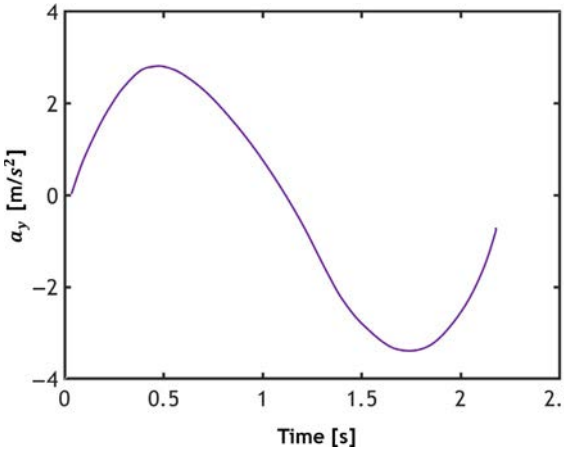

Fig. 4.23 Changes of lateral direction angle and lateral slip angle.

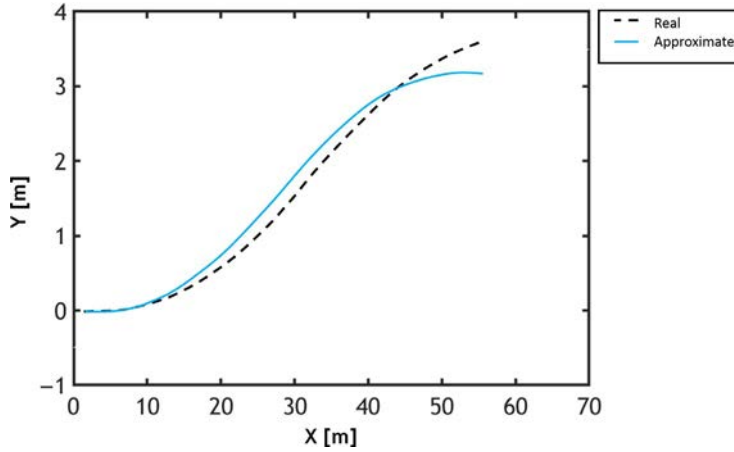

Fig. 4.24 Tracking of an infeasible trajectory for lane-changing maneuvers.

Fig. 4.24 indicates that, as expected, the vehicle is unable to follow this trajectory and completely deviates from the reference trajectory. Eventually, it can be stated that the proposed trajectory planning method correctly assessed the infeasibility of trajectory number 3.

4.8 Conclusions

An algorithm for integrated longitudinal-lateral guidance of vehicles in high-speed lane-changing maneuvers is presented in this chapter. This

algorithm provided proper solutions for optimal trajectory planning and trajectory-tracking problems. The simulation results for a critical collision avoidance maneuver demonstrated the high efficiency and capabilities of the proposed algorithm. The most important features of the proposed algorithm are as follows:

1. To consider the more realistic behavior of the vehicle, the nonlinear dynamics of the tire are taken into account in addition to the longitudinal load transfer of the vehicle, both in the trajectory planning and in the integrated controller design.
2. The proposed method can be used for critical braking/acceleration maneuvers in addition to constant speed maneuvers and yield acceptable results.
3. Because the trajectory planning calculations are performed algebraically, the computational cost is much lower than other studies, which is very valuable in real-time applications.
4. The proposed integrated longitudinal-lateral controller follows the desired trajectory with high accuracy while the stability of the vehicle is guaranteed.
5. The proposed algorithm of trajectory planning and integrated control is based on data that can be obtained by existing equipment.

The following can be used for further improvements on this topic. The movement of vehicles in the adjacent line can be considered in collision avoidance. Also, a four-wheel model of a vehicle can be used for a better representation of the real situation. In this study, the tire formula coefficients were assumed to be known. However, an appropriate method for an online determination of these coefficients is required for a comprehensive, integrated guidance algorithm.

References

[1] Road traffic injuries, Accessed on 2 September 2017; http://www.who.int/mediacentre/factsheets/fs358/en/#content.
[2] Causes of collisions, Accessed on 2 September 2017; http://www.roadsafetymayo.ie/CausesofCollisions.
[3] In the last fourteen years, 315 thousand people have died as a result of road traffic crashes, Accessed on 5 October 2015; http://www.mehrnews.com/news/2933947. (in Persian).
[4] K. Bengler, K. Dietmayer, B. Farber, M. Maurer, C. Stiller, H. Winner, Three decades of driver assistance systems: review and future perspectives, IEEE Intell. Transp. Syst. Mag. 6 (4) (2014) 6–22.
[5] Automated driving, accessed on 5 September 2017; https://www.vda.de/en/topics/innovation-and-technology/ automated-driving/automated-driving.

[6] R. Rajamani, Vehicle Dynamics and Control, second ed., Springer, New York, 2012, pp. 15–46.
[7] J. hwan Jeon, R.V. Cowlagi, S.C. Peters, S. Karaman, E. Frazzoli, P. Tsiotras, Iagnemma, K., Optimal motion planning with the half-car dynamical model for autonomous high-speed driving, in: 2013 American Control Conference, IEEE, 2013, pp. 188–193.
[8] S.C. Peters, Optimal Planning and Control for Hazard Avoidance of Front-Steered Ground Vehicles, Ph.D. Thesis, Department of Mechanical Engineering, Massachusetts Institute Of Technology, Cambridge, 2012.
[9] E. Velenis, P. Tsiotras, J. Lu, Optimality properties and driver input parameterization for trail-braking cornering, Eur. J. Control. 14 (4) (2008) 308–320.
[10] U. Kiencke, L. Nielsen, Automotive Control Systems, second ed., Springer, Berlin, 2005, pp. 301–349.
[11] F. You, R. Zhang, G. Lie, H. Wang, H. Wen, J. Xu, Trajectory planning and tracking control for autonomous lane change maneuver based on the cooperative vehicle infrastructure system, Expert Syst. Appl. 42 (14) (2015) 5932–5946.
[12] S. Samiee, The Design of Vehicle Control System With Drowsy Driver Based on Vehicle-Driver Interaction, Ph.D. Thesis, Department of Mechanical Engineering, K. N. Toosi University of Technology, Tehran, 2016 (in Persian).
[13] Y. Cong, O. Sawodny, H. Chen, J. Zimmermann, A. Lutz, Motion planning for an autonomous vehicle driving on motorways by using flatness properties, in: 2010 IEEE International Conference on Control Applications, IEEE, 2010.
[14] X. Li, et al., A unified approach to local trajectory planning and control for autonomous driving along a reference path, IN: 2014 IEEE International Conference on Mechatronics and Automation, IEEE, 2014.
[15] A. Cadkhodajafarian, A. Analooee, S. Azadi, R. Kazemi, Collision-free navigation and control for autonomous vehicle in complex urban environments, Modares Mech. Eng. 17 (11) (2018) 277–288 (in Persian).
[16] S. Shojaei, A. Rahmani Hanzaki, S. Azadi, M. Saeedi, Collision- design of decision-making lane change algorithm of truck-semitrailer in real dynamic environment, Modares Mech. Eng. 17 (9) (2017) 351–360 (in Persian).
[17] E. Kayacan, H. Ramon, W. Saeys, Robust trajectory tracking error model-based predictive control for unmanned ground vehicles, IEEE/ASME Trans. Mechatron. 21 (2) (2016) 806–814.
[18] P. Petrov, F. Nashashibi, Modeling and nonlinear adaptive control for autonomous vehicle overtaking, IEEE Trans. Intell. Transp. Syst. 15 (4) (2014) 1643–1656.
[19] L. Nehaoua, L. Nouveliere, Backstepping based approach for the combined longitudinal-lateral vehicle control, in: Proceedings of The 2012 IEEE intelligent vehicles symposium, Alcala de Henares, Spain, June 3-7, 2012, 2012.
[20] J. Guo, P. Hu, R. Wang, Nonlinear coordinated steering and braking control of vision-based autonomous vehicles in emergency obstacle avoidance, IEEE Trans. Intell. Transp. Syst. 17 (11) (2016) 3230–3240.
[21] J. Choi, K. Yi, J. Suh, B. Ko, Coordinated control of motor-driven power steering torque overlay and differential braking for emergency driving support, IEEE Trans. Veh. Technol. 63 (2) (2014) 566–579.
[22] R. Attia, R. Orjuela, M. Basset, Combined longitudinal and lateral control for automated vehicle guidance, Veh. Syst. Dyn. 52 (2) (2014) 261–279.
[23] J. Slotine, Sliding controller design for nonlinear systems, Int. J. Control. 40 (2) (1984) 421–434.

CHAPTER 5

String stability and control of a platoon of vehicles

5.1 Introduction

Today, traffic congestion, which has various impacts on modern societies, has become of great importance. Traffic congestion leads to an increase in transportation costs; a reduction in quality, efficiency, and safety; and environmental deterioration due to vehicle emissions and noise pollution. Traffic congestion on highways has continued to be very intense in most countries worldwide, even developed countries [1]. Fig. 5.1 displays an overview of traffic on a highway.

Despite several plans made in route management, infrastructure, and traffic rules, an efficient alternative is needed in terms of fundamental infrastructure due to insufficient land to build more roads and thus eliminate traffic congestion. New approaches have been developed in the field of automated highway systems to address the mentioned dilemma. An automated highway system can increase the traffic flow significantly while also increasing safety [2].

According to a statement from Partners for Advanced Transit and Highway (PATH), several cars with a short interdistance (1–2 m) create a platoon, and the highway infrastructure organizes the platoons. The term "infrastructure" refers to any information group sent, such as speed, route determination, the maximum number of vehicles, and the combination of vehicles in the platoon. In each platoon, the vehicles are electronically linked to the domain and error domain change sensors. Based on this information, each vehicle maintains a certain speed and distance concerning the leading and following vehicles using brake and throttle actuators [3]. The benefits of automated highway systems increase their motivation to use them. The benefits of automated highway systems include:

- The presence of more vehicles with higher speeds in each time and each route [2].
- Safer highways due to reduced human error in driving.

Vehicle Dynamics and Control
https://doi.org/10.1016/B978-0-323-85659-1.00006-9

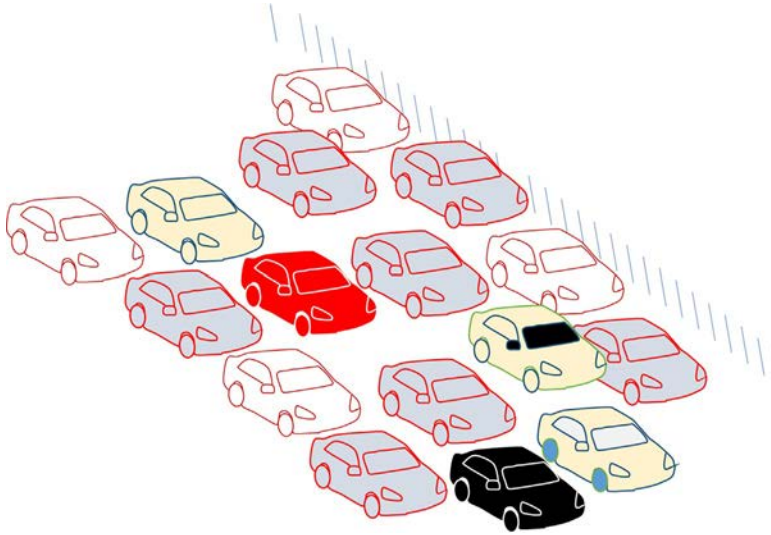

Fig. 5.1 An overview of traffic congestion on a highway.

- Reduced fuel consumption as a result of reduced aerodynamic drag, which is achieved by the short intervehicle distance [4, 5].
- Effective use of land due to the short intervehicle distance on the highway.

In controlling a vehicle platoon on a highway, each vehicle uses the adjacent vehicles' information to maintain the ideal distance. This leads to the creation of a network control system. Issues such as delays and missing data are inevitable in the network control systems due to the transmission of signals in a communication network with limited bandwidth. Hence, this must be taken into account in the communication structure, making the intended system closer to reality. The traffic flow stability is another studied issue related to vehicle platoon control, which refers to the traffic speed and density's microscopic characteristics on part of a highway [6, 7]. This characteristic ensures that density disturbances decrease through flow dispersion.

In general, besides controlling the car itself, it is necessary to design the intervehicle distance and interaction between the vehicles to study a vehicle platoon. Two main strategies used for intervehicle distance are constant spacing [8] and constant time headway [9], in addition to another policy that is designed based on the braking ability and delays in the longitudinal control system of the vehicle [10]. Regarding vehicle interactions, it should be noted that most of the studies have been based on a **unidirectional** structure.

According to the different behavior of vehicles, different traffic volumes are defined to optimize road usage. The problem of vehicle tracking in highways can be divided into three sections. When there is no traffic flow, a simple cruise control structure is used to control the vehicle speed at a predetermined value. In relatively dense and dense traffic flow, an adaptive cruise control structure is used to track the vehicle.

In this section, relatively dense traffic flow is studied using the automatic cruise control structure for situations where traffic density is low or moderate. This chapter aims to address some of the challenges in the design, stability analysis, and performance of multivehicle systems in low or medium traffic. Assuming a definite communication structure and the type of intervehicle spacing policy, the negative impacts on system stability and performance are studied analytically. According to Ghasemi et al. [11], the discussed issues in the relatively dense traffic flow are as follows:

- Time delays and noise interruptions, which are natural and unavoidable features of actuators and sensors in mechanical and control systems.
- The effect of a delay in receiving information from a nearby vehicle on vehicle control.
- Studying unidirectional-bidirectional communication structures and constant spacing–constant time headway policy.
- Investigating the effect of heterogeneity in control parameters and information about leading and following vehicles in a bidirectional communication structure.

After exploring the relatively dense traffic flow issues in this chapter, the required definitions such as string stability, distance segmentation models, communication structure, and vehicle communication will be discussed to clarify the AHS concepts.

5.2 Definitions in the vehicle platoon

A vehicle platoon consists of a group of vehicles located on a straight line, each of which follows its leading vehicle. Several predefined signals follow the speed of the leading vehicle. Generally, there are two types of models for an automated car in a platoon.

- One-dimensional model: vehicles move in a straight line.
- Two-dimensional model: vehicles have a steering system and can move in a plane.

In this chapter, the one-dimensional model is studied based on Ref. [11]. The one-dimensional model of a vehicle platoon includes several vehicles moving

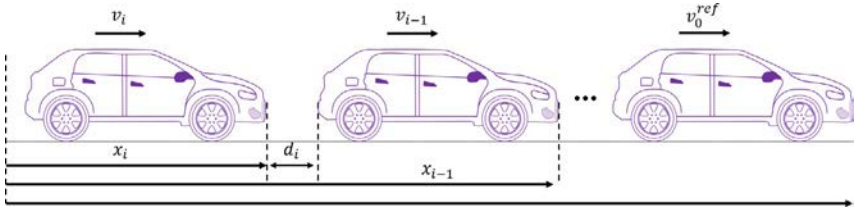

Fig. 5.2 A one-dimensional model of a vehicle platoon.

in a straight line, each of which follows its leading vehicle. For $N + 1$ vehicles moving in a straight line, the position of the leading vehicle is determined by x_0 from a specific reference. Also, the position of the following N vehicles is determined by x_1, x_2, …, x_N, respectively. The distance between the first vehicle from the leading vehicle is determined by $d_1 = x_0 - x_1 - L_0$, and the distance between the ith vehicle from the $i - 1$th vehicle is determined by $d_i = x_{i-1} - x_i - L_{i-1}$, in which L_i indicates the length of the ith vehicle. The speed of the leading vehicle is represented by v_0 and the speed of the rest of the vehicles is expressed by $v_i = dx_i/dt$. Fig. 5.2 displays a one-dimensional model of a vehicle platoon moving in a straight line.

5.2.1 The intervehicle spacing control policy in a vehicle platoon

There are two main types of intervehicle spacing policies. The first one is the constant spacing policy, in which the desired distance between vehicles is always constant. The second is the variable spacing policy, which increases the desired distance at high speeds. Each of the earlier policies has its advantages and disadvantages, which will be discussed in the following.

5.2.1.1 The constant spacing policy

In the constant spacing policy, the distance between two adjacent vehicles in the platoon is controlled by a specific constant value, regardless of the car's speed. Specifically, D_i is the ideal distance to control the separation distance d_i. In this case, if the reference spacing D_i is not large enough, it will cause much danger while moving at high speeds. Also, it is no longer necessary to assume a similar ideal spacing for all vehicles; in fact, they can be different

$$\lim_{t\to\infty}(d_i(t) - D_i) = 0 \tag{5.1}$$

According to Eq. (5.1), this strategic law can increase traffic capacity significantly. Because each vehicle in the platoon must match its position,

speed, and (or) acceleration with the leading vehicle to maintain the intervehicle spacing, the required tracking is challenging.

5.2.1.2 The variable spacing policy

In this scenario, the ideal intervehicle distance changes with the vehicle speed. Although the traffic capacity resulting from this strategy is less than the constant spacing policy, it is easier to achieve string stability.

Constant time headway policy

Time headway denotes a vehicle's required time to reach the preceding vehicle's current position at a constant speed. In constant time headway control, the controlled vehicle adjusts its distance with the preceding vehicle constantly. This distance can be expressed as (5.2):

$$D_i = hv_i + D_{min} \tag{5.2}$$

where h is the time headway and D_{min} is added to prevent a collision at very low speeds.

Variable time headway policy

The time headway constant can be variable, and a nonlinear function can be used [12]

$$h = \text{sat}(h_0 - c_h v_i) = \begin{cases} 1 & h_0 - c_h v_i \geq 1 \\ h_0 - c_h v_i & 0 < h_0 - c_h v_i < 1 \\ 0 & \text{otherwise} \end{cases} \tag{5.3}$$

In Eq. (5.3), h_0, $c_h > 0$ are the design variables. Because the time headway must have a nonnegative value to maintain safety, the lower bound of zero is required. Additionally, the upper bound is required to prevent excessive headways that lead to more distance between vehicles. The latter is considered because bigger intervehicle distances may ruin the purpose of vehicle platooning.

5.2.2 String stability

Creating automated highway systems has been studied to increase highway capacity and efficiency, and various control rules have been considered to achieve the optimal spacing in the vehicle platoon [11–13]. String stability is proposed in the research development of controlling the automated highways. This is a measure of how the distance error is propagated between adjacent vehicles through a platoon or series of vehicles. String stability

can be a description of the increase in the distributed position/speed error through a platoon caused by a maneuver or disturbance in the speed of the leading vehicle. The mentioned increase in distributed errors and the accompanying issues may lead to a serious problem, especially when there are many vehicles in the platoon.

In a simple sense, when the index of the vehicle increases in the platoon, a system in which the error does not increase is said to have string stability. The string stability control structure limits the disturbance and reduces the spacing error along the string; therefore, several researchers have studied string stability for different structural communications, control strategies, and spacing plans [14, 15]. For each vehicle, the tracking errors are defined as Eq. (5.4):

$$\varepsilon_i = x_{i-1} - x_i - L_{i-1} - D_i = d_i - D_i \tag{5.4}$$

where D_i is the ideal distance between the ith and $i-1$th vehicles.

5.2.2.1 Definition 1 (string stability) [16]

In essence, a vehicle platoon is string-stable if

$$\| \varepsilon_1 \|_\infty \geq \| \varepsilon_2 \|_\infty \geq K \geq \| \varepsilon_N \|_\infty \tag{5.5}$$

Eq. (5.5) ensures that the error range is decreased through the vehicle flow. When a linear system is used, the transfer function can be used to check the string stability.

5.2.3 Centralized and decentralized control

Collaborative or centralized control controls a group of dynamic agents that works together to achieve a common goal using state and environmental information that influences the control decision. The basis of the collaborative control plan is the ability to use state information from other vehicles and the environment to create a suitable control input for each vehicle in the system [12].

Collaborative control systems can be found in nature, such as the movement of a group of birds, fish, and insects. In large systems that include identical or near-identical subsystems (these subsystems are called agents), the collaboration between these agents plays a key role. In a large system, agents often interact with each other through a cohesive structure that exists between them. An example of a system with a fixed cohesive structure is a platoon of vehicles on a highway.

In addition to stability and robust analysis, other features may be important for cohesive systems, such as the string stability; this feature is generally used in multiagent systems and is not discussed in the classical control theory. The concepts for a decentralized control system are a little different. For a group of vehicles controlled by a decentralized controller, local information for each vehicle is received only through the sensors installed on the vehicle itself. More specifically, this information is only measured from the preceding vehicle (**unidirectional** structure, Fig. 5.3A), or in addition to the preceding vehicle, the information of the following vehicle is also measured (**bidirectional** structure, Fig. 5.3B). On the other hand, the centralized control strategy assumes a communication network between the vehicles with which different communication patterns can be considered for the platoon. In this case, the communication network can only be limited to the connection of the leading vehicle to all other vehicles in the platoon (Fig. 5.3C), or it may include unlimited communication between all vehicles in the platoon (Fig. 5.3D).

Understanding the dynamics that cover a multivehicle system's behavior is the key to designing a collaborative control rule that will affect how the vehicles interact to achieve a specific goal. Decentralized cooperative control (undistributed control) is a subset of cooperative control. The vehicles automatically use other vehicles' state information to determine the input of their control for achieving the group goals.

The decentralized control method is fundamentally superior to most centralized traditional controllers. All vehicles' control input in the system is determined using environmental and state information in centralized control. The method, as mentioned earlier, is an effective way to control a small number of vehicles. However, centralized control is well known for the computational time in the conditions where the number of vehicles increases. The decentralized control is more resistant to communication errors and structural reconfiguration [12]. The design of a decentralized collaborative control rule mainly depends on the communication structure of multivehicle systems. The communication structure is defined as the available information for each vehicle in the system that may be confined by observations, communications, or processing power limitations. For instance, in many applications, vehicles only communicate with their close neighbors rather than with all vehicles in the system.

It is essential to check the closed-loop stability of the system before analyzing any aspects of a platoon. In general, stability can be proved from two different perspectives. The stability control method can be used to design a

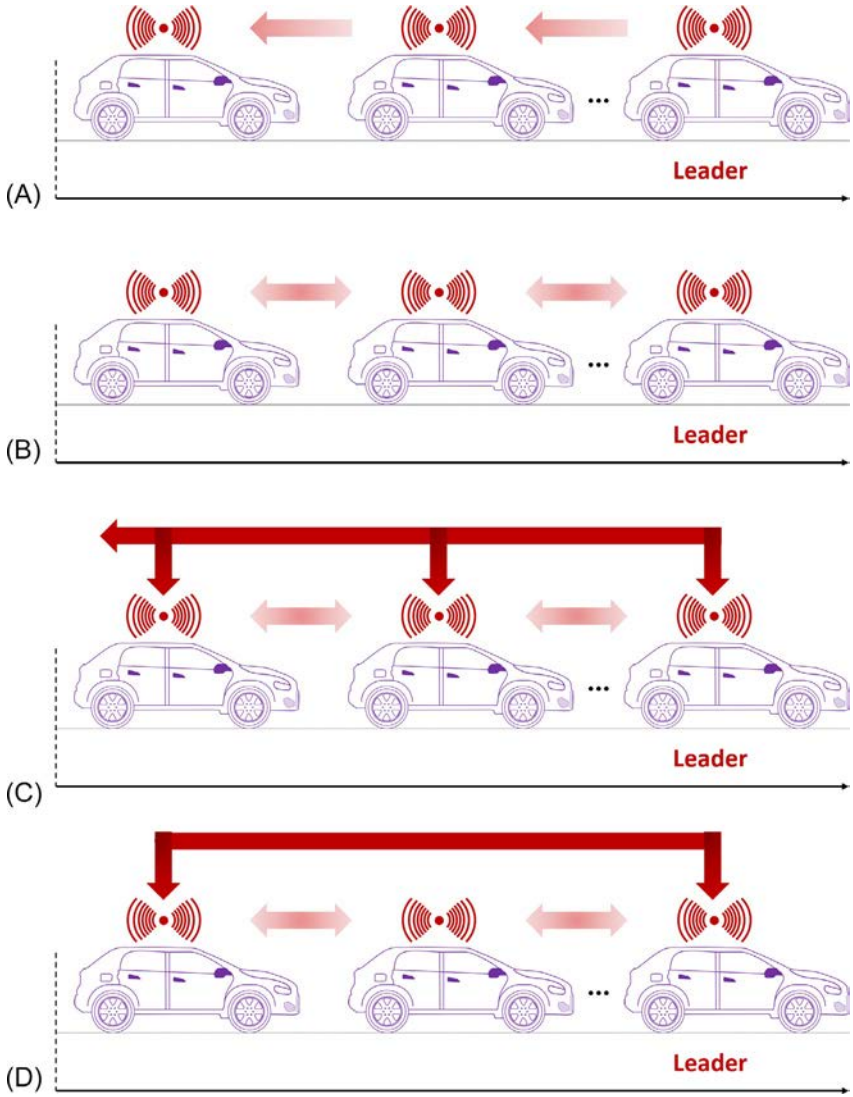

Fig. 5.3 Different communication networks in a vehicle platoon (A) Decentralized control with unidirectional structure, (B) Decentralized control with bidirectional structure, (C) Centralized control limited to the leading vehicle, (D) Centralized control with unlimited common.

controller that makes the system stable. On the other hand, after selecting the controller's structure, necessary conditions can be applied to the controller parameters to achieve a stable system using the stability principles. In this chapter, regarding the considered communication structure and delays, different methods are used to analytically study the conditions that controller parameters must have to obtain system stability.

5.3 Stability analysis

5.3.1 The longitudinal vehicle dynamics model

For modeling a vehicle platoon, the type of vehicle must be specified first. Time delays and noise interruptions are natural and inevitable characteristics of actuators and sensors in mechanical and control systems; therefore, these delays should also be considered in the model. The longitudinal system mainly consists of an engine, a transmission, a propulsion system, and a brake system. A simple description of such a system is shown in Fig. 5.4.

For the longitudinal control, the system can be considered to have two inputs, including the throttle angle and the brake torque commands, and one output of vehicle speed. Other inputs such as aerodynamic drag, road condition, and vehicle mass are considered disturbances. This two-input single-output (TISO) system can be divided into two main sections. The first section includes the engine and transmission systems, and the second one contains the propulsion system.

The longitudinal vehicle dynamic $(\dot{x}_0^* = v_0^*)$ in the platoon is modeled as Eq. (5.6) [18]

$$m_i a_i = F_i - m_i g \sin\theta - \frac{\sigma A_i c_{di}}{2}(v_i + V_{wind})^2 \operatorname{sgn}(v_i + V_{wind}) - d_{mi} \tag{5.6}$$

where m_i is the mass of the vehicle, g is the gravitational acceleration, and θ represents the angle between the road and the horizon surfaces. The term $\frac{\sigma A_i c_{di}}{2}(v_i + V_{wind})^2 \operatorname{sgn}(v_i + V_{wind})$ indicates the air resistance force, σ is the specific mass of the air, A_i is the cross-sectional area of the car, c_{di} is the drag coefficient, V_{wind} is the wind speed, d_{mi} is the mechanical drag, and F_i is the traction force generated by the vehicle engine. The engine dynamics of the vehicle are expressed as Eq. (5.7)

$$\dot{F}_i = -\frac{F_i}{\tau_i(\dot{x}_i)} + \frac{c_i}{\tau_i(\dot{x}_i)} \tag{5.7}$$

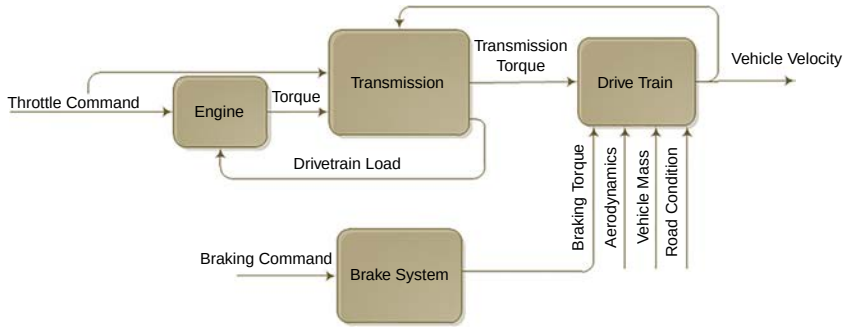

Fig. 5.4 General diagram of a longitudinal vehicle dynamic model.

where τ_i is the time constant of the vehicle engine for when the vehicle is moving at the speed of $\dot{x}_i$, and c_i is the engine input [18]. Assuming that the road surface is horizontal and there is no wind, the car model is simplified as Eq. (5.8)

$$m_i a_i = F_i - \frac{\sigma A_i c_{di}}{2} v_i^2 - d_{mi} \tag{5.8}$$

In the following, the exact linearization method [19] is used to linearize and normalize each vehicle's input–output behavior in the platoon. Eventually, Eq. (5.9) is obtained with mathematical simplifications

$$\dot{a}_i = f_i(v_i, a_i) + g_i(v_i)c_i \tag{5.9}$$

where $f_i(v_i, a_i) = -\frac{1}{\tau_i}\left(a_i + \frac{\sigma A_i c_{di}}{2m_i} v_i^2 + \frac{d_{mi}}{m_i}\right) - \frac{\sigma A_i c_{di} v_i a_i}{m_i}$ and $g_i(v_i) = \frac{1}{\tau_i m_i}$. The control system is designed by defining the engine input as Eq. (5.10)

$$c_i = u_i m_i + 0.5\sigma A_i c_{di} v_i^2 + d_{mi} + \tau_i \sigma A_i c_{di} v_i a_i \tag{5.10}$$

where λ_i is the new input signal on which the design is based. The controller design is a hierarchical control that includes linear control feedback in the first layer and a linear controller in the second layer. Fig. 5.5 displays the structure of this method.

After substitution, the system's dynamic equations are converted to the final form of Eq. (5.11)

$$\tau_i \dot{a}_i + a_i = u_i \tag{5.11}$$

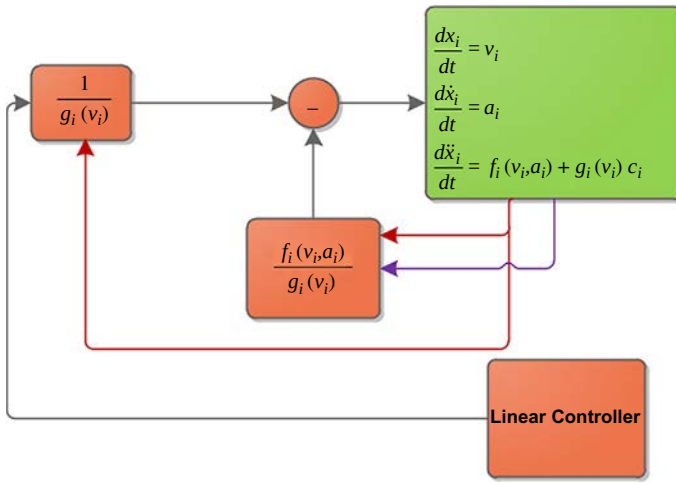

Fig. 5.5 The linearized model of the *i*th car with an input.

Most physical systems deal with noise delays that have a significant effect on system stability in many situations. This delay comes from several sources [20, 21]:

- Delays in engine response.
- Delays in the throttle actuator.
- Delays in the brake actuator.
- Delays due to radar filter.

Due to the noise interruptions of actuators and sensors, the controller's acceleration is not immediately available. Therefore, the equation of the system is rewritten as (5.12)

$$\tau_i \dot{a}_i + a_i = u_i(t - \Delta_i) \tag{5.12}$$

Naus et al. [22] studied the dynamic model by conducting experiments on a Citroen Picasso equipped with an automatic brake system and a throttle valve. The high-level dynamics of the vehicle are expressed by Eq. (5.13)

$$\frac{S_i}{U_i} = \frac{k_i}{s^2(\tau_i s + 1)} e^{-\Delta_i s} \tag{5.13}$$

where U_i and S_i are the Laplace transformation of the input and vehicle position, respectively, and k_i is the gain due to the vehicle's mass. For the mentioned vehicle, the parameters Δ_i, τ_i, k_i take the values of 0.38, 0.76, and 0.18, respectively [22].

5.3.2 The longitudinal controller of the vehicle

In the analysis of a large vehicle platoon, it can be observed that the speed of each vehicle in the platoon can be used as an external signal for the next car. The PD control structure is used for the vehicle's longitudinal control due to simplicity and applicability. The general structure of this control structure is described as (5.14)

$$u_i = P\varepsilon_i + D\dot{\varepsilon}_i \tag{5.14}$$

The selected controller rule states that each vehicle uses the distance error information and its rate relative to the adjacent vehicles. The closed-loop system's stability is controlled based on the previously mentioned rule, and the stability conditions are determined on the control parameters. In other words, the stability boundaries are obtained as certain conditions on the control parameters. However, a group of researchers took a different

approach in this field. Shladover [23] suggested applying other information, including the information related to the leader vehicle, in addition to the use of constant spacing. This approach creates string stability by using the constant spacing policy. However, this theory requires an intervehicle communication protocol to exchange the leader vehicle's information to all vehicles in the platoon. According to the mentioned cases, the concepts of stability will be discussed, and their definitions, utilization, and goals will be reviewed subsequently.

5.3.3 Stability

This section analyzes the controller parameter conditions for system stability by using tools and developing mathematical concepts. The system in hand is a network control system. Issues such as delays are unavoidable in network control systems due to the transmission of signals in the network with limited bandwidth; therefore, two different Lyapunov-Razumikhin methods of cluster treatment of characteristic roots (CTCR) will be used. Subsequently, regarding the different vehicles on a highway, the stability issue will be discussed by considering heterogeneity in control parameters. This is performed by the approximation of partial differential equation.

5.3.3.1 The stability based on constant spacing segmentation policy

The unidirectional structure

A centralized control law is considered in the current section. According to this control law, the controller is designed to use the relative distance of the preceding vehicle and the leading vehicle's speed information. Using centralized control is, in fact, the use of leading vehicle information by selecting a constant spacing policy. In this approach, a platoon is considered with short intervehicle distance. The controlling goal is to design a controller for each vehicle using the front and leading vehicles' information. This is done by assuming that the following information is available for the controlled vehicle.

- The relative distance between the ith and the i-1th vehicle.
- The relative speed between the ith and the leading vehicle.

The control law will be selected as Eq. (5.15) by choosing the control input based on the control goal (zero distance error) and considering the communication delays

$$\begin{aligned} u_i(t) = K\left(\sum_{j\in N_i} a_{ij}\left(x_j(t-r) - x_i(t-r)\right)\right) \\ + K\left(b_i\left(x_0(t-r) - x_i(t-r)\right)\right) \\ + D\left(v_0 - v_i(t)\right) \end{aligned} \tag{5.15}$$

where $r(t)$ is the communication delay, which is considered as a function of time. This function is assumed as a continuous function; in other words, $0 < r(t) < \beta$. In the above equation, a_{ij} and b_i are related to the elements of the Laplacian matrix and the leader proximity matrix, respectively.

The goal of the controller is the convergence of the system; in other words, $x_i \to x_0$ and $v_i \to v_0$ when $t \to \infty$. The problem with this definition is that there are no static equilibrium points in some vehicles. Hence, it is necessary to add an offset (d) to the state variables of the system for obtaining the desired intervehicle distance. d is defined in a way to exist for i, j, and $k(d_{ij} + d_{jk} = d_{ik})$. One method to create such a function is to define an offset of d_{oi} for each vehicle relative to an arbitrary reference, which is presented as (5.16)

$$d_{0i} = \sum_{j=1}^{i}\left(D_{j-1,j} + L_{j-1}\right) \tag{5.16}$$

As a result, the centralized control law is modified as (5.17):

$$\begin{aligned} u_i(t) = K\left(\sum_{j\in N_i} a_{ij}\left(x_j(t-r) - x_i(t-r) - d_{ji}\right)\right) \\ + K\left(b_i\left(x_0(t-r) - x_i(t-r) - d_{0i}\right)\right) \\ + D\left(v_0 - v_i(t)\right) \end{aligned} \tag{5.17}$$

For analyzing the system convergence, it is assumed that the leading vehicle is moving at a constant speed of $(\dot{x}_i^* = v_0^*)$; therefore, the optimal path of the ith vehicle can be expressed as (5.18)

$$x_i^*(t) = x_0^* - D_{0,i} - \sum_{j=l}^{i-1} L_j = x_0^* - \sum_{j=1}^{i}\left(D_{j-1,j} + L_{j-1}\right) \tag{5.18}$$

For simplifying the analysis, the tracking error is defined as follows:

$$\widetilde{x}_i = x_i - x_i^* \to \dot{\widetilde{x}}_i = \dot{x}_i - \dot{x}_i^* \to \ddot{\widetilde{x}}_i = \ddot{x}_i \tag{5.19}$$

By substituting Eq. (5.19) in Eq. (5.17), and by knowing that $x_{i-1}^* - x_i^* = D_{i-1,\,i} - L_{i-1}$ the control law can be modified as below concerning the distance error

$$u_i(t) = K\left(\sum_{j\in N_i} a_{ij}\left(\widetilde{x}_j(t-r) - \widetilde{x}_i(t-r)\right)\right) + K(b_i(-\widetilde{x}_i(t-r))) + D\left(-\dot{\widetilde{x}}_i(t)\right) \tag{5.20}$$

By combining the system's open-loop dynamic equation with the control law of Eq. (5.20), the closed-loop equation of the system will be converted into Eq. (5.21)

$$\tau_i \dddot{\widetilde{x}}_i(t) + \ddot{\widetilde{x}}_i(t) = K\left(\sum_{j\in N_i} a_{ij}\left(\widetilde{x}_j(t-r) - \widetilde{x}_i(t-r)\right)\right) + K(b_i(-\widetilde{x}_i(t-r))) + D\left(-\dot{\widetilde{x}}_i(t)\right) \tag{5.21}$$

Because the unit vector is the eigenvector of the Laplacian matrix, expressing the system's closed-loop dynamics is possible as (5.22)

$$\dot{\varepsilon} = C\varepsilon(t) + E\varepsilon(t-r) \tag{5.22}$$

where

$$\varepsilon(t) = \left[\widetilde{x}_1\dot{\widetilde{x}}_1\ddot{\widetilde{x}}_1 \ldots \widetilde{x}_N\dot{\widetilde{x}}_N\ddot{\widetilde{x}}_N\right]^T$$

$$C = \begin{bmatrix} 0_{N\times N} & I_N & 0_{N\times N} \\ 0_{N\times N} & 0_{N\times N} & I_N \\ 0_{N\times N} & -DI_N/\tau & -I_N/\tau \end{bmatrix}, E = \begin{bmatrix} 0_{N\times N} & 0_{N\times N} & 0_{N\times N} \\ 0_{N\times N} & 0_{N\times N} & 0_{N\times N} \\ -KH/\tau & 0_{N\times N} & 0_{N\times N} \end{bmatrix}, H = L + B$$

where

$I_N = 0_{N\times N}$ are defined as the identity and zero matrices, respectively.

The bidirectional structure

Maintaining the desired distance from the preceding vehicle and ease of driving are defined as the vehicle tracking process's control goals. Using just the preceding vehicle's information to calculate the control inputs is among the common features of control systems in this field. In other words, the controllers do not use the following vehicle's information, and no action is taken to prevent the collision concerning the behavior of the following vehicle. A skilled driver uses the information of both following and preceding vehicles. Hence, doing so is expected to grant better and safer performance to vehicle control.

This approach connects all the following vehicles and leads to a dynamic system similar to a series of mass-spring-damper systems (due to spring-damper dissipation). The system is expected to remain stable if the vehicle control is based on this framework. This section deals with the use of adaptive cruise control (ACC), meaning that the information of the following vehicle is also used in addition to the information of the leading and preceding vehicles. The suggested ACC law guarantees the string stability of the vehicle platoon.

Two different conditions are used to investigate the stability of the bidirectional structure. First, due to the differences of vehicles on a highway, the stability analysis is performed by considering the heterogeneity in the control parameter using the approximation of partial differential equation. Then, two independent time delays are considered for exchanging intervehicle information in a similar group of vehicles. The first delay is considered in the intervehicle communication channel, and the second delay is considered in the exchange of its rate of changes. The *CTCR* method will be used for stability analysis, and the delay under which the system will be stable for specific control parameters is calculated.

The stability by the approximation of partial differential equations

For analyzing system stability, the approximation of partial differential equation is used for the ordinary differential equation (ODE), which indicates the system's closed-loop dynamic model. It should be noted that noise interruptions are not considered in the stability analysis. However, the asymmetry in the position and speed control coefficients is evaluated on both sides. In other words, the heterogeneity is considered in the control law. This is due to the difference in the importance of the intervehicle distance, which is more on the front side compared to the rear; therefore, it is better to consider this subject.

A group of vehicles with a short intervehicle distance is considered for the analysis. The control's objective is to design a controller for each vehicle using the information of the leading, preceding, and following vehicles. Hence, the following information is required for the host vehicle to apply the control law in practice.

- The relative distance and relative speed between the ith and $i-1$th vehicles.
- The relative distance and relative speed between the $i+1$th and ith vehicles.

It should be noted that items above can be measured using the existing sensors and radars. Besides, because there is no following vehicle for the last vehicle, its control is performed by only using the information of the leading and preceding vehicles. For selecting the control input, the control objective is as follows.

- The distance deviation is set to zero.
- The relative speed between the *i*th and the *i*-1th vehicles is set to zero when the ith vehicle is moving at a constant speed.

Here, two different centralized and decentralized control laws are used due to a constant spacing policy. First, centralized control is used (5.23)

$$\begin{aligned} u_i = &- k_i^f (x_i - x_{i-1} + D_{i-1,i} + L_{i-1}) - b_i^f (\dot{x}_i - \dot{x}_{i-1}) \\ &- k_i^b (x_i - x_{i+1} - D_{i,i+1} - L_i) - b_i^b (\dot{x}_i - \dot{x}_{i+1}) \\ &- \beta_i (\dot{x}_i - \dot{x}_0) \end{aligned} \tag{5.23}$$

The coefficients of k_i^f and k_i^b are the front and rear position coefficients for $i = 1, 2, \ldots, N-1$. Similarly, $b_i^f = b_i^b$ are the forward and backward speeds, respectively. Because there is no following vehicle for the last vehicle, its control law is as (5.24):

$$\begin{aligned} u_N = &- k_N^f (x_N - x_{N-1} + D_{N-1,N} + L_{N-1}) - b_N^f (\dot{x}_N - \dot{x}_{N-1}) \\ &- \beta_N (\dot{x}_N - \dot{x}_0) \end{aligned} \tag{5.24}$$

By combining the open-loop dynamic equation of the system with the law of Eq. (5.20), the closed-loop system equation will be as (5.25):

$$\begin{aligned} \tau_i \dot{a}_i + a_i = &- \beta_i (\dot{x}_i - \dot{x}_0) - b_i^f (\dot{x}_i - \dot{x}_{i-1}) - k_i^f (x_i - x_{i-1} + D_{i-1,i} + L_{i-1}) \\ &- b_i^b (\dot{x}_i - \dot{x}_{i+1}) - k_i^b (x_i - x_{i+1} - D_{i,i+1} - L_i) \end{aligned} \tag{5.25}$$

It is assumed that the leading vehicle is moving at a constant speed of $(x_0^* = v_0^*)$ for the analysis of system convergence. Therefore, the ideal path of the *i*th vehicle is defined as Eq. (5.18). The closed-loop equation can be modified as Eq. (5.26) regarding the control error by substituting Eq. (5.19) in Eq. (5.25), and by knowing that $x_{i-1}^* - x_i^* = D_{i-1,\,i} - L_{i-1}$

$$\begin{aligned} \tau_i \dddot{\tilde{x}}_i + \ddot{\tilde{x}}_i = &- k_i^f (\tilde{x}_i - \tilde{x}_{i-1}) - b_i^f \left(\dot{\tilde{x}}_i - \dot{\tilde{x}}_{i-1} \right) - k_i^b (\tilde{x}_i - \tilde{x}_{i+1}) - b_i^b \left(\dot{\tilde{x}}_i - \dot{\tilde{x}}_{i+1} \right) \\ &- \beta_i \dot{\tilde{x}}_i \end{aligned} \tag{5.26}$$

By defining $X = \left[\tilde{x}_1, \dot{\tilde{x}}_1, \ddot{\tilde{x}}_1, \tilde{x}_2, \dot{\tilde{x}}_2, \ddot{\tilde{x}}_2, \ldots, \tilde{x}_N, \dot{\tilde{x}}_N, \ddot{\tilde{x}}_N\right]^T$ the closed-loop equation of the entire system can be rewritten as Eq. (5.27):

$$\dot{X} = AX \tag{5.27}$$

$$A = \begin{bmatrix} A_1 & A_{1b} & 0_{3\times3} & 0_{3\times3} & \ldots & 0_{3\times3} & 0_{3\times3} \\ A_{2f} & A_2 & A_{2b} & 0_{3\times3} & \ldots & 0_{3\times3} & 0_{3\times3} \\ 0_{3\times3} & A_{3f} & A_3 & A_{3b} & \ldots & 0_{3\times3} & 0_{3\times3} \\ \vdots & \vdots & \vdots & \vdots & \vdots & \vdots & \vdots \\ 0_{3\times3} & 0_{3\times3} & 0_{3\times3} & 0_{3\times3} & \ldots & A_{Nf} & A_N \end{bmatrix}$$

$$A_i = \begin{bmatrix} 0 & 1 & 0 \\ 0 & 0 & 1 \\ -\dfrac{k_i^f + k_i^b}{\tau_i} & -\dfrac{b_i^f + b_i^b + \beta_i}{\tau_i} & -\dfrac{1}{\tau_i} \end{bmatrix} A_{ib} = \begin{bmatrix} 0 & 0 & 0 \\ 0 & 0 & 0 \\ k_i^b & b_i^b & 0 \end{bmatrix}, A_{if} = \begin{bmatrix} 0 & 0 & 0 \\ 0 & 0 & 0 \\ k_i^f & b_i^f & 0 \end{bmatrix}$$

Matrix A is the closed-loop state matrix of the system. As a result, the system will be stable when all the eigenvalues of matrix A are left half-plane in a complex domain. The analytical calculation of eigenvalues will not be accessible when the control coefficients are different for each vehicle (heterogeneity in the controlling parameters). Hence, conditions that lead to stability will be calculated by approximating partial differential equation. The parameters are first defined as below for simplicity in writing.

$$k_i^{f+b} = k_i^f + k_i^b k_i^{f-b} = k_i^f - k_i^b$$
$$b_i^{f+b} = b_i^f + b_i^b b_i^{f-b} = b_i^f - b_i^b$$

Also, its substitution in the equation can be rewritten as Eq. (5.28)

$$\begin{aligned} \tau_i \dddot{\tilde{x}}_i + \ddot{\tilde{x}}_i + \beta_i \dot{\tilde{x}}_i = &-\frac{k_i^{f+b} + k_i^{f-b}}{2}(\tilde{x}_i - \tilde{x}_{i-1}) - \frac{k_i^{f+b} - k_i^{f-b}}{2}(\tilde{x}_i - \tilde{x}_{i+1}) \\ &-\frac{b_i^{f+b} + b_i^{f-b}}{2}\left(\dot{\tilde{x}}_i - \dot{\tilde{x}}_{i-1}\right) - \frac{b_i^{f+b} - b_i^{f-b}}{2}\left(\dot{\tilde{x}}_i - \dot{\tilde{x}}_{i+1}\right) \end{aligned} \tag{5.28}$$

The coordinates of the one-dimensional network are expressed in new coordinates in the range of $[0 - 1]$ to simplify the analysis. The ith vehicle in the principal coordinate is described as $(N - i)/N$ in the new coordinate [24] (Figs. 5.6 and 5.7).

The starting point to extract the approximation of partial differential equation is the consideration of $\tilde{x}_i(p, t) : [0, 1] \times [0, \infty) \to R$ and $\tilde{x}_i(t) = \tilde{x}(p, t)|_{p=(N-i)/N}$ functions, in which p is considered as a new variable for the new coordinate. Other scalar functions of $k_i^f(p)$, $k_i^b(p)$, $b_i^f(p)$, $b_i^b(p)$ and $\tau_i(p)$ are defined below regarding the new convention.

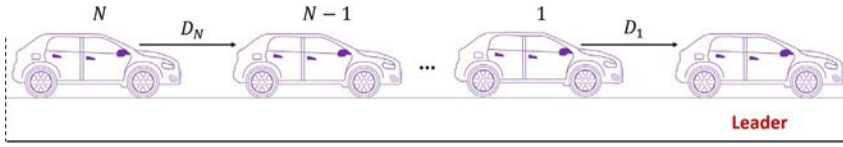

Fig. 5.6 The principal coordinate in the platoon.

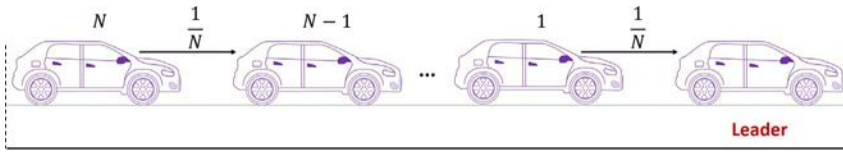

Fig. 5.7 The reexpressed coordinate in the same platoon.

$$k_i^{forb} = k^{forb}(p)\Big|_{p=(N-i)/N}$$
$$b_i^{forb} = b^{forb}(p)\Big|_{p=(N-i)/N}$$
$$\tau_i = \tau_i(p)\big|_{p=(N-i)/N}$$

Finally, a simplified form can be approximated as (5.29)

$$\begin{aligned}&\tau_i\frac{\partial^3\widetilde{x}}{\partial t^3}+\frac{\partial^2\widetilde{x}}{\partial t^2}+\beta_i\frac{\partial\widetilde{x}}{\partial t}\\&=\frac{k_i^{f-b}}{N}\frac{\partial\widetilde{x}}{\partial p}+\frac{k_i^{f+b}}{2N^2}\frac{\partial^2\widetilde{x}}{\partial p^2}+\frac{b_i^{f-b}}{N}\frac{\partial^2\widetilde{x}}{\partial p\partial t}\\&\quad+\frac{b_i^{f+b}}{2N^2}\frac{\partial^3\widetilde{x}}{\partial p^2\partial t}\end{aligned}\tag{5.29}$$

The boundary conditions for the obtained differential equation with partial derivatives depend on the leading vehicle's position in the new coordinate. According to the mentioned conditions, $p = 1$ and $p = 0$ refer to the boundary conditions of the leading and last vehicle, respectively. Therefore,

$$\widetilde{x}(1,t)=0,\frac{\partial\widetilde{x}}{\partial p}(0,t)=0\tag{5.30}$$

This issue is further explained in presenting new theorems in the stability of the bidirectional structure. It is important to note that, proof of some theories is not in this chapter's main content because that was out of boredom. For further reading, you can refer to references [11] and [13].

Theorem 5.1 For the system explained in Eq. (5.25), if the controlling parameters are selected as $b_i^b > \tau_i k_i^b$, the system will exhibit asymptotic stability.

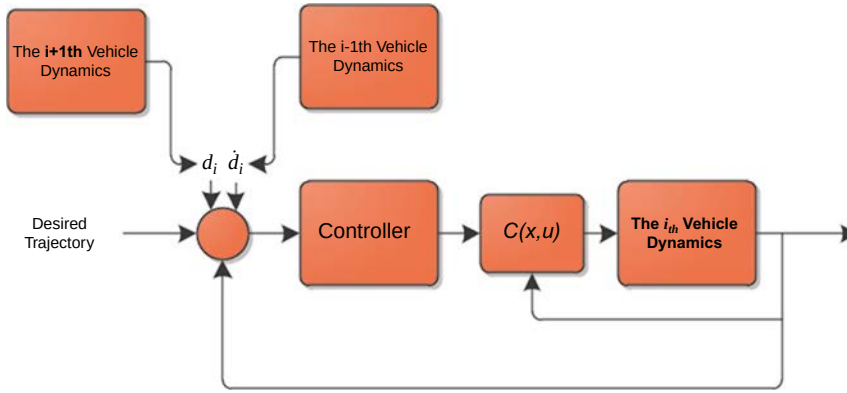

Fig. 5.8 The control structure of the *i*th vehicle.

Now we analyze the system's stability using the approximation of partial differential equation by selecting a decentralized control. The outlines of this case are previously stated about this method; hence, the relations are expressed concisely in this section. The section related to the information of the leading vehicle is omitted (Fig. 5.8) by assuming the control law in the form of (5.31)

$$\begin{aligned} u_i = &-k_i^f(x_i - x_{i-1} + D_{i-1,i} + L_{i-1}) - b_i^f(\dot{x}_i - \dot{x}_{i-1}) \\ &-k_i^b(x_i - x_{i+1} - D_{i,i+1} - L_i) - b_i^b(\dot{x}_i - \dot{x}_{i+1}) \end{aligned} \tag{5.31}$$

The closed-loop equation of the system will be obtained as Eq. (5.32) by combining the open-loop dynamic equation of the system with the control law in Eq. (5.31)

$$\begin{aligned} \tau_i \dot{a}_i + a_i = &-b_i^f(\dot{x}_i - \dot{x}_{i-1}) - k_i^b(x_i - x_{i+1} - D_{i,i+1} - L_i) \\ &-k_i^f(x_i - x_{i-1} + D_{i-1,i} + L_{i-1}) - b_i^b(\dot{x}_i - \dot{x}_{i+1}) \end{aligned} \tag{5.32}$$

By defining the error as before, the closed-loop equation, in terms of control error, can be rewritten as (5.33)

$$\tau_i \dddot{\tilde{x}}_i + \ddot{\tilde{x}}_i = -k_i^f(\tilde{x}_i - \tilde{x}_{i-1}) - k_i^b(\tilde{x}_i - \tilde{x}_{i+1}) - b_i^f\left(\dot{\tilde{x}}_i - \dot{\tilde{x}}_{i-1}\right) - b_i^b\left(\dot{\tilde{x}}_i - \dot{\tilde{x}}_{i+1}\right) \tag{5.33}$$

Eq. (5.33) can be approximated as Eq. (5.34) by performing a procedure similar to centralized control

$$\tau_i \frac{\partial^3 \tilde{x}}{\partial t^3} + \frac{\partial^2 \tilde{x}}{\partial t^2} = \frac{k_i^{f-b}}{N}\frac{\partial \tilde{x}}{\partial p} + \frac{k_i^{f+b}}{2N^2}\frac{\partial^2 \tilde{x}}{\partial p^2} + \frac{b_i^{f-b}}{N}\frac{\partial^2 \tilde{x}}{\partial p \partial t} + \frac{b_i^{f+b}}{2N^2}\frac{\partial^3 \tilde{x}}{\partial p^2 \partial t} \tag{5.34}$$

The controller parameters' stability conditions will be studied for the decentralized control by examining the characteristic equation of partial differential equation. This condition can be expressed as the following theorem.

Theorem 5.2 The closed-loop system is stable if and only if the following conditions are met:

$$b_i^b > \tau_i k_i^b$$

The stability by using CTCR The stability analysis of the closed-loop system is measured based on the real part of the eigenvalues. The delay term causes the characteristic equation of the system to have unlimited roots. Hence, it is difficult to analyze the system by classical methods, especially in the stability analysis and stabilizing controller design. The biggest issue about systems with delays is the lack of analytical solutions, making the analysis difficult. Even for a linear time-invariant system with several constant values as time delays, this will lead to a challenging task. The method used to solve this problem is based on a combination of decoupling and *CTCR*. Decoupling simplifies the system and increases efficiency by reducing the computational load. The *CTCR* method allows for the analysis of the system stability in terms of time delay. This is not a novel method and has been used for delayed systems in the past [25–27]. This process begins with converting the coordinates from the delay space to a new set of coordinates. This mapping reduces the dimension of the problem from an infinite number to a small and controllable number. This method begins with determining all the characteristic equation's imaginary roots for any positive time delay. It is important to note that this transfer is accurate and contains no approximation. A centralized control law is considered in which the relative distance and relative speed between the host vehicle and the preceding and following vehicles, along with the relative velocity between the controlled vehicle and the leading vehicle, are used as the input.

Similar to the law of (5.35):

$$\frac{1}{\tau^2}\left(\begin{bmatrix} 2(D-1) & 1-\tau \\ 1-\tau & 2(1-\tau) \end{bmatrix} \otimes \overline{P}\right) - \frac{K}{\tau^2}\left(\begin{bmatrix} 1 & 1 \\ 1 & 1 \end{bmatrix} \otimes \overline{P}HH^T\overline{P}\right) > 0 \qquad (5.35)$$

The only difference is that the communication between the platoon vehicles is affected by two independent time delays. It is assumed that the first delay is in the position communication channel and the second delay in exchanging speed information. This delay is considered to be constant and uniform throughout the communication. As a result, the control law can be expressed as (5.36)

$$\begin{aligned} u_i(t) = &-\beta_i(\dot{x}_i(t) - \dot{x}_0) - k_i^f\,(x_i\big(t-\tau_p\big) \\ &- x_{i-1}\big(t-\tau_p\big) + D_{i-1,i} + L_{i-1}) - b_i^f\,(\dot{x}_i(t-\tau_v) \\ &- \dot{x}_{i-1}(t-\tau_v)) - b_i^b(\dot{x}_i(t-\tau_v) - \dot{x}_{i+1}(t-\tau_v)) \\ &- k_i^b\big(x_i\big(t-\tau_p\big) - x_{i+1}\big(t-\tau_p\big) - D_{i,i+1} - L_i\big) \end{aligned} \tag{5.36}$$

For $i = 1, 2,\ldots, -1$ the coefficients of k_i^f and k_i^b are the front and rear position coefficients, respectively. Similarly, b_i^f and b_i^b are the forward and backward speed, respectively. τ_p and τ_p are the assumed delay for the exchange position and speed information, respectively.

For analyzing the convergence of the system, it is assumed that the leading vehicle is moving at a constant speed of $x_{i-1}^* - x_i^* = D_i - L_{i-1}$. By simplifying and by knowing that $x_{i-1}^* - x_i^* = D_i - L_{i-1}$, the closed-loop equation can be rewritten as Eq. (5.37) in terms of control error

$$\begin{aligned} \tau_i \dddot{\tilde{x}}_i(t) + \ddot{\tilde{x}}_i(t) = &-k_i^f) - \tilde{x}_{i-1}\big(t-\tau_p\big)) - b_i^f(\dot{\tilde{x}}_i(t-\tau_v) - \dot{\tilde{x}}_{i-1}(t-\tau_v)) \\ &- b_i^b\Big(\dot{\tilde{x}}_i(t-\tau_v) - \dot{\tilde{x}}_{i+1}(t-\tau_v)\Big) \\ &- k_i^b\big(\tilde{x}_i\big(t-\tau_p\big) - \tilde{x}_{i+1}\big(t-\tau_p\big)\big) - \beta_i\dot{\tilde{x}}_i(t) \end{aligned} \tag{5.37}$$

A homogeneous and symmetrical control structure for $N + 1$ strings of cars is considered. In other words:

$$\tau_i = \tau, \beta_i = \beta, k_i^b = k_i^f = k, b_i^b = b_i^f = b$$

If the relations between vehicles are considered as a graph, by defining ω, the closed-loop equation of the entire system can be rewritten in the form of Eq. (5.38) using graph theory

$$\dot{X}(t) = AX(t) + B_1X\big(t-\tau_p\big) + B_2X(t-\tau_v) \tag{5.38}$$

The explicit form of this equation is (5.39)

$$\begin{aligned}\dot{X}(t) = &\left(I_N \otimes \begin{pmatrix} 0 & 1 & 0 \\ 0 & 0 & 1 \\ 0 & -\beta/\tau & -1/\tau \end{pmatrix}\right) X(t) \\ &+ \left(I_N \otimes \begin{pmatrix} 0 & 0 & 0 \\ 0 & 0 & 0 \\ -2k/\tau & 0 & 0 \end{pmatrix}\right) X(t-\tau_p) \\ &+ \left(I_N \otimes \begin{pmatrix} 0 & 0 & 0 \\ 0 & 0 & 0 \\ 0 & -2b/\tau & 0 \end{pmatrix}\right) X(t-\tau_v) \\ &+ \left(C \otimes \begin{pmatrix} 0 & 0 & 0 \\ 0 & 0 & 0 \\ k/\tau & 0 & 0 \end{pmatrix}\right) X(t-\tau_p) \\ &+ \left(C \otimes \begin{pmatrix} 0 & 0 & 0 \\ 0 & 0 & 0 \\ 0 & b/\tau & 0 \end{pmatrix}\right) X(t-\tau_v)\end{aligned} \tag{5.39}$$

where

$$C = \begin{pmatrix} 0 & 1 & 0 & \cdots & 0 & 0 \\ 1 & 0 & 1 & \cdots & 0 & 0 \\ \vdots & \vdots & \vdots & \vdots & \vdots & \vdots \\ 0 & 0 & 0 & \cdots & 1 & 0 \end{pmatrix} \tag{5.40}$$

The C matrix is a matrix that indicates the interactions between the vehicles. The stability analysis of the closed-loop system is measured based on the real part of the eigenvalues. The dynamic complexity increases rapidly as the number of vehicles increases, making the numerical stability analysis difficult

$$\begin{aligned}&CE(s, \tau, k, b, \beta, \tau_p, \tau_v) \\ &= \det\left(sI_{3N} - A - B_1 e^{-\tau_p s} - B_2 e^{-\tau_v s}\right)\end{aligned} \tag{5.41}$$

The stability analysis can be performed by examining the Characteristic Eq. (5.41). The characteristic equation of this group of systems can be easily expressed as a set of factors. These factors are the dynamics of each agent. This method reduces the complexity of the problem significantly.

Theorem 5.3 The characteristic equation of system (5.42) can always be expressed as the product of a set of factors

$$\begin{aligned} &CE(s,\tau,k,b,\beta,\tau_p,\tau_v) = \det\left(sI_{3N} - A - B_1 e^{-\tau_p s} - B_1 e^{-\tau_v s}\right) \\ &= \prod_{i=1}^{N} ce_i(s,\tau,k,b,\beta,\tau_p,\tau_v,\lambda_i) \\ &= \prod_{i=1}^{N} \left(\tau s^3 + s^2 + \beta s + 2be^{-\tau_v s}s + 2ke^{-\tau_p s} - \lambda_i\left(be^{-\tau_v s}s + ke^{-\tau_p s}\right)\right) \end{aligned} \tag{5.42}$$

Proof: There is a nonsingular matrix T, in a way that $T^{-1}CT = \Lambda$ is a diagonal matrix, in which the elements of its main diagonal are equal to the eigenvalues of the Λ matrix. By changing the coordinate as:

$$X = (T \otimes I_3)\xi \epsilon R^{3N}$$

By substituting Eq. (5.39), the following is obtained (5.43)

$$\begin{aligned} \dot{\xi}(t) = &\left(T^{-1}\otimes I_3\right)\left(I_N \otimes \begin{pmatrix} 0 & 1 & 0 \\ 0 & 0 & 1 \\ 0 & -\beta//\tau & -1/\tau \end{pmatrix}\right)(T\otimes I_3)\xi(t) \\ &+ \left(T^{-1}\otimes I_3\right)\left(I_N \otimes \begin{pmatrix} 0 & 0 & 0 \\ 0 & 0 & 0 \\ -2k/\tau & 0 & 0 \end{pmatrix}\right)(T\otimes I_3) \\ &\xi(t-\tau_p) + \left(T^{-1}\otimes I_3\right)\left(I_N \otimes \begin{pmatrix} 0 & 0 & 0 \\ 0 & 0 & 0 \\ 0 & -2b/\tau & 0 \end{pmatrix}\right)(T\otimes I_3) \\ &\xi(t-\tau_v) + \left(T^{-1}\otimes I_3\right)\left(C \otimes \begin{pmatrix} 0 & 0 & 0 \\ 0 & 0 & 0 \\ k/\tau & 0 & 0 \end{pmatrix}\right)(T\otimes I_3) \\ &\xi(t-\tau_p) + \left(T^{-1}\otimes I_3\right)\left(C \otimes \begin{pmatrix} 0 & 0 & 0 \\ 0 & 0 & 0 \\ 0 & b/\tau & 0 \end{pmatrix}\right)(T\otimes I_3)\xi(t-\tau_v) \end{aligned} \tag{5.43}$$

By using the chain multiplication feature in Kronecker multiplication, $(U \otimes V)(W \otimes Z) = UW \otimes VZ$, Eq. (5.43) can be rewritten as Eq. (5.44)

$$\begin{aligned}\dot{\xi}(t) = &\left(I_N \otimes \begin{pmatrix} 0 & 1 & 0 \\ 0 & 0 & 1 \\ 0 & -\beta/\tau & -1/\tau \end{pmatrix}\right)\xi(t) \\ &+ \left(I_N \otimes \begin{pmatrix} 0 & 0 & 0 \\ 0 & 0 & 0 \\ -2k/\tau & 0 & 0 \end{pmatrix}\right)\xi(t-\tau_p) \\ &+ \left(I_N \otimes \begin{pmatrix} 0 & 0 & 0 \\ 0 & 0 & 0 \\ 0 & -2b/\tau & 0 \end{pmatrix}\right)\xi(t-\tau_v) \\ &+ \left(\Lambda \otimes \begin{pmatrix} 0 & 0 & 0 \\ 0 & 0 & 0 \\ k/\tau & 0 & 0 \end{pmatrix}\right)\xi(t-\tau_p) + \left(\Lambda \otimes \begin{pmatrix} 0 & 0 & 0 \\ 0 & 0 & 0 \\ 0 & b/\tau & 0 \end{pmatrix}\right)\xi(t-\tau_v)\end{aligned} \tag{5.44}$$

Because I_N and Λ are diagonal matrices; Eq. (5.44) similar to a diagonal block, which can be expressed as a set of N separate subsystems.

$$\begin{aligned}\dot{\xi}_i(t) = &\begin{pmatrix} 0 & 1 & 0 \\ 0 & 0 & 1 \\ 0 & -\beta/\tau & -1/\tau \end{pmatrix}\xi_i(t) + \begin{pmatrix} 0 & 0 & 0 \\ 0 & 0 & 0 \\ -2k/\tau & 0 & 0 \end{pmatrix}\xi_i(t-\tau_p) \\ &+ \begin{pmatrix} 0 & 0 & 0 \\ 0 & 0 & 0 \\ 0 & -2b/\tau & 0 \end{pmatrix}\xi_i(t-\tau_v) \\ &+ \lambda_i \begin{pmatrix} 0 & 0 & 0 \\ 0 & 0 & 0 \\ k/\tau & 0 & 0 \end{pmatrix}\xi_i(t-\tau_p) \\ &+ \lambda_i \begin{pmatrix} 0 & 0 & 0 \\ 0 & 0 & 0 \\ 0 & b/\tau & 0 \end{pmatrix}\xi_i(t-\tau_v)\end{aligned}$$

For $i = 1, 2, \ldots N$, because the eigenvalues of the matric C are real, it is evident that the characteristic equation of each system can be expressed as (5.45):

$$ce_i(s, \tau, k, b, \beta, \tau_p, \tau_v, \lambda_i) = \tau s^3 + s^2 + \beta s + 2be^{-\tau_v s}s + 2ke^{-\tau_p s} - \lambda_i\left(be^{-\tau_v s}s + ke^{-\tau_p s}\right) \quad (5.45)$$

As a result, the complete characteristic equation of the system, as a product of N factors, is expressed in Eq. (5.45).

Besides, because the only distinguishing element of a factor is the eigenvalues (λ_i), the stability analysis in the field of delay can only be performed once for a general λ_i. Eventually, the entire system's stability can be obtained by using the results of this factor for different factors. In practice, this feature makes the stability analysis independent of the number of factors. Similar to Eq. (5.45), the complexity in determining the stability of the pseudopolynomial is regulated based on determining the eigenvalues of a known matrix C and the repetitive stability analysis of a simple pseudopolynomial. In the following, the stability analysis will be studied without delay and by using the Routh-Hurwitz stability criteria.

Theorem 5.4 The system (5.45) is stable without considering the communication delay if and only if:

$$k < \frac{1}{\tau}\left(\frac{\beta}{2 - \lambda_i} + b\right) \quad (5.46)$$

The analytical stability analysis of a vehicle platoon has received less attention. This section's innovation is due to considering two independent time delays for the communication structure (depending on the information about the intervehicle distance and its rate of change) and considering the time constant of the engine. In the following, the stability conditions for situations related to the constant time headway policy will be examined for two states of unidirectional and bidirectional structures.

5.3.3.2 The stability based on constant headways segmentation policy

As stated earlier, although the constant spacing segmentation policy increases traffic capacity significantly, it is difficult to achieve in practice. The constant time headways segmentation policy is used in this section. This method does not have the same traffic capacity as the previous method; however, it is a policy that is currently used in *ACC* systems. String stability is also easily

achieved in this method. This section also studies the stability for two-way and bidirectional communication situations similar to the previous section.

As a reminder, the goal is to consider a method for all vehicles to follow the leading vehicle, in a way that the distance between two adjacent vehicles is a function of time as $D_{i-1,\,i} = h_i v_i + D_{min}$ instead of being a constant value.

The unidirectional structure

The control objective is to design a controller for each vehicle by using the preceding vehicle's information. This section examines the system's stability by considering the time delays and noise interruptions with the CTCR method. First, a PD controller is used, and then its effect is checked by adding it to a feedforward controller.

This section also uses a decentralized control due to the use of a constant time headway policy

$$u_i(t) = K_p(x_{i-1} - x_i - L_{i-1} - (h_i v_i + D_{min})) + K_d(\dot{x}_{i-1} - \dot{x}_i - h_i \dot{v}_i) \quad (5.47)$$

Due to time delay in the actuators and sensors, the control law is expressed as follows

$$\begin{aligned} u_i(t-\Delta) = & K_p(x_{i-1}(t-\Delta) - x_i(t-\Delta) - L_{i-1} - (h_i v_i(t-\Delta) + D_{min})) \\ & + K_d(\dot{x}_{i-1}(t-\Delta) - \dot{x}_i(t-\Delta) - h_i \dot{v}_i(t-\Delta)) \end{aligned} \quad (5.48)$$

To analyze the stability of the system, it is assumed that the leading vehicle is moving at a constant speed of $(\dot{x}_0^* = v_0^*)$. Hence, the ideal path for the vehicle $x_1, x_2, \ldots, x_N$ is defined as Eq. (5.49) similar to Eq. (5.18)

$$\begin{aligned} x_i^*(t) &= x_0^* - D_{0,i} - \sum_{j=l}^{i-1} L_j = x_0^* - \sum_{j=1}^{i} D_{j-1,j} - \sum_{j=0}^{i-1} L_j \\ &= x_0^* - \sum_{j=1}^{i} \left(D_{j-1,j} + L_{j-1}\right) \end{aligned} \quad (5.49)$$

Also, the tracking error will be defined similarly to Eq. (5.19) to simplify the analysis. By knowing that $x_{i-1}^* - x_i^* = h\dot{x}_0^* - L_{i-1}$, the closed-loop equation can be rewritten in terms of control error as (5.50)

$$\begin{aligned} \tau \dddot{\tilde{x}}_i(t) + \ddot{\tilde{x}}_i(t) = & K_p(\tilde{x}_{i-1}(t-\Delta) - \tilde{x}_i(t-\Delta) - h\dot{\tilde{x}}_i(t-\Delta)) \\ & + K_d\left(\dot{\tilde{x}}_{i-1}(t-\Delta) - \dot{\tilde{x}}_i(t-\Delta) - h\ddot{\tilde{x}}_i(t-\Delta)\right) \end{aligned} \quad (5.50)$$

The Laplace transformation is used for the analysis. The transfer functions are extracted, assuming that the initial conditions are zero. Therefore,

Eq. (5.51) is obtained by performing a Laplace transformation on both sides of Eq. (5.50)

$$\left(\tau s^3 + s^2 + \left(K_d s + K_p\right)(1 + hs)e^{-\Delta s}\right)\widetilde{X}_i(s) = \left(K_d s + K_p\right)e^{-\Delta s}\widetilde{X}_{i-1}(s) \quad (5.51)$$

where $\widetilde{X}_i(s)$ is the Laplace transform of the function $\widetilde{x}_i(s)$. Therefore,

$$\frac{\widetilde{X}_i(s)}{\widetilde{X}_{i-1}(s)} = \frac{\left(K_d s + K_p\right)e^{-\Delta s}}{\tau s^3 + s^2 + \left(K_d s + K_p\right)(1 + hs)e^{-\Delta s}} = G(s) \quad (5.52)$$

The system's internal stability can be examined by analyzing the transfer function between each pair of vehicles. This equation can be rewritten as (5.53)

$$\frac{\widetilde{X}_q(s)}{\widetilde{X}_p(s)} = \frac{\widetilde{X}_q(s)}{\widetilde{X}_{q-1}(s)} \cdots \frac{\widetilde{X}_{p+1}(s)}{\widetilde{X}_p(s)} = (G(s))^{q-p} \quad (5.53)$$

This will be meaningful for $q > p$. The system will be stable for a platoon containing different vehicles and controllers with different coefficients if and only if the transfer function between each pair of consecutive vehicles is stable. The characteristic equation related to the $G(s)$ transfer function will be (5.54)

$$ce = \tau s^3 + s^2 + \left(K_p + \left(hK_p + K_d\right)s + hK_d s^2\right)e^{-\Delta s} = 0 \quad (5.54)$$

Theorem 5.5 The system of Eq. (5.54) is stable without considering the communication delay if the controller parameters are positive.

The bidirectional structure

The stability analysis for a **bidirectional** structure, considering the constant time headways policy, is discussed in this section. The stability analysis of the closed-loop system is measured based on the real part of the eigenvalues. The utilized method is based on a combination of decoupling and CTCR.

Delays in sensors and actuators, along with the communication delays due to data transfer, are considered. Besides, heterogeneity is also considered in the control law because the intervehicle distance is more important at the front compared to the rear. Hence, the control law is defined based on the PD structure (5.55)

$$u_i(t) = k(1-\rho)\varepsilon_i - k\rho\varepsilon_{i+1} + b(1-\rho)(v_{i-1} - v_i) + b\rho(v_{i+1} - v_i) \quad (5.55)$$

where $\rho \in (0,1)$ indicates the penetrance of the front side information compared to the rear side. In other words:

$$\begin{aligned} u_i(t) = & k(1-\rho)(x_{i-1} - x_i - L_{i-1} - (hv_i + D_{min})) \\ & -k\rho(x_i - x_{i+1} - L_i - (hv_{i+1} + D_{min})) \\ & + b(1-\rho)(v_{i-1} - v_i) \\ & + b\rho(v_{i+1} - v_i) \end{aligned} \tag{5.56}$$

Because the error $\varepsilon_{i+1} = x_i - x_{i+1} - L_i - (hv_{i+1} + D_{min})$ is controlled by the ith vehicle, the term can substitute in $\varepsilon_{i+1}{}' = x_i - x_{i+1} - L_i - (hv_i + D_{min})$. Therefore, the control law of Eq. (5.55) can be expressed as (5.57)

$$u_i(t) = k(1-\rho)\varepsilon'_{i+1} - k\rho\varepsilon_{i+1} + b(1-\rho)(v_{i-1} - v_i) + b\rho(v_{i+1} - v_i) \tag{5.57}$$

By considering the communication delay and assuming the same communication delay for the position and speed signals, the control law of Eq. (5.57) can be rewritten as (5.58)

$$\begin{aligned} u_i(t) = & k(1-\rho)(d_i(t-\tau_{com}) - (hv_i(t) + D_{min})) \\ & + b(1-\rho)\dot{d}_i(t-\tau_{com}) \\ & -k\rho(d_{i+1}(t-\tau_{com}) - L_i - (hv_i + D_{min})) \\ & + b\rho\dot{d}_{i+1}(t-\tau_{com}) \end{aligned} \tag{5.58}$$

where $d_i = x_{i-1} - x_i - L_{i-1}$ indicates the intervehicle distance. Due to the presence of noise interruptions in the actuators and sensors, the control law (5.58) is expressed as (5.59)

$$\begin{aligned} & u_i(t-\Delta) = b(1-\rho)(v_{i-1}(t-\tau_{com}-\Delta) - v_i(t-\tau_{com}-\Delta)) \\ & +k(1-\rho)(x_{i-1}(t-\tau_{com}-\Delta) - x_i(t-\tau_{com}-\Delta) - L_{i-1} - (hv_i(t-\Delta) + D_{min})) \\ & -k\rho(x_i(t-\tau_{com}-\Delta) - x_{i+1}(t-\tau_{com}-\Delta) - L_i - (hv_i(t-\Delta) + D_{min})) \\ & +b\rho(v_{i+1}(t-\tau_{com}-\Delta) - v_i(t-\tau_{com}-\Delta)) \end{aligned} \tag{5.59}$$

For simplification, by defining $\Delta = \tau_1$, $\tau_{com} + \Delta = \tau_2$, the control law of Eq. (5.59) can be rewritten as (5.60)

$$\begin{aligned} & u_i(t-\Delta) = k(1-\rho)(x_{i-1}(t-\tau_2) - x_i(t-\tau_2) - L_{i-1} - (hv_i(t-\tau_1) + D_{min})) \\ & -k\rho(x_i(t-\tau_2) - x_{i+1}(t-\tau_2) - L_i - (hv_i(t-\tau_1) + D_{min})) \\ & +b(1-\rho)(v_{i-1}(t-\tau_2) - v_i(t-\tau_2)) + b\rho(v_{i+1}(t-\tau_2) - v_i(t-\tau_2)) \end{aligned} \tag{5.60}$$

For the last vehicle, the control law is as (5.61)

$$u_N(t-\Delta) = k(x_{N-1}(t-\tau_2) - x_N(t-\tau_2) - L_{i-1} - (hv_N(t-\tau_1) + D_{min}())) + b(v_{N-1}(t-\tau_2) - v_N(t-\tau_2)) \tag{5.61}$$

For analyzing the convergence of the system, it is assumed that the leading vehicle is moving at a constant speed of $(\dot{x}_0^* = v_0^*)$. By knowing that $d_i = x_{i-1} - x_i - L_{i-1}$, the closed-loop equation can be rewritten as follows in terms of error

$$\begin{aligned}\tau \dddot{\tilde{x}}_i + \ddot{\tilde{x}}_i = {} & k(1-\rho)(\tilde{x}_{i-1}(t-\tau_2) - \tilde{x}_i(t-\tau_2) - h\tilde{v}_i(t-\tau_1)) \\ & - k\rho(\tilde{x}_i(t-\tau_2) - \tilde{x}_{i+1}(t-\tau_2) - h\tilde{v}_i(t-\tau_1)) \\ & + b(1-\rho)(\tilde{v}_{i-1}(t-\tau_2) - \tilde{v}_i(t-\tau_2)) \\ & + b\rho(\tilde{v}_{i+1}(t-\tau_2) - \tilde{v}_i(t-\tau_2))\end{aligned} \tag{5.62}$$

By defining $X = \left[\tilde{x}_1, \dot{\tilde{x}}_1, \ddot{\tilde{x}}_1, \tilde{x}_2, \dot{\tilde{x}}_2, \ddot{\tilde{x}}_2, \ldots, \tilde{x}_N, \dot{\tilde{x}}_N, \ddot{\tilde{x}}_N\right]^T$, the closed-loop equation of the whole system can be rewritten as (5.63)

$$\dot{X}(t) = AX(t) + B_1X(t-\tau_1) + B_2X(t-\tau_2) \tag{5.63}$$

The explicit form of Eq. (5.63) is Eq. (5.64)

$$\begin{aligned}\dot{X}(t) = {} & \left(I_N \otimes \begin{pmatrix} 0 & 1 & 0 \\ 0 & 0 & 1 \\ 0 & 0 & -\frac{1}{\tau} \end{pmatrix}\right) X(t) \\ & + \left(I_N \otimes \begin{pmatrix} 0 & 0 & 0 \\ 0 & 0 & 0 \\ 0 & -\frac{kh(1-2\rho)}{\tau} & 0 \end{pmatrix}\right) X(t-\tau_1) \\ & \left(I_N \otimes \begin{pmatrix} 0 & 0 & 0 \\ 0 & 0 & 0 \\ -\frac{k}{\tau} & -\frac{b}{\tau} & 0 \end{pmatrix}\right) X(t-\tau_2) \\ & + \left(C \otimes \begin{pmatrix} 0 & 0 & 0 \\ 0 & 0 & 0 \\ \frac{k}{\tau} & \frac{b}{\tau} & 0 \end{pmatrix}\right) X(t-\tau_2)\end{aligned} \tag{5.64}$$

where

$$C=\begin{pmatrix} 0 & \rho & 0 & \dots & 0 & 0 & 0 \\ 1-\rho & 0 & 0 & \dots & 0 & 0 & 0 \\ 0 & 1-\rho & 0 & \dots & 0 & 0 & 0 \\ \vdots & \vdots & \vdots & \vdots & \vdots & \vdots & \vdots \\ 0 & 0 & 0 & \dots & 1-\rho & 0 & \rho \\ 0 & 0 & 0 & \dots & 0 & 1 & 0 \end{pmatrix}$$

The stability analysis of the closed-loop system is measured based on the real part of the eigenvalues. The system's complexity increases rapidly as the number of vehicles increases, which makes the numerical analysis of the stability difficult (5.65)

$$CE(s,\tau,k,b,\rho,\tau_1,\tau_2)=\det\left(sI_{3N}-A-B_1e^{-\tau_1 s}-B_2e^{-\tau_2 s}\right) \tag{5.65}$$

The stability analysis can be performed by examining the characteristic Eq. (5.65). The characteristic equation of this group of systems can be easily expressed as the product of factors that are each agent's dynamics.

According to Theorem 5.3, the characteristic equation of system (5.65) can always be expressed as the product of a set of factors

$$\begin{aligned} &CE(s,\tau,k,b,\rho,\tau_1,\tau_2)=\det\left(sI_{3N}-A-B_1e^{-\tau_1 s}-B_2e^{-\tau_2 s}\right) \\ &=\prod_{i=1}^{N} ce_i(s,\tau,k,b,\rho,\tau_1,\tau_2) \\ &=\prod_{i=1}^{N}\left(\tau s^3+s^2+kh(1-2\rho)se^{-\tau_1 s}+(1-\lambda_i)(k+bs)e^{-\tau_2 s}\right) \end{aligned} \tag{5.66}$$

where $i=1,\ldots,N$ are the eigenvalues of the matrix C.

Because the only distinguishing element between the factors is the eigenvalues of λ_i, the stability analysis in the field of delay can only be performed once for a general λ_i, and the stability of different factors can be obtained by using the obtained results from this factor. Therefore, the stability analysis will be studied without delay and by using the Routh-Hurwitz stability criteria as before.

Theorem 5.6 The system of Eq. (5.66) is stable without considering communication delay if and only if:

$$b>k\left(\tau-\frac{h(1-2\rho)}{(1-\lambda_i)}\right),\quad \rho<0.5 \text{ and } k>0 \tag{5.67}$$

5.4 String stability analysis

One of the objectives of automated highways is to allow a more significant number of vehicles to travel in one direction at a time. Specific conditions must be applied to the vehicle platoons to fulfill the mentioned goal. In other words, in addition to the stability analysis, the convergence analysis of a vehicle platoon and the error propagation through the string (due to disturbances) should be considered. String stability ensures that the range of error is reduced throughout the vehicle flow. The string stability problem is solved by the use of transfer functions, which are related to the distance error between two pairs of consecutive vehicles. The performance of string stability is determined by the control structure and spacing segmentation policy. Section 5.6 will evaluate the string stability conditions for situations in which the stability was studied.

The output error domain (host vehicle) must be smaller or equal to the input error domain (preceding vehicle) to prevent the infinite propagation of domain errors throughout the string of vehicles. As mentioned earlier, the widely used definition of string stability for a vehicle platoon is as (5.68) [28, 29]

$$\left|\frac{E_i(j\omega)}{E_{i-1}(j\omega)}\right| < 1 \forall \omega > 0 \tag{5.68}$$

where $E_i(s)$ is the Laplace transform of $\varepsilon_i(t) = x_{i-1} - x_i - L_{i-1} - D_i = d_i - D_i$. It can be shown that the string stability conditions for a platoon of similar vehicles are as (5.69)

$$\left|\frac{V_i(j\omega)}{V_{i-1}(j\omega)}\right| < 1 \forall \omega > 0 \tag{5.69}$$

where $V_i(s)$ represents the Laplace transformation of $v_i(t)$.

Because the system's performance must be considered in addition to stability, the string stability problem will be discussed in the following. The string stability is in line with automated highways; therefore, it increases the number of vehicles with smaller intervehicle distances.

5.4.1 The string stability based on constant spacing policy

5.4.1.1 Providing a new theorem in string stability of the unidirectional structure

The goal is to find areas of control parameters that satisfy Eq. (5.68). Therefore, the control law can be expressed as (5.70)

$$u_i(t) = K(\widetilde{x}_{i-1}(t-r) - \widetilde{x}_i(t-r) + D\left(-\dot{\widetilde{x}}_i\right) \quad \forall i = 1, \ldots, N \tag{5.70}$$

Therefore, by substituting the control law of Eq. (5.70) in the system's closed-loop dynamics, the system's closed-loop equation can be expressed as (5.71)

$$\tau_i \dddot{\widetilde{x}}_i(t) + \ddot{\widetilde{x}}_i(t) = K(\widetilde{x}_{i-1}(t-r) - \widetilde{x}_i(t-r)) - D\dot{\widetilde{x}}_i(t) \tag{5.71}$$

The communication delay is assumed to be constant and equal to its bound β in the string stability; therefore, Eq. (5.72) is as follows

$$G(s) = \frac{\widetilde{X}_i(s)}{\widetilde{X}_{i-1}(s)} = \frac{Ke^{-\beta s}}{\tau s^3 + s^2 + Ds + Ke^{-\beta s}} \tag{5.72}$$

The equation above indicates the distance error dynamics for two consecutive vehicles.

Theorem 5.7 The string stability is guaranteed if the following conditions are met.

$$K\beta + \sqrt{K^2\beta^2 + 2K} < D < \frac{1}{2\tau} - 0.5K\tau$$

This theorem explains that the delay negatively affects the string stability and creates more strict constraints on the control parameters.

5.4.1.2 Providing new theorems in string stability of the bidirectional structure

The string stability for the model of the approximation of partial differential equations

The analytical study of the bidirectional structure's string stability, which is performed by the approximation of partial differential equation, is among the topics addressed in this section. It first begins with string stability based on decentralized control.

The dynamic equation of position and speed error can be obtained by applying derivatives on both sides in the form of (5.73):

$$\tau_i \ddot{a}_i + \dot{a}_i = -k_i^f(\dot{x}_i - \dot{x}_{i-1}) - k_i^b(\dot{x}_i - \dot{x}_{i+1}) - b_i^f(\ddot{x}_i - \ddot{x}_{i-1}) - b_i^b(\ddot{x}_i - \ddot{x}_{i+1}) \tag{5.73}$$

Laplace transformation is used to obtain the transfer function when the initial condition is assumed to be zero. Therefore, the following is obtained by applying Laplace transformation on both sides of (5.74)

$$\left(\tau_i s^3 + s^2 + \left(b_i^f + b_i^b\right)s + \left(k_i^f + k_i^b\right)\right) V_i = \left(k_i^f + s b_i^f\right) V_{i-1} + \left(k_i^b + s b_i^b\right) V_{i+1} \tag{5.74}$$

The above equation can be rewritten as (5.75)

$$V_i = G_{i-} V_{i-1} + G_{i+} V_{i+1} \tag{5.75}$$

where

$$G_{i-} = \frac{k_i^f + s b_i^f}{\tau_i s^3 + s^2 + \left(b_i^f + b_i^b\right)s + \left(k_i^f + k_i^b\right)},$$

$$G_{i+} = \frac{k_i^b + s b_i^b}{\tau_i s^3 + s^2 + \left(b_i^f + b_i^b\right)s + \left(k_i^f + k_i^b\right)}$$

Each vehicle's controller has access to the information of the preceding and following vehicles as well as the host vehicle's information. As a result, the speeds of consecutive vehicles are expressed by the following equation. The following is obtained by dividing both sides of Eq. (5.75) by V_{i-1}.

$$\frac{V_i}{V_{i-1}} = G_{i-} + G_{i+}\frac{V_{i+1}}{V_{i-1}} = G_{i-} + G_{i+}\frac{V_{i+1}}{V_i}\frac{V_i}{V_{i-1}}$$

$$\frac{V_i}{V_{i-1}}\left(1 - G_{i+}\frac{V_{i+1}}{V_i}\right) = G_{i-} \Rightarrow \frac{V_i}{V_{i-1}} = \frac{G_{i-}}{1 - G_{i+}\dfrac{V_{i+1}}{V_i}}$$

According to the definition, string stability is obtained if Eq. (5.76) is satisfied

$$\|G_{i-}\|_\infty < \left\|1 - G_{i+}\frac{V_{i+1}}{V_i}\right\|_\infty \tag{5.76}$$

The last vehicle in the platoon uses the preceding vehicle's information only; therefore, the string stability is studied from the end of the platoon. By assuming that $\|V_N/V_{N-1}\|_\infty < 1$ is satisfied, the string stability is achieved if Eq. (5.76) is satisfied

$$\|G_{i-}\|_\infty < 0.5, \|G_{i+}\|_\infty < 0.5 \tag{5.77}$$

It should be noted that these conditions are sufficient conditions to ensure stability. Therefore, theorems will be provided on the control parameters to obtain string stability so that the conditions of Eq. (5.77) can be achieved. Eventually, the assumption about $\|V_N/V_{N-1}\|_\infty < 1$ will be studied. This issue is stated in the forms of Theorems 5.8, 5.9, and 5.10.

Theorem 5.8 If the conditions of $k_i^b > \Delta_i^k/\sqrt{2}$, $(\mathrm{b_i^b})^2 > 2\mathrm{k_i^b} + \Delta_\mathrm{i}^\mathrm{k} + 0.5(\Delta_\mathrm{i}^\mathrm{k})^2$, *and* $\mathrm{b_i^b} < 0.25/\tau_\mathrm{i} - 0.5\Delta_\mathrm{i}^\mathrm{b}$ *are met, then* $\|\mathrm{G_{i-}}\|_\infty < 0.5$.

As mentioned before, because low frequencies have the most significant impact on string stability, the constant coefficient, that is, $k_i^b > \Delta_i^k/\sqrt{2}$, will be the governing condition of stability.

Theorem 5.9 If the condition of Theorem 5.8 is established, then $\|G_{i+}\|_\infty < 0.5$.

Theorem 5.10 If $k_N^f = 0$ and $b_N^f < \frac{1}{2\tau_N}$. *Then* $\left\|\dfrac{V_N}{V_{N-1}}\right\|_\infty < 1$.

In the string stability analysis, the propagation of distance errors is not acceptable, even for a few centimeters. It is known that under real conditions, a distance error propagation of only a few centimeters may be acceptable. As a result, a satisfactory solution can be obtained by selecting the appropriate control parameters.

Theorem 5.11 If $k_i^b > \frac{\Delta_i^k}{\sqrt{2}}$ then $\|G_{i-}\|_\infty < 0.5$.

Theorem 5.12 $\|G_{i-}\|_\infty < 0.5$.

Theorem 5.13 If

$$\frac{1}{2\tau_N} > \beta_N > -b_N^f + \sqrt{\left(b_N^f\right)^2 + 2k_N^f}$$

Therefore,

$$|V_N/V_{N-1}(j\omega)| < 1.$$

The string stability for CTCR

This section discusses the string stability of a group of vehicles equipped with similar ACC. The error dynamics equation of position and speed can be written in the form of (5.78)

$$\begin{aligned}\tau_i\ddot{a}_i(t)+\dot{a}_i(t)=&-k\left(\dot{x}_i\left(t-\tau_p\right)-\dot{x}_{i-1}\left(t-\tau_p\right)\right)\\&-b\left(\ddot{x}_i(t-\tau_v)-\ddot{x}_{i-1}(t-\tau_v)\right)\\&-b\left(\ddot{x}_i(t-\tau_v)-\ddot{x}_{i+1}(t-\tau_v)\right)\\&-k\left(\dot{x}_i\left(t-\tau_p\right)-\dot{x}_{i+1}\left(t-\tau_p\right)\right)-\beta\ddot{x}_i(t)\end{aligned}\tag{5.78}$$

The Laplace transformation is used to obtain the transfer function for further analysis by assuming zero initial conditions

$$V_i=G_{i-}V_{i-1}+G_{i+}V_{i+1}\tag{5.79}$$

where

$$G=\frac{ke^{-\tau_p s}+sbe^{-\tau_v s}}{\tau s^3+s^2+(2be^{-\tau_v s}+\beta)s+2ke^{-\tau_p s}}$$

Assuming $|V_N/V_{N-1}(j\omega)|<1$, the string stability will be established if Eq. (5.77) is satisfied. The analysis of this issue is in the form of Theorem 5.14.

Theorem 5.14 The string stability is obtained if the following conditions are met.

$$\text{(a)}\quad 2b^2+\beta^2-4k-4kb\left|\tau_p-\tau_v\right|-4b\beta-4k\beta\tau_p\geq 0$$

$$\text{(b)}\quad a1-2\beta\tau-4b\tau_v-4b\tau-4k\tau\tau_p\geq 0$$

$$\text{(c)}\quad \beta^2-2k-2b\beta-2k\beta\tau_p\geq 0$$

5.4.2 The string stability based on constant headways policy

5.4.2.1 Providing new theorems in string stability of the unidirectional structure

The objective of this section is to find control parameters that satisfy Eq. (5.68). It is primarily necessary to obtain the transfer function for achieving such a condition. The transfer function indicates the distance error between two pairs of consecutive vehicles. Hence, the error dynamics equation of position and speed in the frequency domain can be rewritten (5.80)

$$\frac{\widetilde{X}_i(s)}{\widetilde{X}_{i-1}(s)}=\frac{\left(K_d s+K_p\right)e^{-\Delta s}}{\tau s^3+s^2+\left(K_d s+K_p\right)(1+hs)e^{-\Delta s}}=G(s)\tag{5.80}$$

This case is stated as Theorem 5.15.**Theorem 5.15** String stability is achieved if the following conditions are met.

$$h > \sqrt{2/K_p}$$

5.4.2.2 Providing a new theorem in string stability of the bidirectional structure

This section performs an analytical study on the **bidirectional** structure's string stability for the constant time headways policy. Therefore, the control parameters' conditions must ensure that the string stability will be expressed analytically. The dynamic equation between position and speed error can be explained as (5.81):

$$\begin{aligned}\tau\dddot{\widetilde{x}}_i + \ddot{\widetilde{x}}_i = {} & k(1-\rho)(\widetilde{x}_{i-1}(t-\tau_2) - \widetilde{x}_i(t-\tau_2) - h\dot{\widetilde{v}}_i(t-\tau_1)) \\ & + b(1-\rho)(\widetilde{v}_{i-1}(t-\tau_2) - \widetilde{v}_i(t-\tau_2)) \\ & - k\rho(\widetilde{x}_i(t-\tau_2) - \widetilde{x}_{i+1}(t-\tau_2) - h\dot{\widetilde{v}}_i(t-\tau_1)) \\ & + b\rho(\widetilde{v}_{i+1}(t-\tau_2) - \widetilde{v}_i(t-\tau_2))\end{aligned} \tag{5.81}$$

This equation can be rewritten as (5.82)

$$\widetilde{X}_i = G_{i-}\widetilde{X}_{i-1} + G_{i+}\widetilde{X}_{i+1} \tag{5.82}$$

where

$$G_{i-} = \frac{(1-\rho)(k+bs)e^{-\tau_2 s}}{\tau s^3 + s^2 + kh(1-2\rho)se^{-\tau_1 s} + (k+bs)e^{-\tau_2 s}}$$

$$G_{i+} = \frac{\rho(k+bs)e^{-\tau_2 s}}{\tau s^3 + s^2 + kh(1-2\rho)se^{-\tau_1 s} + (k+bs)e^{-\tau_2 s}}$$

By assuming that $\left|\widetilde{X}_N/\widetilde{X}_{N-1}(j\omega)\right| < 1$ is satisfied, the string stability is achieved if the conditions of Eq. (5.77) are established.

Theorem 5.16 String stability is achieved if the following conditions are met.

$$\text{(a)} \quad kh \geq \frac{2(1+hb)}{h - 2(\tau_2 - \tau_1)}$$

$$\text{(b)} \quad b \leq \frac{1 + 2k\tau\tau_2 - 2kh(\tau + \tau_1)}{2(\tau_2 + \tau)}$$

$$\text{(c)}\quad 0.5 \geq \rho \geq 1 - \sqrt{\frac{1}{2}}$$

$$\text{(d)}\quad (kh(1-2\rho))^2 + b^2\left(1-2(1-\rho)^2\right) - 2khb(1-2\rho) \\ -2k^2h(1-2\rho)(\tau_2-\tau_1) - 2k \geq 0$$

In addition to analyzing the system stability and behavior, it is generally inferred that evaluating a feature titled string stability is necessary to achieve the ideal system performance in multiactuator systems. In other words, in addition to the conditions that must be applied to the control parameters to make the system stable, the conditions of string stability are also required to achieve the system goals.

5.5 Validation based on simulation

The validation of the extracted theorems expressed as boundaries on control parameters is studied using computer simulations. This means that the system will have the ideal conditions of stability and string stability if control parameters are selected to meet the extracted theorems' requirements. The real dynamics are highly nonlinear, and its behavior is different from the simple conditions. Also, the internal control loop and the throttle valve/brake control loop are not negligible problems due to the complexity and asymmetry of the throttle valve and brake subsystems. However, based on the published experimental results, the $\tau_i \dot{a}_i + a_i = u_i(t - \Delta_i)$ model can be accepted as a valid model for the longitudinal control of the vehicle [22, 30].

The computer simulation is performed for a platoon with 10 consecutive vehicles ($N = 10$) to validate the performance of the proposed controller algorithm. As mentioned before, the ability to maintain the intervehicle distance is important for the safety of vehicle platoons in the presence of disturbances. The most important disturbances in a platoon are the increase/decrease of the leading vehicle's acceleration. In other words, a disturbance means the presence of a source that ensures that the vehicle platoon does not maintain its constant speed. In the simulation, the length of the car is considered to be $L_i = 4m$, and other simulation parameters are based on Ref. [31] given in Table 5.1.

Without losing the generality of the case, it is assumed that the leading vehicle initially moves at a constant speed of $v_{initial} = 20$ m/s, and reaches

Table 5.1 The parameters of the system.

Value	Symbol	Parameter
1 N/m^3	σ_i	The specific weight of air
2.2 m^2	A_i	The cross-sectional area of the vehicle
0.35	c_{di}	Drag coefficient
1500 kg	m_i	Vehicle mass
150 N	d_{mi}	Mechanical drag

$v_{final} = 40$ m/s through acceleration. The acceleration procedure of the leading vehicle is as below:

$$a_{des} = \begin{cases} 0 & t \leq 20 \text{ s} \\ 2 \text{ m/s}^2 & 20 \text{ s} \leq t \leq 30 \text{ s} \\ 0 & t \geq 30 \text{ s} \end{cases}$$

5.5.1 Stability

The validation of stability theorems of a vehicle platoon is examined in this section. The process is performed for four conditions, including different spacing policies and structural communications.

5.5.1.1 The stability based on constant spacing policy

The ideal intervehicle distance is assumed to be $D_{i-1,\,i} = 8$ m in this policy.

The unidirectional structure in stability analysis

The stability analysis in the **unidirectional** structure is performed based on Theorem 5.17.

Theorem 5.17 By considering the conditions below for the controlling parameters of system (5.22),

$$K < \frac{2\overline{\mu}}{\gamma\overline{\lambda}} \text{ and } D > 1 + \frac{1-\tau}{4}$$

Then $\lim_{t\to\infty} \varepsilon(t) = 0$, if and only if the vertex of the leading vehicle is fully accessible in the platoon.

The validity of the extracted Theorem 5.17 is checked by performing a simulation. In the first step, the defined parameters and values in the mentioned theorem are calculated. These parameters are necessary to obtain stability boundaries on control parameters and to achieve a sufficient stability condition. Therefore, a delay that is variable with time is assumed

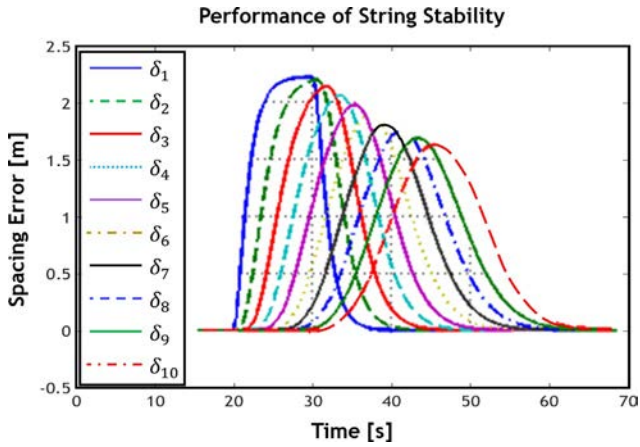

Fig. 5.9 The stability of 10 tracking vehicles under the time-variable communication delay by considering $D = 1.9$, where $\boldsymbol{\delta_i = x_{i-1} - x_i - L_{i-1} - D_i}$ indicates the distance error relative to the ideal distance with the preceding vehicle.

as $r(t) = 0.03|\cos(t)|$. The required parameters in the extracted theorem can be calculated by solving the Lyapunov equation, which is equal to $\overline{\lambda} = 0.2554, \overline{\mu} = 1.5964$. By considering the control parameter $D = 1.9$, the value of γ will be equal to 1.6486. As mentioned in Theorem 5.17, it states a sufficient condition for stability. Two different conditions are examined on the control parameters to indicate two different system behaviors under different conditions. In the first condition, the control parameters are selected so that the condition expressed in the stated theorem is met. As observed in Fig. 5.9, the system exhibits stable behavior, emphasizing the accuracy of Theorem 5.17.

The bidirectional structure in stability analysis

The stability by the use of approximation of partial differential equations

The control parameters are selected as $\tau_i = 0.2\,\text{s}$, $k_i^b = 2$, $b_i^b = 3$, $\beta_i = 4$, and $\Delta_i^b = 0.2$ in the simulation. The response of this system is displayed in Fig. 5.11. As expected, Fig. 5.1 shows a stable behavior in the system. It should be noted that the system will have a stable behavior for all values in Theorem 5.1. Fig. 5.10 is only displayed as an example of confirmation. If the stability condition is not met, it does not necessarily mean that the system will be unstable, but the system will not always be stable.

The system behavior undergoes a fundamental change by the slightest changes in the controlling parameters relative to the stability boundary.

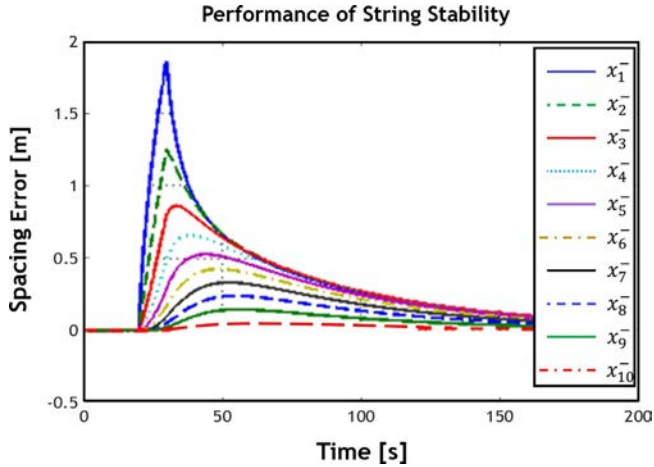

Fig. 5.10 The stability of the system for centralized control under $b_i^b > \tau_i k_i^b$ condition.

Table 5.2 The controlling parameters.

Parameter	State 1	State 2
τ_i	0.2	0.2
k_i^b	5	5
b_i^b	1.1	0.9
Conditions	$b_i^b > \tau_i k_i^b$	$b_i^b < \tau_i k_i^b$

To illustrate this, two groups of different parameters are assumed relative to the stability boundary in Table 5.2.

Fig. 5.11 illustrates State 1 in Table 5.2, which indicates the stability conditions of the system. Fig. 5.12 shows State 2 in Table 5.2, which suggests the instability conditions of the system.

The stability using CTCR The stability analysis based on the bidirectional structure using *CTCR* is performed in this section. This section aims to find delay boundaries for specific control parameters in which the system exhibits stable behavior. Therefore, k_i^b are the eigenvalues of the matrix k_i^f for the considered communication structure. All the eigenvalues are real, and the SDS stability boundaries are depicted for all factors generated by these eigenvalues. The structural blocks can be observed in Figs. 5.13, 5.14, and 5.15 by assuming the longitudinal parameters as $k = 2$, $b = 1$, $\tau = 0.2$, and $\beta = 1$.

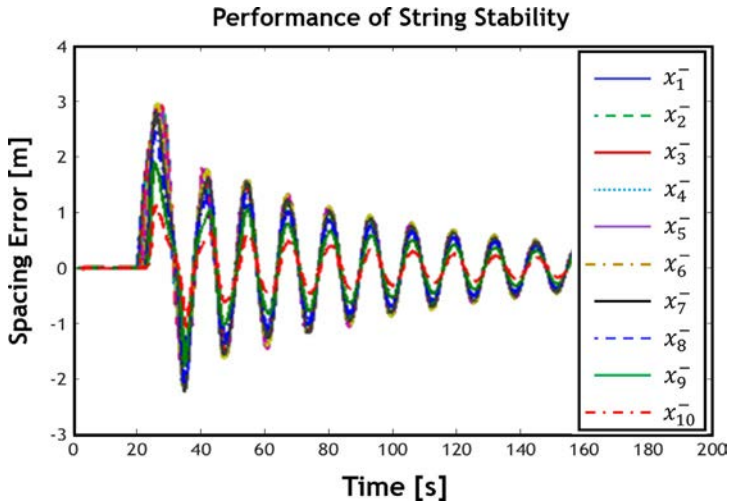

Fig. 5.11 The stability of the system for decentralized control under $b_i^b > \tau_i k_i^b$ condition.

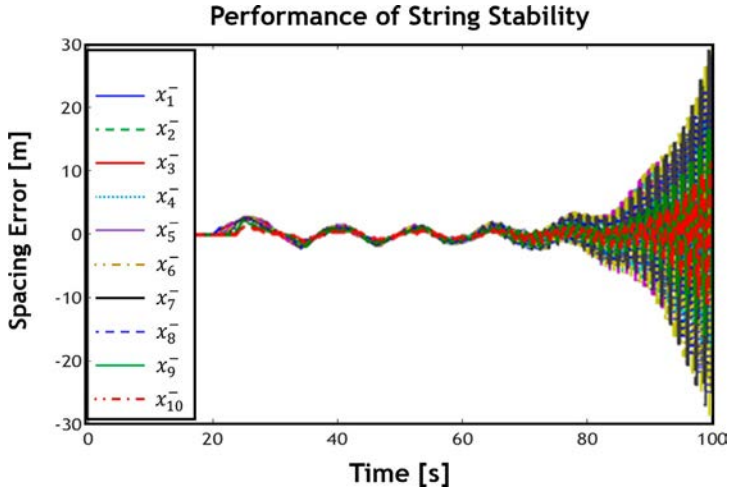

Fig. 5.12 The instability of the system for decentralized control under $b_i^b < \tau_i k_i^b$ conditions.

The red lines (lines in regions $[0, 2\pi]$) indicate the structural curves in the mentioned figures.

5.5.1.2 The stability based on constant time headways policy

The unidirectional structure in stability analysis

This section examines the stability of a **unidirectional** structure based on the CTCR method. The objective is to show the delay space in which the system

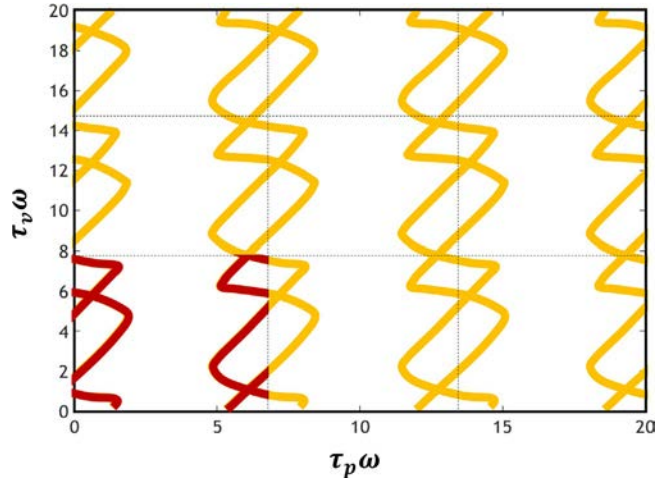

Fig. 5.13 The SDS illustration for factors related to eigenvalues of $\lambda = -1.919, -1.6825, -1.3097$.

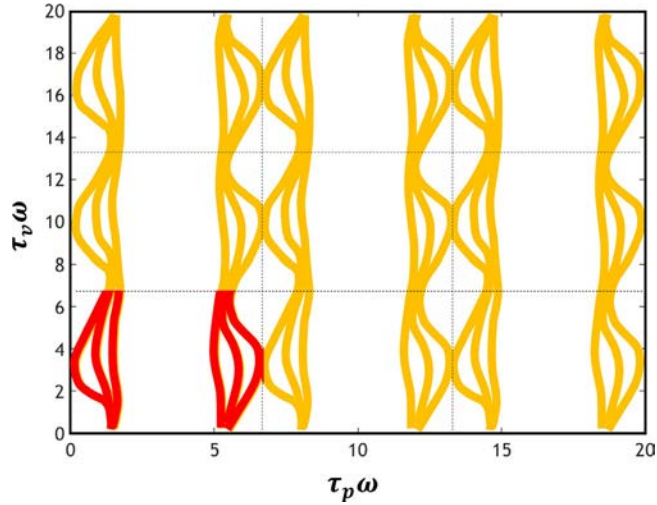

Fig. 5.14 The SDS illustration for factors related to eigenvalues of $\lambda = 1.919, 1.6825, 1.3097, 1.3097$.

exhibits stable behavior for specific control parameters. This section also attempts to indicate the variation of stability boundaries in delay space for control parameter changes. By assuming $h = 1.5$, $\tau = 0.2$ s, and $K_p = 2$, the stable areas in the (K_d, Δ) domain are shown in Fig. 5.16. This is a two-dimensional (2D) illustration for better comprehension. The shaded areas

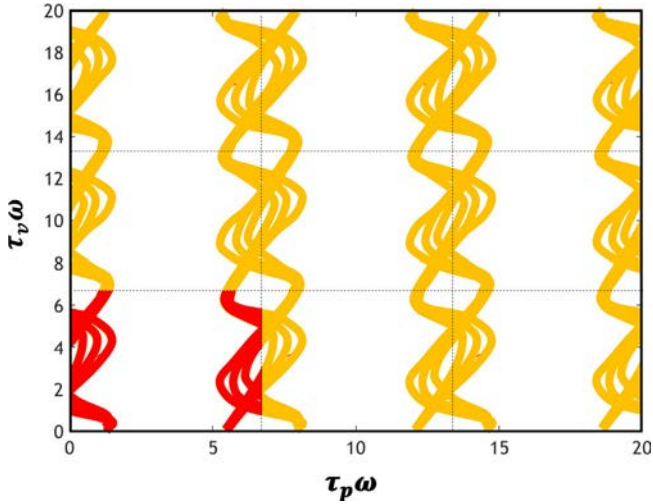

Fig. 5.15 The SDS illustration for factors related to eigenvalues of $\lambda = \pm$ **0.8308**, $\lambda = \pm$ **0.2846**.

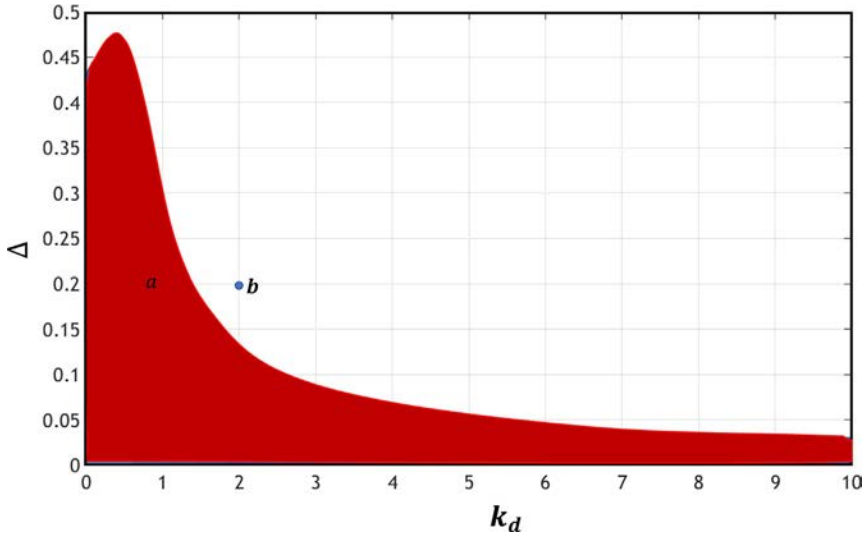

Fig. 5.16 The stability boundaries in the domain of (k_d, Δ) and $k_d = 2$.

indicate the stability of the system. In other words, the system will be stable by selecting the parameters in these areas. As seen in Fig. 5.16, for smaller values of K_p, the system will be unstable for higher delays. This value decreases significantly by increasing the control gain.

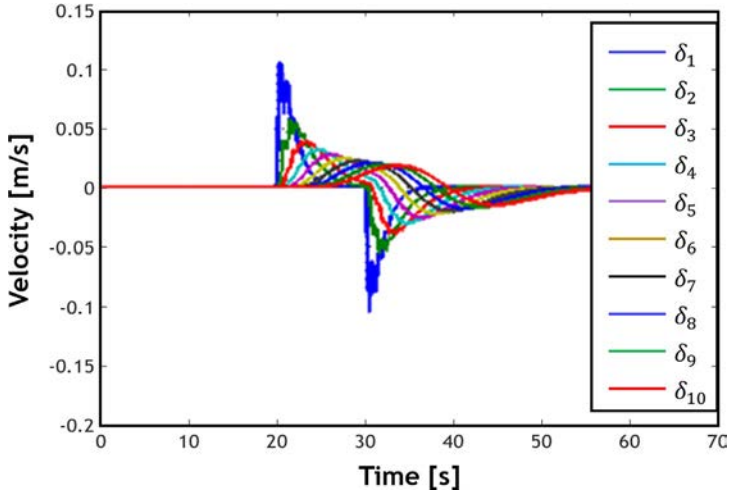

Fig. 5.17 The stable behavior of 10 tracking vehicles corresponding to the point (a) in Fig. 5.16.

Figs. 5.17 and 5.18 illustrate the distance and speed errors of 10 tracking vehicles by assuming the parameter values as $K_d = 1$ and $\Delta = 0.2$. These illustrations are performed to validate the results that indicate the stable state of the system.

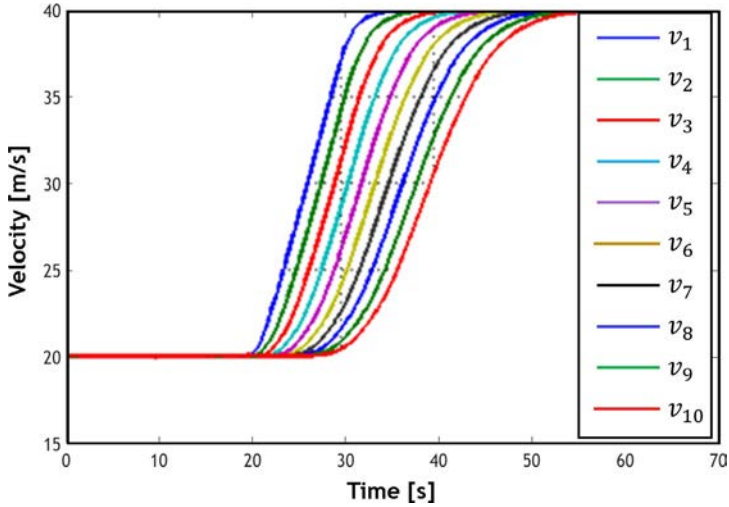

Fig. 5.18 The speed behavior of 10 tracking vehicles corresponding to the point (a) in Fig. 5.16.

The bidirectional structure in stability analysis

This section aims to find delay boundaries for specific control parameters in which the systems exhibit stable behavior. By assuming $\rho = 0.4$, the eigenvalues of matrix C are $\{\pm 0.9544, \pm 0.8571, \pm 0.6795, \pm 0.1503, \pm 0.4361\}$. All eigenvalues are real. The instability boundaries in SDS are displayed in Fig. 5.19 for some of the factors generated by these eigenvalues. The assumed control parameters are $k = 4$, $b = 1$, $\tau = 0.2$, and $h = 1.5$.

The stable area is shown in a 2D shape for better illustration. Hence, one of the control parameters is assumed to be a constant value, and the stable boundaries are shown in delay space in terms of another control variable. The stability boundaries are shown in Figs. 5.20 and 5.21. The process of drawing these figures is based on considering stable zones.

The lines shown in these figures represent the stability boundaries, meaning that the lower values represent stable regions. As can be seen in the figures, the system is more stable against communication delays.

5.5.2 String stability

The string stability of a vehicle platoon is also analyzed in the same way as the stability; therefore, it is necessary to check the validity of the proposed theorems by simulation. This validation will be performed in the following.

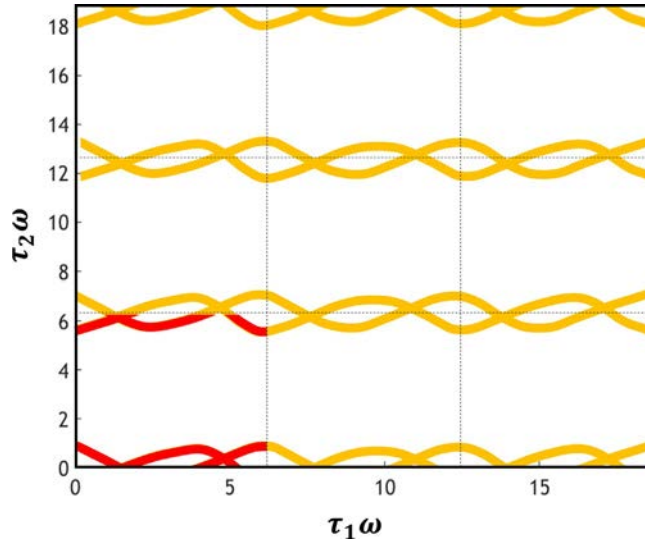

Fig. 5.19 The SDS illustration for factors related to eigenvalues of $\lambda = \pm 0.4361, \pm 0.1503$.

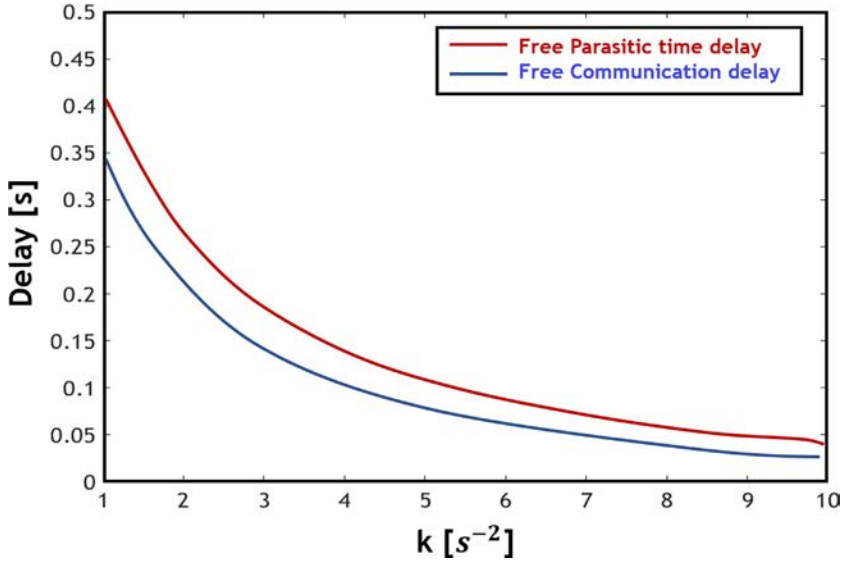

Fig. 5.20 The stable areas by assuming $b = 1$.

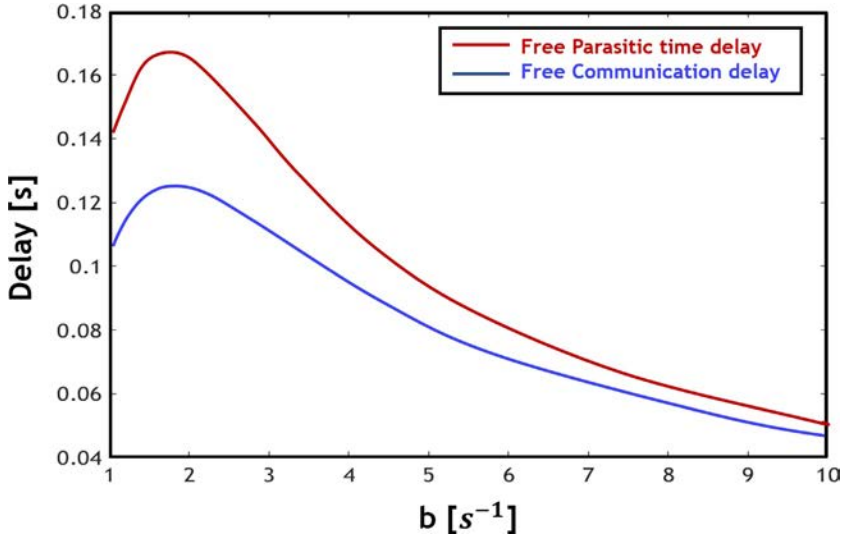

Fig. 5.21 The stable areas by assuming $k = 4$.

5.5.2.1 The string stability based on constant spacing policy

The ideal intervehicle distance is assumed as 8 m in this policy.

The unidirectional structure in string stability analysis

For this purpose, the control parameters, engine time constant, and delay are assumed in three different situations. In Table 5.3, the string stability is examined for the three cases based on Theorem 5.7. These cases include a stable situation, a boundary situation, and an unstable case.

Where $\rho = K\beta + \sqrt{K^2\beta^2 + 2K}$, and it should be noted that the condition $D < 0.5/\tau - 0.5K\tau$ is applied in all cases. The reason for this is that the low frequencies have the most significant impact on string stability. Fig. 5.22 illustrates State 1 in Table 5.3, which shows the string stability under the condition of $D > \rho$. As observed, the distance error decreases smoothly throughout the string. Fig. 5.23 also shows the speed behavior of the tracking vehicles in the platoon under the mentioned conditions.

Figs. 5.24 and 5.25 indicate State 2 in Table 5.3, which shows the critical string stability.

Fig. 5.26 indicates State 3 in Table 5.3, which shows the string instability under $D < \rho$ condition. As observed, the distance error does not decrease throughout the string. Besides, Fig. 5.27 illustrates the speed behavior of tracking vehicles in the platoon under the mentioned conditions.

The bidirectional structure in string stability analysis

The string stability for the model of approximation of partial differential equations To validate the mentioned theorems, and by assuming the control parameters as $\tau_i = 0.1$ sec , $k_i^b = 2$, $b_i^b = 2.2$, and $\Delta_i^b = 0.3$, we will have $k_i^b - \Delta_i^k/\sqrt{2} = 1.807$, $0.25/\tau_i - 0.5\Delta_i^b - b_i^b = 0.15$, and $(b_i^b)^2 - (2k_i^b + \Delta_i^k + 0.5(\Delta_i^k)^2) = 1.045$. Hence, as expected, the time response of the intervehicle distance error is an ideal response under the selected control parameters (Fig. 5.28).

Table 5.3 The system parameters.

Parameters	State 1	State 2	State 3
τ	0.1	0.1	0.1
β	0.03	0.03	0.03
k	2	2	2
D	2.5	2.06	1.5
Conditions	$D > \rho$	$D = \rho$	$D < \rho$

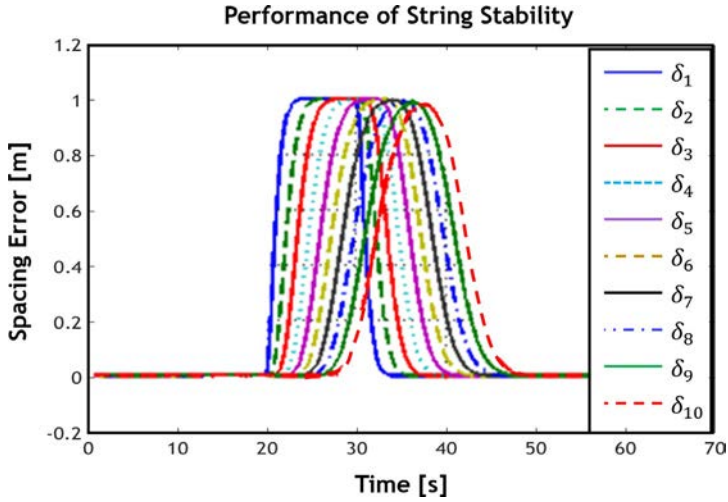

Fig. 5.22 The string stability of 10 tracking vehicles under $D > \rho$ condition.

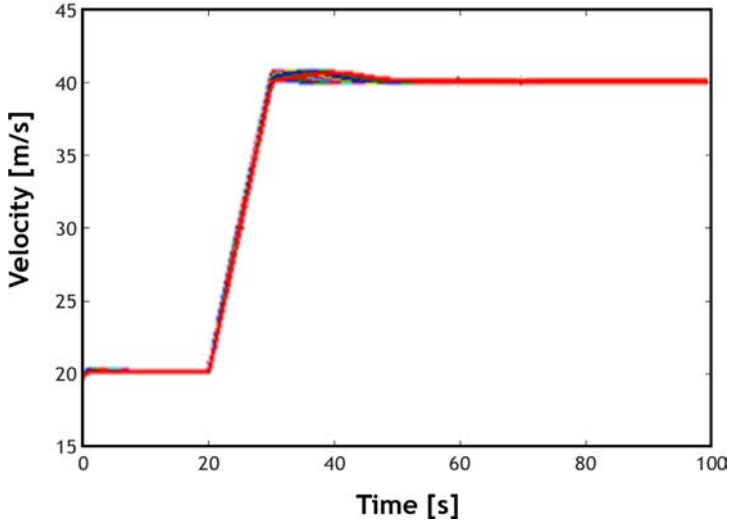

Fig. 5.23 The speed behavior of 10 tracking vehicles under $D > \rho$ condition.

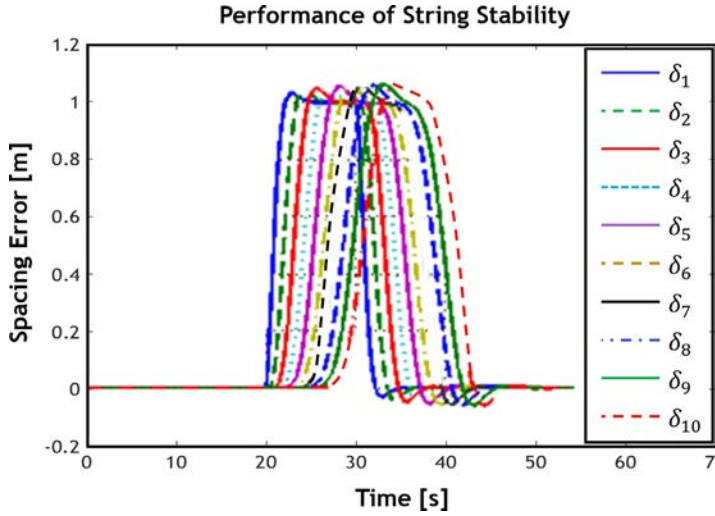

Fig. 5.24 The critical string stability of 10 tracking vehicles under $D = \rho$ condition.

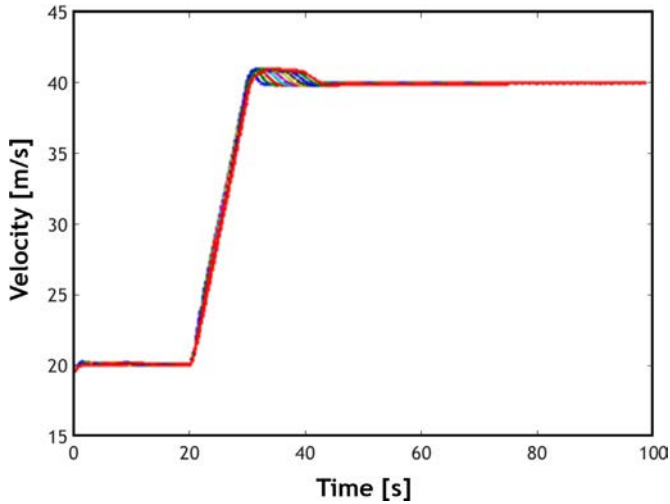

Fig. 5.25 The speed behavior of 10 tracking vehicles under $D = \rho$ condition.

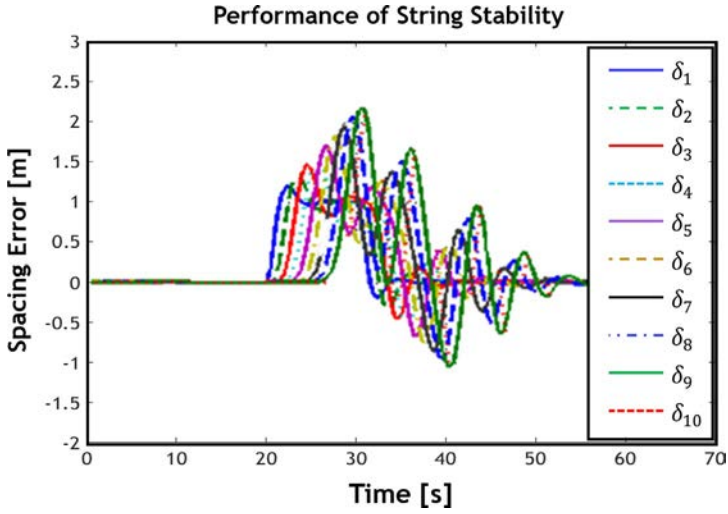

Fig. 5.26 The string instability of 10 tracking vehicles under $D < \rho$ condition.

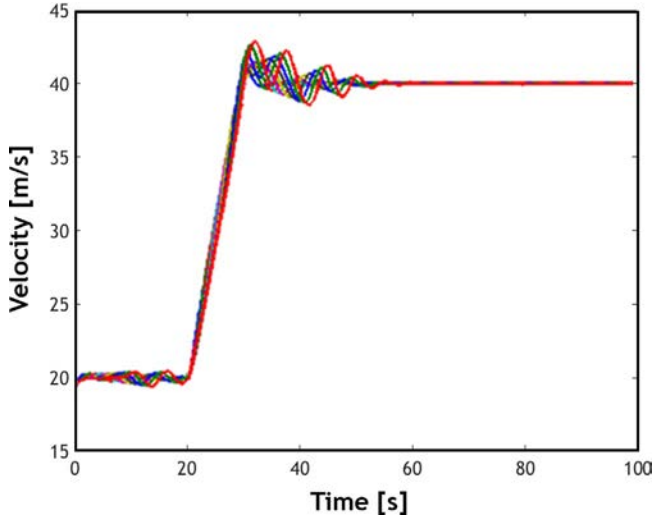

Fig. 5.27 The speed behavior of 10 tracking vehicles under $D < \rho$ condition.

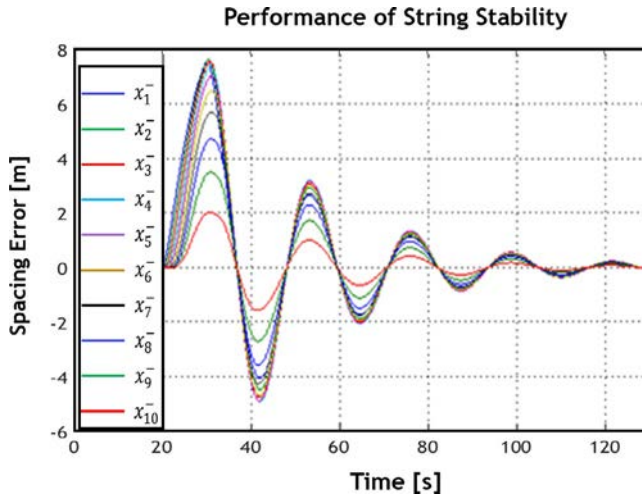

Fig. 5.28 The stability of 10 tracking vehicles.

Because the range of low frequencies has the greatest impact on the string stability, the condition $k_i^b - \Delta_i^k/\sqrt{2}$ will have the greatest effect on string stability. By assuming the parameters as $\tau_i = 0.1\ sec$, $k_i^b = 5$, $b_i^b = 4$, and $\Delta_i^b = 0.3$, we will have $k_i^b - \Delta_i^k/\sqrt{2} = 4.735$ and $0.25/\tau_i - 0.5\Delta_i^b - b_i^b = -1.65$. As can be observed, $k_i^b - \Delta_i^k/\sqrt{2}$ is the only established condition among the conditions.

The string stability for CTCR A simulation is carried out to validate the previously mentioned theorem. Hence, the string stability of a vehicle platoon is studied by assuming the control parameters as $k = 2.5$, $b = 1$, $\tau = 0.2$, $\beta = 4$, $\tau_p = 0.05$ s, and $\tau_v = 0.05$ s. It should be noted that the parameters are selected in such a way that they satisfy Theorem 5.14.

As can be observed in Fig. 5.29, the system is string stable (Fig. 5.30).

5.5.2.2 The string stability based on the constant time headways policy

The unidirectional structure in string stability analysis

A computer simulation is performed to validate the extracted theorem by assuming the control parameters as $K_p = 4$, $K_d = 2$, $h = 1$, $\tau = 0.2$, $\Delta = 0.1$ (Figs. 5.31 and 5.32).

As shown in Fig. 5.31, the distance error decreases smoothly throughout the string. Fig. 5.32 shows the string stability of the vehicle platoon,

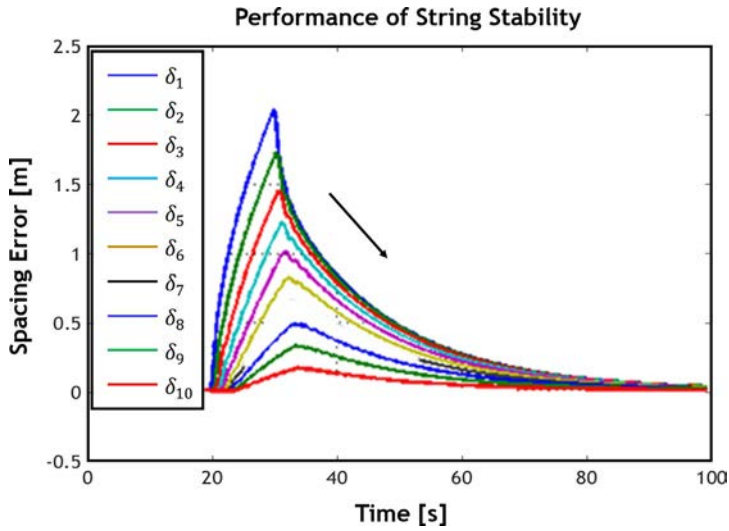

Fig. 5.29 The string stability of 10 tracking vehicles.

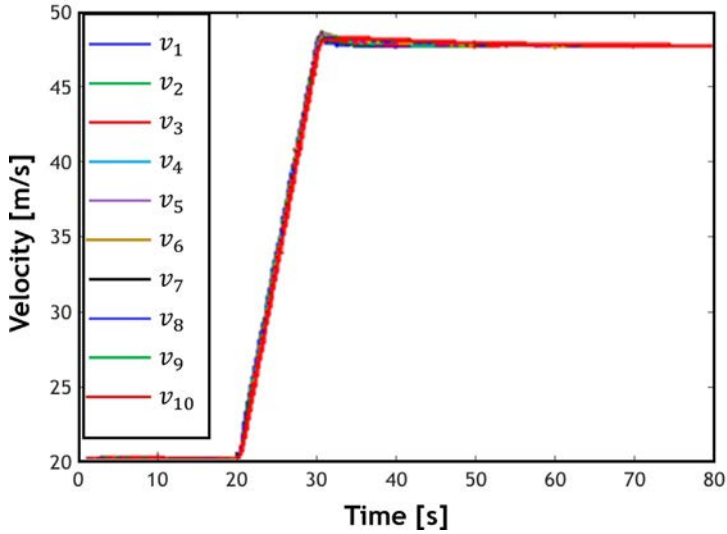

Fig. 5.30 The speed behavior of 10 tracking vehicles.

which confirms Theorem 5.15. Subsequently, the effect of adding a feedforward controller will be investigated. As illustrated analytically in Theorem 5.16, the performance of the system increases by adding a feedforward controller. A simulation is performed by assuming the parameter

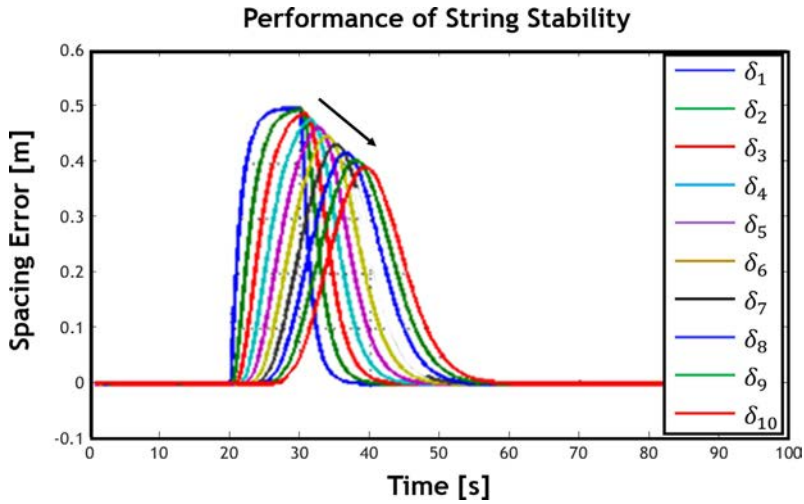

Fig. 5.31 The string stability of 10 tracking vehicles without considering the feedforward controller.

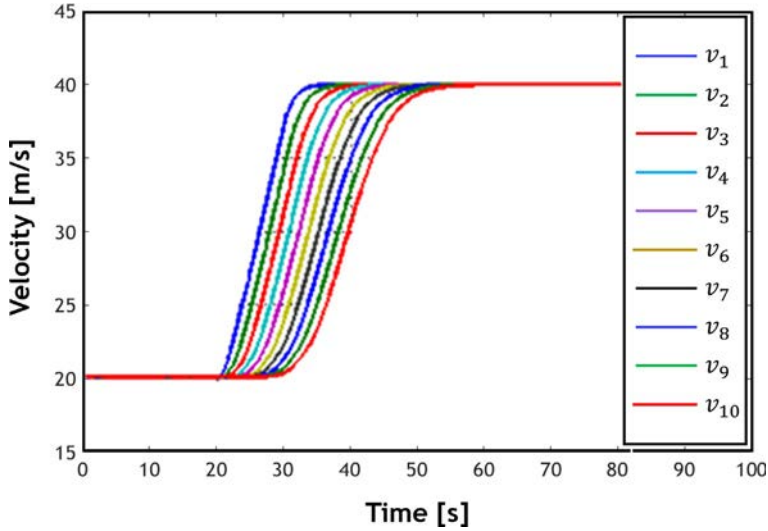

Fig. 5.32 The speed behavior of 10 tracking vehicles without considering the feedforward controller.

controls as $K_p = 1$, $K_d = 2$, $h = 1$, $\tau = 0.2$, and $\Delta = 0.1$ to validate the extracted theorems for two conditions with and without consideration of the feedforward controller. The system response is displayed in Figs. 5.33–5.36 for the mentioned conditions.

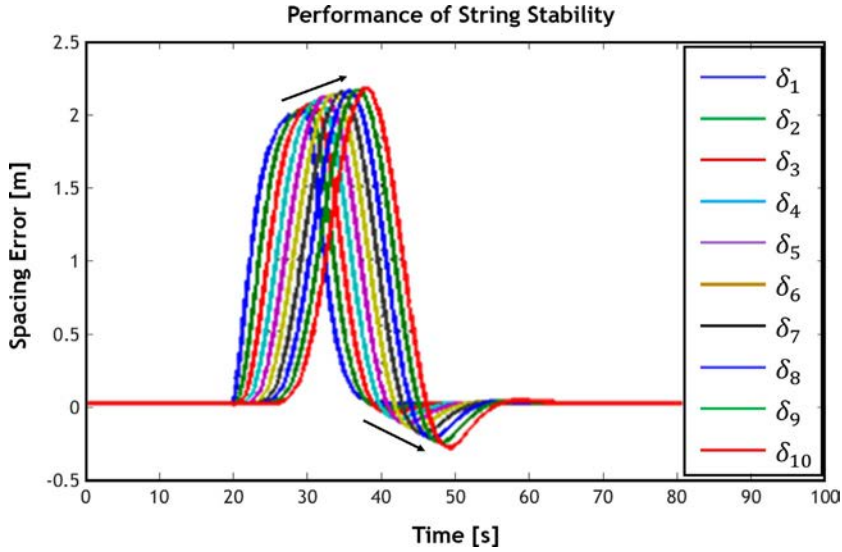

Fig. 5.33 The string instability of 10 tracking vehicles without considering the feedforward controller.

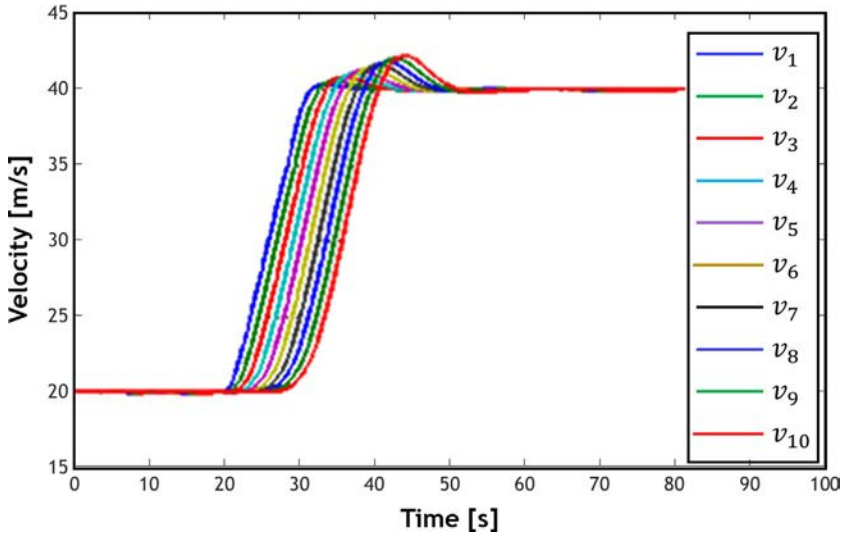

Fig. 5.34 The speed behavior of 10 tracking vehicles without considering the feedforward controller.

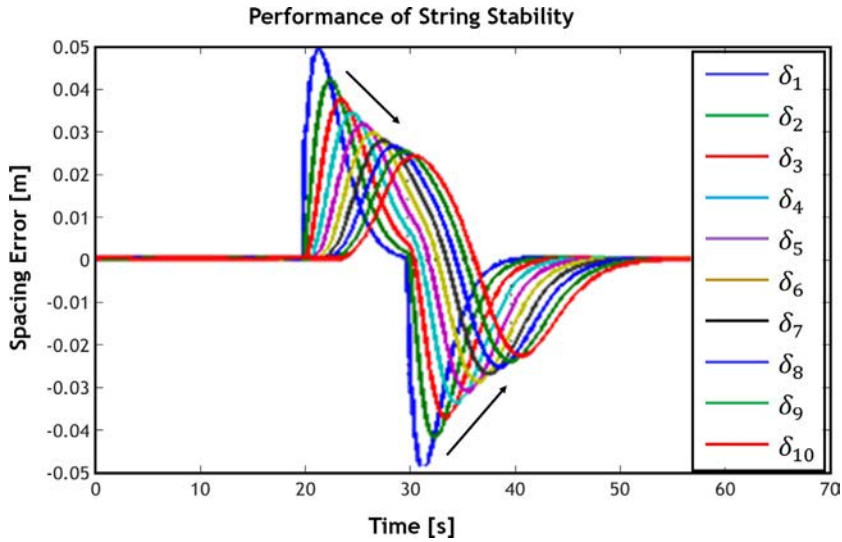

Fig. 5.35 The string stability of the 10 tracking vehicles considering the feedforward controller.

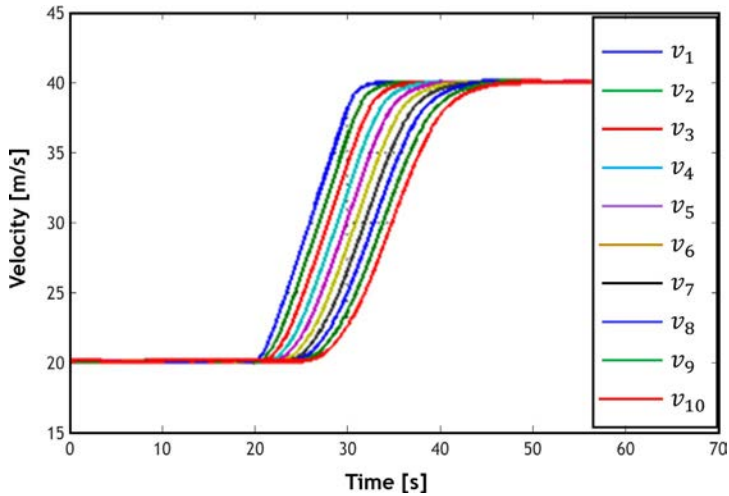

Fig. 5.36 The speed behavior of 10 tracking vehicles with considering the feedforward controller.

As can be seen in Figs. 5.35 and 5.36, the system goes from string instability to string stability. This indicates the improvement of system performance and validates Theorem 5.6. Besides, the error rate is significantly reduced, which also emphasizes the improvement of system performance.

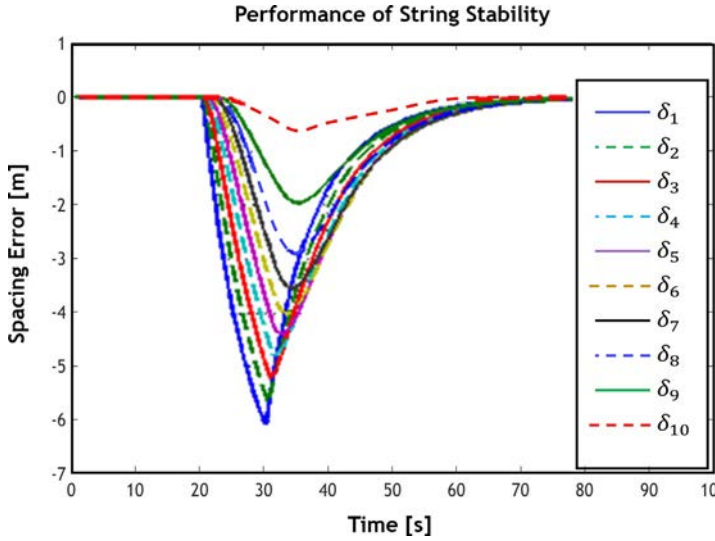

Fig. 5.37 The string stability of 10 tracking vehicles without considering the feedforward controller.

Bidirectional structure in the string stability analysis

For the validation of the proposed theorem, the system response is shown in Figs. 5.37 and 5.38 by assuming the control parameters as $k = 2.5$, $b = 1$, $\tau = 0.2$, $\Delta = 0.04$, $\tau = 0.06$, $\rho = 0.3$, and $h = 1.5$.

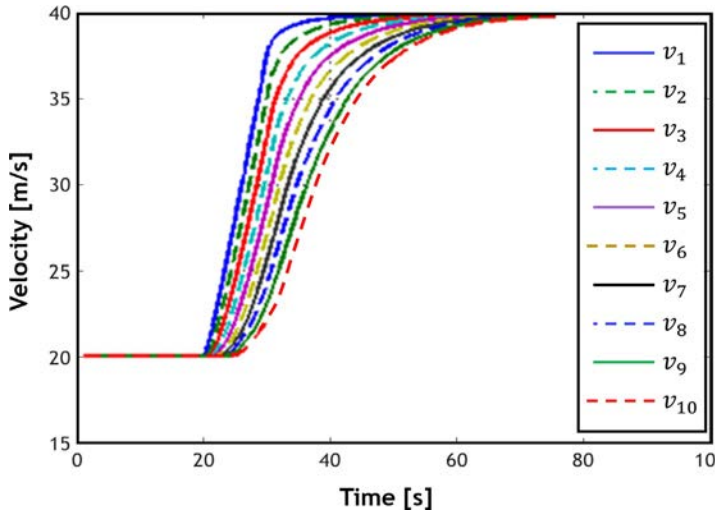

Fig. 5.38 The speed behavior of 10 tracking vehicles without considering the feedforward controller.

It is observed that the distance error decreases smoothly throughout the string, which indicates string stability. Due to different vehicles on a highway, this problem will also be studied for dissimilar vehicle platoons. Hence, the system will be stable if the control parameters are selected in a way that they have string stability conditions. The system parameters are assumed similar to parameters in Table 5.4 for the numerical validation of the problem. Fig. 5.39 shows the distance error for the parameters of Table 5.4. As can be seen, the distance error decreases smoothly throughout the string,

Table 5.4 The system parameters for a platoon of heterogeneous vehicles.

Vehicle	L_i	m_i	τ_i	Δ_i	τ_{com}	b_i	k_i	ρ_i	h_i
1	4	1500	0.1	0.05	0.05	1	5	0.4	2
2	4.5	1600	0.2	0.02	0.04	1.5	5	0.4	1.5
3	5	1550	0.3	0.04	0.06	2	5	0.3	1.5
4	5	1650	0.1	0.02	0.03	1	6	0.4	2
5	4.5	1500	0.2	0.02	0.05	2	6	0.45	1.5
6	3.5	1400	0.2	0.01	0.015	1	5	0.4	1
7	4	1550	0.35	0.02	0.04	1	4	0.3	1.5
8	4	1550	0.15	0.05	0.04	1	5	0.4	2
9	5	1700	0.2	0.02	0.02	4	7	0.35	1.5
10	4.5	1600	0.2	0.05	0.06	2	5	–	1.5

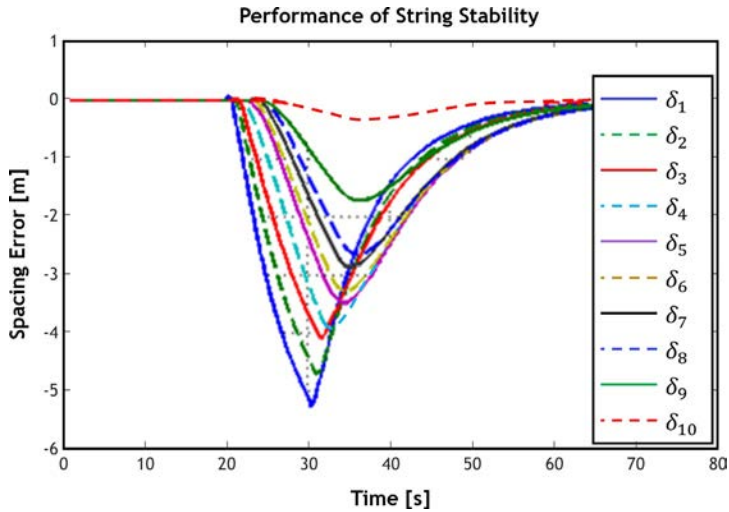

Fig. 5.39 The string stability of 10 tracking vehicles by considering the parameters of Table 5.4.

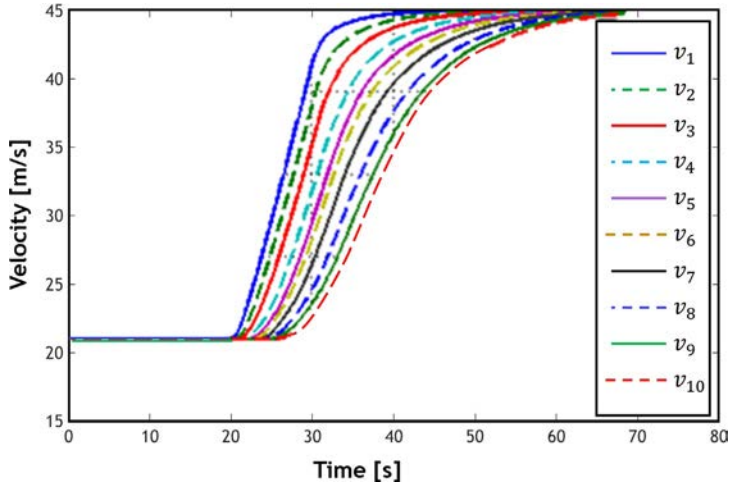

Fig. 5.40 The speed behavior of 10 tracking vehicles by considering the parameters of Table 5.4.

which indicates string stability. Fig. 5.40 shows the speed behavior of the tracking vehicles in the platoon under the mentioned conditions.

5.6 Conclusion

The purpose of this chapter was to analytically investigate the stability and string stability of a vehicle platoon. The analysis is performed based on constant spacing and constant time headways policies, along with the unidirectional and bidirectional communication structures. The communication structure and distance policy must be determined in advance to analyze the system. The unidirectional and bidirectional communication structures were examined because each vehicle can only communicate with the preceding and following vehicles. This is due to the limitations of the existing communication structure. The bidirectional structure exhibits a better performance because each vehicle uses the information of the preceding vehicle and the information of the following vehicle. However, the system's stability is more difficult to achieve, and the system is more sensitive to changes. Because time delays and noise interruptions are among the natural and inevitable mechanical and control systems, these factors are considered in the vehicle's longitudinal model. The negative effect of these delays is investigated on the system's performance and stability, and it is observed that the system is always stable without considering them. This emphasizes the need

to consider these delays. Each vehicle is controlled by the information received from the adjacent vehicles. This information is always delayed due to the limitations of communication tools; therefore, the effect of these delays was also considered. It should also be noted that communication delays do not have constant values. In this study, the upper bound of delays that leads to instability of the system is calculated. It is shown that regardless of the structure used to express the delay in the simulation, the system will be stable if the magnitude of delay is less than the calculated bound. The stability and string stability, which indicate the system performance, are studied by considering the mentioned factors. Furthermore, the stability boundaries are calculated on the control parameters; if obtained, the system will be stable and exhibit the desired performance.

References

[1] D. Schrank, Annual Urban Mobility Report, Technical Report, Texas Transportation Institute, 2003.
[2] P. Varaiya, Smart cars on smart roads: problems of control, IEEE Trans. Autom. Control 38 (2) (1993) 195–207.
[3] D.B. Maciua, J.K. Hedrick, Brake dynamics effect on AHS lane capacity, in: SAE Systems and Issues in ITS (SP-1106), 1995, pp. 81–86. SAE Paper No. 951929.
[4] M. Zabat, N. Stabile, S. Frascaroli, F. Browand, The Aerodynamic Performance of Platoon: Final Report, Technical Report UCB-ITS-PRR-95-35, California PATH, Berkeley, California, 1995.
[5] M. Barth, J.M. Norbeck, Transportation Modeling for the Environment: Final Report, Technical Report UCB-ITS-PRR-95-35, California PATH, Berkeley, California, 1996.
[6] D. Ngoduy, Platoon-based macroscopic model for intelligent traffic flow, Transportmetrica B: Transport Dyn. 1 (2) (2013) 153–169.
[7] T. Petrinic, R. Elektroprimorje, M. Lošinj, I. Croatia, Petrovic, longitudinal spacing control of vehicles in a platoon for stable and increased traffic flow, in: IEEE International Conference on Control Applications (CCA), 2012, pp. 178–183.
[8] F.M. Tangerman, J.J.P. Veerman, B.D. Stosic, Asymmetric decentralized flocks, IEEE Trans. Autom. Control 57 (11) (2012) 2844–2853.
[9] L. Xiao, F. GAO, Practical string stability of platoon of adaptive cruise control vehicles, IEEE Trans. Intell. Transp. Syst. 12 (4) (2011) 1184–1194.
[10] J. Zhao, M. Oya, A.E. Kamel, A. Safety Spacing, Policy and its impact on highway traffic flow, in: IEEE Intelligent Vehicles Symposium, 2009, pp. 960–965.
[11] A. Ghasemi, R. Kazemi, S. Azadi, Stable decentralized control of a platoon of vehicles with heterogeneous information feedback, IEEE Trans. Veh. Technol. 62 (9) (2013) 4299–4308.
[12] D.D. Siljak, Decentralized Control of Complex Systems, Academic, New York, 1991 (chapter 9).
[13] A. Ghasemi, R. Kazemi, S. Azadi, Stability analysis of unidirectionaladaptive cruise control with asymmetric information flow, Proc. Inst. Mech. Eng. C J. Mech. Eng. Sci. 229 (2) (2015) 216–226.

[14] D. Swaroop, J.K. Hedrick, String stability of interconnected systems, IEEE Trans. Autom. Control 41 (3) (1996) 349–357.
[15] X. Liu, A. Goldsmith, S.S. Mahal, J.K. Hedrick, Effects of communication delay on string stability in vehicle platoons, in: Proceeding of: Intelligent Transportation Systems, 2001.
[16] S. Butenko, R. Murphey, P. Pardalos (Eds.), Recent Developments in Cooperative Control and Optimization, Kluwer Academic Publishers, Boston, Massachusetts, 2004.
[17] X. Ling-yun, G. Feng, Effect of information delay on string stability of platoon of automated vehicles under typical information frameworks, J. Cent. South Univ. Technol. 17 (2010) 1271–1278.
[18] S. Sheikholeslam, C.A. Desoer, Longitudinal Control of a Platoon of Vehicles III: Nonlinear Model, PATH, Res. Rep. UCB-ITS-PRR-90-1, 1990.
[19] Isidori, Nonlinear Control Systems, second ed., Springer-Verlag, 1989.
[20] D. Yanakiev, I. Kanellakopoulos, Longitudinal control of automated CHVs with significant actuator delays, IEEE Trans. Veh. Technol. 50 (5) (Sep. 2001) 1289–1297.
[21] X. Lu, K. Hedrick, Practical string stability for longitudinal control of automated vehicles, in: Proc. IAVSD Conf., Kanagawa, Japan, 2003.
[22] G. Naus, R. Vugts, J. Ploeg, R.V. Molengraft, M. Steinbuch, String-stable cacc design and experimental validation: a frequency-domain approach, IEEE Trans. Veh. Technol. 59 (November 2010) 4268–4279.
[23] S. Shladover, Operation of Automated Guideway Transit Vehicles in Dynamically Reconfigured Trains and Platoons, Rep. UMTA-MA-06- 0085–79, 1979.
[24] H. Hao, P. Barooah, Control of Large 1D Networks of Double Integrator Agents: Role of Heterogeneity and Asymmetry on Stability Margin, August 2011. http://arxiv.org/abs/1011.0791v2.
[25] Thowsen, The Routh–Hurwitz method for stability determination of linear differential-difference systems, Int. J. Control. 33 (5) (1981) 991–995.
[26] H. Fazelinia, R. Sipahi, N. Olgac, Stability robustness analysis of multiple time-delayed systems using building block Concept, IEEE Trans. Autom. Control 52 (2007) 799–810.
[27] R. Cepeda-Gomez, N. Olgac, An exact methodology for the stability analysis of linear consensus protocols with time delay, IEEE Trans. Autom. Control 56 (2011) 1734–1740.
[28] D. YanaKiev, I. Kanellakopoulos, A simplified framework for string stability analysis in AHS, in: Proc. of the 13th IFAC world congress, Volume Q, 1996, pp. 177–182.
[29] P. Cook, Conditions for string stability, Syst. Control Lett. 54 (2005) 991–998.
[30] M.R.I. Nieuwenhuijze, String stability analysis of Unidirectional Adaptive cruise control, Master's Thesis, Eindhoven University of Technology, Eindhoven, 2010.
[31] G. Guo, W. Yue, Hierarchical platoon control with heterogeneous information feedback, IET Control Theory Appl. 5 (15) (2011) 1766–1781.

CHAPTER 6

Dynamic behavior and stability of an articulated vehicle carrying fluid

6.1 Introduction

In order to study the fluid motion and its combination with vehicle dynamics, there are different methods such as quasistatic and equivalent mechanical methods. Each method has limitations on the calculation of forces and moments arising from the transient response and the parameters required for analysis. In this regard, only the mechanical-fluid methods allow the accurate modeling of fluid behavior in different conditions, including different inputs for vehicle dynamics and different shapes of the tanker, different fill percentages, etc. It is also essential to note that the modeling, coupling the mechanical model of the fluid with the vehicle dynamics, and how data transfer between these two systems are processes of great complexity.

Fluid motion inside the moving tanker plays an essential role in the stability of the fluid-carrying vehicle. Fluid-carrying systems such as tankers and tanker ships, when filled partially and exposed to external stimulations, are exposed to a higher risk of rollover than when they carry a rigid load. Fluid motion is considered in many engineering applications. For example, the fuel motions in the tank can cause instability in rockets and spacecraft. Also, the loads exposed by earthquakes can cause severe fluid motion inside the tanks that leads to significant damage to their structures. According to maneuver or road conditions, the fluid inside a partially filled tanker can usually experience large or small amplitude motions. The motion of fluid with a large amplitude generally occurs in acceleration, rotation, or lane change maneuvers. Generally, fuel-carrying tanks are partially loaded because of the tolerances of the axes with the existence of fluids with different densities. Tankers are used to carry hazardous substances such as toxic or flammable materials, and as a result, any damage to them can cause severe environmental pollution.

Vehicle Dynamics and Control
https://doi.org/10.1016/B978-0-323-85659-1.00001-X

Fuel-carrying vehicles are divided into two categories: articulated vehicles (a trailer or tanker, and separated tractor) or nonarticulated vehicles. Heavy vehicles have less stability than other types of vehicles because their center of gravity is located at a high-level point. Roll instability is the most dangerous type of instability, and it is more likely to occur than other events. A comparison between 1984 and 1987 in the United States showed that rollover is the most dangerous road hazard (41.4% of road accidents) [1]. More than 15,000 cars roll over per year in the United States, almost 62.67% of which are associated with articulated vehicles [2]. Also, a rollover occurs for nearly every 4 million miles traveled by heavy trucks.

Trucks carrying partially filled tanks have lower stability compared to other heavy vehicles. This is due to the effect of the dynamic of fluid motion and its interaction with vehicle dynamics, which undermines the stability of the fluid-carrying vehicle. The ultimate threshold of tolerable acceleration for a tanker with an ellipsoid cross-section in a steady steer maneuver is roughly half that of a vehicle with a rigid load [3]. Because a fluid-carrying vehicle's stability threshold is low, a small maneuver such as a rotation, a lane change, or vehicle braking in cornering can cause them to roll over.

Although fluid motion is an essential factor in vehicle instability, fluid motions and their effect on vehicle dynamics have not been thoroughly investigated and identified. The relevant studies are limited to developing different fluid motion methodologies in tankers with different shapes or simplified equations related to fluid motion. When fluid motion is considered in a static or nontransient state, the calculated instability will be lower than the actual values. The amount of transient forces due to fluid motion is larger than the forces calculated for rigid or solid loads [4].

In this chapter, we try to calculate the forces exposed by fluids transiently and accurately and couple them with vehicle dynamics to calculate the effect of fluid motion on the vehicle's dynamics and stability.

6.2 Dynamics of articulated vehicles

Heavy vehicles generally tend toward instability in lateral accelerations of more than 0.3 g [5, 6]. On the other hand, the rollover moments include centrifugal forces, which are derived from different maneuvers. When the vehicle wheels are locked, it loses control. Such a case occurs in braking or braking-dependent maneuvers [7, 8]. The properties of an articulated vehicle are quite complex, especially when carrying a moving load. The load

transfer at the case of braking is related to the magnitude of the deceleration and the trailer brake force.

Articulated vehicles carrying a partially filled tanker will also be subject to the load driven from fluid motion that negatively affects the braking, even using the antilock brake system. Recognizing the brake force's optimum distribution is very complicated in the presence of different loads exposed to axes of the fluid-carrying vehicles. Meanwhile, the jackknifing phenomenon is the most vital type of instability for the yaw motion that will cause a high yaw speed at the trailer section. Although it has little effect on the trailer instability, switching motion can be dangerous for other vehicles. Also, the quick input from the steering wheel can cause a swing motion around the joint point.

The instability of heavy vehicles with a static rollover threshold has been investigated extensively. Concerning the constant steering wheel maneuver, the balance of moments around the roll axis is considered in this method. Although the rollover events are not static in reality, the roll's static stability correctly estimates the potential of rollover. The ultimate threshold for static rollover can be defined as "the maximum amount of acceleration the vehicle can tolerate without being overturned." This technique is a comparative method, and the static rollover threshold for heavy vehicles is higher than the dynamics rollover threshold (about 5%) [9, 10].

6.3 Fluid dynamics

Fluid motion in mobile tankers has been investigated in various studies since 1960. These studies are based on experimental or theoretical work on spacecraft [4] and fluid motion and its interaction with tankers by focusing on factors affecting the vehicle's stability under different maneuvers.

The fundamental problems of fluid motion are associated with the calculating force, moment, and natural frequency of the fluid's free surface. In the partially filled tankers, these forces and moments are coupled with the vehicle's dynamics to describe the motion and stability of this type of vehicle due to external stimulations. These external stimulations are applied through different maneuvers such as braking, acceleration, lane change, or stimulations caused by road roughness [11, 12]. The preliminary investigation of fluid motion and its effect on vehicle dynamics is possible by the following three methods:

- Quasistatic method.
- Equivalent mechanical methods.
- Dynamics methods.

6.3.1 Quasistatic methods

Using the quasistatic methods is a common technique for estimating the fluid's free surface in a moving tanker. In this method, the center of gravity of the moving fluid is calculated under different stimulus factors. A straight line–smooth surface replaces the free surface of the fluid, and the new free surface of the fluid is determined based on the lateral acceleration in the roll plane, or longitudinal acceleration. Then the displacement effect of the center of gravity is applied to the lateral dynamics of the vehicle.

By assuming an incompressible and homogenous fluid, and steady steer maneuver, the momentum conservation equations in the coordinate axis (Fig. 6.1), the center of which is attached to the tanker, are defined as (6.1 and 6.2):

$$-\rho g \sin\theta - \frac{\partial p}{\partial y} + (R - y\cos\theta)\omega^2 \rho \cos\theta = 0 \tag{6.1}$$

$$-\rho g \cos\theta - \frac{\partial p}{\partial z} + (R - y\cos\theta)\omega^2 \rho \sin\theta = 0 \tag{6.2}$$

where r, p, g, and ω are the density of the fluid, the pressure, the acceleration of gravity, and the rotational speed, respectively. Also, R describes the distance between the center of rotation and the coordinate center connected to the tanker's floor. These equations are associated with the fluid's free surface and the low roll angles for the vehicle. For tankers with a large radius compared to the tanker width, the term $y \cos\theta$ can be ignored concerning the term R [12].

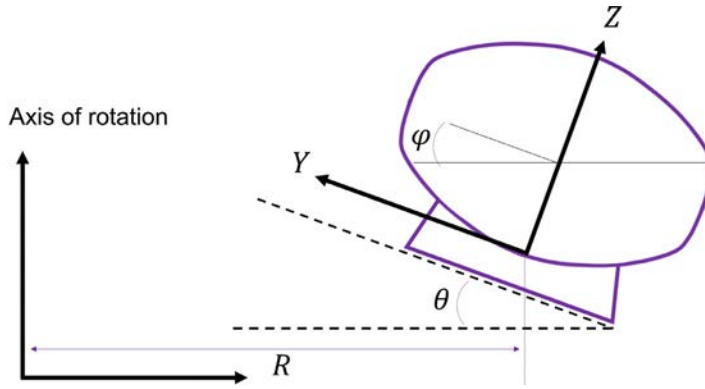

Fig. 6.1 The position of the coordinate axis in the quasistatic method.

By applying the lateral acceleration a_y in Eqs. (6.1) and (6.2) and assuming $\partial p = 0$ at the free surface of the fluid, Eq. (6.3) is obtained:

$$\left(-\rho g \sin\theta + \rho a_y \cos\theta\right) dy + \left(-\rho g \cos\theta - \rho a_y \sin\theta\right) dz = 0 \tag{6.3}$$

For a two-dimensional (2D) model in the roll plane and steady steer maneuver, the equation for the free surface of the fluid is defined as (6.4):

$$\frac{dz_s}{dy_s} = \frac{a_y \cos\theta - g \sin\theta}{g \cos\theta + a_y \sin\theta} \tag{6.4}$$

and the angle of free surface assuming low values for the roll angle is defined as (6.5):

$$\tan \varnothing_p = \frac{\frac{a_x}{g} - \theta_p}{1 + \frac{a_x}{g}\theta_p} \tag{6.5}$$

where $\varnothing_p$ is the slope of the free surface of the fluid in the pitch plane, a_x is the longitudinal acceleration, and θ_p is the pitch angle of the tanker. The fill percentage of the tanker and its shape, the fluid motion, and its center of gravity can be calculated based on the fluid's free surface. The coordinates of the center of gravity in the roll plane can be calculated as (6.6):

$$Y = \frac{\iint_\Omega y dy dz}{\iint_\Omega dy dz}, Z = \frac{\iint_\Omega z dy dz}{\iint_\Omega dy dz} \tag{6.6}$$

where Ω is the volume of fluid filling the tanker.

The quasistatic method is an efficient method for calculating the forces applied in the steady state by the fluid inside the tanker. This method cannot model the transient forces due to fluid motion, and hence the use of this method for the stability analysis of the fluid-carrying vehicles is accompanied by many limitations. Also, although fluid analysis on the partially filled tankers using quasistatic methods allows determining the center of gravity of the fluid, which is related to the average force and dynamic response, the transient behavior of the fluid cannot be examined in this method. The dynamic forces can be high for the high fill percentage and the low amplitude of input [12–16]. Hence, this method is suitable for problems in which the input frequency is lower than the fluid motion's natural frequency.

6.3.2 Dynamics methods for fluid motion

In the dynamic methods, the fluid motion is demonstrated by solving the Navier-Stokes equations. The investigation of fluid motion using this method is possible in two ways. In the first method, the fluid's amplitude of motion is considered small, and by considering the ideal fluid assumption (nonviscose, incompressible, and rotational fluid flow), the Navier-Stokes equations are converted into the potential equations with linear boundary conditions on the free surface [4]. It should be noted that this method is known as a linear method. Fluid motion with large amplitudes is investigated in the nonlinear method, and this can be possible through solving the Navier-Stokes equations using methods of computational fluid dynamics. Given the recent developments in computer technology and numerical analysis, the attention of many researchers has been attracted to numerical methods for solving nonlinear problems; these are briefly discussed in the following. Numerical methods can be divided into four categories:

- Lagrangian methods.
- Eulerian methods.
- ALE (smoothed arbitrary Lagrangian-Eulerian) methods.
- SPH (particle hydrodynamic method) methods.

In the Lagrangian method, the mesh moves with the fluid flow across the domain. In this method, the finite element technique is used for the discretization of the domain. Although the Lagrangian method is faster than the Eulerian method, and the mesh motion can model the free surface properly, the fluid dynamics cause changes in the elements shape, resulting in unstable and noncorrect solutions. So, the meshing of the domain has to be done again, which is very difficult. In contrast to the Lagrangian method, a constant mesh is used in the Eulerian approach, and therefore, the change of the free surface does not change the shape of the mesh. In this method, the free surface of fluid must be modeled with other techniques. The volume of fluid (VOF) method is one of the most common methods in this field. Many researchers have applied this method. This method was originally developed by Hirt [17] and later extended by other researchers. In this method, if the volume fraction of the ith cell, f_i, is zero, the cell is empty. If the volume fraction is one, it is full of fluid. Therefore, its value for a cell is variable between zero and one and defined as (6.7):

$$\frac{\partial f}{\partial t} + u \cdot \nabla f = 0 \tag{6.7}$$

Navier-Stokes equations simultaneously solve (6.7) to determine the shape and properties of the fluid's free surface.

The ALE method combines the advantages of Lagrangian and Eulerian methods. In this method, the nodes can move by fluid or be fixed. The possibility of shifting the meshes gives the possibility to model large deformations of the free surface. The basic idea of the SPH method is based on interpolation. The conservation of mass and moment equations is transformed into the particle form by integral interpolation.

6.3.3 Equivalent mechanical model

Another method for analyzing the fluid motion in a moving tanker is to consider fluid motion as an equivalent mechanical system. The key idea is that the moving fluid inside the tanker serves as two parts: a fixed part relative to the tanker and a moving part that represents the fluid motion. This is done based on two components of the hydrodynamic pressure of the fluid moving inside the tanker. One component of the pressure is proportional to the acceleration, and another one is the convective pressure. The fluid's moving parts can be modeled as a series of mass and springs or a pendulum with a linear spring assumption, as shown in Fig. 6.2.

The equivalent mechanical system parameters are determined by the equalization of the mass, the moment of inertia, the center of gravity, the natural frequency, the applied force, and the moment. For this purpose,

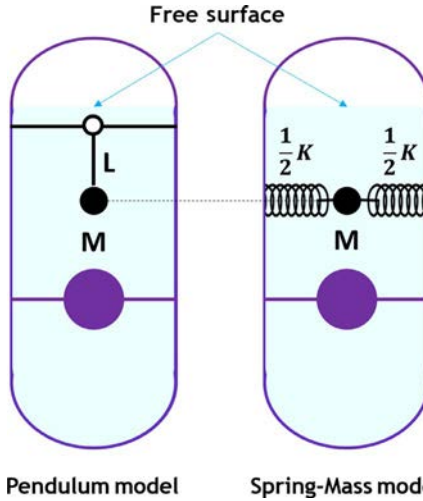

Fig. 6.2 Mechanical systems equivalent to (1) system of mass and spring, (2) pendulum system.

the mass difference between the fluid and the fixed part is considered as the mass of fluid in different modes. The spring constant is derived from the natural frequency of the fluid motion. The simple relation of the equivalent mechanical model with the vehicle model allows for simultaneous analyses. However, the equivalent linear mechanical models will have the same limitations of the linear models for fluid motion, such as the amplitude of motion, the frequency, and the shape of the tanker. The parameters of the equivalent linear mechanical systems for different tankers must be determined experimentally.

6.4 Dynamics modeling of vehicle and fluid inside the tanker

Some limitations accompany approximate methods for fluid analysis, such as quasistatic methods and equivalent mechanical models, but dynamics methods involving solving the Navier-Stokes equations don't have the above limitations. These methods can be applied to model large fluid motions properly. However, dynamic methods have significant advantages over other methods, but the difficulties of coupling them with the vehicle dynamics model and the long runtime are still the main issues of these methods.

In this chapter, a model with five degrees of freedom, the Eulerian approach, and the volume of the fluid technique are used for examining the dynamics of the articulated vehicle, modeling the fluid dynamics, and modeling the free surface of the fluid, respectively. This modeling analysis is carried out for the full-scale system. When the articulated vehicle is modeled as a full-scale vehicle, the quality of the mesh is essential, considering the large volume of fluid inside the tanker. The mesh sizes must be optimized because by scaling down the mesh dimensions or increasing the quality of the mesh, the number of grids and the analysis runtime increase rapidly. Therefore, it is essential to determine the mesh's optimal dimensions without affecting the accuracy of the results. Thus, it is very efficient to use a powerful tool such as *FLUENT software* for fluid dynamics modeling.

The model of the articulated vehicle consists of two rigid sections, including the tractor and trailer. The tractor part has the degree of freedom in the lateral slip, yaw, and roll direction while the trailer section has the degree of freedom of yaw and roll relative to the tractor.

6.4.1 Fluid dynamics modeling

The fluid inside the partially filled tanker can be considered as two-phase flow. For example, in the water-air tank, the water's density is approximately 815 times the air. In this type of flow, the mass forces are dominated by the viscosity, and the effects of viscosity can be neglected [19]. Due to the fluid's flow velocity in different maneuvers, the flow is considered in the laminar regime. In the two-phase model, the air is a gas phase, and water is a liquid phase. In this model, the air is considered as the primary phase and water as the secondary phase. The continuity equation of the incompressible transient flow is expressed as (6.8).

$$\nabla \cdot V = 0 \tag{6.8}$$

The Navier-Stokes equation is defined as (6.9).

$$\frac{\partial V}{\partial t} + V \cdot \nabla V = -\frac{1}{\rho}\nabla \cdot \mu\left(\nabla V + (\nabla V)^T\right) + F_b \tag{6.9}$$

where ∇ is the gradient operator, $\nabla\cdot$ is the divergence operator, ρ is density, μ is viscosity, V is the velocity vector, and F_b is the mass force vector, which indicates the force generated due to the acceleration of gravity or external disturbances such as a vehicle maneuver, which is defined as (6.10):

$$F_b = g + a \tag{6.10}$$

where g is the acceleration due to gravity, and a is the acceleration due to the vehicle maneuver. For example, a sinusoidal function cycle can be applied for lane change maneuvers without considering the vehicle's dynamics and a ramp function for a steady steer maneuver. This acceleration is applied to the momentum equation through defined functions in *FLUENT* software. For the boundary of the fluid and air, the volume fraction equation for the air-fluid boundary can be defined as (6.11):

$$\frac{\partial f}{\partial t} + \nabla \cdot (Vf) = 0 \tag{6.11}$$

Where f is the volume fraction. In the range of calculations, the value of f is *one* for a cell that is entirely occupied by the fluid, and for a cell that is filled with gas, the number is *zero*. When the cell contains a percentage that is filled by fluid, the volume fraction is a number between zero and one concerning the occupied volume. Although the fluid is two-phase, a series of continuity equations and momentum equations is solved by the volume fraction function [20]. The fluid properties such as density and viscosity for different

phases in the Navier-Stokes equations are calculated by volume fraction related to a cell. For example, for fluid on the boundary, the density or viscosity of the fluid for each cell is calculated by Eq. (6.12):

$$\varnothing = f_2\varnothing_2 + (1 - f_2)\varnothing_1, \quad (\varnothing = \rho \text{ or } \mu) \tag{6.12}$$

where $\varnothing_1$ and $\varnothing_2$ are the density or viscosity of the fluid, and f_2 is the volume fraction of the liquid phase in a cell. The model described in Eq. (6.12) is implemented in the *FLUENT* software. The Navier-Stokes equations are implemented using a finite volume method for discretizing and solving the Navier-Stokes equations. Flow equations are solved based on pressure correction and the pressure-velocity coupling technique. Also, using the pressure-implicit relation, the number of iterations for convergence, especially in transient flow, is greatly reduced. The first-order upwind method is used for meshing the solution domain because the second-order method will lead to slow convergence. The body force weighted method is then applied for determining the large mass forces in two-phase flow and pressure interpolation. In this case, the segregated algorithm has weak convergence and the implicit body force method, which has good convergence, has to be used for determining the pressure gradient and body force. The equations are discretized by the first-order implicit method in the time domain. Also, the nonslip condition is applied to the tanker's surface. The geo-reconstruct method has been used to calculate the surface flux between two fluids in the VOF method. This method is employed for the interpolation of cells closed to the contact surface of two phases. This method assumes that the contact surface has a linear slope within each cell and uses this linear form to compute fluid displacement from the cell level near the contact surface.

Because the *FLUENT* software uses gauge pressure, the pressure reference location is very important and must be fixed. During two-phase VOF, the reference pressure must be placed in the lighter phase. Because large amounts of force are calculated when the fluid moves violently and strikes the reference point, it is considered the highest point in the tanker. *FLUENT* software does not compute the displacement of the center of gravity, fluid motion forces, and the resulting moments, so they have to be calculated and used by programming in the software.

6.4.1.1 Calculating the fluid's center of gravity, forces, and moments

As explained above, *FLUENT* software does not calculate the center of gravity. It needs to compute these variables through programming capability

embedded within the software. In Eqs. (6.13)–(6.15), equations are presented along the length, width, and height.

$$CG_x = \frac{\sum_{\Omega} X_{ci} A_i}{\sum_{\Omega} A_i} \tag{6.13}$$

$$CG_y = \frac{\sum_{\Omega} Y_{ci} A_i}{\sum_{\Omega} A_i} \tag{6.14}$$

$$CG_z = \frac{\sum_{\Omega} Z_{ci} A_i}{\sum_{\Omega} A_i} \tag{6.15}$$

In the above equations CG_x, CG_y, and CG_z are the coordinates of the center of gravity of the fluid along the length, width, and height; $\boldsymbol{\Omega}$ is the space occupied by the fluid; X_{ci}, Y_{ci}, and Z_{ci} are the coordinates of the center of the ith cell; and A_i is the volume of the ith cell. The applying forces on the tanker's body due to the presence and motion of a fluid are denoted with F_x, F_y, and F_z, which will be calculated by integrating from the fluid pressure on the tanker's wet surface and the boundary of the middle plates. Eqs. (6.16)–(6.18) indicate this.

$$F_x(t) = \sum_{\partial\Omega} \left(P_i \overline{A}_{xi}\right) \tag{6.16}$$

$$F_y(t) = \sum_{\partial\Omega} \left(P_i \overline{A}_{yi}\right) \tag{6.17}$$

$$F_z(t) = \sum_{\partial\Omega} \left(P_i \overline{A}_{zi}\right) \tag{6.18}$$

where P_i is the pressure of the ith cell, A_i is the surface vector associated with the ith surface cell, and $\partial\boldsymbol{\Omega}$ is the domain of wet surfaces on the boundary wall. Roll (M_x), pitch (M_y), and yaw (M_z) moments are obtained by integrating the multiplication of the force and position vectors, shown in Eqs. (6.19)–(6.21):

$$M_x(t) = \sum_{\partial\Omega} F_{zi} Y_{fi} - \sum_{\Omega} F_{yi} Z_{fi} \tag{6.19}$$

$$M_y(t) = \sum_{\partial\Omega} F_{xi} Z_{fi} - \sum_{\Omega} F_{zi} X_{fi} \tag{6.20}$$

$$M_z(t) = \sum_{\partial\Omega} F_{yi} X_{fi} - \sum_{\Omega} F_{xi} Y_{fi} \tag{6.21}$$

where X_{fi}, Y_{fi}, and Z_{fi} are the coordinates of the center of the tank's ith wet wall, and F_{xi}, F_{yi}, and F_{zi} are the longitudinal, lateral, and vertical components of the force, which is applied to the ith surface of the wet wall.

6.4.1.2 Type of mesh and number of cells

The mesh dimensions significantly influence the simulations carried out in the software, so it is important to select the optimal number of cells with the lowest effects on the results. Different types of meshes can be used in FLUENT software, as shown in Fig. 6.3. The hexahedral and wedge shape cells are commonly used in the present study. In Fig. 6.4, an example of the meshed tanker is represented, and the number of cells is 92,040. To verify the model's sensitivity against the number of cells, we can use the ramp and sinusoidal inputs, but considering the coupled model for the vehicle motion and fluid dynamics, it is better to refine the mesh based on the real conditions. Therefore, the method of coupling the fluid and vehicle dynamics is explained first.

6.4.2 Coupling of the fluid motion model and vehicle dynamics

The coordinate center of $(x, y, z)^I$ is attached to the center of the tanker according to Fig. 6.5, and the tanker is moving toward the center of G with angular velocity Ω, and linear velocity U, relative to the coordinates

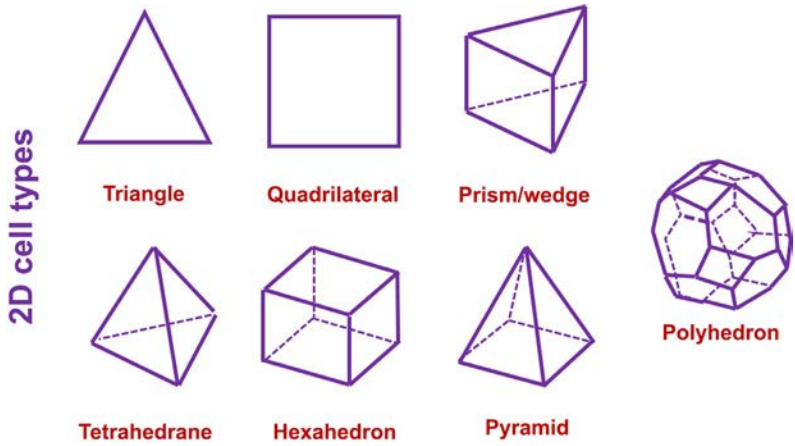

Fig. 6.3 Types of meshes that can be used in FLUENT software.

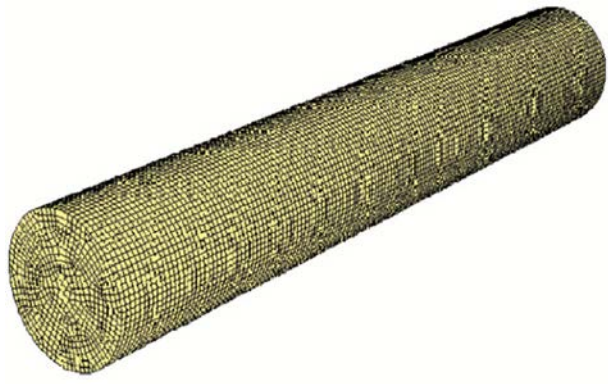

Fig. 6.4 An example of a hexahedral mesh.

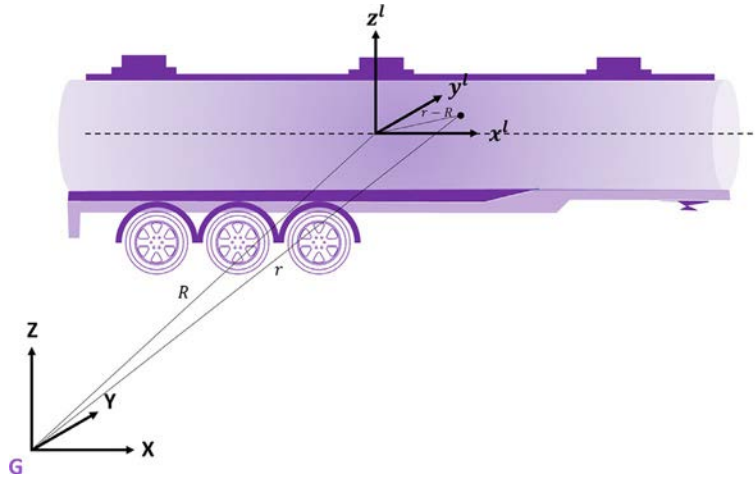

Fig. 6.5 The schematic of the fixed and moving center of the coordinate for the tanker.

of X, Y, Z. The lateral force is the sum of the gravitational force, the force generated from rotation, and so on; this is defined by Eq. (6.22).

$$F_b = g - \frac{dU}{dt} - \frac{d\Omega}{dt} \times (r - R) - 2 \times \Omega \times \frac{d(r - R)}{dt} - \Omega \times [\Omega \times (r - R)] \tag{6.22}$$

where r and R are the position vector of a fluid particle and the tanker's center relative to the fixed coordinate center. Eq. (6.22) is applied to calculate the external forces applied to the fluid and substituted in the Navier-Stokes equations.

The dynamics model of the vehicle is modeled in moving coordinates, the center of which is located on the center of the mass for the tractor and trailer, and the fluid model in the tanker's coordinate $(x, y, z)^l$, whose center is located on the center of the tanker based on Fig. 6.6.

The model is first solved with the static conditions for the fluid. In the first step, the steering input is applied to the model and the response of the dynamics system of the vehicle in the coordinates $(x, y, z)^l$ is calculated. Then, the dynamics system response from this coordinate system will be transferred to the coordinate system $(x, y, z)^l$. The external force applied to the fluid elements can be calculated concerning the linear and rotational acceleration terms. At this stage, knowing the body force, the fluid system can be resolved alone. The outputs of the fluid model are the forces and moments of the fluid applied on the tanker wall, which have been calculated in the coordinate $(x, y, z)^l$, and must be transferred to the coordinate system of (x, y, z). Then these transferred forces and moments are used for calculating the dynamics model of the vehicle.

In each time step, two subsystems (vehicle dynamics system and fluid dynamics) are solved simultaneously. The process described above will continue until the end of the analysis. For convergence behavior of subsystems,

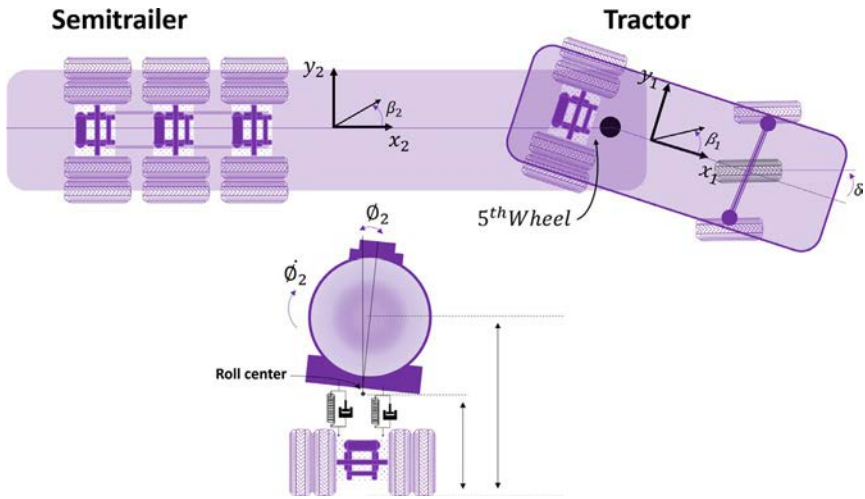

Fig. 6.6 Arrangement of the coordinate systems.

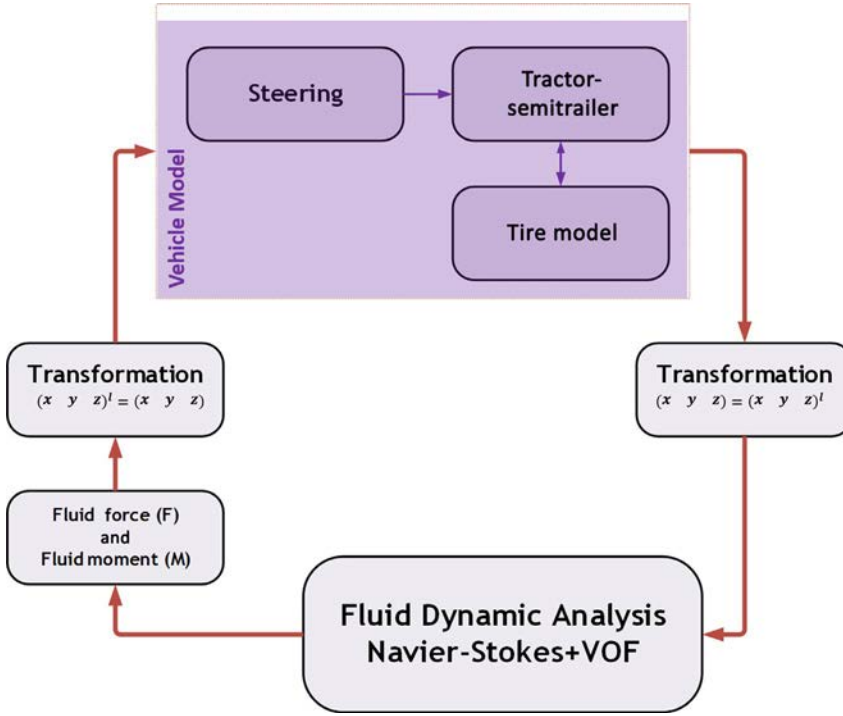

Fig. 6.7 Simultaneous solving stages of the fluid dynamics and the vehicle model.

small time-step values must be considered; for example, a fraction of a thousandth of a second would be appropriate for such analyzes. Fig. 6.7 shows the simultaneous solving process of the vehicle and fluid dynamic systems.

6.4.3 Model sensitivity to the number of cells

As noted, the type of mesh can influence the accuracy of the results. Therefore, the mesh size must be chosen so that reducing the number of cells does not significantly affect the results. In this chapter, two models have been proposed. Model A with 213,210 hexahedral cells and model B with 92,040 cells are indicated in Fig. 6.8, where the size of the mesh and the number of cells will have the most significant effect on the forces applied by the fluid.

As shown in Fig. 6.9, model B with larger cells did not significantly change the lateral and vertical forces (F_y and F_z). A small difference is observed in the F_x values, and because the values of the longitudinal force (100 N) are very small relative to the lateral force (about 0.2%), so the error generated in the longitudinal direction is negligible.

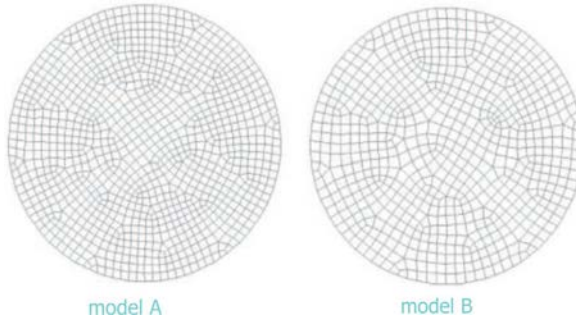

Fig. 6.8 Schematic of meshes with hexahedral cells used for model A and model B.

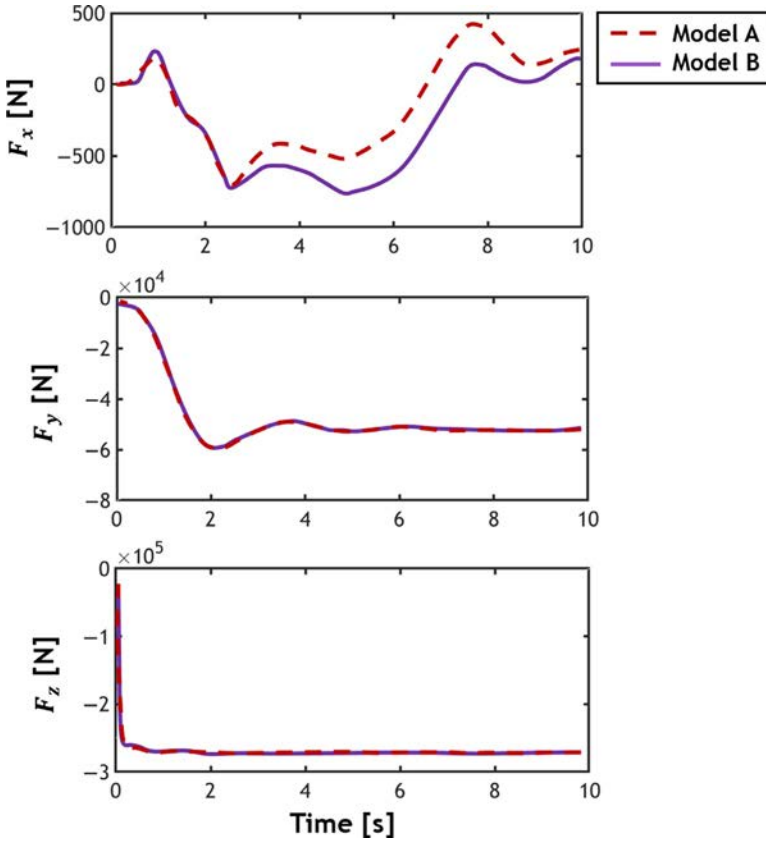

Fig. 6.9 Comparison of the forces exposed on the tanker by moving fluid for two types of the selected mesh.

6.5 Numerical dynamics analysis of the articulated vehicle carrying fluid

It was noted that the velocities of each particle are obtained from the angles, velocity, and angular velocities derived from the vehicle dynamics model and applied as input to the fluid model. Concerning these variables, the force and moment of the fluid are calculated and applied to the vehicle dynamics. This cycle is repeated each time step. The vehicle dynamics model's input is the steering angle, which can be one of the two common types of steady steer and lane-change maneuvers.

In the case of vehicle dynamics, roll angles, yaw rates, the acceleration of the center of mass, and the tractor and trailer's undertires, forces are plotted and investigated at different times. Due to fluid motion, the position of the center of gravity of fluid along the longitudinal and lateral direction as well as forces applied on the tanker's hull due to fluid presence and resulting moments are investigated. The fluid inside the tanker is water with a density of 998 kg/m^3.

6.5.1 Fixed input–steady steer

The five-axis vehicle's response behavior is first investigated at a constant input, and a speed of 60 km/h as shown in Fig. 6.10.

Fig. 6.11 displays the condition of the free surface of the fluid in the middle of the fluid-carrying tanker at times of 1 and 2.5 s. In this figure, the fill percentage is 50%, and the steady steer maneuver is considered for the

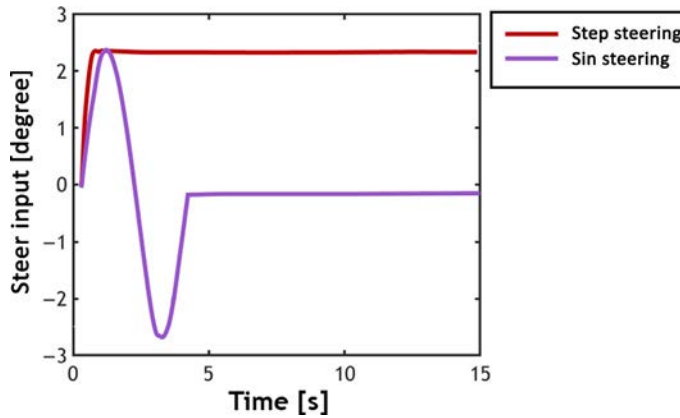

Fig. 6.10 Steering input (steady steer and lane change).

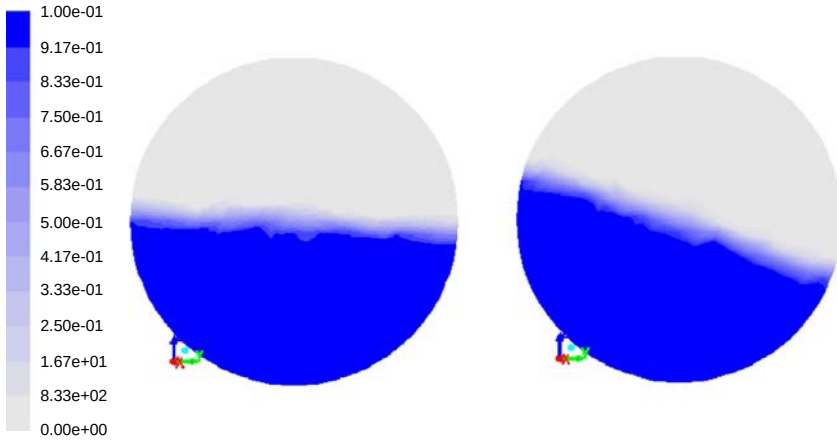

Fig. 6.11 The free surface of the fluid at the time of 1 and 2.5 s at $x = 0$.

vehicle. As can be seen, the slope of the fluid's free surface is very low in the first second and increases over time, which will have significant values at 2.5 s. Fig. 6.12 shows the dynamics behavior of the fluid-carrying vehicle and the vehicle with a rigid load under constant input. This figure displays the main responses of the tractor and the trailer considering the variation of the roll angle φ and the yaw rate angle $\dot{\psi}$.

The analysis also has been carried out for the equivalent rigid load, and the response is compared to the fluid load. As a result, the roll angle of the fluid-carrying vehicle is significantly larger than that of a rigid load carrier. Compared with the rigid load, the roll angle of the fluid-carrying tanker is 65% higher for the steady-state response condition and 70% higher for the maximum response condition. The fluid-carrying tractor and trailer have an oscillating response compared to the vehicle response with a rigid load. In the steady steer maneuver, at the end of long periods, the fluid becomes stable in its position, causing a constant roll angle relative to the rigid load. The yaw rate value is slightly higher than that of the rigid load, but it will eventually reach the value obtained for the rigid load. In the fluid-carrying vehicle, the yaw angle behavior similar to the roll angle has some oscillations compared to that of the vehicle with a rigid load.

Fig. 6.13 shows the motions of the center of mass along the longitudinal direction CG_x and the lateral direction CG_y. As expected, the variation of the coordinates of the center of mass is greater in the lateral than the

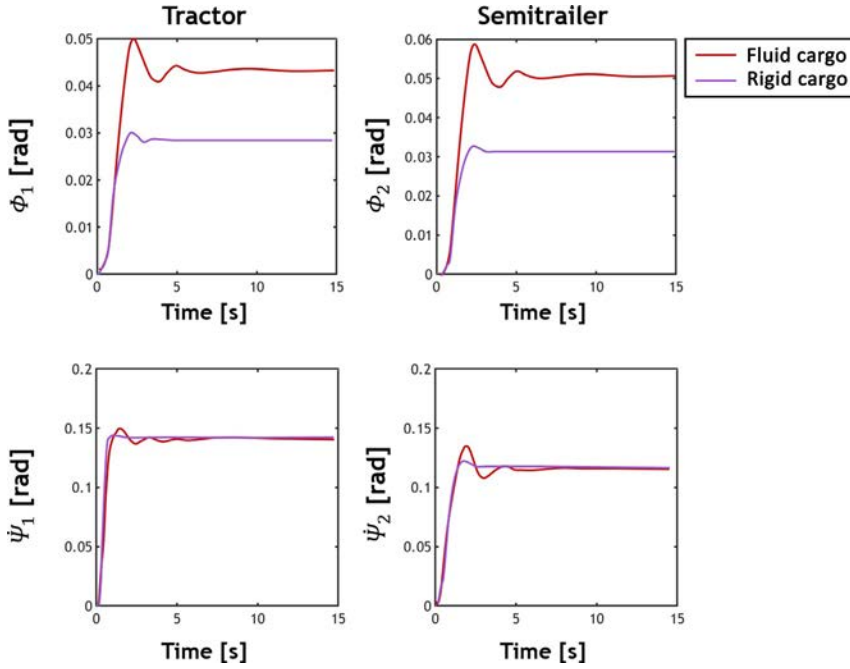

Fig. 6.12 The transient response of the tractor and trailer.

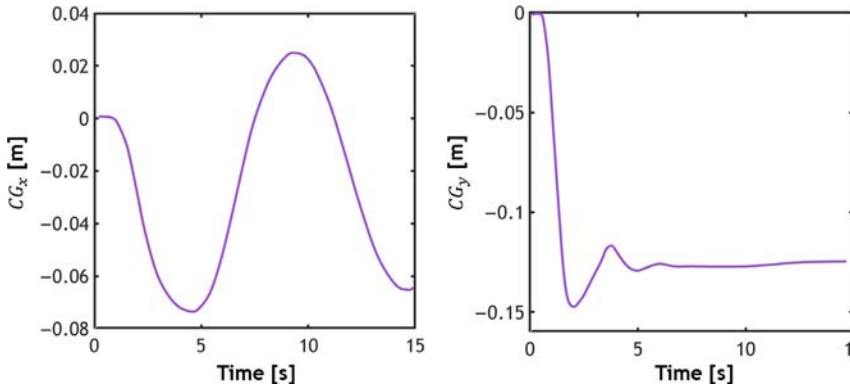

Fig. 6.13 Displacement of the center of gravity of the fluid (longitudinal and transverse) inside the tanker.

longitudinal direction, and the oscillatory behavior of the coordinate center is always expected. The low frequency of motion of the coordinate center along the longitudinal direction is due to the length of the pipe's length to its diameter. This is because surface waves require more time to go through the tanker's length compared to the width or the same diameter of the tanker. However, the vehicle dynamics and the steering input dynamics also affect the motion frequency of the center of gravity.

Fig. 6.14 shows the resulting forces of the fluid applied to the tanker's body. The total fluid force on the tanker's body is obtained from the aggregation of pressure product at the surface for each cell of the tanker's body. Because the lateral direction's acceleration component is greater than the longitudinal one, the lateral force is also greater than the longitudinal one. The amount of force in the lateral direction has some fluctuations,

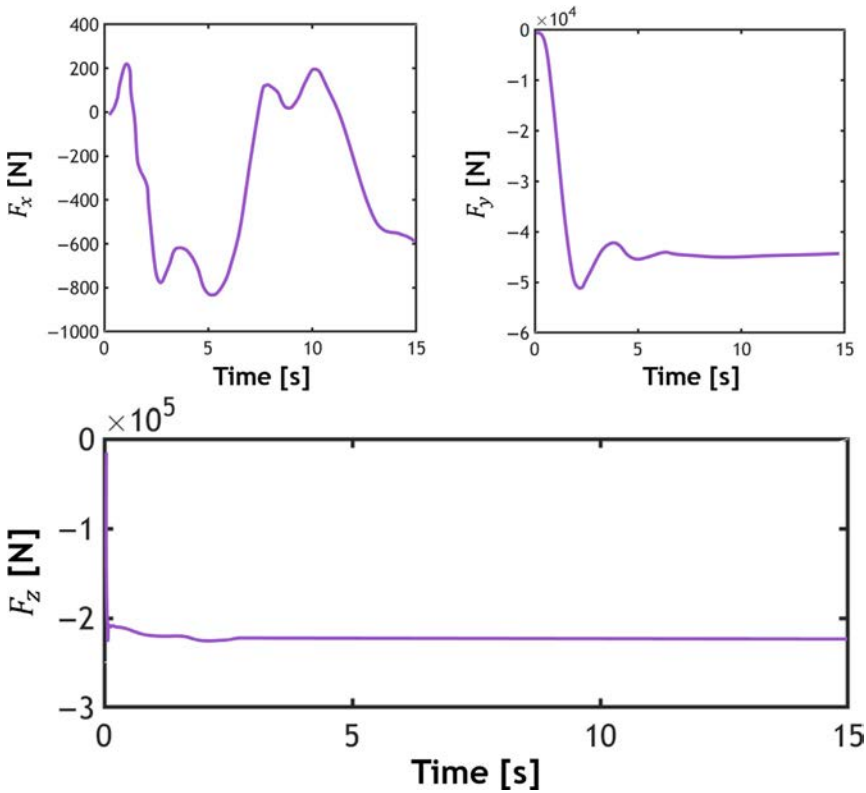

Fig. 6.14 The forces applied to the tanker's body due to the presence of fluid.

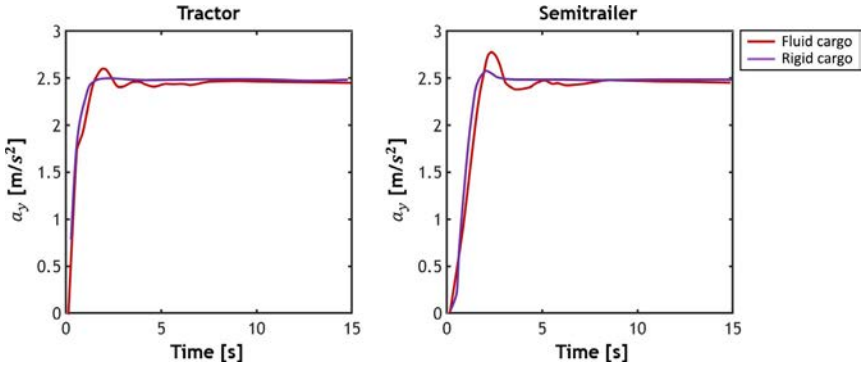

Fig. 6.15 Accelerations of the center of gravity for the trailer and tractor.

but its value is negative during the analysis. The force in the vertical direction F_z is affected by the force of gravity and will oscillate around the weight.

Fig. 6.15 shows the center of gravity's accelerations for the tractor and trailer, where the solid lines show the fluid-carrying vehicle and the dashed line represents the vehicle carrying a rigid load. The acceleration of the center of gravity for the trailer is a little more than that of the tractor, and the maximum value of this acceleration for the fluid-carrying vehicle is greater than that of the vehicle carrying a rigid load. The acceleration response of the fluid-carrying vehicle has an oscillatory behavior around the vehicle's acceleration response carrying a rigid load. These oscillations will be eliminated by time, and in the steady state, its value reaches the acceleration of the vehicle with the rigid load.

Vehicle rollover behavior is interpreted in terms of dynamic load factor. The dynamic load factor is defined from the vertical load ratio on the right or the left to the static load of that axis corresponding to (6.23).

$$DLF_r = \frac{2F_{zr}}{F_{zr} + F_{zl}},\ DLF_l = \frac{2F_{zl}}{F_{zr} + F_{zl}} \tag{6.23}$$

F_{zr} and F_{zl} are normal loads applied perpendicular to the right and left wheel of an axis. During a steady steer maneuver, DLF is one and may reach zero when the tire loses contact with the ground. In this case, the load dynamic factor for the other wheel will have a maximum value of *two*. The last axis is always prone to rollover. The dynamics stability of the vehicle is generally defined with the term dynamics load transfer ratio. This ratio is calculated from the sum of the difference between the loads of the right and left wheels to the total static load of all axes, according to (6.24).

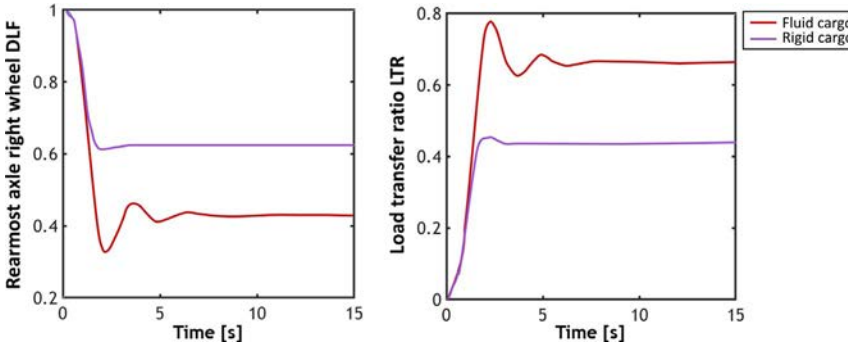

Fig. 6.16 Dynamic load factor and load transfer ratio for the last axis.

$$LTR = \sum_{j=1}^{N} \frac{\left|F_{zrj} - F_{zlj}\right|}{F_{zrj} + F_{zlj}} \tag{6.24}$$

In this equation, N is the number of axes. For vehicles that are independent of the roll, LTR is calculated for independent units. The front axis is generally excluded because of its high roll resistance. LTR's value is zero initially and reaches 1 when the wheel is separated from the Earth's surface in the road turning.

Fig. 6.16 shows the dynamics load factor for the last axis and the load transfer ratio for the fluid load and the equivalent rigid load. It is shown that the DLF for the fluid-carrying vehicle is less than that of the vehicle with a rigid load (45% lower at maximum values and 30% lower in steady response mode). This figure also shows that the possibility of rollover for fluid-carrying vehicles is higher than vehicles with a rigid load.

6.6 Effects of fill percentage and viscosity on the dynamics of fluid and vehicle

6.6.1 Fill percentage effects

The percentage of the tanker's filled volume affects the fluid inertia, the height of the center of gravity, and the potential of mass displacement that causes the creation of destructive forces and moments. Figs. 6.17 and 6.18 show that the roll angle changes are presented for three fill percentages of 25%, 50%, and 75% for the steady steer and lane-change maneuvers. These figures reflect that an increase in fill percentage will increase the roll angle of

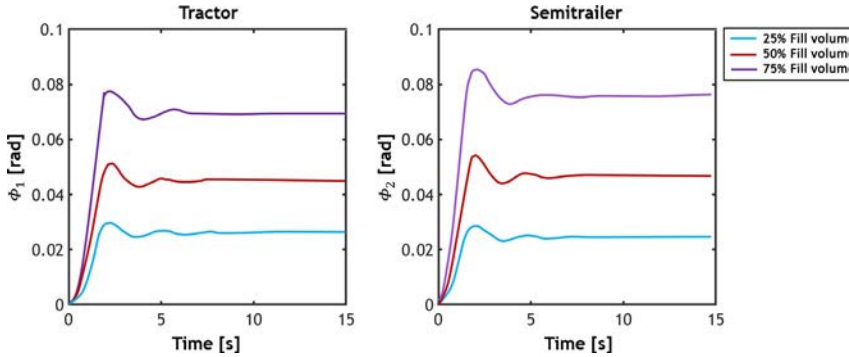

Fig. 6.17 Dynamic behavior of the fluid-carrying vehicle with steady steer input.

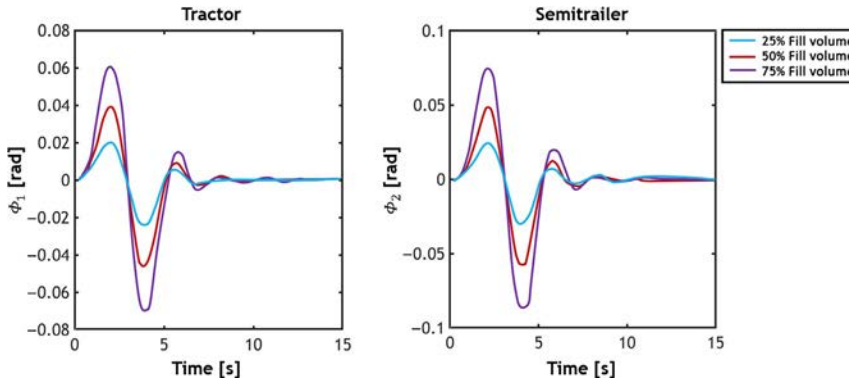

Fig. 6.18 Dynamic behavior of the fluid-carrying vehicle with the lane-change maneuver.

the tractor and trailer. As can be seen, changes in roll angle in the second half of the lane change maneuver are more than the first half of the maneuver due to fluid motion and its effect on vehicle dynamics. Because of the constant displacement of the fluid's center of coordinate in the steady steer maneuvering, the roll angle shows a shift relative to zero value. But in the lane-change maneuver, because the center of gravity is returned to the initial state, the center of the mass coordinate is also returned to the initial state (zero).

Figs. 6.19 and 6.20 show the effect of fluid motion on the vehicle dynamics and its stability for the three values of fill percentage and two intended maneuvers. The dynamic load factor is displayed in these figures. The figures show that an increase in the fill percentage leads to a reduction in

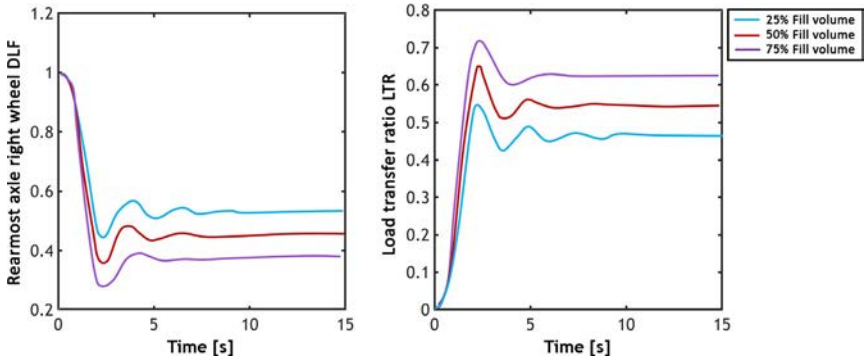

Fig. 6.19 Dynamic load factor (DLF) and load transfer ratio (LTR) for the steady steer maneuver.

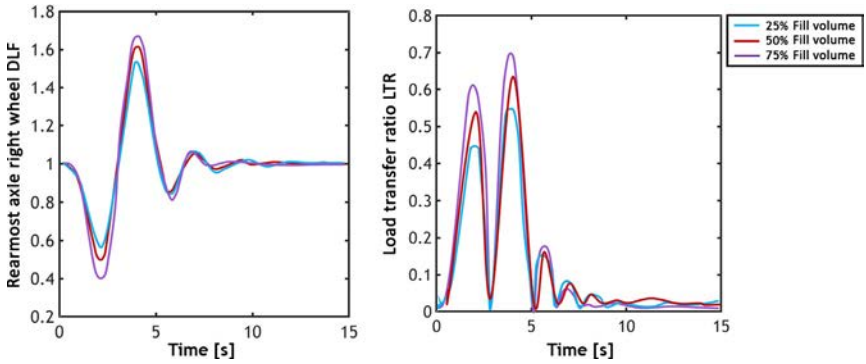

Fig. 6.20 Dynamic load factor (DLF) and load transfer ratio (LTR) for the lane-change maneuver.

fluid carrier stability, which does not depend on maneuver type. Fig. 6.20 shows that the worst stability condition occurs for the left wheel and in the second maximum of DLF.

6.6.2 Effects of viscosity

In order to investigate the net effect of viscosity on vehicle dynamics, an equivalent fluid has been introduced so that this fluid must have water properties, with the viscosity of 1 kg/m s, which is almost a thousand times the viscosity of the water and close to the oil viscosity. In Figs. 6.21 and 6.22, the

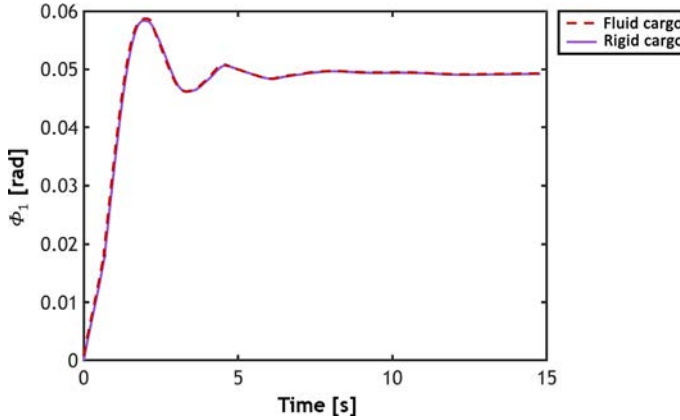

Fig. 6.21 The transient response of the roll angle for the trailer.

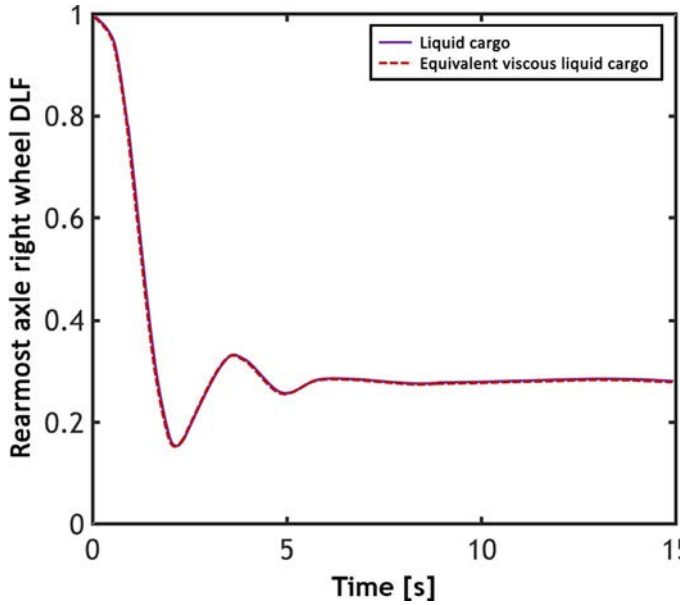

Fig. 6.22 Dynamic load factor (DLF).

fill percentage is considered to be 50%, and the steering input is a steady steer by a constant radius. This indicates that the effects of the viscosity on the roll angle of the trailer will be insignificant. Fig. 6.22 shows the dynamic load factor for the water and the equivalent fluid, which indicates that, despite it being imagined that viscosity can play a significant role in the vehicle dynamics, its effects on vehicle dynamics will be insignificant.

6.7 Effects of the tanker's geometrical shape on the roll response of an articulated vehicle

The force applied from fluid motion depends on the boundary constraints created by the tanker's geometrical shape. The geometrical shape of the cross-sectional area and the tanker's length will affect the fluid motion and the stability of the fluid-carrying vehicle. The amount of force applied to a tanker vehicle is dependent on the shape and fill percentage of the tanker, vehicle dynamics, and maneuver type. Three types of tankers–circular cross-section, modified ellipsoid, and triangular with round corners–are shown in Fig. 6.23. The circular cross-section with a radius of 1.015 m and the modified ellipsoid cross-section with the following properties are the most common form of the cross-sectional area for fluid-carrying tankers:

$$R_1 = R_2 = 1.78, R_3 = 0.39, H_1 = 2.44\,\text{m}, H_2 = 1.65\,\text{m}, c.g.height = 0.825\,\text{m}$$

From the perspective of roll stability, the modified ellipsoid shape has a low-level center of gravity but has more load transfer in the partially filled state. The cross-section with the circular shape has less load transfer concerning the low width, but the height of its center of gravity is considerably more than the ellipsoid one.

The tanker with a triangular cross-sectional area with the following properties

$$H_1 = 2.15\,\text{m}, H_2 = 1.88\,\text{m}, c.g.height = 0.84\,\text{m}$$

has a relatively low-level center of gravity and a lower load transfer in the partially filled state [21]. This cross-sectional area is called the optimal cross-section, and in the following, the lateral dynamics and stability of the mentioned cross-sections are investigated using the coupled model of a vehicle with a three-dimensional model of fluid.

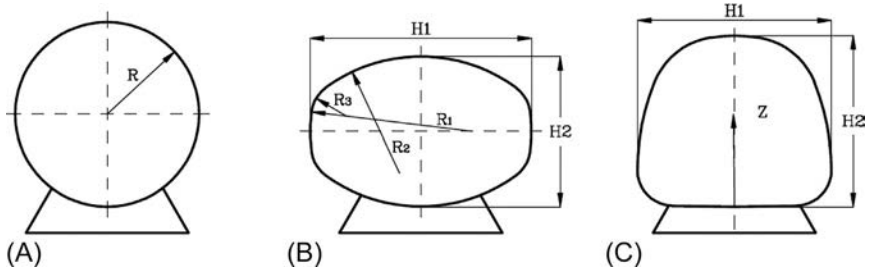

Fig. 6.23 The cross-section of the tankers used in the investigations. (A) circular, (B) modified oval, (C) Reuleaux triangle.

Table 6.1 The number of elements considered for different tanker shapes.

Shape of tanker	Cylindrical	Modified oval	OPT
Number of cells	92,040	80,910	86,800

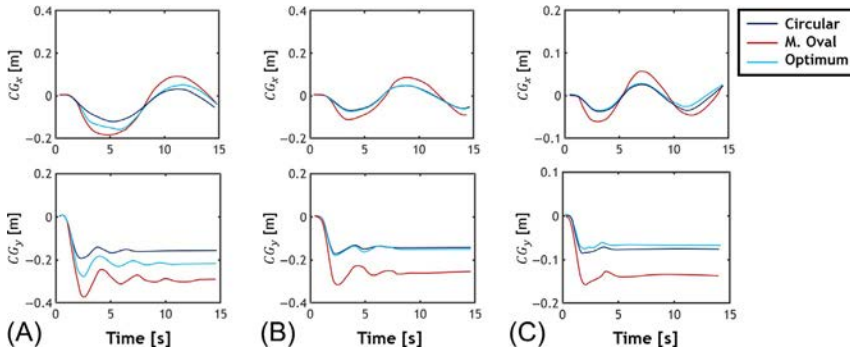

Fig. 6.24 Longitudinal and lateral displacement of the center of gravity for the fluid at fill percentages of A: 30%, B: 50%, and C: 70%.

FLUENT software is used to model the fluid behavior. To model the joint boundary of the fluid and the air, the VOF method is used. Meshes with hexahedral cells are used for numerical analysis, and Table 6.1 demonstrates the number of elements used for different tankers.

The simulation of the dynamic behavior of the vehicle is done with fill percentages of 30, 50, and 70. The fluid inside the tanker is also water. The results for the displacement of the center of gravity of the fluid in Fig. 6.24 indicate that CG_x will decrease with an increase in the fill percentage regardless of the cross-sectional area of the tankers. In all three cases, the longitudinal displacement of the center of gravity related to the modified ellipsoid cross-sectional area is higher than that of other tankers. An investigation of the displacement of the center of gravity in the lateral direction also has impressive results. For all three fill percentages, the center of mass's lateral displacement for the fluid has the maximum value for the modified ellipsoid cross-section. For fill percentages of 50% and 70%, the displacement of the center of mass in the lateral direction is very close for tankers of both circular and optimal cross-sections, so the load transfer is expected to be in good agreement for both of them. In the case of a 30% fill percentage, the tanker with the cylindrical cross-sectional area will have the minimum displacement of the center of gravity, and as a result, the minimum load transfer.

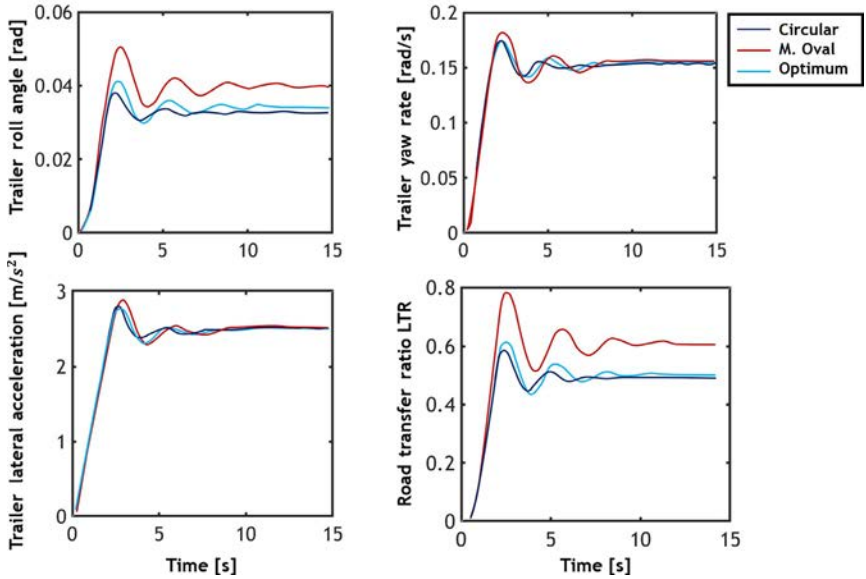

Fig. 6.25 Transient response of the fluid-carrying vehicle for a 30% fill percentage.

In Figs. 6.25–6.27, the roll angle, lateral acceleration, yaw rate, and load transfer ratio of the trailer are given. It can be observed that the vehicle equipped with the tanker of the modified ellipsoid cross-section has a higher roll angle than the tankers with the circular and optimal cross-sectional areas. This is due to the greater load transfer that arises from a broader cross-section. The tanker's roll angle with the optimal cross-sectional area at a 30% fill percentage is slightly higher than that of the circular cross-sectional area. But at 50% and 70% fill percentages, the roll angle of the optimal cross-sectional area is less than the circular one. At these fill percentages, the lateral load transfer is the same for both circular and optimal cross-sectional areas. This can be seen from the diagram for the center of coordinate motion in the lateral direction. Therefore, the height of the center of gravity will play a significant role in the response of the roll angle, and because the height of the center of gravity for the optimal cross-section is lower than the circular one, so its roll angle response has also lower values.

Accelerations and yaw angle rates indicate that the cross-sectional area's effects on the general response are small and only affect the dynamics cases (abrupt changes of steering input). The tanker with

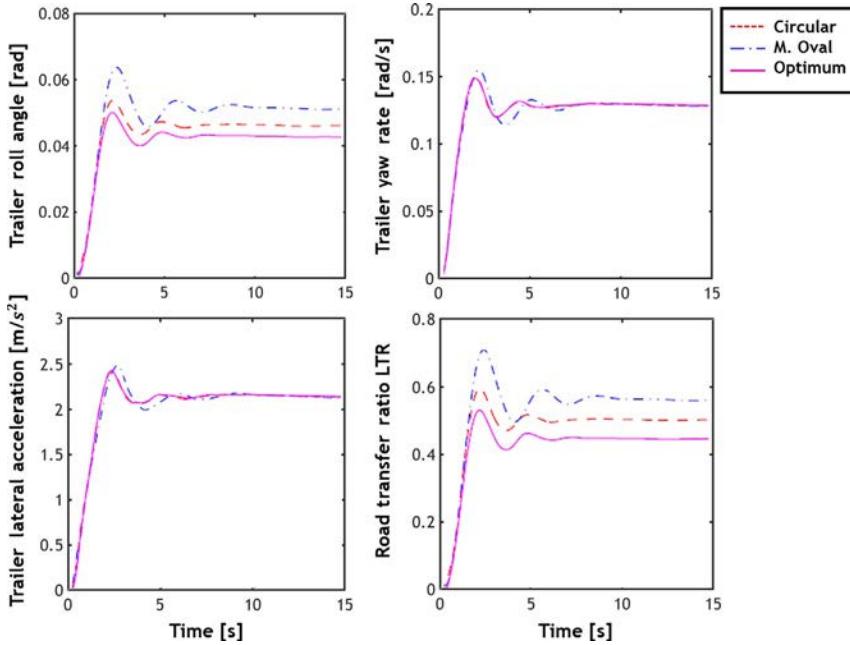

Fig. 6.26 Transient response of the fluid-carrying vehicle for a 50% fill percentage.

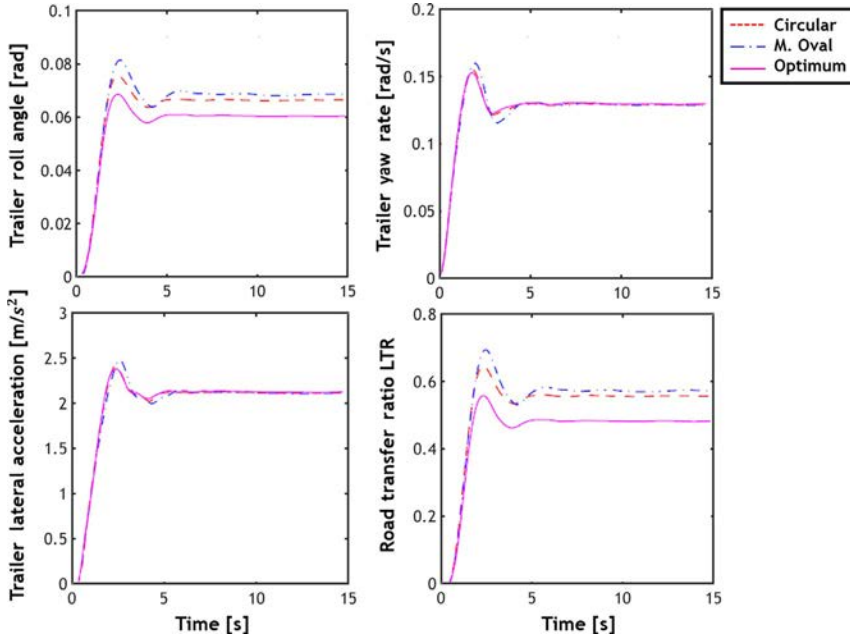

Fig. 6.27 Transient response of the fluid-carrying vehicle for a 70% fill percentage.

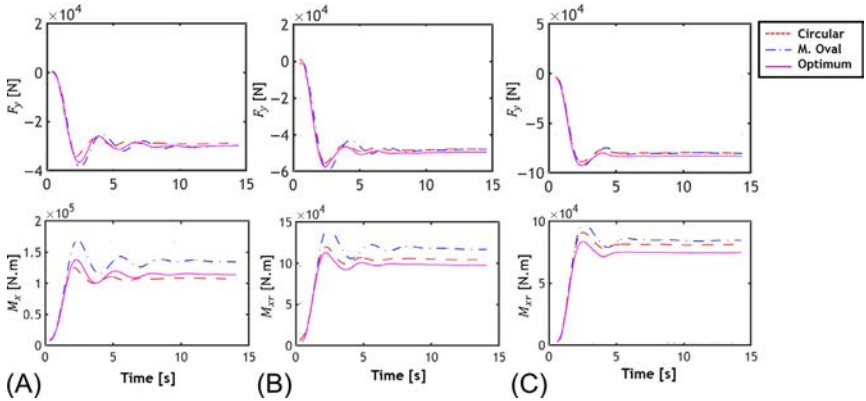

Fig. 6.28 Moments arose from the fluid flow and motion, in 30%, 50%, and 70% fill percentages, respectively.

the modified ellipsoid cross-sectional area has the greatest variation compared to the other cross-sectional areas. In Fig. 6.28, the forces and moments of fluid are drawn around the roll axis of the trailer, where the effects of load transfer as well as the height of the center of gravity can be observed at the same time. In all the fill percentages, the moments of the modified ellipsoid cross-section are higher than the rest of the cases. Also, it results in more fluctuating behavior compared to other shapes of the cross-sectional area. This indicates that the load transfer due to a wide cross-sectional area is the main factor that influences the amount of moment and, thus, the dynamics of the vehicle. For a 30% fill percentage, the amount of moment corresponding to the circular cross-sectional area is slightly less than that of the optimal one, but at other fill percentages, the optimal one has the lowest moment.

6.8 Effects of holder plates on the vehicle dynamics of and fluid motion inside the tanker

Different methods have been proposed to reduce fluid motion and, consequently, the fluid motion force in which the holder plates as a tool can improve the dynamic behavior of the vehicle [3]. Although the installation of holder plates has positive effects on vehicle dynamics, it will also introduce limitations such as cleaning the tanker, increasing its weight, and stress concentration at the connection points of the holder plates with the tanker. The results of the investigations [22–24] represent the fact that baffle plates can be

an essential factor in limiting fluid motion and, consequently, fluid forces. As mentioned earlier, the fluid motion force is directly related to the tanker's geometry, middle plate layout, fill percentage, vehicle dynamics, and type of maneuvers. During a given maneuver, the fluid motion causes the forces and moments generated on the tanker's body, which increases the probability of rollover for the fluid-carrying vehicle. To overcome this challenge, baffle plates are proposed to reduce the likelihood of rollover while reducing fluid motion forces over the tanker's body.

A cylindrical tanker with a radius of 1.015 m and a length of 12.04 m with three arrangements of baffle plates ($a = b = 1$ m, $c = 0.4$ m) is considered, as shown in Fig. 6.29. In these arrangements, baffle plates are extended along the length of the tanker.

6.8.1 Lane change maneuver

In this section, an analysis has been carried out for a fill percentage of 50% and three arrangements of baffle plates. The results are compared with corresponding values for the tanker without an inner plate to determine the effect of the midplate arrangement on the fluid-carrying vehicle dynamics. The effect of fluid motion on the vehicle's lateral dynamics and the stability of the fluid-carrying vehicle can be considered from three perspectives. The first is the mass force resulting from the cumulative motion of the fluid that creates a moment on the body, which is a function of fluid type, the shape of the tanker, and the fill percentage. The second is due to the displacement of the fluid's center of gravity inside the tanker, which will also generate moments. The third will be related to the equality of the natural frequency of fluid motion with the vehicle frequency or the lateral frequency of the vehicle [25].

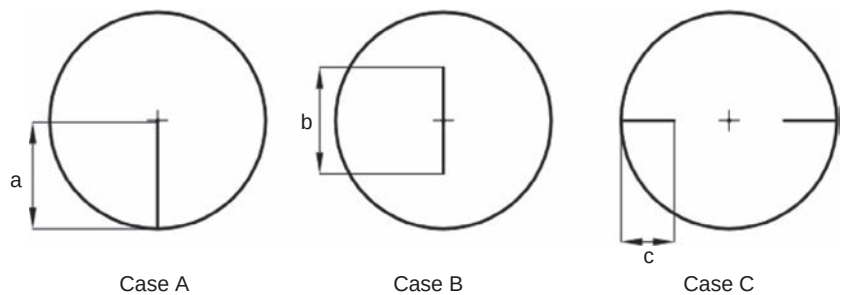

Fig. 6.29 Three arrangements of baffle plates inside the tanker.

6.8.2 Dynamics of vehicle and fluid at 50% fill percentage

Fig. 6.30 shows moments on the tanker's body around the trailer's roll axis for the three arrangements of baffle plates and a 50% fill percentage. This figure shows the displacement of the fluid and also the effect of the center of gravity displacement. As seen in Fig. 6.30, the center of gravity is sensitive to the middle plate design. In the case of A, the displacement value at the maximum value ($t = 2$, 4 s) is less than the rest of the cases. As a result, it is possible to compare the results of the displacement in figures. In this case (case A), due to the limitation of the displacement of the center of mass, the load transfer is lower and, therefore, better lateral dynamics may be compared to any other cases. Fig. 6.31 shows that case A has the lowest moment around the roll axis compared to other cases, indicating the efficiency of this arrangement in limiting fluid motion as well as the scattering of energy.

In the case of C, the maximum lateral displacement of the center of mass of the fluid in the first half of the maneuver is close to the tanker's behavior without the middle plate, but in the second part of the maneuver, the peak value is reduced and approaches case A. The same results can also be observed for the resulting moments. This reduction of the moment in the second half of the maneuver can also be interpreted in terms of fluid motion of Fig. 6.33. In the first half of the maneuver ($t = 2$ s), the arrangement of

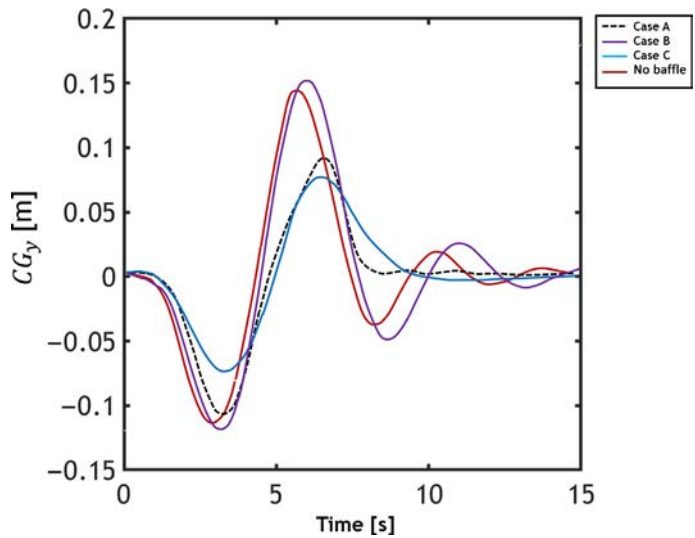

Fig. 6.30 Lateral motion of the center of gravity at a 50% fill percentage (lane-change maneuver).

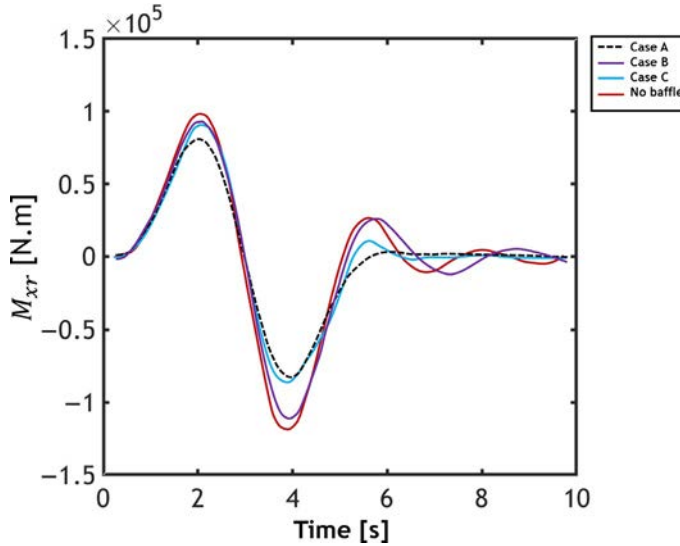

Fig. 6.31 The resulting moment around the roll axis at a 50% fill percentage (lane-change maneuver).

the baffle plates did not have a significant effect on the fluid motion, but in the second half of the maneuver ($t = 4$ s), the fluid energy decreased, and the fluid motion was damped because of collision with these plates.

In the case of B, the maximum lateral displacement of the center of mass is higher than the tanker without holder plates, and consequently, higher values of moments are expected. However, the shape of moments in Fig. 6.32 shows another thing. This means that although this arrangement failed to limit the fluid motion, it could reduce fluid energy through changes in the fluid regime and limit surface waves.

The roll angle and yaw rate can show the effects of fluid motion on the vehicle dynamics. Fig. 6.34 shows the results of the roll angle of the trailer for a fill percentage of 50%. The highest and lowest values of the roll angle are associated with the tanker without plates and the case A arrangement. Fig. 6.35 shows the dynamic effects of different arrangements on the rate of yaw angle changes at a 50% fill percentage. The lateral load transfer ratio (LTR) for the 50% fill percentage is shown in Fig. 6.36. The stability of the vehicle has been weakened by the increase in the tanker's fill percentage. This figure shows that the worst stability condition occurs in the second half of the maneuver. In this fill percentage, case A has the lowest LTR

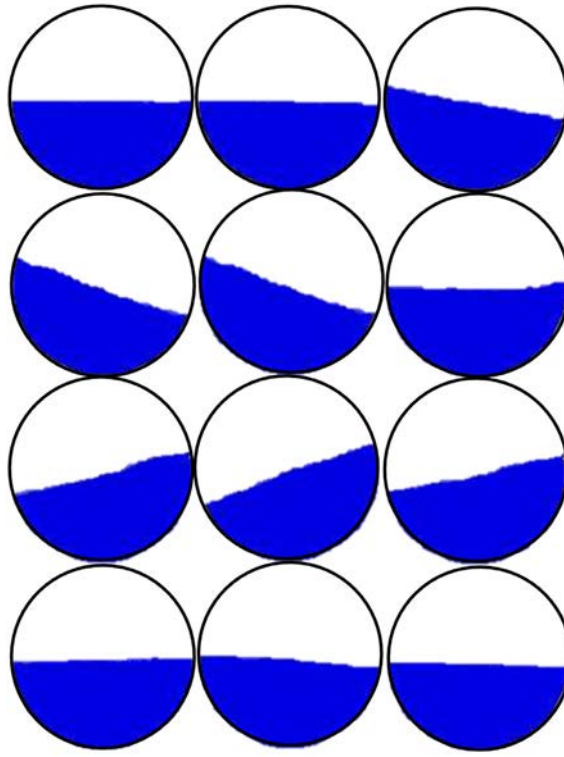

Fig. 6.32 Fluid motion in the tanker without baffle plates (0–5.5 s with a 0.5 s interval and a lane-change maneuver).

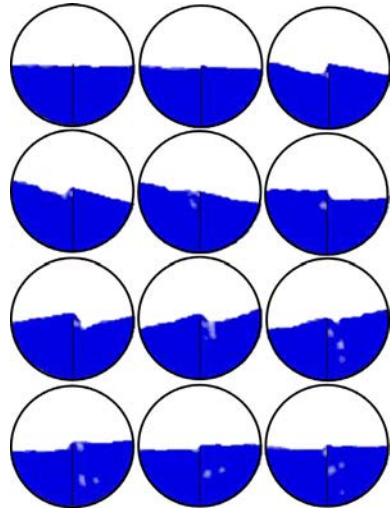

Fig. 6.33 Fluid motion in the tanker with the baffle plates case A (0–5.5 s with a 0.5 s interval and a lane-change maneuver).

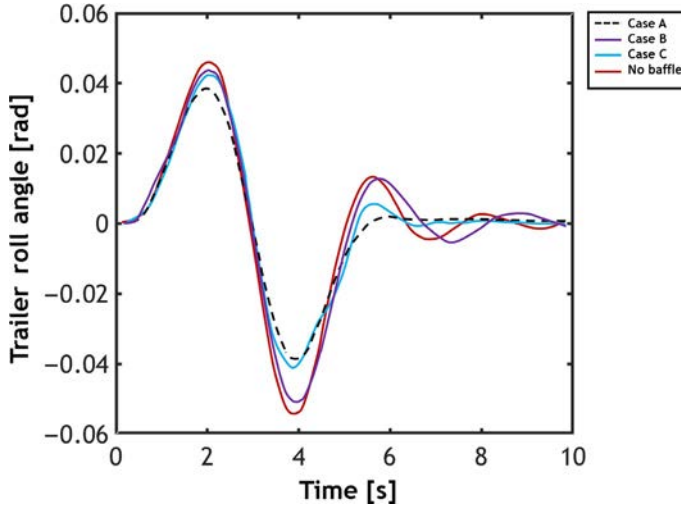

Fig. 6.34 Trailer roll angle of the trailer at a 50% fill percentage (lane-change maneuver).

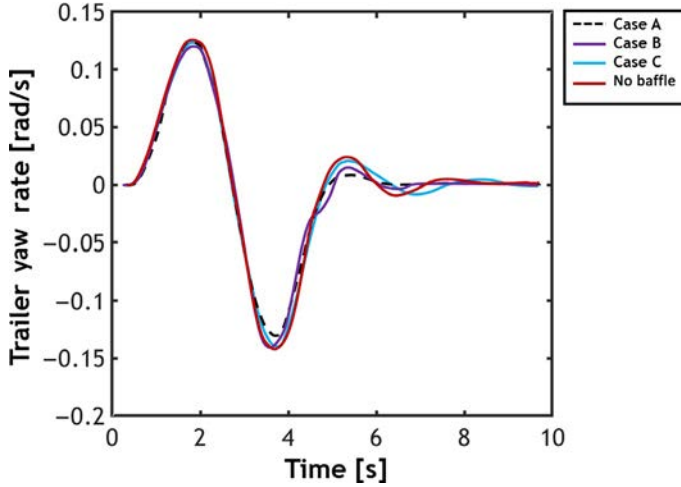

Fig. 6.35 Trailer yaw angle at a 50% fill percentage (lane-change maneuver).

(better stability) in the maximum values, and the response is nonfluctuating after the end of the maneuver.

In the case of C, the LTR value in the first half of the maneuver is as large as the tanker without baffle plates, but its value is reduced in the second half of the maneuver and approaches case A (optimum one). The arrangement

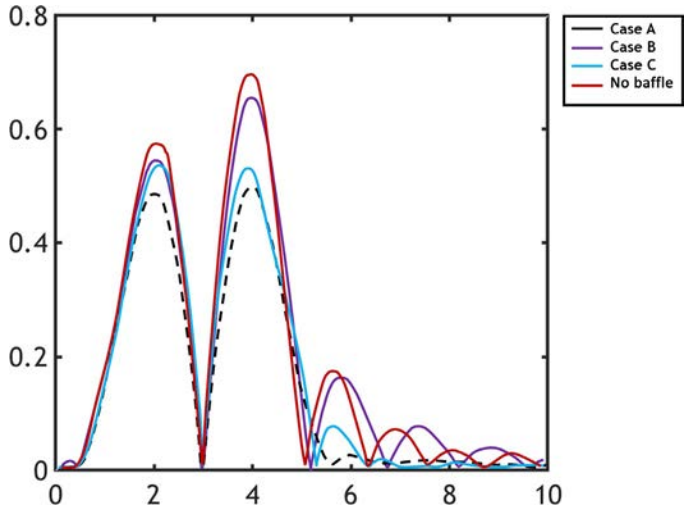

Fig. 6.36 The load transfer ratio at a 50% fill percentage (lane-change maneuver).

B of baffle plates in this fill percentage improves the dynamics behavior of the vehicle but is not as good as case A. At the end of the lane-change maneuver, the diagram of the load transfer ratio for case B and the tanker without baffle plates shows an oscillatory behavior compared to other arrangements. It should be taken into account that the fill percentage has a significant effect on fluid and vehicle behavior. For example, according to Fig. 6.37, the baffle plates have no significant effect on the vehicle dynamics at a fill percentage of 75% compared to a fill percentage of 50%.

6.9 Improving the design of baffle plates

The three patterns presented for the middle plates have different applications concerning the type of maneuver and the fill percentage. For example, the design of A at a 50% fill percentage and both of the steering inputs improve the stability, but as soon as the fill percentage increases to 75%, its efficiency is significantly reduced. Design B has improved the vehicle's stability with the steering input of the lane-change in 50% and 70% fill percentages, but the design has no significant improvement in the stability in the steady steer maneuver and a 50% fill percentage. Regarding design C, with the lane-change input and a 50% fill percentage, considerable improvement is achieved in stability, especially in the second half of the maneuver. In the

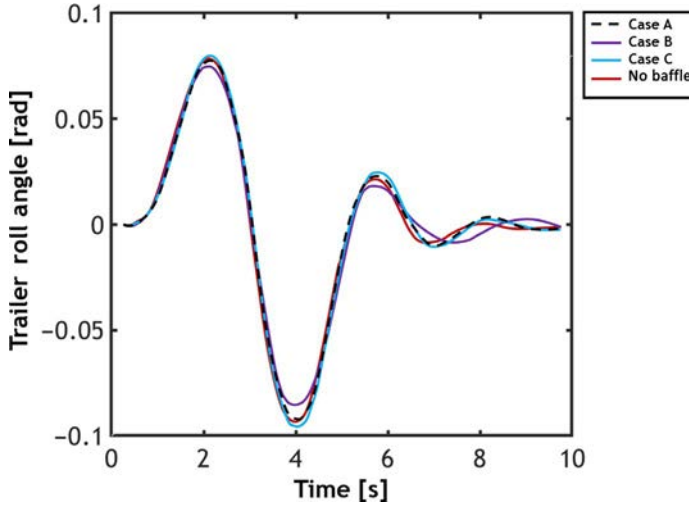

Fig. 6.37 The roll angle of the trailer at a 75% fill percentage (lane-change maneuver).

steady steer maneuver for 50% and 75% fill percentages, the effect on stability is low and may be negligible. Therefore, it is important to develop patterns that are guaranteed in different conditions.

6.9.1 Improved design A

As indicated, case A loses its effectiveness severely by increasing the fill percentage. In order to address this problem, it is proposed to increase the height of the median plate. Then, increase the middle plate's height to the tanker's end so that the tanker is divided into two equal parts. We call this EA Case. By drawing the load transfer ratio for two values of fill percentage and two maneuvers, we examine the new case's effectiveness and compare the obtained results with the results of case A and the tanker without middle plates. In a lane-change maneuver and at a 50% fill percentage, case A led to the dynamic stability of the vehicle, but it is noticed in Fig. 6.38 that an improved version has better performance than case A. Case A shows a 30% improvement in stability compared to the tanker without baffle plates while the improvement in case EA is about 37%. In the EA, the volume of baffle plates is greater than case A (by almost two times).

In Fig. 6.39, the variation of the load transfer ratio is shown for a 75% fill percentage and the lane-change maneuver. As can be seen, case A has lost its

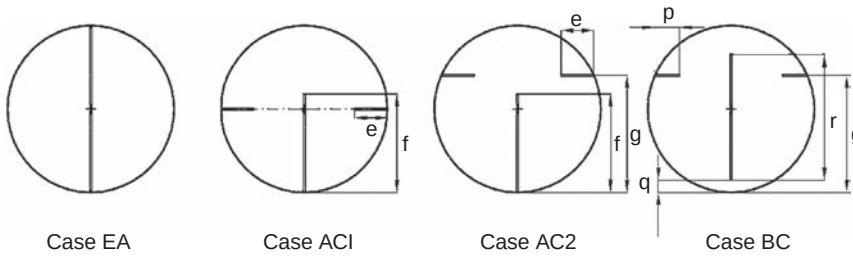

Fig. 6.38 Improved arrangements of the baffle plates inside the tanker.

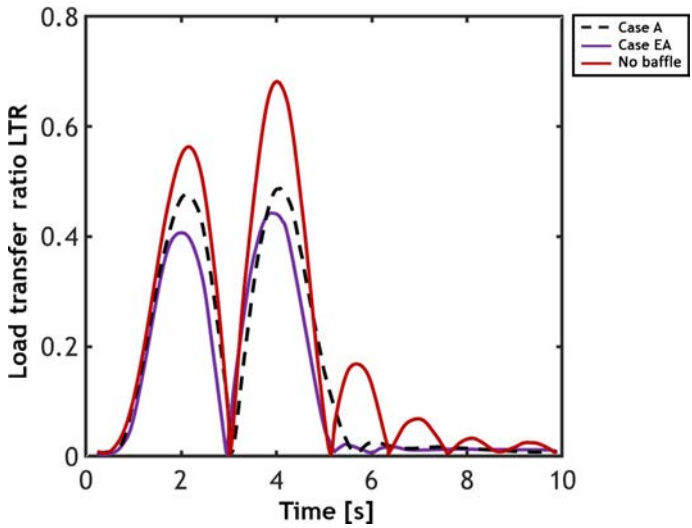

Fig. 6.39 The load transfer ratio for a 50% fill percentage (lane-change maneuver).

effectiveness completely while case EA maintains its effectiveness and improves stability by about 25% relative to the tanker without baffle plates. Fig. 6.40 shows the load transfer ratio for a 50% fill percentage and the steady steer maneuver. As shown in this figure, case A shows a 15% improvement in the maximum value while in the steady state, the scheme does not lead to any improvement. Case EA shows a 30% improvement in the maximum response, and in the steady state, the model shows a 20% improvement in the load transfer ratio compared to the tanker without baffle plates. This analysis means that the EA has improved the stability of the vehicle in the dynamic state and also improves the stability of the articulated vehicle in

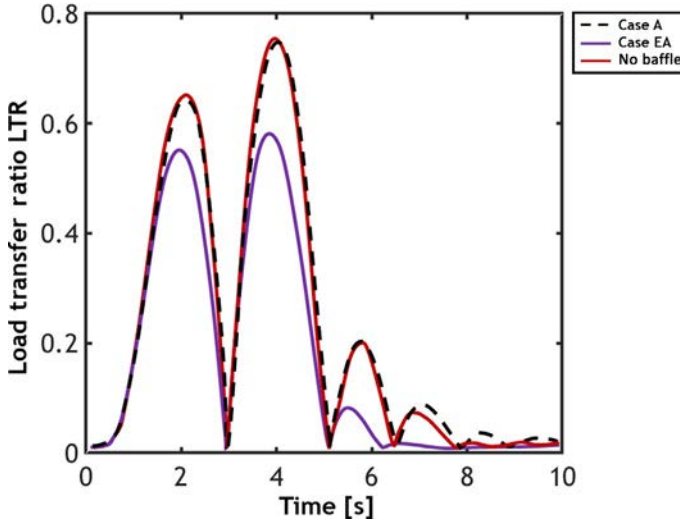

Fig. 6.40 The load transfer ratio for a 75% fill percentage (lane-change maneuver).

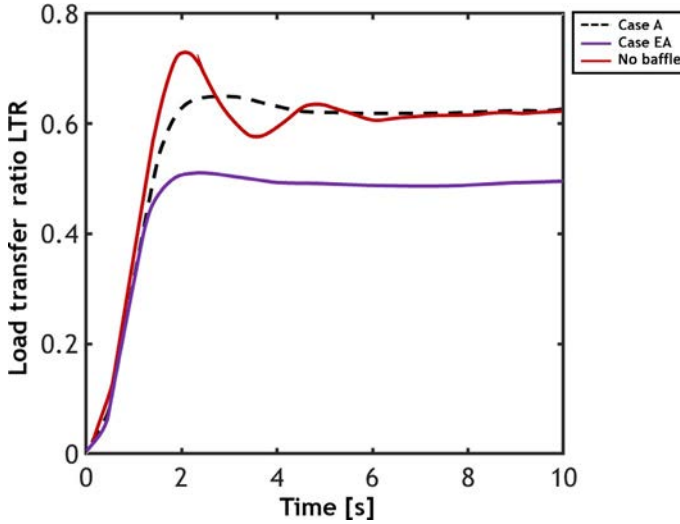

Fig. 6.41 The load transfer ratio for a 50% fill percentage (steady steer maneuver).

the steady state. Fig. 6.41 depicts the load transfer ratio for the steady steer maneuver at a 75% fill percentage. Case A loses its effectiveness with an increase in the fill percentage, and the EA responds to a 17% improvement in terms of maximum load transfer and a 10% improvement in steady-state response (Fig. 6.42).

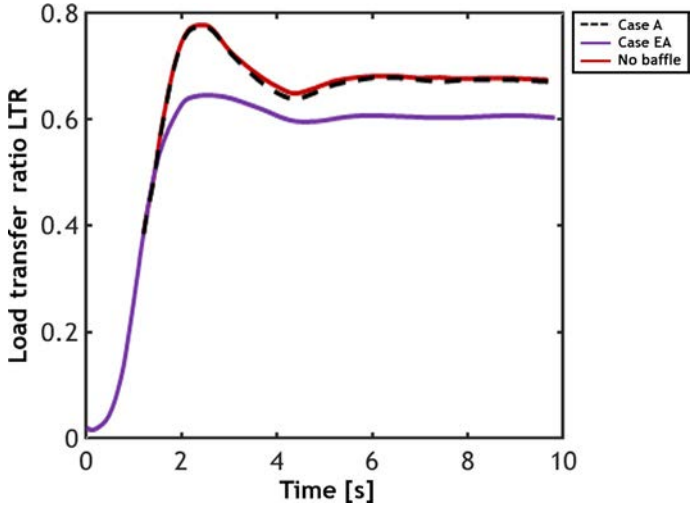

Fig. 6.42 The load transfer ratio for a 75% fill percentage (steady steer maneuver).

6.9.2 Combinations of patterns to form the optimum shape of baffle plates

6.9.2.1 Combination of cases A and C

We call the initially combined design AC1. In this scheme, case A is modified and combined with case C. The size and shape of the layout of the plates are shown in Fig. 6.38 ($f = 1.2$ m, $e = 0.4$ m). Figs. 6.43–6.46 show the load transfer ratio for the modified design and compare it with designs A and C, and a tanker without baffle plates at 50% and 75% fill percentages for steady steer and lane-change maneuvers. The modified design is better than cases of A and C at a 50% fill percentage. This design shows a 45% improvement in the lane-change maneuver and a 28% improvement in the steady steer maneuver at a 50% fill percentage. For a 75% fill percentage, the lane-change maneuver shows only a 5% improvement in stability. In the same percentage, it does not provide improvement in stability for the steady steer steering input.

According to the obtained results, although the AC1 design created an appropriate improvement for a 50% fill percentage, it will still lack the necessary effect for the high fill percentage values. Therefore, we introduce our proposed AC2 design. It is the same as the AC1 scheme, with the elevation of the lateral midplates increased and placed at a height of 50% of the tanker ($g = 1.425$ m). In order to improve the performance of the baffle plates, this design has been proposed to fill percentages of more than 50%. The variation

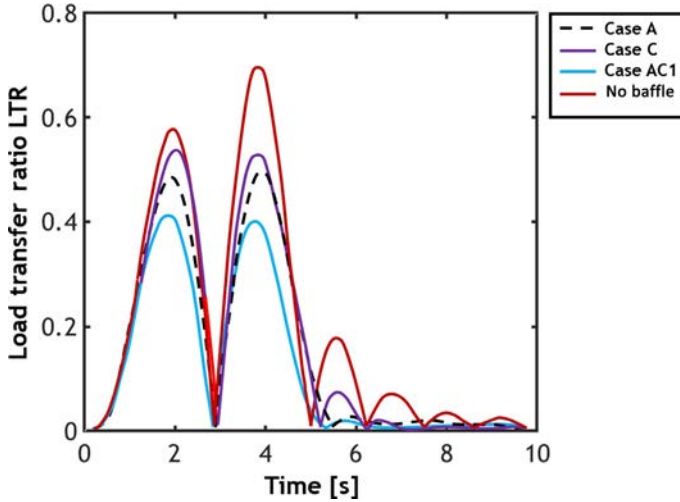

Fig. 6.43 The load transfer ratio for a 50% fill percentage (lane-change maneuver).

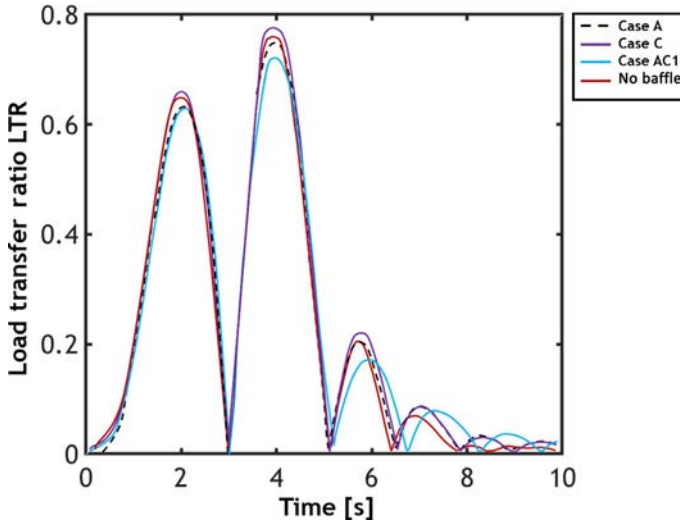

Fig. 6.44 The load transfer ratio for a 75% fill percentage (lane-change maneuver).

of load transfer ratio of the tanker equipped with baffle plates of design AC2 is plotted in Figs. 6.47–6.50.

As shown in Fig. 6.47, an increase in the height of the lateral plates causes a loss in stability relative to the AC1 design at a 50% fill percentage. However, by increasing the fill percentage, as shown in Fig. 6.48, an increase of

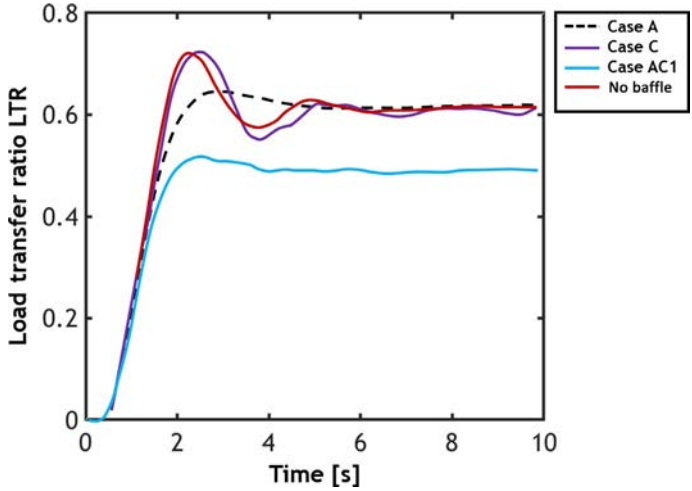

Fig. 6.45 The load transfer ratio for a 50% fill percentage (steady steer maneuver).

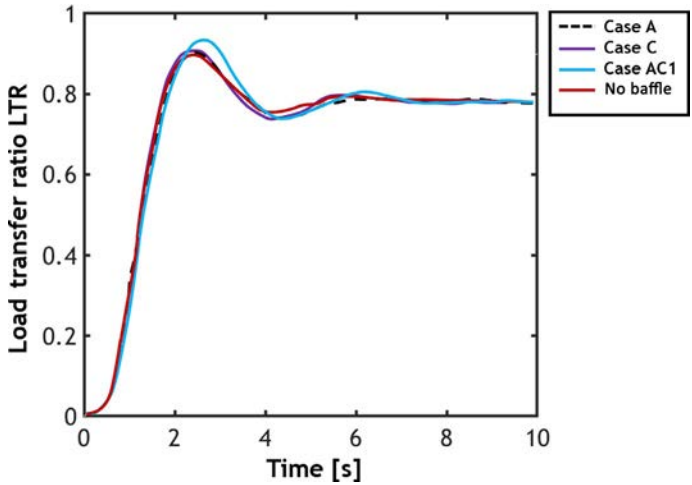

Fig. 6.46 The load transfer ratio for a 75% fill percentage (steady steer maneuver).

18% in improvement is observed for the AC2 scheme. In the AC1 design, the improvement is about 5%. In the case of a steady steer input at a 50% fill percentage, the AC1 design has a better performance than the AC2, and in a 75% fill percentage, both are ineffective. In other words, the improved designs of AC1 and AC2 in maneuvers with a dynamic nature have their efficiency and are ineffective in transporting the load caused by a steady-state motion.

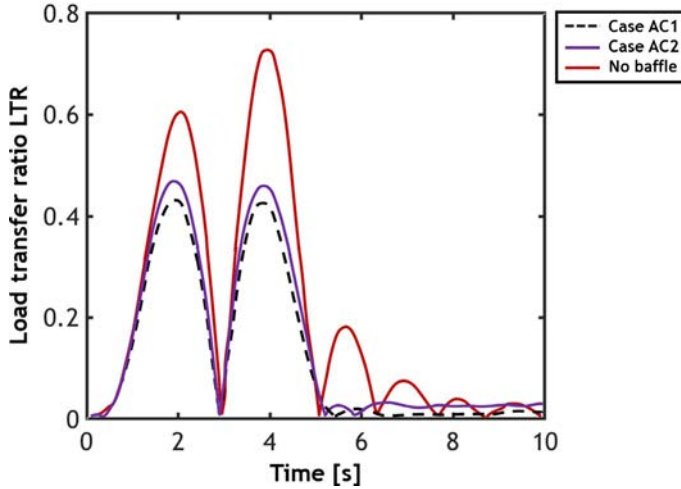

Fig. 6.47 The load transfer ratio for a 50% fill percentage (lane-change maneuver).

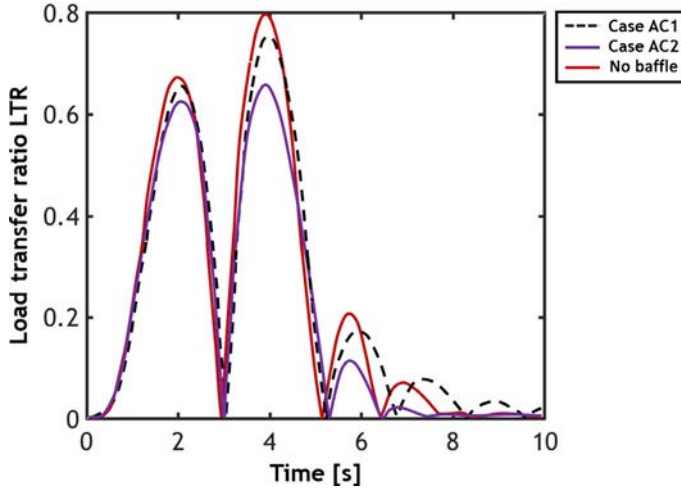

Fig. 6.48 The load transfer ratio for a 75% fill percentage (lane-change maneuver).

6.9.2.2 Combination of cases B and C

In the initial designs, cases A and B are similar, except that in B, the middle plate is placed with a distance from the tanker's floor, allowing it to move the fluid from two parts between the middle plate and the tanker's body. Therefore, this capability is considered an advantage, but on the other hand, the distance has to be chosen to allow the displacement of the fluid and also to

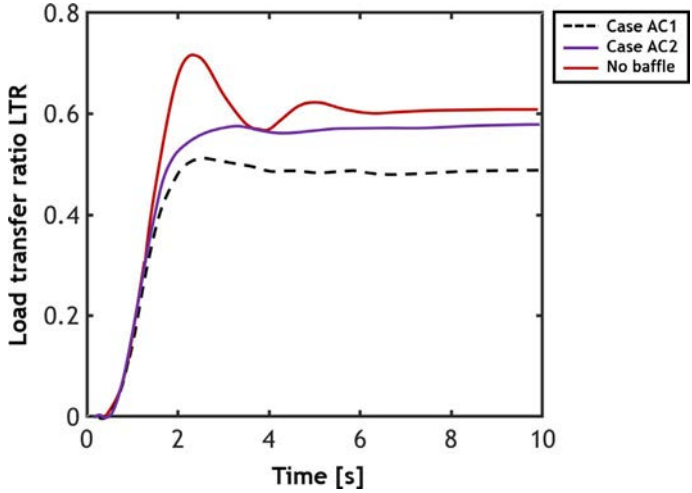

Fig. 6.49 The load transfer ratio for a 50% fill percentage (steady steer maneuver).

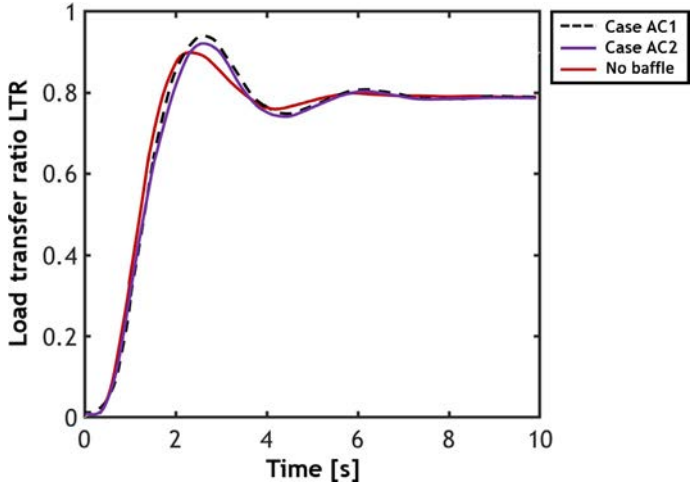

Fig. 6.50 The load transfer ratio for a 75% fill percentage (steady steer maneuver).

provide stability in different maneuvers. Therefore, in this section, introducing BC, a combination of designs B and C, also changes the middle plate distance from the bottom (three BC1, BC2, and BC3 designs) to investigate the effect of this variation. According to the previous section, we consider the elevation of the lateral midplates similar to the AC2 scheme at a 75% fill

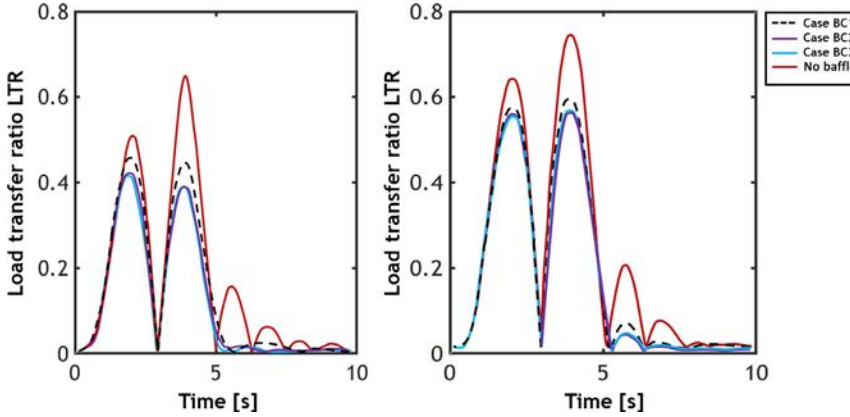

Fig. 6.51 The load transfer ratio for 50% and 75% fill percentages (lane-change maneuver).

percentage. We also consider the elevation of the median baffle plate to be higher than the fluid height at a 75% fill percentage ($r = 1.45$ m, $p = 0.3$ m). The median baffle plate spacings to the bottom of the tanker in the BC1, BC2, and BC3 designs are $q = 10$ cm, $q = 5$ cm, and $q = 2.5$ cm, respectively.

In Fig. 6.51, the load transfer ratio for the lane-change maneuver is plotted for two fill percentages of 50% and 75% and three designs of BC1, BC2, and BC3. It is observed for a 50% fill percentage that by reducing the median plate distance to the tanker's floor from 10 cm to 5 cm, stability in this maneuver has improved, but reducing this distance to 2.5 cm has no significant effect on stability. The issue also poses approximately a 75% fill percentage. In other words, a 5 cm distance from the tanker's floor is suitable for this maneuver, and the reduction will not have a significant effect on stability. The differences in the maximum value of the load transfer ratio ($t = 5$ s) between the BC1, BC2, and BC3 schemes are evident in Fig. 6.52, which is plotted for a 50% fill percentage. In BC1, because the median plate distance to the tanker's floor is 10 cm, the fluid motion between the two parts of the tanker is available, reducing this distance to 5 cm and 2.5 cm, thus decreasing the load transfer ratio and ultimately, there will be no stability at the time of 5.5 s. When the fluid provides a second, the load transfer ratio is equal to each other in different designs, indicating when the fluid needs to move from one part to another and reach the steady state. In the steady steer maneuver and for a 75% fill percentage, different BC schemes have similar performances and lead to a little improvement in the stability.

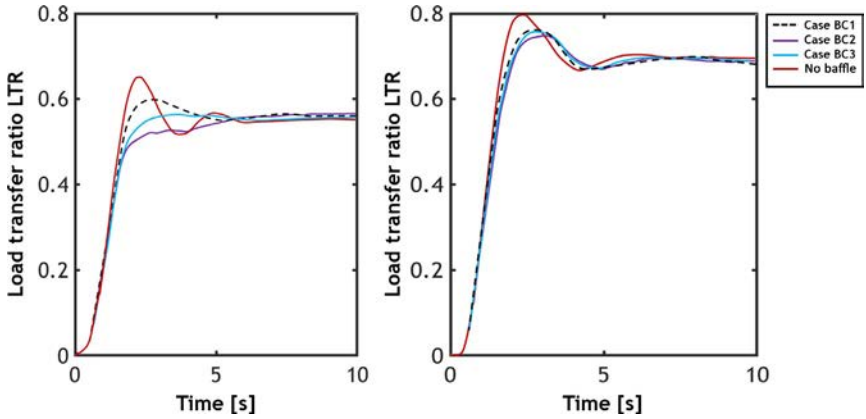

Fig. 6.52 The load transfer ratio for 50% and 75% fill percentages (steady steer maneuver).

According to all examinations, BC3 and EA can provide better performance than other cases. Although EA has a good performance in providing stability, its implementation is associated with some problems. For example, two entirely distinct parts do not allow fluid to transfer from one part to another, and it is also challenging to clean them. Therefore, the designs can be considered as a combination of the BC design or by changing the EA design to an appropriate design.

6.10 Conclusion

In this chapter, an accurate 3D fluid model has been created in FLUENT software for analysis in various situations. The potential of the 3D fluid model has been used, depending on the type of maneuvers applied. Because the shape of the tanker affects the vehicle dynamics and the fluid dynamics, the effect of the shape of the tanker cross-section on the vehicle lateral dynamics has been analyzed simultaneously with the exact 3D model. Besides, the three shapes of the middle plates and their comparison in different maneuvers with the exact model have been studied. Then, by combining these three shapes, a new design has been extracted and its efficiency has been examined.

References

[1] K.L. Campbell, K.P. Sullivan, Heavy truck cab safety study, in: Proceedings of the 35th Stapp Car Crash Conference, University of Michigan Transportation Research Institute, MI, US, 1991, pp. 199–225.

[2] C. Winkler, Rollover of heavy commercial vehicles, in: UMTRI Research Review, vol. 31, No. 4, University of Michigan Transportation Research Institute, 2000. October December.

[3] L. Strandberg, Lateral Stability of Road Tankers, National Road TracRes Inst Report 138A, Sweden, 1978.

[4] H.N. Abramson, The Dynamic Behavior of Liquids in Moving Containers, NASA SP-106, 1966.

[5] A.G. Nalecz, J. Genin, Dynamic stability of heavy articulated vehicles, Int. J. Veh. Des. 5 (4) (1984) 417–426.

[6] R. Ranganathan, Stability Analysis and Directional Response Characteristics of Heavy Vehicles Carrying Liquid Cargo (Ph.D. thesis), Concordia University, Montreal, 1990.

[7] J.Y. Wong, Theory of Ground Vehicles, third ed., John Wiley & Sons, INC., 2001.

[8] E.C. Mikulcik, The Dynamics of Tractor-Semitrailer Vehicles: The Jackknifing Problem, SAE paper, No. 710045, 1971.

[9] P.J. Liu, S. Rakheja, A.K.W. Ahmed, Dynamic rollover threshold of articulated freight vehicles, Int. J. Heavy Veh. Syst. 5 (3/4) (1998) 300–322.

[10] R.D. Ervin, The Influence of Size and Weight Variables on the Roll Stability of Heavy Duty Trucks, SAE paper, No. 831163, 1983.

[11] V.N. Pilipchuk, R.A. Ibrahim, T. Ikeda, Recent advances in liquid sloshing dynamics, Appl. Mech. Rev. 54 (2) (2001) 133–198.

[12] G. Popov, Dynamics of Liquid Sloshing in Road Containers (Ph.D. thesis), Concordia University, Montreal, Quebec, 1991.

[13] S. Azadi, A. Jafari, M. Samadian, Effect of tank shape on roll dynamic response of an articulated vehicle carrying liquids, Int. J. Heavy Veh. Syst. 21 (3) (2014) 221–240.

[14] S. Rakheja, S. Sankar, R.N. Sabounghi, Stability analysis of liquid tank vehicle, in: International Symposium on Heavy Vehicle Weights and Dimensions, June 8-13, 1986, 1986.

[15] S. Rakheja, S. Sankar, R. Ranganathan, Roll plane analysis of articulated tank vehicles during steady turning, Veh. Syst. Dyn. 17 (1988) 81–104.

[16] R. Ranganathan, S. Rakheja, S. Sankar, Kineto-static roll plane analysis of articulated tank vehicles with arbitrary tank geometry, Int. J. Veh. Des. 10 (1) (1989) 89–111.

[17] C.W. Hirt, B.D. Nichols, Volume of fluid (VOF) method for the dynamics of free boundaries, J. Comput. Phys. 39 (1) (1981) 209–225.

[18] R. Ranganathan, Y. Ying, J.B. Miles, Development of a mechanical analogy model to predict the dynamic behavior of liquids in partially filled tank vehicles, No. 942307, SAE Technical Paper, 1994.

[19] M.T. Korang, Analysis of Transient Liquid Slosh Inside a Partly Filled Tank Subjected to Lateral and Longitudinal Acceleration Fields (Master's thesis), Concordia University, 2004.

[20] ANSYS, Inc., ANSYS FLUENT User's Guide, Canonsburg, PA, 2011.

[21] X.D. Kang, Optimal Tank Design and Directional Dynamic Analysis of Liquid Cargo Vehicles Under Steering and Braking (Ph.D. thesis), Department of Mechanical and Industrial Engineering, Concordia University, 2001.

[22] I.M. Ibrahim, Anti Slosh Damper Design for Improving the Roll Dynamic Behavior of Cylindrical Tank Trucks, SAE technical paper series, SAE 1999-01-3729, 1999.

[23] T. Kandasamy, Analysis of Bafle Design for Limiting Fluid Slosh in Partly Filled Vehicle Tanks (MASc thesis), Concordia University, Montreal, 2008.
[24] R. Miralbes, L. Castejon, M. Carrera, D. Valladares, Response analyses of a two-phase cryogenic tank to longitudinal and lateral accelerations, Int. J. Heavy Veh. Syst. 17 (2010) 237–255.
[25] O. Ramirez, J.M. Fortanell, M. Martinez, J.A. Romero, A. Lozano, Analysis of lateral sloshing forces within road containers with high levels, Proc. Inst. Mech. Eng. D J. Automob. Eng. 220 (2006) 303–312.

CHAPTER 7

Adaptive robust controller in lateral dynamics of an articulated vehicle carrying liquid

7.1 Introduction

In its most common form, a heavy liquid-carrying articulated vehicle consists of a tractor unit and a semitrailer unit containing the liquid-carrying tanker, which is connected via mechanical couplings. The tractor unit is in the front of the articulated vehicle, usually has a diesel engine and several axles, and is guided by the driver. Despite the development of rail, aerial, and marine transportation, good transit using road transportation is of utmost significance due to some countries' strategic position. Therefore, a large volume of goods is transported using heavy articulated vehicles. For this reason, the safety of these vehicles on roads is very important because of their large weight. Among items carried by liquid-carrying heavy articulated vehicles are water, gasoline, diesel, and oil. Financial saving is an important principle in trade. Two costly elements in good transport are labor (specifically the driver) and vehicle fuel. Undoubtedly, the larger the vehicle is, the larger the load transported by one driver and less fuel consumption due to one power train. According to research conducted in Sweden, using heavy articulated vehicles has reduced fuel costs by 15%, labor costs by 23%, and trips by 32% [1]. According to the results of research conducted in Canada, employing articulated vehicles has decreased the transportation costs by 29%, traveled distance by 44%, fuel consumption by 32%, and road damage by 40% [2]. Enlarging the vehicle means increasing its length. This imposes many performance limitations on rigid (nonarticulated) vehicles.

For example, when turning at low velocities, the unsteerable rear axle wheels cannot follow the front axle wheels' path and goes off-track toward the inside of the bend. It can be proven using geometrical principles that the rear axles' off-tracking is proportional to the vehicle length square. This is considered a significant performance limitation. However, by configuring a vehicle as a combination of short parts connected via joints, it is possible to

Vehicle Dynamics and Control
https://doi.org/10.1016/B978-0-323-85659-1.00009-4

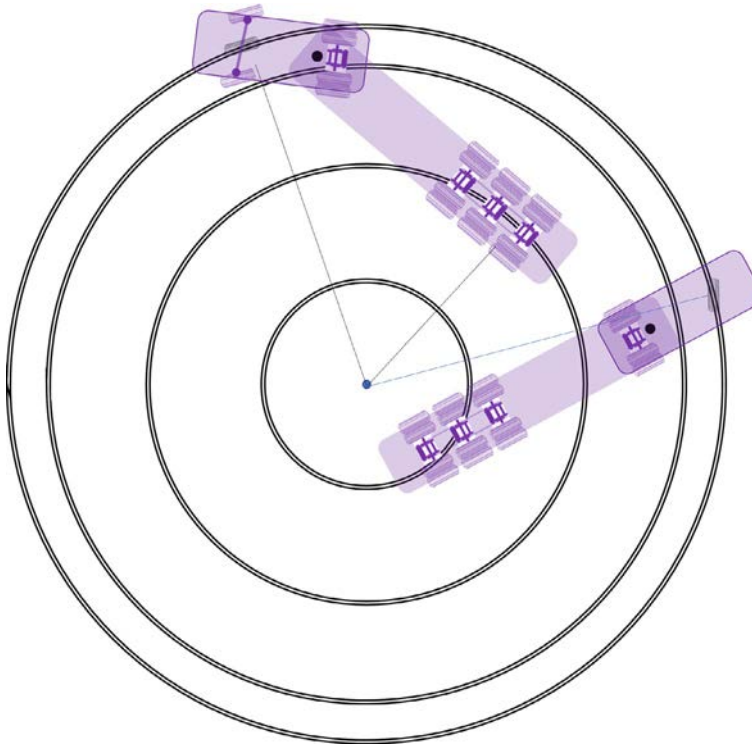

Fig. 7.1 Reduction of off-tracking by making the vehicle articulated.

achieve a long vehicle with acceptable maneuverability and significantly reduce off-tracking. The mentioned points are schematically shown in Fig. 7.1.

It must be noted that by configuring the vehicle as articulated, increasing the trailer units' acceleration relative to the tractor unit is possible. The performance criterion representing this phenomenon is the rearward amplification, which is denoted by RA and shows the maximum lateral acceleration of the last trailer unit to the tractor unit's maximum lateral acceleration.

Despite the advantages mentioned for heavy articulated vehicles, these vehicles are considered significant causes of road accidents. According to statistical studies performed in the United States and Canada, the number of road accidents involving these vehicles is twice that involving passenger vehicles. The main reason is lateral instability during lateral maneuvers such as lane changes, braking during turns, and performing U-turns. This issue bears more significance for liquid-carrying heavy articulated vehicles due to their lower lateral stability due to an interaction between the vehicle and the liquid. The instability of these vehicles is directly attributed to

the liquid forces and moments resulting from lateral maneuvers. In a statistical study conducted in the United States between 1984 and 2004, the most important factor in accidents was a rollover, claiming about 41.4% of casualties [3]. It has been reported by the US Department of Transportation that every year, 1300 rollover incidents involving liquid-carrying tankers occur, 56% of which happen on straight roads. Furthermore, more than 31% of heavy vehicle rollovers involve liquid-carrying vehicles. In 86% of the incidents involving these vehicles, which are mostly used to carry hazardous materials, the liquid spills, leading to fire and explosions in 50% of these cases. The economic loss reported for these vehicles' rollovers is estimated to be about $150 million and increases annually. In Canada, this loss has been estimated to be more than $84 million over 8 years. Numerous studies on liquid-carrying vehicles have been carried out so far in North America due to this issue's importance.

7.1.1 Performance criteria of an articulated vehicle

A set of performance standards has been codified to evaluate the performance of heavy vehicles in various fields. These standards can be used to assess heavy vehicle performance and the control systems utilized in these vehicles. A complete collection of these performance standards, named performance-based standards (PBS), has been compiled by Australia's National Road Transport Commission. This collection consists of 16 standards. This standard considers the longitudinal, lateral, and ride performance of heavy vehicles. The goal of studying these criteria is to seek ideas for identifying the control variables in articulated vehicles.

7.1.1.1 Handling quality

A vehicle must be sufficiently controllable and stable and must acceptably trace the path desired by the driver in response to the steering input. The maneuverability quality, expressed as oversteer and understeer, indicates the driver's feeling of controlling the vehicle steering and changes considerably with lateral acceleration. In some cases, the changes are so intense that controlling the vehicle becomes problematic, and even instability might occur.

7.1.1.2 Lateral stability during braking

A vehicle's ability to maintain the stability, handling, and motion between lines in bends during intense braking is a key factor in road transportation. Vehicle rollover in a bend is highly risky and might result in serious harm. Intense braking in a road bend is a challenging maneuver that subjects the vehicle to a complicated combination of longitudinal and lateral

accelerations and seriously threatens travel safety. For this reason, PBS has specified certain conditions for braking, as follows:

- When a braking force with −0.45 g is applied to a heavy vehicle moving at 65 [km/h] on a dry road, none of the front wheels must lock, and the vehicle must maintain itself within the track.
- A heavy vehicle moving in bending paths must be able to maintain itself within the track.

7.1.1.3 Steady-state off-tracking

This criterion states that the articulated vehicle must require minimal road space during steady-state turning in a curved path. When a long vehicle turns slowly at an intersection, the vehicle's end will travel a path inside the path traveled by the front vehicle. This phenomenon is known as steady-state off-tracking. Large off-tracking is undesirable because the vehicle sweeps a wider path and, hence, occupies a larger space on the road. This may cause the vehicle to divert off-road or toward the opposite lane, colliding with parked vehicles, pedestrians, and roadside objects. As an example, the articulated vehicle in Fig. 7.2 slowly travels along a 90 degree bend. The maximum swept width (SPW_{max}) in this bend is measured, and the turning performance of the articulated vehicle at low speeds is measured accordingly [4].

7.1.1.4 Transient off-tracking

As shown in Fig. 7.2, the lateral displacement of the end of the semitrailer unit of the articulated vehicle has an overshoot relative to the path traveled

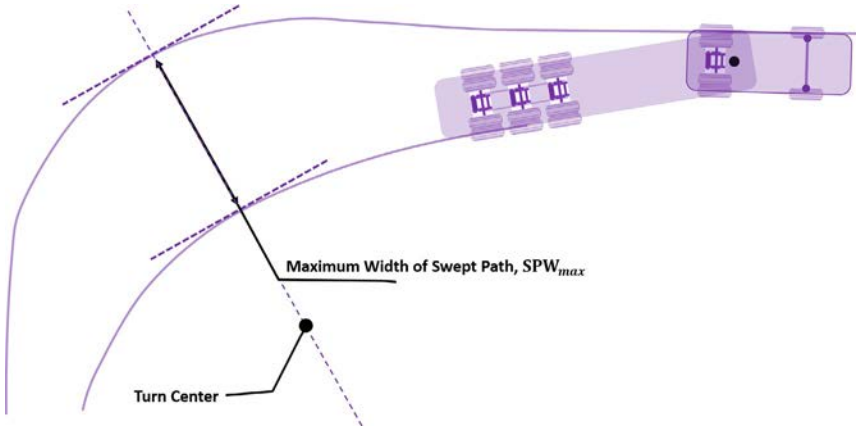

Fig. 7.2 Performance evaluation of an articulated vehicle in the steady-state turning test.

by the tractor unit's front axle. This parameter is known as the trailer swing. The rate of accidents increases with an increase in this parameter [4].

7.1.1.5 Rearward amplification

This quantity represents the connected trailers' tendency to gain an acceleration larger than that of the tractor unit. This phenomenon is dangerous in lane-change maneuvers and results in vehicle rollover. A lower RA value represents a better performance of the articulated vehicle, and higher RA values indicate a higher rollover probability. RA is improved by using fewer joints and a smaller distance between the tractor's mass center and the joint point. According to PBS, this quantity is defined as the ratio of the maximum lateral acceleration of the mass center of the last unit of the articulated vehicle to the lateral acceleration at the center of the steerable axle of the tractor unit [5].

7.1.1.6 Static rollover threshold

The main objective of this quantity is to minimize the probability of vehicle rollover during turns. When the vehicle moves along a curved path, it is subjected to a centrifugal force proportional to the lateral acceleration. Rollover occurs when the lateral acceleration exceeds the stability threshold of the vehicle. The basic criterion for rollover stability is the static rollover threshold, which is usually expressed as acceleration per gravity unit. This quantity represents the acceleration a vehicle can have while turning with its wheels maintaining contact with the ground. Rollover stability is sensitive to the vehicle width ratio to the height of its center of gravity: rollover stability increases with an increase in this ratio. The tires belonging to the steerable axle can be ignored for articulated vehicles having one tractor unit and a flexible chassis. The rollover threshold of articulated vehicles equals the sum of all the units' lateral accelerations at the rollover point and is calculated as (7.1).

$$AY_{rcu} = \frac{m_1 h_1 AY_1 + m_2 h_2 AY_2}{m_1 h_1 + m_2 h_2} \tag{7.1}$$

where m, h, and AY respectively represent the mass, the height of the mass center, and the lateral acceleration of the tractor and semitrailer units. For an articulated vehicle, rollover instability occurs when the vertical force in all the tires on one side of every unit or all joined units becomes zero.

7.1.2 Hazardous behavior modes of an articulated vehicle

In the previous section, the performance standards of an articulated vehicle were studied, and it was mentioned that this study aimed to provide a suitable pattern for selecting the appropriate control variables in articulated vehicles [6, 7]. It is necessary to pay attention to the unstable modes of the articulated vehicle while selecting the control variables and implementing the control system. One unstable mode of this type of vehicle is a rollover, which was explained in the previous section. This section will examine the unstable modes of the lateral dynamics of an articulated vehicle.

7.1.2.1 Lateral instability of liquid-carrying vehicles

A liquid-solid interaction is present in some mechanical systems. The dynamic motions of these systems cause the liquid to move. Liquid sloshing can disturb the system and adversely affect its correct performance. Consequently, studying the liquid-solid interaction in these systems is of considerable significance. The liquid moves inside the tanker due to changes in velocity and impacts by the vehicle's road, resulting in a sloshing phenomenon. Liquid sloshing in tankers is the fluctuation of the liquid due to the motion of the tanker. The tanker's fluid motion depends on tanker geometry, liquid height, excitation frequency, and vehicle maneuver type. The forces and moments resulting from the pressure distribution on the tanker wall will significantly affect both the tanker and the overall structure, changing the liquid's motion inside the tanker. These fluid motions influence vehicle stability and brake system performance. Excessive liquid fluctuation inside the tanker can cause the vehicle to veer and increase the braking time, the stopping distance, and, ultimately, the number of road accidents. Hence, measures must be taken in these systems to minimize these effects and optimize the system.

Liquid motion inside a tank and dynamic interaction between the vehicle and the liquid have always been important topics related to road transportation systems. The dynamic coupling between the liquid and the vehicle, which is a key factor in analyzing lateral vehicle dynamics, can be examined from different aspects. Liquid motion inside a tank plays a vital role in the dynamic behavior and stability of liquid-carrying vehicles. Due to the forces and moments resulting from liquid motion in the tanker, liquid-carrying vehicles exhibit a lower stability threshold than conventional heavy vehicles. Accordingly, the rollover threshold of an articulated vehicle with a rigid load during a unit step maneuver is about 0.34 g. In contrast, it is under

0.2 g for the same vehicle with a tanker 50% filled with liquid [8]. These effects result from the moment exerted by the liquid on the vehicle due to the displacements in the mass center of the former. The stability threshold is related to the transmission of the liquid's dynamic load along with longitudinal and lateral directions under lateral maneuvers. Transportation systems such as trucks, articulated vehicles, and ships carrying liquid are more prone to rollovers than vehicles that transport rigid loads in case of external disturbances and excitations. Generally, the liquid inside a half-filled tank experiences different motions depending on the vehicle maneuver and road conditions. The liquid has large-amplitude motions when the vehicle performs braking, accelerating, and lane-change maneuvers.

Given that these vehicles are employed to transport flammable liquids and toxic chemicals, road accidents involving these vehicles can inflict severe casualties and economic loss. Lateral instability in heavy vehicles is attributed to their high mass center, heavy weight, and large dimensions. Furthermore, rollover is one of the most dangerous lateral instability modes and has a considerably higher probability of occurrence in these vehicles.

7.1.3 Dynamics of liquid-carrying heavy vehicles

The study of the stability and dynamics of articulated vehicles came to attention in 1970. Conventional heavy vehicle models and common liquid behavior modeling methods are used for the dynamic modeling of liquid-carrying heavy vehicles. Numerous researchers have studied free surface sloshing in tanks since 1960. The following approaches have been used in modeling the liquid behavior in the studies carried out:

- Equivalent mechanical systems in the form of masses and springs or pendulums for simulating liquid motion in a container.
- Modeling liquid motion using the potential function, which has the advantage of good accuracy as demonstrated by validations carried out using actual tests.
- Numerical solutions of the Navier-Stokes equations to model liquid dynamics.

In addition to the above methods, experimental methods are observed in a limited number of studies about liquid-carrying vehicles. However, the obtained results are unacceptable due to the limitations associated with using small-scale tank models. One of the most important reasons is the considerable difference in liquid motion in different tanks.

7.1.3.1 Literature

This section presents some of the previous studies conducted to improve the dynamic behavior and stability of liquid-carrying heavy vehicles. Strandberg [9] showed in his studies that the rollover threshold of a liquid-carrying vehicle with a 50% filled oval tank is almost half that of a vehicle with a full tank in a uniform turning maneuver. The simulation results showed that the vehicle with an oval tank has a smaller rollover threshold than a circular tank during a transient maneuver. In 2000, Winkler [10] used Strandberg's results for further analyses on rollover stability in liquid-carrying vehicles and showed that these vehicles' rollover threshold decreases with an increase in the liquid volume. In 2001, Kang [11] studied the lateral dynamic response for various tanks with different cross-sections by using a 7-DOF model for the articulated vehicle and the potential function for modeling the liquid. His analysis focused on liquid volume, cross-sectional shape, and type of maneuver. The simulation results for lane-change and steady-state turning maneuvers indicated that the liquid's motion load transfer has an undesirable effect on the lateral dynamics of the articulated vehicle for a small volume of liquid inside the tank. In 2003, Mantriota [12] investigated vehicle yaw stability using a 2-DOF linear model for an articulated vehicle and the pendulum model for interpreting the liquid behavior. The nonviscosity fluid was considered as several lateral elements. Each element was a fixed-weight pendulum with only a roll motion. The simulation results showed considerable instability for a vehicle with a 70% filled tank and moving with constant velocity during a steady-state turn maneuver. In 2008, Yan [13] studied the effect of liquid motion on a liquid-carrying truck's braking performance and rollover stability. He utilized a 7-DOF model for the vehicle, and three-dimensional Navier-Stokes equations and the volume fraction technique for modeling the liquid behavior inside the tank.

Moreover, he employed a laboratory sample in a conventional tank and a tank with baffles to validate his liquid model and the experimental studies. The simulation results showed that the rollover stability threshold decreased compared to previous analyses involving transient liquid behavior and that considerable interaction was observed between the vehicle and the liquid during the braking maneuver. In 2013, Zheng et al. [14] investigated the baffles' effect in restricting sloshing inside a half-filled tank. Three lateral plates, namely conventional, circular, and perpendicular alternating, were created to reduce the negative effects of liquid sloshing on braking. Furthermore, Fluent software, along with Navier-Stokes equations numerical methods, were used to model the liquid. They recognized the baffle installation angle and the hole size as the most important factors in restricting liquid motion inside the tank in

their simulations. In 2014, Samadian [15] examined the impact of various parameters on a liquid-carrying articulated vehicle's dynamic roll response. In this research, a three-dimensional model and numerical methods based on the Navier-Stokes equations, the volume fraction technique, and FLUENT software were used to model the liquid. He considered the liquid volume and the vehicle maneuver type as influential in the dynamic interaction between the vehicle and the liquid. Simulation results for steady-state and transient modes indicated that the viscosity of the liquid has a negligible effect on the dynamic characteristics of the vehicle and that an increase in the liquid volume results in an increase in the roll angle, a decrease in the motion of the mass center of the liquid along with longitudinal and lateral directions, and an increase in the frequency of liquid motion.

7.2 Dynamic modeling of a liquid-carrying articulated vehicle

An accurate dynamic model of the vehicle must be developed to shed light on the vehicle's actual behavior and the vehicle simulation software's validity. If the vehicle behavior is unpredictable at the design stage, it can lead to inappropriate handling behavior or even inappropriate motions such as rollover of the vehicle. Using mathematical models and computer simulation tools, one can study the dynamic behavior and safety without the need to manufacture or test the vehicle on the road, which is very costly.

The chapter aims to develop, simulate, and validate the 16-DOF dynamic model of the articulated vehicle using experimental data to investigate these vehicles' ride comfort and handling performance.

7.2.1 Assumptions and simplifications

The dynamic modeling of a liquid-carrying articulated vehicle consists of the following three subsystems:

7.2.1.1 First system: Articulated vehicle dynamic system

To simulate the dynamics of an articulated vehicle, a full model comprising longitudinal, lateral, yaw, and roll DOFs for the tractor unit; yaw and roll DOFs for the semitrailer unit; and rotational DOF for the wheels has been used.

7.2.1.2 Second system: Wheel and tire system

The road and driver inputs are applied to the wheel via the steering wheel and the brake pedal, and inputs such as linear and angular velocity and mass effect from the dynamic system are applied to the tire. As a result of these

inputs and the tires' overall effect, a force is exerted on the vehicle dynamic system. Hence, it seems necessary to use a nonlinear tire in order to display suitable performances.

7.2.1.3 Third system: Liquid dynamic system

The inputs of this system are from the vehicle dynamic system. The vehicle's instantaneous vehicle velocity and acceleration are applied to the liquid-carrying tanker via the vehicle dynamic system, resulting in the motion of liquid inside the tanker. This motion on the tanker walls will be in the form of forces and moments, which is then applied to the vehicle dynamics.

7.2.2 16-DOF dynamic model of the articulated vehicle

7.2.2.1 System dynamic equations

The model mentioned in this research is a 16-DOF model of the articulated vehicle, which simulates this vehicle's lateral dynamics. The DOFs of this model consist of longitudinal and lateral velocities of the tractor unit (u_t, v_t), yaw rate of the tractor unit (r_t), yaw rate of the semitrailer (r_s), roll angle of the tractor (φ_t), roll angle of the semitrailer (φ_s), and angular velocities of the wheels $(\omega_i = 1, 2\ldots, 10)$. The front wheels of the tractor unit are considered as steerable in this model.

7.2.2.2 Problem kinematics

As shown in Fig. 7.3, the coordinate system $x_n y_n z_n$ is the inertial coordinate system. The overall mass center of the tractor, including the sprung and unsprung masses, is located at the point CG_t. The point P_t is the intersection of the normal line passing through CG_t and the roll axis of the tractor unit.

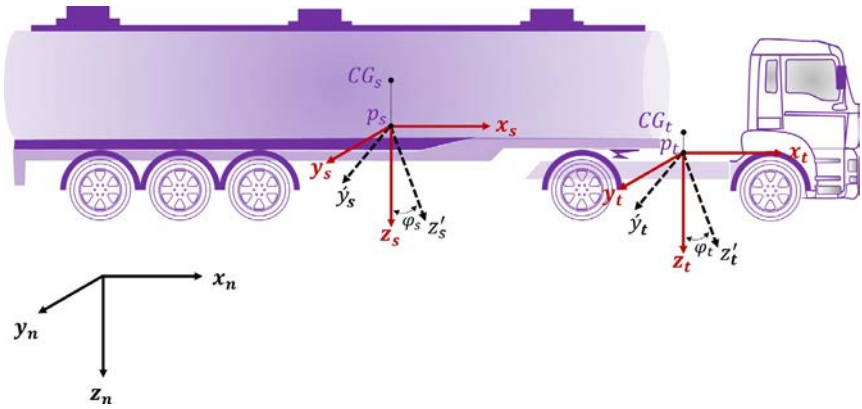

Fig. 7.3 16-DOF dynamic model of the articulated vehicle.

This point has been selected as the origin of the coordinate system $x_t y_t z_t$. This coordinate system is fixed at the unsprung masses of the tractor. Therefore, it performs longitudinal, lateral, and rotational motions along with them but does not roll.

The rotation matrix between the inertial coordinate system $x_n y_n z_n$ and the coordinate system $x_t y_t z_t$ can be defined as follows:

$$\begin{bmatrix} i_n \\ j_n \\ k_n \end{bmatrix} = \begin{bmatrix} \cos\psi_t & -\sin\psi_t & 0 \\ \sin\psi_t & \cos\psi_t & 0 \\ 0 & 0 & 1 \end{bmatrix} \begin{bmatrix} i_t \\ j_t \\ k_t \end{bmatrix} \tag{7.2}$$

$$\begin{bmatrix} i_t \\ j_t \\ k_t \end{bmatrix} = \begin{bmatrix} \cos\psi_t & \sin\psi_t & 0 \\ -\sin\psi_t & \cos\psi_t & 0 \\ 0 & 0 & 1 \end{bmatrix} \begin{bmatrix} i_n \\ j_n \\ k_n \end{bmatrix} \tag{7.3}$$

Moreover, the rotation matrices between the tractor and semitrailer units are as follows:

$$\begin{bmatrix} i_t \\ j_t \\ k_t \end{bmatrix} = \begin{bmatrix} \cos\Gamma & -\sin\Gamma & 0 \\ \sin\Gamma & \cos\Gamma & 0 \\ 0 & 0 & 1 \end{bmatrix} \begin{bmatrix} i_s \\ j_s \\ k_s \end{bmatrix} \tag{7.4}$$

$$\begin{bmatrix} i_s \\ j_s \\ k_s \end{bmatrix} = \begin{bmatrix} \cos\Gamma & \sin\Gamma & 0 \\ -\sin\Gamma & \cos\Gamma & 0 \\ 0 & 0 & 1 \end{bmatrix} \begin{bmatrix} i_t \\ j_t \\ k_t \end{bmatrix} \tag{7.5}$$

The angular velocities of the coordinate systems attached to the tractor unit and semitrailer unit and the time derivatives of the corresponding unit vectors are defined as follows: The angular velocities of the coordinate systems $x_t y_t z_t$ and $x_t' y_t' z_t'$ are as (7.6) (Fig. 7.4):

$$\omega_t = \dot{\psi}_t k_t \tag{7.6}$$

$$\omega'_t = \dot{\varphi}_t i'_t + \dot{\psi}_t k'_t$$

Furthermore, the angular velocities of the coordinate systems $x_s y_s z_s$ and $x_s' y_s' z_s'$ are as (7.7):

$$\omega_s = \dot{\psi}_s k_s \tag{7.7}$$

$$\omega'_s = \dot{\varphi}_s i'_t + \dot{\psi}_s k'_s$$

The acceleration of the mass center of the tractor unit is equal to (7.8):

$$a_{s_t} = \left(\dot{u}_t - v_t\dot{\psi}_t - c_t\dot{\psi}_t^2 - h_t\dot{\varphi}_t\dot{\psi}_t\right)i'_t + \left(u_t\dot{\psi}_t + \dot{v}_t + c_t\ddot{\psi}_t + h_t\ddot{\varphi}_t\right)j'_t \tag{7.8}$$

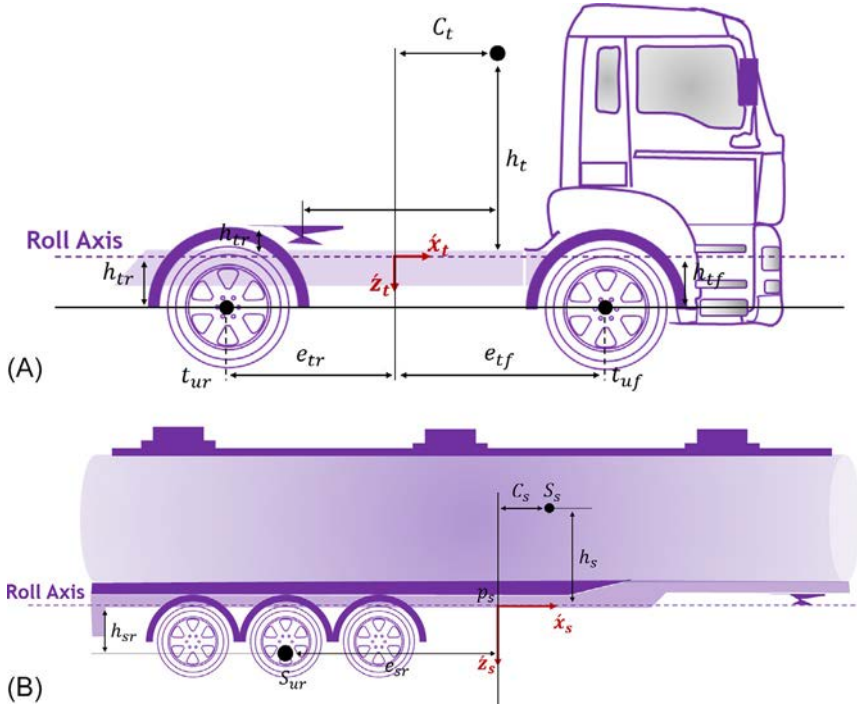

Fig. 7.4 Tractor unit and semitrailer unit of the articulated vehicle.

And the acceleration of the mass center of the semitrailer unit is equal to (7.9):

$$a_{S_s} = \left(\dot{u}_s - v_s\dot{\psi}_s - c_s\dot{\psi}_s^2 - h_s\dot{\varphi}_s\dot{\psi}_s\right)i_s' + \left(u_s\dot{\psi}_s + \dot{v}_s + c_s\ddot{\psi}_s + h_s\ddot{\varphi}_s\right)j_s' \qquad (7.9)$$

7.2.2.3 Equations of motion of longitudinal and lateral dynamics of the tractor unit and the semitrailer unit

The forces exerted on the system to present the longitudinal and lateral dynamics equations must be introduced. The equations of motion are presented individually for the tractor unit and the semitrailer unit. In both systems, the sprung and unsprung masses are considered in the form of one system. Therefore, the internal forces between these components are omitted, and only the external forces exerted on the tractor and semitrailer systems are taken into account.

Tractor unit

According to Fig. 7.5, the system dynamics' external forces are the longitudinal and lateral forces generated at the contact between the tire and the road surface and the joint's constraint forces.

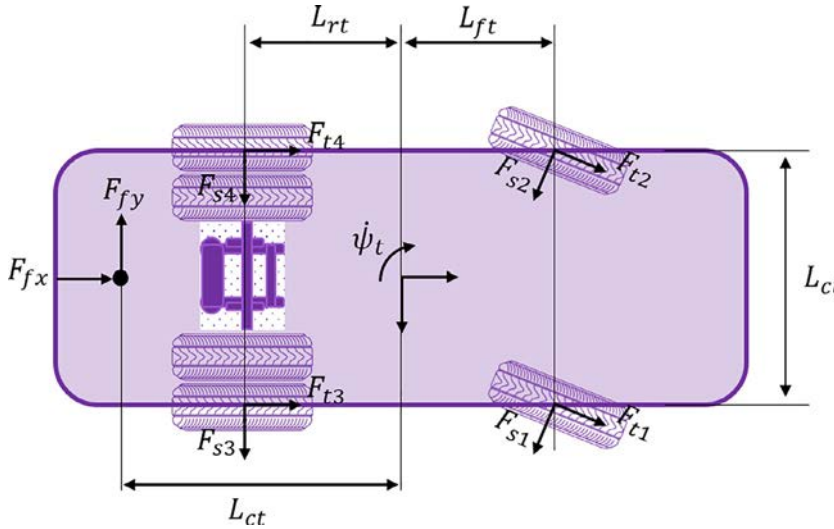

Fig. 7.5 External forces affecting the tractor unit.

The longitudinal and lateral forces of each tire are denoted by F_{ti} and F_{si}, respectively. Now, we can develop the equations of motion using Newton's second law. The terms F_{xi}, F_{yi} , which respectively represent the forces in the tires of the tractor along the coordinate axes x_t and y_t , are defined as (7.10):

$$\begin{aligned} F_{xi} &= F_{ti}\cos\delta_i - F_{si}\sin\delta_i \\ F_{yi} &= F_{ti}\sin\delta_i + F_{si}\cos\delta_i \end{aligned} \tag{7.10}$$

where δ_i represents the steering angle. The sum of the longitudinal and lateral forces of the tractor tires are defined as (7.11):

$$\begin{aligned} F_{xtt} &= F_{x1} + F_{x2} + F_{x3} + F_{x4} \\ F_{ytt} &= F_{y1} + F_{y2} + F_{y3} + F_{y4} \end{aligned} \tag{7.11}$$

Also, the yaw moment created in the tractor unit is equal to (7.12):

$$M_{ptz} = (F_{x2} + F_{x4} - F_{x1} - F_{x3})T_w/2 + (F_{y1} + F_{y2})L_{ft} - (F_{y3} + F_{y4})L_{rt} \tag{7.12}$$

And the roll moment exerted on the tractor unit is equal to (7.13):

$$M_{p_{tsx}} = m_{st}gh_t\sin(\varphi_t) - KS_t\varphi_t - CS_t\dot{\varphi}_t + KS_w(\varphi_t - \varphi_s) + CS_w(\dot{\varphi}_t - \dot{\varphi}_s) \tag{7.13}$$

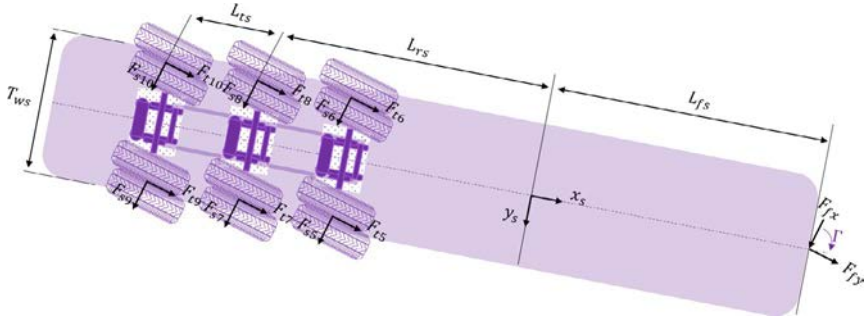

Fig. 7.6 External forces affecting the semitrailer unit.

Semitrailer unit

The external forces exerted on the semitrailer unit are as in Fig. 7.6.

The sum of the longitudinal and lateral forces of the semitrailer tires are defined as (7.14):

$$\begin{aligned} F_{xss} &= F_{x5} + F_{x6} + F_{x7} + F_{x8} + F_{x9} + F_{x10} \\ F_{yss} &= F_{y5} + F_{y6} + F_{y7} + F_{y8} + F_{y9} + F_{y10} \end{aligned} \tag{7.14}$$

Also, the yaw moment created in the semitrailer unit is equal to (7.15):

$$\begin{aligned} M_{psz} = &\left(F_{x6} + F_{x8} + F_{x10} - F_{x5} - F_{x7} - F_{x9}\right) T_{ws}/2 \\ &- \left(F_{y5} + F_{y6}\right)\left(L_{rs} - L_{ts}\right)\left(F_{y7} + F_{y8}\right) L_{rs} - \left(F_{y9} + F_{y10}\right)\left(L_{rs} + L_{ts}\right) \end{aligned} \tag{7.15}$$

And the roll moment exerted on the semitrailer unit is equal to (7.16):

$$M_{p_{ssx}} = m_{ss} g h_s \sin\varphi_s - KS_s\varphi_s - CS_s\dot{\varphi}_s - KS_w(\varphi_t - \varphi_s) - CS_w(\dot{\varphi}_t - \dot{\varphi}_s) \tag{7.16}$$

Hence, the main equations governing the articulated vehicle dynamics are obtained as (7.17–7.24):

$$m_t\dot{u}_t = m_t v_t\dot{\psi}_t + m_{st}h_t\dot{\varphi}_t\dot{\psi}_t + F_{xtt} + F_{fx} \tag{7.17}$$

$$m_t\dot{v}_t + m_{st}h_t\ddot{\varphi}_t = -m_t u_t\dot{\psi}_t + F_{ytt} - F_{fy} \tag{7.18}$$

$$I_{zz_t}\ddot{\psi}_t - I_{xz_{pt}}\ddot{\varphi}_t = M_{p_{tz}} + F_{fy}L_{ct} \tag{7.19}$$

$$I_{xx_{pt}}\ddot{\varphi}_t - I_{xz_{pt}}\ddot{\psi}_t + m_{st}h_t\dot{v}_t = M_{p_{tsx}} - m_{st}h_t u_t\dot{\psi}_t \tag{7.20}$$

$$m_s\dot{u}_s = m_s v_s\dot{\psi}_s + m_{ss}h_s\dot{\varphi}_s\dot{\psi}_s + F_{xss} - F_{fx}\cos(\Gamma) + F_{fy}\sin(\Gamma) \tag{7.21}$$

$$m_s\dot{v}_s + m_{ss}h_s\ddot{\varphi}_s = -m_s u_s\dot{\psi}_s + F_{yss} + F_{fx}\sin(\Gamma) + F_{fy}\cos(\Gamma) \tag{7.22}$$

$$I_{zz_s}\ddot{\psi}_s - I_{xz_{ps}}\ddot{\varphi}_s = \left(F_{fx}\sin(\Gamma) + F_{fy}\cos(\Gamma)\right)L_{ws} + M_{p_{sz}} \tag{7.23}$$

$$I_{xx_{ps}}\ddot{\varphi}_s - I_{xz_{ps}}\ddot{\psi}_s + m_{ss}h_s\dot{v}_s = M_{p_{ssx}} - m_{ss}h_s u_s\dot{\psi}_s \tag{7.24}$$

7.2.2.4 Wheel dynamics

The wheel is one of the most important subsystems in studying vehicle dynamics during braking and accelerating. The equation of motion of the wheels is as (7.25):

$$I_w\dot{\omega} = -R_w F_{ti} + T_i \tag{7.25}$$

where T_i is the moment exerted on the ith wheel.

7.2.2.5 Lateral slip angle of the tire

The slip angle of the tire is the angle between the tire plane and the direction of motion. The tire slip angle is a very important parameter in tire dynamic modeling. According to the figure, the tire slip angle is calculated as follows [16]:

$$\alpha_2 = \delta_f - \tan^{-1}\left(\frac{v_t + L_{ft}r_t}{u_t + r_t\dfrac{T_w}{2}}\right) \qquad \alpha_1 = \delta_f - \tan^{-1}\left(\frac{v_t + L_{ft}r_t}{u_t - r_t\dfrac{T_w}{2}}\right)$$

$$\alpha_4 = -\tan^{-1}\left(\frac{v_t - r_t L_{rt}}{u_t + r_t\dfrac{T_w}{2}}\right) \qquad \alpha_3 = -\tan^{-1}\left(\frac{v_t - r_t L_{rt}}{u_t - r_t\dfrac{T_w}{2}}\right)$$

$$\alpha_6 = -\tan^{-1}\left(\frac{v_t - r_t(L_{rt} + L_{tt})}{u_t + r_t\dfrac{T_w}{2}}\right) \qquad \alpha_5 = -\tan^{-1}\left(\frac{v_t - r_t(L_{rt} + L_{tt})}{u_t - r_t\dfrac{T_w}{2}}\right)$$

$$\alpha_8 = -\tan^{-1}\left(\frac{v_s - r_s(L_{rs} - L_{ts})}{u_s + r_s\dfrac{T_{ws}}{2}}\right) \qquad \alpha_7 = -\tan^{-1}\left(\frac{v_s - r_s(L_{rs} - L_{ts})}{u_s - r_s\dfrac{T_{ws}}{2}}\right)$$

$$\alpha_{10} = -\tan^{-1}\left(\frac{v_s - r_s L_{rs}}{u_s + r_s\dfrac{T_{ws}}{2}}\right) \qquad \alpha_9 = -\tan^{-1}\left(\frac{v_s - r_s L_{rs}}{u_s - r_s\dfrac{T_{ws}}{2}}\right) \tag{7.26}$$

7.2.2.6 Tire dynamics

The tire plays a vital role in vehicle dynamics because the vehicle is controlled by the longitudinal and lateral forces resulting from the contact between the tire and the road to move on the road, turn, or stop. Any force required to accelerate, brake, and navigate the vehicle results from the small contact area between the tire and the road. Given that the tire model abandons linear behavior and, instead, exhibits nonlinear behavior at high speeds and large slip angles, the tire model becomes more complicated and realistic compared to the linear model. The Dugoff tire model is used here to calculate the longitudinal and lateral forces, as follows [17]:

$$\begin{aligned}
\lambda &= \frac{\mu F_{zi}\left[1-\varepsilon_r u_i\sqrt{S_i^2+\tan^2\alpha_i}\right](1-S_i)}{2\sqrt{C_i^2S_i^2+C_\alpha^2\tan^2\alpha_i}} \\
f(\lambda) &= \begin{cases} \lambda(\lambda-2) \text{ if } \lambda<1 \\ 1 \qquad \text{if } \lambda>1 \end{cases} \\
F_{si} &= \frac{C_\alpha\tan\alpha_i}{1-S_i}f(\lambda) \\
F_{ti} &= \frac{C_iS_i}{1-S_i}f(\lambda)
\end{aligned} \tag{7.27}$$

In the above equations, F_{si} and F_{ti} respectively denote lateral and tractive forces.

7.2.3 Dynamic modeling of a liquid-carrying articulated vehicle

The potential function model is used in this research to model the liquid inside the tank and investigate the effects of sloshing on the articulated vehicle's lateral dynamics. In this model, the liquid's mass center's position is considered a function of the tank cross-section, liquid volume, and the gradient of the free surface of the liquid. Assuming steady-state conditions, the nonviscous liquid moves as a rigid body in the tank. The gradient of the liquid free surface is determined by assuming nonviscous and using Newton's second law [11], as shown in Fig. 7.7.

$$\begin{aligned}
-\frac{\partial P}{\partial y}+\rho a_l\cos\varphi_s+\rho g\sin\varphi_s=0 \\
-\frac{\partial P}{\partial z}-\rho a_l\sin\varphi_s+\rho g\cos\varphi_s=0
\end{aligned} \tag{7.28}$$

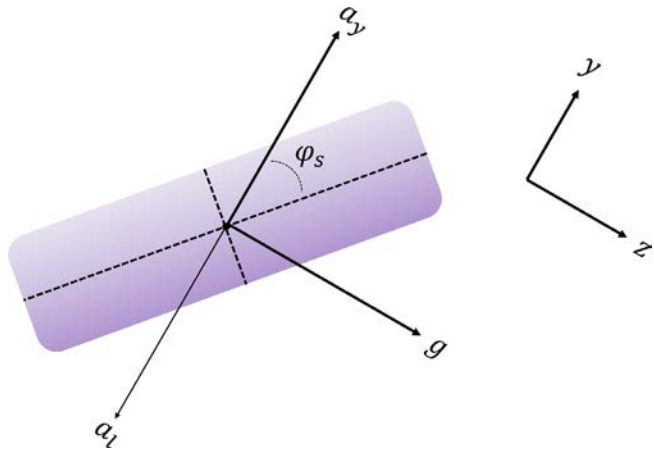

Fig. 7.7 Acceleration of the mass center of the liquid.

Now

$$dP = \frac{\partial P}{\partial y}dy + \frac{\partial P}{\partial z}dz = 0$$

The liquid free surface gradient is computed by dividing $\frac{\partial P}{\partial y}$ by $\frac{\partial P}{\partial z}$:

$$\tan\varnothing = -\frac{dz}{dy} = \frac{\frac{\partial P}{\partial y}}{\frac{\partial P}{\partial z}} = \frac{\rho a_l \cos\varphi_s + \rho g \sin\varphi_s}{-\rho a_l \sin\varphi_s + \rho g \cos\varphi_s}$$
$$\tan\varnothing = \frac{-a_{l1} + \varphi_s}{a_l \varphi_s + 1} \tag{7.29}$$

Hence, the liquid's free surface gradient is calculated, assuming non-viscous fluid and using the semitrailer unit's lateral acceleration and roll angle.

For tanks with circular cross-sections, the position of the mass center of the liquid along the lateral and vertical directions is calculated using relation (7.30) [11]:

$$Z = R - (R - Z_0)\cos\varnothing$$
$$Y = (R - Z_0)\sin\varnothing \tag{7.30}$$

According to Fig. 7.8, in the above equation, R denotes the tank radius, and Z_0 is the height of the liquid mass center in the absence of the roll angle and lateral acceleration of the semitrailer unit.

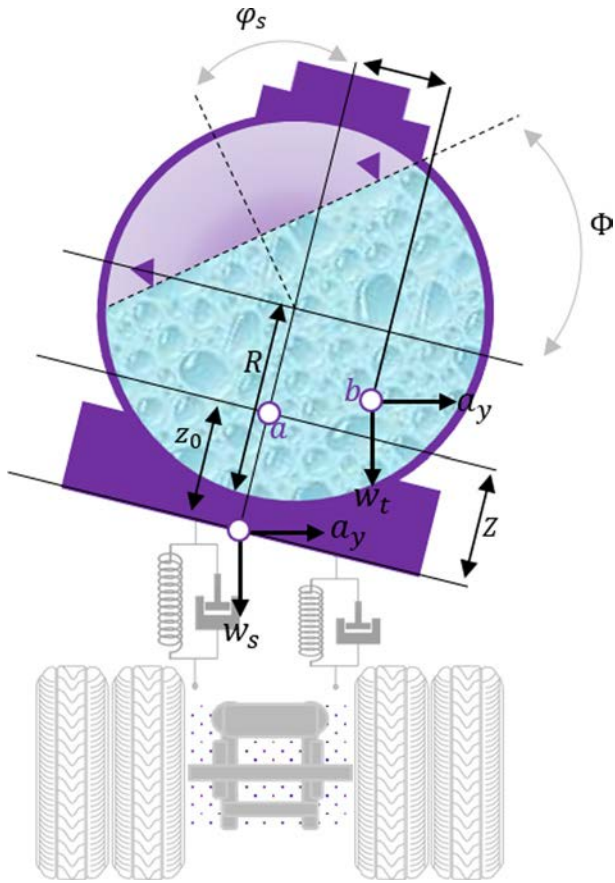

Fig. 7.8 Potential function model for a cylindrical tank with a circular cross-section.

Furthermore, the moment of inertia of the liquid moving inside the tank is determined using the product of the moment of inertia and the conversion matrix via (7.31).

$$I_{xl} = I_{xl}^0$$
$$I_{zl} = I_{zl}^0(\cos\varnothing)^2 \tag{7.31}$$

Where I_{xl}^0 and I_{zl}^0 are the moments of inertia of the liquid for when the free surface gradient is zero.

7.2.3.1 Computing the acceleration of the liquid mass center

Using the relative acceleration relationship and considering the acceleration of the mass center of the semitrailer unit, the acceleration of the liquid mass center is obtained as (7.32):

$$\begin{aligned} a_l = & \left(\dot{u_s} - v_s\dot{\psi}_s - h_s\dot{\varphi}_s\dot{\psi}_s - Z\dot{\varphi}_s\dot{\psi}_s - X{\dot{\psi}_s}^2 - Y\ddot{\psi}_s\right)\hat{i} \\ & + \left(\dot{v_s} + u_s\dot{\psi}_s + h_s\ddot{\varphi}_s - Y{\dot{\varphi}_s}^2 - Y{\dot{\psi}_s}^2 + Z\ddot{\varphi}_s + X\ddot{\psi}_s\right)\hat{j} \\ & + \left(Z{\dot{\varphi}_s}^2 + X\dot{\varphi}_s\dot{\psi}_s + Y\ddot{\varphi}_s\right)\hat{k} \end{aligned} \tag{7.32}$$

7.2.3.2 Dynamic equations of a liquid-carrying articulated vehicle

As explained in detail previously, this research's main objective is controlling the lateral dynamics of a liquid-carrying articulated vehicle. For this reason, we try to model the liquid so that the dynamic behavior shows the sloshing effect, and it is possible to simultaneously solve the vehicle nonlinear dynamic equations and equations related to sloshing. In the previous section, the effect of rotational motion, especially roll angle, was taken into account in the computation of liquid free surface gradient in a simple manner and assuming a nonviscous liquid. However, when the effect of liquid motion, especially in the rotation of the vehicle, is modeled, it is not possible to take into account the impact of the moment of inertia of the liquid, which is effective in the rotation, in the equations if the liquid is assumed to be nonviscous. As a result of this assumption, the effects of liquid rotation are not considered in the vehicle's simulation. Hence, it must be assumed that the liquid is viscous and takes into account the moment of inertia of the liquid in the vehicle model. With this assumption, it becomes possible to avoid more run time of the simulation by Navier-Stokes equations and to make it possible to control the vehicle dynamics during a short time. The dynamic equations of the liquid-carrying articulated vehicle are obtained by using the equations of motion of the articulated vehicle and assuming the acceleration of the liquid mass center, Eqs. (7.33)–(7.40).

$$m_t\dot{u}_t = m_t v_t\dot{\psi}_t + m_{st}h_t\dot{\varphi}_t\dot{\psi}_t + F_{xtt} + F_{fx} \tag{7.33}$$

$$m_t\dot{v}_t + m_{st}h_t\ddot{\varphi}_t = -m_t u_t\dot{\psi}_t + F_{ytt} - F_{f\dot{y}} \tag{7.34}$$

$$I_{zz_t}\ddot{\psi}_t - I_{xz_{pt}}\ddot{\varphi}_t = M_{p_{tz}} + F_{f\dot{y}}L_{ct} \tag{7.35}$$

$$I_{xx_{pt}}\ddot{\varphi}_t - I_{xz_{pt}}\ddot{\psi}_t + m_{st}h_t\dot{v}_t = M_{p_{tsx}} - m_{st}h_t u_t\dot{\psi}_t \tag{7.36}$$

$$m_s\dot{u}_s + m_l a_l \hat{i} = m_s v_s \dot{\psi}_s + m_{ss} h_s \dot{\varphi}_s \dot{\psi}_s + F_{xss} - F_{fx}\cos(\Gamma) + F_{fy}\sin(\Gamma) \quad (7.37)$$

$$m_s\dot{v}_s + m_{ss} h_s \ddot{\varphi}_s + m_l a_l \hat{j} = -m_s u_s \dot{\psi}_s + F_{yss} + F_{fx}\sin(\Gamma) + F_{fy}\cos(\Gamma) + (m_s + m_l) g \sin(\varphi_s) \quad (7.38)$$

$$(I_{zz_s} + I_{zl})\ddot{\psi}_s - I_{xz_{ps}}\ddot{\varphi}_s = \left(F_{fx}\sin(\Gamma) + F_{fy}\cos(\Gamma)\right) L_{ws} + M_{p_{sz}} + m_l a_l \hat{j} X - m_l a_l \hat{i} Y \quad (7.39)$$

$$\left(I_{xx_{ps}} + I_{xl}\right)\ddot{\varphi}_s - I_{xz_{ps}}\ddot{\psi}_s + m_{ss} h_s \dot{v}_s = M_{p_{ssx}} - m_{ss} h_s u_s \dot{\psi}_s + m_l a_l \hat{j} Z + m_l a_l \hat{k} Y + m_l g (Z \sin(\varphi_s) + Y) \quad (7.40)$$

In this simulation, the vehicle parameters are shown in Table 7.1.

Table 7.1 Articulated vehicle parameters.

Parameter	Value	Unit
$CS_{tf(tr)}$	4.05 (6.88)	kN m s/rad
CS_s	23.9	kN m s/rad
C_w	700	kN m s/rad
D	2.03	m
$h_{t(s)}$	0.438 (1.8)	m
$h_{wt(ws)}$	0.63 (1)	m
I_{wi}	11.63	kg m^2
$I_{xx_{pt(ps)}}$	3335 (120,024)	kg m^2
$I_{xz_{pt(ps)}}$	602 (5756)	kg m^2
$I_{zz_{t(s)}}$	20,679 (238,898)	kg m^2
KS_s	800	kN m/rad
$KS_{tf(tr)}$	380 (684)	kN m/rad
K_w	30,000	kN m/rad
L	10	m
L_{ct}	1.959	m
$L_{fs}(L_{rs})$	5.653 (2.047)	m
$L_{ft}(L_{rt})$	1.115 (2.583)	m
$L_{tt}(L_{ts})$	1.31	m
$m_{t(st)}$	6525 (4819)	kg
$m_{s(ss)}$	33,221 (30,821)	kg
R_{wi}	0.4	m
$T_{wt(s)}$	2.04 (2)	m
ρ	1000	kg/m^3

7.2.4 Validation of the dynamic model of the articulated vehicle

In order to validate the vehicle dynamic model, the TruckSim software has been used [18]. To this end, the above model's physical properties have been considered identical to those of the test vehicle.

7.2.4.1 Double lane-change maneuver

In this analysis, the vehicle has started moving with an initial speed of 70 km/h on a dry road, and a steering input has been applied to it, as shown in Fig. 7.9.

The validation results corresponding to the standard double lane-change maneuvers are shown in Fig. 7.10. In this figure, as can be seen from the diagrams of angular velocity, articulation angle, and the path of the articulated vehicle, the simulated model results and the TruckSim software tests are acceptable. Moreover, the roll angle plot shows disparities between the model and test results between 5 s and 7 s, despite a good overall agreement.

7.2.5 Validation of the dynamic model of the liquid-carrying articulated vehicle

The dynamic model of the liquid-carrying articulated vehicle presented in this research has been validated using the test results [11]. To this end, the proposed model's physical properties have been considered identical to

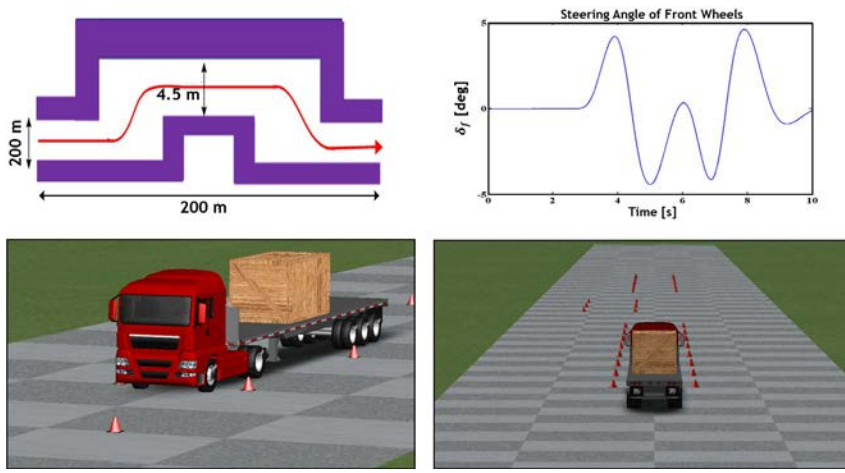

Fig. 7.9 Double lane-change maneuver in TruckSim software.

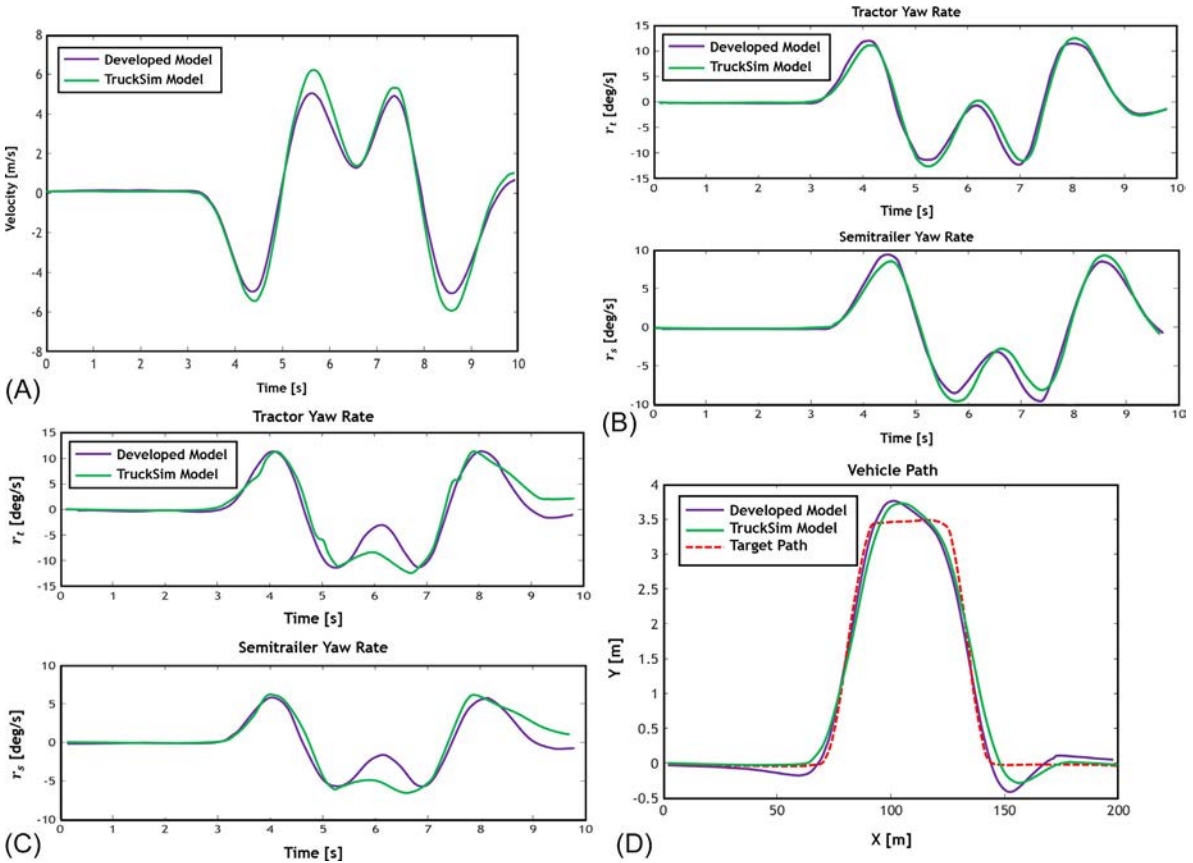

Fig. 7.10 (A) Articulation angle, (B) yaw rate, (C) roll angle, (D) vehicle path.

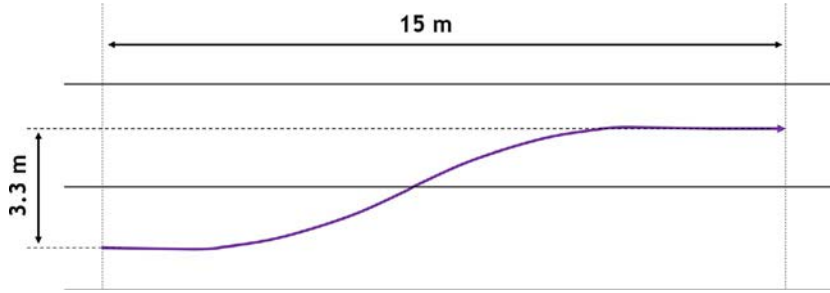

Fig. 7.11 Lane-change maneuver.

those of the dynamic model of the liquid-carrying articulated vehicle in this reference. The validation has been performed for a 70% filled liquid-carrying articulated vehicle moving at 45 km/h performing a lane-change maneuver, as shown in Fig. 7.11.

The simulation has been carried out based on the steering angle obtained from the test results. The dynamic responses of the liquid-carrying articulated vehicle, including the yaw angle, roll angle, and lateral acceleration of the semitrailer unit, have been compared to actual test results in Fig. 7.12. As shown in Fig.7.12B, the yaw angle shows a good match with the test results. Despite the acceptable adaptation of Fig. 7.12C to the test results, the roll angle's peak value related to the semitrailer is still 0.3 degrees higher than the test results. Also, the lateral acceleration of the developed model in the first peak is 0.2 g and in the second peak is 0.15 g compared to the test results.

7.2.6 Selection of the controlled state variables

Given the increase in the lateral load transfer, due to liquid sloshing in the tank, for liquid-carrying articulated vehicles compared to articulated vehicles with rigid loads and the resulting increase in the rollover probability for the former, it seems necessary to use a control system to improve the lateral stability of this kind of vehicle. Thus, considering the significant increase in the roll angles of the tractor unit and the semitrailer unit, due to the increase in the filled volume and sloshing, compared to articulated vehicles with rigid loads, the use of an active roll control system to restrict the roll angles of the tractor and semitrailer units is a suitable solution for improving the roll stability of the vehicle. In the active roll control system, the tractor and semitrailer units' roll angle are the two controlled state

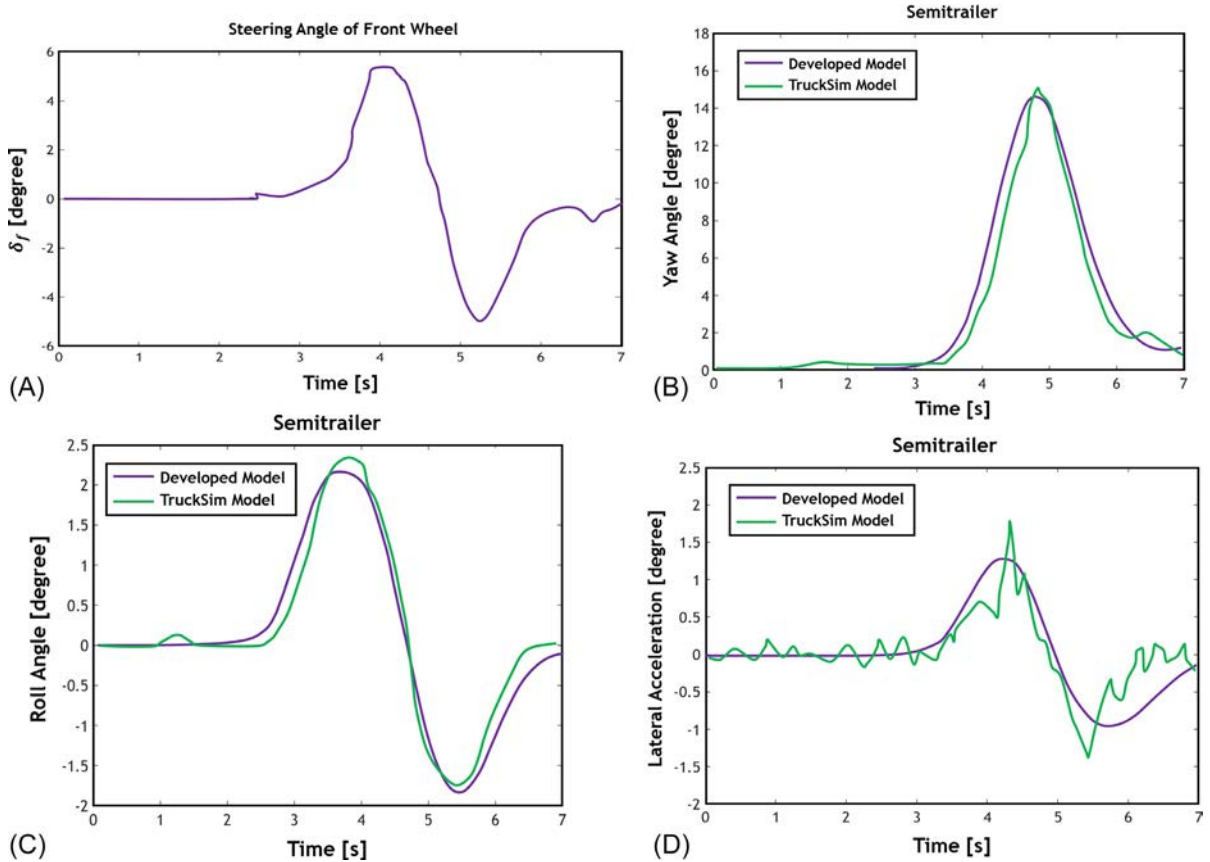

Fig. 7.12 (A) Steering angle, (B) yaw angle, (C) roll angle, (D) lateral acceleration.

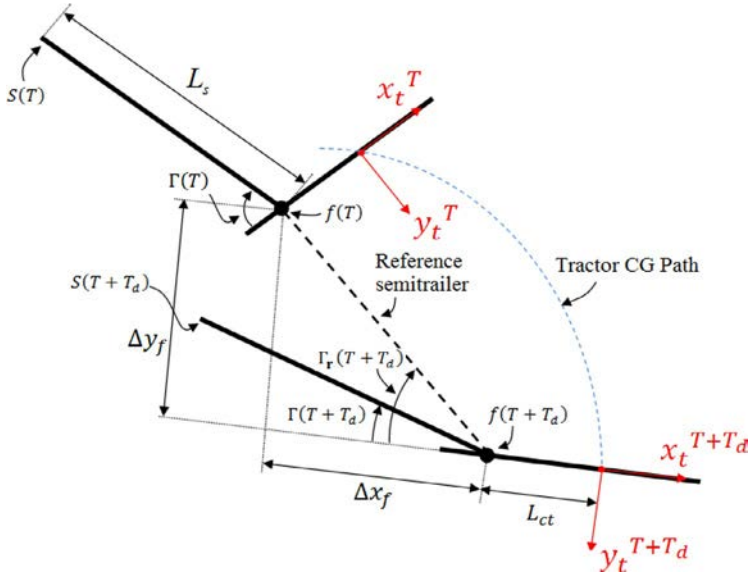

Fig. 7.13 The schematic of the articulated vehicle at instants T and $T + T_d$ [19].

variables that must trace their desired values. The desired values of these controlled state variables are assumed to be zero. This restricts the roll angles and increases the rollover stability of the liquid-carrying articulated vehicle under critical conditions.

In controlling the passenger vehicles' lateral dynamics, the yaw rate and the lateral velocity are the main state variables to improve handling and increase stability, respectively, and the lateral dynamics of the vehicle are controlled by controlling these variables. However, there is another control variable in articulated vehicles, called the articulation angle, which must be paid attention to for preventing jackknifing. Also, controlling this variable omits the off-tracking of the articulated vehicle during steady-state and transient maneuvers. In this chapter, the tractor unit's yaw rate, the lateral velocity of the tractor unit, and the articulation angle are considered the controlled state variables that must trace their desired values to improve handling and avoid jackknifing an articulated vehicle.

The reference model for each of these control variables is given below:

7.2.6.1 The angular velocity of the tractor unit

The yaw rate's most common desired model is a steady-state one based on the bicycle model in passenger vehicles. In this chapter, the yaw rate's

desired value in the steady state is obtained from a single-track articulated vehicle model [20] (7.41).

$$r_d = \frac{u_t}{L_g + K_u u_t^2}\delta$$
$$K_u = m_t \frac{L_{rt}C_{rt} - L_{ft}C_{ft}}{C_{rt}C_{ft}\left(L_{ft} + L_{rt}\right)} + m_s L_{rs} \frac{\left(L_{rt} - L_{ct}\right)C_{rt} - \left(L_{ft} + L_{ct}\right)C_{ft}}{C_{rt}C_{ft}\left(L_{ft} + L_{rt}\right)\left(L_{fs} + L_{rs}\right)} \tag{7.41}$$
$$L_g = L_{ft} + L_{rt}$$

Where L_g is the wheelbase and K_u is the understeer factor.

7.2.6.2 The lateral velocity of the tractor unit

The lateral velocity of the vehicle is indicative of its stability performance to a large extent. Numerous researchers have stressed the importance of restricting the lateral velocity to maintain a passenger vehicle [21, 22]. Hear, the desired value of the lateral velocity is considered zero to avoid jackknifing and the semitrailer unit's swinging and restricting the tractor unit's lateral velocity.

7.2.6.3 Articulation angle

The study of Tabatabaee et al. [19] is used for the desired value of the articulation angle. Based on a geometric-kinematic analysis, a formula is presented. Accordingly, following the articulation angle in some situation (including both low and high speeds, steady-state maneuvers, transient maneuvers, and at small and large articulation angles) eliminates off-tracking. To define this value, the articulated vehicle is considered at times T and $T + T_d$. The time interval T_d is the duration required for the articulated vehicle to travel the distance between the end of the semitrailer unit and the fifth wheel. According to Fig. 7.13, the desired value can be defined as (7.42) and (7.43).

$$\Gamma_r(T + T_d) = \tan^{-1}\frac{\Delta y_f}{\Delta x_f} \tag{7.42}$$

$$\Delta x_f = -L_{ct} + L_{ct}\cos\left[\sum_{k=n}^{j-1}\dot{\psi}_t(T + k\Delta T)\Delta T\right] + \sum_{k=\mathrm{n}}^{j-1}\left\{u_t(T + k\Delta T)\Delta T\cos\left[\sum_{m=k}^{j-1}\dot{\psi}_t(T + m\Delta T)\Delta T\right]\right\}$$

$$+ [v_t(T + k\Delta T)\Delta T] \sin \left[\sum_{m=k}^{j-1} \dot{\psi}_t(T + m\Delta T)\Delta T \right] \Bigg\}$$

$$\Delta\gamma_f = -L_{ct} \sin \left[\sum_{k=n}^{j-1} \dot{\psi}_t(T + k\Delta T)\Delta T \right]$$

$$- \sum_{k=n}^{j-1} \Bigg\{ u_t(T + k\Delta T)\Delta T \sin \left[\sum_{m=k}^{j-1} \dot{\psi}_t(T + m\Delta T)\Delta T \right]$$

$$- [v_t(T + k\Delta T)\Delta T] \cos \left[\sum_{m=k}^{j-1} \dot{\psi}_t(T + m\Delta T)\Delta T \right] \Bigg\} \quad (7.43)$$

7.3 Control system design

The dynamic roll responses of the liquid-carrying articulated vehicle are strongly affected by sloshing inside the tank due to the interaction between the vehicle and the road and the maneuvers applied to the dynamic system. The forces and moments resulting from the distribution of liquid pressure on the tank wall lead to a reduction in the rollover stability threshold of liquid-carrying articulated vehicles at various velocities during critical maneuvers. Besides, an excessive height of the mass center in articulated vehicles is another factor in the occurrence of unstable modes of lateral dynamics for these vehicles. Therefore, it seems necessary to use active control systems to help the driver during critical maneuvers. To this end, this section concerns the design of an active roll control system for improving the rollover stability of a liquid-carrying articulated vehicle. The aim of designing the active roll control system is to generate a moment from the antiroll bar to increase the liquid-carrying articulated vehicle's rollover stability. In the control system's design, the roll angles of the tractor and semitrailer units are the controlled state variables that must trace their desired values. These desired values are considered to be zero. The output of this system is the control moment to be applied to the tractor and semitrailer units.

7.3.1 Active roll control system design

7.3.1.1 Tractor unit

The simplified dynamic model in Eq. (7.35) is used to design the control system [23, 24].

$$\begin{aligned} I_{xx_{pt}}\ddot{\varphi}_t - I_{xz_{pt}}\ddot{\psi}_t + m_{st}h_t\dot{v}_t &= M_{p_{tsx}} - m_{st}h_t u_t\dot{\psi}_t + M_A \\ I_{xx_{pt}}\ddot{\varphi}_t &= M_{p_{tsx}} - m_{st}h_t(\dot{v}_t + u_t\dot{\psi}_t) + M_A \end{aligned} \tag{7.44}$$

Now:

$$f_1 = M_{p_{tsx}} - m_{st}h_t(\dot{v}_t + u_t\dot{\psi}_t) \tag{7.45}$$

By substituting Eq. (7.45) into Eq. (7.44):

$$I_{xx_{pt}}\ddot{\varphi}_t = f_1 + M_A \tag{7.46}$$

We define the error as the difference in the roll angle of the tractor unit and its desired value:

$$e_1 = \varphi_t - \varphi_d \tag{7.47}$$

The sliding surface is considered as (7.48):

$$s_t = \left(\frac{d}{dt} + \lambda_1\right)^2 \int (\varphi_t - \varphi_d)dt \tag{7.48}$$

By simplification:

$$\begin{aligned} s_t &= \left(\frac{d^2}{dt^2} + 2\lambda_1\frac{d}{dt} + \lambda_1^2\right)\int (\varphi_t - \varphi_d)dt \\ s_t &= \dot{\varphi}_t + 2\lambda_1(\varphi_t - \varphi_d) + \lambda_1^2\int (\varphi_t - \varphi_d)dt \end{aligned} \tag{7.49}$$

By differentiating (7.50):

$$\dot{s}_t = \ddot{\varphi}_t + 2\lambda_1\dot{\varphi}_t + \lambda_1^2(\varphi_t - \varphi_d) \tag{7.50}$$

By considering the exponential rule in the (7.51) form:

$$\dot{s}_t = -k_1 s_t - k_2\, sgn(s_t) \tag{7.51}$$

where $\dot{s}_t = -k_1 s_t$ is the exponential term and is solved as $s_t = s_t(0)e^{-k_1 t}$. It is clear that adding the term $-k_1 s_t$ causes the controlled state variables to move faster toward the switching surfaces. Given Eqs. (7.50) and (7.51) and by substituting $\ddot{\varphi}_t$ from Eq. (7.46).

$$\frac{1}{I_{xx_{pt}}}f_1 + \frac{1}{I_{xx_{pt}}}M_A + 2\lambda_1\dot{\varphi}_t + \lambda_1^2(\varphi_t - \varphi_d) = -k_1 s_t - k_2\, sgn(s_t) \tag{7.52}$$

Therefore,

$$M_A = -I_{xx_{pt}}\left(\frac{1}{I_{xx_{pt}}}f_1 + 2\lambda_1\dot{\varphi}_t + \lambda_1^2(\varphi_t - \varphi_d) + k_1 s_t + k_2\, sgn(s_t)\right) \tag{7.53}$$

The control input is equal to (7.54).

$$M_A = -I_{xx_{pt}}\left(\frac{1}{I_{xx_{pt}}}f_1 + (2\lambda_1 + k_1)\dot{\varphi}_t + \left(\lambda_1^2 + 2\lambda_1 k_1\right)(\varphi_t - \varphi_d) + k_1\lambda_1^2 \int(\varphi_t - \varphi_d)dt + k_2\, sgn(s_t)\right) \tag{7.54}$$

7.3.1.2 Semitrailer unit

Similarly to deriving the control input of the tractor unit, the semitrailer unit control input is obtained as (7.55).

$$\left(I_{xx_{ps}} + I_{xl}\right)\ddot{\varphi}_s - I_{xz_{ps}}\ddot{\psi}_s + m_{ss}h_s\dot{v}_s = M_{p_{ssx}} - m_{ss}h_s u_s\dot{\psi}_s + m_l a_l\hat{j}Z + m_l a_l\hat{k}Y + m_l g(Z\sin(\varphi_s) + Y) + M_B \tag{7.55}$$

Now

$$f_2 = M_{p_{ssx}} - m_{ss}h_s(\dot{v}_s + u_s\dot{\psi}_s) + m_l a_l\hat{j}Z + m_l a_l\hat{k}Y + m_l g(Z\sin(\varphi_s) + Y) \tag{7.56}$$

Eq. (7.55) is turned into the following.

$$\left(I_{xx_{ps}} + I_{xl}\right)\ddot{\varphi}_s = f_2 + M_B \tag{7.57}$$

The error equals

$$e_2 = \varphi_s - \varphi_d \tag{7.58}$$

The sliding surface is considered as (7.59).

$$s_s = \left(\frac{d}{dt} + \lambda_2\right)^2 \int(\varphi_s - \varphi_d)dt \tag{7.59}$$

By differentiating Eq. (7.59);

$$\dot{s}_s = \ddot{\varphi}_s + 2\lambda_2\dot{\varphi}_s + \lambda_2^2(\varphi_s - \varphi_d) \tag{7.60}$$

Thus, the control input of the semitrailer unit is computed as (7.61).

Table 7.2 Robust active roll control system parameters.

SMC parameter	Value
λ_1	15
λ_2	38
k_1	10
k_2	0.02
k_3	2
k_4	0.02

$$M_B = -\left(I_{xx_{ps}} + I_{xl}\right)\left(\frac{1}{\left(I_{xx_{ps}} + I_{xl}\right)} f_2 + (2\lambda_2 + k_3)\dot{\varphi}_s + \left(\lambda_2^2 + 2\lambda_2 k_3\right)(\varphi_s - \varphi_d)\right.$$
$$\left. + k_3\lambda_2^2 \int (\varphi_s - \varphi_d)dt + k_4\, sgn(s_s)\right) \tag{7.61}$$

The active roll control system parameters are shown in Table 7.2.

7.3.2 Active steering control system design

In this section, an active steering control system is presented in order to prevent yaw instability and a jackknife of the liquid-carrying articulated vehicle. In controlling the passenger vehicles' lateral dynamics, the yaw rate and the lateral velocity are the main state variables to improve handling and increase stability, respectively, and the lateral dynamics of the vehicle are controlled by controlling these variables. However, there is another control variable in articulated vehicles, called the articulation angle, which must be paid attention to for preventing jackknifing. Thus, in the design of the control system, the tractor unit's yaw rate, the lateral velocity of the tractor unit, and the articulation angle are considered the controlled state variables that must trace their desired values. The controller is designed based on a 3-DOF model of the liquid-carrying articulated vehicle, including DOFs for the tractor's yaw rate, lateral velocity of the tractor, and articulation angle. Moreover, the sliding mode control method is used to design the controller [25].

By considering the simple articulated vehicle model, according to Tabatabaee et al. [19], Fig. 7.14, the equations governing the lateral and yaw dynamics of the articulated vehicle in the coordinate system $x_t y_t$ are presented as (7.62–7.65).

$$m_t(\dot{v}_t + u_t\dot{\psi}_t) = F_{yft} + F_{yrt} - F_{fy} \tag{7.62}$$

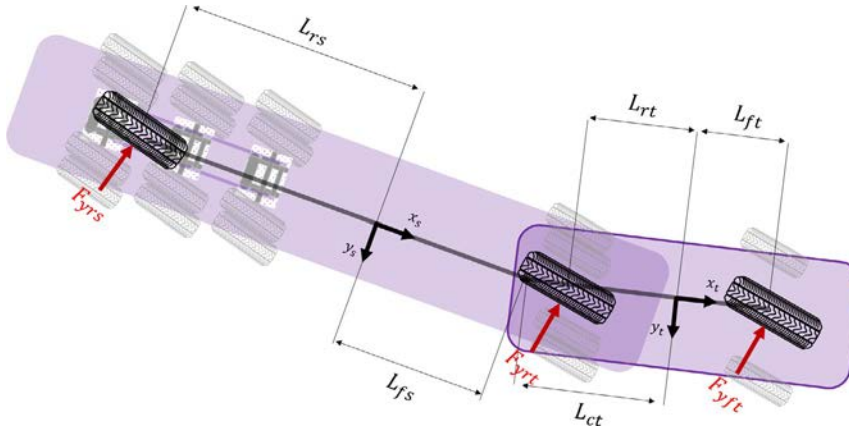

Fig. 7.14 Simplified articulated vehicle model.

$$I_{zz_t}\ddot{\psi}_t = +F_{fy}L_{ct} + F_{yft}L_{ft} - F_{yrt}L_{rt} \tag{7.63}$$

$$(m_s + M_h)\left(\dot{v}_t + u_t\dot{\psi}_t - \left(L_{ct} + L_{fs}\right)\ddot{\psi}_t - L_{fs}\ddot{\Gamma}\right) + M_hX\left(\ddot{\psi}_t + \ddot{\Gamma}\right) = F_{yrs} + F_{fy} \tag{7.64}$$

$$\begin{aligned}&\left(I_{zz_s} + I_{zzl}\right)\left(\ddot{\psi}_t + \ddot{\Gamma}\right) + M_hX\left(\dot{v}_t + u_t\dot{\psi}_t - \left(L_{ct} + L_{fs}\right)\ddot{\psi}_t - L_{fs}\ddot{\Gamma}\right)\\ &+ M_hX^2\left(\ddot{\psi}_t + \ddot{\Gamma}\right) + M_hY^2\left(\ddot{\psi}_t + \ddot{\Gamma}\right) = F_{fy}L_{fs} - F_{yrs}L_{rs}\end{aligned} \tag{7.65}$$

7.3.2.1 Dynamic equations of the simplified model of a liquid-carrying articulated vehicle

The dynamic equations of the liquid-carrying articulated vehicle are obtained by considering the liquid mass center's acceleration and the equations of motion of the articulated vehicle, as (7.66–7.68).

$$\begin{aligned}&\text{Eq.}(7.19) + \text{Eq.}(7.21) \xrightarrow{\text{yields}} m_t(\dot{v}_t + u_t\dot{\psi}_t)\\ &+ (m_s + M_h)\left[\dot{v}_t + u_t\dot{\psi}_t - \left(L_{ct} + L_{fs}\right)\ddot{\psi}_t - L_{fs}\ddot{\Gamma}\right] + M_hX\left(\ddot{\psi}_t + \ddot{\Gamma}\right)\\ &= F_{yft} + F_{yrt} + F_{yrs}\end{aligned} \tag{7.66}$$

$$\begin{aligned}&\text{Eq.}(7.20) + \text{Eq.}(7.22) - \left(L_{ct} + L_{fs}\right)\text{Eq.}(7.21) \xrightarrow{\text{yields}} I_{zz_t}\ddot{\psi}_t\\ &+ \left(I_{zz_s} + I_{zzl}\right)\left(\ddot{\psi}_t + \ddot{\Gamma}\right) + M_hX\left(\dot{v}_t + u_t\dot{\psi}_t - \left(L_{ct} + L_{fs}\right)\ddot{\psi}_t - L_{fs}\ddot{\Gamma}\right)\\ &+ M_hX^2\left(\ddot{\psi}_t + \ddot{\Gamma}\right) - M_hY^2\left(\ddot{\psi}_t + \ddot{\Gamma}\right)\\ &- (m_s + M_h)\left(\dot{v}_t + u_t\dot{\psi}_t - \left(L_{ct} + L_{fs}\right)\ddot{\psi}_t - L_{fs}\ddot{\Gamma}\right)\left(L_{ct} + L_{fs}\right)\\ &+ M_hX\left(\ddot{\psi}_t + \ddot{\Gamma}\right)\left(L_{ct} + L_{fs}\right)\\ &= F_{yft}L_{ft} - F_{yrt}L_{rt} - F_{yrs}\left(L_{ct} + L_{fs} + L_{rs}\right)\end{aligned} \tag{7.67}$$

$$\begin{aligned}&\text{Eq.}(7.22)-L_{fs}\text{Eq.}(7.21)\xrightarrow{\text{yields}}\left(I_{zz_s}+I_{zzl}\right)\left(\ddot{\psi}_t+\ddot{\Gamma}\right)\\&+M_hX\left(\dot{v}_t+u_t\dot{\psi}_t-\left(L_{ct}+L_{fs}\right)\ddot{\psi}_t-L_{fs}\ddot{\Gamma}\right)+M_hX^2\left(\ddot{\psi}_t+\ddot{\Gamma}\right)\\&-M_hY^2\left(\ddot{\psi}_t+\ddot{\Gamma}\right)-L_{fs}\left(m_s+M_h\right)\left(\dot{v}_t+u_t\dot{\psi}_t-\left(L_{ct}+L_{fs}\right)\ddot{\psi}_t-L_{fs}\ddot{\Gamma}\right)\\&+M_hX\left(\ddot{\psi}_t+\ddot{\Gamma}\right)=-F_{yrs}\left(L_{fs}+L_{rs}\right)\end{aligned}\tag{7.68}$$

By writing the equations in state-space form (7.69).

$$A\dot{X}+f=U\tag{7.69}$$

where

$$A_{11}=m_t+m_s+M_h$$

$$A_{12}=-\left(m_s+M_h\right)\left(L_{ct}+L_{fs}\right)+M_hX$$

$$A_{13}=-\left(m_s+M_h\right)L_{fs}+M_hX$$

$$A_{21}=-\left(m_s+M_h\right)\left(L_{ct}+L_{fs}\right)+M_hX$$

$$A_{22}=I_{zz_t}+I_{zz_s}+I_{zzl}+M_h\left(X^2-Y^2\right)+\left(m_s+M_h\right)\left(L_{ct}+L_{fs}\right)^2$$

$$A_{23}=I_{zz_s}+I_{zzl}+M_h\left(X^2-Y^2+X\right)-M_hX\left(L_{ct}+L_{fs}\right)+\left(m_s+M_h\right)L_{fs}\left(L_{ct}+L_{fs}\right)$$

$$A_{31}=-\left(m_s+M_h\right)L_{fs}+M_hX$$

$$A_{32}=\left(I_{zz_s}+I_{zzl}\right)-M_hX\left(L_{ct}+L_{fs}\right)+M_h\left(X^2-Y^2+X\right)+\left(m_s+M_h\right)\left(L_{ct}+L_{fs}\right)L_{fs}$$

$$A_{33}=\left(I_{zz_s}+I_{zzl}\right)+M_h\left(-XL_{fs}+X^2-Y^2+X\right)+\left(m_s+M_h\right)L_{fs}^2$$

The error is defined as follows:

$$e=X-X_d\tag{7.70}$$

By defining the sliding surface as (7.71).

$$s=e\tag{7.71}$$

By differentiating the Eq. (7.71);

$$\begin{aligned}\dot{s}=0\rightarrow\dot{X}-\dot{X}_d=0\\A^{-1}(-f+U)-\dot{X}_d=0\\\hat{U}=\hat{A}\dot{X}_d+\hat{f}\end{aligned}\tag{7.72}$$

The control input is equal to (7.73).

$$\begin{aligned}U=\hat{U}-k\text{sgn}(s)\\U=\hat{A}\dot{X}_d+\hat{f}-k\text{sgn}(s)\end{aligned}\tag{7.73}$$

According to Eq. (7.69):

$$U = MF\gamma_i, \quad M = \begin{bmatrix} 1 & 1 & 1 \\ L_{ft} & -L_{rt} & -\left(L_{ct} + L_{fs} + L_{rs}\right) \\ 0 & 0 & -\left(L_{fs} + L_{rs}\right) \end{bmatrix} \tag{7.74}$$

$$\text{with } i = ft, rt, rs$$

By considering the lateral tire force.

$$F\gamma_i = C_{\alpha i}\alpha_i \tag{7.75}$$

By equating Eqs. (7.74) and (7.75).

$$\alpha_i = \frac{M^{-1}U}{C_{\alpha i}} \tag{7.76}$$

Hence, the control angles of the axles of the tractor and semitrailer units are computed as (7.77):

$$\begin{aligned} \delta_{ft} &= \alpha_{ft} + \tan^{-1}\left(\frac{v_t + \dot{\psi}_t L_{ft}}{u_t}\right) \\ \delta_{rt} &= \alpha_{rt} + \tan^{-1}\left(\frac{v_t - \dot{\psi}_t L_{rt}}{u_t}\right) \\ \delta_s &= \alpha_s + \tan^{-1}\left(\frac{v_s - \dot{\psi}_s L_{rs}}{u_s}\right) \end{aligned} \tag{7.77}$$

By equating the lateral forces of the semitrailer axles, the control angles of the other two axles are computed as (7.78):

$$\begin{aligned} \delta_{fs} &= \arctan\left(\tan(\delta_s) + \frac{L_{ts}}{u_s}\dot{\psi}_s\right) \\ \delta_{rs} &= \arctan\left(\tan(\delta_s) - \frac{L_{ts}}{u_s}\dot{\psi}_s\right) \end{aligned} \tag{7.78}$$

7.3.2.2 Stability analysis

In this section, the stability of the system is analyzed using the Lyapunov stability theory. The Lyapunov function is considered as (7.79):

$$V = \frac{1}{2}s^T As \tag{7.79}$$

The derivative V is computed as (7.80):

$$\dot{V} = s^T A\dot{s} = s^T\left(A\dot{X} - A\dot{X}_d\right) = s^T\left(-f + U - A\dot{X}_d\right)$$
$$\dot{V} = s^T\left(-f + \hat{A}\dot{X}_d + \hat{f} - k\,\mathrm{sgn}(s) - A\dot{X}_d\right) = s^T\left(\hat{A}\dot{X}_d + \hat{f} - A\dot{X}_d - f - k\,\mathrm{sgn}(s)\right) \tag{7.80}$$

And:

$$\left|\hat{A}\dot{X}_d + \hat{f} - A\dot{X}_d - f\right| \le F \tag{7.81}$$

k is selected in such a way that:

$$k = F + \eta \tag{7.82}$$

Therefore:

$$\dot{V} = s^T\left(\hat{A}\dot{X}_d + \hat{f} - A\dot{X}_d - f - k\,\mathrm{sgn}(s)\right) = s^T\left(\hat{A}\dot{X}_d + \hat{f} - A\dot{X}_d - f\right) - k\left|s^T\right|$$
$$\le F\left|s^T\right| - F\left|s^T\right| - \eta\left|s^T\right| \le -\eta\left|s^T\right| \rightarrow \dot{V} \le -\eta\left|s^T\right| \tag{7.83}$$

Hence, the system is stable in the sense of Lyapunov. In order to omit the chattering in the control input, the *sgn* function is replaced by the sat($s/\varnothing$) function. The sat($s/\varnothing$) function is defined as (7.84):

$$\mathrm{sat}(s/\varnothing) = \begin{cases} \dfrac{s}{\varnothing}, & \text{if } |s| \le \varnothing \\ \mathrm{sgn}\left(\dfrac{s}{\varnothing}\right), & \text{if } |s| > \varnothing \end{cases} \tag{7.84}$$

where $\varnothing$ is the boundary layer thickness.

7.3.2.3 Active steering control system modification

Given previous research and the fact that commercial vehicle power train systems are placed on the tractor unit's rear axle, this axle's steerability seems unpractical. For this reason, we attempt to modify the control system so that only the front axle of the tractor unit and the semitrailer axles are steerable.

According to Eqs. (7.66)–(7.68), the lateral forces of the front axle of the tractor unit and the axle of the semitrailer unit are considered as (7.85).

$$F_{yft1} + F_{yrs1} = \mathrm{U_1} - \hat{F}_{yrt}$$
$$F_{yft1}L_{ft} - F_{yrs1}\left(L_{ct} + L_{fs} + L_{rs}\right) = \mathrm{U_2} + \hat{F}_{yrt}L_{rt} - F_{yrs1}\left(L_{rs} + L_{fs}\right) = \mathrm{U_3} \tag{7.85}$$

In the above equations, $\hat{F}_{yrt}$ is the estimate of F_{yrt}, and the target is finding the new lateral forces of the front axle of the tractor unit and the axle of the semitrailer unit. The idea in Boada et al. [22] is used in this section. To obtain the response, the function J_s is considered as (7.86):

$$J_s = \omega_1\left[F_{yft} + F_{yrs} - \left(\mathrm{U_1} - \hat{F}_{yrt}\right)\right]^2$$
$$+ \omega_2\left[F_{yft}L_{ft} - F_{yrs}\left(L_{ct} + L_{fs} + L_{rs}\right) - \left(\mathrm{U_2} + \hat{F}_{yrt}L_{rt}\right)\right]^2$$
$$+ \omega_3\left[F_{yrs}\left(L_{rs} + L_{fs}\right) + \mathrm{U_3}\right]^2 \tag{7.86}$$

where ω_1, ω_2, and ω_3 are weighting factors. The lateral forces are corrected by minimizing the above function:

$$\begin{aligned}\frac{\partial J_s}{\partial F_{yft}} &= \left(2\omega_1 + 2\omega_2 L_{ft}^2\right)F_{yft} + \left(2\omega_1 - 2\omega_2 L_{ft}\left(L_{ct} + L_{fs} + L_{rs}\right)\right)F_{yrs} \\ &\quad -2\omega_1\left(\mathrm{U}_1 - \hat{F}_{yrt}\right) - 2\omega_2 L_{ft}\left(\mathrm{U}_2 + \hat{F}_{yrt}L_{rt}\right) = 0 \\ \frac{\partial J_s}{\partial F_{yrs}} &= \left(2\omega_1 - 2\omega_2 L_{ft}\left(L_{ct} + L_{fs} + L_{rs}\right)\right)F_{yft} \\ &\quad + \left(2\omega_1 + 2\omega_2\left(L_{ct} + L_{fs} + L_{rs}\right)^2 + 2\omega_3\left(L_{rs} + L_{fs}\right)^2\right)F_{yrs} \\ &\quad -2\omega_1\left(\mathrm{U}_1 - \hat{F}_{yrt}\right) + 2\omega_2 L_{cs}\left(\mathrm{U}_2 + \hat{F}_{yrt}L_{rt}\right) + 2\omega_3 L_{rf}\mathrm{U}_3 = 0\end{aligned} \tag{7.87}$$

Now:

$$\begin{bmatrix} 2\omega_1 + 2\omega_2 L_{ft}^2 & 2\omega_1 - 2\omega_2 L_{ft}\left(L_{ct} + L_{fs} + L_{rs}\right) \\ 2\omega_1 - 2\omega_2 L_{ft}\left(L_{ct} + L_{fs} + L_{rs}\right) & 2\omega_1 + 2\omega_2\left(L_{ct} + L_{fs} + L_{rs}\right)^2 + 2\omega_3\left(L_{rs} + L_{fs}\right)^2 \end{bmatrix}$$

$$\begin{Bmatrix} F_{yft} \\ F_{yrs} \end{Bmatrix} = \begin{Bmatrix} 2\omega_1\left(\mathrm{U}_1 - \hat{F}_{yrt}\right) + 2\omega_2 L_{ft}\left(\mathrm{U}_2 + \hat{F}_{yrt}L_{rt}\right) \\ 2\omega_1\left(\mathrm{U}_1 - \hat{F}_{yrt}\right) - 2\omega_2\left(L_{ct} + L_{fs} + L_{rs}\right)\left(\mathrm{U}_2 + \hat{F}_{yrt}L_{rt}\right) - 2\omega_3\left(L_{rs} + L_{fs}\right)\mathrm{U}_3 \end{Bmatrix} \tag{7.88}$$

Using Eqs. (7.62)–(7.65), an estimate is obtained for the lateral force of the tractor unit's rear axle.

$$\begin{aligned}\hat{F}_{yrs} &= \frac{\left(I_{zz_s} + I_{zzl}\right)\left(\ddot{\psi}_t + \ddot{\Gamma}\right) + M_h X\left(\dot{v}_t + u_t\dot{\psi}_t - \left(L_{ct} + L_{fs}\right)\ddot{\psi}_t - L_{fs}\ddot{\Gamma}\right) + M_h X^2\left(\ddot{\psi}_t + \ddot{\Gamma}\right) - }{L_{rs} + L_{fs}} \\ &\quad \frac{M_h Y^2\left(\ddot{\psi}_t + \ddot{\Gamma}\right) - L_{fs}(m_s + M_h)\left(\dot{v}_t + u_t\dot{\psi}_t - \left(L_{ct} + L_{fs}\right)\ddot{\psi}_t - L_{fs}\ddot{\Gamma}\right) + M_h X\left(\ddot{\psi}_t + \ddot{\Gamma}\right)}{L_{rs} + L_{fs}} \\ \hat{F}_{fy} &= (m_s + M_h)\left[\dot{v}_t + u_t\dot{\psi}_t - \left(L_{ct} + L_{fs}\right)\ddot{\psi}_t - L_{fs}\ddot{\Gamma}\right] + M_h X\left(\ddot{\psi}_t + \ddot{\Gamma}\right) - \hat{F}_{yrs} \\ \hat{F}_{yrt} &= \frac{\hat{F}_{fy}\left(L_{ct} + L_{ft}\right) + m_t(\dot{v}_t + u_t\dot{\psi}_t)L_{ft} - I_{zz_t}\ddot{\psi}_t}{L_{rt} + L_{ft}} \\ \hat{F}_{yft} &= \hat{F}_{fy} + m_t(\dot{v}_t + u_t\dot{\psi}_t) - \hat{F}_{yrt}\end{aligned} \tag{7.89}$$

Where $\hat{F}_{yft}$, $\hat{F}_{yrt}$, and $\hat{F}_{yrs}$ are estimates for the lateral forces in the front axle of the tractor unit, the rear axle of the tractor unit, and the axle of the semi-trailer unit, respectively.

7.4 Hybrid control system consisting of the active steering and active roll control systems

In this section, a combination of the two control systems designed in the previous section is used to benefit both control systems' advantages. Hence, active steering control is utilized to improve maneuverability and prevent jackknifing. Another goal is to increase rollover stability using active roll control. Another advantage of the above system is the lack of conflict between the performances of the subsystems. Furthermore, the hybrid control system makes it possible to control the tractor unit's lateral acceleration, which plays a direct role in the unstable rollover and handling modes by controlling the yaw rate, lateral velocity, and roll angle. The diagram of the control system is shown in Fig. 7.15.

In an active steering control system, the tractor's yaw rate, the lateral velocity of the tractor, and the articulation angle are the controlled state variables that must trace their desired values. The above control system's output is all the control angles, including the tractor front axle's steering angle, the tractor rear axle's steering angle, and the angles of the semitrailer axles. For the active roll control system, the controlled state variables that must trace their desired values are the tractor and semitrailer units' roll angles. The above system's output is the control moments exerted on the tractor and semitrailer units, which are provided by an active antiroll bar.

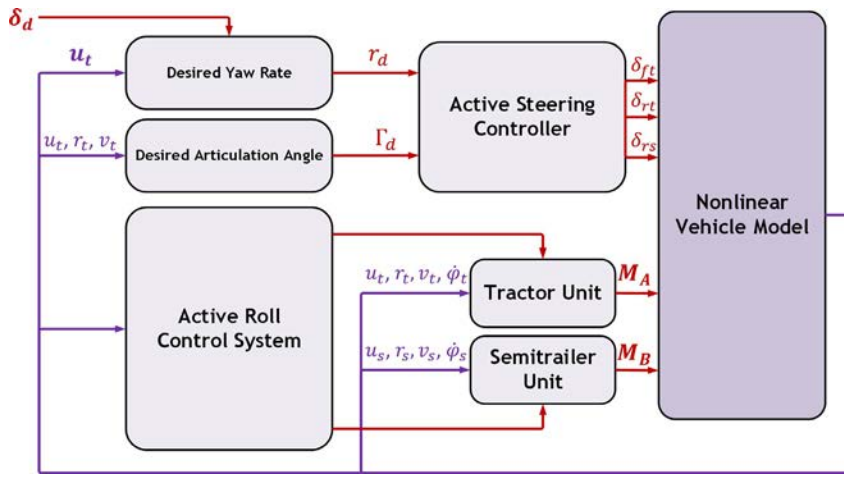

Fig. 7.15 Hybrid control system diagram.

7.4.1 Performance evaluation of the hybrid control system

In this section, the hybrid control system's performance is evaluated for 20%, 50%, and 80% filling volume.

7.4.1.1 Fishhook maneuver

In this analysis, the vehicle has started moving with an initial speed of 80 km/h on the road with a friction coefficient of 0.7, and a steering input has been applied to it as shown in Fig. 7.16.

Small, medium, and large filling volumes are considered for this maneuver. The simulation results for the tractor unit's yaw rate, the lateral velocity of the tractor unit, the articulation angle, the control inputs, and the roll angles of the tractor and semitrailer units are displayed in Figs. 7.17–7.19. As shown in Fig. 7.17, the uncontrolled vehicle is stable for all three filling volumes. Still, the deviations in the tractor's yaw rate and the articulation angle relative to their desired values increase with an increase in the filling volume. This increase intensifies with time for a filling volume of 80% due to the dynamic interaction between the vehicle and the liquid. In addition, the lateral velocity of the tractor unit has an increasing trend for the uncontrolled vehicle. For the controlled mode, the hybrid system is able to make the controlled vehicle state variables to trace the desired values on an acceptable level. According to Fig. 7.17A and B, the tractor's yaw rate and the

Fig. 7.16 Fishhook maneuver.

articulation angle trace well their desired values in the steady-state and tractor modes. Moreover, the robust controller exhibits an acceptable performance by limiting the tractor unit's lateral velocity to a narrow range. Fig. 7.18 displays the results related to the tractor unit's roll angles and semitrailer unit and the lateral-load transfer ratio. As shown in the figure, the tractor and semitrailer units' roll angles increase with an increase in the tank's

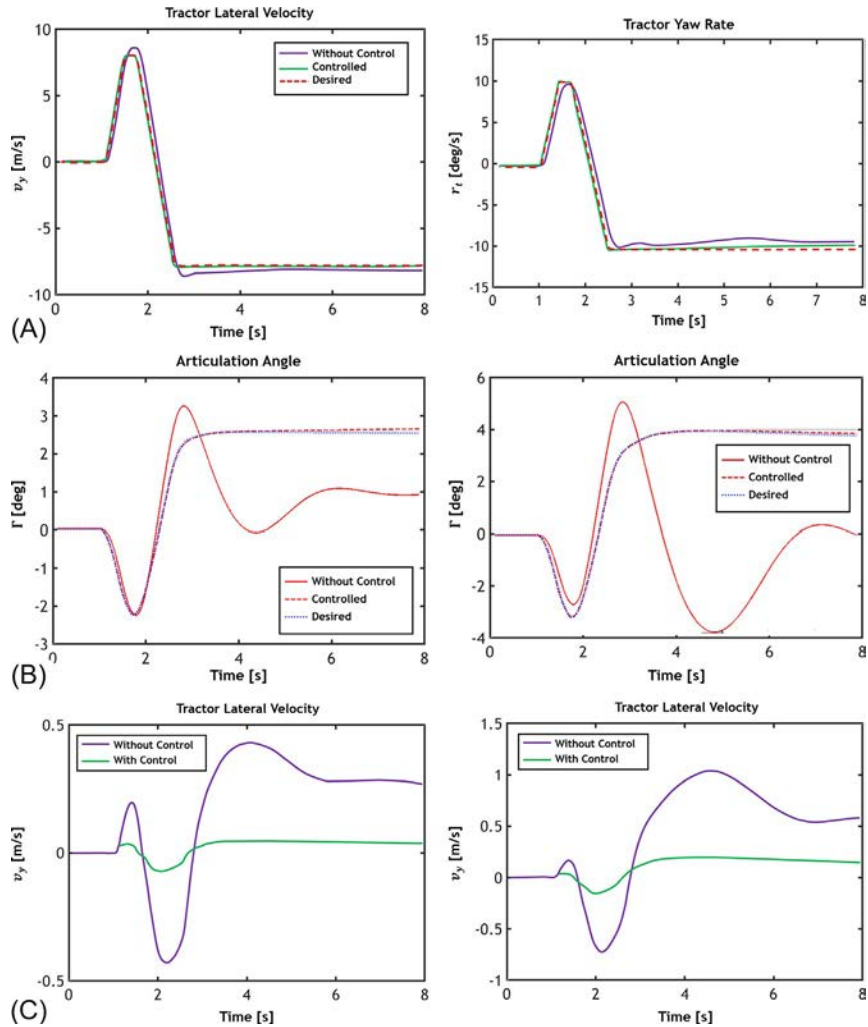

Fig. 7.17 (A) Tractor unit yaw rate,

(Continued)

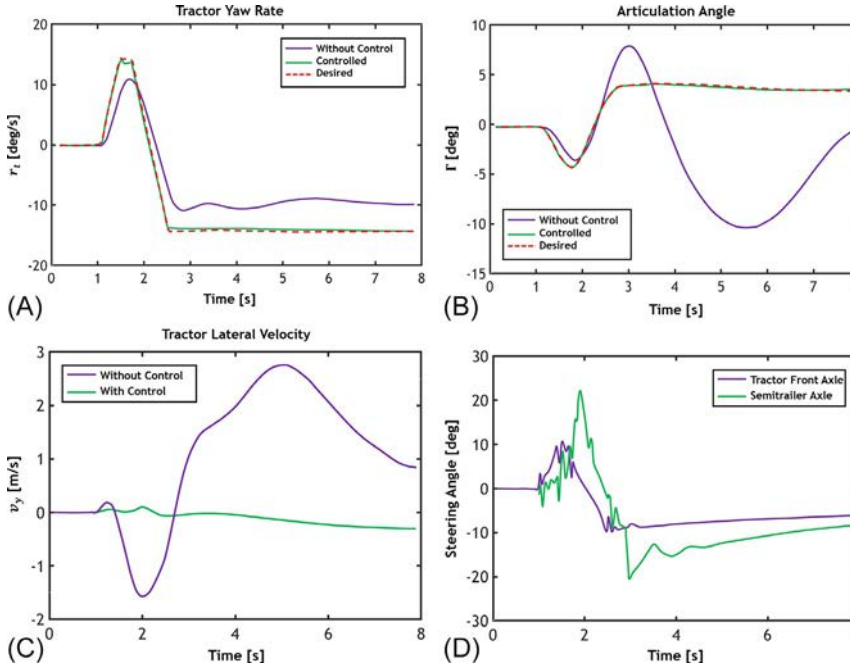

Fig. 7.17, Cont'd (B) articulation angle, (C) tractor unit lateral velocity, (D) control inputs.

liquid volume. However, the control system reduces the overshoot and the roll angle's settling time for both units at all three filling volumes. For example, at a filling volume of 80%, the maximum overshoot of the tractor unit's roll angle shows 80% and 91.3% reductions in the first and second peaks, respectively, compared to the uncontrolled mode. As can be seen, this situation becomes zero after 5 s. The roll angle reduces by 71.4% and 85% in the first and second peaks for the semitrailer unit, respectively. In other words, the rollover stability of the liquid-carrying articulated vehicle increases with a decrease in the roll angle. The tractor and semitrailer units' control moments are displayed in Fig. 7.19 for the three filling volumes. As shown in the figure, the control moment has a smooth form for each unit's three filling volumes.

As shown in Fig. 7.20, the semitrailer unit's rear axle is off-track concerning the fifth wheel path for the uncontrolled mode. However, the active steering system has been able to omit the off-tracking and make the rear axle of the semitrailer unit trace the fifth wheel's path by controlling the tractor unit's yaw rate articulation angle.

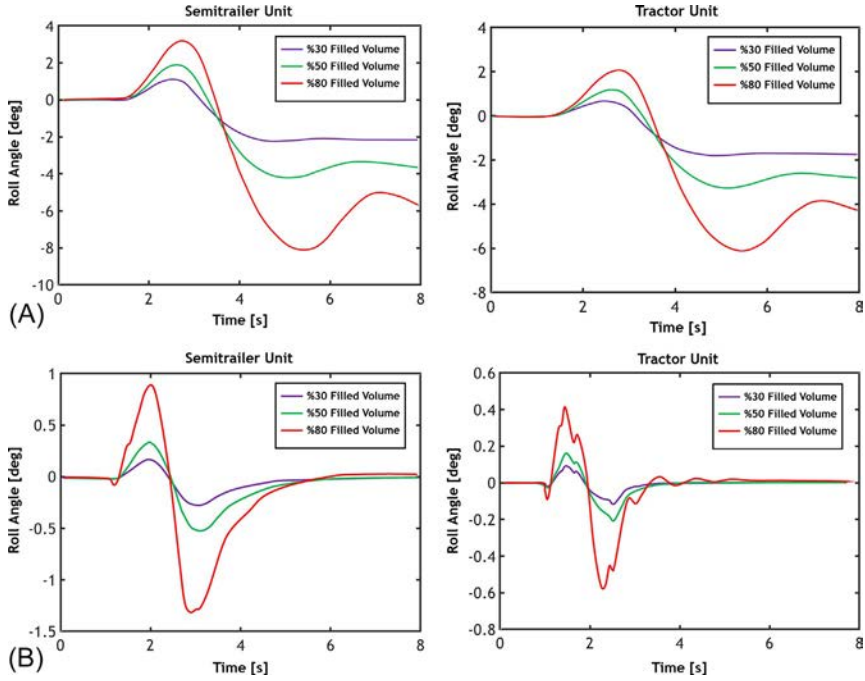

Fig. 7.18 Roll angles, (A) uncontrolled, (B) controlled.

7.4.2 The adaptive sliding mode controller

In the last section, sliding mode control was used to compute the control input. Utilizing this method is simple, with the added advantage that the modeling uncertainties can be taken into account in the control law. Nevertheless, sliding mode control, in which the error range is determined and the control law is designed based on the error range, has the disadvantage that the boundary layer thickness increases with the increase in the variation range of modeling errors and the presence of uncertainty in the control system parameters, increasing the tracing error and control effort. In such cases, an adaptive law must be derived for the parameters that have uncertainty and that change under different operational conditions.

The main idea of adaptive control is estimating the system's uncertain parameters (or, equivalently, the controller parameters) based on the system signals measured online. The control input is obtained using the estimated parameters. Therefore, an adaptive control system can be considered as a control system along with a parameter estimator.

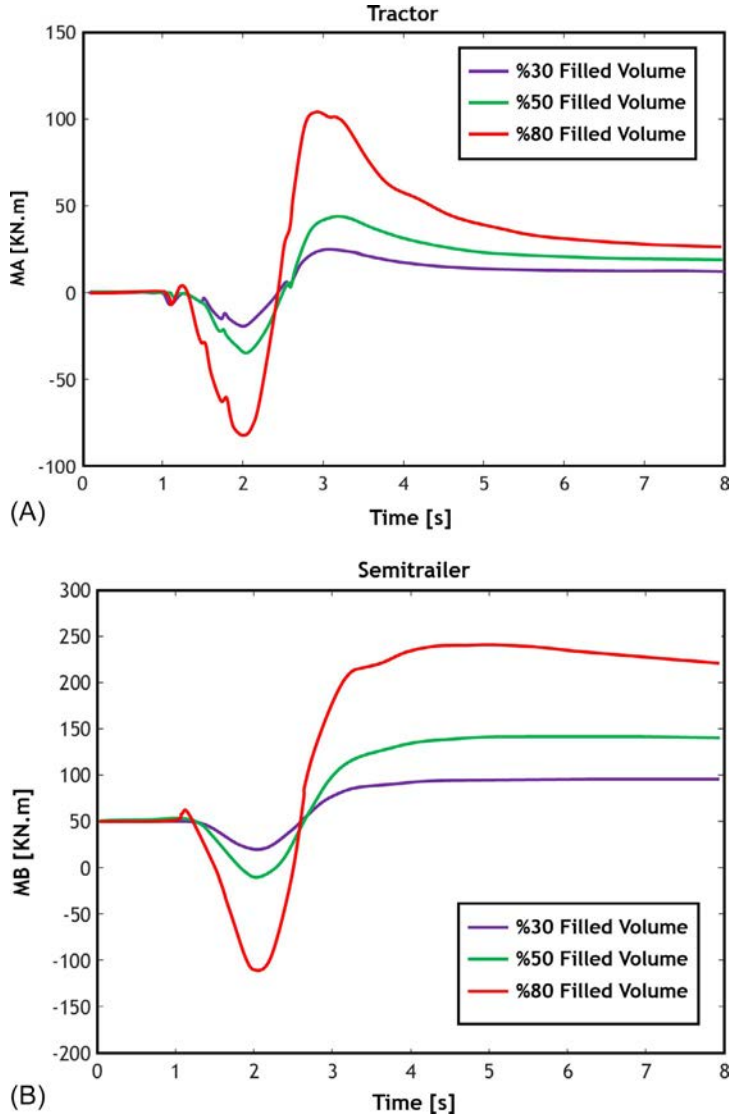

Fig. 7.19 Control inputs, (A) tractor unit, (B) semitrailer unit.

As seen in the previous section, robust control methods are employed when there are uncertainties in the system parameters. Nevertheless, using adaptive control methods for parameter estimation when there are uncertainties in the system parameters has the following advantages over using robust control methods:

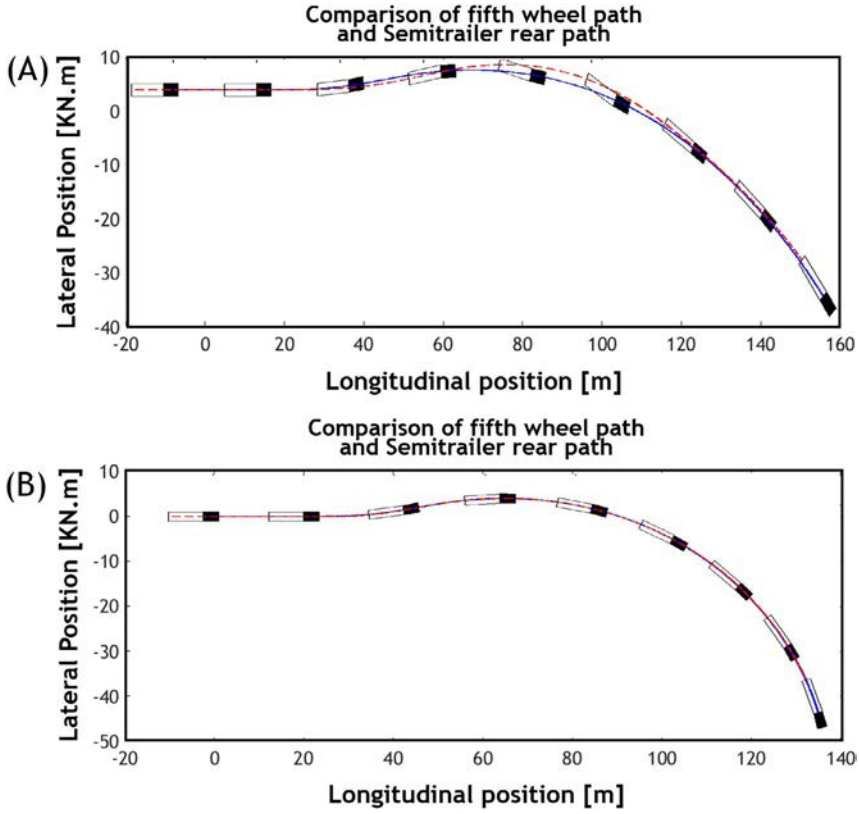

Fig. 7.20 Path of the liquid-carrying articulated vehicle, (A) uncontrolled, (B) controlled.

- An adaptive controller improves its performance as time passes by estimating the system parameters more accurately, whereas a robust controller attempts to provide suitable performance.
- An adaptive controller does not require initial data about the system parameters or requires little data. In contrast, a robust controller needs a suitable initial approximation of the range variation of the parameters.

On the other hand, robust control has some advantages over adaptive control. For example, a robust control system offers better performance when there are disturbances in the system, when the system has time-varying parameters, or when the system has unmodeled dynamics. Hence, it can be said that the use of an adaptive robust controller provides the advantage

of reducing the parametric uncertainties in the system using adaptive control and considering the effect of the rest of system uncertainties such as structural uncertainties or unmodeled dynamics using robust control.

Most dynamic systems have constant or variable uncertain parameters. Adaptive control is generally used to control systems with uncertain and unknown parameters. The fundamental idea of adaptive control is estimating the system's uncertain parameters based on the data obtained from the system and using the estimated parameters to compute the control input.

In this section, we use the standard least-squares method to estimate the control system parameters.

7.4.2.1 Standard least-squares method

The basis of parameter estimation is obtaining data related to the parameter using available system data. Therefore, an estimation model is required to attribute the available data to the unknown parameters [26]. A general model for parameter estimation is the linear form (7.90):

$$y = wa \tag{7.90}$$

where the n-dimensional vector y consists of the system outputs, the m-dimensional vector a consists of the unknown parameters that must be estimated, and the $n \times m$ matrix w is the signal matrix. It must be noted that both matrices y and w can be identified by measuring the system data; hence, the unknown values in Eq. (7.90) are present in the vector a.

The value of y can be predicted using the estimated parameter and based on the model in Eq. (7.90).

$$\hat{y} = w\hat{a} \tag{7.91}$$

Where $\hat{y}$ denotes the predicted output at time t. The difference between the predicted output and the measured output y is named the prediction error and is denoted by e_1.

$$e_1 = \hat{y} - y \tag{7.92}$$

The prediction error can be related to the parameter estimation error as (7.93):

$$e_1 = w\hat{a} - wa \tag{7.93}$$

where $\tilde{a} = a - \hat{a}$ is the parameter estimation error vector.

In the standard least-squares method, the parameters are estimated by minimizing the total prediction error with respect to $\hat{a}(t)$. This error is equal to (7.94):

$$J = \int_0^t e_1^T(r)e_1(r)dr = \int \|y(r) - W(r)\hat{a}(t)\|^2 dr \tag{7.94}$$

By differentiating J concerning $\hat{a}(t)$:

$$\frac{\partial J}{\partial \hat{a}(t)} = 0 \rightarrow \left(\int_0^t w^T(r)w(r)dr\right)\hat{a}(t) = \int_0^t w^T(r)y(r)dr \tag{7.95}$$

By the following definition:

$$P(t) = \left[\left(\int_0^t w^T(r)w(r)dr\right)\hat{a}(t)\right]^{-1} \tag{7.96}$$

Hence:

$$P(t) = \left[\left(\int_0^t w^T(r)w(r)dr\right)\hat{a}(t)\right]^{-1} \tag{7.97}$$

As such, the above relationship is written as follows:

$$P^{-1}(t)\hat{a} = \int_0^t w^T(r)y(r)dr \tag{7.98}$$

By differentiating:

$$\dot{\hat{a}} = -P(t)w^T e_1 \tag{7.99}$$

where $P(t)$ is the estimator gains matrix. For the online tuning of the matrix $P(t)$, the following is performed:

$$\dot{P} = -Pw^T wP \tag{7.100}$$

In order to use Eqs. (7.99) and (7.100) we must make an initial guess for the parameters $\hat{a}(0)$ and an initial guess for the estimation rule gain $P(0)$.

7.4.2.2 Active roll system parameter estimation

In this system, the vehicle's moment of inertia about the longitudinal axis and the vehicle mass center's height have uncertainties and are estimated using the standard least-squares method.

Tractor unit

By considering the roll equation of the tractor unit:

$$\begin{aligned} I_{xx_{pt}}\ddot{\varphi}_t + m_{st}h_t\dot{v}_t &= M_{p_{tsx}} - m_{st}h_t u_t\dot{\psi}_t + M_A \\ I_{xx_{pt}}\ddot{\varphi}_t &= M_{p_{tsx}} - m_{st}h_t(\dot{v}_t + u_t\dot{\psi}_t) + M_A \end{aligned} \tag{7.101}$$

The above equation is considered as (7.102):

$$\begin{aligned} I_{xx_{pt}}\ddot{\varphi}_t = {} & m_{st}gh_t\sin(\varphi_t) - KS_t\varphi_t - CS_t\dot{\varphi}_t + KS_w(\varphi_t - \varphi_s) + CS_w(\dot{\varphi}_t - \dot{\varphi}_s) \\ & - m_{st}h_t(\dot{v}_t + u_t\dot{\psi}_t) + M_A \end{aligned} \tag{7.102}$$

Now:

$$\begin{aligned} a_1 &= I_{xx_{pt}} \\ a_2 &= h_t \end{aligned} \tag{7.103}$$

By substituting Eq. (7.103) into Eq. (7.102):

$$\begin{aligned} & -KS_t\varphi_t - CS_t\dot{\varphi}_t + KS_w(\varphi_t - \varphi_s) + CS_w(\dot{\varphi}_t - \dot{\varphi}_s) - M_A \\ & = a_1\ddot{\varphi}_t + a_2(m_{st}(\dot{v}_t + u_t\dot{\psi}_t) - gh_t\sin(\varphi_t)) \end{aligned} \tag{7.104}$$

And:

$$\begin{aligned} & -KS_t\varphi_t - CS_t\dot{\varphi}_t + KS_w(\varphi_t - \varphi_s) + CS_w(\dot{\varphi}_t - \dot{\varphi}_s) - M_A \\ & = [\ddot{\varphi}_t \;\; m_{st}(\dot{v}_t + u_t\dot{\psi}_t) - gh_t\sin(\varphi_t)] \begin{bmatrix} a_1 \\ a_2 \end{bmatrix} \end{aligned} \tag{7.105}$$

By rewriting the above equation in the (7.106) form:

$$\begin{aligned} y &= wa \\ y &= -KS_t\varphi_t - CS_t\dot{\varphi}_t + KS_w(\varphi_t - \varphi_s) + CS_w(\dot{\varphi}_t - \dot{\varphi}_s) - M_A \\ w &= [\ddot{\varphi}_t \;\; m_{st}(\dot{v}_t + u_t\dot{\psi}_t) - gh_t\sin(\varphi_t)] \\ a &= \begin{bmatrix} a_1 \\ \\ a_2 \end{bmatrix} \end{aligned} \tag{7.106}$$

Semitrailer unit

By considering the equation of the semitrailer unit:

$$\left(I_{xx_{ps}} + I_{xl}\right)\ddot{\varphi}_s - I_{xz_{ps}}\ddot{\psi}_s + m_{ss}h_s\dot{v}_s = M_{p_{ssx}} - m_{ss}h_s u_s\dot{\psi}_s + m_l a_l\hat{j}Z + m_l a_l\hat{k}Y$$

$$
\begin{aligned}
&+ m_l g(Z\sin(\varphi_s) + Y) + M_B\left(I_{xx_{ps}} + I_{xl}\right)\ddot{\varphi}_s + m_{ss}h_s\dot{v}_s \\
&= m_{ss}gh_s\sin(\varphi_s) - KS_s\varphi_s - CS_s\dot{\varphi}_s - KS_w(\varphi_t - \varphi_s) - CS_w(\dot{\varphi}_t - \dot{\varphi}_s) \\
&\quad - m_{ss}h_s u_s\dot{\psi}_s + m_l Z\left(\dot{v}_s + u_s\dot{\psi}_s + h_s\ddot{\varphi}_s - Y\dot{\varphi}_s{}^2 - Y\dot{\psi}_s{}^2 + Z\ddot{\varphi}_s + X\ddot{\psi}_s\right) \\
&\quad + m_l Y\left(Z\dot{\varphi}_s{}^2 + X\dot{\varphi}_s\dot{\psi}_s + Y\ddot{\varphi}_s\right) + m_l g(Z\sin(\varphi_s) + Y) + M_B
\end{aligned}
\tag{7.107}
$$

The above equation is considered as (7.108):

$$
\begin{aligned}
\left(I_{xx_{ps}} + I_{xl}\right)\ddot{\varphi}_s = {} & m_{ss}gh_s\sin(\varphi_s) - KS_s\varphi_s - CS_s\dot{\varphi}_s - KS_w(\varphi_t - \varphi_s) \\
& - CS_w(\dot{\varphi}_t - \dot{\varphi}_s) - m_{ss}h_s(\dot{v}_s + u_s\dot{\psi}_s) + m_l h_s Z\ddot{\varphi}_s \\
& + m_l Z\left(\dot{v}_s + u_s\dot{\psi}_s - Y\dot{\varphi}_s{}^2 - Y\dot{\psi}_s{}^2 + Z\ddot{\varphi}_s + X\ddot{\psi}_s\right) \\
& + m_l Y\left(Z\dot{\varphi}_s{}^2 + X\dot{\varphi}_s\dot{\psi}_s + Y\ddot{\varphi}_s\right) + m_l g(Z\sin(\varphi_s) + Y) + M_B
\end{aligned}
\tag{7.108}
$$

Now:

$$
\begin{aligned}
a_3 &= I_{xx_{ps}} \\
a_4 &= h_s
\end{aligned}
\tag{7.109}
$$

By substituting Eq. (7.109) into Eq. (7.108):

$$
\begin{aligned}
&-KS_s\varphi_s - CS_s\dot{\varphi}_s - KS_w(\varphi_t - \varphi_s) - CS_w(\dot{\varphi}_t - \dot{\varphi}_s) \\
&+ m_l Z\left(\dot{v}_s + u_s\dot{\psi}_s - Y\dot{\varphi}_s{}^2 - Y\dot{\psi}_s{}^2 + Z\ddot{\varphi}_s + X\ddot{\psi}_s\right) \\
&+ m_l Y\left(Z\dot{\varphi}_s{}^2 + X\dot{\varphi}_s\dot{\psi}_s + Y\ddot{\varphi}_s\right) + m_l g(Z\sin(\varphi_s) + Y) - M_B \\
&= a_3\ddot{\varphi}_s + a_4(m_{ss}(\dot{v}_s + u_s\dot{\psi}_s) - gh_s\sin(\varphi_s))
\end{aligned}
\tag{7.110}
$$

And

$$
\begin{aligned}
&-KS_s\varphi_s - CS_s\dot{\varphi}_s - KS_w(\varphi_t - \varphi_s) - CS_w(\dot{\varphi}_t - \dot{\varphi}_s) \\
&+ m_l Z\left(\dot{v}_s + u_s\dot{\psi}_s - Y\dot{\varphi}_s{}^2 - Y\dot{\psi}_s{}^2 + Z\ddot{\varphi}_s + X\ddot{\psi}_s\right) \\
&+ m_l Y\left(Z\dot{\varphi}_s{}^2 + X\dot{\varphi}_s\dot{\psi}_s + Y\ddot{\varphi}_s\right) + m_l g(Z\sin(\varphi_s) + Y) - M_B \\
&= \left[\ddot{\varphi}_s \quad m_{ss}(\dot{v}_s + u_s\dot{\psi}_s) - gh_s\sin(\varphi_s)\right]\begin{bmatrix} a_3 \\ a_4 \end{bmatrix}
\end{aligned}
\tag{7.111}
$$

7.4.2.3 Active steering system parameter estimation

Given Eqs. (7.66)–(7.68):

$$\begin{bmatrix} m_t+m_s+M_h & 0 & 0 \\ M_hX & M_h(X^2-Y^2) & M_h(X^2-Y^2) \\ M_hX & M_h(X^2-Y^2+X) & M_h(X^2-Y^2+X) \end{bmatrix} \begin{bmatrix} \dot{v}_t \\ \ddot{\psi}_t \\ \ddot{\Gamma} \end{bmatrix}$$

$$+ \begin{bmatrix} 0 & -(m_s+M_h)\left(L_{ct}+L_{fs}\right) & -(m_s+M_h)L_{fs} \\ -(m_s+M_h)\left(L_{ct}+L_{fs}\right) & I_{zz_t}+I_{zz_s}+I_{zzl}+(m_s+M_h)\left(L_{ct}+L_{fs}\right)^2 & I_{zz_s}+I_{zzl}-M_hXL_{ct}+(m_s+M_h)L_{fs}\left(L_{ct}+L_{fs}\right) \\ -(m_s+M_h)L_{fs} & -M_hX\left(L_{ct}+L_{fs}\right)+(m_s+M_h)\left(L_{ct}+L_{fs}\right)L_{fs} & \left(I_{zz_s}+I_{zzl}\right)-M_hXL_{fs}+(m_s+M_h)L_{fs}^2 \end{bmatrix} \begin{bmatrix} \dot{v}_t \\ \ddot{\psi}_t \\ \ddot{\Gamma} \end{bmatrix}$$

$$+ \begin{bmatrix} m_t+m_s+M_h \\ M_hX \\ M_hX \end{bmatrix} u_t\dot{\psi}_t + \begin{bmatrix} 0 \\ -(m_s+M_h)\left(L_{ct}+L_{fs}\right) \\ -(m_s+M_h)L_{fs} \end{bmatrix} u_t\dot{\psi}_t = U \tag{7.112}$$

The seven parameters of the active steering system that have uncertainties are;

$$\begin{aligned} a_1 &= L_{ct}+L_{fs} \\ a_2 &= L_{fs} \\ a_3 &= I_{zzt} \\ a_4 &= I_{zzs}+I_{zl} \\ a_5 &= \left(L_{ct}+L_{fs}\right)^2 \\ a_6 &= L_{fs}\left(L_{ct}+L_{fs}\right) \\ a_7 &= L_{fs}^2 \end{aligned} \tag{7.113}$$

Now

$$Y = \begin{bmatrix} -(m_s+M_h)\ddot{\psi}_t & -(m_s+M_h)\ddot{\Gamma} & 0 & 0 & 0 & 0 & 0 \\ -(m_s+M_h)\dot{v}_t & 0 & \ddot{\psi}_t & \ddot{\psi}_t+\ddot{\Gamma} & (m_s+M_h)\ddot{\psi}_t & -M_hX\ddot{\Gamma}+(m_s+M_h)\ddot{\Gamma} & 0 \\ -(m_s+M_h)u_t\dot{\psi}_t & & & & & & \\ -M_hX\ddot{\psi}_t & -(m_s+M_h)\dot{v}_t & 0 & \ddot{\psi}_t+\ddot{\Gamma} & 0 & (m_s+M_h)\ddot{\psi}_t & (m_s+M_h)\ddot{\Gamma} \\ & -(m_s+M_h)u_t\dot{\psi}_t & & & & & \end{bmatrix}$$

$$w = \begin{bmatrix} -(m_s+M_h)\ddot{\psi}_t & -(m_s+M_h)\ddot{\Gamma} & 0 & 0 & 0 & 0 & 0 \\ -(m_s+M_h)\dot{v}_t & 0 & \ddot{\psi}_t & \ddot{\psi}_t+\ddot{\Gamma} & (m_s+M_h)\ddot{\psi}_t & -M_hX\ddot{\Gamma}+(m_s+M_h)\ddot{\Gamma} & 0 \\ -(m_s+M_h)u_t\dot{\psi}_t & & & & & & \\ -M_hX\ddot{\psi}_t & -(m_s+M_h)\dot{v}_t & 0 & \ddot{\psi}_t+\ddot{\Gamma} & 0 & (m_s+M_h)\ddot{\psi}_t & (m_s+M_h)\ddot{\Gamma} \\ & -(m_s+M_h)u_t\dot{\psi}_t & & & & & \end{bmatrix}$$

$$a = \begin{bmatrix} a_1 \\ a_2 \\ a_3 \\ a_4 \\ a_5 \\ a_6 \\ a_7 \end{bmatrix} \tag{7.114}$$

In the presented diagram in Fig. 7.21, the control system's uncertain parameters are identified using adaptive control. The estimation process for the active steering and active roll subsystems is performed using the least-squares algorithm. Parameters such as the distance between the tractor mass center and the joint, the distance between the semitrailer mass center and the joint, and the moments of inertia of the tractor and semitrailer units about the vertical axis are estimated for the active steering subsystem. Besides, the height

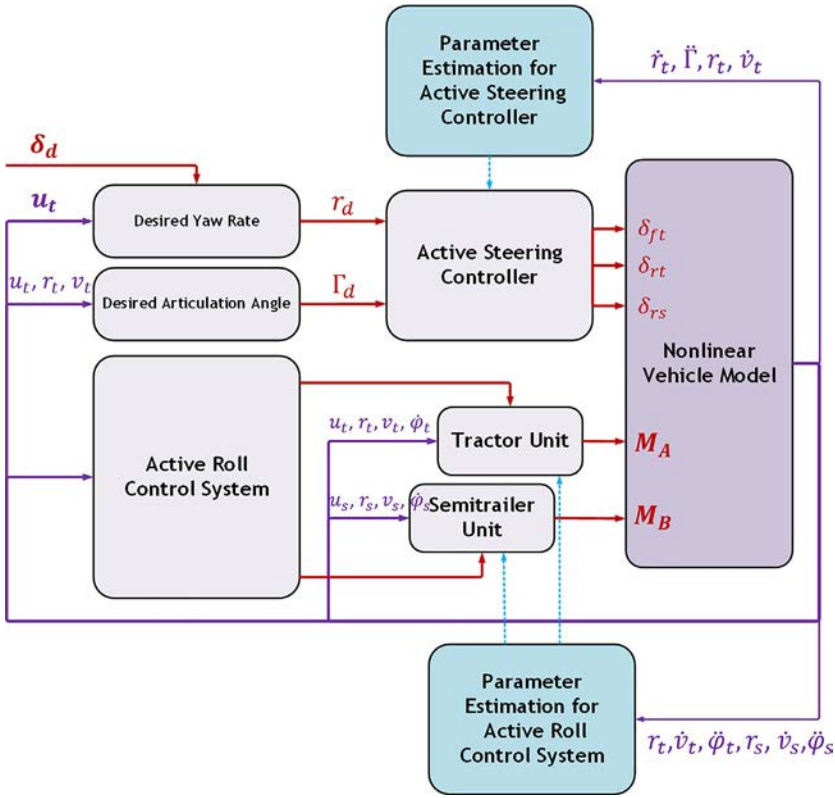

Fig. 7.21 Hybrid adaptive robust control system diagram.

Table 7.3 Sensors used in the adaptive robust control system.

Sensor	Sensor type	Measured variable	Sensor dynamics	Manufacturer
Angular Rate Gyro (SAG, DAG, TAG)	KCD16008 KCD16922	Yaw rate, roll angle rate Articulation angle rate	$T_s(s)=\frac{\omega_n^2}{s^2+2\xi\omega_n s+\omega_n^2}$ $T_a(s)=\frac{\omega_n}{s+\omega_n}$	Kistler
Wheel Speed Sensor	CWPTA	Longitudinal speed	$T_s(s)=\frac{\omega_n^2}{s^2+2\xi\omega_n s+\omega_n^2}$	Kistler
Optical Sensor (SFII-P)	CSF2A	Longitudinal speed, lateral speed, yaw angle, and roll angle	$T_s(s)=\frac{\omega_n^2}{s^2+2\xi\omega_n s+\omega_n^2}$	Kistler
Triaxial Sensors	8395A2D0	Lateral acceleration	$T_s(s)=\frac{\omega_n^2}{s^2+2\xi\omega_n s+\omega_n^2}$	Kistler

of the mass centers of the tractor and semitrailer units from the ground and the moments of inertia of the tractor and semitrailer units about the longitudinal axis are estimated for the active roll subsystem. Sensors are also available to measure each of the state variables used in the robust adaptive control system. The type of sensors used and their dynamics are presented separately in Table 7.3.

7.4.2.4 Performance evaluation of the adaptive robust control system

In this section, the adaptive robust control system's performance in the previous section is evaluated for standard maneuvers under different road conditions and various filling volumes. As shown in the diagram of Fig. 7.21, the hybrid control system consists of the active steering subsystem and the active roll subsystem, in which the uncertain parameters are identified using the estimation algorithm and used in the control law. Moreover, the state variables used in the adaptive robust control system are measured using sensors, and the dynamic model of each of these sensors is shown in Table 7.3 using a transfer function.

Fishhook maneuver

In this analysis, the steering input and road friction condition are the same as in Section 7.4.1.1 and Fig. 7.16.

In this section, the adaptive sliding mode control performance is evaluated for the maneuver performed in the previous section. Figs. 7.22–7.26

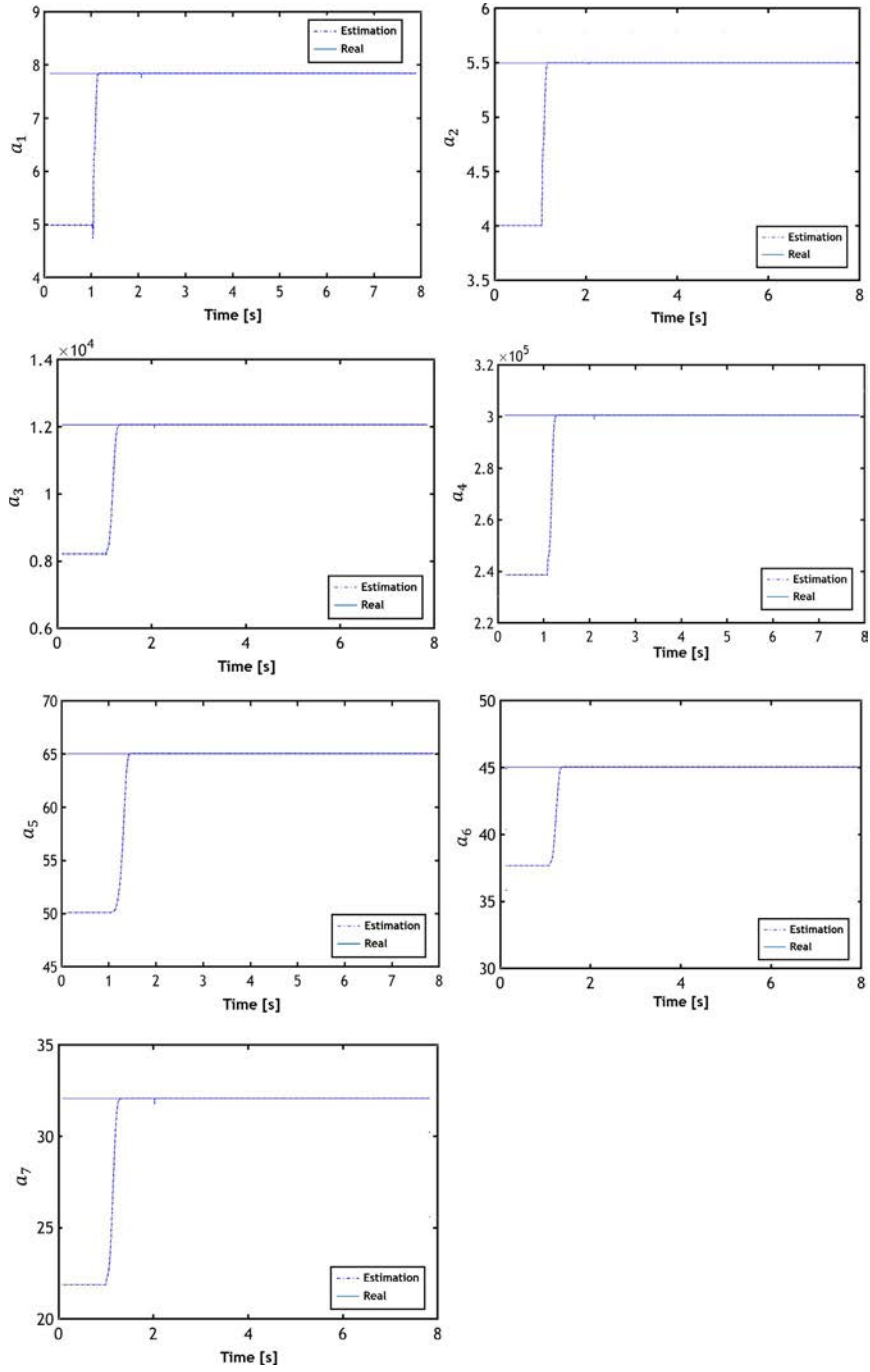

Fig. 7.22 Parameter estimation.

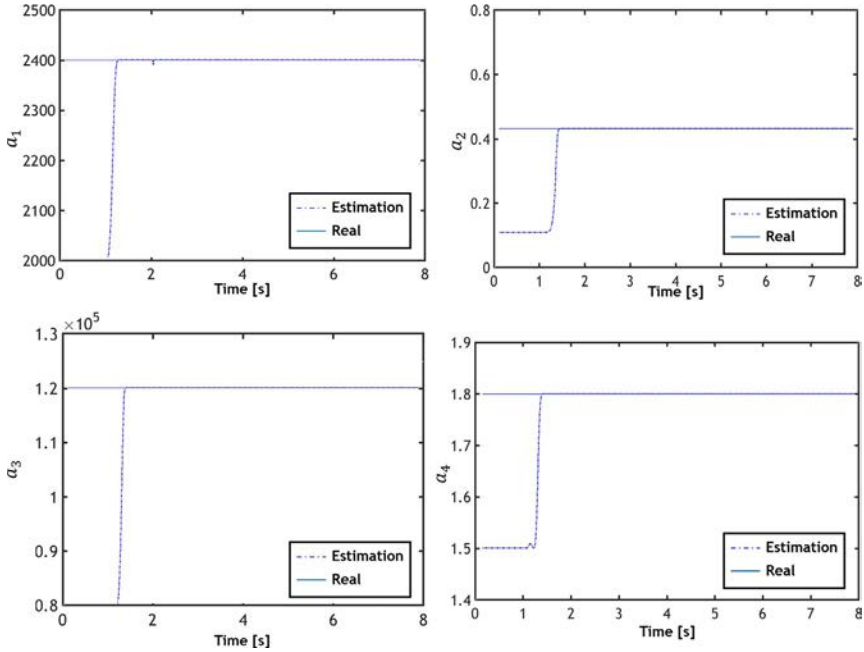

Fig. 7.23 Parameter estimation.

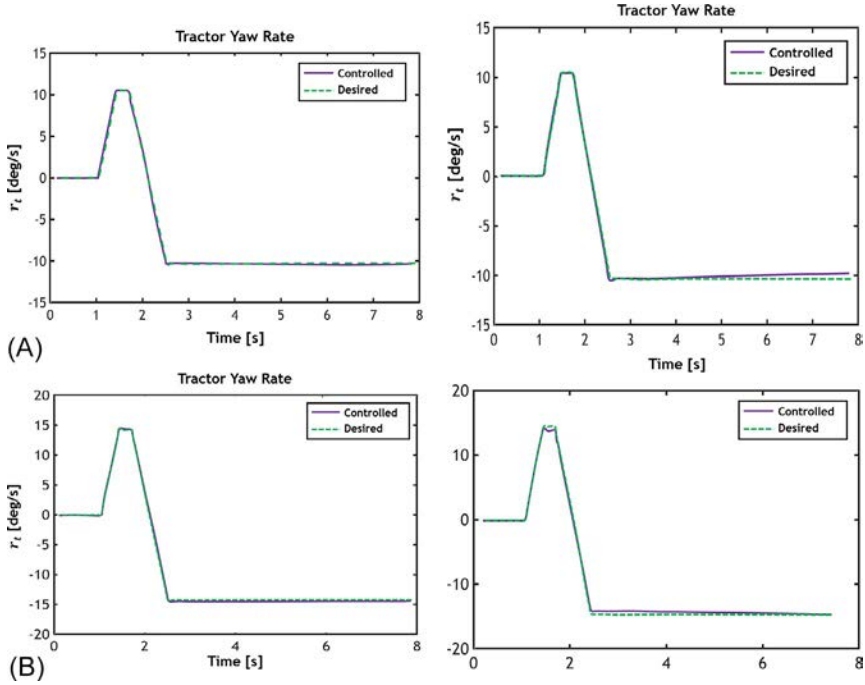

Fig. 7.24 Yaw rate, (A) 50% filling volume, (B) 80% filling volume.

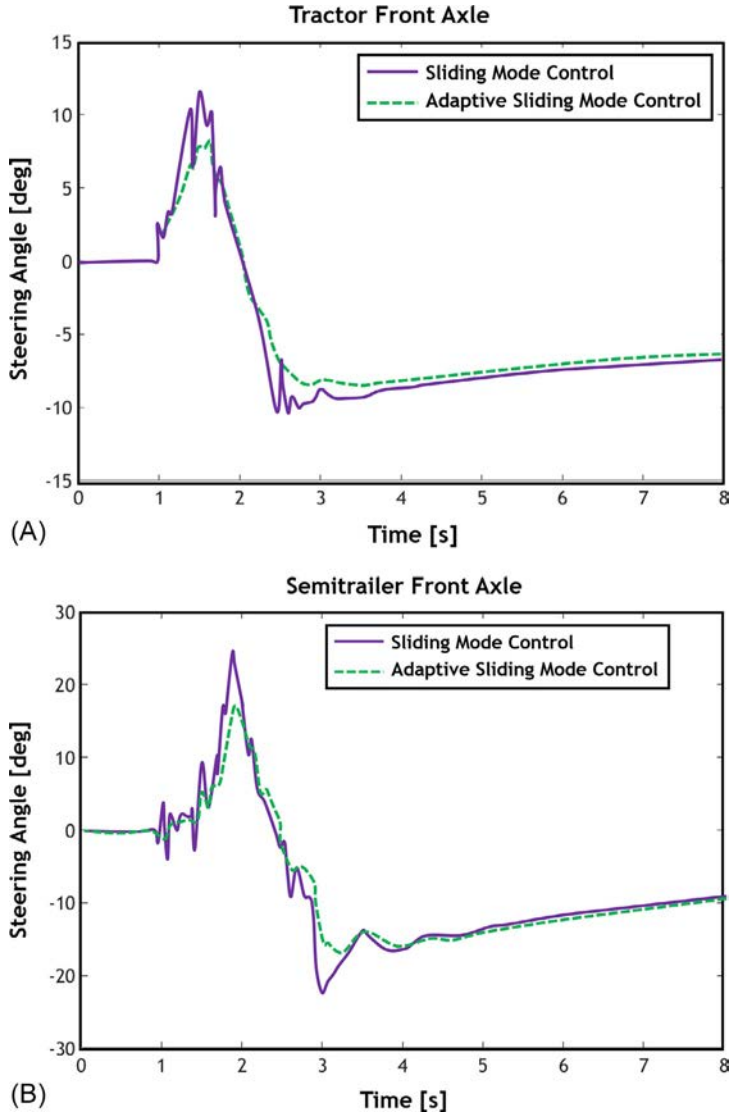

Fig. 7.25 Control inputs (A) tractor front axle (B) semitrailer axle.

indicate the results of estimating the parameters, namely the tractor's yaw rate, the control effort, and the roll angles of the tractor and semitrailer units.

Active steering system parameter estimation

See Fig. 7.23.

Active roll system parameter estimation (see Fig. 7.24) In this section, the two control systems' performances in tracing the controlled state

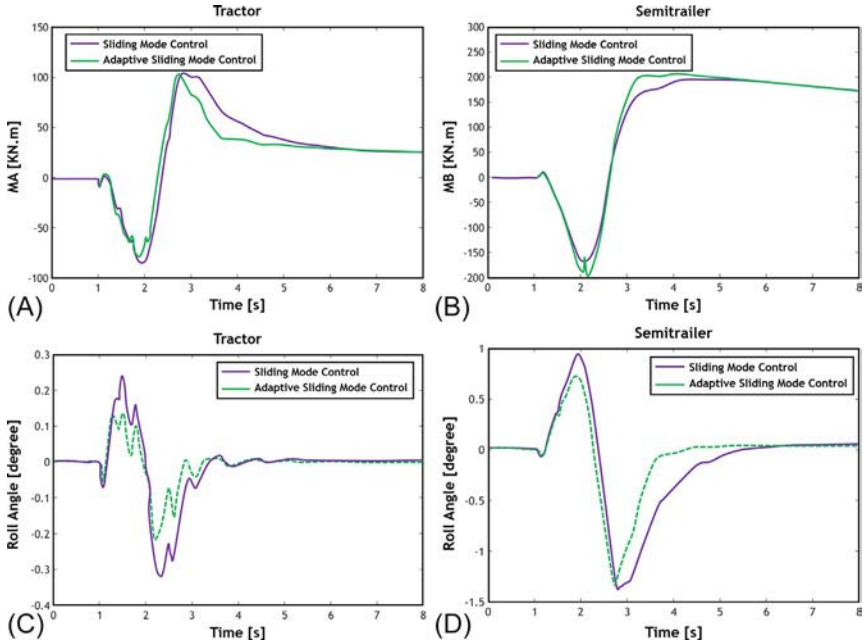

Fig. 7.26 (A) Control effort of the tractor unit, (B) control effort of the trailer unit, (C) roll angle of the tractor unit, (D) roll angle of the semitrailer unit.

variables are compared. Given that the results related to the performances of the two control systems for the articulation angle and lateral velocity of the tractor unit are almost identical and that the largest difference was observed for the tractor unit's yaw rate, the results of this last state variable are compared. The adaptive sliding mode controller exhibits good performance in tracing the desired yaw rate for both filling volumes based on the simulation results. According to Fig. 7.24, both controllers perform well in tracing the tractor's desired yaw rate in the transient mode. However, the tractor's yaw rate deviates from the desired value after 5 s in the steady-state mode and for a 50% filling volume. For an 80% filling volume, this deviation is remarkable from 1.5 s to 1.8 s and from 2.5 s to 5.5 s. On the other hand, the tractor's yaw rate traces the desired value well for both steady-state and transient modes and both filling volumes when the adaptive sliding mode controller is utilized.

The control inputs for the robust control and adaptive robust control methods are compared in Fig. 7.25. As shown in the figure, for robust adaptive control, the control effort has decreased in the first and second peaks, and the curve representing the control angles is smoother for both axles compared to that for the robust control method. For example, the tractor

unit's steering angle of the front axle decreases by 35% and 22% at the first and second peaks, respectively.

The adaptive robust control system results for the control effort and roll angles of the tractor and semitrailer units are displayed in Fig. 7.26. According to Fig. 7.26, the tractor unit's control effort is considerably lower for adaptive control than for robust control. Still, the semitrailer unit's control moment has increased by 14% for adaptive control compared to robust control. Besides, the roll angle results show that despite the increase in the control effort for the semitrailer unit, the peak roll angle for both units has decreased remarkably, and the settling time for the tractor unit has reached 3.8 s.

7.5 Conclusion

Due to changes in the velocity and impacts from the road, the liquid inside the tanker moves, resulting in sloshing. This factor causes mutual interaction between the liquid and the vehicle, which strongly affects the dynamic roll responses of the liquid-carrying articulated vehicle. The liquid motion inside the tank depends on tank geometry, liquid height, excitation frequency, and vehicle maneuver type. The forces and moments resulting from the pressure distribution on the tank wall will significantly affect both the tank and the overall structure, changing the liquid's motion inside the tank. These liquid motions influence the stability and dynamic system performance. Hence, measures must be taken in these systems to minimize these effects and optimize the system. A review of the literature on liquid-carrying vehicles shows that the attempts to investigate the stability and to improve the dynamics of these vehicles mainly involve selecting and optimally designing liquid-carrying tanks, using lateral plates to restrict the liquid motion inside the tank, and the like. Also, only a few works have improved the lateral motion of the vehicle using control systems. For this reason, the present research attempts to design an adaptive robust control system for improving the dynamic performance of the vehicle at various speeds and various road conditions by studying the weaknesses present in the literature and considering the operational modes of an articulated vehicle. The results of this research are as follows:

- First, a 16-DOF dynamic model of an articulated vehicle was simulated. Then, this model was validated using the TruckSim software for standard maneuvers. Subsequently, the dynamic interaction between the liquid and the vehicle was investigated by using a pseudodynamic

method for modeling the liquid inside the tank and a nonlinear dynamic model for the articulated vehicle.

- Studies show that the tank's liquid sloshing significantly affects the tractor and semitrailer units' roll angles and the lateral-load transfer ratio. As a result, a considerable increase in both units' roll angles and the lateral-load transfer ratio is observed compared to articulated vehicles with rigid loads. Moreover, an increase in the filling volume increases the roll angle, lateral load transfer, and forces and moment exerted on the tank wall and decreases the lateral displacement of the liquid mass center. The conducted stability analysis shows that an increase in the distance between the mass center of the tractor unit and the front axle leads to tractor oversteer and, hence, jackknifing. Besides, higher vehicle instability is observed with an increase in the filling volume. Moreover, a rise in the tires' lateral stiffness leads to understeer in the liquid-carrying articulated vehicle and an increase in its stability.
- Given the increase in the rollover probability due to sloshing in the tank and an increase in the lateral load transfer in this vehicle, an active roll control system was proposed for controlling the roll angles of the tractor and semitrailer units. Furthermore, an active steering control system was designed to improve maneuverability and prevent the liquid-carrying articulated vehicle from jackknifing. In the active steering controller, the tractor's yaw rate, the lateral velocity of the tractor, and the articulation angle are the state variables that are controlled and the desired values of which must be traced.
- In order to design the active steering control system, a 3-DOF model of the liquid-carrying articulated vehicle was developed, and the control inputs were derived according to this model. Moreover, both control systems were designed based on the sliding mode control method.
- In order to compensate for the weaknesses present in the robust controller, an estimation algorithm was used to identify the parameters that change during the driving process and have uncertainties. The advantages of adaptive robust control systems include the smoothness of the control effort curve and its ability to trace the controlled state variables under critical conditions when the robust controller fails.
- The performance of the adaptive robust control system was evaluated under critical conditions. Under these conditions, the control system improves the dynamic performance during critical maneuvers involving increased longitudinal speed and reduced road friction coefficient by tracing the controlled state variables' desired values.

References

[1] S. Kharrazi, Steering Based Lateral Performance Control of Long Heavy Vehicle Combinations (Ph.D. thesis), Department of Applied Mechanics, Chalmers University of Technology, 2012.

[2] J. Woodrooffe, L. Ash, Economic Efficiency of Long Combination Transport Vehicles in Alberta, Woodrooffe & Associates, Report, 2001.

[3] K.L. Campbell, K.P. Sullivan, Heavy truck cab safety study, in: Proceedings of the 35th Stapp Car Crash Conference, 1991, pp. 199–225.

[4] Rules for the Assessment of Potential Performance-Based Standards. Discussion Paper, National Transport Commission (NTC), Australia, 2008.

[5] C. MacAdam, M. Hagan, P. Fancher, C. Winkler, R. Ervin, J. Zhou, S. Bogard, Rearward Amplification Suppression, University of Michigan Transportation Research Institute, Report UMTRI-2000-47, 2000.

[6] A. Hac, Stability and Control Consideration of Vehicle-Trailer Combination, SAE technical paper, 2008-01-1228, 2008.

[7] A. Goodarzi, An optimized braking force distribution strategy for articulated heavy vehicles, Veh. Syst. Dyn. 46 (2008) 849–865.

[8] C. Bechtold James, Vehicle Stability and 102 inches, Modern Bulk Transporter, 1983, pp. 65–69.

[9] L. Strandberg, Lateral Stability of Road Tankers, National Road &Traffic Research Institute Report 138A, Sweden, 1978.

[10] C. Winkler, Rollover of Heavy Commercial Vehicles, Final Report, vol. 31, No. 4, University of Michigan Transportation Research Institute, 2000.

[11] X.D. Kang, Optimal Tank Design and Directional Dynamic Analysis of Liquid Cargo Vehicles Under Steering and Braking (Ph.D. thesis), Department of Mechanical and Industrial Engineering, Concordia University, 2001.

[12] G. Mantriota, Directional stability of articulated tank vehicles: a simplified model, Int. J. Veh. Des. 10 (12) (2003) l44–165.

[13] G. Yan, Liquid Slosh and Its Influence on Braking and Roll Responses of Partly Filled Tank Vehicles (Ph.D. thesis), Concordia University, 2008.

[14] X. Zheng, X. Li, Y. Ren, Y. Wang, J. Ma, Effects of transverse baffle design on reducing liquid sloshing in partially filled tank vehicles, Math. Probl. Eng. 2013 (2013) Article ID 130570, https://doi.org/10.1155/2013/130570.

[15] S. Azadi, A. Jafari, M. Samadian, Effect of parameters on roll dynamic response of an articulated vehicle carrying liquids, J. Mech. Sci. Technol. 9 (2014) 837–848.

[16] M.A. Saeedi, R. Kazemi, S. Azadi, Liquid sloshing effect analysis on lateral dynamics of an articulated vehicle carrying liquid for various filled volumes, Int. J. Eng. 28 (11) (2015) 1671–1679.

[17] H. Dugoff, C. Fancher, L. Segel, An Analysis of Tire Traction Properties and Their Influence on Vehicle Dynamic Performance, SAE paper 700377, 1970.

[18] Mechanical Simulation Corporation (MSC), TruckSim 8.0 Reference Manual, 1999.

[19] S.H. Tabatabaee, R. Kazemi, S. Azadi, Tractor Semi-Trailer Integrated Control System for Lateral Stability and Improvement of Maneuverability (Ph.D. thesis), KNT University, Mechanical Engineering Department, 2013.

[20] M.K. Salaani, The application of understeer gradient in stability analysis of articulated vehicles, Int. J. Heavy Veh. Syst. 16 (1) (2009) 3–25.

[21] S. Inagaki, I. Kshiro, M. Yamamoto, Analysis on vehicle stability in critical cornering using phase-plane method, in: Proceedings of the International Symposium on Advanced Vehicle Control, 1994.

[22] B.L. Boada, M.J.L. Boada, V. Dfaz, Fuzzy-logic applied to yaw moment control for vehicle stability, Veh. Syst. Dyn. 43 (10) (2005) 753–770.

[23] M.A. Saeedi, R. Kazemi, S. Azadi, Improvement in the rollover stability of a liquid-carrying articulated vehicle via a new robust controller, Proc. Inst. Mech. Eng. D J. Automob. Eng. (2016), https://doi.org/10.1177/0954407016639204.
[24] M.A. Saeedi, R. Kazemi, S. Azadi, Analysis of roll control system to eliminate liquid sloshing effect on lateral stability of an articulated vehicle carrying liquid, Int. J. Eng. 29 (3) (2016) 386–393.
[25] M.A. Saeedi, R. Kazemi, S. Azadi, A new robust controller to improve the lateral dynamic of an articulated vehicle carrying liquid, Proc. Inst. Mech. Eng. K J. Multibody Dyn. (2017), https://doi.org/10.1177/1464419316663028.
[26] K.J. Astrom, B. Wittenmark, Adaptive Control, Addison-Wesley, 1995.

CHAPTER 8

Directional stability analysis and integrated control of articulated heavy vehicles

8.1 Introduction

The popularity and application of articulated heavy vehicles (AHVs) are growing rapidly because of their great commercial benefits. The majority of AHVs are commonly used for the transportation of goods as well as materials due to their cost effectiveness in both labor requirements and fuel consumption. Fig. 8.1 shows a view of an AHV on the road as a commercial vehicle for moving more payloads with a lower tare weight than a single unit. According to research conducted in Sweden, 15% of fuel costs, 23% of human costs, and 32% of travel have been reduced by the use of articulated heavy vehicles [1].

A fundamental understanding of the stability and control concepts of articulated heavy vehicles is required to comprehend the effects of the various layouts and parameters. This knowledge can be used to quickly assess risks, critical situations, and critical vehicle configurations when evaluating new stability control functions. The instability of AHVs is considered a

Fig. 8.1 View of an articulated heavy vehicle on the road as a commercial vehicle.

Vehicle Dynamics and Control
https://doi.org/10.1016/B978-0-323-85659-1.00004-5

danger to road transportation due to the high moment of inertia and mass because the accidents caused by this type of vehicle have more severe losses than passenger cars. Therefore, it is essential to apply control devices to increase stability and improve the handling of heavy vehicles. As a result, using active safety systems plays a vital role in heavy vehicles. These systems help drivers in difficult driving situations, and they are also accessible to control vehicle motion. With the increasing growth as well as the deployment of technologies in the automotive industry, the role of the driver has changed dramatically. In other words, an expert system consisting of a number of mechatronic units will be responsible for controlling the vehicle. The basic idea is to turn the vehicle handling behavior to be closed to linear vehicle characteristics (that the driver is familiar with) and to restrain the vehicle lateral dynamics to be within a stable region in aggressive maneuvers. When it comes to the approach of this chapter on articulated vehicles, the controlling objectives take another form. For example, following the trajectory of a tractor by the trailer unit is one of the important/cardinal control targets in this area, where various systems such as active suspension, active steering, and active braking have all been used to improve the lateral dynamics [2].

The two popular approaches in this field, which are applied to all vehicles in different classes (i.e., heavy vehicles as well as passenger cars), include using the steering angle of wheels and applying differential braking forces on the selected vehicle tires. The systems that control the vehicle dynamics by changing the steering angle are referred to as active front steering (AFS) or steering angle (four-wheel steering).

In another type, the differential braking method, the vehicle dynamics behavior is modified by a yaw moment generated by the asymmetric distribution of the braking forces on the selected tires. The most famous title used for this type of system is the electronic stability program (ESP), which was first developed by the Bosch Company in 1995 for Mercedes-Benz. In maneuvers with high lateral acceleration, the quality of the active steering system is greatly reduced due to the nonlinear nature of the tires because these systems are not able to provide enough lateral force to maintain the vehicle in turn (and the physical limit of adhesion between the tires and the road is reached). In other words, the active steering system could not properly control the vehicle in aggressive maneuvers, and its performance has been limited to rather low lateral accelerations in most cases. On the other hand, the active braking system could effectively control the vehicle lateral dynamics in both the linear and nonlinear regions of the tire. It is common to use this subsystem within boundary conditions because

continuous braking accelerates the tire wear process and also reduces the vehicle velocity, which makes the driver feel uncomfortable.

In light of the above, an intelligent method of control system design is developed in a way that takes the proper performance of each braking and steering subsystem into account and applies them in such a way that the minimum interference and maximum efficiency are reached.

Researchers have considered two types of approaches in this field. In the first approach, the active steering system and active braking system are designed separately for two independent control targets, and then the performance of these subsystems is regulated based on the condition by a supervisor system. This approach is called bottom-up integration [3–6]. In the second approach, a system is designed as a multivariable controller, and the control variables are adjusted simultaneously. To implement this top-down method in the vehicle framework, several control theories have been developed, such as optimal control [7–10], predictive control [11], and robust control [12].

8.2 Modeling of an articulated heavy vehicle

According to the definition, modeling helps researchers analyze a system in a systematic manner and predict its behavior. In this section, a complete nonlinear model will be presented for articulated vehicles based on the method given by the automotive scientist Masato Abe to model the roll motion in vehicles [13]. As briefly mentioned upon introducing articulated heavy vehicles, the given vehicle consists of two parts, the tractor and semitrailer, as shown in Fig. 8.2 [14]. The presented model of the vehicle is a complete

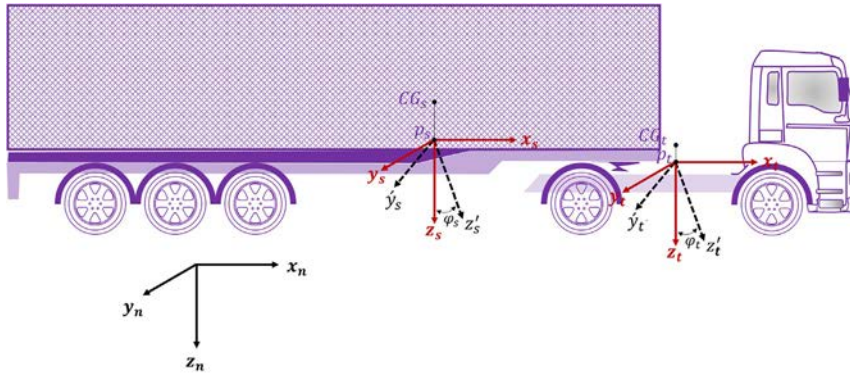

Fig. 8.2 Sixteen degree-of-freedom model for the articulated vehicle.

nonlinear model, namely the 16 degree-of-freedom model. The degree-of-freedom considered for the dynamic model includes the longitudinal and lateral motion of the tractor unit, the yaw motion of the tractor unit around the z_t axis, and the roll motion of this unit around the roll axis of the tractor. For the semitrailer part, the yaw and roll motion are also considered independently from the tractor. The remaining 10 degree-of-freedom belong to the wheel rotation. In this method, we assume that the tractor and trailer units have sprung and unsprung masses separately. The tractor unit's sprung mass is the body (cabin), and unsprung masses of this unit include the suspension system, axles, and the front also rear wheels. The semitrailer unit also consists of a body and an unsprung mass, including the total suspension system, axles, and rear wheel masses.

8.2.1 Introducing the applied coordinate systems in modeling

As shown in Fig. 8.2, the coordinate system of $x_n y_n z_n$ is an inertial coordinate. The center of mass of the tractor unit, including the sprung and unsprung masses, is located in the point of CG_t. The point P_t is the intersection of the vertical line passing from CG_t and the roll axis of the tractor unit, which is selected as the origin of the coordinate system $x_n y_n z_n$. The recent coordinate system has been fixed on the tractor unsprung masses. Because of that, it moves in longitudinal and lateral directions and performs the yaw motion without a roll, as given in Eq. (8.1) [14, 15].

$$\begin{bmatrix} i_n \\ j_n \\ k_n \end{bmatrix} = \begin{bmatrix} \cos\psi_t & -\sin\psi_t & 0 \\ \sin\psi_t & \cos\psi_t & 0 \\ 0 & 0 & 1 \end{bmatrix} \begin{bmatrix} i_t \\ j_t \\ k_t \end{bmatrix} \tag{8.1}$$

where ψ_t is the rotation of the tractor longitudinal axis over the x_n axis of the inertial coordinate system. The coordinate system $x_t' y_t' z_t'$ is fixed on the tractor body and the point P_t is its origin. This coordinate system also has additional roll motion. By assuming that the roll angle (φ_t) is small, the angular velocities of two coordinate systems, $x_t y_t z_t$ and $x_t' y_t' z_t'$, are measured as the following:

$$\omega_t = \dot{\psi}_t k_t \tag{8.2}$$

$$\omega'_t = \dot{\varphi}_t i'_t + \dot{\psi}_t k'_t \tag{8.3}$$

Similar to the tractor unit, in the trailer unit, the point P_s as the origin of the coordinate system $x_s y_s z_s$ is the intersection of the vertical line passing from CG_s and the roll axis. The above coordinate system is fixed on the

trailer unsprung mass and has a rotation about the coordinate system $x_t y_t z_t$, which equals the articulation angle between the tractor and trailer (Γ) units. So, we could simply infer:

$$\begin{bmatrix} i_t \\ j_t \\ k_t \end{bmatrix} = \begin{bmatrix} \cos\Gamma & -\sin\Gamma & 0 \\ \sin\Gamma & \cos\Gamma & 0 \\ 0 & 0 & 1 \end{bmatrix} \begin{bmatrix} i_s \\ j_s \\ k_s \end{bmatrix} \tag{8.4}$$

Assuming the angular rotation of the coordinate system $x_t y_t z_t$ as ψ_s, the articulation angle is calculated as Eq. (8.5):

$$\Gamma = \psi_s - \psi_t \tag{8.5}$$

Similar to the tractor unit, the coordinate system $x_s' y_s' z_s'$ is addressed with the origin P_s. The given coordinate system with the trailer body also performs the roll motion (φ_s). The angular velocities of both $x_s y_s z_s$ and $x_s' y_s' z_s'$ are:

$$\omega_s = \dot{\psi}_s k_s \tag{8.6}$$

$$\omega'_s = \dot{\varphi}_s i'_t + \dot{\psi}_s k'_s \tag{8.7}$$

8.2.2 Calculating the velocity and acceleration of the tractor and semitrailer center of masses

8.2.2.1 Tractor unit

Fig. 8.3 represents the tractor unit consisting of the body sprung mass and the unsprung masses. The points S_t, t_{uf}, and t_{ur} are the center of mass of the tractor body, the front sprung mass, and the rear sprung mass, respectively, where the velocity and acceleration of these points are presented.

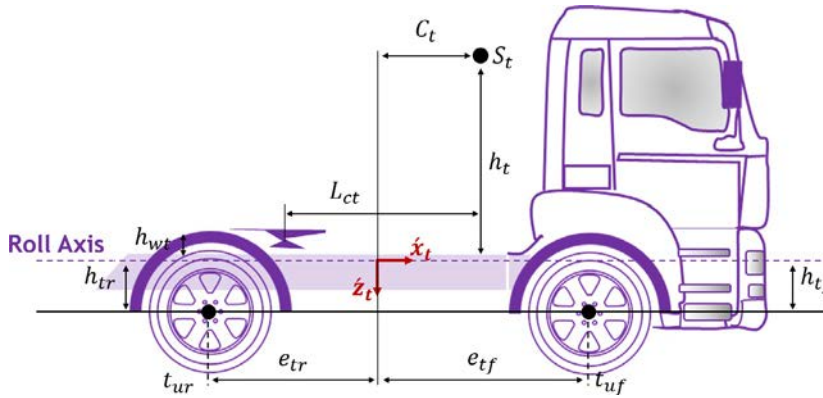

Fig. 8.3 Tractor unit in the articulated heavy vehicle.

The center of mass velocity and acceleration of the tractor body are obtained as:

$$V_{S_t} = u_t i'_t + \left(v_t + c_t\dot{\psi}_t + h_t\dot{\varphi}_t\right)j'_t \tag{8.8}$$

$$a_{s_t} = \left(\dot{u}_t - v_t\dot{\psi}_t - c_t\dot{\psi}_t^2 - h_t\dot{\varphi}_t\dot{\psi}_t\right)i'_t + \left(u_t\dot{\psi}_t + \dot{v}_t + c_t\ddot{\psi}_t + h_t\ddot{\varphi}_t\right)j'_t \tag{8.9}$$

where u_t and v_t represent the longitudinal and lateral velocity of point P_t, respectively. The velocity and acceleration of the front sprung mass are calculated as:

$$V_{t_{uf}} = u_t i_t + \left(v_t + e_{ft}\dot{\psi}_t\right)j_t \tag{8.10}$$

$$a_{t_{uf}} = \left(\dot{u}_t - v_t\dot{\psi}_t - e_{tf}\dot{\psi}_t^2\right)i_t + \left(u_t\dot{\psi}_t + \dot{v}_t + e_{tf}\ddot{\psi}_t\right)j_t \tag{8.11}$$

Similarly, the velocity and acceleration of the rear sprung mass are given as:

$$V_{t_{ur}} = u_t i_t + \left(v_t - e_{tr}\dot{\psi}_t\right)j_t \tag{8.12}$$

$$a_{t_{ur}} = \left(\dot{u}_t - v_t\dot{\psi}_t + e_{tr}\dot{\psi}_t^2\right)i_t + \left(u_t\dot{\psi}_t + \dot{v}_t - e_{tr}\ddot{\psi}_t\right)j_t \tag{8.13}$$

8.2.2.2 Semitrailer unit

Fig. 8.4 shows the trailer schematic. Furthermore, points S_s and s_{ur} indicate the center of mass of the trailer body and its rear sprung mass, respectively, for which the velocity and acceleration are calculated as in the previous section.

The velocity and acceleration of point S_s are obtained by Eqs. (8.14) and (8.15).

$$V_{S_s} = u_s i'_s + \left(v_s + c_s\dot{\psi}_s + h_s\dot{\varphi}_s\right)j'_s \tag{8.14}$$

$$a_{S_s} = \left(\dot{u}_s - v_s\dot{\psi}_s - c_s\dot{\psi}_s^2 - h_s\dot{\varphi}_s\dot{\psi}_s\right)i'_s + \left(u_s\dot{\psi}_s + \dot{v}_s + c_s\ddot{\psi}_s + h_s\ddot{\varphi}_s\right)j'_s \tag{8.15}$$

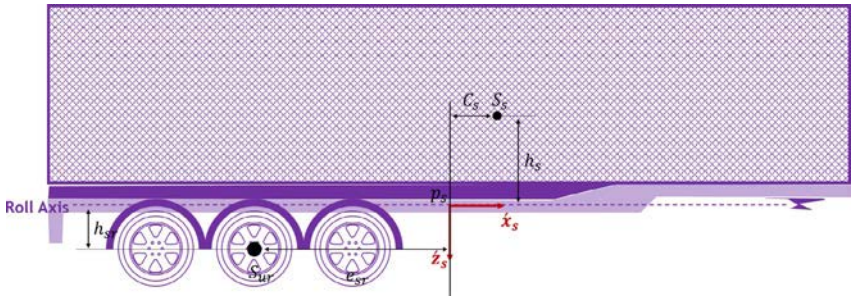

Fig. 8.4 Semitrailer unit in the articulated heavy vehicle.

where u_s and v_s represent the longitudinal and lateral velocity of point P_t, respectively. The velocity and acceleration of point s_{ur} are obtained as:

$$V_{s_{ur}} = u_s i_s + (v_s - e_{sr}\dot{\psi}_s) j_s \tag{8.16}$$

$$a_{s_{ur}} = \left(\dot{u}_s - v_s\dot{\psi}_s + e_{sr}\dot{\psi}_s^2\right) i_s + (u_s\dot{\psi}_s + \dot{v}_s - e_{sr}\ddot{\psi}_s) j_s \tag{8.17}$$

8.2.3 Longitudinal and lateral dynamics motion equations of tractor and trailer units

It is necessary to address the applied forces on the system to present the equations of longitudinal and lateral dynamics. A brief introduction to the forces is given in the following.

8.2.3.1 Tractor unit

As shown in Fig. 8.5, the external forces affecting the vehicle dynamics include the longitudinal and lateral forces applied on the contact patch (i.e., the contact surface between the tire and road) and the constraint forces in the joint.

It is evident that the representation of forces in the direction of x_t and y_t would be as in Eqs. (8.18) and (8.19)

$$F_{xi} = F_{ti}\cos\delta_i - F_{si}\sin\delta_i \tag{8.18}$$

$$F_{yi} = F_{ti}\sin\delta_i + F_{si}\cos\delta_i$$
$$\text{with } i = 1,2,3,4 \tag{8.19}$$

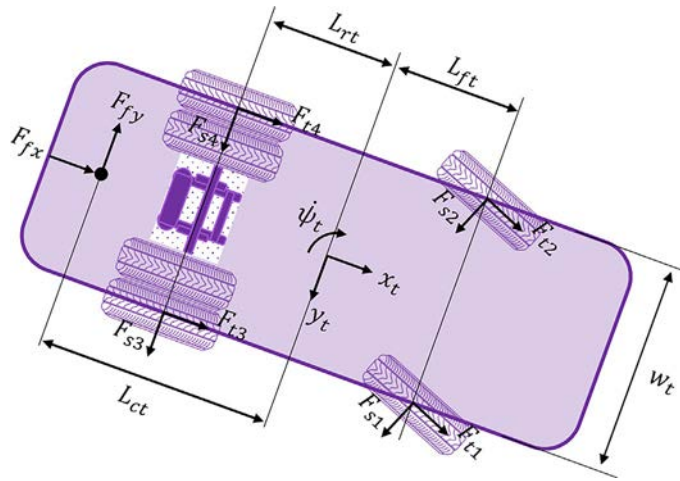

Fig. 8.5 External forces affecting the tractor unit.

where δ_i is the steering angle of the front axle wheels, defined as the steering angle applied by the driver. The sums of the longitudinal (F_{xtt}) and lateral (F_{ytt}) forces of the tractor tires are given by:

$$F_{xtt} = F_{x1} + F_{x2} + F_{x3} + F_{x4} \tag{8.20}$$

$$F_{ytt} = F_{y1} + F_{y2} + F_{y3} + F_{y4} \tag{8.21}$$

Considering mathematical simplification, the longitudinal and lateral dynamics equations of the tractor are obtained as in Eqs. (8.22) and (8.23):

$$m_t(\dot{u}_t - v_t\dot{\psi}_t) - m_{st}h_t\dot{\varphi}_t\dot{\psi}_t = F_{xtt} + F_{fx} \tag{8.22}$$

$$m_t(\dot{v}_t + u_t\dot{\psi}_t) + m_{st}h_t\ddot{\varphi}_t = F_{ytt} - F_{fy} \tag{8.23}$$

here, F_{fx} and F_{fy} represent the articulation forces in the longitudinal and lateral directions, respectively. Also, m_t is the total sprung and unsprung masses and m_{st} indicates the tractor's body mass.

8.2.3.2 Semitrailer unit

Similarly, the equations of longitudinal and lateral dynamics obtained for the semitrailer unit are the same as the tractor unit. Fig. 8.6 shows the forces affecting the semitrailer. In this section, the steering angle $\delta_t(\delta_{5:10})$ for the trailer rear axle wheels, the total longitudinal forces (F_{xss}) of the tractor tires, and the total lateral forces of the tractor tires are given as:

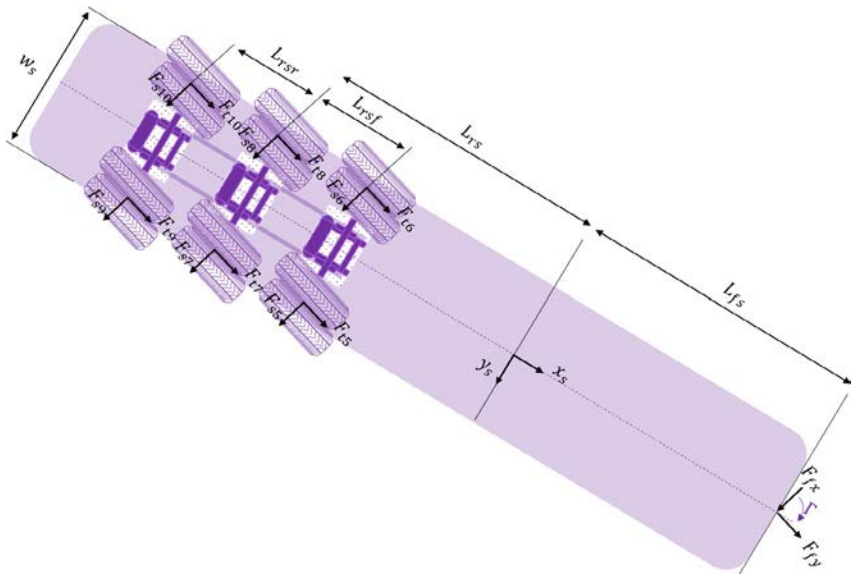

Fig. 8.6 External forces affecting the semitrailer unit.

$$F_{xss} = F_{x5} + F_{x6} + F_{x7} + F_{x8} + F_{x9} + F_{x10} \tag{8.24}$$

$$F_{yss} = F_{y5} + F_{y6} + F_{y7} + F_{y8} + F_{y9} + F_{y10} \tag{8.25}$$

The longitudinal and lateral dynamics equations of the semitrailer are given as:

$$m_s(\dot{u}_s - v_s\dot{\psi}_s) - m_{ss}h_s\dot{\varphi}_s\dot{\psi}_s = F_{xss} - F_{fx}\cos(\Gamma) + F_{fy}\sin(\Gamma) \tag{8.26}$$

$$m_s(\dot{v}_s + u_s\dot{\psi}_s) + m_{ss}h_s\ddot{\varphi}_s = F_{yss} + F_{fx}\sin(\Gamma) + F_{fy}\cos(\Gamma) \tag{8.27}$$

where m_s shows the total sprung and unsprung masses and m_{ss} represents the trailer sprung mass.

8.2.4 Roll and yaw motion equations of tractor and trailer units

8.2.4.1 Tractor unit

Fig. 8.7 shows the free diagram of a tractor unit for calculating the total roll moment.

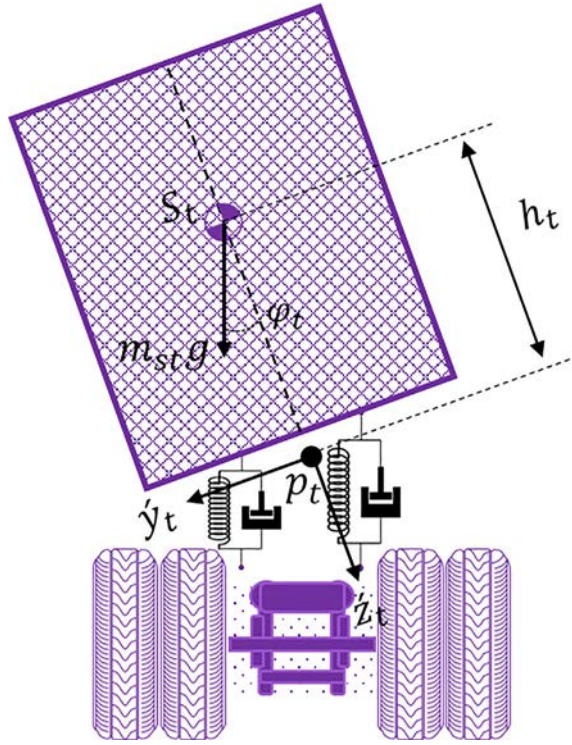

Fig. 8.7 Front view of the tractor unit.

The roll moment of the external forces applied to the tractor unit is obtained by:

$$M_{p_{tsx}} = \underbrace{\left(I_{xx_{st}} + m_{st}h_t^2\right)}_{I_{xx_{pt}}}\ddot{\varphi}_t - \underbrace{\left(I_{xz_{st}} - m_{st}h_t c_t\right)}_{I_{xz_{pt}}}\ddot{\psi}_t + m_{st}h_t\left(u_t\dot{\psi}_t + \dot{v}_t\right) \xrightarrow{\text{yields}} M_{p_{tsx}}$$

$$= I_{xx_{pt}}\ddot{\varphi}_t - I_{xz_{pt}}\ddot{\psi}_t + m_{st}h_t\left(u_t\dot{\psi}_t + \dot{v}_t\right) \tag{8.28}$$

As Fig. 8.7 shows, the roll torques on the tractor unit include the following cases: (a) the roll moment caused by the body mass center motion due to the vehicle rolling; (b) the roll torque caused by the suspension system among sprung and unsprung masses, which could be replaced with a spring and torsion damper; and (c) the transitional roll torque between the tractor and semitrailer modeled as a spring-torsion damper according to the mentioned explanations. As a consequence, the roll torque applied on a tractor unit is obtained by:

$$M_{p_{tsx}} = m_{st}gh_t\sin\varphi_t - KS_t\varphi_t - CS_t\dot{\varphi}_t + KS_w(\varphi_t - \varphi_s) + CS_w(\dot{\varphi}_t - \dot{\varphi}_s) \tag{8.29}$$

where KS_t represents the total torsional stiffness and CS_t is the total torsional damping coefficient of the tractor suspension system. Moreover, KS_w and CS_w indicate the torsional stiffness and coupling torsional damping between the tractor and trailer, respectively. In what follows, the yaw equations of the tractor unit are given. In this section, the equation of the tractor yaw dynamics around the axis z_t passing from point P_t is given for the total sprung and unsprung masses. It is noteworthy that a simple form of the equations could be obtained by considering some remarks, as in Eqs. (8.30) and (8.31).

$$F_{fy}L_{ct} + M_{p_{tz}} = I_{zz_t}\ddot{\psi}_t - I_{xz_{pt}}\ddot{\varphi}_t \tag{8.30}$$

$$M_{p_{tz}} = \left(F_{x2} + F_{x4} - F_{x1} - F_{x3}\right)\frac{w_t}{2} + \left(F_{y1} + F_{y2}\right)L_{ft} - \left(F_{y3} + F_{y4}\right)L_{rt} \tag{8.31}$$

Where $M_{p_{tz}}$ is the yaw torque of the tractor tire forces around axis z_t. Also, I_{zz_t} and $I_{xz_{pt}}$ are calculated as follows:

$$I_{zz_t} = I_{zz_{st}} + I_{zz_{ufl}} + I_{zz_{urt}} + m_{st}c_t^2 + m_{ufl}e_{tf}^2 + m_{urt}e_{tr}^2 \tag{8.32}$$

$$I_{xz_{pt}} = I_{xz_{st}} - m_{st}c_t h_t \tag{8.33}$$

where $I_{zz_{st}}$, $I_{zz_{ufl}}$, $I_{zz_{urt}}$, and $I_{xz_{st}}$ represent the sprung mass moment of inertia around the axis z_{ts}', the moment of inertia around the vertical axis that is

parallel with z_t and passing from the tractor front and rear unsprung masses, and the last one is product inertia moment in $x_{ts}'z_{ts}'$ around point S_t. m_{uft} and m_{urt} are the tractor unit's front and rear sprung masses.

8.2.4.2 Semitrailer unit

Similar to the tractor unit, the roll and yaw dynamics equations of the semitrailer unit are obtained in this section. If we represent the total torque affecting the semitrailer unit around the roll axis by $M_{p_{ssx}}$, the dynamics equation of the semitrailer unit would be obtained by:

$$M_{p_{ssx}} = I_{xx_{ps}}\ddot{\varphi}_s - I_{xz_{ps}}\ddot{\psi}_s + m_{ss}h_s(u_s\dot{\psi}_s + \dot{v}_s) \tag{8.34}$$

where $I_{xx_{ps}}$ is the semitrailer body moment of inertia around axis x_s' and $I_{xz_{ps}}$ is the semitrailer body moment product of inertia in $x_s'z_s'$ around point P_s. The $M_{p_{ssx}}$ applied on the semitrailer is gained as the tractor unit by Eq. (8.35):

$$M_{p_{ssx}} = m_{ss}gh_s\sin\varphi_s - KS_s\varphi_s - CS_s\dot{\varphi}_s - KS_w(\varphi_t - \varphi_s) - CS_w(\dot{\varphi}_t - \dot{\varphi}_s) \tag{8.35}$$

here, KS_s and CS_s are the total torsional stiffness and the total torsional damping for the semitrailer suspension system, respectively. In order to present the yaw dynamics of the semitrailer unit, Eq. (8.36) is given as:

$$\left(F_{fx}\sin\Gamma + F_{fy}\cos\Gamma\right)L_{fs} + M_{p_{sz}} = I_{zz_s}\ddot{\psi}_s - I_{xz_{ps}}\ddot{\varphi}_s \tag{8.36}$$

where I_{zz_s} is the inertia torque of the whole semitrailer unit and $M_{p_{sz}}$ represents the yaw torque originated from/generated through the trailer tires, given by:

$$\begin{aligned} M_{p_{sz}} = {} & \left(F_{x6} + F_{x8} + F_{x10} - F_{x5} - F_{x7} - F_{x9}\right)\frac{w_s}{2} - \left(F_{y5} + F_{y6}\right)\left(L_{rs} - L_{frs}\right) \\ & - \left(F_{y7} + F_{y8}\right)L_{rs} - \left(F_{y5} + F_{y6}\right)\left(L_{rs} + L_{rrs}\right) \end{aligned} \tag{8.37}$$

8.2.5 Articulated vehicle dynamics equations and constraint equations

Eqs. (8.38)–(8.45) represent the eight significant vehicle equation dynamics rewritten as follows:

$$m_t\dot{u}_t = m_t v_t\dot{\psi}_t + m_{st}h_t\dot{\varphi}_t\dot{\psi}_t + F_{xtt} + F_{fx} \tag{8.38}$$

$$m_t\dot{v}_t + m_{st}h_t\ddot{\varphi}_t = -m_t u_t\dot{\psi}_t + F_{ytt} - F_{fy} \tag{8.39}$$

$$I_{zz_t}\ddot{\psi}_t - I_{xz_{pt}}\ddot{\varphi}_t = M_{p_{tz}} + F_{fy}L_{ct} \tag{8.40}$$

$$I_{xx_{pt}}\ddot{\varphi}_t - I_{xz_{pt}}\ddot{\psi}_t + m_{st}h_t\dot{v}_t = M_{p_{tsx}} - m_{st}h_t u_t\dot{\psi}_t \tag{8.41}$$

$$m_s\dot{u}_s = m_s v_s\dot{\psi}_s + m_{ss}h_s\dot{\varphi}_s\dot{\psi}_s + F_{xss} - F_{fx}\cos(\Gamma) + F_{fy}\sin(\Gamma) \tag{8.42}$$

$$m_s\dot{v}_s + m_{ss}h_s\ddot{\varphi}_s = -m_s u_s\dot{\psi}_s + F_{yss} + F_{fx}\sin(\Gamma) + F_{fy}\cos(\Gamma) \tag{8.43}$$

$$I_{zz_s}\ddot{\psi}_s - I_{xz_{ps}}\ddot{\varphi}_s = \left(F_{fx}\sin\Gamma + F_{fy}\cos\Gamma\right)L_{ws} + M_{p_{sz}} \tag{8.44}$$

$$I_{xx_{ps}}\ddot{\varphi}_s - I_{xz_{ps}}\ddot{\psi}_s + m_{ss}h_s\dot{v}_s = M_{p_{ssx}} - m_{ss}h_s u_s\dot{\psi}_s \tag{8.45}$$

The above eight differential equations consist of eight dynamics variables (u_t, v_t, ψ_t, φ_t, u_s, v_s, ψ_s, φ_s) and two conditional forces, F_{fy} and F_{fx}. Therefore, another two equations must be added to the above equations to simulate the vehicle motion where these two equations are obtained due to the existing condition between the tractor and trailer. The velocity of the articulation point could be measured in either of the coordinate systems $x_t'y_t'z_t'$ or $x_s'y_s'z_s'$. By equating these two values, two conditional equations are extracted along the longitudinal and lateral axes, which would simulate the articulated vehicle motion with the eight significant vehicle equations. Two following equations are employed to simulate the vehicle dynamics behavior in addition to the eight above equations.

$$\begin{aligned}&\dot{u}_t - \dot{u}_s\cos\Gamma + \dot{v}_s\sin\Gamma + L_{fs}\ddot{\psi}_s\sin\Gamma + h_{ws}\ddot{\varphi}_s\sin\Gamma\\ &= -\dot{u}_s\Gamma\sin\Gamma - \dot{\Gamma}v_s\cos\Gamma - L_{fs}\dot{\Gamma}\dot{\psi}_s\cos\Gamma - h_{ws}\dot{\Gamma}\dot{\varphi}_s\cos\Gamma\end{aligned} \tag{8.46}$$

$$\begin{aligned}&\dot{v}_t - L_{wt}\ddot{\psi}_t + h_{ct}\ddot{\varphi}_t - \dot{u}_s\sin\Gamma - \dot{v}_s\cos\Gamma - L_{fs}\ddot{\psi}_s\cos\Gamma - h_{ws}\ddot{\varphi}_s\sin\Gamma\\ &= u_s\dot{\Gamma}\cos\Gamma - \dot{\Gamma}v_s\sin\Gamma - L_{fs}\dot{\Gamma}\dot{\psi}_s\sin\Gamma - h_{ws}\dot{\Gamma}\dot{\varphi}_s\sin\Gamma\end{aligned} \tag{8.47}$$

8.2.6 Wheel rotational equations of motion

By neglecting the wheels' vertical motion, a degree of freedom corresponding to each wheel rotation is considered. The dynamics equation of each tire rotation is represented as:

$$\begin{aligned}I_{wi}\dot{\Omega}_i &= Torque_i - F_{ti}R_{wi}\\ &\text{with } i = 1:10\end{aligned} \tag{8.48}$$

where $Torque_i$ shows the torque applied on each wheel, R_{wi} is the tire radius, and I_{wi} is the polar inertia moment for each tire.

8.2.7 Tire normal forces

The effective longitudinal and lateral forces on the tire originate from the contact patch. The tire longitudinal and lateral forces would be established

for vehicle acceleration as well as direction setting. In order to simulate the tire behavior, various models have been presented, such as *Pejka*, *Dugoff*, etc. Each model has its specific features and particular inputs. For example, the inputs of the Magic Formula tire model include tire lateral slip angle, the slip ratio, and the tire normal forces. Generally, the tire normal force is one of the most important parameters in nearly every tire model. Fig. 8.8 shows the free diagram of the articulated vehicle in which the tire longitudinal forces, articulation, and inertia forces are observed in both tractor and trailer units in addition to the normal forces. Fig. 8.9 depicts the lateral and inertia forces along the lateral direction.

After conducting a series of mathematical calculations, finally, six normal forces are computed for tires considering the effect of lateral load transfer under the lateral acceleration of two units, the lateral force established in the articulation, and the transferred lateral load caused by the vehicle roll motion:

$$F_{z1}=\frac{m_t g L_{rt}-m_t a_{tx} h_{ct}-F_{fx} h_f+F_{fz}\left(L_{rt}-L_{ct}\right)}{2\left(L_{ft}+L_{rt}\right)}-\frac{m_t a_{ty} h_{ct} L_{rt}}{W_t\left(L_{ft}+L_{rt}\right)}-\frac{F_{fy} h_f\left(L_{rt}-L_{ct}\right)}{W_t\left(L_{ft}+L_{rt}\right)}+\frac{KS_{tf}\varphi_t+CS_{tf}\dot{\varphi}_t}{W_t} \tag{8.49}$$

$$F_{z2}=\frac{m_t g L_{rt}-m_t a_{tx} h_{ct}-F_{fx} h_f+F_{fz}\left(L_{rt}-L_{ct}\right)}{2\left(L_{ft}+L_{rt}\right)}+\frac{m_t a_{ty} h_{ct} L_{rt}}{W_t\left(L_{ft}+L_{rt}\right)}+\frac{F_{fy} h_f\left(L_{rt}-L_{ct}\right)}{W_t\left(L_{ft}+L_{rt}\right)}-\frac{KS_{tf}\varphi_t+CS_{tf}\dot{\varphi}_t}{W_t} \tag{8.50}$$

$$F_{z3}=\frac{m_t g L_{ft}+m_t a_{tx} h_{ct}+F_{fx} h_f+F_{fz}\left(L_{ft}+L_{ct}\right)}{2\left(L_{ft}+L_{rt}\right)}-\frac{m_t a_{ty} h_{ct} L_{ft}}{W_t\left(L_{ft}+L_{rt}\right)}-\frac{F_{fy} h_f\left(L_{ft}+L_{ct}\right)}{W_t\left(L_{ft}+L_{rt}\right)}+\frac{KS_{tr}\varphi_t+CS_{tr}\dot{\varphi}_s}{W_t} \tag{8.51}$$

$$F_{z4}=\frac{m_t g L_{ft}+m_t a_{tx} h_{ct}+F_{fx} h_f+F_{fz}\left(L_{ft}+L_{ct}\right)}{2\left(L_{ft}+L_{rt}\right)}\frac{m_t a_{ty} h_{ct} L_{ft}}{W_t\left(L_{ft}+L_{rt}\right)}+\frac{F_{fy} h_f\left(L_{ft}+L_{ct}\right)}{W_t\left(L_{ft}+L_{rt}\right)}-\frac{KS_{tr}\varphi_t+CS_{tr}\dot{\varphi}_s}{W_t} \tag{8.52}$$

$$F_{z5}=\frac{m_s g L_{fs}+m_s a_{sx} h_{cs}-F_{fx} h_f}{2\left(L_{fs}+L_{rs}\right)}-\frac{m_s a_{sy} h_{cs}}{W_s}+\frac{F_{fy} h_f}{W_s}+\frac{KS_s\varphi_s+CS_s\dot{\varphi}_s}{W_s} \tag{8.53}$$

$$F_{z6}=\frac{m_s g L_{fs}+m_s a_{sx} h_{cs}-F_{fx} h_f}{2\left(L_{fs}+L_{rs}\right)}+\frac{m_s a_{sy} h_{cs}}{W_s}-\frac{F_{fy} h_f}{W_s}-\frac{KS_s\varphi_s+CS_s\dot{\varphi}_s}{W_s} \tag{8.54}$$

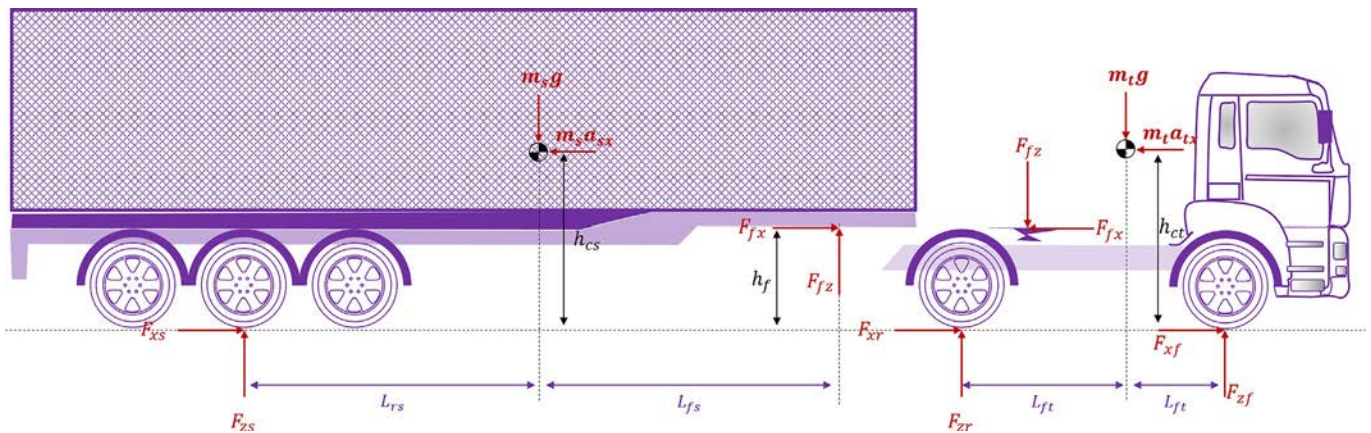

Fig. 8.8 Free diagram of tractor and semitrailer to calculate tire normal forces.

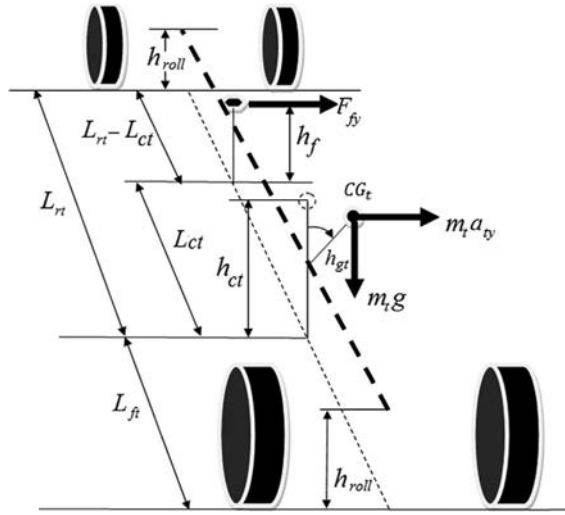

Fig. 8.9 Free diagram of tractor during turning.

In the proposed vehicle configuration, the semitrailer unit has three axles where, as can be seen, the normal forces are calculated for the center of wheels and then $\frac{1}{3}$ of the obtained values are considered for the tires of each side. This assumption is correct because the mechanism of connecting triple axles is designed in such a way that the normal load is distributed equally among the one side wheels.

8.2.8 Simplified dynamics model

Typically, simplified linear models are used to design the control systems. In these models in which the complexities of high degrees of freedom models are ignored, the proper behavior of the system can be achieved in the linear region. The given model is shown in Fig. 8.10 for the articulated vehicle. The longitudinal and roll dynamics are excluded, and the tires on both sides are collapsed into one. Other than that, the six rear wheels of the semitrailer are modeled as a tire in the center of the middle axle. As can be seen in Fig. 8.10, the equations of lateral and yaw dynamics of the tractor unit are calculated in the coordinate system $x_t y_t$ as follows:

$$m_t(\dot{v}_t + u_t\dot{\psi}_t) = F_{yft} + F_{yrt} - F_{fy} \tag{8.55}$$

$$I_{zz_t}\ddot{\psi}_t = + F_{fy}L_{ct} + F_{yft}L_{ft} - F_{yrt}L_{rt} \tag{8.56}$$

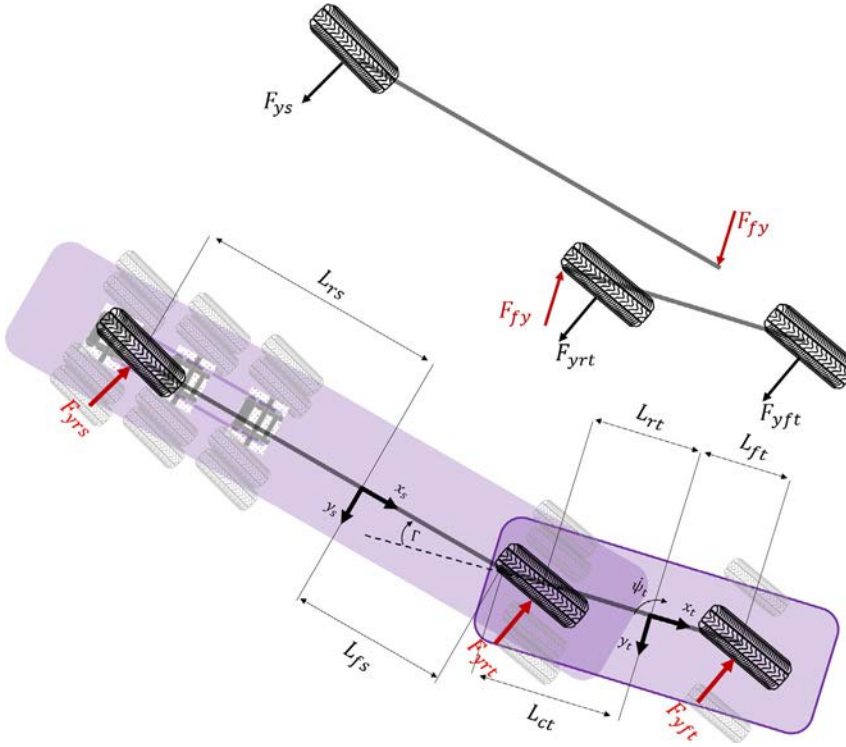

Fig. 8.10 Vehicle simplified model.

The equations of the trailer lateral and yaw dynamics are given as:

$$m_s\left[\dot{v}_t + u_t\dot{\psi}_t - \left(L_{ct} + L_{fs}\right)\ddot{\psi}_t - L_{fs}\ddot{\Gamma}\right] = F_{yrs} + F_{fy} \tag{8.57}$$

$$I_{zz_s}\left(\ddot{\psi}_t + \ddot{\Gamma}\right) = F_{fy}L_{fs} - F_{yrs}L_{rs} \tag{8.58}$$

By eliminating the articulation force from the above equations, three main equations of the articulated vehicle directional dynamic are acquired as (8.59, 8.60, and 8.61).

$$\left(m_t + m_s\right)\left(\dot{v}_t + u_t\dot{\psi}_t\right) - m_s\left[\left(L_{ct} + L_{fs}\right)\ddot{\psi}_t + L_{fs}\ddot{\Gamma}\right] = F_{yft} + F_{yrt} + F_{yrs} \tag{8.59}$$

$$I_{zz_t}\ddot{\psi}_t + m_t\left(\dot{v}_t + u_t\dot{\psi}_t\right)L_{ct} = F_{yft}\left(L_{ct} + L_{ft}\right) + F_{yrt}\left(L_{ct} - L_{rt}\right) \tag{8.60}$$

$$I_{zz_s}\left(\ddot{\psi}_t + \ddot{\Gamma}\right) - m_s\left[\dot{v}_t + u_t\dot{\psi}_t - \left(L_{ct} + L_{fs}\right)\ddot{\psi}_t - L_{fs}\ddot{\Gamma}\right]L_{fs} = -F_{yrs}\left(L_{rs} + L_{fs}\right) \tag{8.61}$$

The above model is linearized under an assumption that the lateral force is only a linear function of the tire slip angle:

$$F_{yi} = C_i \alpha_i \tag{8.62}$$

In other words, the slip angle is expressed for each axle as follows:

$$\alpha_{ft} = \delta_{ft} - \tan^{-1}\left(\frac{v_t + \dot{\psi}_t L_{ft}}{u_t}\right) \approx \delta_{ft} - \frac{v_t + \dot{\psi}_t L_{ft}}{u_t} \tag{8.63}$$

$$\alpha_{rt} = \delta_{rt} - \tan^{-1}\left(\frac{v_t - \dot{\psi}_t L_{rt}}{u_t}\right) \approx \delta_{rt} - \frac{v_t - \dot{\psi}_t L_{rt}}{u_t} \tag{8.64}$$

$$\begin{aligned}\alpha_{rs} &= \delta_{rs} - \tan^{-1}\left(\frac{v_s - \dot{\psi}_s L_{rs}}{u_s}\right) \\ &\approx \delta_{rs} - \frac{v_t - \dot{\psi}_t\left(L_{ct} + L_{fs} + L_{rs}\right) - \dot{\Gamma}\left(L_{fs} + L_{rs}\right)}{u_s} - \Gamma\end{aligned} \tag{8.65}$$

The fourth-order linear equations are calculated considering Eqs. (8.63)–(8.65), substituting them in Eqs. (8.59)–(8.61) and using tractor lateral velocity (v_t), tractor yaw velocity ($\dot{\psi}_t$), articulation angle variation rate ($\dot{\Gamma}$), and articulation angle (Γ) as the linear system state variables:

$$\begin{aligned}&\begin{bmatrix} m_t + m_s & -m_s\left(L_{ct} + L_{fs}\right) & -m_s L_{fs} & 0 \\ m_t L_{ct} & I_{zz_t} & 0 & 0 \\ -m_s L_{fs} & I_{zz_s} + m_s L_{fs}\left(L_{ct} + L_{fs}\right) & I_{zz_s} + m_s L_{fs}^2 & 0 \\ 0 & 0 & 0 & 1 \end{bmatrix} \begin{Bmatrix} \dot{v}_t \\ \ddot{\psi}_t \\ \ddot{\Gamma} \\ \dot{\Gamma} \end{Bmatrix} \\ &= \begin{bmatrix} a_{11} & a_{12} & a_{13} & a_{14} \\ a_{21} & a_{22} & 0 & 0 \\ a_{31} & a_{32} & a_{33} & a_{34} \\ 0 & 0 & 1 & 0 \end{bmatrix} \begin{Bmatrix} v_t \\ \dot{\psi}_t \\ \dot{\Gamma} \\ \Gamma \end{Bmatrix} \\ &+ \begin{bmatrix} C_{ft} & C_{rt} & C_{rs} \\ C_{ft}\left(L_{ct} + L_{ft}\right) & C_{rt}\left(L_{ct} - L_{rt}\right) & 0 \\ 0 & 0 & C_{rs}\left(L_{fs} + L_{rs}\right) \\ 0 & 0 & 0 \end{bmatrix} \begin{Bmatrix} \delta_{ft} \\ \delta_{rt} \\ \delta_{rs} \end{Bmatrix}\end{aligned} \tag{8.66}$$

The above parameters are listed in Table 8.1. Table 8.2 also shows the parameters used in computer simulations.

Table 8.1 Vehicle parameters.

$$a_{11} = -\frac{C_{fi} + C_{rt} + C_{rs}}{u_t}$$
$$a_{12} = \frac{C_{rt}L_{rt} - C_{fi}L_{fi} + C_{rs}\left(L_{ct} + L_{fs} + L_{rs}\right) - (m_t + m_s)u_t^2}{u_t}$$
$$a_{13} = \frac{C_{rs}\left(L_{fs} + L_{rs}\right)}{u_t}$$
$$a_{14} = C_{rs}$$
$$a_{21} = -\frac{C_{fi}\left(L_{fi} + L_{ct}\right) + C_{rt}(L_{ct} - L_{rt})}{u_t}$$
$$a_{22} = \frac{-C_{fi}\left(L_{fi}L_{ct} + L_{fi}^2\right) + C_{rt}(L_{ct} - L_{rt})L_{rt} - m_t L_{ct} u_t^2}{u_t}$$
$$a_{31} = \frac{C_{rs}\left(L_{rs} + L_{fs}\right)}{u_t}$$
$$a_{32} = \frac{-C_{rs}\left(L_{rs} + L_{fs}\right)\left(L_{rs} + L_{fs} + L_{ct}\right) + m_s L_{fs} u_t^2}{u_t}$$
$$a_{33} = \frac{-C_{rs}\left(L_{rs} + L_{fs}\right)^2}{u_t}$$
$$a_{34} = -C_{rs}(L_{rs} + L_{fs})$$

Table 8.2 Articulated vehicle parameters used in computer simulations.

Symbol	Value	Unit	Description
$CS_{tf(tr)}$	4.05 (6.88)	$\frac{\text{kN m s}}{\text{rad}}$	Tractor torsional damping of the front (rear) suspension
CS_s	23.9		Torsional damping of semitrailer suspension
C_w	700		Torsional damping of the coupling between the tractor unit and the semitrailer
$h_{t(s)}$	0.438 (1.8)	m	Height of center of gravity of the sprung mass of the tractor (semitrailer) from the rolling axis
$h_{ct(s)}$	1.05 (1.9)		Height of center of gravity of the sprung mass of the tractor (semitrailer) from the rolling axis
h_f	1.22		The height of the fifth wheel from the ground
$h_{wt(ws)}$	0.63 (1)		Height of the fifth wheel from the roller axis of the tractor (semitrailer)
$I_{zz_{t(s)}}$	20,679 (238,898)	kg m^2	Yaw moment of inertia of the whole tractor unit (semitrailer) around the vertical axis passing through the center of gravity of the semitrailer unit of inertia

Table 8.2 Articulated vehicle parameters used in computer simulations—cont'd

Symbol	Value	Unit	Description
$I_{xx_{pt(ps)}}$	3335 (120,024)		Rolling inertia moment of the tractor (semitrailer) around the rolling axis
$I_{xz_{pt(ps)}}$	602 (5756)		The cross moment of inertia the sprung mass of the tractor (semitrailer)
I_{wi}	11.63		Wheel moment of inertia
$KS_{tf(tr)}$	380 (684)	$\frac{\text{kN m}}{\text{rad}}$	Torsional stiffness of the front (rear) suspension of the tractor unit
KS_s	800		Torsional stiffness of semitrailer suspension
K_w	30,000		Torsional stiffness of the coupling between the tractor unit and the semitrailer
$L_{ft}(L_{rt})$	1.115 (2.583)	m	Distance between center of mass and front axle of tractor (rear axle of tractor)
$L_{fs}(L_{rs})$	5.653, 2.047		The distance between the center of mass of the semitrailer and the fifth wheel (middle axis of the semitrailer)
L_{ct}	1.959		The distance between the center of mass of the tractor and the fifth wheel
$L_{rsf(rsr)}$	1.31		The distance between the center axle of the semitrailer and its front (rear) axle
L_s	9		The distance between the fifth wheel and the end of the semitrailer
$m_{t(st)}$	6525 (4819)	kg	Total mass (sprung mass) of the tractor
$m_{s(ss)}$	33,221 (30,821)		Total mass (sprung mass) of the semitrailer
R_{wi}	0.4	m	Radius of each wheel
$W_{t(s)}$	2.04 (2)		Tractor (semitrailer) width

8.3 Control variables

The first step in designing a control system is to determine the control targets that must be specified for the control algorithm. In vehicle lateral dynamics control, the yaw velocity and lateral slip angle (lateral velocity) are addressed

to provide suitable steering and vehicle stability as the main motion variables and the vehicle lateral dynamic is enhanced by controlling them [6, 16].

By studying the performance standards/characteristics of the articulated vehicle's directional dynamics/behavior, examining dangerous modes, and conducting dynamics analysis based on phase plane, we could have a clearer view of the role of different motion variables in improving the stability as well as maneuverability of an articulated vehicle. These variables must be selected in such a way that controlling them results in the stability of the articulated vehicle.

In order to evaluate the performance of heavy vehicles in different fields, a set of standards has been codified. These standards could be used to assess the performance of heavy vehicles and also evaluate the developed control systems. The complete set of these standards has been compiled by Australia's National Road Transport Commission, and that set is called the Performance-Based Standard (PBS) [17]. The mentioned standards include longitudinal performance, lateral performance, rollover performance, and ride performance of heavy vehicles. Several standards related to the lateral dynamics and also dangerous modes of articulated vehicle motion include handling quality, steady-state off-tracking, transient off-tracking, lateral stability in braking, and tire friction demand. Furthermore, hazardous modes of articulated vehicle motion include the first dangerous motion, which is divergence instability covering jackknifing and trailer swing, and the second unstable oscillating motion, which is when the trailer starts to oscillate toward the tractor and its oscillation domain increases progressively. This unstable mode is the so-called snaking [18].

It should also be noted that the directional stability of the articulated vehicle when braking, minimizing the required friction and preventing dangerous motion modes, also depend on how the control system is designed and implemented. This issue should be considered in the design of integrated control systems.

8.3.1 Tractor yaw velocity and its desired value

The vehicle handling quality implies the capability of a vehicle to meet the driver's demand. It should be noted that handling quality is a subjective criterion. So far, no theoretical method has been presented that can express the extent of handling or vehicle controllability analytically. For this reason, only

empirical truth-based and practical tests can be carried out to appraise handling [13]. However, the yaw velocity is the most important factor among the vehicle motion variables by which drivers could evaluate vehicle handling as far as researchers are concerned [6]. In other words, the driver tries to adjust the vehicle yaw velocity by changing the steering angle. But, it should be noted that a typical driver drives at low accelerations and is subjectively familiar with the vehicle performance range in the linear region. Hence, the best situation is that under extreme acceleration conditions and high lateral acceleration maneuvers, the driver would feel a subjective motion in the linear conditions [15]. Accordingly, the desired yaw velocity value is measured as the following:

$$\frac{\dot{\psi}_r}{\delta_{driver}} = G_r \frac{1}{1 + t_r S} \tag{8.67}$$

where $\dot{\psi}_r$ is the desired yaw velocity, δ_{driver} is the steering angle applied by the driver, t_r is delay time, and G_r is the steady-state yaw velocity gain. Therefore, based on Eq. (8.67), the vehicle's linear behavior is determined for the driver, and adjusting the vehicle motion becomes easier for him/her. The desired yaw velocity could also be obtained in the articulated heavy vehicle, just the same as the idea implemented in the passenger vehicle. The desired yaw velocity gain is obtained for a linear model of the articulated vehicle shown in Fig. 8.11 [19]:

$$G_{r\_heavy} = \frac{u_t}{L_g + K_{ug} u_t^2} \tag{8.68}$$

where L_g and K_{ug} are the extended length and the understeer gradient for the articulated heavy vehicle, respectively. These two parameters are obtained for the arbitrary number of tractor and trailer axles as the following [19]:

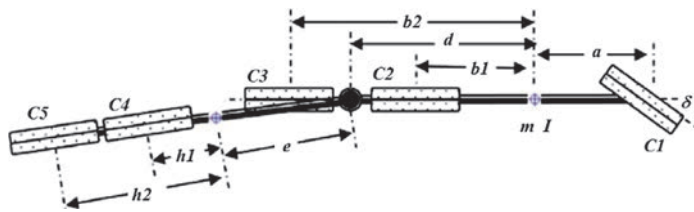

Fig. 8.11 The simplified model of the articulated vehicle to calculate the steady-state yaw velocity gain.

$$K_u = m\frac{\sum_{i=2}^{N}(b_{i-1}C_i) - aC_1}{C_1\sum_{i=2}^{N}(a+b_{i-1})C_i} + m_1\frac{\sum_{j}^{M}h_jC_{N+j}}{\sum_{j}^{N}(h_j+e)C_{N+j}}\frac{\sum_{i=2}^{N}(b_{i-1}-d)C_i-(a+d)C_1}{C_1\sum_{i=2}^{N}(a+b_{i-1})C_i} \tag{8.69}$$

$$L_g = m\frac{\sum_{i=2}^{N}(b_{i-1}C_i) - aC_1}{C_1\sum_{i=2}^{N}(a+b_{i-1})C_i}\left(\sum_{i=1}^{N}C_i\left(\frac{\sum_{i=2}^{N}(b_{i-1}^2C_i)+a^2C_1}{\sum_{i=2}^{N}b_{i-1}C_i - aC_1}\right) - \left(\sum_{i=2}^{N}b_{i-1}C_i - aC_1\right)\right)$$
$$+ \frac{\sum_{i=2}^{N}(b_{i-1}-d)C_i-(a+d)C_1}{C_1\sum_{i=2}^{N}(a+b_{i-1})C_i}\left(\sum_{j=1}^{M}C_{N+j}\frac{\sum_{j=1}^{M}h_j(h_j+e)C_{N+j}}{\sum_{j}^{N}(h_j+e)C_{N+j}} - \sum_{j=1}^{N}h_jC_{N+j}\right) \tag{8.70}$$

where N is the number of tractor axles, and M is the number of semitrailer axles. The rest of the parameters have been given in Fig. 8.11.

8.3.2 Lateral velocity and its desired value

Adjusting the tractor yaw velocity and the side slip angle is an effective way to maintain stability and specifically prevent the vehicle from jackknifing. It must be noted that adjusting both the lateral velocity (v_t) and the side slip angle (β_t) based on the following equation is two equivalent tasks:

$$\beta_t = \arctan\left(\frac{v_t}{u_t}\right) \tag{8.71}$$

Well-known automotive scientists have focused on limiting the side slip angle to maintain the lateral stability of the riding vehicle [20, 21]. Limiting the tractor side slip angle is of prime importance to prevent tractor jackknifing and trailer swing. Because vehicle stability depends on the side slip angle directly, this angle should be limited to place the vehicle in the linear condition [16] in which its desired value could be considered zero.

8.3.3 Articulation angle and its desired value

The articulation angle is considered a critical variable in the articulated vehicle. The idea of following the turning angle to track the path was proposed for the first time in 1991 [22]. The desired articulation angle is determined in such a way that the steady-state off-tracking as well as transient off-tracking are eliminated. On the other hand, it is obvious that adjusting the articulation angle, particularly limiting it, could result in preventing trailer swing and snaking. In this section, the desired articulation angle (Γ_r) is obtained to such a degree that tracking Γ_r helps the trailer end to track the fifth wheel path at all velocities. This procedure has been shown in Fig. 8.12, schematically [15].

Fig. 8.13 shows the articulated vehicle at times T and $T + T_d$ schematically. The time interval T_d is the required time duration for the articulated vehicle to traverse the distance between the end of the semitrailer and the fifth wheel. Besides, the location of the fifth wheel is represented by $f(T)$ and $f(T + T_d)$ at T and $T + T_d$. Additionally, the location of the end of the semitrailer is shown by $S(T)$ and $S(T + T_d)$ at T and $T + T_d$, respectively. Moreover, it is feasible to track the reference articulation angle $\Gamma_r(T + T_d)$ by removing the off-tracking (i.e., removing the position deviation between $f(T)$ and $(T + T_d)$).

As can be seen in Fig. 8.13, Eq. (8.72) can be defined as an equivalent for $\Gamma_r(T + T_d)$:

$$\Gamma_r(T + T_d) = \tan^{-1}\frac{\Delta y_f}{\Delta x_f} \tag{8.72}$$

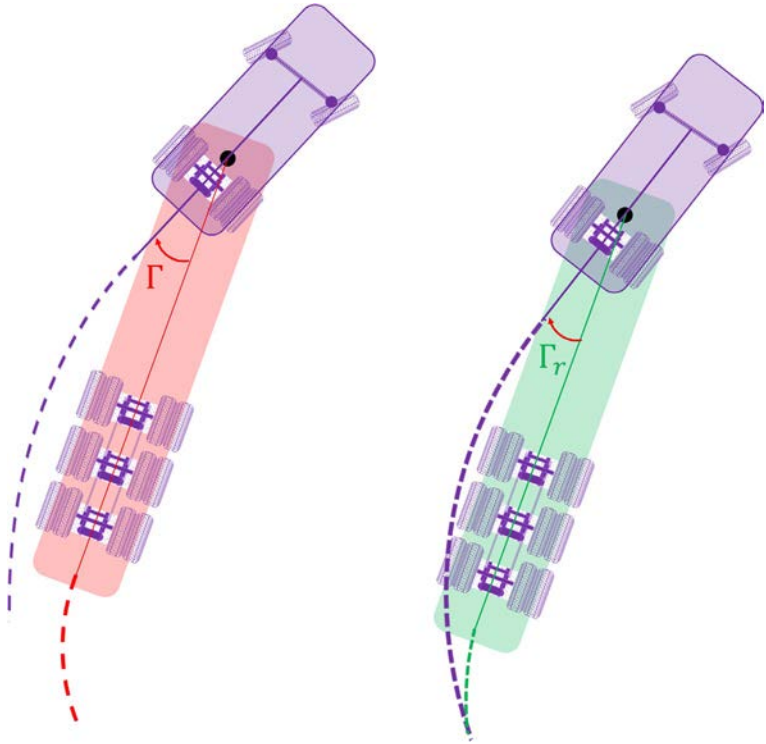

Fig. 8.12 Right image: The articulated vehicle when it follows the desired articulation angle. Left image: The articulated vehicle when the articulation angle has an arbitrary value.

where Δx_f and Δy_f are the longitudinal and lateral displacement of the fifth wheel at the T_d interval, respectively. It is worth knowing that Δx_f and Δy_f are calculated within the coordinate system attached to the tractor at $T + T_d$ (namely, in the $x_t^{T+T_d} y_t^{T+T_d}$ coordinate system). Other than that, it must be considered that due to the motion of the $x_t y_t$ coordinate system, it is not straightforward to calculate Δx_f and Δy_f. To perform this, the T_d time interval is divided into j equal periods, each as ΔT where j is calculated $j = T_d/\Delta T$ and the ΔT period must be small enough. Fig. 8.14 shows the idea proposed in this research (it should be noticed that at arbitrary $T + k\Delta T$, the coordinates fixed on the tractor unit are shown by $x_t^{T+k\Delta T} y_t^{T+k\Delta T}$).

According to Fig. 8.13, Δx_f and Δy_f are defined as follows:

$$\Delta x_f = x_f(T + T_d) - x_f(T) \tag{8.73}$$

$$\Delta y_f = y_f(T + T_d) - y_f(T) \tag{8.74}$$

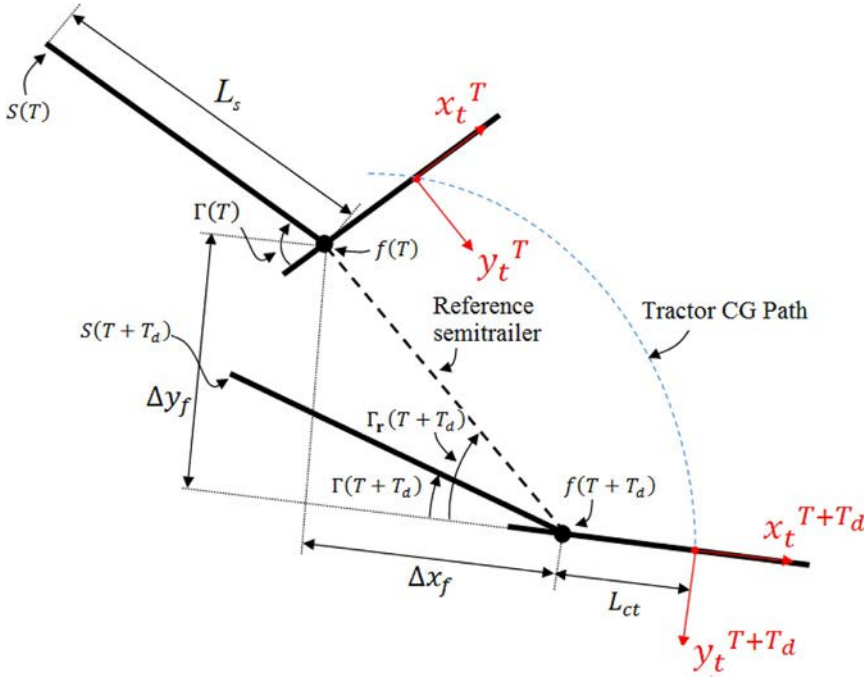

Fig. 8.13 Schematic of the articulated vehicle at T and $T + T_d$.

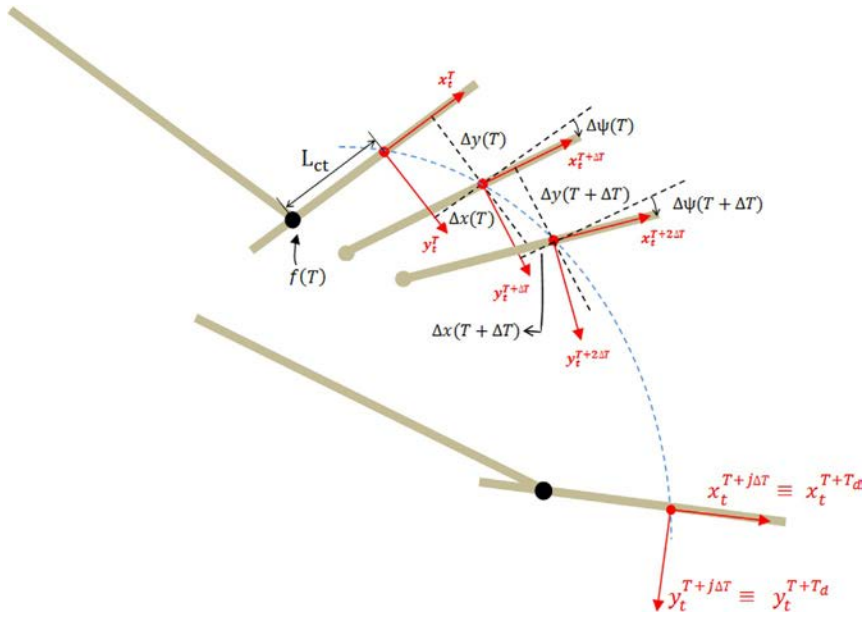

Fig. 8.14 Representation of the proposed idea to define the desired articulation angle [15].

where $x_f(T+T_d)$ and $y_f(T+T_d)$ are simply defined in the $x_t^{T+T_d}y_t^{T+T_d}$ coordinate system:

$$x_f(T+T_d) = -L_{ct} \tag{8.75}$$

$$y_f(T+T_d) = 0 \tag{8.76}$$

The idea represented in

Fig. 8.14 is used to calculate $x_f(T)$ and $y_f(T)$ in $x_t^{T+T_d}y_t^{T+T_d}$. In the first step, through simple geometrical analysis, the longitudinal and lateral locations of $f(T)$ are determined in $x_t^{T+\Delta T}y_t^{T+\Delta T}$:

$$x_f(T) = -[\Delta x(T) + L_{ct}]\cos[\Delta\psi(T)] - \Delta y(T)\sin[\Delta\psi(T)] \tag{8.77}$$

$$y_f(T) = +[\Delta x(T) + L_{ct}]\sin[\Delta\psi(T)] - \Delta y(T)\cos[\Delta\psi(T)] \tag{8.78}$$

where $\Delta x(T)$, $\Delta y(T)$, and $\Delta\psi(T)$ are the longitudinal, lateral, and yaw alterations of the tractor gravity center at the T and ΔT interval, respectively. Concerning the above mentioned, $x_f(T)$ and $y_f(T)$ could be represented in $x_t^{T+2\Delta T}y_t^{T+2\Delta T}$:

$$\begin{aligned} x_f(T) = &-[\Delta x(T) + L_{ct}]\cos[\Delta\psi(T) + \Delta\psi(T+\Delta T)] \\ &- \Delta x(T+\Delta T)\cos[\Delta\psi(T+\Delta T)] \\ &- \Delta y(T)\sin[\Delta\psi(T) + \Delta\psi(T+\Delta T)] \\ &- \Delta y(T+\Delta T)\sin(\Delta\psi(T+\Delta T)) \end{aligned} \tag{8.79}$$

$$\begin{aligned} y_f(T) = &+[\Delta x(T) + L_{ct}]\sin[\Delta\psi(T) + \Delta\psi(T+\Delta T)] \\ &+ \Delta x(T+\Delta T)\sin[\Delta\psi(T+\Delta T)] \\ &- \Delta y(T)\cos[\Delta\psi(T) + \Delta\psi(T+\Delta T)] \\ &- \Delta y(T+\Delta T)\cos(\Delta\psi(T+\Delta T)) \end{aligned} \tag{8.80}$$

Finally, by applying the same method, the location of $f(T)$ is presented in $x_t^{T+T_d}y_t^{T+T_d}$:

$$\begin{aligned} x_f(T) = &-L_{ct}\cos\left[\sum_{k=n}^{j-1}\Delta\psi(T+k\Delta T)\right] \\ &+ \sum_{k=n}^{j-1}\left\{-\Delta x(T+k\Delta T)\cos\left[\sum_{m=k}^{j-1}\Delta\psi(T+m\Delta T)\right]\right\} \\ &- \sum_{k=n}^{j-1}\left\{\Delta y(T+k\Delta T)\sin\left[\sum_{m=k}^{j-1}\Delta\psi(T+m\Delta T)\right]\right\} \end{aligned} \tag{8.81}$$

$$\gamma_f(T) = L_{ct}\sin\left[\sum_{k=n}^{j-1}\Delta\psi(T+k\Delta T)\right] + \sum_{k=n}^{j-1}\left\{\Delta x(T+k\Delta T)\sin\left[\sum_{m=k}^{j-1}\Delta\psi(T+m\Delta T)\right]\right\} - \sum_{k=n}^{j-1}\left\{\Delta\gamma(T+k\Delta T)\cos\left[\sum_{m=k}^{j-1}\Delta\psi(T+m\Delta T)\right]\right\} \tag{8.82}$$

where in both equations, n is an integer number that is initialized zero at the beginning of the simulation. The equations of $\Delta x(T)$, $\Delta\gamma(T)$, $\Delta\psi(T)$ and the vehicle motion variables could be explained approximately as:

$$\Delta x(T+i\Delta T) = u_t(T+i\Delta T)\Delta T \tag{8.83}$$

$$\Delta\gamma(T+i\Delta T) = v_t(T+i\Delta T)\Delta T \tag{8.84}$$

$$\Delta\psi(T+m\Delta T) = \dot{\psi}_t(T+i\Delta T)\Delta T \tag{8.85}$$

Finally, Δx_f and $\Delta\gamma_f$ are defined by:

$$\Delta x_f = -L_{ct} + L_{ct}\cos\left[\sum_{k=n}^{j-1}\dot{\psi}_t(T+k\Delta T)\Delta T\right] + \sum_{k=n}^{j-1}\left\{u_t(T+k\Delta T)\Delta T\cos\left[\sum_{m=k}^{j-1}\dot{\psi}_t(T+m\Delta T)\Delta T\right] + [v_t(T+k\Delta T)\Delta T]\sin\left[\sum_{m=k}^{j-1}\dot{\psi}_t(T+m\Delta T)\Delta T\right]\right\} \tag{8.86}$$

$$\Delta\gamma_f = -L_{ct}\sin\left[\sum_{k=n}^{j-1}\dot{\psi}_t(T+k\Delta T)\Delta T\right] - \sum_{k=n}^{j-1}\left\{u_t(T+k\Delta T)\Delta T\sin\left[\sum_{m=k}^{j-1}\dot{\psi}_t(T+m\Delta T)\Delta T\right] - [v_t(T+k\Delta T)\Delta T]\cos\left[\sum_{m=k}^{j-1}\dot{\psi}_t(T+m\Delta T)\Delta T\right]\right\} \tag{8.87}$$

Substituting Eqs. (8.86) and (8.87) into Eq. (8.72) presents the desired articulation angle at any time. In the proposed method, $T + T_d$ has not been specified clearly. As mentioned above, T_d is the required time interval for the articulated vehicle to traverse the distance between the end of the semitrailer and the fifth wheel. According to Fig. 8.13 and using the Pythagorean

Theorem, it can be determined whether the articulated vehicle has traversed the distance L_s.

$$\Delta x_f{}^2 + \Delta y_f{}^2 \geq L_s^2 \tag{8.88}$$

Fig. 8.15 shows the proposed method to determine the desired articulation angle. The u_t, v_t, and $\dot{\psi}_t$ instances are stored. Δx_f and Δy_f are calculated by using Eqs. (8.86) and (8.87) at any time. In the next step, it must be determined whether the articulated vehicle has been displaced as much as the L_s. If the given condition in Eq. (8.88) is satisfied, then the desired articulation angle will be determined as Eq. (8.72) and the old instances of u_t, v_t, and $\dot{\psi}_t$ are ignored by defining $n = n + 1$. Otherwise, the desired articulation angle obtained by the previous step is considered as the new articulation angle.

8.4 Active steering controller

One of the directional dynamics control methods of articulated heavy vehicles is to use the steering subsystem. The optimal control method based on the linear model of the articulated vehicles is considered as the most popular method to regulate the directional dynamics of such vehicles. Meanwhile, the powerful control techniques such as the sliding mode control method

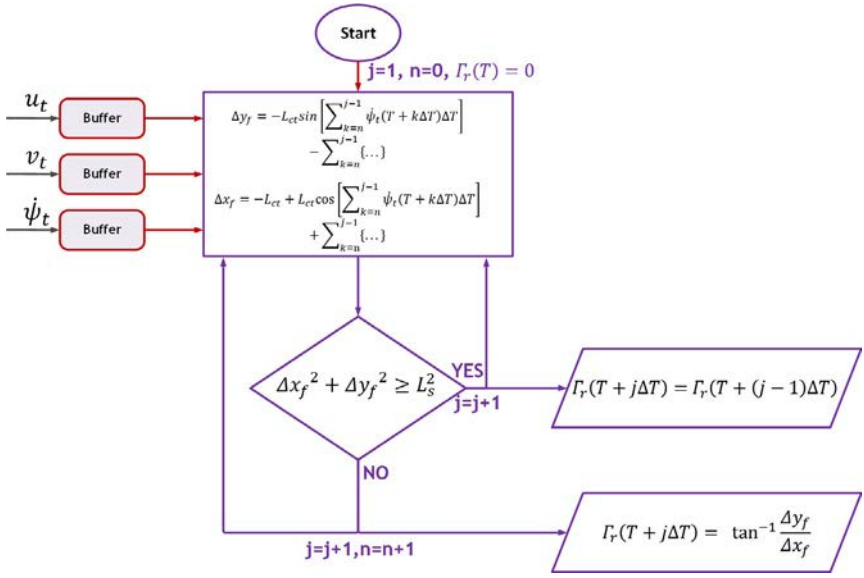

Fig. 8.15 Flowchart of the desired articulation angle calculation.

have become so popular in studies on vehicle handling and stability, and prominent scholars have proposed various control structures to implement these methods [23, 24]. Also, the lack of applying nonlinear control methods such as sliding mode control [15] is observable in this field as well.

8.4.1 Active steering controller using linear optimal control method

By considering the tractor lateral velocity (v_t), the tractor yaw velocity ($\dot{\psi}_t$), the articulation angle rate ($\dot{\Gamma}$), and the articulation angle (Γ) as the linear system state variable, Eq. (8.66) can be presented in the following matrix form:

$$M^*\dot{x}_l = A^*x_l + C^*u_l \tag{8.89}$$

where

$$x_l = \left[v_t \dot{\Psi}_t \dot{\Gamma} \Gamma\right]^T \tag{8.90}$$

The above equation can be stated as the following state-space form by multiplying two sides by M^{*-1}:

$$\begin{gathered} \dot{x}_l = A_l x_l + B_l u_l \\ A_l = M^{*-1}A^* B_l = M^{*-1}C^* \end{gathered} \tag{8.91}$$

The controller consists of two feed-forward and feedback compensators that apply the optimal response and its error over the real system response to regulate the motion of the articulated vehicle. In order to design a controller, the tracking error can be defined as:

$$e_l = x_l - x_r \tag{8.92}$$

Differentiating from Eq. (8.92) and substituting the right term of Eq. (8.90), the differential equation of the tracking error is calculated as:

$$\dot{e}_l = \dot{x}_l - \dot{x}_r = A_l e_l + B_l u_l - \dot{x}_r + A_l x_r \tag{8.93}$$

Now, we define the control input as two parts of feed-forward u_{ff} and feedback u_{fb} as follows:

$$u_l = u_{ff} + u_{fb} \tag{8.94}$$

Substituting Eq. (8.94) in Eq. (8.93) gives the following equation:

$$\dot{e}_l = A_l e_l + B_l u_{fb} + B_l u_{ff} - \dot{x}_r + A_l x_r \tag{8.95}$$

The feed-forward control input is defined as:

$$u_{ff} = B_l^{-1}(\dot{x}_r - A_l x_r) \tag{8.96}$$

It is worth noting that the matrix B_l is not a square matrix and ${B_l}^{-1}$ is a pseudoinverse that is used to calculate the feed-forward input. By combining Eqs. (8.95) and (8.96), the error state equation is obtained as:

$$\dot{e}_l = A_l e_l + B_l u_{fb} \tag{8.97}$$

The optimal u_{fb} can be obtained using the optimal control rule with the performance index minimization condition:

$$J = \int_0^\infty \left({e_l}^T Q_l e_l + u_{fb}^T R_l u_{fb} \right) dt \tag{8.98}$$

where Q_l is the positive definite matrix (or semidefinite) and R_l is the symmetric positive definite matrix. By adjusting the elements of the matrix Q_l, we could change the significance degree of adjusting each control variable and achieve a suitable articulated vehicle directional dynamics response. Moreover, by regulating the elements of R_l, the conditions of the control operators can be considered. Finally, the control input is defined by Eq. (8.99):

$$\begin{aligned} u_{fb} &= -K_l e_l \\ K_l &= {R_l}^{-1} {B_l}^{-1} P_l \end{aligned} \tag{8.99}$$

where $P_l$is the result of the *Riccati* equation:

$${A_l}^T P_l + P_l A_l - P_l B_l {R_l}^{-1} {B_l}^T P_l + Q_l = 0 \tag{8.100}$$

8.4.2 Active steering controller using the sliding mode control method

In this section, the articulated vehicle model is considered in the form of a multiinput-multioutput nonlinear system, and the controller is designed based on the sliding mode method. In the first step, a dynamic model of an articulated vehicle is required. The articulation force is removed from the above equations using the four equations presented for the 3-degree-of-freedom vehicle model in Eqs. (8.55)–(8.58). In this way, the inertia matrix would be symmetric. Ultimately, the articulated vehicle directional dynamics equation can be represented in the matrix form as:

$$\mathrm{M}\dot{\mathrm{q}} + \mathrm{D}\dot{\psi}_t u_t = \mathrm{U} \tag{8.101}$$

where

$$\mathrm{M}=\begin{bmatrix} m_t+m_s & -m_s\left(L_{ct}+L_{fs}\right) & -m_sL_{fs} \\ -m_s\left(L_{ct}+L_{fs}\right) & I_{zz_t}+I_{zz_s}+m_s\left(L_{ct}+L_{fs}\right)^2 & I_{zz_s}+m_sL_{fs}\left(L_{ct}+L_{fs}\right) \\ -m_sL_{fs} & I_{zz_s}+m_sL_{fs}\left(L_{ct}+L_{fs}\right) & I_{zz_s}+m_sL_{fs}^2 \end{bmatrix}$$

$$\mathrm{D}=\begin{bmatrix} \left(m_t+m_s\right) \\ -m_s\left(L_{ct}+L_{fs}\right) \\ -m_sL_{fs} \end{bmatrix},\mathrm{U}=\begin{bmatrix} \mathrm{U}_1 \\ \mathrm{U}_2 \\ \mathrm{U}_3 \end{bmatrix}$$

$$=\begin{bmatrix} F_{yft}+F_{yrt}+F_{yrs} \\ F_{yf}L_{ft}-F_{yr}L_{rt}-F_{yrs}\left(L_{ct}+L_{fs}+L_{rs}\right) \\ -F_{yrs}\left(L_{rs}+L_{fs}\right) \end{bmatrix},\mathrm{q}=\begin{bmatrix} v_t \\ \dot{\psi}_t \\ \dot{\Gamma} \end{bmatrix} \tag{8.102}$$

where U is the control input vector, and q is the vector of control variables that must track the optimal response. The sliding surfaces that could force variables to track the optimal responses are presented by Eq. (8.103). The integral terms have been used in this equation to eliminate the steady-state error. On the other hand, parameters $\Lambda_{0,\,1,\,2,\,3}$ have positive values where $s_{1,\,2,\,3}$ can be obtained in the matrix form:

$$\mathrm{S}=\mathrm{q}-\mathrm{q}_\mathrm{r} \tag{8.103}$$

where;

$$\mathrm{S}=\begin{bmatrix} s_1 \\ s_2 \\ s_3 \end{bmatrix},\quad \mathrm{q}_\mathrm{r}=\begin{bmatrix} -\Lambda_0\int_0^t v_t\,dt \\ \dot{\psi}_r-\Lambda_1\int_0^t\left(\dot{\psi}_t-\dot{\psi}_r\right)dt \\ \dot{\Gamma}_r-\Lambda_2\left(\Gamma-\Gamma_r\right)-\Lambda_3\int_0^t\left(\Gamma-\Gamma_r\right)dt \end{bmatrix}\Lambda_{0,1,2,3}>0 \tag{8.104}$$

In Eq. (8.101), matrix M is symmetric. Using the Sylvester-Gallai theorem, it can easily be shown that the matrix mentioned above is also a positive definite matrix. Therefore, we can define the following *Lyapunov* function:

$$\mathrm{V}(t)=\frac{1}{2}\mathrm{S}^\mathrm{T}\mathrm{MS} \tag{8.105}$$

The aim of control is to keep the scalars $s_{1,\,2,\,3}$ in zero. As such, the time derivative of Eq. (8.105) is defined as:

$$\dot{\mathrm{V}}\,(t) = \mathrm{S}^{\mathrm{T}}\mathrm{M}\dot{\mathrm{S}} = \mathrm{S}^{\mathrm{T}}\mathrm{M}(\dot{\mathrm{q}} - \dot{\mathrm{q}}_{\mathrm{r}}) = \mathrm{S}^{\mathrm{T}}(\mathrm{U} - \mathrm{D}\dot{\psi}_t u_t - \mathrm{M}\dot{\mathrm{q}}_{\mathrm{r}}) \tag{8.106}$$

The proper control rule is defined by Eq. (8.107)

$$\mathrm{U} = \widehat{\mathrm{U}} - \mathrm{K}\,\mathrm{sgn}(\mathrm{S}) \tag{8.107}$$

where K = diag $[k_1, k_2, k_3]$, $\mathrm{sgn}(\mathrm{S}) = [\mathrm{sgn}(s_1), \mathrm{sgn}(s_2), \mathrm{sgn}(s_3)]^{\mathrm{T}}$, and $\widehat{\mathrm{U}}$ are control inputs. If the system dynamics are defined accurately, then $\dot{\mathrm{V}}$ becomes zero. Consequently, $\widehat{\mathrm{U}}$ is given as:

$$\widehat{\mathrm{U}} = \widehat{\mathrm{M}}\dot{\mathrm{q}}_{\mathrm{r}} + \widehat{\mathrm{D}}\dot{\psi}_t u_t \tag{8.108}$$

where $\widehat{\mathrm{M}}$ and $\widehat{\mathrm{D}}$ are the nominal values of matrices M and D. To this end, the following limits are considered as the modeling errors:

$$\widetilde{\mathrm{M}} \geq \left|\widehat{\mathrm{M}} - \mathrm{M}\right| \widetilde{\mathrm{D}} \geq \left|\widehat{\mathrm{D}} - \mathrm{D}\right| \tag{8.109}$$

Therefore, the time derivative of the *Lyapunov* function is rewritten as:

$$\dot{\mathrm{V}}\,(t) \leq \mathrm{S}^{\mathrm{T}}\left(\widetilde{\mathrm{D}}\dot{\psi}_t u_t + \widetilde{\mathrm{M}}\,\dot{\mathrm{q}}_{\mathrm{r}}\right) - \sum_{i=1}^{3} k_i |s_i| \tag{8.110}$$

As a consequence, the parameters k_i are given as:

$$k_i \geq \left|\left[\widetilde{\mathrm{D}}\dot{\psi}_t u_t + \widetilde{\mathrm{M}}\,\dot{\mathrm{q}}_{\mathrm{r}}\right]_i\right| + \eta_i \tag{8.111}$$

where η_i are positive parameters and satisfy the sliding condition of Eq. (8.112):

$$\dot{\mathrm{V}}\,(t) \leq -\sum_{i=1}^{3} \eta_i |s_i| \tag{8.112}$$

This slip condition guarantees that we could reach surface $s = 0$ $(S = 0)$ during the limited time [25]. The control rule defined in Eq. (8.107) is discontinuous while passing from $s_i = 0$, which leads to the chattering phenomenon. In an attempt to counteract the detrimental effects of the so-called chattering phenomenon, function *sgn*(0) is replaced by a saturation function defined by Eq. (8.113):

$$\mathrm{sat}\left(\frac{s_i}{\phi_i}\right) = \begin{cases} \dfrac{s_i}{\phi_i} & \text{if } |s_i| < \phi_i \\ \mathrm{sgn}\left(\dfrac{s_i}{\phi_i}\right) & \text{if } |s_i| \geq \phi_i \end{cases} \quad \text{with } i = 1, 2, 3 \tag{8.113}$$

where $\phi_{1,\ 2,\ 3}$ is the thicknesses of the boundary layer. In the last step, the steering angle of each wheel must be determined. According to Eq. (8.100), the relationship between the control input vector and the lateral force vector is given as:

$$\mathrm{U} = Z_f F_y \tag{8.114}$$

where in Eq. (8.114) we have:

$$Z_f = \begin{bmatrix} 1 & 1 & 1 \\ L_{ft} & -L_{rt} & -\left(L_{ct} + L_{fs} + L_{rs}\right) \\ 0 & 0 & -\left(L_{fs} + L_{rs}\right) \end{bmatrix}, F_y = \begin{bmatrix} F_{yft} \\ F_{yrt} \\ F_{yrs} \end{bmatrix} \tag{8.115}$$

The Z_f matrix is reversible, and the lateral forces could be determined easily by $F_y = {Z_f}^{-1}\mathrm{U}$. Therefore, the lateral forces of each axle are specified. In the next step, by using a tire reverse model, the tractor front axle side slip angle (α_{ft}), the tractor rear axle (α_{rt}), and the semitrailer rear axle (α_{rs}) are computed by a 3-degree-of-freedom model. By using them in the last step, the related axle wheels' steering angle could be simply calculated. To model the tire behavior and avoid complex calculations, the simple lateral model proposed by *Masato Abe* is used to measure the slip angles [26].

$$F_{yi} = \begin{cases} -\left[C_i\alpha_i - \mathrm{sgn}(\alpha_i)\dfrac{C_i^2}{4\mu F_{zi}}\alpha_i^2\right]\sqrt{\left(1 - \left(\dfrac{F_{xi}}{\mu F_{zi}}\right)^2\right)} \text{ when } |\alpha_i| < \dfrac{2\mu F_{zi}}{C_i} \\ -\mathrm{sgn}(\alpha_i)\mu F_{zi}\sqrt{\left(1 - \left(\dfrac{F_{xi}}{\mu F_{zi}}\right)^2\right)} \text{ when } |\alpha_i| \geq \dfrac{2\mu F_{zi}}{C_i} \end{cases}_{i = ft, rt, rs} \tag{8.116}$$

The controller has been designed in such a way that the lateral force of each axle is calculated, and the slip angle must be determined for each axle. So, Eq. (8.116) is reversed as the following over the lateral force. The result is given as Eqs. (8.116) and (8.117). If the lateral force is less than the saturation threshold (μF_{zi}), the slip angle will be obtained by (8.117):

$$\alpha_i = -\mathrm{sgn}\left(F_{yi}\right)\frac{-b - \sqrt{b^2 - 4ac}}{2a}$$
$$\text{where } a = \frac{C_i^2}{4\mu F_{zi}}, b = -C_i, \text{and } c = \frac{\left|F_{yi}\right|}{\sqrt{\left(1 - \left(\dfrac{F_{xi}}{\mu F_{zi}}\right)^2\right)}} \tag{8.117}$$
$$i = ft, rt, rs$$

Otherwise,

$$\alpha_i = -\operatorname{sgn}(F_{yi})\frac{2\mu F_{zi}}{C_i} \tag{8.118}$$

As a result, the slip angle of an individual axle can be determined by using Eqs. (8.117) and (8.118) when it comes to the lateral force of each axle. Finally, after calculating the slip angles of each axle, the steering angle of each axle is defined by:

$$\begin{aligned}
\delta_{ft} &= \alpha_{ft} + \tan^{-1}\left(\frac{v_t + \dot{\psi}_t L_{ft}}{u_t}\right) \\
\delta_{rt} &= \alpha_{rt} + \tan^{-1}\left(\frac{v_t - \dot{\psi}_t L_{rt}}{u_t}\right) \\
\delta_{rs} &= \alpha_{rs} + \tan^{-1}\left(\frac{v_s - \dot{\psi}_s L_{rs}}{u_s}\right)
\end{aligned} \tag{8.119}$$

It is worth mentioning that the steering angle (δ_{rs}) has been given for all three axles of the semitrailer end. Based on these explanations, the block diagram of the proposed controller is shown in Fig. 8.16.

8.5 Comparison between simulation and performance

The aim of this section pertains to the performance of these two systems, which is tested once in a relatively simple maneuver and once in a relatively hard maneuver. In the first maneuver, the articulated vehicle with a 70 km/h speed moves on a road with a 0.7 friction coefficient. In the first second, the driver applies a 3 degree steering angle with a 0.5 frequency to the front wheels of the tractor. The simulation results without control and both controllers given in previous sections are shown in Fig. 8.17. It can be

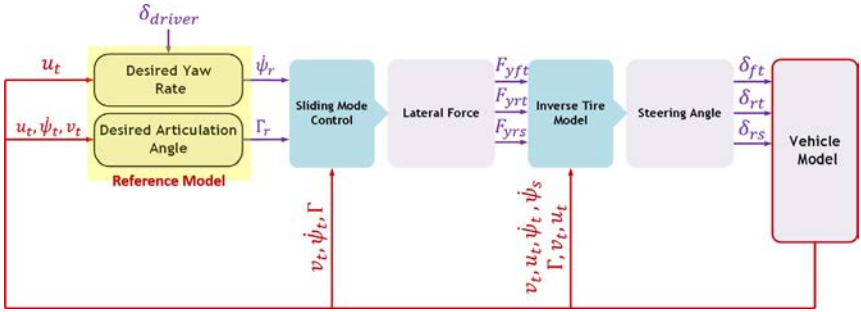

Fig. 8.16 Block diagram of the steering control system.

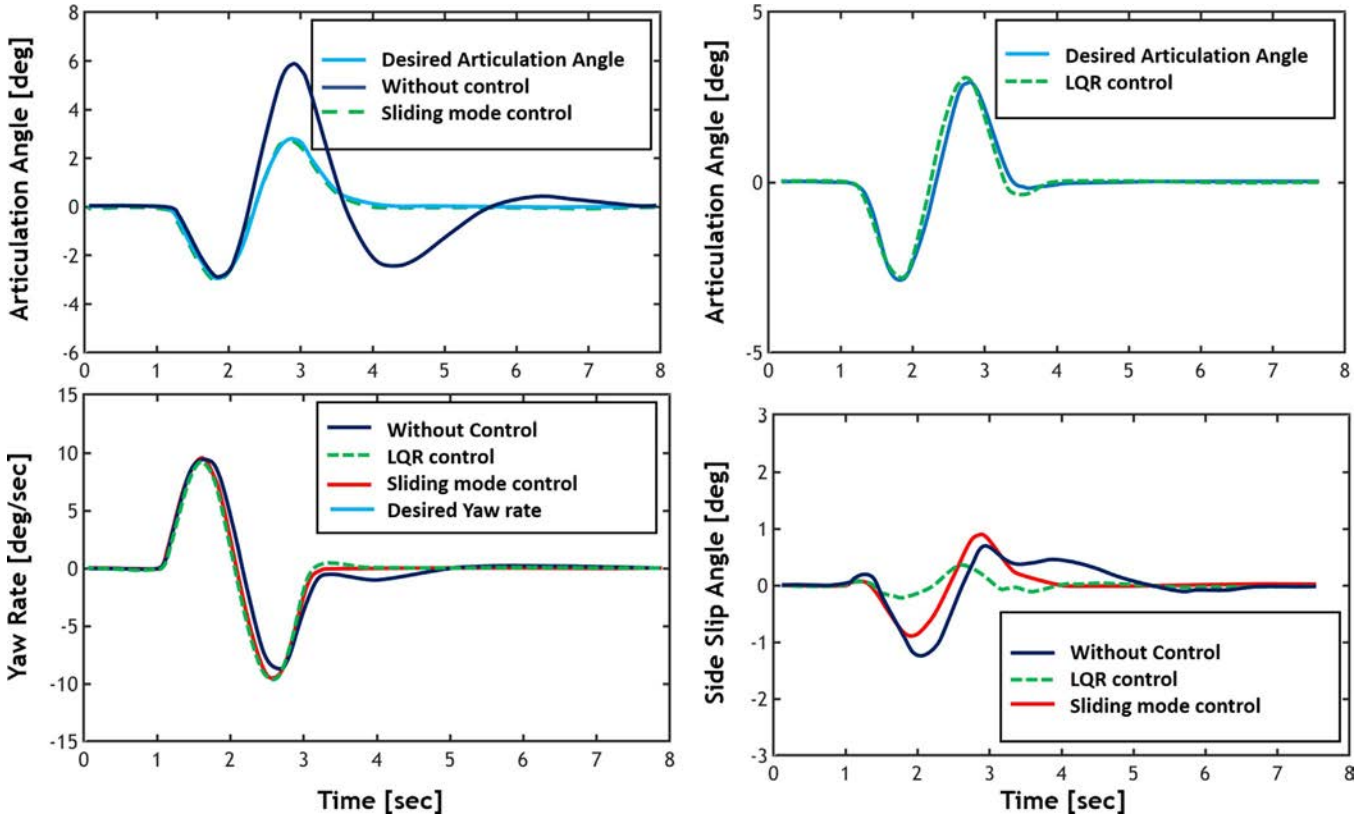

Fig. 8.17 System responses to simple line swap maneuvers.

seen that both controllers can adjust the control variables. Furthermore, it can be easily noticed from Fig. 8.17 that the only motion variable that has a significant deviation from its desired value is the articulation angle.

Herein, to evaluate the robustness of both controllers against the tire performance condition conversion from the linear to the nonlinear state, the previous maneuver is simulated with a 90 km/h speed and a 0.2 friction coefficient. In Fig. 8.18, the response has been compared in three different cases without a controller, an LQR controller, and a sliding mode controller. Considering Fig. 8.18, it is obvious that unlike the sliding model control approach, the linear optimal controller has feeble performance for following the optimal articulation angle as well as optimal yaw velocity.

Fig. 8.19 shows the lateral force of one wheel against the tire slip angle in both maneuvers. It can be seen from Fig. 8.19 that in the first maneuver, the given tire has linear behavior, and in the second maneuver, the tire behavior has intensively become nonlinear. Therefore, in tire nonlinear conditions, the sliding mode controller has a significant superiority over the linear controller.

8.5.1 Brake compared with steering to set directional dynamics

Another effective approach to adjust the directional dynamics of the articulated heavy vehicle is to apply braking forces. The implementation of the control systems based on the brake actuator is much simpler than active steering systems. The main drawback of these systems is a direct effect on the vehicle longitudinal dynamic, which results in unpleasant feelings for the driver. In an articulated heavy vehicle, another ambiguity comes from brake actuator-based controllers. The fundamental question is whether this actuator has the required capacity and power to adjust the vehicle directional dynamics.

According to the initial evaluations, the asymmetric braking method over the semitrailer wheels is inefficient in adjusting the articulation angle, and it is not possible to track the optimal articulation angle through the distribution of braking forces because the braking subsystem is weaker than the steering subsystem in adjusting the control variables, especially the articulation angle. However, since the lateral force of steering input always has the saturation problem in slippery roads as well as critical conditions, the brake actuator can be used as an auxiliary system in such situations.

In consideration of the above, by using the linear model of the articulated vehicle, we could compare the capacity of the braking and steering actuators.

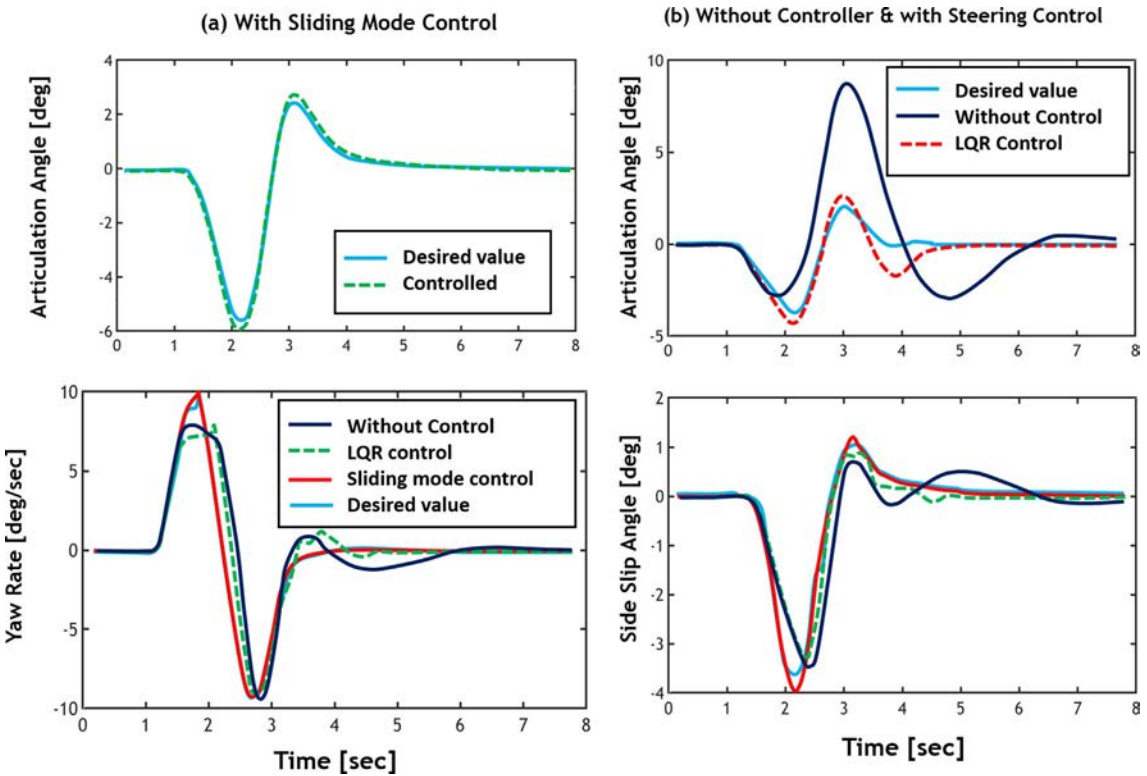

Fig. 8.18 System responses to hard line swap maneuvers.

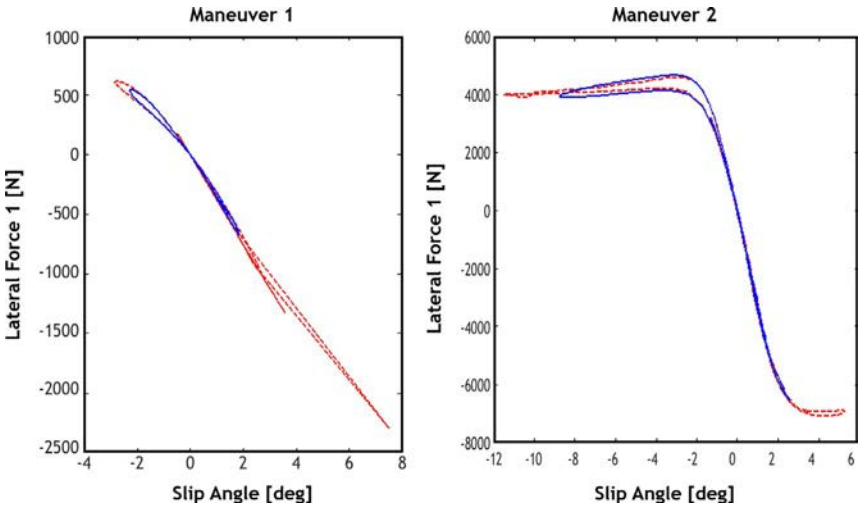

Fig. 8.19 Variations of tractor right front wheel lateral force against lateral slip angle in both maneuvers. The sliding mode controller *(bold line)* and the linear optimal controller *(dotted line)*.

It should be noted that the tractor front axle and trailer rear axle have been assumed steerable, and as a consequence, steering actuators are these two axles. It is also possible to apply the braking torque on all the wheels of the articulated vehicle.

To compare these two actuators by using the presented linear model, the steady-state gain of each control variable is calculated for each control input, and its amount is compared in various lateral accelerations.

Fig. 8.20 shows this comparison in which the articulated vehicle model has been exposed to multiple steady-state maneuvers in different lateral accelerations at 100 km/h where the horizontal axis represents the lateral acceleration, which has increased from 1 m/s^2 to 5 m/s^2. Besides, it is assumed that the maximum steering angle that can be applied on each wheel is 10 degrees ($\frac{\pi}{18}$), and the maximum braking torque is 10,000 N m. Furthermore, the related steady-state gains have been normalized so that the capability of the braking and steering actuators becomes comparable. First line images of this in Fig. 8.20 compare the capability of the tractor front axle steering angle and the braking torque applied over the wheels of this unit in adjusting the tractor control variables. It can be seen from Fig. 8.20 that the tractor steering angle with respect to the braking torque has a significant capability in adjusting the tractor lateral and yaw velocity. On the other hand, it is observed that the tractor steering actuator is so sensitive to the

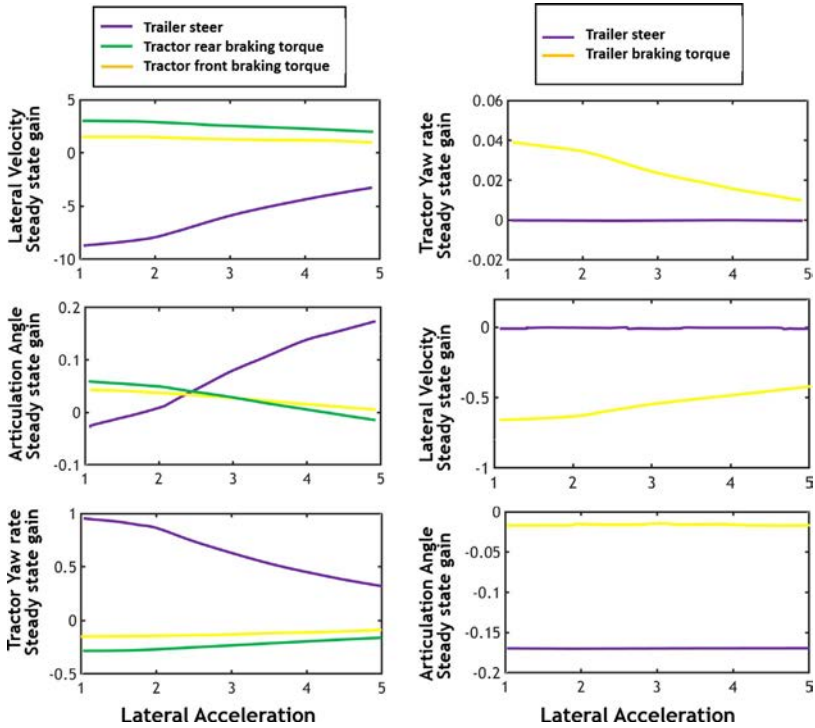

Fig. 8.20 The steady-state gains in different accelerations at 100 km/h velocity.

lateral acceleration variations and its capability has decreased by 1/3 through increasing the lateral acceleration up to 5 m/s^2,which is a significant value for the articulated vehicle. Moreover, it can be seen that the braking actuator shows less sensitivity to this acceleration variation. Other than that, in addition to reducing the capability of the steering actuator in adjusting two given variables, its superiority over the braking actuators is also specified in extreme situations.

In the second row of this figure, adjusting the articulation angle by the two above-mentioned actuators has been considered. It is observed that by increasing the lateral acceleration for both actuators, the direction change occurs in the control command. Further, we can see that the trailer steering actuator could not have any influence on the tractor lateral and rotational velocity. Also, in the last image, the considerable weakness of the semitrailer braking actuator over the steering actuator of this unit is observable in adjusting the articulation angle. According to a study conducted in this regard, the semitrailer braking actuator could not simply force the articulation angle to follow its optimal value.

8.6 Integrated control of braking and steering subsystems

As previously mentioned, the steering inputs could regulate the directional dynamics efficiently compared with the braking inputs. Therefore, in normal motion situations, the steering actuators adjust the vehicle directional dynamics. As the vehicle motion conditions become severe and the lateral acceleration increases, the capability of the steering actuators is reduced and, in this case, the braking inputs could be used as an auxiliary option. Meanwhile, we would keep the steering input in extreme conditions according to the previously obtained results.

The above paragraph gives the basis of the integrated control system design. For designing the control system, a sliding mode control approach is employed, provided in the previous section. According to the conducted measurements, three major inputs U_1, U_2, and U_3 have been determined. In this step, the aim is to assess the contribution of each steering and braking actuator of the tractor and semitrailer in providing the major inputs.

If we repeat the presented computation procedure for Eq. (8.101) with yaw torques caused by the braking forces, the relationship between the major inputs and the modified forces and torques would be obtained by:

$$F_{yft} + F_{yrs} = U_{1N} \tag{8.120}$$

$$F_{yft}L_{ft} - F_{yrs}L_{cs} + M_{zbt} + M_{zbs} = U_{2N} \tag{8.121}$$

$$M_{zbs} - F_{yrs}L_{rf} = U_3 \tag{8.122}$$

where M_{zbt} and M_{zbs} are the yaw torques caused by the braking forces while they are approximated by assuming small steering angles, as follows:

$$M_{zbt} = \frac{\left((F_{t2} + F_{t4}) - (F_{t1} + F_{t3})\right)W_t}{2} \tag{8.123}$$

$$M_{zbs} = \frac{(F_{t6} - F_{t5})W_s}{2} \tag{8.124}$$

We should note that $U_{1N} = U_1 - \hat{F}_{yrt}$ and $U_{2N} = U_2 + \hat{F}_{yrt}L_{rt}$. Therefore, a cost function is given as Eq. (8.125):

$$\begin{aligned} J_{int} = {} & \frac{1}{2}\omega_1\left[F_{yft} + F_{yrs} - U_{1N}\right]^2 \\ & + \frac{1}{2}\omega_2\left[F_{yft}L_{ft} - F_{yrs}L_{cs} + M_{zbt} + M_{bs} - U_{2N}\right]^2 \\ & + \frac{1}{2}\omega_3\left[M_{zbs} - F_{yrs}L_{rf} - U_3\right]^2 + \frac{1}{2}\omega_4 F_{yft}^2 + \frac{1}{2}\omega_5 M_{zbt}^2 + \frac{1}{2}\omega_6 F_{yrs}^2 \\ & + \frac{1}{2}\omega_7 M_{zbs}^2 \end{aligned} \tag{8.125}$$

The first three terms of this equation are taken from Eqs. (8.122)–(8.124). The other four terms have been inserted into the cost function in order to determine what the contribution of each actuator is in generating the braking and lateral forces. For example, a very high value for ω_4 could reduce the contribution of the tractor front steering angle in adjusting the vehicle directional dynamic. In addition, by adjusting the weighting coefficients ($\omega_{1:7}$) in an appropriate manner, the constraints of the braking and steering operators are satisfied, and a suitable dynamics behavior is available for the articulated vehicle. The necessary conditions to minimize J_{int} include $(\frac{\partial J_{int}}{\partial F_{yft}} = \frac{\partial J_{int}}{\partial F_{yrs}} = \frac{\partial J_{int}}{\partial M_{zbt}} = \frac{\partial J_{int}}{\partial M_{zbs}} = 0)$.

By applying the method given in the previous section, the following equation is obtained. Eq. (8.126) can be applied to determine the modified lateral forces and rotational torques caused by the braking forces at any time.

$$\begin{bmatrix} \omega_1 + \omega_2 L_{ft}^2 + \omega_4 & \omega_1 - \omega_2 L_{ft} L_{cs} & \omega_2 L_{ft} & \omega_2 L_{ft} \\ \omega_1 - \omega_2 L_{ft} L_{cs} & \omega_1 + \omega_2 L_{cs}^2 + \omega_3 L_{rf}^2 + \omega_6 & -\omega_2 L_{cs} & \omega_2 L_{cs} + \omega_3 L_{rf} \\ \omega_2 L_{ft} & \omega_2 L_{ft} & \omega_2 + \omega_5 & \omega_2 \\ \omega_2 L_{ft} & \omega_2 L_{cs} + \omega_3 L_{rf} & \omega_2 & \omega_2 + \omega_3 + \omega_7 \end{bmatrix}$$

$$\begin{Bmatrix} F_{yft} \\ F_{yrs} \\ M_{zbt} \\ M_{zbs} \end{Bmatrix} = \begin{Bmatrix} \omega_1 U_{1N} + \omega_2 L_{ft} U_{2N} \\ \omega_1 U_{1N} - \omega_2 L_{cs} U_{2N} - \omega_3 L_{rf} U_3 \\ \omega_2 U_{2N} \\ \omega_2 U_{2N} + \omega_3 U_{3N} \end{Bmatrix} \tag{8.126}$$

Once the modified lateral forces have been determined by using the method given in the previous section (applying the Abe Reverse Tire Model), the modified steering angle is achieved. Then, the braking torque applied to each wheel must be calculated. To minimize the interference of the control braking torque in the performance of the tractor front active steering system, the braking torque is applied only to the tractor rear axle wheels. There are three axles for the semitrailer unit, where it is assumed that a control braking torque can be used for all wheels of one side at any time. In terms of Eqs. (8.119) and (8.120) as well as assuming the relation of braking torque and longitudinal force of each wheel ($T_{bi} = F_{ti} R_{wi}$), the braking torques of tractor wheels (T_{bt}) and semitrailer wheels (T_{bs}) are obtained as the following pseudocode:

for tractor unit

if $M_{zbt} \geq 0$ *then*

$$for\ right\ wheels: T_{bt} = -\frac{R_w M_{zbt}}{W_t} \qquad for\ left\ wheels: T_{bt} = 0$$

else

$$for\ right\ wheels: T_{bt} = 0 \qquad for\ left\ wheels: T_{bt} = \frac{R_w M_{zbt}}{W_t}$$

end

for semitrailer unit

if $M_{zbs} \geq 0$ *then*

$$for\ right\ wheels: T_{bs} = -\frac{2R_w M_{zbs}}{3W_s} \qquad for\ left\ wheels: T_{bs} = 0$$

else

$$for\ right\ wheels: T_{bs} = 0 \qquad for\ left\ wheels: T_{bs} = \frac{2R_w M_{zbs}}{3W_s}$$

end

(8.127)

8.6.1 Limiting wheel slip ratio

Applying braking torque on each wheel can lead to tire slip. As can be noticed from Fig. 8.21, the longitudinal force (braking force) at each tire is a function of tire slip ratio (γ). In Fig. 8.21, it can be seen that the max-

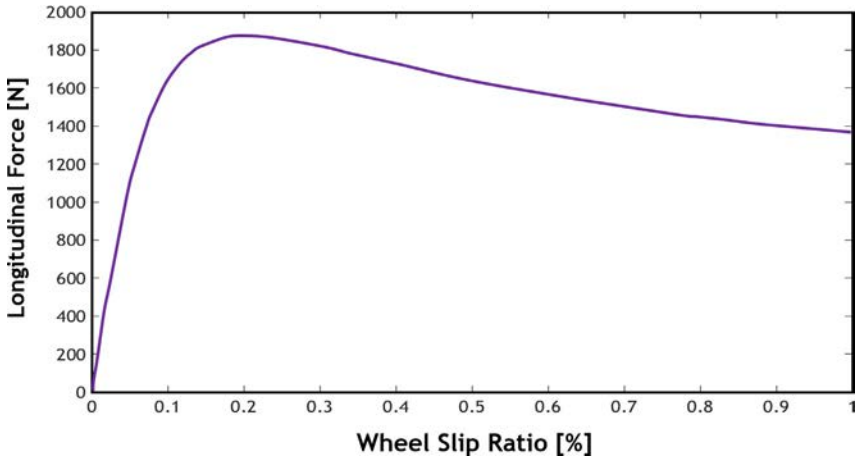

Fig. 8.21 Longitudinal force as a function of slip ratio.

imum braking force occurs at a 0.2 slip ratio. Therefore the antilock braking systems do not let the slip ratio exceed the predefined threshold.

However, this problem must be considered from another viewpoint in the integrated controller. The major question is that when the braking subsystem as an assistant to the steering subsystem starts to adjust the directional dynamics in the semitrailer unit, is it suitable to choose 0.2 for the maximum allowed slip ratio? Nevertheless, it must be noted that a maximum 0.2 slip ratio seems suitable for a time when our aim is just braking and shortening the stop distance.

The steering subsystem adjusts the motion through lateral forces. On the other hand, we know that increasing the slip ratio has an inverse effect on the lateral force and reduces its value. In Fig. 8.22, a semitrailer has been shown in the extreme conditions where both braking and steering actuators are active. For this purpose, both the braking force and lateral force create torque around the articulation point, as mentioned in Eq. (8.128), and this adjusts the articulation angle of AHV. In these calculations, the steering angle is assumed to be small.

$$M_{z\_fifth} = F_t \frac{W_s}{2} + F_s \frac{L_{fs} + L_{rs}}{2} \tag{8.128}$$

We should take notice that increasing the slip ratio by 0.2 can cause a longitudinal force increase. However, it might be in contradiction with the major demand, which is the maximum value of M_{z_fifth}, while to find

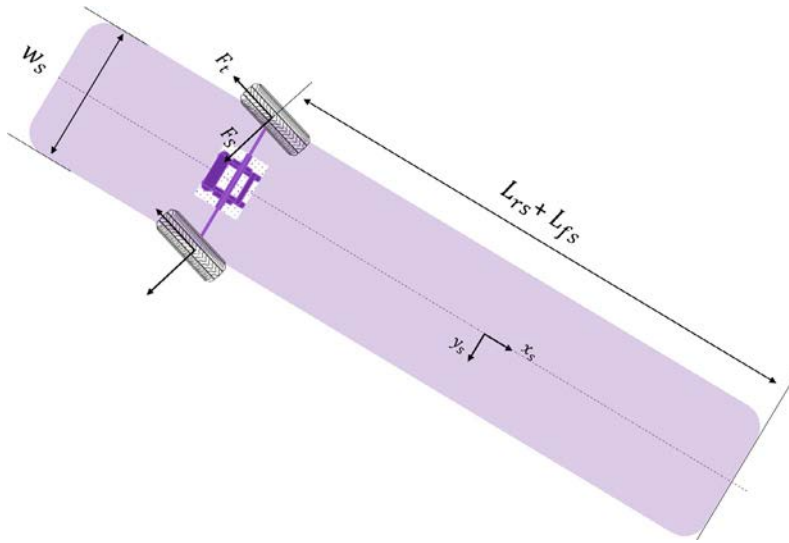

Fig. 8.22 Semitrailer in the extreme condition with both actuators.

the maximum allowed slip, we could plot the curve M_{z_fifth} in terms of slip ratio.

In Fig. 8.23, the curves of the longitudinal force (dotted), lateral force (dashed line), and rotational torque M_{z_fifth} (bold line) have been shown as functions of slip (λ) at three different slip angles ($\alpha = 1, 5, 10$ degrees) for two normal forces ($F_z = 20{,}000, 40{,}000$ N) and two friction coefficients ($\mu = 0.2, 0.4$).

It can be concluded that the maximum allowed slip ratio for the semitrailer wheels in activating the braking subsystem so as to help the steering subsystem is a value less than 0.1 and about 0.05. Therefore, it should be arranged such that the wheel slip ratio is not allowed to exceed 0.05. To prevent the wheel slip ratio from exceeding the allowed threshold, we use a simple fuzzy system where reverse tangent functions have been used. The left side of Fig. 8.24 shows the schematic of this system where the input of this system is the slip ratio, and its output is the weight function (ρ) in the range of 0–1. If the value of the slip ratio (λ) exceeds the allowed value of λ_{ref}, ρ is minimized quickly and regulates the braking torque (T_b) before being applied to the wheels. As mentioned above, the curve (ρ) has been defined as a reverse tangent function based on Eq. (8.129). This curve is plotted for multiple λ_{ref} on the right side of Fig. 8.24.

$$\rho = 0.55 \tan^{-1}\left(160\left(\lambda + \lambda_{ref}\right)\right) \tag{8.129}$$

Therefore, for activation of the braking subsystem to adjust the directional dynamics, the suitable value of the allowed slip ratio is 0.05 for the semitrailer axles. However, to stop quicker than normal situations, this value increases to 0.2.

8.6.2 The performance of the integrated controller

In this section, the performance of the integrated controller is evaluated in several maneuvers. The structure of the integrated controller is shown in Fig. 8.25.

8.6.2.1 Lane change maneuver

In this maneuver, the performances of two integrated controllers and a hybrid control system are compared. The given hybrid control system has a structure similar to the integrated control system. The only difference is in considering the weight coefficients $\omega_{5,\,6,\,7}$ as a constant value where these coefficients are updated within the integrated control system. The basic

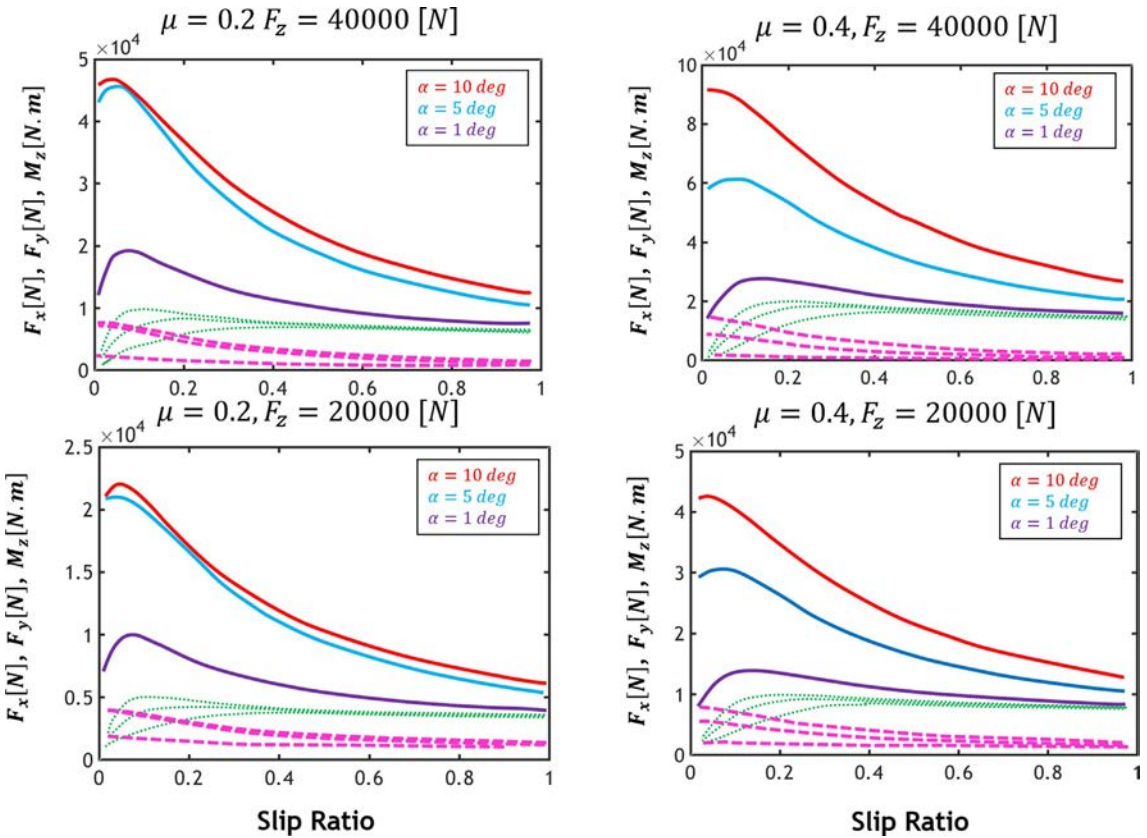

Fig. 8.23 Torque is given in Eq. (8.128) *(bold line)*, braking force *(dotted)*, lateral force *(dashed line)* as a function of slip.

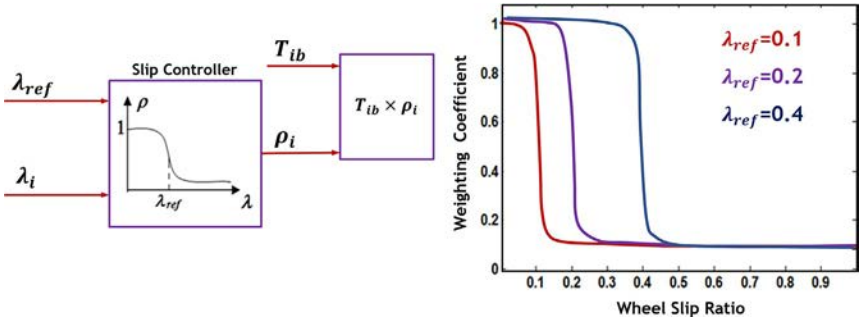

Fig. 8.24 Slip ratio limiting system.

velocity for the lane change maneuver is considered as 120 km/h, and the minimum friction coefficient is 0.22 by which the hybrid system can adjust the vehicle motion. Consequently, the performances of the hybrid as well as the integrated controllers are compared in this situation.

In Fig. 8.26, it is shown that both control techniques have similar performances in adjusting the articulation angle, the yaw velocity, and the lateral slip angle. However, their difference is in the variation of vehicle longitudinal velocity. It can be seen from Fig. 8.26 that in the hybrid controller, the vehicle velocity has decreased more than 5 km/h, whereas by using the integrated controller, the velocity reduction is less than 1.5 km/h. This slight velocity reduction implies the on-time usage of the braking actuator in an integrated controller.

Fig. 8.27 shows the variations of weight coefficients during the maneuver. The effect of these variations, particularly the integrated controller braking torques, is represented in Fig. 8.28.

It is evident that by considering the weight coefficient of the tractor steering and also the fewer variations of the semitrailer's steering actuator, there is not any significant difference among the control steering angles of both studied methods. The evident difference is in the modified yaw torques based on the braking actuator, where the integrated controller applies them in a short period of motion while the torque is used for the hybrid controller in a vibrated manner during the maneuver. It must be noted that according to the conducted study, the proposed integrated controller can adjust the vehicle motion on slippery roads at 120 km/h. Fig. 8.29 shows the system response at 0.16 friction rates/coefficient. Moreover, it is seen that the control variables have been adjusted in an acceptable limit. Fig. 8.30 represents the vehicle motion path with and without the controller.

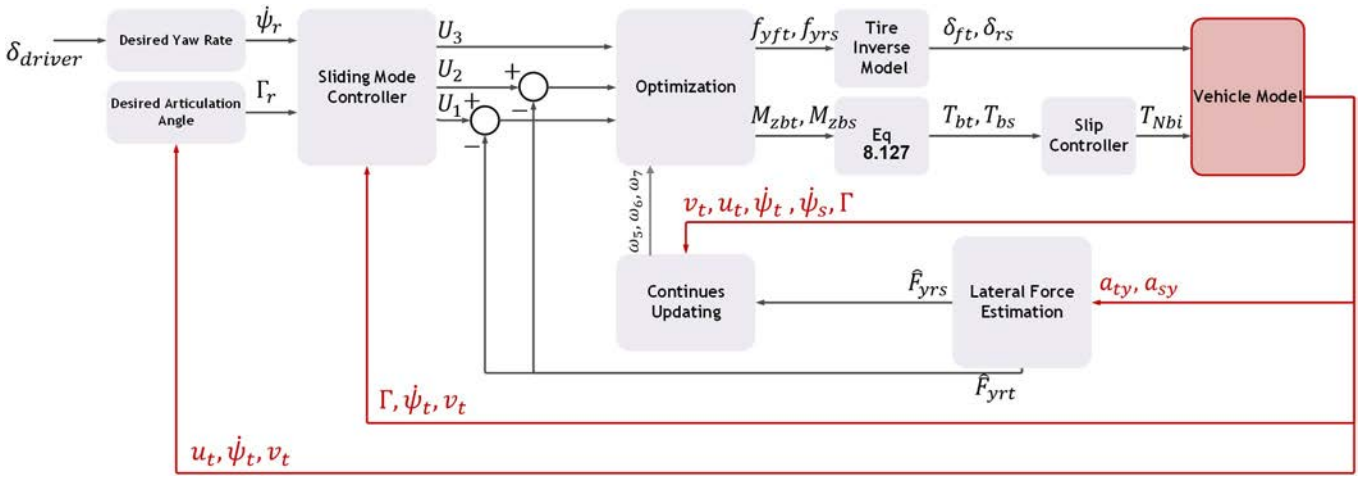

Fig. 8.25 Integrated control system.

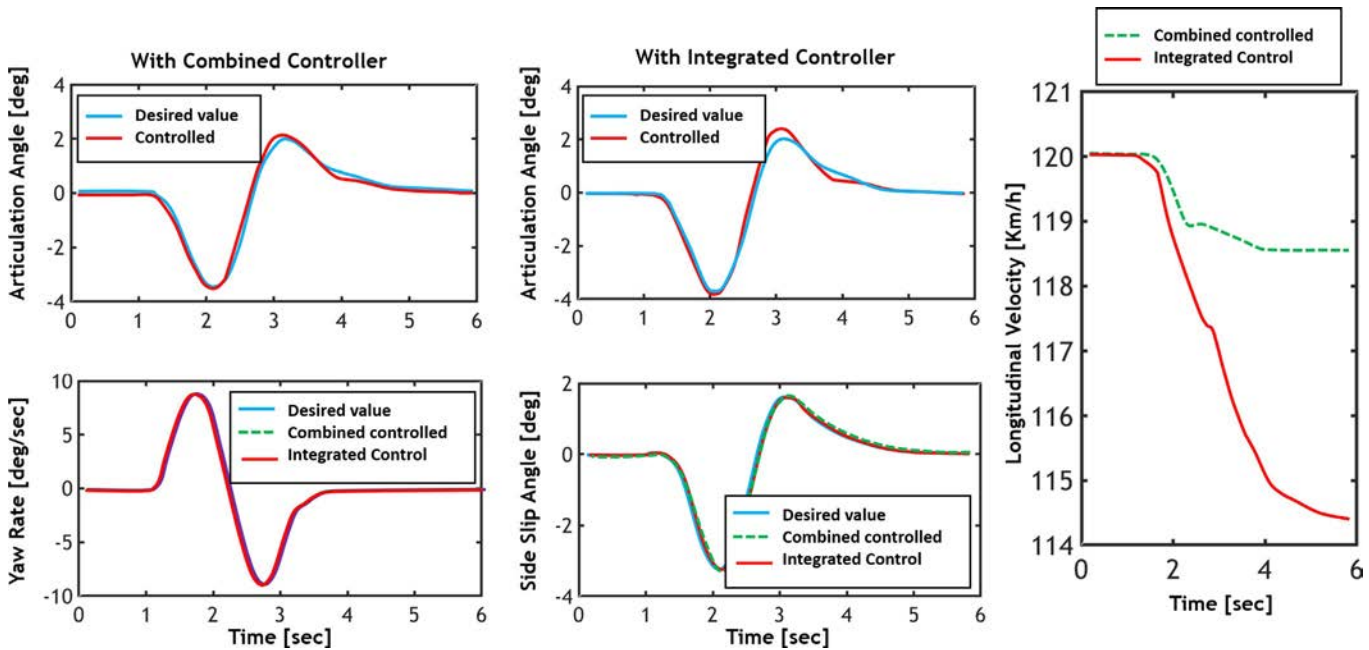

Fig. 8.26 Comparison of hybrid and integrated controller responses.

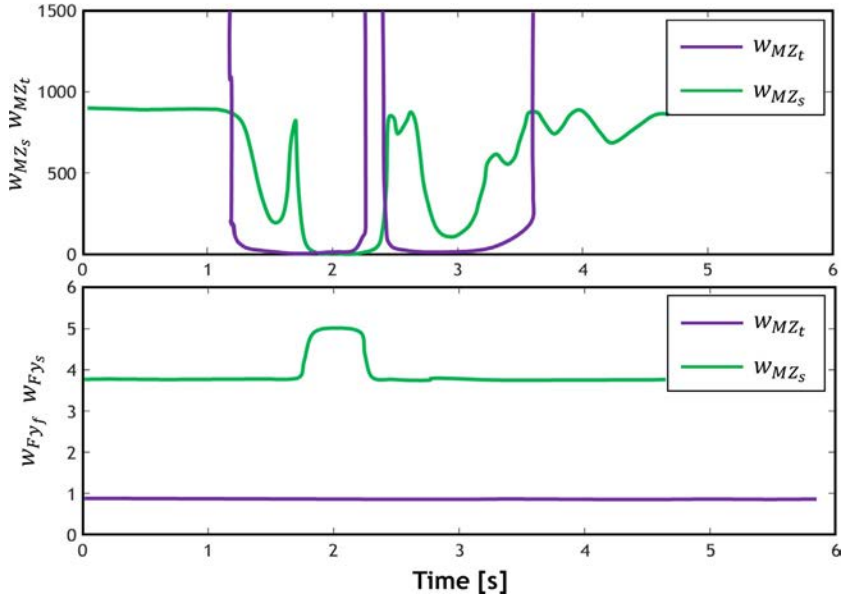

Fig. 8.27 Weight coefficient variations of the integrated controller.

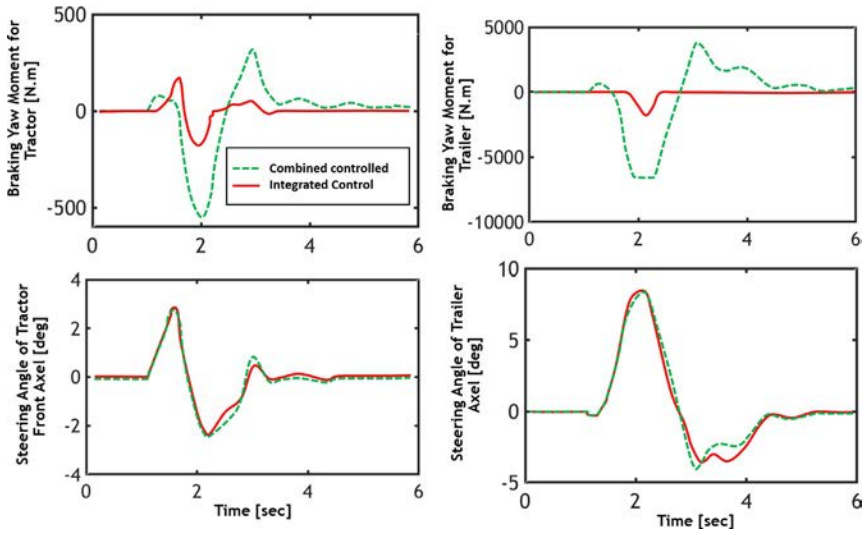

Fig. 8.28 Two upper images: Braking yaw torques (M_{zbt}, M_{zbs}) for both tractor and semitrailer units; two lower images: the control steering angle of the tractor front axle and semitrailer rear axle.

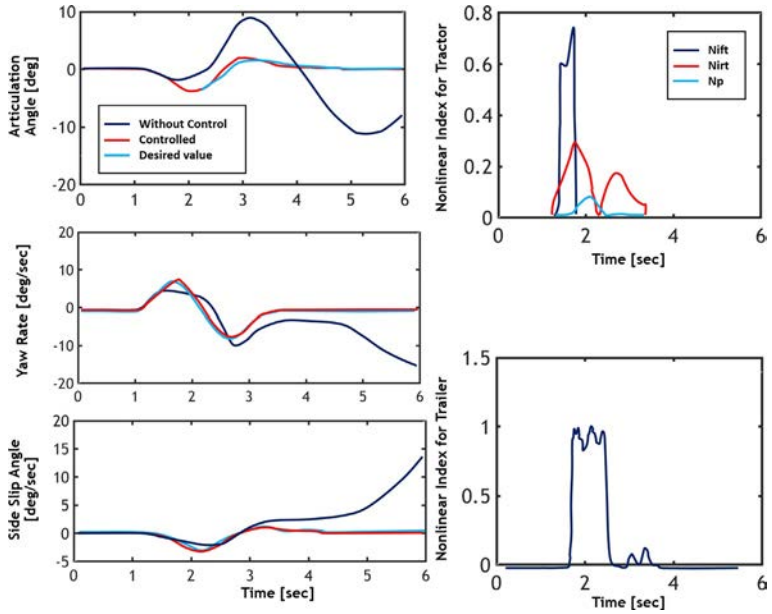

Fig. 8.29 Comparison of vehicle response with and without control by using the proposed integrated controller at 120 km/h and a 0.16 friction coefficient.

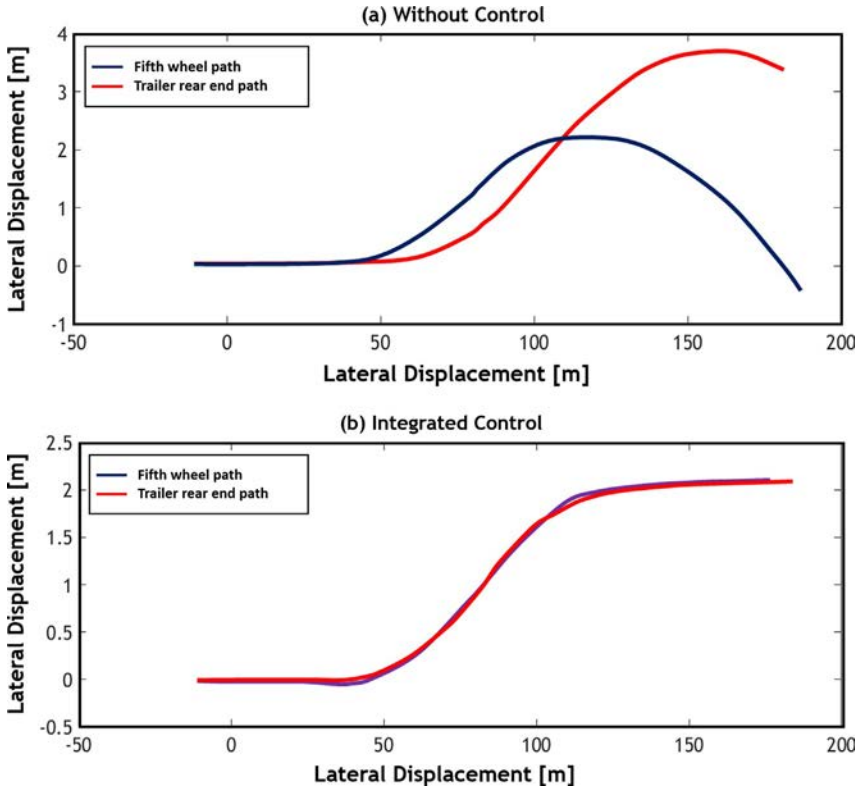

Fig. 8.30 Comparison of vehicle path in controlled and uncontrolled vehicles.

8.6.2.2 Slalom maneuver on the semislippery road

In this maneuver, the articulated vehicle moves at 140 km/h on the road with a 0.5 friction rate/coefficient, where the steering angle shown in Fig. 8.31 is applied on the vehicle front wheel. In Fig. 8.32, the vehicle response is compared in three modes: without control, hybrid control, and integrated control. In adjusting the articulation angle, it is seen from Fig. 8.31 that in the final seconds, the integrated control outperforms the hybrid control. Also, the vehicle longitudinal velocity has less reduction by applying integrated control. Fig. 8.32 shows the control inputs where the unprofitable use of a hybrid controller is evident from the braking actuator. Fig. 8.33 also represents the tractor and semitrailer lateral accelerations in three given modes. It is shown that by using the control system, the acceleration of the tractor unit has been significantly limited. Fig. 8.34 represents a lateral acceleration in the slalom maneuver.

8.6.3 Evaluation of the controller robustness against error and noise over control variables

In this section, the vehicle is exposed to the critical maneuver again. The given maneuver is the lane-change maneuver, which has been performed at 110 km/h on the 0.3 friction coefficient. In Fig. 8.35, the system response

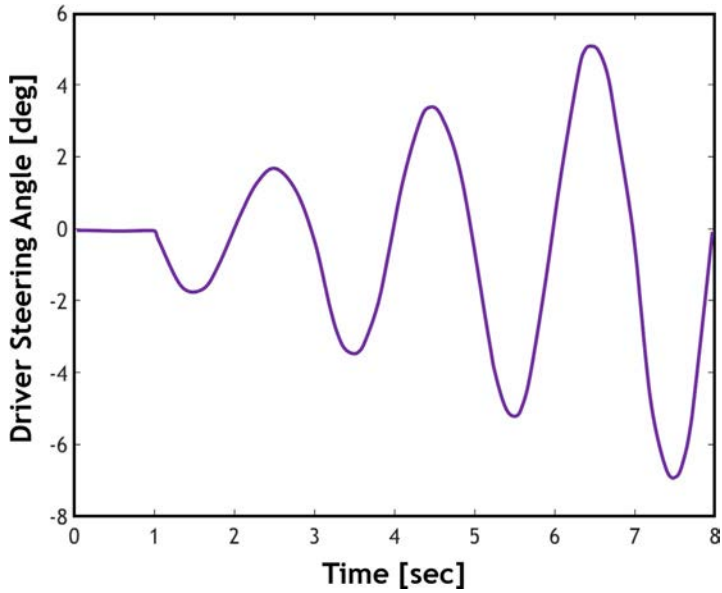

Fig. 8.31 Steering angle in the slalom maneuver.

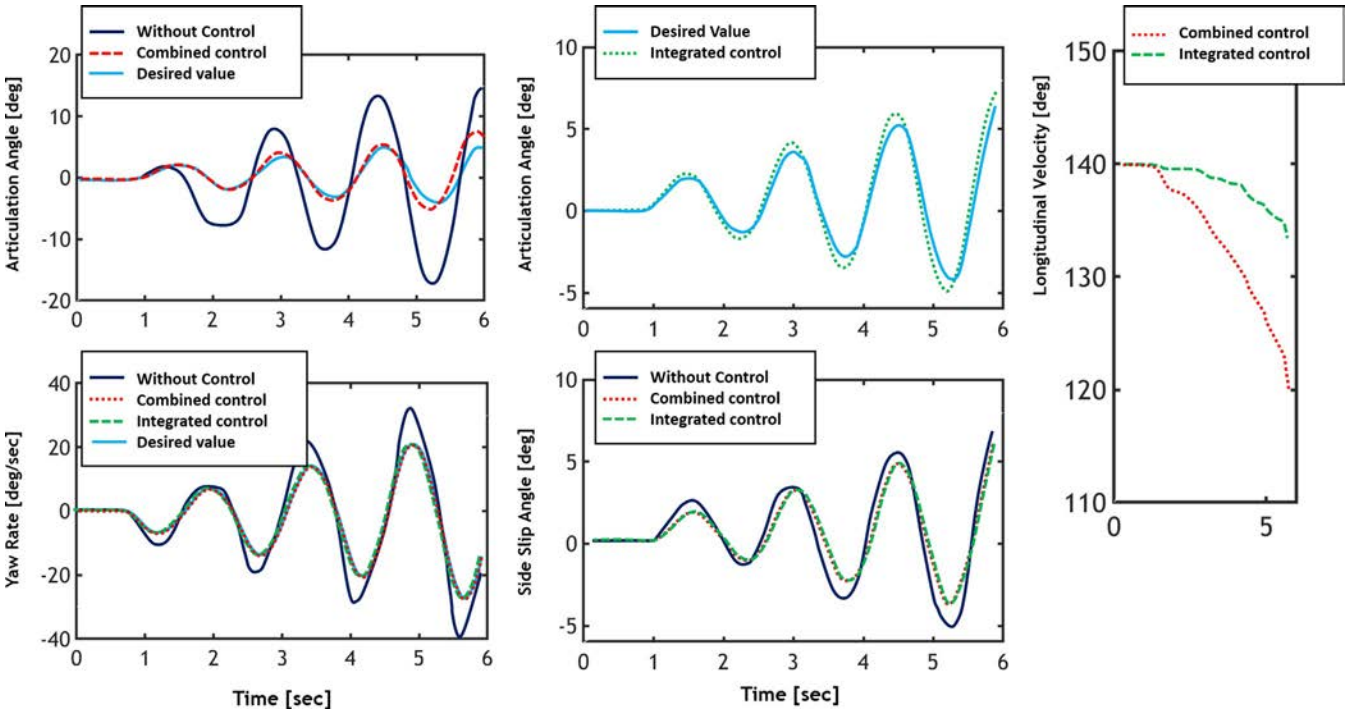

Fig. 8.32 Vehicle response in the slalom maneuver.

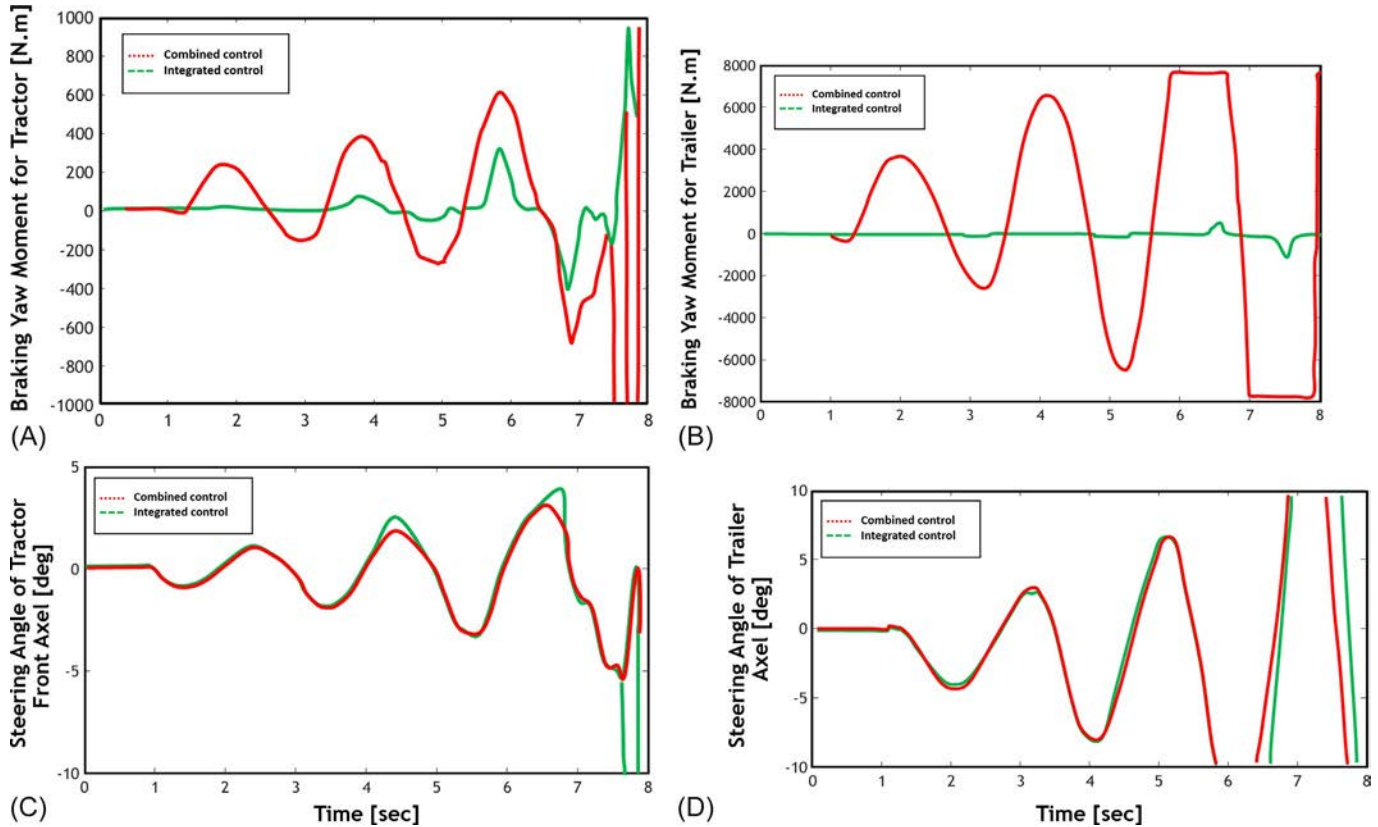

Fig. 8.33 Control inputs in the slalom maneuver.

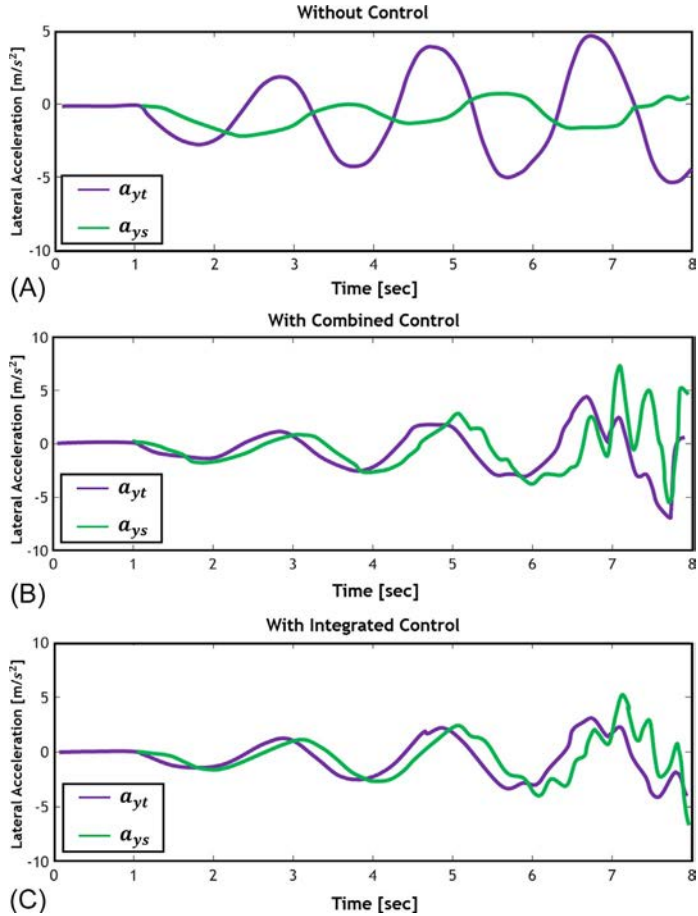

Fig. 8.34 Lateral acceleration in the slalom maneuver.

is shown without the controller being active. Later, the performance of the controller has been studied with the noise and error over the motion variables. The yaw velocity sensor can measure the tractor yaw velocity. Due to the measuring noise, it is assumed that this variable has a white noise with 10^{-5} variance. Furthermore, for the longitudinal and lateral velocities to be evaluated, 10% error and noise have been considered with 10^{-4} variance. Moreover, it is observed that in the presence of a controller, the defined maneuver has been performed well, and the condition of semitrailer off-tracking over the tractor with additional noise and error is negligible against without control mode, as shown in Fig. 8.36.

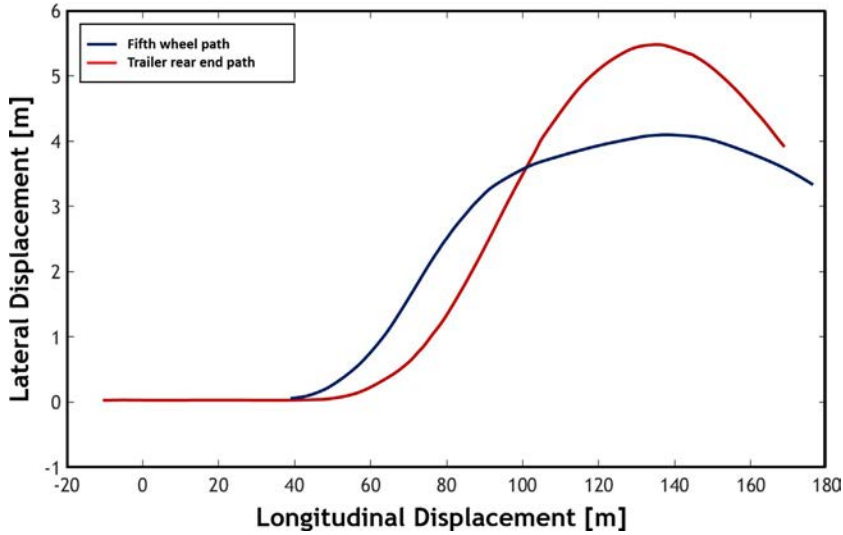

Fig. 8.35 Vehicle motion path in the line change maneuver without using the controller.

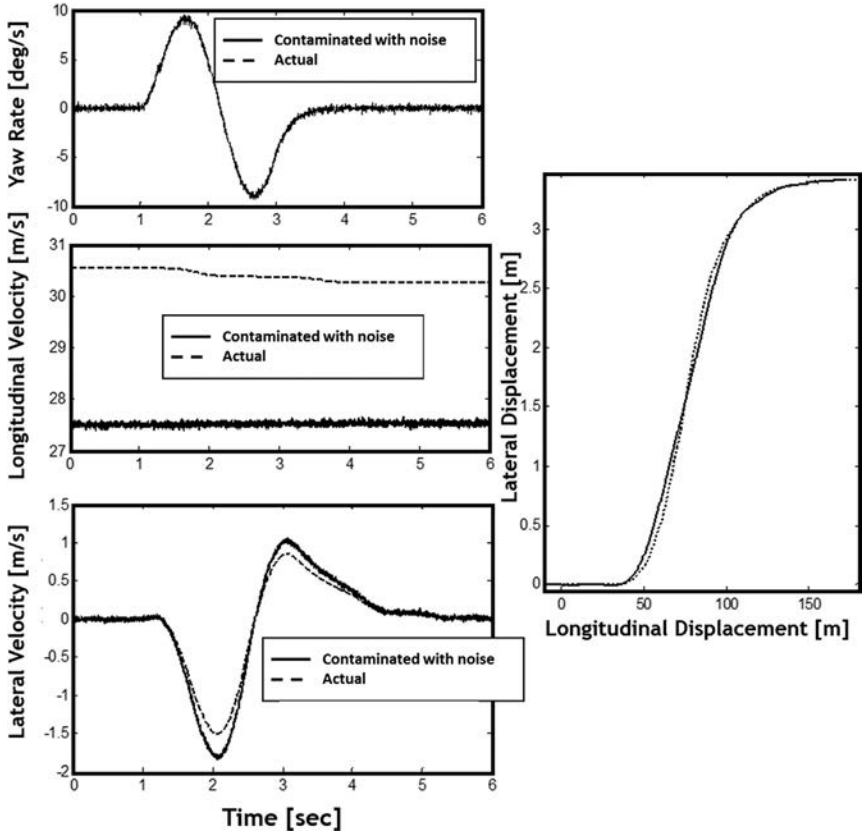

Fig. 8.36 Left: Noisy displacement variables, right: increasing off-tracking.

8.7 Conclusion

In this chapter, a systematic method to define a reference articulation angle was developed. The linear model has been used to design the controller and to generate the reference response while the nonlinear model has been used to evaluate the system responses. The reference model for generating the desired response of the tractor yaw rate, the tractor lateral velocity, and the articulation angle has been proposed. Three output variables, including tractor yaw rate, tractor lateral velocity, and articulation angle, have been controlled for the reference responses. Furthermore, the steering angle of the tractor front axle, the tractor rear axle, and the trailer rear axles are used to make the state variables follow the desired responses. The simulation results revealed that the tracking of the proposed desired articulation angle can eliminate the off-tracking between the trailer rear end path and the fifth wheel path and that the control of the lateral velocity as well as the yaw rate can improve the vehicle handling responses at high speed in the lane change maneuver.

References

[1] S. Kharrazi, Steering Based Lateral Performance Control of Long Heavy Vehicle Combinations, Chalmers University of Technology, 2012.
[2] M. Doumiati, O. Sename, L. Dugard, J.J. Martinez-Molina, P. Gaspar, Z. Szabo, Integrated vehicle dynamics control via coordination of active front steering and rearbraking, Eur. J. Control. 19 (2) (2013) 121–143.
[3] J. He, D.A. Crolla, M.C. Levesley, W.J. Manning, Coordination of active steering, driveline, and braking for integrated vehicle dynamics control, Proc. Inst. Mech Eng. D Automob. Eng. 220 (10) (2006) 1401–1420.
[4] B.A. Guvenç, T. Acarman, L. Guvenç, Coordination of steering and individual wheel braking actuated vehicle yaw stability control, in: Proceedings of the IEEE Intelligent Vehicle Symposium, 2003, pp. 288–293.
[5] Y. Furukawa, M. Abe, On-board-tyre-model reference control for cooperation of4ws and direct yaw moment control for improving active safety of vehicle handling, in: Proceedings of the 3rd International Symposium on Advanced Vehicle Control, 1996, pp. 507–526.
[6] J. He, Integrated Vehicle Dynamics Control Using Active Steering, Driveline and Braking (Ph.D. thesis), University of Leeds, 2005.
[7] M. Nagai, H. Yutaka, Y. Sachiko, Integrated control of active rear wheel steering and direct yaw moment control, Veh. Syst. Dyn. 27 (5–6) (1997) 357–370.
[8] M. Nagai, S. Motoki, G. Feng, Study on integrated control of active front steer angle and direct yaw moment, JSAE Rev. 23 (2003) 309–315.
[9] F. Mobini, A. Ghaffari, M. Alirezaei, Nonlinear optimal control of articulated-vehicle planar motion based on braking utilizing the state-dependent Riccati equation method, Proc. Inst. Mech. Eng. D J. Automob. Eng. 229 (13) (2015) 1774–1787.
[10] J. Wang, R.G. Longoria, Coordinated and reconfigurable vehicle dynamics control, IEEE Trans. Control Syst. Technol. 17 (3) (2009) 723–732.

[11] S. Di Cairano, H.E. Tseng, Driver-assist steering by active front steering and differential braking: design, implementation and experimental evaluation of a switched model predictive control approach, in: Proceedings of the 49th IEEE Conference on Decision and Control, Atlanta, USA, 2010, pp. 2886–2891.
[12] B.A. Guvenc, L. Guvenc, S. Karaman, Robust yaw stability controller design and hardware-in-the-loop testing for a road vehicle, IEEE Trans. Veh. Technol. 58 (2) (2009) 555–571.
[13] M. Abe, Vehicle Handling Dynamics, first ed., 2009, ISBN: 9781856177498. Printbook, and Release.
[14] S.H.T. Oreh, R. Kazemi, S. Azadi, A new desired articulation angle for directional control of articulated vehicles, Proc. Inst. Mech. Eng. K J. Multi-body Dyn. 226 (4) (2012) 298–314.
[15] S.H.T. Oreh, R. Kazemi, S. Azadi, A sliding-mode controller for directional control of articulated heavy vehicles, Proc. Inst. Mech. Eng. D J. Automob. Eng. 228 (3) (2014) 245–262.
[16] X. Yang, Z. Wang, W. Peng, Coordinated control of AFS and DYC for vehicle handling and stability based on optimal guaranteed cost theory, Veh. Syst. Dyn. 47 (1) (2009) 57–79.
[17] Rules for the Assessment of Potential Performance-Based Standards. Discussion Paper, National Transport Commission (NTC), Australia, 2008.
[18] A. Hac, et al., Stability and Control Consideration of Vehicle-Trailer Combination, SAE Technical Paper, 2008-01-1228, 2008.
[19] M.K. Salaani, The application of understeer gradient in stability analysis of articulated vehicles, Int. J. Heavy Veh. Syst. 16 (1) (2009) 3–25.
[20] S. Inagaki, I. Kshiro, M. Yamamoto, Analysis on vehicle stability in critical cornering using phase-plane method, in: Proceedings of the International Symposium on Advanced Vehicle Control, 1994.
[21] Y. Shibahata, K. Shimada, T. Tomari, The improvement of vehicle maneuverability by direct yaw moment control, in: Proceedings of AVEC '92, Yokohama, Japan, 1992.
[22] S. Notsu, R. Takahashi, Y. Watanabe, Investigation Into Turning Behavior of Semi-Trailer With Additional Trailer-Wheel Steering—A Control Method for Trailer-Wheel Steering to Minimize Trailer Rear—Overhang Swing in Short Turns, SAE Technical paper, No.912570, 1991.
[23] J. Wang, R.G. Longoria, Coordinated and reconfigurable vehicle dynamics control, IEEE Trans. Control Syst. Technol. 17 (3) (2009) 723–732.
[24] O. Mokhyamar, M. Abe, Simultaneous optimal distribution of lateral tire forces for the model following control, J. Dyn. Syst. Meas. Control. 126 (2004) 753–763.
[25] J.-J.E. Slotine, W. Li, Applied Nonlinear Control, Prentice Hall, 1991.
[26] M. Abe, A. Kato, K. Suzuki, Y. Kano, Y. Furukawa, Y. Shibahata, Estimation of vehicle sideslip angle for DYC by using on-board-tire-model, in: Proceedings 4th International Symposium on Advanced Vehicle Control, Nagoya, Japan, 1998, pp. 437–442.

CHAPTER 9

Automatic parking of articulated vehicles using a soft computing approach

9.1 Introduction

Despite the widespread use of vehicles in daily routines, it has been problematic for less-experienced drivers to navigate the vehicles properly. This is especially the case when it comes to parallel parking or reverse driving. Automatic parking systems have contributed significantly to improved safety and the comfort of driving. Parking is one of the most challenging tasks. First, the driver is required to find and identify the location of the park. Then, running with a backward maneuver, try to steer the vehicle and place it in the desired location. This procedure is associated with high collision risks [1]. On a busy street, parking may take an extended amount of time for a junior driver, thereby interrupting the flow of traffic. Stats have shown that the presence of automatic parking systems can significantly mitigate particular traffic problems in metropolitan areas [2]. An automatic parking system is of great help for navigation in situations where the environmental constraints require high precision and driving experience [3]. A vehicle can be appropriately parked in a smaller parking space if it is equipped with an automatic parking system; this increases the parking capacity of the streets. Fig. 9.1 presents an example of a parallel and perpendicular parking maneuver. Considering what was mentioned above, as a subclass of automatic navigation systems, automatic vehicle parking has gained a great deal of attention from numerous research centers [4–7].

The research on the problem of vehicle parking has emerged from the general motion planning problem, making it usually defined as finding a path that connects the initial and target position of the vehicle under collision avoidance constraint while observing one or more nonholonomic constraints [8]. Automatic parking refers to the smart act of a vehicle to undertake the parking maneuver, which is not an easy task for a vehicle. For this purpose, first of all, the vehicle must be capable of sensing the environment to find an appropriate parking space and detect possible obstacles within the

Vehicle Dynamics and Control
https://doi.org/10.1016/B978-0-323-85659-1.00008-2

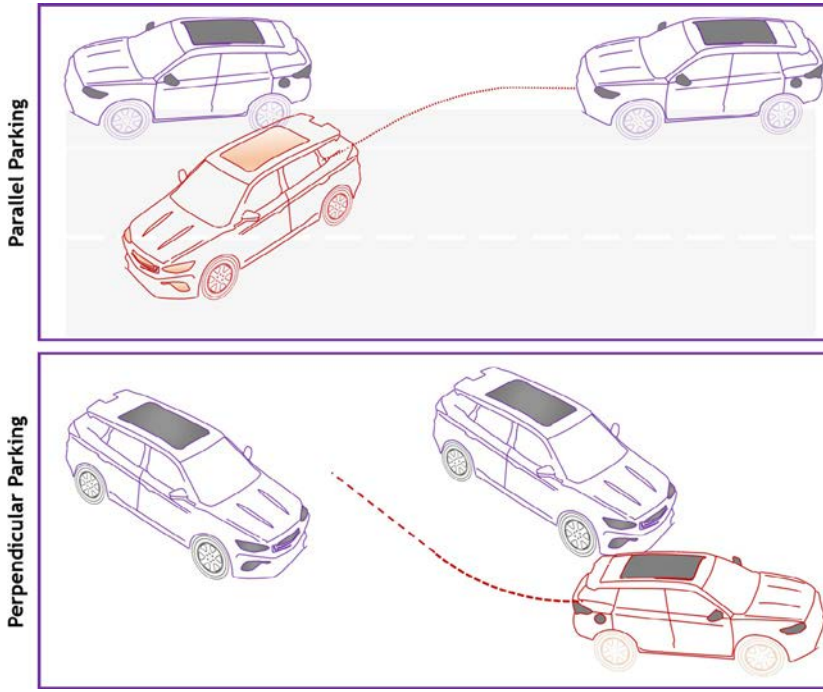

Fig. 9.1 Parallel and perpendicular parking of a passenger car.

surrounding space. Next, the vehicle must be able to autonomously plan for movement and then follow successive moves and verify them against the planned moves to ensure that the vehicle will end up at the target position. For the most part, existing automatic parking systems rely on the data acquired from visionary and active sensors (e.g., ultrasonic or laser) to reconstruct a local image for navigating the vehicle. According to Hsu et al. [9], the automatic parking problems can be classified into two broad categories, namely parallel parking and garage parking. These two classes of problems have been extensively investigated in many research works. From another point of view, Hsu et al. [9] stipulate that a group of works on the automatic parking problem sought to follow a reference path.

In contrast, some others focused on stabilizing the vehicle status while trying to reach the target position from any arbitrary initial condition. In general, for a vehicle with nonholonomic constraints, the kinematic equations are nonlinear and time-variant. Accordingly, it is almost impossible to design and practically establish an alternative controller (to replace the driver) for automatic handling of the vehicle through a parking maneuver using classic control methodologies.

The subject matter of navigation and kinematic control of articulated vehicles has been visited by many researchers [10]. Such a vehicle is made up of two main components, namely a tractor and a trailer. As is clear from the terminology, the tractor provides the traction force for the vehicle while the trailer is connected to the tractor at an articulation assemblage. The term *articulated vehicle* refers to a vehicle where one or more trailers is passively (providing no active traction force) connected to a tractor. Considering the working framework laid out in this chapter, we focus on the single-trailer articulated vehicles. The primary application of reverse parking for an articulated vehicle is that for cargo loading/unloading purposes in garages, custom spaces, plants, etc., where it is desired for the articulated vehicle to timely undertake the parking maneuver with no collision with the obstacles within the parking space (Fig. 9.2).

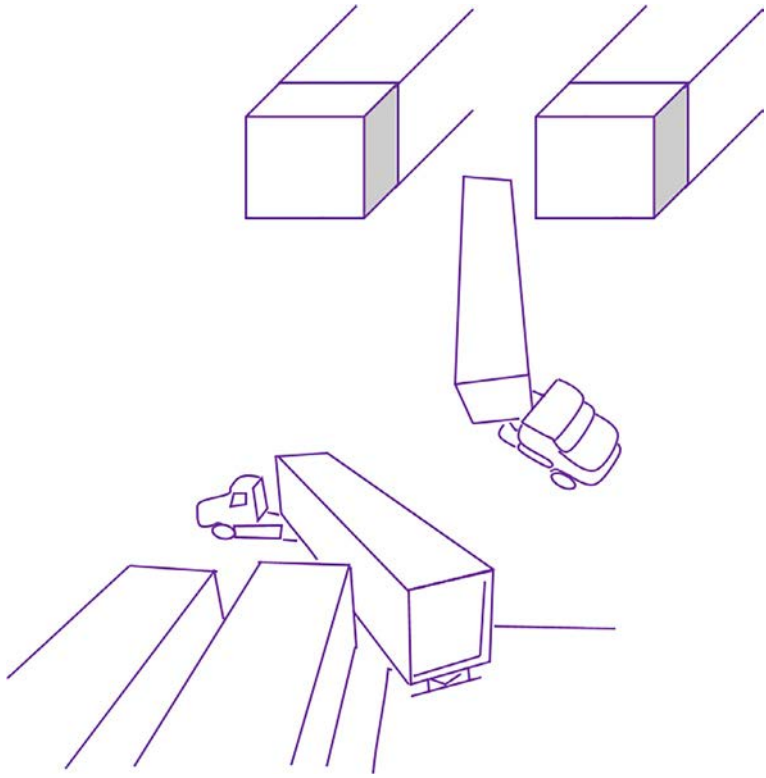

Fig. 9.2 An example of loading an articulated vehicle in a garage.

In the following, we present a quick review of the research works performed on this topic. The subject matter of automatic parking is significantly more complicated in an articulated vehicle rather than a passenger car because, as detailed in Zöbel et al. [11], the articulated vehicles are nonholonomic, and this makes their navigation and control more complicated. Accordingly, junior drivers reportedly experience many difficulties undertaking reverse maneuvers on a trailer either along a straight or curved path. Kelber et al. [12] took a step forward and suggested that reverse driving and parking of an articulated vehicle are hard to accomplish even for expert drivers.

Various solutions have been proposed based on control theories; examples include optimal control, nonlinear control, and hybrid control theories. As an alternative approach, the combination of fuzzy logic with ANN has been proposed as a workaround for path planning, navigation, and control of articulated vehicles; this has been extensively researched in the recent literature [11].

Among other research works focusing on the parking of articulated vehicles, one may refer to the research by Zimic and Mraz [13], who employed a decomposition technique to address the problem of numerous fuzzy rules in classic control theory for reverse parking of an articulated vehicle. Zobel et al. [14] elaborated on the problems associated with minimum-path parallel parking of articulated vehicles, extracted fundamental equations of motion, and presented precise definitions of the minimum-path parallel parking for articulated vehicles. Zobel et al. [14] explain the flow of automatic vehicle parking as follows. The radar scans the surrounding environment across the width of the parking space. Accordingly, it transmits a signal to the driver to inform that enough space for parking is detected. Finally, the driver must make the final decision to use the recognized parking space. Upon such a decision, the articulated vehicle stops at the proper location before implementing the control strategy (e.g., controlling the throttle/brake and the steering wheel) onto the articulated vehicle to navigate it into the parking space using forward and backward moves.

Presenting the kinematic model of a center-articulated vehicle, Delrobaei and McIsaac [15] proposed a control technique for following a reference path by satisfying geometric and nongeometric constraints, before analyzing the stability of a controller-equipped system through the Lyapunov function. Kelber et al. [12] proposed a control strategy that was made up of a controller for the articulation angle and another controller for following the path. The proposed controller possessed a layered cascade structure with an internal layer that was in charge of controlling the engine and an external

layer that addressed the vehicle dynamics. Sharafi and Nikpoor [16] defined the problem of articulated vehicle parking via an optimal path in the presence of fixed and moving obstacles. They also emphasized the significant roles played by such factors as the type, size, and velocity of the obstacles and the time constraint for reaching the target in making the problem even more complex. They acknowledged the automatic parking of an articulated vehicle as a nonlinear problem for which no conventional controller or method can achieve an appropriate control strategy. In contrast, one could design a control strategy for an articulated vehicle by simulating the human's behavior (provided the driver's experiences are known). For this purpose, they adopted two fuzzy controllers separately, one for identifying the path (the target) and another one for avoiding the obstacles.

Introducing the advanced driver assistance system (ADAS), Morales et al. [17] highlighted the advantages of such systems in improving driver safety and comfort through the complex maneuver required to park multitrailer articulated vehicles. This paper proposed a driver assistance system where the steerable wheels and throttle of the vehicle could be applied in such a way as to simulate a situation where the traction force is exerted at the tail of the last trailer when the vehicle is being maneuvered in a reverse direction. This was realized by adopting several cameras.

Elaborating on the necessity of using articulated vehicles, Roh and Chung [18] suggests that single- or multitrailer articulated vehicles are much more cost-efficient than multiple vehicles. This, however, does not undermine the main challenge with such systems: the control problem. This work focused on "pushing" rather than "pulling." The authors believed that the problem was much more complicated with pushing rather than pulling. The kinematics were extracted accordingly. This article further proposed a highly efficient method for the automatic parking maneuver of articulated vehicles. It proceeded to verify the proposed methodology by both simulating the procedure and implementing it on a model vehicle in the laboratory.

Hoel and Falcone [19] investigated the slow-motion maneuver of a heavy-duty articulated vehicle for its application in the automatic parking of such a class of vehicles. The technique used was the state feedback optimal controller design. They claim that the proposed method, with great accuracy, will perform the desired maneuvers. Mohamed et al. [20] described a motion planning algorithm for articulated vehicles and urged that the system could ensure a collision-avoided maneuver via predetermined paths. The proposed methodology was a combination of the so-called artificial potential field (AFP) and the optimal control theory.

Investigating the problems associated with the parking of articulated vehicles, it is obvious that the focus has been on inefficient conventional methods that were founded on the driver's skill rather than a simple, easily implementable smart system. Accordingly, the reverse parking function of an articulated vehicle has been generally achieved through successive forward/backward moves or by help from a nondriver human assistant. Moreover, this conventional parking scheme has proved to be slow and is associated with a high risk of colliding with the walls in the parking space, which can damage not only the vehicle but also the parking space due to an inappropriate assessment of the parking space by the driver. Therefore, this chapter considers the subject matter of the automatic parking of articulated vehicles. In this respect, such an automatic system is expected to move the vehicle forward from an arbitrary initial condition to an appropriate position[a] followed by a reverse maneuver to place the end of the trailer in the parking space. For an articulated vehicle, the reverse maneuver is generally performed in garages and exclusive parking space when the vehicle is expected to place the back of its trailer(s) appropriately for cargo loading/unloading purposes while satisfying a set of initial and final conditions without collision. Due to several reasons, including the nonlinear nature of the motion kinematics of articulated vehicle and the successful application of the fuzzy logic and ANNs in the field of vehicle control given the robustness and mathematical model-independence of the control systems based on adaptive neuro-fuzzy schemes, an adaptive neuro-fuzzy inference system is herein proposed for solving the problem of automatic parking in articulated vehicles.

9.2 Modeling the kinematics of motion of an articulated vehicle

The fundamentals of developing equations of motion for parking maneuvers by an articulated vehicle are based on the no-slip motion. This approach is very consistent with reality. From a parking perspective, vehicle kinematics can be simplified. For instance, as the vehicle velocity is so low in a parking maneuver, then the no-slip condition is satisfied beneath the tires so that the vehicle can be considered as a rigid body moving across a plane [21–23]. Nonslip motion means that the speed will only be in the tires' direction, and we will not have a velocity perpendicular to the tire. At lower velocities,

[a] Where proper distance between the vehicle and the walls in the parking space is observed.

the tire forces are too small that justify the no-slip motion assumption at the tires. Based on this assumption, the front and back tires were reduced to single wheels at the center of the respective axle. This approach helped achieve a simplified description of the kinematics of the vehicle [24].

The local coordinate system deployed in Fig. 9.3 and the velocity directions imply that *ft* is the front of the tractor, *rt* is the end of the tractor, and *rs* is the end of the trailer. Moreover, θ is the steering wheel angle, φ_t is the tractor yaw angle, and φ_s is the trailer yaw angle. Furthermore, L_t and L_s denote the tractor and trailer wheelbase, respectively.

Taking a look at Fig. 9.3, the velocity at point *ft* can be calculated via Eqs. (9.1) and (9.2) for the horizontal and vertical velocity components, respectively. Considering the assumption described earlier, Eqs. (9.3) and (9.4) express the velocities at *rt* and *rs*, respectively.

$$\dot{x_{ft}} = v\cos(\theta + \varphi) \tag{9.1}$$

$$\dot{y_{ft}} = v\sin(\theta + \varphi) \tag{9.2}$$

$$v_{rt} = v\cos(\theta) \tag{9.3}$$

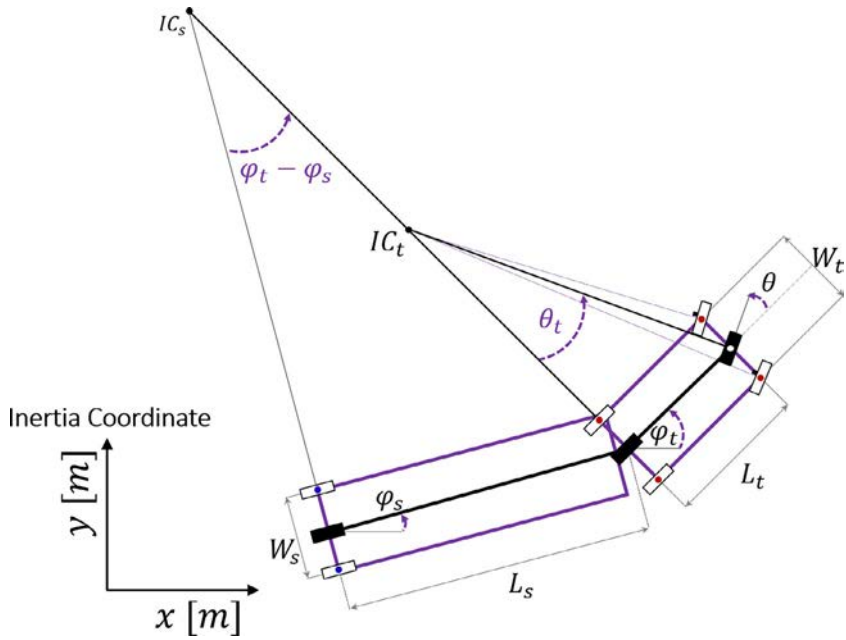

Fig. 9.3 The local coordinate system for determining instantaneous velocity-position.

$$v_{rs} = v\cos(\theta)\cos(\varphi_t - \varphi_s) \tag{9.4}$$

Following this work, applying the instantaneous center of rotation and considering the geometric relations (Fig. 9.3), that is, $\left(\overline{ft-rt} \perp \overline{rt-o}\right)$ and $\left(\overline{rt-rs} \perp \overline{rs-o'}\right)$, we have[b]:

$$v_{rt} = \left(\overline{rt-o}\right)\dot{\varphi}_t \tag{9.5}$$

$$\left(\overline{rt-o}\right) = \frac{L_t}{\tan(\theta)} \tag{9.6}$$

$$v_{rs} = \left(\overline{rs-o'}\right)\dot{\varphi}_s \tag{9.7}$$

$$\left(\overline{rs-o'}\right) = \frac{L_s}{\tan(\varphi_t - \varphi_s)} \tag{9.8}$$

Combining Eqs. (9.3), (9.5), and (9.6), and also Eqs. (9.4), (9.7), and (9.8) and applying algebraic simplifications, Eqs. (9.9) through (9.11) are obtained for calculating the angles of the tractor and trailer.

$$\Delta\varphi = \varphi_t - \varphi_s \tag{9.9}$$

$$\dot{\varphi}_t = \frac{v}{L_t}\sin\theta \tag{9.10}$$

$$\dot{\varphi}_s = \frac{v}{L_s}\cos(\theta)\sin(\Delta\varphi) \tag{9.11}$$

$$\Delta\dot{\varphi} = \frac{v}{L_t}\sin\theta - \frac{v}{L_s}\cos(\theta)\sin(\Delta\varphi) \tag{9.12}$$

Considering the coordinate system in Fig. 9.3, the velocity components along the x and y axes are given in Eqs. (9.13) and (9.14) (at rt) and Eqs. (9.15) and (9.16) (at rs).

$$\dot{x}_{rt} = v\cos(\theta)\cos(\varphi_t) \tag{9.13}$$

$$\dot{y}_{rt} = v\cos(\theta)\sin(\varphi_t) \tag{9.14}$$

$$\dot{x}_{rs} = v\cos(\theta)\cos(\Delta\varphi)\cos(\varphi_s) \tag{9.15}$$

$$\dot{y}_{rs} = v\cos(\theta)\cos(\Delta\varphi)\cos(\varphi_s) \tag{9.16}$$

9.2.1 Extracting optimal steering angle by moving the trailer end along optimal path using inverse kinematics

In this subsection, appropriate path extraction is discussed. Here the objective is to keep the vehicle following a proper path for the parking maneuver.

[b] The $\perp$ symbol refers to orthogonality.

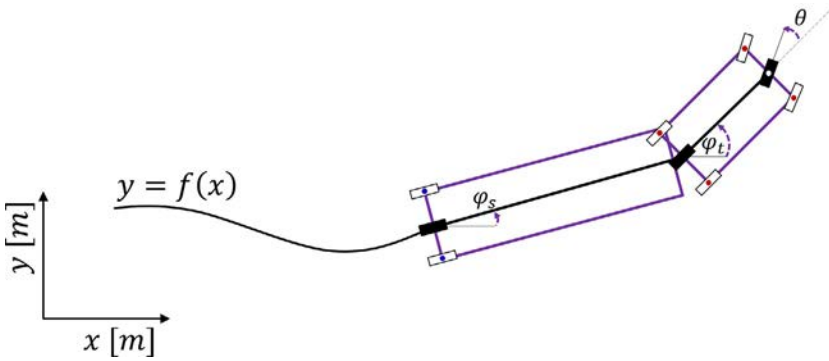

Fig. 9.4 Movement of the articulated vehicle through the optimal path.

Mathematically speaking, this is equivalent to saying that the point *rs* in Fig. 9.4 must pass through the specific path $y_s = f(x_s)$. Accordingly, one must extract an appropriate steering angle for accomplishing this objective.

Taking the derivative of both sides of the equation path $y_s = f(x_s)$, with respect to time, using the derivative chain rule, Eq. (9.17) is developed:

$$\dot{y}_s = \frac{\partial f(x_s)}{\partial x_s}\dot{x}_s \tag{9.17}$$

On the other hand, a simple look at Eqs. (9.15)–(9.17) leads to Eq. (9.18), as follows:

$$\frac{\dot{y}_s}{\dot{x}_s} = \tan(\varphi_s) \tag{9.18}$$

Using Eqs. (9.17) and (9.18), one can obtain Eq. (9.19). Taking the derivative of Eq. (9.19) and reapplying the chain rule, one can get Eq. (9.20). The substitution of tan (φ_s) into Eq. (9.19) gives Eq. (9.20) as well.

$$\tan(\varphi_s) = \frac{\partial f(x_s)}{\partial x_s} \tag{9.19}$$

$$\dot{\varphi}_s = \frac{\dfrac{\partial^2 f(x_s)}{\partial {x_s}^2}}{\left(1 + \left(\dfrac{\partial f(x_s)}{\partial x_s}\right)^2\right)}\dot{x}_s \tag{9.20}$$

Given the definitions of $\dot{x}_s$ and $\dot{\varphi}_s$ from Eqs. (9.11) and (9.15) and applying some algebraic simplifications as well as trigonometric functions calculations, Eq. (9.21) is obtained:

$$\tan(\varphi_t - \varphi_s) = L_s \frac{\dfrac{\partial^2 f(x_s)}{\partial {x_s}^2}}{\left(1 + \left(\dfrac{\partial f(x_s)}{\partial x_s}\right)^2\right)^{\frac{3}{2}}} \tag{9.21}$$

Eq. (9.23) is obtained by introducing $G(x_s)$ by Eq. (9.22) and considering Eq. (9.21). The proceeding calculations were performed in a similar way to that followed up to this stage. Accordingly, taking the derivative of Eq. (9.23) leads to Eq. (9.24) and the substitution of Eqs. (9.10), (9.11), and (9.15) into Eq. (9.24) and performing some algebraic simplifications give rise to Eq. (9.25)

$$G(x_s) \equiv L_s \frac{\dfrac{\partial^2 f(x_s)}{\partial {x_s}^2}}{\left(1 + \left(\dfrac{\partial f(x_s)}{\partial x_s}\right)^2\right)^{\frac{3}{2}}} \tag{9.22}$$

$$\tan(\varphi_t - \varphi_s) = G(x_s) \tag{9.23}$$

$$(\dot{\varphi}_t - \dot{\varphi}_s)\left(1 + \tan(\varphi_t - \varphi_s)^2\right) = \frac{\partial G(x_s)}{\partial x_s}\dot{x}_s \tag{9.24}$$

$$\theta = \tan^{-1}\left(\frac{L_t}{\left(1 + \dfrac{\partial f(x_s)^2}{\partial x_s}\right)^{\frac{1}{2}}} \frac{\dfrac{\partial G(x_s)}{\partial x_s}}{\left(1 + G(x_s)^2\right)^{\frac{3}{2}}} + \frac{L_t}{L_s}\frac{G(x_s)}{\left(1 + G(x_s)^2\right)^{\frac{1}{2}}}\right) \tag{9.25}$$

9.3 Design of control system

In this chapter, three main reasons led to introducing the ANFIS technique in the controller design for automatic parking in articulated vehicles. These reasons include:

- The nonlinear nature of kinematic articulated vehicle motion.

- Successful applications of fuzzy logic and artificial neural networks in similar fields.
- ANFIS robustness to environmental and vehicle uncertainties.

The ANNs and fuzzy inference systems have gained much attention from many researchers in various fields of engineering and science. This has been a consequence of the increasing need for smart adaptive systems for addressing the problems encountered in the real world, including vehicle control, pattern recognition, human-machine interaction, medical and economic issues, etc. [25]. Thanks to the nature of a fuzzy system, no exact mathematical model of either the vehicle or the surrounding environment is required for navigating the vehicle based on fuzzy logic. Also, we must mention the robustness of a fuzzy system to possible sensor data errors and dynamic fluctuations of the system and environment [26]. ANN can be defined as a model for data processing that is inspired by the structure of the human brain [27]. Computational intelligence tools, such as ANN and fuzzy logic, have been regarded mainly due to their widespread application in various problems; this has led to increasing interest in combining the two approaches to come up with an even better solution [28, 29]. The proposed control system in this chapter tends to combine fuzzy logic with ANN. To clarify the concept, we proceed with brief introductions of a fuzzy controller structure and the ANN, as the understanding of the formation of a combined neuro-fuzzy algorithm is based on a proper understanding of the two concepts. Interested readers may refer to the literature for more information [30–36]. Finally, the structure of the proposed ANFIS algorithm is described, followed by implementing the proposed model onto an articulated vehicle as a closed-loop system.

9.3.1 Fuzzy control

As of the present, fuzzy systems have found applications in a wide spectrum of science and technical fields, including control, signal processing, communication, integrated circuit manufacturing, news broadcasting systems, trading, medicine, social science, etc. One of the most important applications of fuzzy systems has been their use for solving the problems encountered in control systems. In the following, we further introduce fuzzy control by presenting parts of "*Fuzzy Systems and Fuzzy Control*" [37, 38]. A fuzzy controller is a fuzzy system that is used as a controller. The structure of a classic fuzzy controller is made up of five primary parts. These include the fuzzifier, a database,

a rule base, a decision-making or inference unit, and a defuzzifier. Usually, a preprocessor and a postprocessor are deployed upstream and downstream of a fuzzy controller. It is worth mentioning that, as the fuzzy system is fed real numbers in many cases, we must establish interfaces between the fuzzy inference engine and the environment. These are, in fact, the fuzzifier and defuzzifier functions. Fig. 9.5 shows the structure of a classic fuzzy controller.

For a fuzzy system, the starting point is to develop a set of fuzzy if-then rules based on a knowledge base provided by experts in the field. A common approach to the design of a neuro-fuzzy system is the Takagi-Sugeno-Kang (TSK) inference system, where the input is fuzzy while the output is non-fuzzy. Thoroughly described in Lee [37], this system models a nonlinear phenomenon by dividing it into regions within the input and output ranges, with each region described by a particular fuzzy if-then rule. The inputs into and the outputs out of the TSK system are variables with real values. This condition is based on the assumption that no complex defuzzification stage is required in the controller. As an example, this fuzzy system applies the rules as follows:

If the vehicle $\boldsymbol{x}$ *is moving at a high velocity, then the force exerted to the acceleration pedal can be calculated as* $\boldsymbol{y} = \boldsymbol{cx}$ *(where c is a constant)*

Comparisons have shown that the *then* part of a fuzzy rule can be easily turned into a single mathematical relationship using a lingual descriptor; this mapping simplifies the combination of fuzzy rules. Indeed, the TSK fuzzy system represents a weighted average over the *then* parts of the rules. Interested readers may refer to the study of Naderloo et al. [36], Lee [37], Jang et al. [38], and Haykin [39] for more information on fuzzy inference systems.

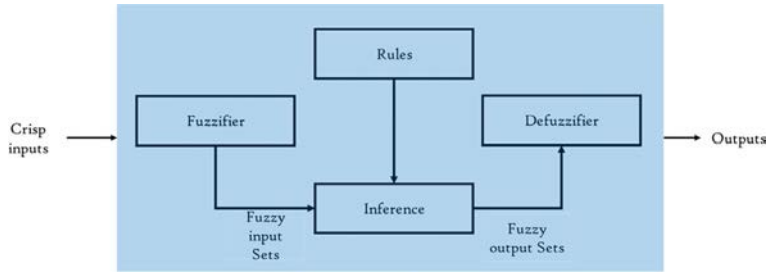

Fig. 9.5 Structure of a classic fuzzy controller.

9.3.2 Artificial neural networks

Although exact mechanisms by which the human (or other animals) brain operates are yet to be comprehensively identified, there are well-known parts of the brain that have inspired the theory of neural networks. The extraordinary power of the human brain is fueled by the very large number of neurons and their interconnections. The structure of even a single neuron is highly complicated. Each neuron is composed of numerous parts and subsystems wherein complex control mechanisms are deployed. Neural cells can transmit information via electrochemical mechanisms. According to the mechanisms incorporated into the structure of neurons, they have been classified into more than 100 categories.

Technically speaking, the neurons and their interconnections are neither binary, stable, nor synchronous. A computer-assisted simulated neural network may hardly represent a small portion of the actual characteristics of the respective biologic neural system. From an engineering point of view, the aim of building a neural network is not to simulate the human brain, but rather to establish a mechanism for solving the relevant engineering problems based on inspiration by the behavior pattern of biologic networks. In this respect, ANN can be defined as a model for data processing that is inspired by the structure of the human brain. An ANN is made up of a large number of parallel processing units, called neurons, that work together to solve a particular problem. The ANNs are trained by their surrounding environment, where known input-output data are used to adjust interneuron synaptic communications. As far as an ANN is concerned, the training means to adjust weights for synaptic communications between neurons. These communications store the required knowledge for solving a particular problem.

Fig. 9.6 shows the structure of a bioneuron. In this structure, each neuron is made up of three primary parts:

1. A cell body, which is composed of a nucleus and some protective components.
2. Dendrites, which receive electrical signals.
3. An exon, which serves as a communication channel.

The segment where an exon links a cell to the dendrites of another cell is referred to as a synapse. Across a neural network, the neural messages flow in a unidirectional way: from dendrites to the cell body and then to the exon. One of the most surprising properties of a neural network is its ability to learn. This is done by applying training algorithms based on a set of known cases for training. Throughout the training phase, the weights or parameters

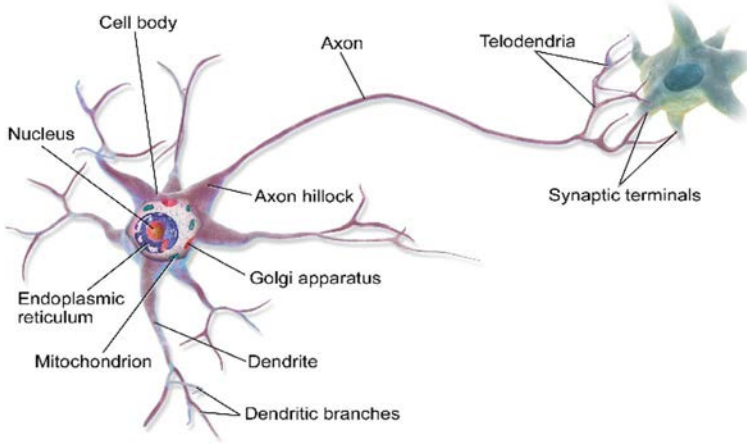

Fig. 9.6 Structure of a bioneuron [27].

of the stimulation functions are adjusted. A common challenge is to determine the time when the network is sufficiently trained. Because the present research seeks to apply soft computation algorithms and techniques for control system design, further details are avoided, and interested readers may refer to the study of Minhaj [27], Haykin [39], and Rojas [40] to build a deeper understanding of the concept of the ANN.

9.3.3 Adaptive neuro-fuzzy inference system (ANFIS)

Neuro-fuzzy networks can be designed into various structures. ANFIS is a well-known structure that was first introduced by Roger Jang in 1993 [30]. In this structure of a fuzzy network, first, fuzzy systems are modeled by various fuzzy techniques before the developed fuzzy model is used to develop an equivalent NN. In the following, the ANFIS structure is presented based on Jang [30].

9.3.3.1 Introduction of ANFIS network structure

In order to describe the network structure, let us consider a system with two inputs and a single output. The inputs are herein denoted by x and y, with the output designated as f. Assume that each input variable has only two membership functions. That is, the input x has the membership functions A_1 and A_2 while the input y has the membership functions expressed as B_1 and B_2 (Fig. 9.7).

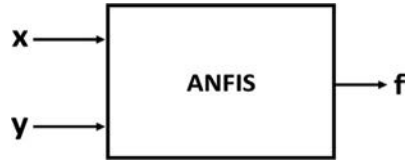

Fig. 9.7 Demonstration of ANFIS with two inputs and a single output.

Now assume that we have only two first-order Sugeno rules, as follows:

$$\text{if } x \text{ is } A_1 \text{ and } y \text{ is } B_1 \text{ Then } f_1 = p_1 x + q_1 y + r_1$$

$$\text{if } x \text{ is } A_2 \text{ and } y \text{ is } B_2 \text{ Then } f_2 = p_2 x + q_2 y + r_2$$

It is trivial that we practically have four control rules (equal to the product of the numbers of membership functions of x and y); the other two are not mentioned here. Fig. 9.8 illustrates the fire rule and layered structure of the ANFIS network. Here, w_1 and w_2 are the inference products or the weighting factor corresponding to the firing rule (9.26).

$$f = \frac{w_1}{w_1 + w_2} f_1 + \frac{w_2}{w_1 + w_2} f_2 = \overline{w_1} f_1 + \overline{w_2} f_2 \tag{9.26}$$

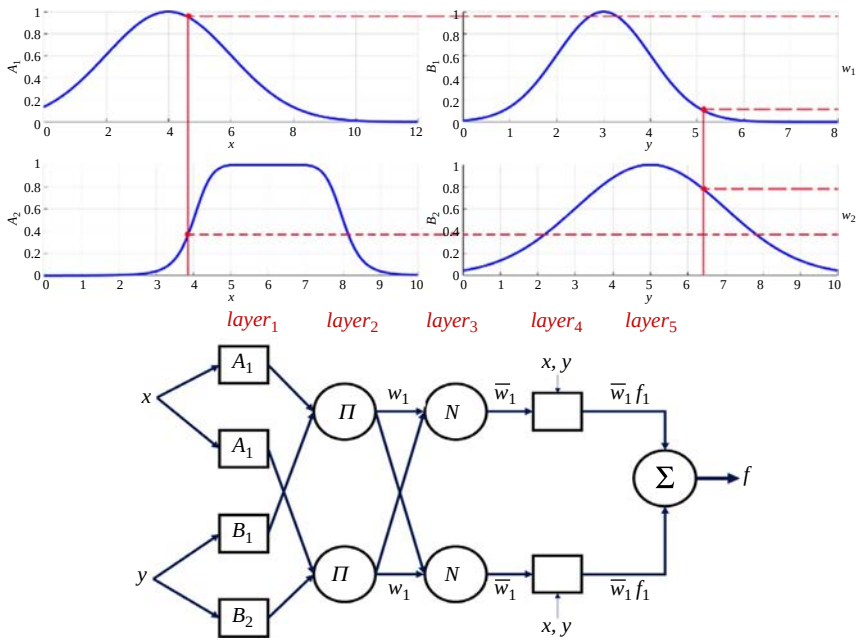

Fig. 9.8 The firing rule and the layered structure of the ANFIS network.

Different layers of the ANFIS network are explained in the following:

Layer 1: This is an adaptive layer, meaning that its parameters are subject to adjustment (and this is why squares mark the nodes). The corresponding functions to each node in the first layer are the same as the fuzzy membership functions (denoted by A_1, A_1, A_1, and A_1, or $\mu_{A_1}(x)$, $\mu_{A_2}(x)$, $\mu_{B_1}(y)$, and $\mu_{B_2}(y)$). Therefore, each node corresponds to a membership function whose parameters are subject to adjustment (e.g., each node has two, three, or more parameters). The parameters x and y are the inputs into Layer 1, with the outputs of the layer being the membership functions corresponding to each node. Denoting the outputs of each node in the layer by O_{l_i} (the output of the ith node in ith layer), the outputs of Layer 1 are as follows:

$$\begin{aligned} O_{11} &= \mu_{A_1}(x) \\ O_{12} &= \mu_{A_2}(x) \\ O_{13} &= \mu_{B_1}(x) \\ O_{14} &= \mu_{B_2}(x) \end{aligned} \tag{9.27}$$

In Eq. (9.27), the term $\mu_{A_1}(x) = \frac{1}{1+\left|\frac{x-c_1}{a_1}\right|^{2b_1}}$, for example, where the parameters a_1, b_1, and c_1 correspond to the first node in Layer 1, together with similar terms for the second to the fourth nodes in Layer 1 that are referred to as "primary parameters."

Layer 2: This is not an adaptive layer but rather a fixed layer (and this is why the nodes are marked by circles). The output of each node in this layer is the product of the inputs into that node (9.28). This layer is denoted by the multiplication symbol (Π).

$$O_{2i} = w_i = \mu_{A_i}(x) \times \mu_{B_i}(y) \quad i = 1,2 \tag{9.28}$$

In the following example, this layer contains no more than two nodes as the fuzzy system was defined only as (A_1, B_1) and (A_2, B_2). However, one can consider four cases, as detailed in Eq. (9.29):

$$\begin{aligned} O_{21} &= w_1 = \mu_{A_1}(x) \times \mu_{B_1}(y) \\ O_{22} &= w_2 = \mu_{A_2}(x) \times \mu_{B_2}(y) \\ O_{23} &= w_3 = \mu_{A_3}(x) \times \mu_{B_3}(y) \\ O_{24} &= w_4 = \mu_{A_4}(x) \times \mu_{B_4}(y) \end{aligned} \tag{9.29}$$

Therefore, the output of Layer 2 is indeed the fire power of the corresponding rule. It is worth mentioning that, in Layer 2, one can replace the multiplication (Π) with any other T-norm operator that implies AND for the node function.

Layer 3: In this layer, the nodes are fixed, and each node is represented by N_1 and N_2. Outputs of the nodes in this layer express the "normalized fire power." This concept is expressed by (9.30).

$$O_{3i} = \overline{w_i} = \frac{w_i}{w_1 + w_2} \quad i = 1, 2 \tag{9.30}$$

Layer 4: This layer has once more the parameters x and y as inputs. It is an adaptive layer where the output of each node is as follows:

$$O_{4i} = \overline{w_i} f_i = \overline{w_i}(p_i x + q_i y + r_i) \quad i = 1, 2 \tag{9.31}$$

In Eq. (9.31), one should determine the parameters p_i, q_i, and r_i for these two nodes in Layer 4.

Layer 5: As a nonadaptive layer, Layer 5 has the sum of inputs as the node output or function (9.32).

$$f = \sum_{i=1}^{n} \overline{w_i} f_i, n = 2 \tag{9.32}$$

9.3.4 Closed-loop control system for automatic parking of articulated vehicles

The ANFIS network is trained based on the requirements defined for parking maneuvers according to the expert driver's behaviors. It should be noted that the trained network is indeed a modeled version of the expert driver's behavior who performs well in a parking maneuver. Following this section, the proposed ANFIS structure is applied to the articulated vehicle in the form of a closed-loop control scheme, with the results presented and interpreted.

9.3.4.1 Computer simulation of articulated vehicle kinematics

The kinematics of the articulated vehicle were simulated in MATLAB Simulink software on a PC, with details of the simulated model reported in Table 9.1 (according to the standard model discussed in RTA website [41]). Fig. 9.9 demonstrates the standard dimensions of the refrigerated semitrailer [41] that were used as a model in the computer simulations in this study. The simulations were performed based on the kinematic equations for the articulated vehicle, as expressed earlier (Fig. 9.10).

Table 9.1 Information on the computer-assisted simulation of the articulated vehicle and the parking space.

Parameter	Symbol	Value	Unit
Tractor length	l_t	5.4	m
Trailer length	l_s	13.9	m
Articulated vehicle width	–	2.5	m
Parking space span	–	7	m
Simulation time interval	–	0.1	s
Steering angle range	θ	$\left[-\frac{\pi}{6}+\frac{\pi}{6}\right]$	rad
Articulation angle range	$\Delta\varphi$	$\left[-\frac{\pi}{2}+\frac{\pi}{2}\right]$	rad
Forward motion velocity	ν	+1	m/s
Backward motion velocity		−1	
Initial condition	$\varphi_t\ (o)$	0	degree
	$\varphi_s\ (o)$	0	degree

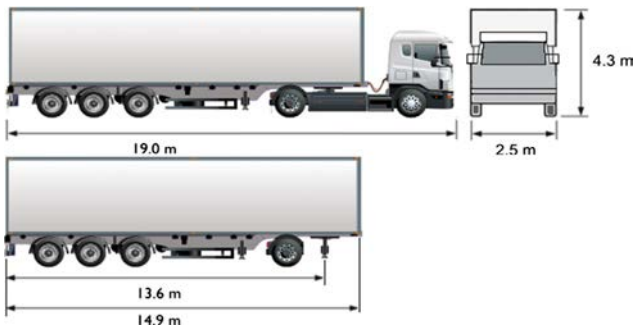

Fig. 9.9 Standard dimensions of a particular class of articulated vehicles.

9.3.4.2 Training the ANFIS based on expert driver's behavior

Before proceeding to train the ANFIS based on the expert driver's behavior, one must define the appropriate parking maneuver scenario. Accordingly, based on the scenario designed in Azadi et al. [24], the parking maneuver of the articulated vehicle was divided into two motion phases: (1) moving forward from the arbitrary initial condition, and (2) the reverse maneuver. Notably, the first phase is switched to the second phase when an expert driver finds the distance between the back of the trailer and the parking space span long enough to place the trailer in the desired position so that the reverse maneuver can be performed with no collision. For an automated control system, this information is practically provided by the distance

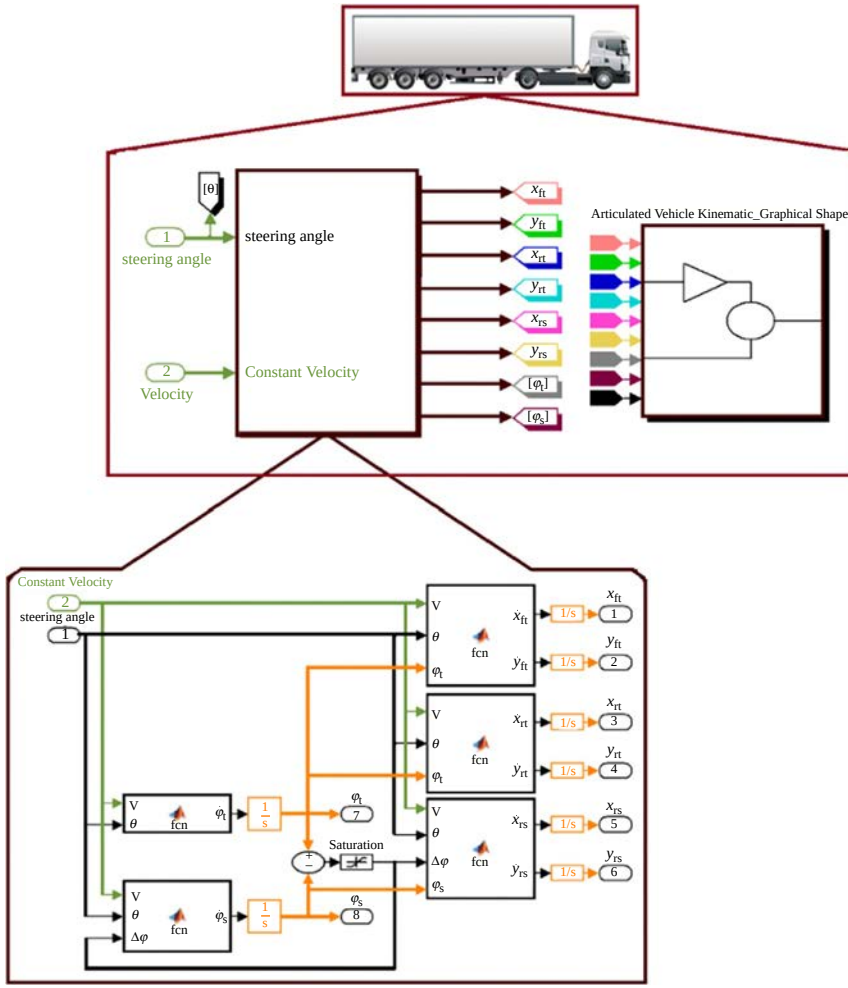

Fig. 9.10 Computer-assisted simulation of the kinematics of the articulated vehicle.

sensors. The flowchart shown in Fig. 9.11 helps better understand vehicle behavior throughout a parking maneuver. Table 9.2 reports the simulation information concerning the inputs and desired outputs for training the ANFIS network.

Next, to have the articulated vehicle move along the desired path to perform the parking maneuver appropriately, the appropriate steering angle and velocity must the applied to the vehicle. This purpose is realized by employing expert drivers' experience. The necessary skills were obtained by analyzing

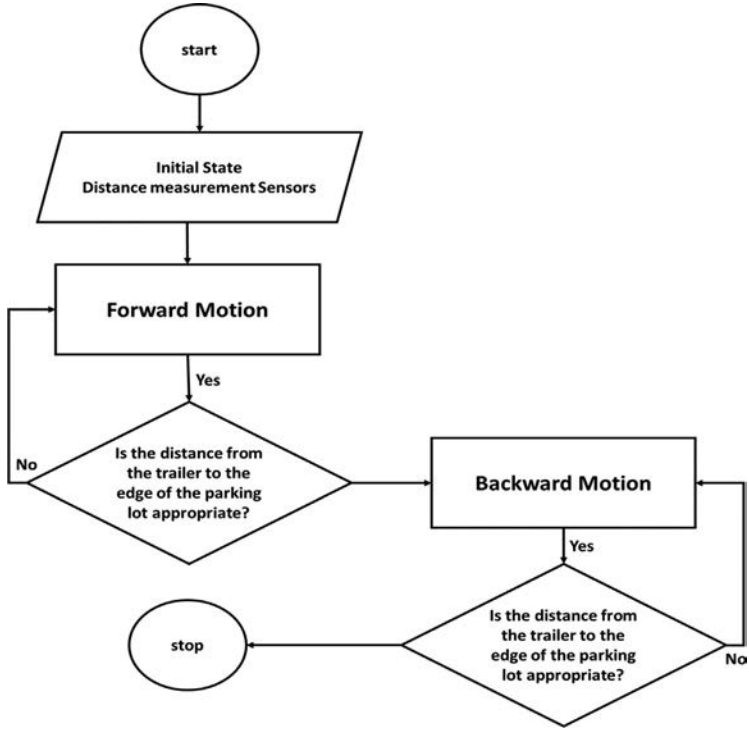

Fig. 9.11 Flowchart of the articulated vehicle behavior in a parking maneuver.

Table 9.2 The simulation information in relation to the inputs and desired outputs for training the ANFIS network.

Parameter description	Symbol	Range	Phase	Unit
Tractor yaw angle	φ_t	$[-1.2\ \ 0]$	1	rad
		$[-0.86\ \ 1.6]$	2	rad
Trailer yaw angle	φ_s	$[-0.7\ \ 0]$	1	rad
		$[0\ \ 1.6]$	2	rad
Steering wheel angle	θ	$\left[-\frac{\pi}{6}\ \ \frac{\pi}{6}\right]$		rad
Horizontal distance from the wall	Distance	$[0\ \ 22.7]$		m

the responses to a questionnaire and massive simulation runs, examples of which are demonstrated in Figs. 9.12 and 9.13, on which the motion path and inputs/outputs are indicated.

As shown by the flowchart in Fig. 9.11, the transition in the motion phase of the articulated vehicle during the parking maneuver is evident. Under the scenario where the parking maneuver is implemented

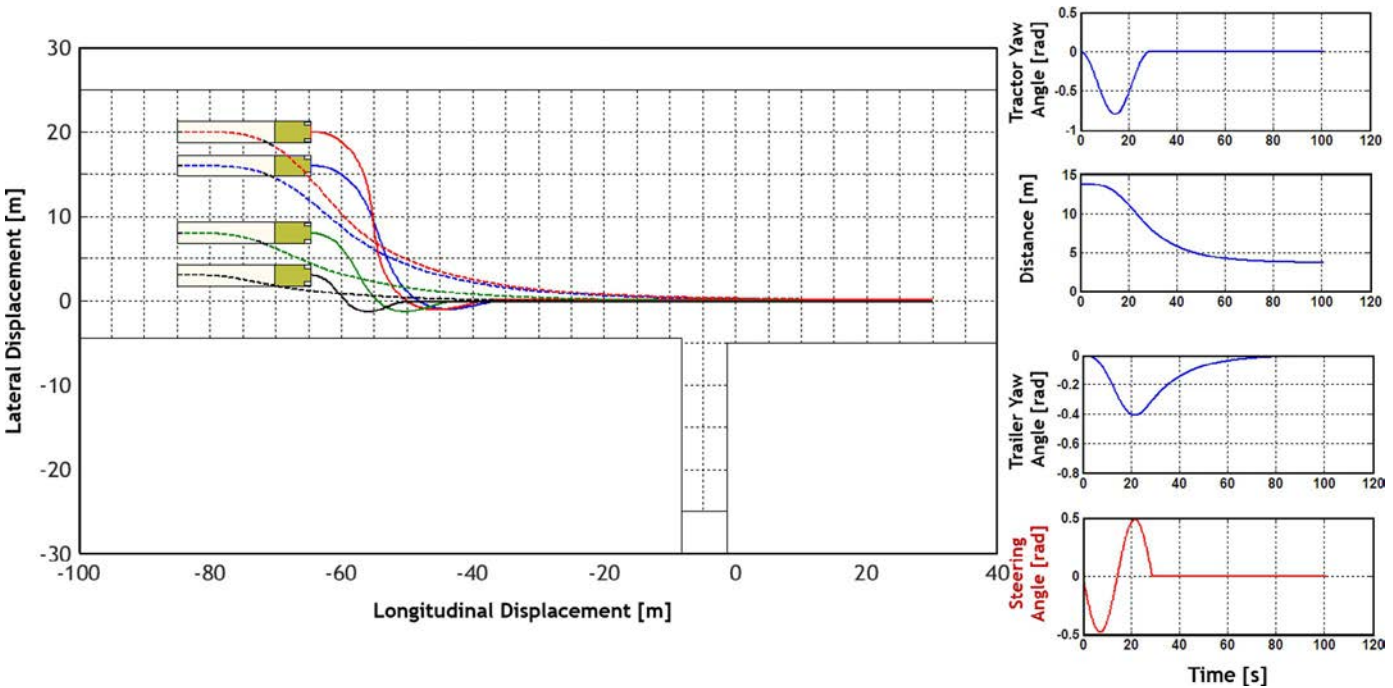

Fig. 9.12 Examples of desired paths for the first phase considering various initial conditions.

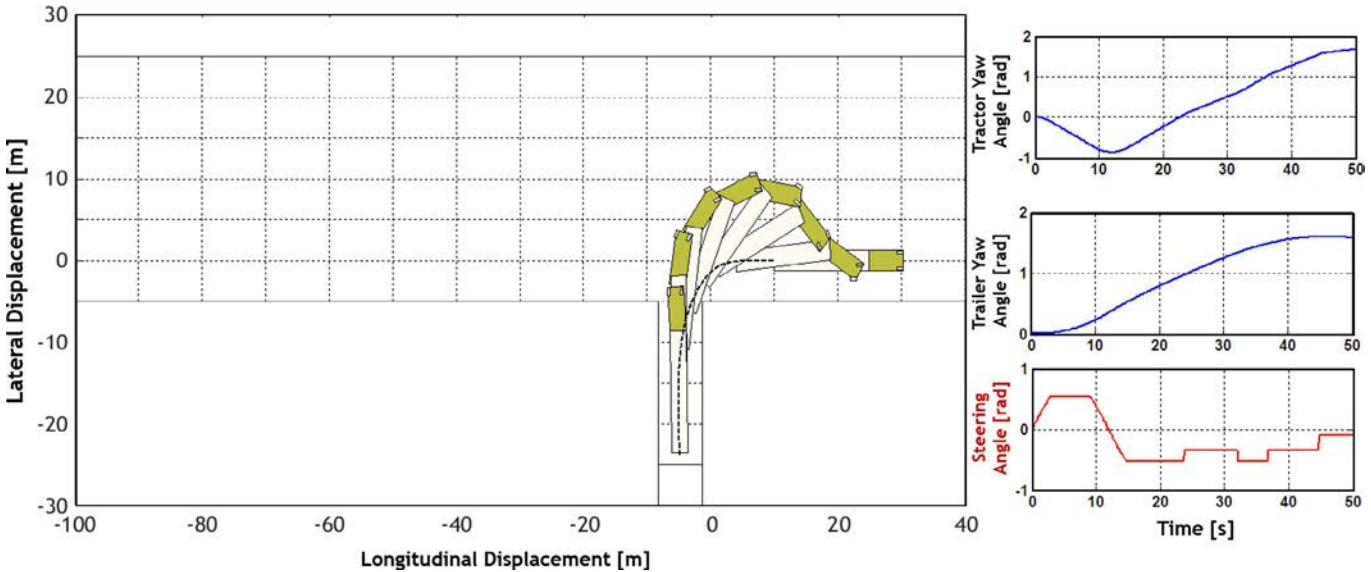

Fig. 9.13 Examples of desired paths for the second phase.

automatically, the transition from the first phase to the second phase is triggered based on a signal to the control system by which the distance between the back of the trailer and the parking space span is reported to the system. This distance is also related to the changes in the velocity direction of the vehicle. The objective is to design a network that helps us achieve an appropriate nonlinear map. This nonlinear map is developed through a set of data. This dataset contains input-output pairs describing the appropriate driver's behavior, which we are seeking to model, as discussed earlier. In other words, the adaptive neuro-fuzzy network is used to model a subject system, that is, the expert driver's behavior. This dataset is usually referred to as a *training dataset*. The methodology deployed to adjust the network parameters for improved performance of the network is known as learning rules or adaptive algorithms. Usually, the performance of an adaptive neuro-fuzzy network is evaluated by comparing the outputs of the network against those of the real system for given input parameters. The training based on the expert driver's behavior is demonstrated in Fig. 9.14.

As indicated in Fig. 9.14, it is evident that the training is achieved with the training dataset containing the input-output pairs corresponding to the expert driver's behavior. In order to train the ANFIS, the desired input data includes the tractor yaw angle (φ_t), the trailer yaw angle (φ_s), and distance between the back of trailer and the parking space wall. Representing the expert driver's behavior, this information serves as the training database for the ANFIS. Upon compiling the training dataset and performing the training task, the input membership functions of the controller, the neural structure of the controller, and the control level in both phases are shown in Figs. 9.15 and 9.16. It is worth mentioning that in the simulation runs, the stopping criterion for the parking maneuver was set to be a particular distance between the back of the trailer and the parking space wall.

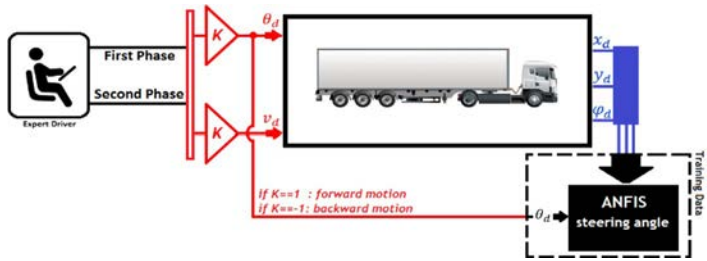

Fig. 9.14 Training the ANFIS based on the desired input-output pairs according to the expert driver's behavior.

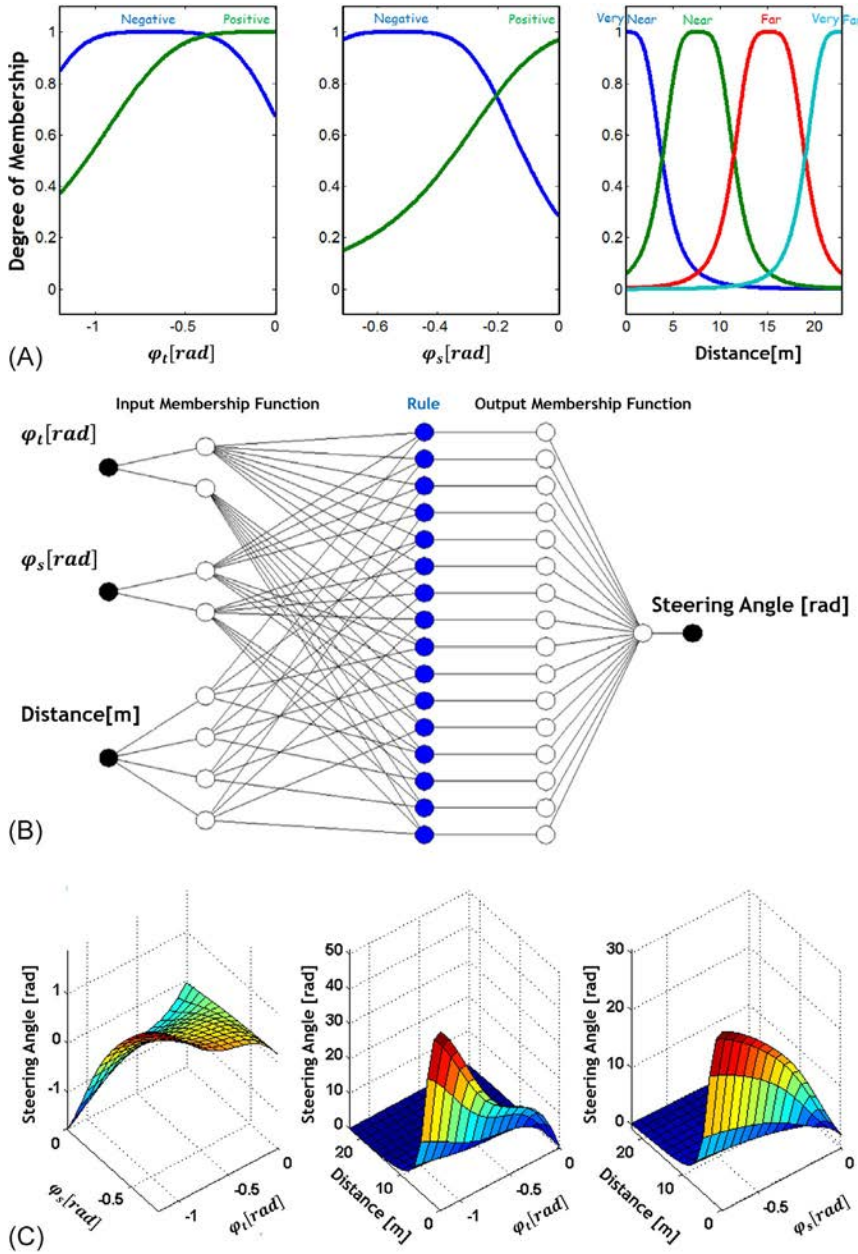

Fig. 9.15 Phase 1 of motion, including the input membership functions of the controller, the neural structure of the controller, and the fuzzy rules level.

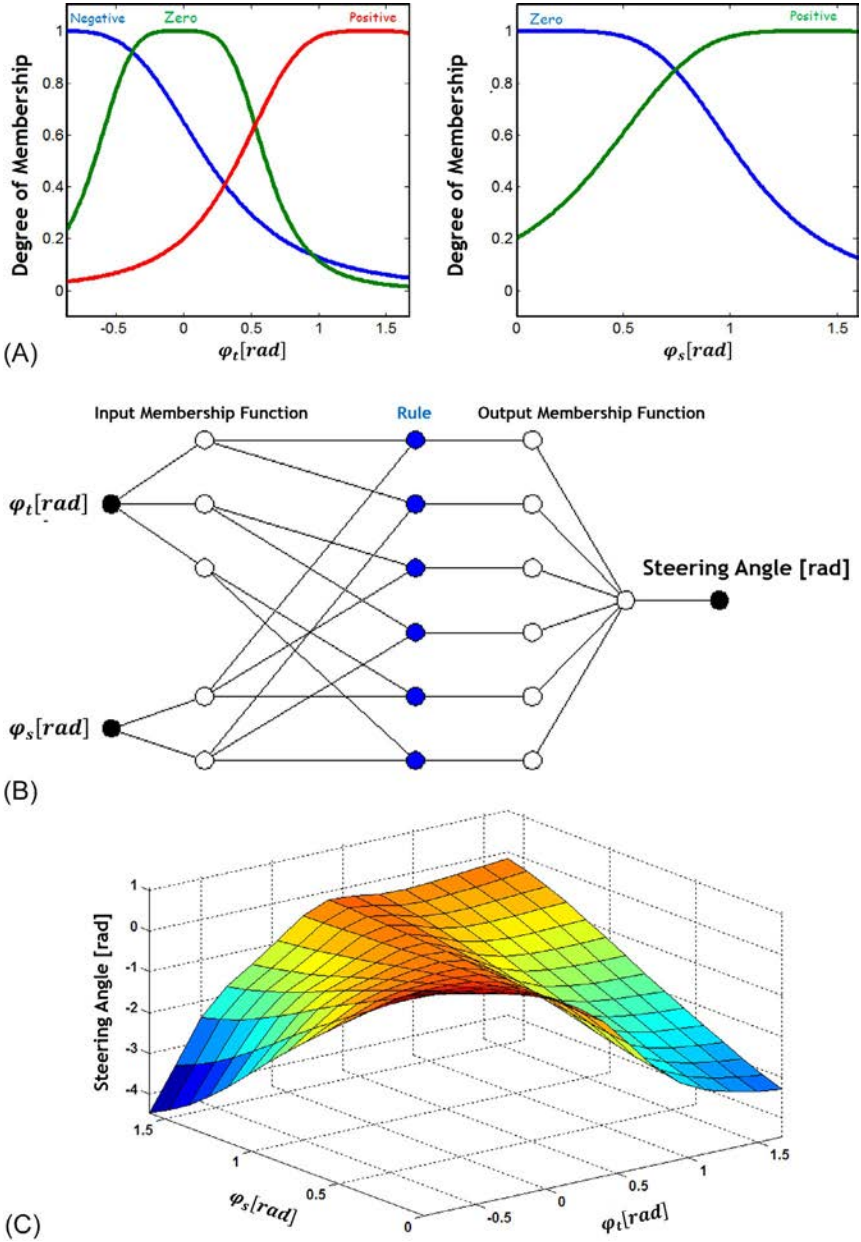

Fig. 9.16 Phase 2 of motion, including the input membership functions of the controller, the neural structure of the controller, and the fuzzy rules level.

Table 9.3 The fuzzy rules for the forward motion (Phase 1).

No.	φ_t(rad)	φ_s(rad)	Distance (m)	outMF
1	Negative	Negative	Very near	192.6
2	Negative	Negative	Near	3.745
3	Negative	Negative	Far	1.042
4	Negative	Negative	Very far	0.9004
5	Negative	Positive	Very near	−47.23
6	Negative	Positive	Near	−6.599
7	Negative	Positive	Far	−4.434
8	Negative	Positive	Very far	−3.838
9	Positive	Negative	Very near	−129.5
10	Positive	Negative	Near	−2.541
11	Positive	Negative	Far	0.0378
12	Positive	Negative	Very far	−0.645
13	Positive	Positive	Very near	31.75
14	Positive	Positive	Near	4.439
15	Positive	Positive	Far	2.573
16	Positive	Positive	Very far	2.461

Table 9.4 The fuzzy rules for the backward motion (Phase 2).

No.	φ_t(rad)	φ_s(rad)	outMF
1	Negative	Zero	3.18
2	Negative	Positive	−7.38
3	Zero	Zero	−0.23
4	Zero	Positive	2.38
5	Positive	Zero	−4.44
6	Positive	Positive	0.69

Tables 9.3 and 9.4 list the fuzzy rules characterizing the designed ANFIS network for the forward-motion and backward-motion phases, respectively.

These rules can be interpreted according to the logic presented in Eqs. (9.33) and (9.34), respectively:

$$\text{Rule1}: \text{If } \varphi_t \text{ is Negative and } \varphi_s \text{ is Negative and Distance is Very near Then out MF1} \tag{9.33}$$

$$\text{Rule2}: \text{If } \varphi_t \text{ is Negative and } \varphi_s \text{ is Zero Then out MF1} \tag{9.34}$$

9.3.4.3 Closed-loop control system for automatic parking of articulated vehicle

In this section, having finished the design of the proposed ANFIS algorithm, it was applied to a closed-loop control structure. Fig. 9.17 shows the closed-loop control structure. As demonstrated in the previous section, the data on φ_t (rad), φ_s (rad), and the horizontal distance to the wall were supplied to the control system as the input data, and the control system returned the steering angle (θ) and velocity (v) as output. The two-phase nature of the maneuver required that the proposed control system was also composed of two parts. As shown in Fig. 9.17, these two parts are meant to control the forward and backward motions, respectively. The transition of the phase-1 to the phase-2 should occur when the vehicle identifies the appropriate distance to the parking space span so that the backward motion of the vehicle to place the trailer within the parking space appropriately would lead to no collision.

9.3.4.4 Results of applying the ANFIS controller

The proposed ANFIS model in the closed-loop structure shown in Fig. 9.17 resembles an expert driver's behavior for parking an articulated vehicle

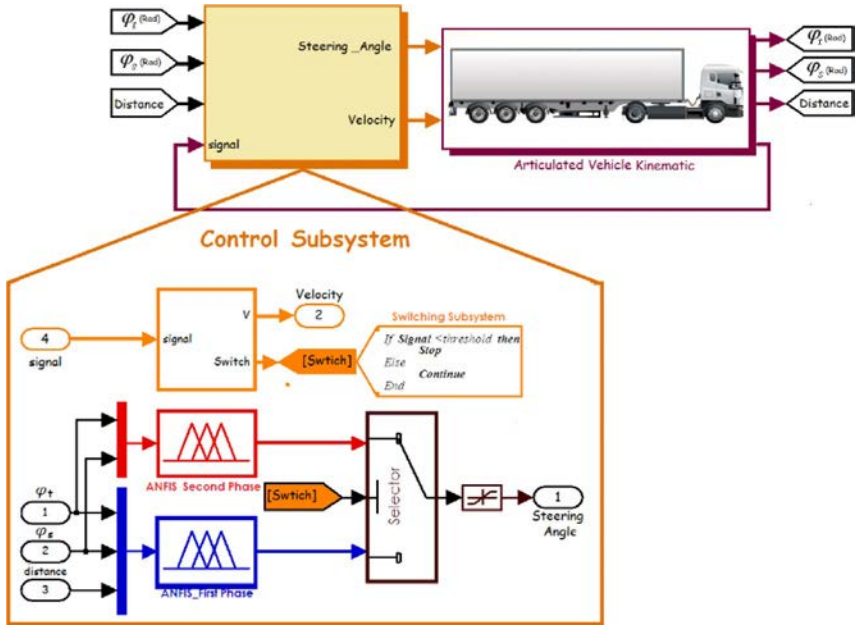

Fig. 9.17 Closed-loop system for the automatic parking of the articulated vehicle.

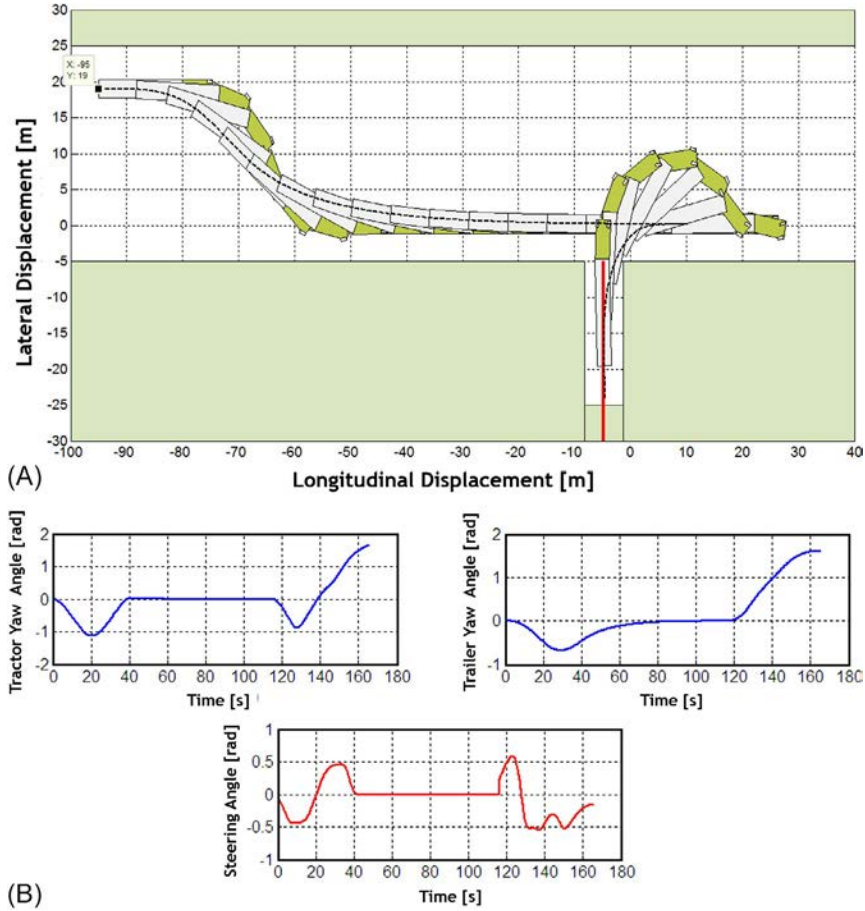

Fig. 9.18 Automatic parking maneuver for an articulated vehicle under initial conditions (−95 m, 19 m).

through two motion phases. As observed, the results of applying the ANFIS in the closed-loop structure are well evident in Figs. 9.18–9.20.

9.3.4.5 Error calculation

Considering the final values obtained from Eq. (9.35), the errors associated with distance (from the desired final position) and trailer angle (from the desired angle at the final condition) are calculated by Eqs. (9.36) and (9.37), respectively. Eq. (9.38) gives the distance between the initial and final positions of the back of the trailer. The final results of error calculation for 14 maneuvers from various initial conditions are reported in Table 9.5.

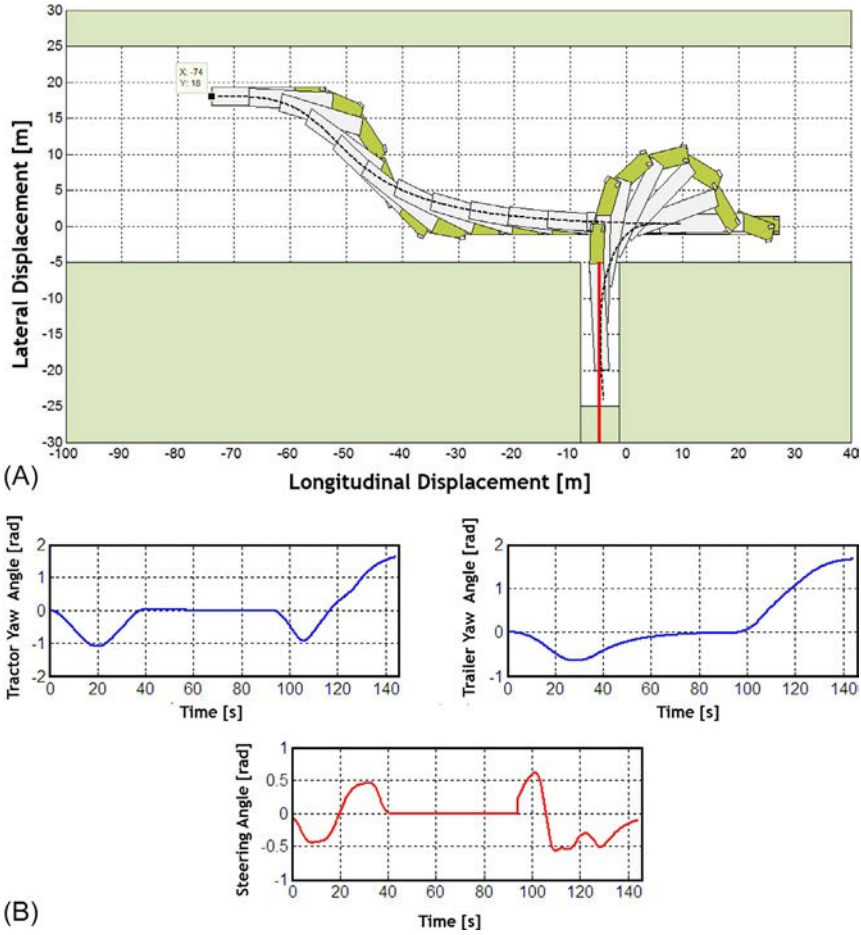

Fig. 9.19 Automatic parking maneuver for an articulated vehicle under initial conditions (−74 m, 18 m).

Moreover, Figs. 9.21 and 9.22 show the distance and trailer angle errors relative to the distance between the initial and final positions, together with the frequency of error values, respectively.

$$\begin{aligned} x_{final} &= -4.75\,\text{m} \\ x_{final} &= -24\,\text{m} \\ \varphi_{final} &= \frac{\pi}{2}\,\text{rad} \end{aligned} \tag{9.35}$$

$$Distance_{error} = \sqrt{\left(x_{final} - x_s\right)^2 + \left(y_{final} - y_s\right)^2} \tag{9.36}$$

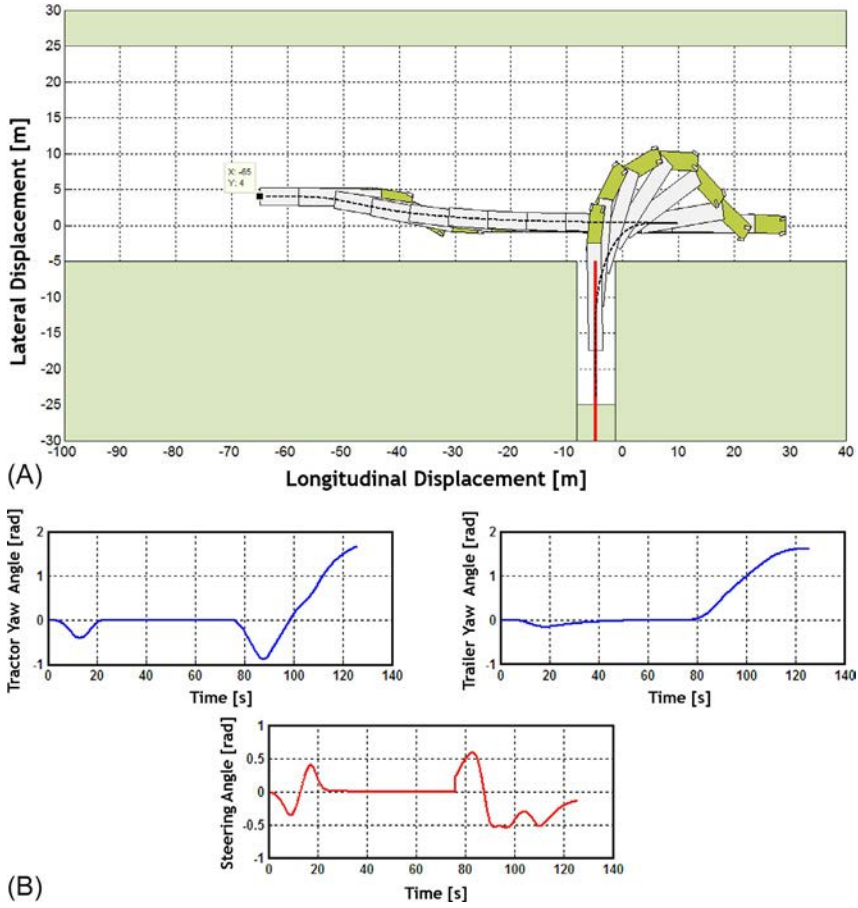

Fig. 9.20 Automatic parking maneuver for an articulated vehicle under initial conditions (−65 m, 4 m).

$$\varphi_{error} = \left| \varphi_{final} - \varphi_s \right| \tag{9.37}$$

$$N_{\{IC_x,\, IC_y\}} = \sqrt{\left(x_{final} - IC_x\right)^2 + \left(y_{final} - IC_y\right)^2} \tag{9.38}$$

Analyzing the data tabulated in Table 9.5 and demonstrated on Figs. 9.21 and 9.22 where the parking maneuver errors are reported, one can determine that the proposed adaptive neuro-fuzzy controller performed well and could successfully implement both phases of the parking maneuver from different initial positions without hitting the walls of the parking space within acceptable ranges of error. The distribution of error in Figs. 9.21

Table 9.5 Associated errors with automatic parking of the articulated vehicle with different initial conditions.

No.	IC_{φ_s} [rad]	IC_x [m]	IC_y [m]	$N_{\{IC_x,ICy\}}$	$Distance_{error}$	φ_{error}
1	0	−65	4	66.4	0.14	2.21
2	0	−72	12	76.2	0.37	3.57
3	0	−74	18	80.9	0.69	5.01
4	0	−79	10	81.6	0.23	1.91
5	0	−80	11	82.9	0.22	1.97
6	0	−83	15	87.4	0.22	2.12
7	0	−85	16.7	89.9	0.15	2.45
8	0	−87	12.5	89.9	0.32	1.58
9	0	−88	14.5	91.7	0.29	1.73
10	0	−90	11	92.1	0.18	1.24
11	0	−90	14	93.3	0.43	1.54
12	0	−90	20	95.9	0.32	2.26
13	0	−92	16.5	96.2	0.24	1.66
14	0	−95	19	99.9	0.26	1.67
Mean Value of Error					0.29	2.21

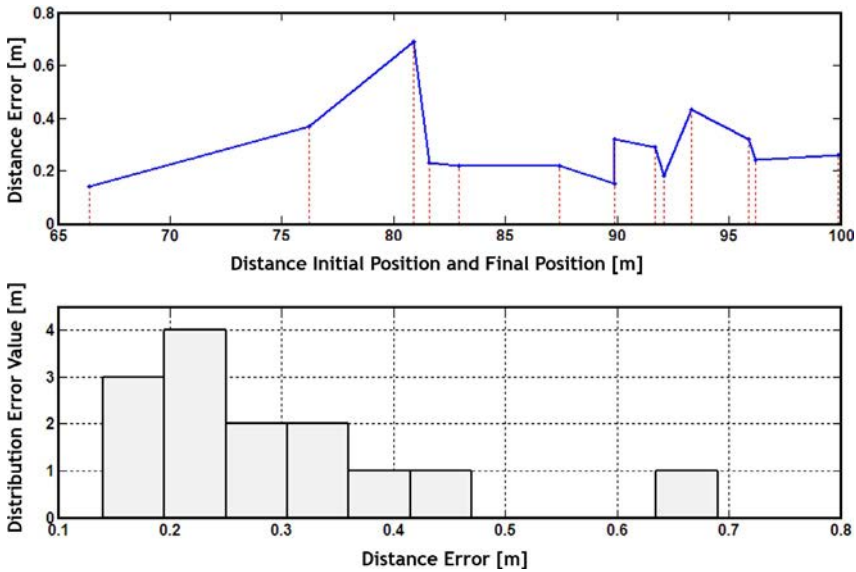

Fig. 9.21 Diagram of the distance error relative to the distance between the initial and final positions.

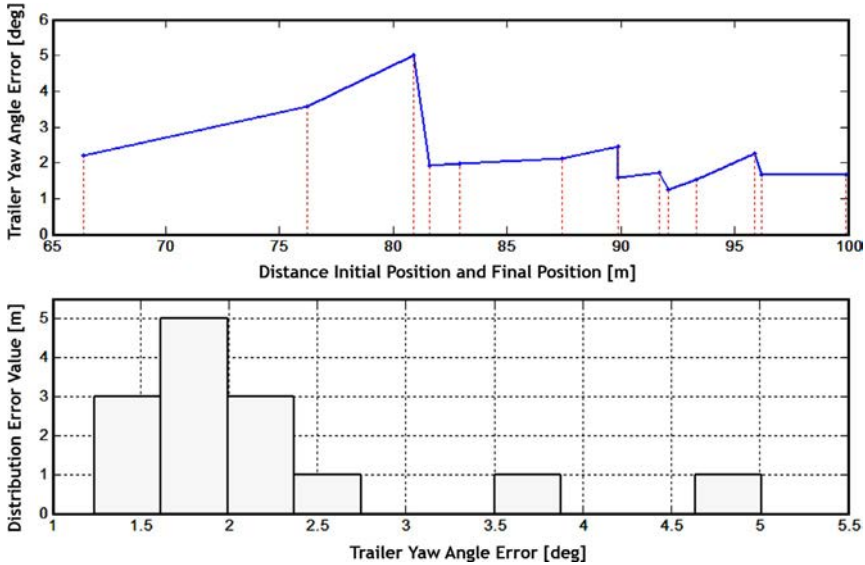

Fig. 9.22 Diagram of the yaw angle error relative to the distance between the initial and final positions.

and 9.22 shows that the highest frequency of distance error was seen for the distance error of about 0.2 m, while that of the trailer yaw angle was about 2 degrees.

9.3.5 Application of inverse kinematic equations in parking maneuvers for articulated vehicles

9.3.5.1 Verification of inverse kinematic equations using computer simulations

Fig. 9.23 shows, schematically, the relationship between the desired path along which the vehicle must go, $y = f(x)$, the steering angle, and the vehicle velocity. In this figure, the function $f(x)$ serves as input into the structure (provided by the user for the computer-assisted simulation). Here, considering the scenario considered for the automatic parking of the articulated vehicle, the fifth-order polynomial expressed in Eq. (9.39) was adopted to approximate $f(x)$.

$$f(x) = a_0 + a_1 x + a_2 x^2 + a_3 x^3 + a_4 x^4 + a_5 x^5 \tag{9.39}$$

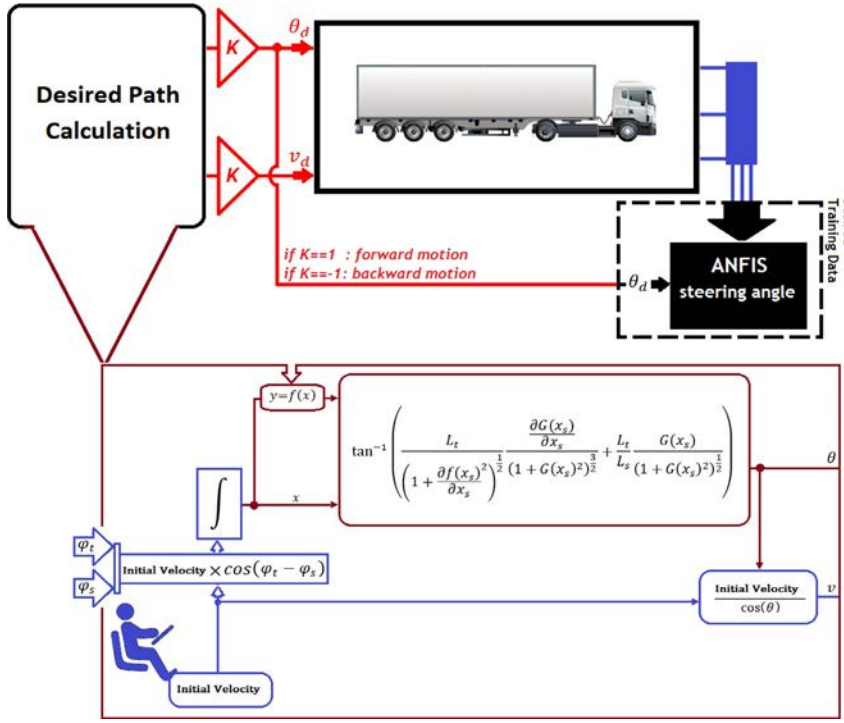

Fig. 9.23 Schematic demonstration of the simulation of an articulated vehicle to verify the proposed inverse kinematic method.

This polynomial must meet three key constraints: (1) it must satisfy at the initial (x_i, y_i) and final points (x_f, y_f), at which points the (2) slope and (3) convexity of the polynomial must be zero. The polynomial coefficients that satisfy these properties are under Eq. (9.40):

$$\underbrace{\begin{bmatrix} a_0 \\ a_1 \\ a_2 \\ a_3 \\ a_4 \\ a_5 \end{bmatrix}}_{A} = \underbrace{\begin{bmatrix} 1 & x_i & x_i^2 & x_i^3 & x_i^4 & x_i^5 \\ 1 & x_f & x_f^2 & x_f^3 & x_f^4 & x_f^5 \\ 0 & 1 & 2x_i & 3x_i^2 & 4x_i^3 & 5x_i^4 \\ 0 & 1 & 2x_f & 3x_f^2 & 4x_f^3 & 5x_f^4 \\ 0 & 0 & 2 & 6x_i & 12x_i^2 & 20x_i^3 \\ 0 & 0 & 2 & 6x_f & 12x_f^2 & 20x_f^3 \end{bmatrix}}_{X}^{-1} \underbrace{\begin{bmatrix} y_i \\ y_f \\ 0 \\ 0 \\ 0 \\ 0 \end{bmatrix}}_{Y} \tag{9.40}$$

Table 9.6 Verification errors are associated with the calculations performed by the proposed inverse kinematic method.

Initial Condition $x_i(m)$, $y_i(m)$	*Final Condition* $x_f(m)$, $y_f(m)$	$\frac{\max\lvert error_x\rvert}{\lvert x_i - x_f\rvert} \times 100$	$\frac{\max\lvert error_x\rvert}{\lvert y_i - y_f\rvert} \times 100$
$(-75, 10)$	$(10, 0)$	0.0527	0.4919
$(-75, 10)$	$(10, 0)$	0.0524	0.2591
$(-80, 13)$	$(7, 2)$	0.0513	0.4490
$(-85, 20)$	$(5, 2)$	0.0497	0.4313
$(-90, 22)$	$(10, 2)$	0.0449	0.3632

Given the subject of this research (automatic parking of heavy-duty articulated vehicles with one joint and two links), computer-assisted simulations were run to verify (9.25) (Table 9.6).

9.3.5.2 Training the articulated vehicle with desired data-fed ANFIS for the inverse kinematic method

In the proposed methodology, similar to the methodology implemented previously, the ANFIS was prepared for the phase-1 motion based on the desired path and extracted steering angle data to develop the parking maneuver. For both motion phases, the required information was provided based on the desired data in Fig. 9.24. Here, we once more used the feedback related to φ_t (rad), φ_s (rad), and horizontal distance to the wall. Table 9.7 lists the initial condition (IC) and final condition (FC) for the desired paths, as used for training the ANFIS network. The position (0, 15) was set as the FC

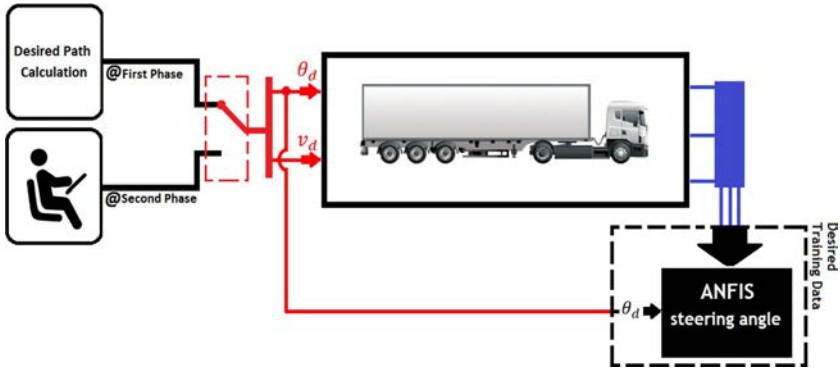

Fig. 9.24 Schematic demonstration of receiving information for the two motion phases based on the desired motion information.

Table 9.7 Information on initial condition (IC) and final condition (FC) for the desired paths, as used for training the ANFIS network in the inverse kinematic method.

No.	(IC_x, IC_y)	(FC_x, FC_y)	No.	(IC_x, IC_y)	(FC_x, FC_y)
1	(−65, 5)	(15, 0)	7	(−80, 10)	(15, 0)
2	(−70, 8)	(15, 0)	8	(−80, 14)	(15, 0)
3	(−70, 16)	(15, 0)	9	(−85, 18)	(15, 0)
4	(−75, 15)	(15, 0)	10	(−90, 15)	(15, 0)
5	(−75, 19)	(15, 0)	11	(−90, 18)	(15, 0)
6	(−80, 5)	(15, 0)	12	(−95, 15)	(15, 0)

for phase-1 as the control strategy for phase-2 required that the vehicle started phase-2 at this position (IC for phase-2). In this regard, Table 9.7 presents (0, 15) as the FC for phase-1. As seen in this table, the information related to a total of 12 different ICs was used to train the ANFIS network. Next, for the phase-1 motion, the information on the desired path and extracted steering wheel angles (Fig. 9.23) was utilized. For the second phase, as explained earlier, the expert driver's behavior was used.

Fig. 9.25 shows three examples of the articulated vehicle motion along the paths determined based on the extracted desired steering angle according

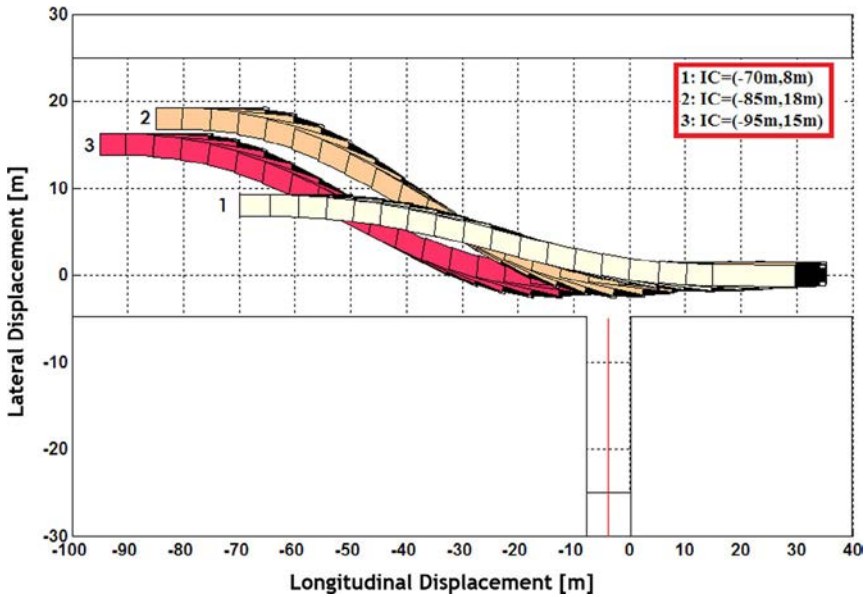

Fig. 9.25 An example of the paths of the phase-1 and phase-2 motions for training the ANFIS network in the inverse kinematic method.

to Eq. (9.25). Indeed, the vehicle motion along these paths with different ICs has been practiced to provide a database for training the ANFIS network. As explained earlier, in order to go through the desired path at the desired steering angle, the control system needs to explore not only the appropriate steering angle, but also the vehicle velocity. Following this line of reasoning, the output of the ANFIS system is not limited to the steering angle only, but rather extends to the vehicle velocity. The similarities between the methodology described in this section and the one explained previously provide for not repeating the similar concepts over but rather emphasizing the most important issues. Accordingly, the designed ANFIS is herein solely represented by the input membership functions and the fuzzy rules levels with the two output parameters, namely the steering angle and the vehicle velocity (Figs. 9.26 and 9.27, respectively), not mentioning the other common characteristics such as the fuzzy rules, the structure of the fuzzy network, etc.

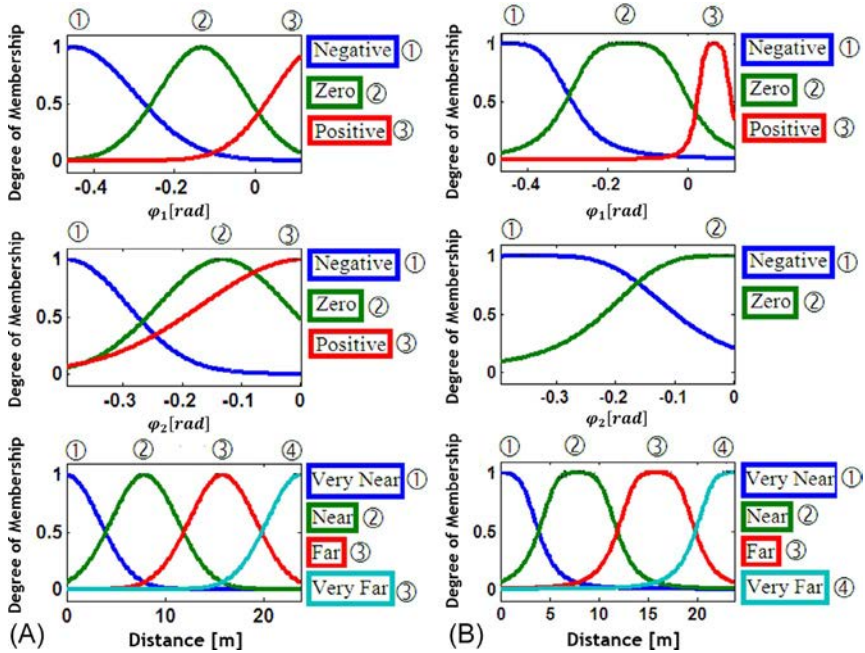

Fig. 9.26 Input membership functions and outputs (steering angle and velocity) for the phase-1 motion based on the inverse kinematic method.

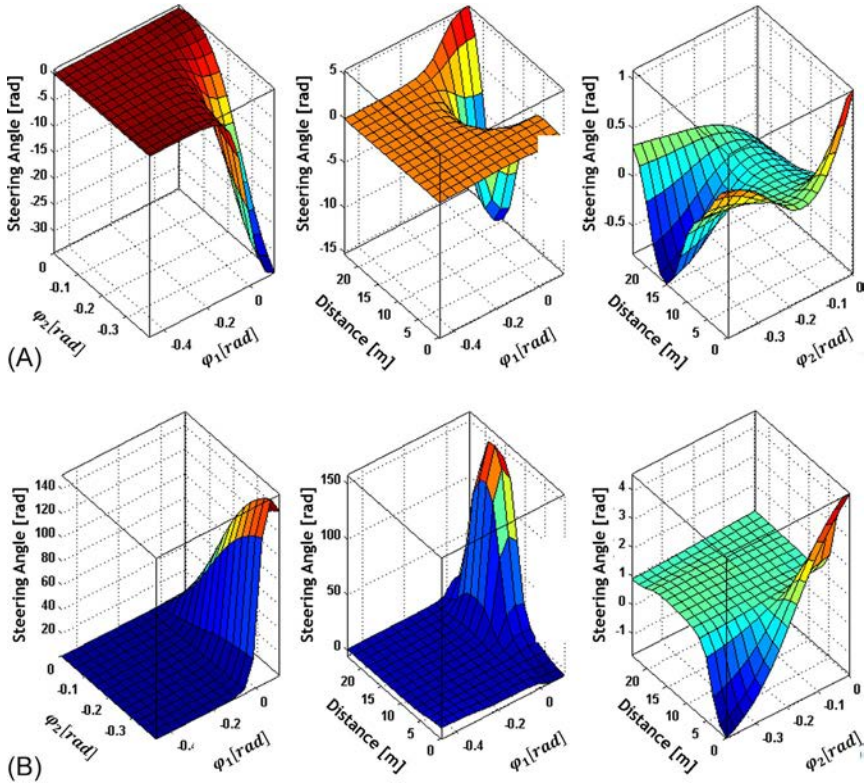

Fig. 9.27 Fuzzy rules levels and outputs (steering angle and velocity) for the phase-1 motion.

9.3.5.3 Closed-loop control system with neuro-fuzzy controller in inverse kinematic method

The incorporation of the designed ANFIS system into the considered closed-loop structure is demonstrated in Fig. 9.28. In this figure, it is clear that the controller itself is composed of two components corresponding to the two motion phases. The important point to note is that both parts produce as outputs both the steering angle and the longitudinal velocity of the vehicle. In the first phase of motion, the longitudinal velocity signal is obtained as an input of the ANFIS network, just like the steering angle. For the second phase of motion, the velocity is set to be fixed at $v = -1$ (m/s).

The parking error is herein calculated from the values obtained in Eq. (9.41) using Eqs. (9.36) and (9.37). Table 9.8 reports the parking maneuver error associated with different ICs, and Fig. 9.29 demonstrates two cases

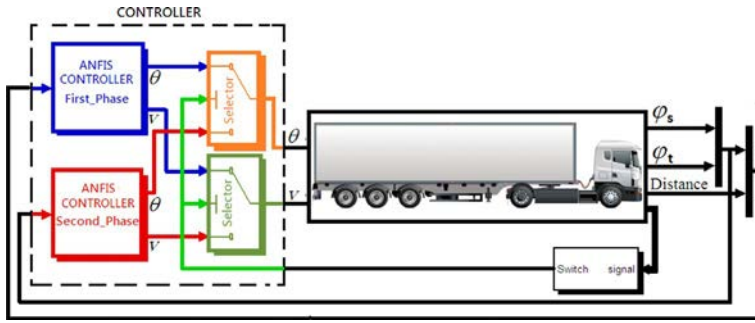

Fig. 9.28 The closed-loop control system for the automatic parking of the articulated vehicle.

Table 9.8 The articulated vehicle parking maneuver error is associated with different ICs.

No.	IC_x(m)	IC_y(m)	$Distance_{error}$(m)	$\varphi_{t_{error}}$(rad)	$\varphi_{s_{error}}$(rad)
1	−73	11.2	0.1733	0.1158	0.0042
2	−80	15.4	0.1334	0.1568	0.0336
3	−83.2	13.7	0.1075	0.1369	0.0147
4	−93.2	18	0.1509	0.1397	0.013
5	−95	17.2	0.0382	0.1325	0.0071
6	−68.6	5.6	0.5420	0.0505	0.0799
7	−89.6	14.25	0.1962	0.1314	0.062
8	−77.2	10.25	0.0073	0.1077	0.0115
Error Mean Value			0.1686	0.1214	0.0283

of automatic parking maneuvers for articulated vehicles based on the inverse kinematic method.

$$\begin{aligned} x_{final} &= -3.85\,\text{m} \\ x_{final} &= -24\,\text{m} \\ \varphi_{final} &= \frac{\pi}{2}\,\text{rad} \end{aligned} \tag{9.41}$$

An investigation into the results presented in Fig. 9.29 shows that the development of a database using the newly proposed equations in this chapter contributed well to improved training of the ANFIS network and hence to increased performance of the proposed adaptive neuro-fuzzy controller within a closed-loop structure. Indeed, in eight cases with different ICs, the system could successfully handle the maneuver and position the end of the vehicle appropriately without hitting the walls and within acceptable ranges of parking error.

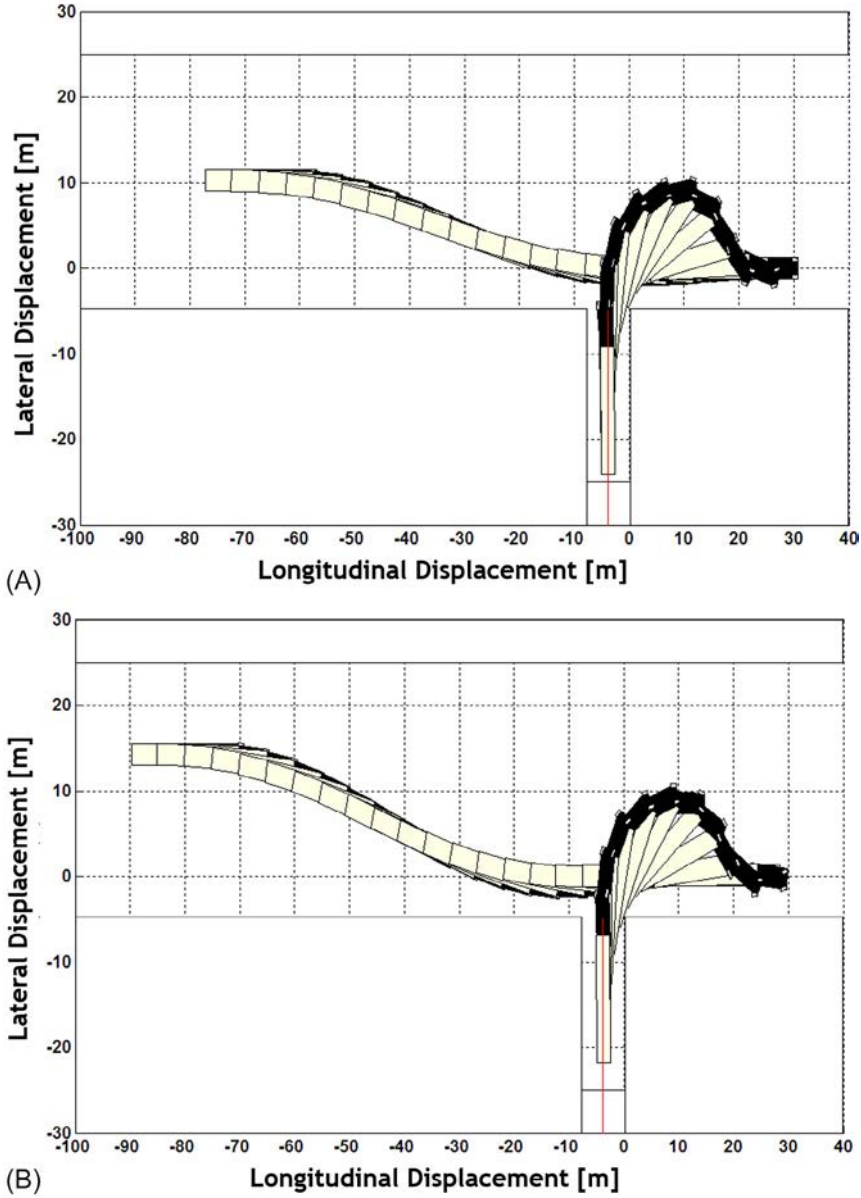

Fig. 9.29 Automatic parking maneuver of an articulated vehicle with different ICs: (−77.2 m, 10.25 m) and (−86.6 m, 1.25 m).

9.4 Design and implementation of mechanical equipment for articulated vehicle experimental model

This section is dedicated to the verification of the proposed control method for the automatic parking of the articulated vehicle. The audit was conducted by implementing a model articulated vehicle in the laboratory. The design verification should be done by performing the design steps successively to ensure that the obtained product would meet the expected requirements. In this approach to the verification, the goal is to make sure that the ideal model built through mathematical modeling in the computer exhibits no significant difference to the manufactured model. The model manufacturing verification begins with designing the CAD model and proceeds to select appropriate driving power equipment and sensors, considering the physical and real-problem constraints. It should be noted that the connection between the control system, which is the decision-making unit, and the sensors as well as the driving power equipment was established by providing interface circuits. The circuits are only briefly discussed in this section as their design is beyond the scope of this chapter.

Fig. 9.30 presents a complete view of the implemented articulated vehicle experimental model for the verification stage. Fig. 9.31 demonstrates the main components of the vehicle, with each component numbered appropriately. The name of the different components of the system is given in Table 9.9. As mentioned earlier, to have the model articulated vehicle be able to move, we need to utilize particular electronic equipment such as a driving power system, sensors, and interface circuits. The relevant information and a brief explanation of the mentioned items of equipment and their applications are presented in Table 9.10.

A PCB populated with electronic components is called a printed circuit assembly (PCA), a printed circuit board assembly, or a PCB assembly (PCBA). The IPC-preferred term for assembled boards is circuit card assembly (CCA), and for assembled backplanes, it is backplane assemblies. Fig. 9.32 shows the final assembly of the PCB, and Fig. 9.33 presents the manufactured physical model of the articulated vehicle in the laboratory.

Following this chapter, as proposed in the parking scenario, the vehicle was first moved along the desired paths, and the information extracted from the sensors as the model vehicle moved along the desired path (four maneuvers) was used to train the ANFIS network. To better understand the process of training the ANFIS network using the input-desired output data on the model articulated vehicle, please see Figs. 9.34 and 9.35, where the

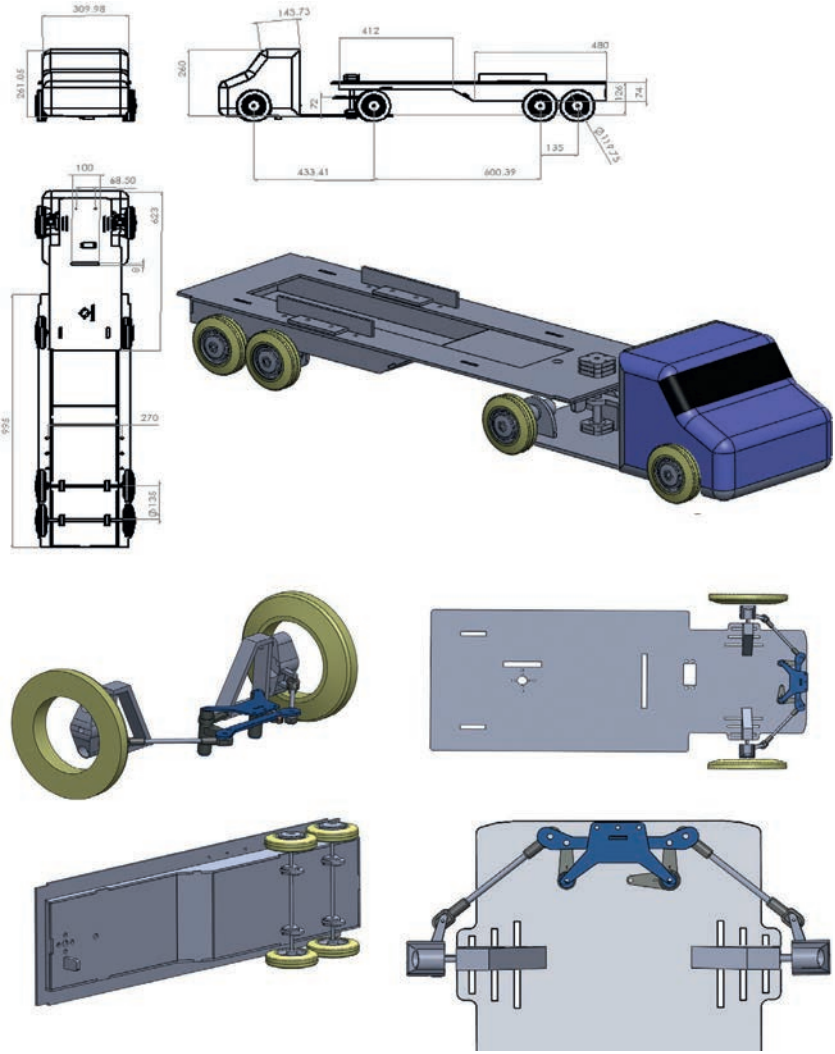

Fig. 9.30 Demonstration of the model articulated vehicle and its main components.

closed-loop control system is presented. It is worth mentioning that the limitations encountered in laboratory experiments, such as the limited space of the laboratory, the manufacturing and modeling precision, the proper function of the mechanical and electronic equipment, and the difficulties faced when implementing the control system required that the control system be made to maximum simplicity to avoid the negative impacts of the mentioned issues (e.g., velocity, etc.) on the system performance. In this regard,

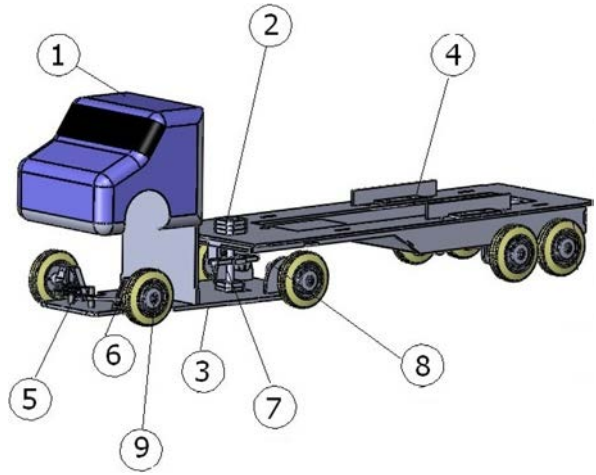

Fig. 9.31 Demonstration of the main components of the model articulated vehicle.

Table 9.9 Names of different components of the designed model articulated vehicle.

Part no.	Part name	Quantity
1	Cabin	1
2	Tractor-trailer joint	1
3	Tractor	1
4	Trailer	1
5	Steering system	1
6	Rigid suspension system	2
7	Joint angle physical constraint	1
8	Driving power system	2
9	Tire	8

Fig. 9.36 shows the structure and input membership functions of the ANFIS controller with the minimum number of membership functions in the two phases of the automatic parking of the model articulated vehicle in the laboratory.

The designed parking space is about 1 m in span and 1.5 m in length. Fig. 9.37 shows the parking space, together with images of the maneuvering model vehicle under an automatic parking scheme. Figs. 9.38 and 9.39 show the results of the sensors and control signals with the ICs (75 cm, 158 cm) and (75 cm, 83 cm), respectively, for both phases of the automatic parking of the model articulated vehicle. Table 9.11 presents the parking error from

Table 9.10 Electrical and electronic equipment used to manufacture the model articulated vehicle in the laboratory.

No.	Part	Specifications	Application
Engine	DC motor	10:1 Gearbox Operating voltage: 24 V Rotational velocity: 5000 RPM	Supplying driving force for the vehicle
	Servo motor	Rotational velocity at 6 V: 0.27 (seconds per 60 degrees) Rotational velocity at 4.8 V: 0.33 (seconds per 60 degrees) Torque at 6 V: 8 kg/cm Torque at 4.8 V: 8 kg/cm	Steering angle operator
Electronic components	SRF05	Power supply: 5 V Operating current: 4 mA Operating frequency: sonar 40 kHz Range: 3–4 cm Resolution: 3–4 cm TTL-level echo signal transmitter	Distance measurement
	Potentiometer	10 kΩ and single RPM	Vehicle joint angle measurement
	L298	Operating voltage: up to 46 V with a low saturation voltage Peak DC current: up to 4 A High-temperature resistance 0–1.5 V logical input Low noise admission	DC motor startup
	4n35	Isolation voltage: 5 kV Output voltage: 70 V Operating ranges: 55–100°C Number of channels: 1	

Continued

Table 9.10 Electrical and electronic equipment used to manufacture the model articulated vehicle in the laboratory—cont'd

No.	Part	Specifications	Application
	7805	Output voltage: 5 V Minimum input voltage: 7.3 V	Voltage regulator
	ZIG110A	The ZIG-110 assembly is composed of two moduli, namely a SIG-100 and a ZIG-110 The ZIG-100 board can be assembled onto RC-100, ZIGSerial, and/or CM-5. The ZIG-110 modulus can be connected to CM-510 and/or CM-700	Transmitter-receiver
Microcontroller	AVR ATMEGA128	Flash memory (programmable): 128 kB EEPROM: 4 kB SRAM: 4 kB Equipped with internal calibrated oscillator Number of slots: 64 (TQFP) The number of input and output pins: 53 Power supply: 4.5–5.5 V (ATmega 128) 2.7–5.5 V (ATmega 128L) Operating Frequency: 0–16 5 V (ATmega 128) 0–8 V (ATmega 128L)	
Power supply	Battery Battery	12 V, three cells, Lithium polymer 12 V, atomic	Supplying the main board Powering the startup board

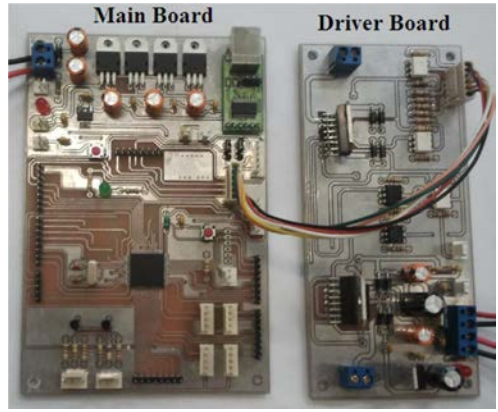

Fig. 9.32 Demonstration of the manufactured electronic board together with the designed circuit.

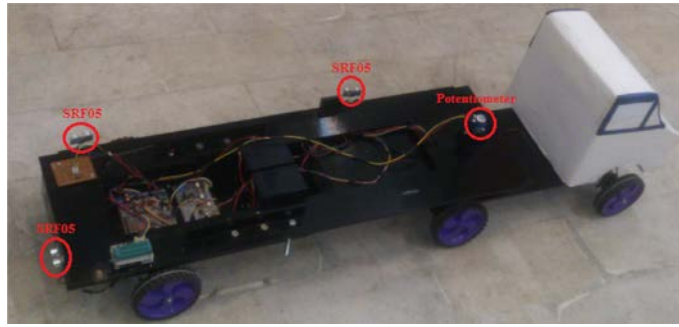

Fig. 9.33 The manufactured physical model articulated vehicles together with the sensors from two different views.

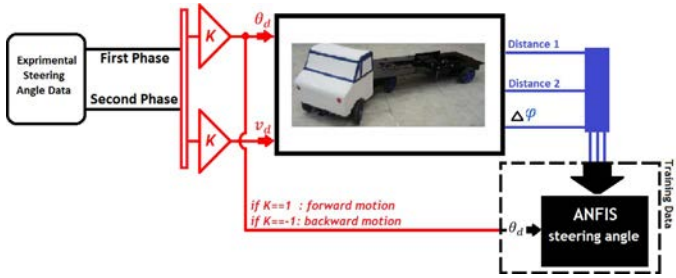

Fig. 9.34 Training the ANFIS based on the experimental desired input–output pairs for the experimental model.

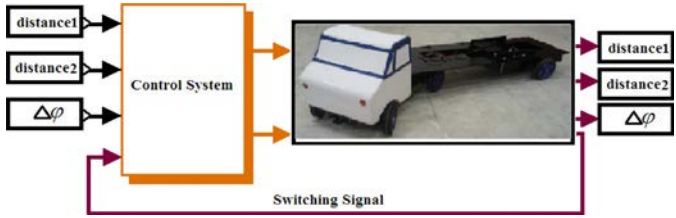

Fig. 9.35 Closed-loop control system for the automatic parking of the model articulated vehicle in the laboratory.

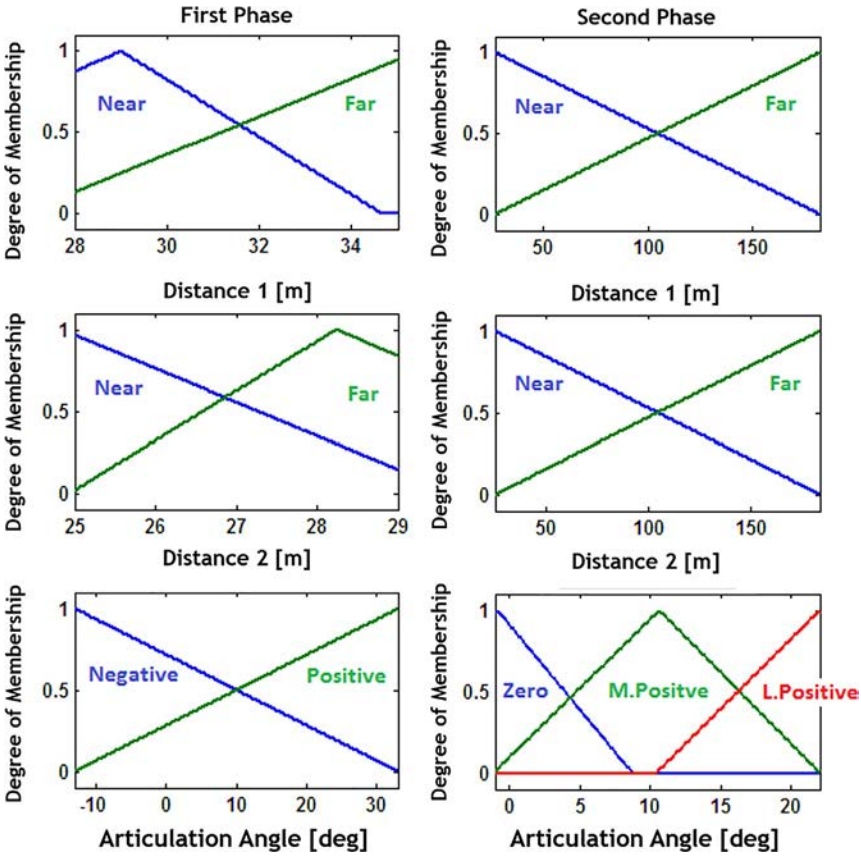

Fig. 9.36 Demonstration of the input membership functions of the ANFIS controller in the phases of motion.

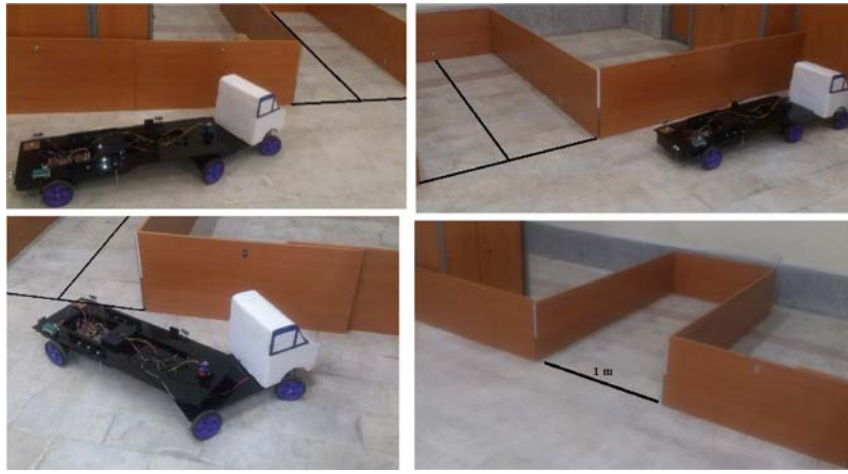

Fig. 9.37 Parking space and parking maneuver for the automatic parking of the model articulated vehicle.

two different ICs. Two error terms are defined to evaluate the performance of the proposed parking scheme, namely deviation from the desired final position and tractor and trailer yaw angle errors regarding the desired values.

Due to the limitations encountered in the laboratory and the problems faced when measuring and starting up the system, we had no choice, unfortunately, but to present only two error terms and demonstrate one signal (Table 9.11). In the similar maneuvers, the vehicle could go into the parking space without hitting any wall.

9.5 Conclusion

Due to the nonlinear nature of the motion kinematics in an articulated vehicle and acknowledging the successful application of fuzzy logic and artificial networks (ANNs), ANFIS was proposed for designing a controller for the automatic parking of articulated vehicles. Indeed, the proposed system tended to reproduce the behavior exhibited by an expert driver as he/she would undertake the parking maneuver. An ANFIS network was built based on the expert driver's experiences of desirably parking an articulated vehicle. The control structure was designed accordingly. Following with the chapter, simulations were performed, and the proposed technique was practically implemented on a model articulated vehicle in the laboratory to verify the proper performance of the proposed methodology for the automatic parking of the articulated vehicle.

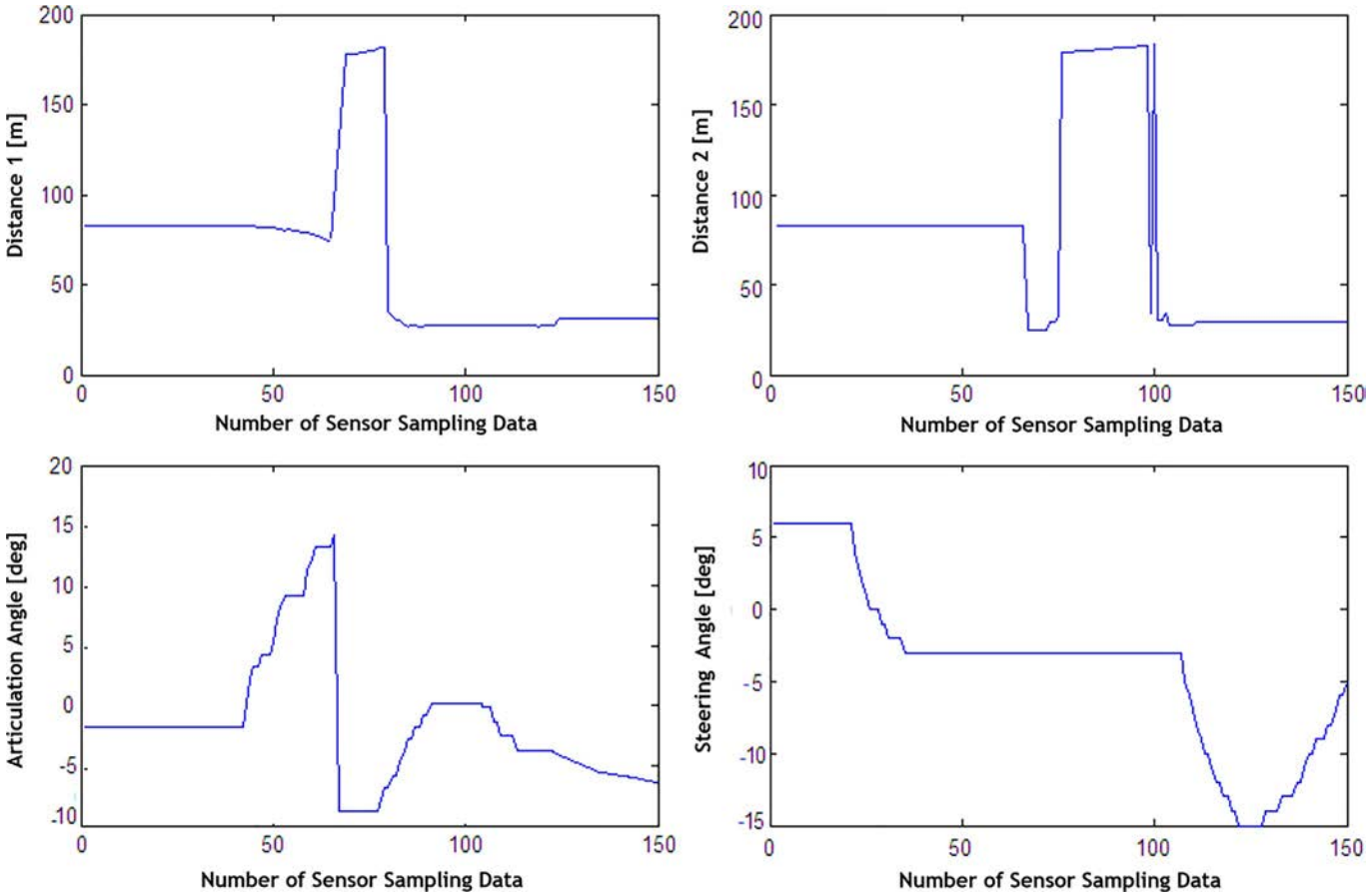

Fig. 9.38 Demonstration of the data from sensors and the control signal with the IC (75 cm, 158 cm), first motion phase.

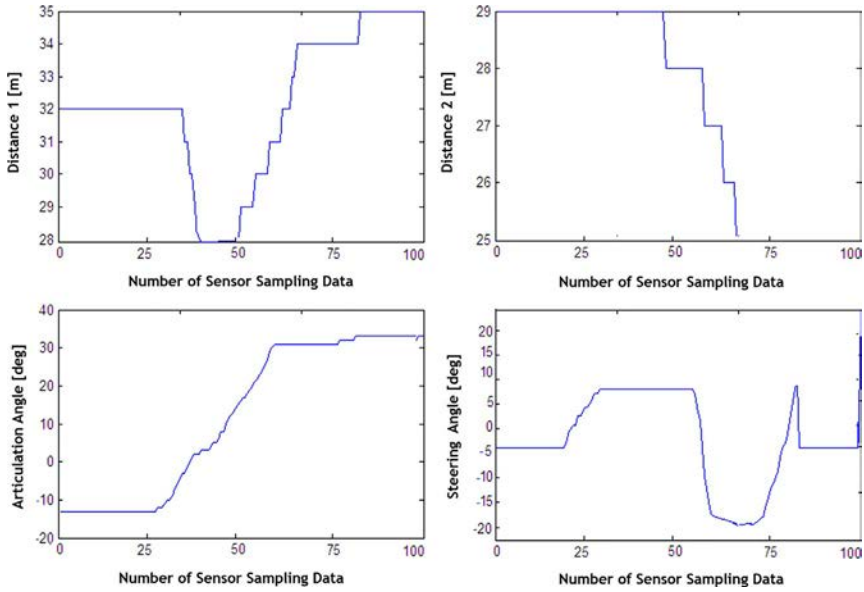

Fig. 9.39 Demonstration of the data from sensors and the control signal with the IC (75 cm, 83 cm), second motion phase.

Table 9.11 Parking error with the model articulated vehicle.

No.	Articulation angle initial condition (degrees)	Distance initial condition (cm)	Deviation error (cm)	Articulation angle error (degrees)
1	3	(75, 83)	13.5	31
2	−2	(75, 158)	7	8

References

[1] J. Xu, G. Chen, M. Xie, Vision-guided automatic parking for smart car, in: Proceedings of the IEEE Intelligent Vehicles Symposium 2000 (Cat. No. 00TH8511), IEEE, 2000.
[2] https://www.whichcar.com.au/car-advice/self-parking-technologies-in-cars.
[3] Y.J. Huang, C.H. Chang, Auto-parking system via intelligent computation intelligence, World Acad. Sci. Eng. Technol. Int. J. Comput. Electr. Autom. Control Inf. Eng. 6 (5) (2012) 687–690.
[4] M.-H. Li, P.-K. Tseng, Implementation of an autonomous driving system for parallel and perpendicular parking, in: 2016 IEEE/SICE International Symposium on System Integration (SII), IEEE, 2016.
[5] B. Li, K. Wang, Z. Shao, Time-optimal maneuver planning in automatic parallel parking using a simultaneous dynamic optimization approach, IEEE Trans. Intell. Transp. Syst. 17 (11) (2016) 3263–3274.

[6] Y. Song, C. Liao, Analysis and review of state-of-the-art automatic parking assist system, in: 2016 IEEE International Conference on Vehicular Electronics and Safety (ICVES), IEEE, 2016.
[7] Y. Jeong, et al., Design and Implementation of Parking Control Algorithm for Autonomous Valet Parking, No. 2016-01-0146. SAE Technical Paper, 2016.
[8] Z. Taherkhani, Design and Simulation of Controller for Automatic Car Park (Master thesis in Mechanical Engineering), Khajeh University, Nasir al-Din al-Tusi, Summer 2011 (in Persian).
[9] T.-h. Hsu, et al., Development of an automatic parking system for vehicle, in: Vehicle Power and Propulsion Conference, 2008. VPPC'08. IEEE, IEEE, 2008.
[10] T.-H.S. Li, S.-J. Chang, Autonomous fuzzy parking control of a car-like mobile robot, IEEE Trans. Syst. Man Cybern. A Syst. Hum. 33 (4) (2003) 451–465.
[11] D. Zöbel, D. Polock, P. Wojke, Steering assistance for backing up articulated vehicles, Syst. Cybern. Inf. 1 (5) (2003) 101–106.
[12] C.R. Kelber, F.S. Osório, L.B. Becker, Assistance controller for driving backwards and parking an articulated vehicle, in: 2008 IEEE Intelligent Vehicles Symposium, IEEE, 2008.
[13] N. Zimic, M. Mraz, Decomposition of a complex fuzzy controller for the truck-and-trailer reverse parking problem, Math. Comput. Model. 43 (5) (2006) 632–645.
[14] D. Zobel, E. Balcerak, T. Weidenfeller, Minimum parking maneuvers for articulated vehicles with one-axle trailers, in: 9th International Conference on Control, Automation, Robotics and Vision, 2006. ICARCV'06, IEEE, 2006.
[15] M. Delrobaei, K.A. McIsaac, Parking control of a center-articulated mobile robot in presence of measurement noise, in: 2010 IEEE Conference on Robotics Automation and Mechatronics (RAM), IEEE, 2010.
[16] M. Sharafi, S. Nikpoor, Intelligent parking method for truck in presence of fixed and moving obstacles and trailer in presence of fixed obstacles: advanced Fuzzy logic technologies in industrial applications, in: 2010 International Conference on Electronics and Information Engineering (ICEIE), vol. 2, IEEE, 2010.
[17] J. Morales, et al., Driver assistance system for backward maneuvers in passive multi-trailer vehicles, in: 2012 IEEE/RSJ International Conference on Intelligent Robots and Systems (IROS), IEEE, 2012.
[18] J. Roh, W. Chung, Reversing control of a car with a trailer using the driver assistance system, Int. J. Adv. Robot. Syst. 8 (2) (2011) 23.
[19] C.-J. Hoel, P. Falcone, Low speed maneuvering assistance for long vehicle combinations, in: 2013 IEEE Intelligent Vehicles Symposium (IV), IEEE, 2013.
[20] A. Mohamed, et al., Optimal collision free path planning for an autonomous articulated vehicle with two trailers, in: 2017 IEEE International Conference on Industrial Technology (ICIT), IEEE, 2017.
[21] Z. Liang, G. Zheng, J. Li, Application of fuzzy control strategy in automatic parking path planning, in: 2012 4th International Conference on Intelligent Human-Machine Systems and Cybernetics (IHMSC), vol. 2, IEEE, 2012.
[22] Z.-J. Wang, et al., Application of fuzzy logic for autonomous bay parking of automobiles, Int. J. Autom. Comput. 8 (4) (2011) 445–451.
[23] H. Masaki, L. Kangzhi, Automatic parking benchmark problem: experimental comparison of nonholonomic control Methods, in: Control Conference, 2007. CCC 2007. Chinese, IEEE, 2007.
[24] S.H. Azadi, H.R.R. Nedamani, R. Kazemi, Automatic parking of an articulated vehicle using ANFIS, Glob. J. Sci. Eng. Technol. 2322-2441, (2013) 93–104.
[25] P.R. Pande, P.L. Paikrao, D.S. Chaudhari, Digital ANFIS model design, Int. J. Soft Comput. Eng. 3 (1) (2013) 314–318.

[26] K.-Y. CAI, Robustness of fuzzy reasoning and/spl delta/-equalities of fuzzy sets, IEEE Trans. Fuzzy Syst. 9 (5) (2001) 738–750.
[27] M.B. Minhaj, Fundamentals of Computational Intelligence Neural Networks, fourth ed., Amirkabir University of Technology Press, 2007 (in Persian).
[28] S.H. Azadi, Z. Taherkhani, Autonomous parallel parking of a car based on parking space detection and fuzzy controller, Int. J. Automot. Eng. 2 (1) (2012) 30–37.
[29] A. Subasi, Application of adaptive neuro-fuzzy inference system for epileptic seizure detection using wavelet feature extraction, Comput. Biol. Med. 37 (2) (2007) 227–244.
[30] J.-S.R. Jang, ANFIS: adaptive-network-based fuzzy inference system, IEEE Trans. Syst. Man Cybern. 23 (3) (1993) 665–685.
[31] R.M. Tong, A control engineering review of fuzzy systems, Automatica 13 (6) (1977) 559–569.
[32] H.B. Demuth, et al., Neural Network Design, Martin Hagan, 2014.
[33] M.Y. Rafiq, G. Bugmann, D.J. Easterbrook, Neural network design for engineering applications, Comput. Struct. 79 (17) (2001) 1541–1552.
[34] C.-T. Lin, C.S.G. Lee, Neural Fuzzy Systems, PTR Prentice Hall, 1996.
[35] H. Zhang, Y.U. Yuefeng, W.A.N.G. Qiang, Modeling and simulation applying adaptive neural-fuzzy inference system (ANFIS), Comput. Simul. 4 (2002) 012.
[36] L. Naderloo, et al., Application of ANFIS to predict crop yield based on different energy inputs, Measurement 45 (6) (2012) 1406–1413.
[37] Lee Wang, Translator: Mohammad Tashneh Lab, Nima Safapour, Dariush Afyoni, Fuzzy Systems and Fuzzy Control, Khajeh Nasir al-Din al-Tusi University of Technology Press, fourth ed., 2007 (in Persian).
[38] J.-S.R. Jang, C.-T. Sun, E. Mizutani, Neuro-fuzzy and soft computing-a computational approach to learning and machine intelligence [Book Review], IEEE Trans. Autom. Control 42 (10) (1997) 1482–1484.
[39] S. Haykin, Neural Networks: A Comprehensive Foundations, second ed., Pearson, 2004.
[40] R. Rojas, Neural Networks: A Systematic Introduction, Springer Science & Business Media, 2013.
[41] http://www.rta.nsw.gov.au.

CHAPTER 10

Trajectory planning of tractor semitrailers

10.1 Introduction

Driving is among the tasks that can put human life at risk if not performed with sufficient concentration and care. The World Health Organization (WHO) studied global road safety in its report on October 22, 2015, based on data collected from 180 countries. This report puts the number of fatalities and the number of seriously injured people due to road accidents at 1.25 million and between 20 and 50 million, respectively. The report also mentions that the highest severity of road accidents leading to death (almost 90%) occurs in medium- and low-income countries. In contrast, merely 54% of vehicles in the world are on the road in these countries. Because such accidents impose an enormous financial burden on the victims, they can be considered one of the factors in the economic gap between these countries and high-income countries. Road accidents currently rank as the ninth most common cause of death, with a 2.2% share of all global deaths. The Association for Safe International Road Travel (ASIRT) has predicted that this rank will rise to fifth by 2030 if a serious effort is not made to improve regulations and use novel technologies in this area.

A study by the US Department of Transportation in the 1990s indicated that fatigue is the cause of 30% of road accidents involving heavy commercial vehicles [1–3]. On the other hand, some studies in some European countries about driver fatigue and its effect on accidents have shown that fatigue is the cause of 20% of road accidents in commercial transportation and, hence, is a significant factor [4]. Therefore, drowsiness in suburban and transit drivers, who often choose articulated vehicles to transport cargo and are driving long distances, plays an essential role in accidents. As a result, it is necessary to design an automatic system capable of navigating the vehicle via safe and accurate decisions in case of driver drowsiness.

Among the works carried out in this area is a system that detects a decrease in the driver's level of consciousness and prevents an accident by sending a warning message and performing automatic cautionary actions.

Vehicle Dynamics and Control
https://doi.org/10.1016/B978-0-323-85659-1.00010-0

In this system, after the parameters are sensed online and sent to the processor, the decision-making system determines the driver's level of consciousness using predefined criteria for sleepiness. This process must occur in real-time throughout driving. After the level of consciousness is determined, the automatic navigation system must go into action if the driver is unable to navigate the vehicle due to sleepiness.

Extensive research has been performed to develop collision avoidance methods using velocity control or motion path planning with lateral guidance along the desired path. The obstacles in most of this research were either stationary or moving at a constant vehicle velocity. Moreover, most of the research was to investigate control systems to be used in robots and was conducted inside laboratory environments. Also, the previous works mostly involved passenger cars, and tractor semitrailers were less commonly addressed. Operational speeds are usually lower in robotics compared to vehicles, and robots benefit from more diverse motion dynamics and fewer motion constraints than vehicles. Also, passenger comfort and safety that are key in vehicles are irrelevant to robots.

This chapter aims to investigate motion planning for tractor semitrailers in single and double lane change maneuvers, assuming a dynamic environment. The automatic navigation system must take action after detecting the driver's inability to navigate the tractor semitrailer due to drowsiness. As we know, the control inputs for vehicle navigation consist of the steering wheel and the accelerator and brake pedals (assuming an automatic transmission). More specifically, the accelerator and brake pedals are the control inputs for longitudinal navigation, and the steering wheel angle is the control input for lateral navigation. Accordingly, various control strategies have been considered by researchers, leading to the design of diverse, intelligent systems. For example, a system concerned with only the longitudinal control of the vehicle that prevents collision with vehicles in front is adaptive cruise control (ACC). Another type of system attempts to change vehicle direction after obstacle detection and collision prediction. To this end, these systems first determine the safe motion path and then attempt to navigate the vehicle toward this path by changing the steering wheel angle. Some novel research in this field has addressed simultaneous longitudinal and lateral vehicle control for collision avoidance. The related systems first determine the suitable method for collision avoidance by analyzing sensor data via the decision-making unit and then control the vehicle accordingly.

In this chapter, motion path determination and the relating algorithms are briefly addressed, after which trajectory generation is analyzed. Two

examples with step-by-step explanations are provided in order to create more understandable analyses of trajectory planning for semitrailers. In the first example, trajectory planning for semitrailers using $\eta^4 - spline$ is examined. In the second example, trajectory planning under dynamic conditions for single and double lane change maneuvers is studied.

10.1.1 An introduction to tractor semitrailers

N-trailers are the most commonly articulated vehicles used in ground transportation. They consist of an active tractor equipped with passive trailers connected via either on-axle hitching or off-axle hitching. On-axle hitching is when the hitching location is directly at the rear axle, and off-axle hitching is when the hitching location is at a distance from the rear axle, as shown in Fig. 10.1. The hitching location is the critical point that determines vehicle behavior [5].

Maneuvering an articulated vehicle is difficult even for expert drivers; hence, automatically controlling its motion is even more complicated. N-trailers are highly nonlinear kinematic systems with unique characteristics such as nonholonomic, operation-readiness, instability in structural connections during backward motion, and articulated angle dynamics. These characteristics make the manual control of these systems complicated [6].

N-trailers can be divided into three general classes:

1. Standard n-trailers (Snt): All trailers are connected at the center of towing via on-axle hitching.
2. Nonstandard n-trailers (nSnt): All trailers are connected at a distance from towing via off-axle hitching.
3. General n-trailers (Gnt): Instances of on-axle and off-axle hitching are used for specific trailers.

10.1.2 Steps in automatic vehicle navigation for collision avoidance

The first step in collision avoidance is obstacle detection. These obstacles are pedestrians and other moving vehicles. Numerous methods have been employed for obstacle detection using various sensors, including ultrasonic sensors and video cameras, and techniques such as image processing. After detecting the obstacle, predicting its motion, and establishing the vehicle state, one can determine whether a collision will occur between the vehicle

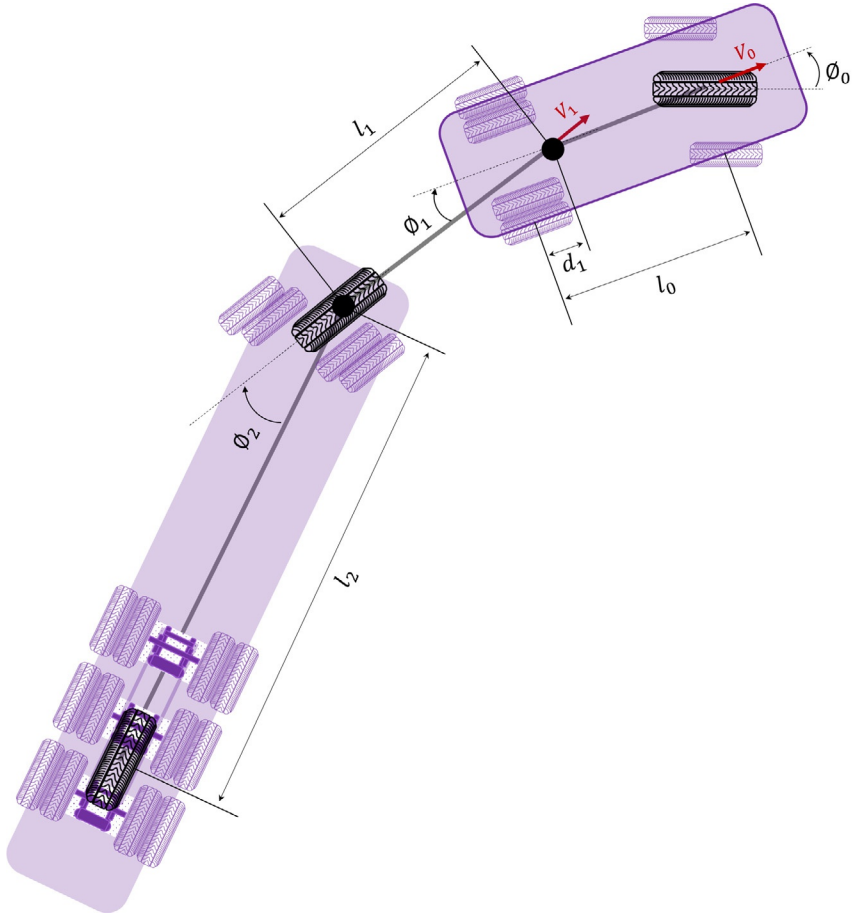

Fig. 10.1 On-axle and off-axle hitching.

and the obstacle. At this moment, the intelligent vehicle system must make the right decision for navigating the vehicle and avoiding the collision. Fig. 10.2 shows the diagram used to analyze the vehicle position and make control decisions.

As shown in Fig. 10.2, the information relating to the position and motion of the obstacle and the vehicle is assessed by the processing unit, and whether a collision will occur and time to the collision are determined.

According to this computation, the necessary warning is sent to the driver, or the automatic navigation system goes into action, depending on the situation. Automatic navigation can be performed via either braking or steering (changing the steering wheel angle). In case of a need for

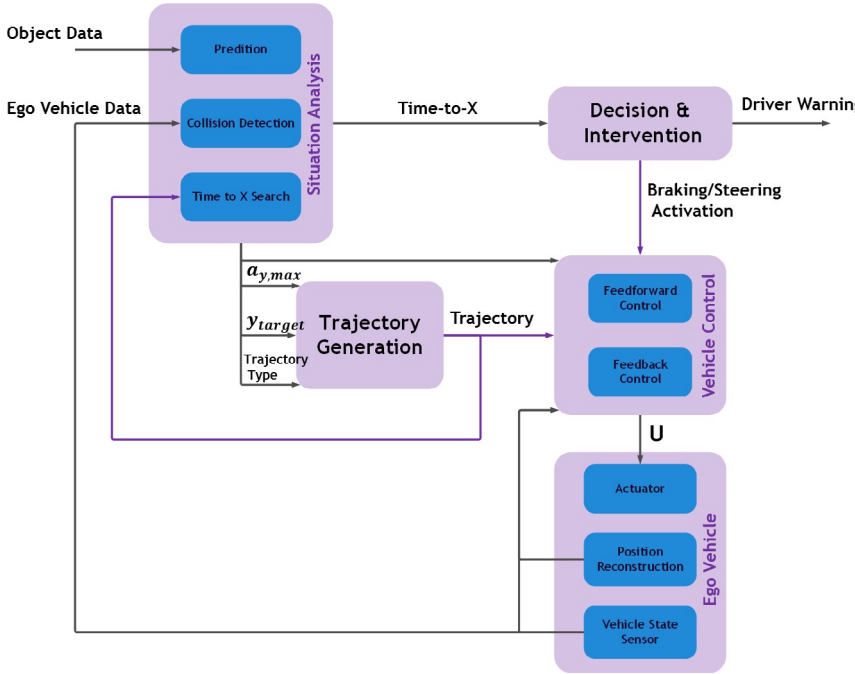

Fig. 10.2 Diagram for analyzing the vehicle position and making control decisions.

maneuvering using steering, the optimal path must first be calculated. After the adoption of a suitable strategy, all the data are transferred to the control system, and control commands are transmitted to the actuators [7].

The controlling complexity of automatic systems in every scenario strongly depends on the traffic, infrastructure, safety characteristics, and customer needs. So far, vehicle manufacturers and R&D centers have introduced some advanced driver assistance systems (ADAS) for road monitoring and semiautomatic control of vehicles and transportation systems. These systems include the following:

1. Emergency braking
2. Keeping intervehicle safe distance
3. Automated parking
4. Obstacle collision avoidance

Furthermore, autonomous emergency braking (AEB) and lane keeping assist (LKA) systems are currently available to some manufacturers. Besides, several platforms have been tested in real-life urban scenarios and highways, including the following:

1. Google driverless car
2. Daimler autonomous car
3. PROUD platform of Parma University

Almost all vehicle manufacturers and vehicle research centers have begun research in this area, which indicates significant progress.

This research field is 25 years old, and during this time, researchers have introduced numerous ways of improving controllers to achieve higher stability and reliability. However, issues such as trajectory generation under dynamic conditions, collision avoidance, and safe and comfortable driving are still either unsolved or without highly accurate solutions. Recently, online maneuver generation methods have been proposed for path planning and collision avoidance.

10.2 Path planning

Path planning is the most important issue in vehicle navigation. It is defined as finding a geometrical path from the current location of the vehicle to a target location such that it avoids obstacles. This path must be navigable by the vehicle and optimal in terms of at least one variable so that it can be considered a suitable path. For different target distance situations, the smoothest path, the shortest path, or the path along which the vehicle can move with the highest speed can become the most important path. In other words, the optimal path is determined concerning these characteristics. A standard method of path planning is discretizing the space and considering the center of each unit a movement point. Every movement point either has an obstacle that must be avoided or is free of obstacles that can be entered. Different discretization methods lead to different motion paths. The important point in discretizing the space is that the individual units must be convex to allow the movement to and from any point in them in case they can be passed. Uniform and Quadtree space discretization are typical to square discretization methods. Triangular and trapezoidal space discretization are two other, more accurate discretization types, meaning every unit is either an obstacle or free, and no unit is half obstacle and half free. All the mentioned methods lead to a graph that determines the acceptable locations for the vehicles. The next step in path planning is finding the path within this graph. This can be done using various methods, for example, the breadth-first search (BFS) or the A^* method.

Path planning is divided into two main categories based on assumptions:

1. *Global planning methods* are methods in which the surrounding environment is globally known, assuming the availability of a map.

These methods include the road-map algorithm, cell decomposition, Voronoi diagrams, occupancy grinds, and new potential field techniques. In most cases, the last step in the trajectory generation involves applying a Bézier curve [8].

2. *Local planning methods* are methods in which the surroundings are known locally and can be reconstructed based on reactive methods using sensors, such as infrared and ultrasonic sensors, and local video cameras.

The most well-known methods in this group are Bug algorithms, which navigate vehicles via local path planning based on a minimum set of sensors and with reduced complexity of online implementation. Bug1 and Bug2 are among the most common types of local path planning algorithms. Bug1 and Bug2 are utilized in cases where path planning is based on a predetermined rule and is most effective in fixed environments. In the Bug1 algorithm, the vehicle takes a path straight toward the target. It swerves past the potential obstacles from the right or left, returning to the original path and separating from the obstacle, as shown in Fig. 10.3. The sensor current data play a

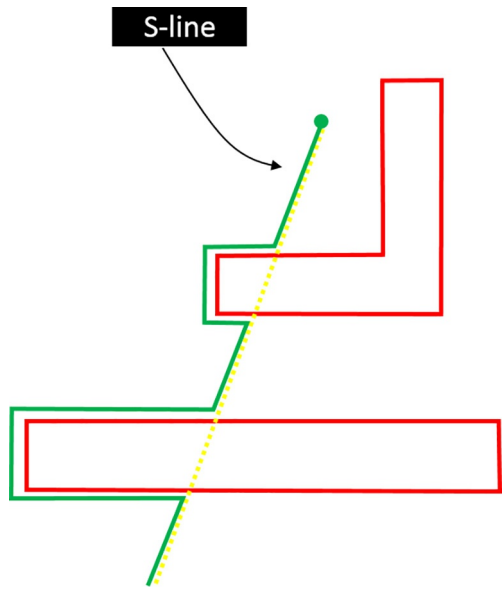

Fig. 10.3 Path planning using Bug1.

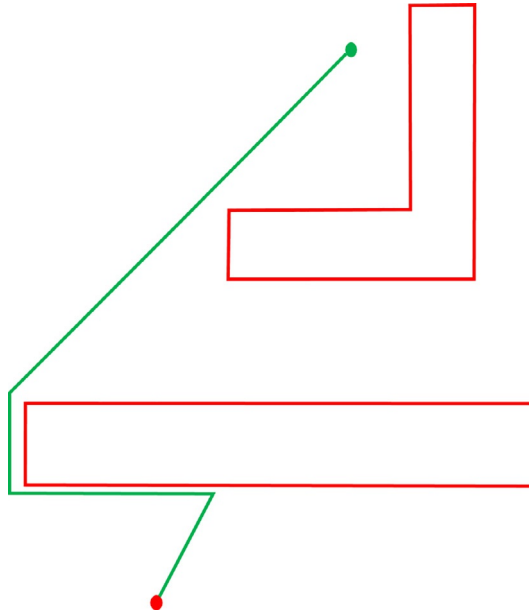

Fig. 10.4 Path planning using Bug2.

crucial role in this algorithm. The weaknesses of this method are that the vehicle remains for too long near the obstacles and that the path it suggests is far from the shortest path [9].

Bug2 behaves similarly to Bug1 except that it follows a fixed-line from start to end. In this algorithm, the vehicle moves on the line connecting the start point and the target. If it encounters an obstacle, it swerves past it until it reaches a point on the line joining the start point and the target, at which point it leaves the obstacle. In this method, too, the vehicle spends a long time moving alongside the obstacles, although this time is usually shorter than that in the previous algorithm. Fig. 10.4 displays the Bug2 algorithm [9].

Among other Bug algorithms that use a minimal number of sensors are TangentBug [10], DistBug [11], and VisBug [12]. The Tangent Bug algorithm is an upgraded version of Bug2 and is capable of determining a shorter path to reach the target using an environment recognition sensor with an infinite 360-degree resolution. The DistBug algorithm has guaranteed convergence if a path exists. Moreover, it needs to understand the position of the vehicle, the position of the target, and data from the environment recognition sensors. The VisBug algorithm requires comprehensive information to

Table 10.1 Characteristics of various path planning algorithms.

No.	Path planning algorithm	Required memory	Required processing	Special advantages and disadvantages
1	Uniform discretization	Large	Average	Simplicity of implementation
2	Quadtree discretization	Average	Large	More uniform path and large computations in case of moving obstacles
3	Triangular discretization	Small	Average	Good distance from obstacles
4	Trapezoidal discretization	Small	Average	Good distance from obstacles
5	Voronoi algorithm	Average	Large	Largest distance from obstacles
6	Visibility graph	Average	Average	Shortest path
7	Bug1	Very small	Small	High implementation simplicity and attachment to obstacles
8	Bug2	Very small	Small	High implementation simplicity and attachment to obstacles
9	Gradient field	Large	Large	Sticking to local points
10	Vector field histogram	Average	Large	Suitable for path planning using sonar output

update the minimum distance to the target point while pursuing the boundary and for determining the end of a loop during convergence toward the target. In all the path planning algorithms presented, the vehicle is modeled as a point in space without any motion constraints. Furthermore, the actual vehicle kinematics, which are especially important for nonholonomic vehicles, are ignored.

The Voronoi and the visibility graph algorithms are two other methods of finding the optimal path in which the graph consists of various short paths and, in effect, a sequence of paths is searched. Path planning can also be performed using gradient field methods.

In summary, the general characteristics of path planning algorithms are presented in Table 10.1.

10.3 Trajectory generation

Trajectory generation or reference time path is the addition of time data to the path, resulting in the determination of the set point for the motion actuators based on the path determined by the path planning algorithm. In space

discretization methods, the trajectory is specified via the coordinates of the connection points. The method of reaching these points and some parameters, such as vehicle speed, at these points, are not considered in selecting these points. In other words, there are no time requirements for vehicles at the connection points in this method. In trajectory generation, the vehicles must move continuously along this path, meaning that the motion characteristics of the vehicles such as direction, velocity, and acceleration must be specified between any two given points and on the points themselves.

In mathematical terms, the trajectory generation problem is equivalent to specifying a function $p(t)$ where t is time and $p(t)$ is the position of the vehicle. Given the determined connection points, $p_i = p(t_i)$, where p_i is the position of a given connection point, and t_i is the time when the vehicle is expected to be at that point. This function must be determined under physical constraints (such as the motion of the vehicle) such that the vehicle can follow these positions at times obtained from this function.

The most important variables in the trajectory are the velocity of the vehicle, including the forward speed of the vehicle, the yaw rate, and the vehicle acceleration. These explanations reveal that the trajectory generation problem is the transformation of data at the connection point coordinates to the velocity and acceleration of the vehicle. Trajectories are divided into two major groups: one-dimensional and multidimensional. Generally, the difference in these two groups lies in the fact that a trajectory is one-dimensional if a scalar function defines it, and it is multidimensional if a vector function defines it.

10.3.1 Trajectory generation methods

Numerous methods have been presented for trajectory generation in research conducted so far. Nevertheless, these methods belong to one of the following base groups:

1. Polynomial trajectory
   - **a.** Linear (constant velocity)
   - **b.** Parabolic (constant acceleration)
   - **c.** Trajectory with constant asymmetric acceleration
   - **d.** Cubic
   - **e.** Higher-degree polynomials
2. Trigonometric trajectory
   - **f.** Harmonic
   - **g.** Arch
   - **h.** Elliptical

3. Exponential trajectory
4. Fourier expansion-based trajectory

Most complex trajectories can be generated via a suitable combination of these base functions considering appropriate velocity, acceleration, and jerk constraints. Using a sigmoid motion path based on polynomials is the most common among these methods [13].

10.3.1.1 Cubic polynomial trajectory

In the cubic polynomial trajectory method, a cubic function is considered as the trajectory. In other words, $q(t) = a_0 + a_1 t + a_2 t^2 + a_3 t^3$, where the four constraints of the problem can be satisfied by setting the parameters a_0 to a_3. Two of the constraints are satisfied by $p_i = p(t_i)$ at two connection points and the two other constraints are satisfied by the current and final velocities of the vehicles, namely $\dot{q}(t_f)$ and $\dot{q}(t_s)$, which are obtained by differentiating the above relationship.

The drawback of this method is that the acceleration of the vehicle at the end of the trajectory cannot be considered a specific value. On the other hand, the acceleration at the beginning of the trajectory has a specific value (obtained from the previous path), and a sudden change in acceleration indicates the exertion of a large force. Fig. 10.5 displays a sample trajectory computed via cubic polynomials.

10.3.1.2 High-degree polynomials

High-degree polynomials are used in special applications for a more accurate match. They utilize constraints such as boundary conditions on the velocity, acceleration, jerk, snap, and even higher-degree derivatives along with the conditions at the intermediate points. An nth-degree polynomial, in its vertical form, is expressed as follows:

$$q_N(\tau) = a_0 + a_1 t + a_2 t^2 + a_3 t^3 + \cdots + a_n t^n$$

Assuming unit displacement, $h = q_1\text{-}q_0 = 1$, and duration of $T = t_1 - t_0 = 1$ ($t_0 = 0$ is considered for simplicity).

To calculate the parameters a_i, the following equation is used:

$$Ma = b$$

where $a = [a_0, a_1, a_2, a_3, \ldots, a_n]^T$ and the vector b, which consists of boundary conditions on position, velocity, acceleration, jerk, and even higher-order derivatives, is in the form

$$b = [q_0, V_0, a_0, j_0, \ldots, q_1, V_1, a_1, j_1, \ldots]^T.$$

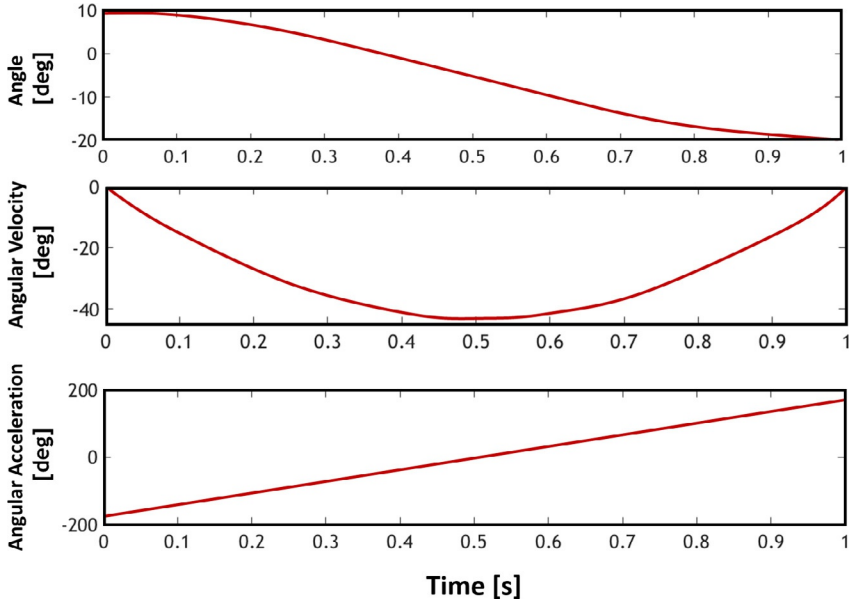

Fig. 10.5 Cubic polynomial trajectory [13].

The initial and final values of velocity, acceleration, jerk, snap, etc., $(V_{Nj}, a_{Nj}, \ldots, j = 1, 0)$ are obtained as $\frac{q_i^{(k)}}{h/T^k} = q_{Nj}^{(k)}$ by normalizing based on the boundary conditions $(V_j, a_j, \ldots)$. This relationship is used everywhere except the start and endpoints, where the values are considered to be zero and one, respectively. The normalized boundary conditions V_{Nj}, a_{Nj}, … are considered as V_0, V_1, a_0, a_1, …, in order to simplify the calculations.

In the end, the matrix M is easily obtained by applying the following boundary conditions to the relationship (q_N).

1. $a_0 = 0$, polynomial at the start point $(q_N(0) = 0)$.
2. $a_1 = V_0$, $a_2 = a_0$, $a_3 = j_0$, …, initial conditions on the velocity, acceleration, etc.; there are n_{ci} initial conditions on the derivatives of $q_N(t)$.
3. $\sum_{i=0}^{n} a_i = 1$: polynomial at the endpoint $(q_N(1) = 1)$.
4. $\sum_{i=1}^{n} i a_i = V_1$: *end condition on velocity*.
5. $\sum_{i=2}^{n} i(i-1) a_i = a_1$: *end condition on acceleration*.
6. $\sum_{i=3}^{n} i(i-1)(i-2) a_i = j_1$: *end condition on jerk*.
7. $\sum_{i=d}^{n} \frac{i!}{(i-d)!} a_i = c_{d1}$: end condition on the dth derivative of $q_N(t)$ (with n_{cf} end conditions).

$q_N(\tau)$ is a polynomial of degree n with $n + 1$ a_i coefficients; hence, the matrix M has $(n + 1) \times (n + 1)$ dimensions, where $n + 1 = 2 + n_{cf} + n_{ci}$.

The parameters a are computed from $a = M^{-1}b$ [13]. The following provides an example of a 9th-degree polynomial for a tractor semitrailer.

10.3.2 Derivation of $\eta^4 - splines$ optimal path for a tractor semitrailer

$\eta^k - splines$ are polynomial curves dependent on the vector η with an order of $2k + 1$. One needs $2k$ members of the vector η to derive these curves. An important feature of these curves is the interdependence between the lower-degree and higher-degree curves, as expressed by the following mathematical relationship [14]:

$$\eta^k - paths \subset \eta^{k+1} - paths \quad \text{for all } k \in N \tag{10.1}$$

This feature can explain the preference of higher degrees over lower degrees. Higher-degree curves have the properties of lower-degree curves, and the increase in the degree of a curve may have an advantage or a disadvantage. For example, $\eta^2 - spline$ can estimate well circular curves or second-degree functions [15, 16], whereas $\eta^3 - spline$, which has the properties of a lower-degree curve, can provide a better estimate only for cubic spirals [17–19].

Given the dynamic configuration of tractor semitrailers, the problem of creating an efficient and flexible method for automatically moving the vehicle from initial conditions to the final desired configuration, which is discussed here as an open-loop control problem, is significant considering the following two conditions: 1. The control signals must be smooth (for example, the velocity and the steering angle and their derivatives are continuous functions). 2. The autonomous vehicle must follow a freely drawn Cartesian path via selecting and changing parameters with specific geometric meanings. This research uses $\eta^4 - spline$, which contains the properties of lower-degree curves, for path planning in forwarding parking maneuvers, where a steep path planning speed is required while the articulated vehicle is moving [20].

$\eta^4 - spline$ is a 9th-degree polynomial curve in which the curvature and the first and second derivatives of curvature are determined via the interpolation of Cartesian points provided as the start and endpoints of the path. Order 4 in the parameter η stems from the concept of fourth-order geometric continuity (G4) [21].

10.4 Smooth open-loop control of a tractor semitrailer

A tractor semitrailer with on-axle hitching (the trailer is connected to the tractor at the center of the rear axle) has been considered, as shown in Fig. 10.6.

In Fig. 10.6, the vehicle has been considered within a Cartesian coordinate. The variables (x_1, y_1) are the coordinates of the middle of the trailer axle. The angles θ_0 and θ_1 respectively represent the directions of the tractor and the trailer to the x-axis. d_0 denotes the distance between the front and rear axles of the tractor, and d_1 indicates the distance between the trailer axle and the hitching location on the tractor axle. Maneuvers are performed via the motion of the tractor with velocity v of the rear wheels and the steering angle δ of the front wheels. The common assumptions for articulated vehicles are that the tractor and the trailer are assumed to be rigid bodies, and the

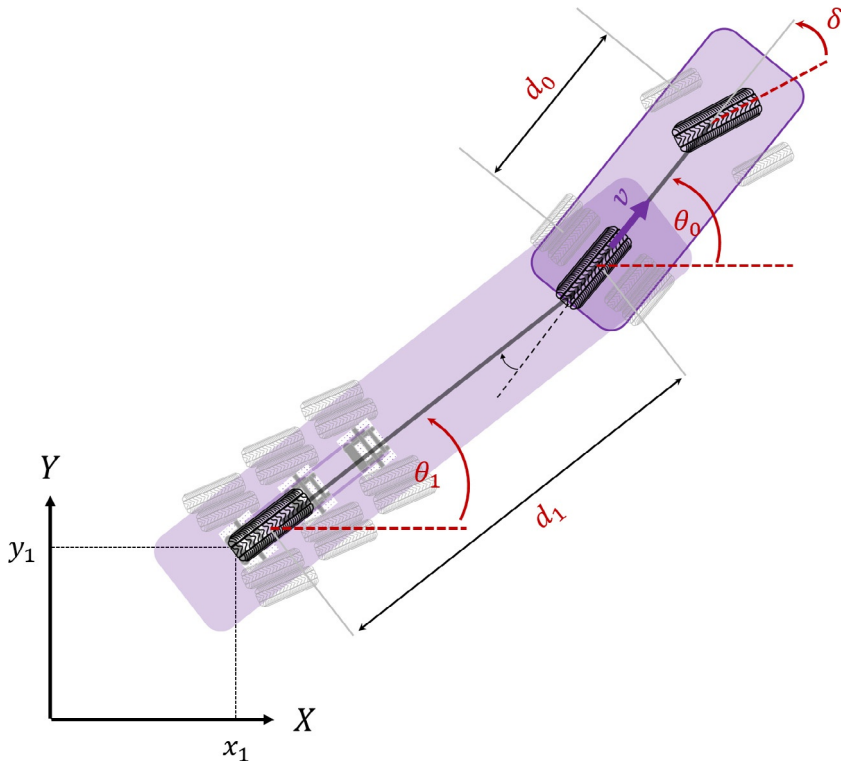

Fig. 10.6 Tractor semitrailer schematic.

rotation of the wheels is assumed to be without slipping. Hence, the nonholonomic model of this articulated vehicle is according to Eq. (10.2):

$$\begin{cases} \dot{x}_1 = v\cos(\theta_0 - \theta_1)\cos\theta_1 \\ \dot{y}_1 = v\cos(\theta_0 - \theta_1)\sin\theta_1 \\ \dot{\theta}_0 = \dfrac{v}{d_0}\delta \\ \dot{\theta}_1 = \dfrac{v}{d_1}\sin(\theta_0 - \theta_1) \end{cases} \tag{10.2}$$

Given the above relationship, the configuration of the articulated vehicle is determined by the inputs and their derivatives, as shown in Eq. (10.3).

$$\left(x_1, y_1, \theta_0, \theta_1, v, \dot{v}, \delta, \dot{\delta}\right) \tag{10.3}$$

On the other hand, according to the definition of geometric continuity, a curve is geometrically continuous of order k if the $k-2$ derivative of curvature to length is parametrically continuous. Therefore, for the curve to be geometrically continuous of order 4, the second-order derivative must be parametrically continuous along the curve. Thus, the path planning problem for an articulated vehicle with the fourth-order geometric continuity must be specified for the start and end points up to the second derivative of curvature (Fig. 10.7).

The relationships governing the unit slope vector, curvature, and first and second derivatives of curvature are presented in Eqs. (10.4), (10.5), (10.6), and (10.7), respectively.

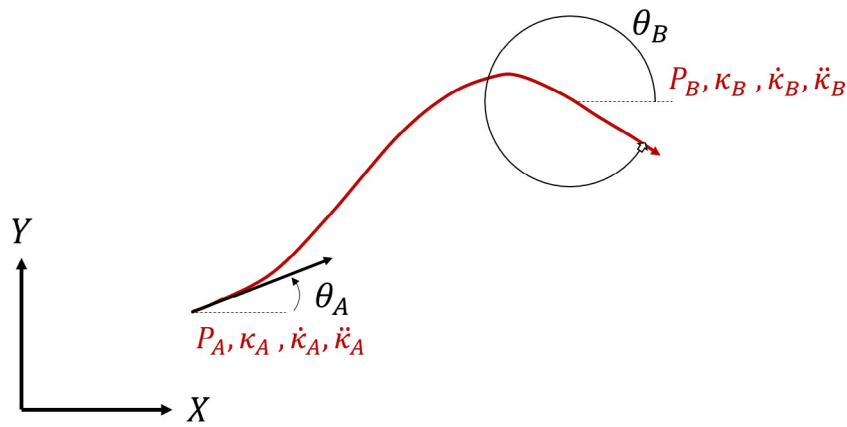

Fig. 10.7 G4 polynomial interpolation problem.

$$\tau(t)=\frac{\left[\dot{x}_1(t)\dot{y}_1(t)\right]^T}{\sqrt{\dot{x}_1^2(t)+\dot{y}_1^2(t)}}=\operatorname{sgn}(v(t))\begin{bmatrix}\cos\theta_1(t)\\ \sin\theta_1(t)\end{bmatrix}. \tag{10.4}$$

$$\kappa=\frac{d\theta_1}{ds}=\frac{d\theta_1}{dt}\frac{1}{\frac{ds}{dt}}=\dot{\theta}_1\frac{1}{\left(\dot{x}_1^2+\dot{y}_1^2\right)^{\frac{1}{2}}}=\frac{v}{d_1}\sin(\theta_0-\theta_1)\frac{1}{|v|\cos(\theta_0-\theta_1)}$$
$$=\operatorname{sgn}(v)\frac{1}{d_1}\tan(\theta_0-\theta_1). \tag{10.5}$$

$$\frac{d\kappa}{ds}=\frac{\frac{1}{d_0}\tan\delta-\frac{1}{d_1}\sin(\theta_0-\theta_1)}{d_1\cos^3(\theta_0-\theta_1)} \tag{10.6}$$

$$\frac{d^2\kappa}{ds^2}=\frac{\dot{\delta}}{|v|d_0d_1\cos^2\delta\cos^4(\theta_0-\theta_1)}-\operatorname{sgn}(v)\frac{\frac{1}{d_0}\tan\delta-\frac{1}{d_1}\sin(\theta_0-\theta_1)}{d_1^2\cos^3(\theta_0-\theta_1)}$$
$$+\operatorname{sgn}(v)\frac{3\left(\frac{1}{d_0}\tan\delta-\frac{1}{d_1}\sin(\theta_0-\theta_1)\right)^2\sin(\theta_0-\theta_1)}{d_1\cos^5(\theta_0-\theta_1)} \tag{10.7}$$

As mentioned in the beginning, a temporary solution for the problem of interpolating the trajectory of an articulated vehicle via smooth open-loop control involves using the $P(u)=[\alpha(u)\ \beta(u)]^T$, $u\in[0,1]$ curve as a 9th-degree polynomial, where $\alpha(u)$ and $\beta(u)$ are defined as follows:

$$\alpha(v)=\sum_{i=0}^{9}\alpha_iu^i,\quad \beta(u)=\sum_{i=0}^{9}\beta_iu^i \tag{10.8}$$

The coefficients α_i, β_i, $i=0,\ldots,9$, are determined based on the above interpolation problem. On the other hand, the relationships governing the unit slope vector, curvature, and first and second derivatives of curvature can be rewritten in parametric form based on α and β, as shown respectively in Eqs. (10.9), (10.10), (10.11), and (10.12):

$$\tau(u)=\frac{\left[\dot{\alpha}\dot{\beta}\right]^T}{\left(\dot{\alpha}^2+\dot{\beta}^2\right)^{\frac{1}{2}}} \tag{10.9}$$

$$k(u)=\frac{\dot{\alpha}\ddot{\beta}-\ddot{\alpha}\dot{\beta}}{\left(\dot{\alpha}^2+\dot{\beta}^2\right)^{\frac{3}{2}}} \tag{10.10}$$

$$\frac{d\kappa(u)}{ds}=\frac{\left(\dot{\alpha}\dddot{\beta}-\dddot{\alpha}\dot{\beta}\right)\left(\dot{\alpha}^2+\dot{\beta}^2\right)-3\left(\dot{\alpha}\ddot{\beta}-\ddot{\alpha}\dot{\beta}\right)\left(\ddot{\alpha}\dot{\alpha}+\ddot{\beta}\dot{\beta}\right)}{\left(\dot{\alpha}^2+\dot{\beta}^2\right)^{\frac{5}{2}}} \tag{10.11}$$

$$\begin{aligned}\frac{d^2k}{ds^2}(u)=&\left[\left(\dot{\alpha}\dddot{\beta}-\dddot{\alpha}\dot{\beta}+\ddot{\alpha}\ddot{\beta}-\ddot{\alpha}\ddot{\beta}\right)\left(\dot{\alpha}^2+\dot{\beta}^2\right)^2\right.\\&-7\left(\dot{\alpha}\dddot{\beta}-\dddot{\alpha}\dot{\beta}\right)\left(\dot{\alpha}\ddot{\alpha}+\dot{\beta}\ddot{\beta}\right)\left(\dot{\alpha}^2+\dot{\beta}^2\right)\\&-3\left(\dot{\alpha}\ddot{\beta}-\ddot{\alpha}\dot{\beta}\right)\left(\ddot{\alpha}^2+\ddot{\beta}^2+\dot{\alpha}\dddot{\alpha}+\dot{\beta}\dddot{\beta}\right)\left(\dot{\alpha}^2+\dot{\beta}^2\right)\\&\left.+18\left(\dot{\alpha}\ddot{\beta}-\ddot{\alpha}\dot{\beta}\right)\left(\dot{\alpha}\ddot{\beta}-\dot{\alpha}\ddot{\alpha}+\dot{\beta}\ddot{\beta}\right)^2\right]\frac{1}{\left(\dot{\alpha}^2+\dot{\beta}^2\right)^{\frac{9}{2}}}\end{aligned} \tag{10.12}$$

By applying the fourth-order geometric continuity interpolation conditions on the endpoints $P(u)$, Eqs. (10.13)–(10.22) below are obtained:

$$P(0)=P_A \tag{10.13}$$

$$P(1)=P_B \tag{10.14}$$

$$\dot{P}(0)=\eta_1\begin{bmatrix}\cos\theta_A\\ \sin\theta_A\end{bmatrix} \tag{10.15}$$

$$\dot{P}(1)=\eta_2\begin{bmatrix}\cos\theta_B\\ \sin\theta_B\end{bmatrix} \tag{10.16}$$

$$k(0)=k_A \tag{10.17}$$

$$k(1)=k_B \tag{10.18}$$

$$\frac{dk}{ds}(0)=\dot{k}_A \tag{10.19}$$

$$\frac{dk}{ds}(1)=\dot{k}_B \tag{10.20}$$

$$\frac{d^2k}{ds^2}(0)=\ddot{k}_A \tag{10.21}$$

$$\frac{d^2k}{ds^2}(1)=\ddot{k}_B \tag{10.22}$$

Given the relationship for $P(u)$, 20 instances of α_i and β_i must be determined; however, there are only 14 scalar equations in Eqs. (10.13)–(10.22), derived from the nonlinear algebraic system. Consequently, a measure must be taken to solve the additional 6 degrees of freedom. To solve this issue, the

parameters $\eta_3, \ldots, \eta_8$ for the remaining 6 degrees of freedom are determined as follows:

$$\left\langle \ddot{P}(0), \begin{bmatrix} \cos\theta_A \\ \sin\theta_A \end{bmatrix} \right\rangle = \eta_3 \tag{10.23}$$

$$\left\langle \ddot{P}(1), \begin{bmatrix} \cos\theta_B \\ \sin\theta_B \end{bmatrix} \right\rangle = \eta_4 \tag{10.24}$$

$$\left\langle \dddot{P}(0), \begin{bmatrix} \cos\theta_A \\ \sin\theta_A \end{bmatrix} \right\rangle = \eta_5 \tag{10.25}$$

$$\left\langle \dddot{P}(1), \begin{bmatrix} \cos\theta_B \\ \sin\theta_B \end{bmatrix} \right\rangle = \eta_6 \tag{10.26}$$

$$\left\langle \dddot{P}(0), \begin{bmatrix} \cos\theta_A \\ \sin\theta_A \end{bmatrix} \right\rangle = \eta_7 \tag{10.27}$$

$$\left\langle \dddot{P}(1), \begin{bmatrix} \cos\theta_B \\ \sin\theta_B \end{bmatrix} \right\rangle = \eta_8 \tag{10.28}$$

In this way, an algebraic system consisting of 20 equations and 20 unknowns is formed, including α_i, β_i, $i = 0, \ldots, 9$, which depend on the parameters η, such that $\eta_1, \eta_2 \in R_+$ and R, $\eta_3, \ldots, \eta_8 \in R$. As such, all the unknowns of the problem can be determined.

The following will discuss the calculation of the unknowns α_i, β_i, $i = 0, \ldots, 9$ using the parameters η.

and

$$\overset{\text{Eqs.(10.13),(10.15)}}{\Rightarrow} \begin{cases} \alpha_0 = x_A, \beta_0 = y_A \\ , \\ \alpha_1 = \eta_1 \cos\theta_A, \beta_1 = \eta_1 \sin\theta_A \end{cases} \tag{10.29}$$

$$\overset{\text{Eq.(10.14)}}{\Rightarrow} \left\{ \alpha(1) = \sum_{i=0}^{9} \alpha_i = x_B, \beta(1) = \sum_{i=0}^{9} \beta_i = y_B \right. \tag{10.30}$$

$$\overset{\text{Eq.(10.16)}}{\Rightarrow} \begin{cases} \dot{\alpha}(1) = \sum_{i=1}^{9} i\alpha_i = \eta_2 \cos\theta_B \\ , \\ \dot{\beta}(1) = \sum_{i=1}^{9} i\beta_i = \eta_2 \sin\theta_B \end{cases} \tag{10.31}$$

Using Eqs. (10.10) and (10.17) and by obtaining α_1 and β_1 from Eq. (10.29), Eq. (10.32) is obtained as follows:

$$-2\eta_1 \sin\theta_A \alpha_2 + 2\eta_1 \cos\theta_A \beta_2 = \eta_1^3 k_A \tag{10.32}$$

$$\overset{\text{Eq.(10.23)}}{\Rightarrow} \quad \{2\cos\theta_A \alpha_2 + 2\sin\theta_A \beta_2 = \eta_3 \tag{10.33}$$

By simultaneously solving Eqs. (10.32) and (10.33), α_2 and β_2 are obtained in the form of Eqs. (10.34) and (10.35):

$$\alpha_2 = \frac{1}{2}\eta_3 \cos\theta_A - \frac{1}{2}\eta_1^2 k_A \sin\theta_A \tag{10.34}$$

$$\beta_2 = \frac{1}{2}\eta_3 \sin\theta_A + \frac{1}{2}\eta_1^2 k_A \cos\theta_A \tag{10.35}$$

On the other hand:

$$\begin{aligned}\overset{\text{Eqs.(10.11), (10.19)}}{\Rightarrow} \quad & \{(6\alpha_1\beta_3 - 6\beta_1\alpha_3)\eta_1^2 - 12(\alpha_1\beta_2 - \alpha_2\beta_1)(\alpha_1\alpha_2 + \beta_1\beta_2) \\ & = \eta_1^6 \dot{k} A. \end{aligned} \tag{10.36}$$

and

$$\overset{\text{Eq.(10.25)}}{\Rightarrow} \quad \{6\cos\theta_A \alpha_3 + 6\sin\theta_A \beta_3 = \eta_5 \tag{10.37}$$

By simultaneously solving Eqs. (10.36) and (10.37), α_3 and β_3 are obtained in the form of Eqs. (10.38) and (10.39):

$$\alpha_3 = -\left(\frac{1}{2}\eta_1\eta_3 k_A + \frac{1}{6}\eta_1^3 \dot{k}_A\right)\sin\theta_A + \frac{1}{6}\eta_5 \sin\theta_A \tag{10.38}$$

$$\beta_3 = \left(\frac{1}{2}\eta_1\eta_3 k_A + \frac{1}{6}\eta_1^3 \dot{k}_A\right)\cos\theta_A + \frac{1}{6}\eta_5 \sin\theta_A \tag{10.39}$$

Similarly, Eq. (10.40) is obtained from Eqs. (10.12) and (10.21), and Eq. (10.41) is derived from Eq. (10.27):

$$\begin{aligned}& 12(2\alpha_1\beta_4 - 2\alpha_4\beta_1 + \alpha_2\beta_3 - \alpha_3\beta_2)\eta_1^4 - 84(\alpha_1\beta_3 - \alpha_3\beta_1)(\alpha_1\alpha_2 + \beta_1\beta_2)\eta_1^2 \\ & - 12(\alpha_1\beta_2 - \alpha_2\beta_1)\left(2\alpha_2^2 + 2\beta_2^2 + 3\alpha_1\alpha_3 + 3\beta_1\beta_3\right)\eta_1^2 + 144(\alpha_1\beta_2 - \alpha_2\beta_1)(\alpha_1\alpha_1 + \beta_1\beta_2)^2 \\ & = \eta_1^9 \ddot{k}_A \end{aligned} \tag{10.40}$$

$$24\cos\theta_A \alpha_4 + 24\sin\theta_A \beta_4 = \eta_7 \tag{10.41}$$

By substituting Eqs. (10.29), (10.34), (10.35), (10.38), and (10.39) into Eqs. (10.40) and (10.41), the parameters α_4 and β_4 are obtained in the form of Eqs. (10.42) and (10.43):

$$\alpha_4 = -\left(\frac{1}{6}\eta_1\eta_5 k_A + \frac{1}{4}\eta_1^2\eta_3\dot{k}_A + \frac{1}{8}\eta_1^4 k_A^3 + \frac{1}{24}\eta_1^4\ddot{k}_A + \frac{1}{8}\eta_3^2 k_A\right)\sin\theta_A + \frac{1}{24}\eta_7\cos\theta_A \tag{10.42}$$

$$\beta_4 = \left(\frac{1}{6}\eta_1\eta_5 k_A + \frac{1}{4}\eta_1^2\eta_3\dot{k}_A + \frac{1}{8}\eta_1^4 k_A^3 + \frac{1}{24}\eta_1^4\ddot{k}_A + \frac{1}{8}\eta_3^2 k_A\right)\cos\theta_A + \frac{1}{24}\eta_7\sin\theta_A \tag{10.43}$$

Eq. (10.44) below is obtained by substituting Eq. (10.31) in Eq. (10.18), and Eq. (10.45) is derived from Eq. (10.45).

$$\eta_2\cos\theta_B\ddot{\beta}(1) - \eta_2\sin\theta_B\ddot{\alpha}(1) = \eta_2^3 k_B \tag{10.44}$$

$$\cos\theta_B\ddot{\alpha}(1) - \sin\theta_B\ddot{\beta}(1) = \eta_4 \tag{10.45}$$

Solving Eqs. (10.44) and (10.45) leads to Eqs. (10.46) and (10.47):

$$\ddot{\alpha}(1) = \eta_4\cos\theta_B - \eta_2^2 k_B\sin\theta_B \tag{10.46}$$

$$\ddot{\beta}(1) = \eta_4\sin\theta_B + \eta_2^2 k_B\cos\theta_B \tag{10.47}$$

Eq. (10.48) below is obtained by substituting Eqs. (10.46), (10.47), and (10.31) in Eq. (10.20), and Eq. (10.49) is derived from Eq. (10.26).

$$\eta_2^3\cos\theta_B\dddot{\beta}(1) - \eta_2^3\sin\theta_B\dddot{\alpha}(1) = \eta_2^6\dot{k}_B + 3\eta_2^4 k_B \tag{10.48}$$

$$\cos\theta_B\dddot{\alpha}(1) + \sin\theta_B\dddot{\beta}(1) = \eta_6 \tag{10.49}$$

By using Eqs. (10.48) and (10.49), $\dddot{\alpha}(1)$ and $\dddot{\beta}(1)$ are determined in the forms of Eqs. (10.50) and (10.51), respectively:

$$\dddot{\alpha}(1) = \eta_6\cos\theta_B - \left(\eta_2^3\dot{k}_B + 3\eta_2\eta_4 k_B\right)\sin\theta_B \tag{10.50}$$

$$\dddot{\beta}(1) = \eta_6\sin\theta_B + \left(\eta_2^3\dot{k}_B + 3\eta_2\eta_4 k_B\right)\cos\theta_B \tag{10.51}$$

Eq. (10.52) is obtained by substituting Eqs. (10.46), (10.47), (10.31), (10.50), and (10.51) in Eq. (10.22), and Eq. (10.53) is derived from Eq. (10.28).

$$-\sin\theta_B\ddot{\alpha}(1) + \cos\theta_B\ddot{\beta}(1) = \eta_2^4\ddot{k}_B + 3\eta_2^4 k_B^3 + 3\eta_4^2 k_B + 4\eta_2\eta_6 k_B + 6\eta_2^2\eta_4\dot{k}_B \tag{10.52}$$

$$\cos\theta_B\ddot{\alpha}(1) + \sin\theta_B\dddot{\beta}(1) = \eta_8 \tag{10.53}$$

Similar to before, the following results from the linear equations (10.52) and (10.53):

$$\ddot{\alpha}(1)=\eta_8\cos\theta_B-\left(3\eta_4^2k_B+3\eta_2^4k_B^3+4\eta_2\eta_6k_B+6\eta_2^2\eta_4\dot{k}_B+\eta_2^4\ddot{k}_B\right)\sin\theta_B \quad (10.54)$$

$$\dddot{\beta}(1)=\eta_8\sin\theta_B+\left(3\eta_4^2k_B+3\eta_2^4k_B^3+4\eta_2\eta_6k_B+6\cos\theta_B\eta_4\dot{k}_B+\eta_2^4\ddot{k}_B\right)\cos\theta_B \quad (10.55)$$

Using $\alpha(1)$, $\dot{\alpha}(1)$, $\ddot{\alpha}(1)$, $\dddot{\alpha}(1)$, and $\ddot{\dddot{\alpha}}(1)$, which are specified in Eqs. (10.30), (10.31), (10.46), (10.50), and (10.54), respectively, one can form a linear system of equations with five equations and five unknowns, from which α_5, α_6, α_7, α_8, and α_9 can be determined.

$$\begin{cases}\alpha(1)=\sum_{i=0}^{9}\alpha_i=x_B\rightarrow\alpha_5+\alpha_6+\alpha_7+\alpha_8+\alpha_9=x_B-\alpha_0-\alpha_1-\alpha_2-\alpha_3-\alpha_4\\ \dot{\alpha}(1)=(31)\rightarrow5\alpha_5+6\alpha_6+7\alpha_7+8\alpha_8+9\alpha_9=\eta_2\cos\theta_B-\alpha_1-2\alpha_2-3\alpha_3-4\alpha_4\\ \ddot{\alpha}(1)=(46)\rightarrow20\alpha_5+30\alpha_6+42\alpha_7+56\alpha_8+72\alpha_9=\eta_2\cos\theta_B\\ \qquad-\eta_2^2k_B\sin\theta_B-2\alpha_2-6\alpha_3-12\alpha_4\\ \alpha\ldots(1)=(50)\rightarrow60\alpha_5+120\alpha_6+210\alpha_7+336\alpha_8+504\alpha_9=\eta_6\cos\theta_B\\ \qquad-\left(\eta_2^3\dot{k}_B+3\eta_2\eta_4k_B\right)\sin\theta_B-6\alpha_3-24\alpha_4\\ \dddot{\alpha}(1)=(54)\rightarrow12\alpha_5+360\alpha_6+840\alpha_7+168\alpha_8+3024\alpha_9=\eta_8\cos\theta_B\\ \qquad-\left(3\eta_4^2k_B+3\eta_2^4k_B^3+4\eta_2\eta_6k_B+6\eta_2^4\eta_4\dot{k}_B\right)\sin\theta_B-24\alpha_4.\end{cases} \quad (10.56)$$

Similarly, a linear system of equations with five equations and five unknowns is formed to determine β_5, β_6, β_7, β_8, and β_9, whereby these parameters can be written in the form of Eq. (10.57):

$$\begin{cases}\beta(1)=\sum_{i=0}^{9}\beta_i=\gamma_B\rightarrow\beta_5+\beta_6+\beta_7+\beta_8+\beta_9=\gamma_B-\beta_0-\beta_1-\beta_2-\beta_3-\beta_4\\ \dot{\beta}(1)=(31)\rightarrow5\beta_5+6\beta_6+7\beta_7+8\beta_8+9\beta_9=\eta_2\sin\theta_B-\beta_1-2\beta_2-3\beta_3-4\beta_4\\ \ddot{\beta}(1)=(46)\rightarrow20\beta_5+30\beta_6+42\beta_7+56\beta_8+72\beta_9=\eta_4\sin\theta_B+\eta_2^2k_B\cos\theta_B\\ \qquad-2\beta_2-6\beta_3-12\beta_4\\ \beta\ldots(1)=(51)\rightarrow60\beta_5+120\beta_6+210\beta_7+336\beta_8+504\beta_9=\eta_6\sin\theta_B\\ \qquad+\left(\eta_2^3\dot{k}_B+3\eta_2\eta_4k_B\right)\cos\theta_B-6\beta_3-24\beta_4\\ \dddot{\beta}(1)=(55)\rightarrow12\beta_5+360\beta_6+840\beta_7+168\beta_8+3024\beta_9=\eta_8\sin\theta_B\\ \qquad+\left(3\eta_4^2k_B+3\eta_2^4k_B^3+4\eta_2\eta_6k_B+6\eta_2^2\eta_4\dot{k}_B+\eta_2^4\ddot{k}_B\right)\cos\theta_B-24\beta_4.\end{cases} \quad (10.57)$$

The values of α_i and β_i and the relevant code are presented in Appendix.

The following presents a sample path planned for a tractor semitrailer in an environment without obstacles using the η^4 polynomial method. The reference point in the tractor semitrailer is the middle point of the axle, and the

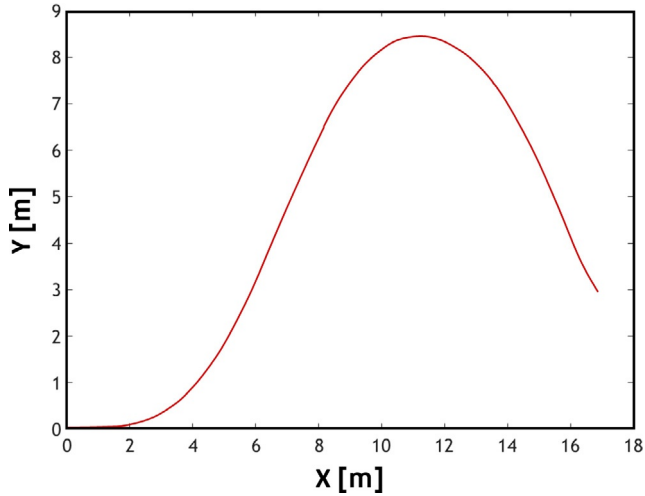

Fig. 10.8 Path planning based on $\eta^4 - spline$ for a tractor semitrailer.

path shown in the figure below corresponds to this point. The maneuver was performed from the start point PA to the endpoint PB.

$$\mathrm{P_A} = [18\,3]^{\mathrm{T}} \overset{\text{parameters}}{\Rightarrow} \left\{ \begin{array}{c} \theta_A = \frac{3}{4}\pi \\ k_A = 0.25\,m^{-1} \\ \dot{k}_A = 0.1882\,m^{-2} \\ \ddot{k}_A = free \end{array} \right\}$$

and

$$\mathrm{P_B} = [0\,0]^{\mathrm{T}} \overset{\text{parameters}}{\Rightarrow} \left\{ \begin{array}{c} \theta_B = \pi \\ k_B = 0\,m^{-1} \\ \dot{k}_B = 0\,m^{-2} \\ \ddot{k}_B = free \end{array} \right\}$$

Fig. 10.8 displays the path planned for the tractor semitrailer based on the $\eta^4 - spline$ method.

10.5 Trajectory generation for tractor semitrailers performing a lane change

Assume a tractor semitrailer is moving along a highway when the intelligent drowsiness detector system recognizes the sleepiness of the driver. As a

result, the system issues warnings to alert the driver. However, the driver's level of sleepiness is beyond the possibility of the driver regaining consciousness. At this moment, the automatic navigation springs into action and takes control of the articulated vehicle. This system is responsible for navigating the vehicle to a parking space along the path and stopping it when a collision with the front vehicle is inevitable. The vehicle must change the paths, as shown in Fig. 10.9. This is done by receiving data from sensors while the front vehicle may change speed and direction at any moment.

Fig. 10.10 displays in a flowchart the procedure followed by the automatic navigation system and the strategy considered for the tractor semitrailer during maneuvering.

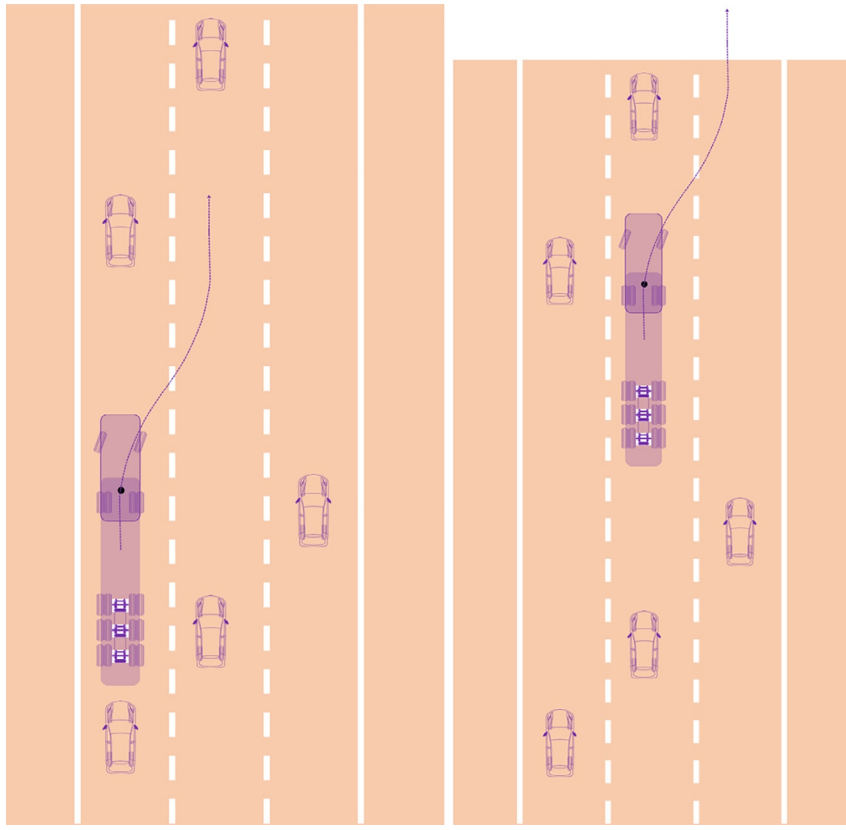

Fig. 10.9 Navigation of the vehicle to the right-side lane in the presence of mobile obstacles.

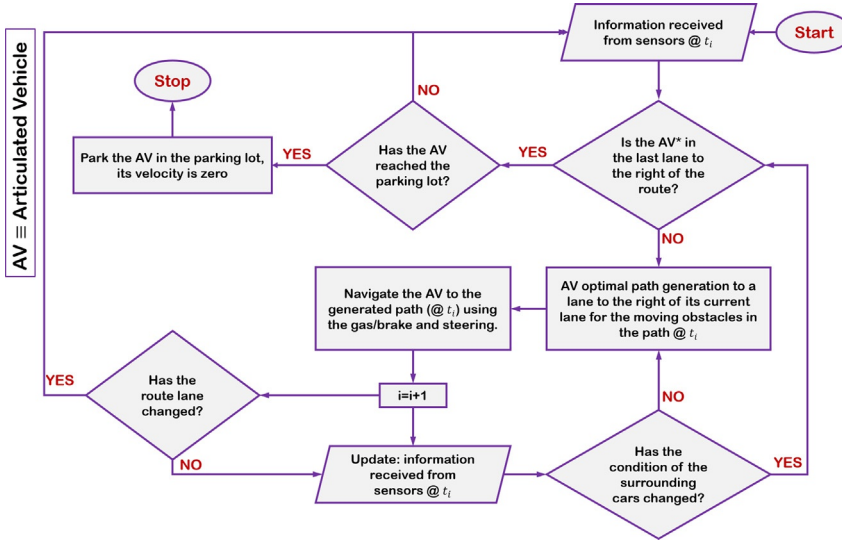

Fig. 10.10 Flowchart of the steps used in the research.

In most of the previous studies, the decision-making unit has not been designed under real dynamic conditions where the conditions of the surrounding vehicles change sometime after the start of the maneuver. Moreover, the inclusion of vehicle dynamic conditions in designing the decision-making unit has been less often considered, and trajectory planning has been performed merely for passenger cars. Hence, this section is concerned with the design of the decision-making unit for the lane-change maneuver of tractor semitrailers under real dynamic conditions using three innovations. These innovations are the extension of trajectory planning to tractor semitrailers by determining general constraints, determining the minimum time for a two-piece vehicle to perform the maneuver under real dynamic conditions (changing conditions of the surrounding vehicles during the maneuver), and the derivation of an equation for the minimum time for the lane-change maneuver of a tractor semitrailer based on the off-line dynamic method. Furthermore, single and double lane-change maneuvers are examined to validate the proposed method. The process is structured as follows:

10.5.1 Trajectory equation

A 5th-degree polynomial is the most common and lowest-degree polynomial that can satisfy the minimum requirements of a lane-change trajectory due to being simple and satisfying the continuity of position, velocity, and acceleration. It is assumed in this research that the longitudinal velocity of the vehicle is constant throughout the lane-change maneuver, and, hence, the longitudinal acceleration is ignored.

The equation for a 5th-degree polynomial can be determined by specifying six boundary conditions on the position, velocity, and acceleration of the start and endpoints, as shown in Eq. (10.58).

$$y(t) = y_0 + a_1 t + a_2 t^2 + a_3 t^3 + a_4 t^4 + a_5 t^5 \tag{10.58}$$

In Eq. (10.58), the vehicle's lateral position and velocity are zero at the start and end of the maneuver. Given the assumption of constant longitudinal velocity during the lane-change maneuver, the lateral acceleration at the beginning and end of the maneuver is zero. The above assumptions are expressed in Eq. (10.59).

$$\begin{cases} y(0) = 0 \\ \dot{y}(0) = 0 \\ \ddot{y}(0) = 0 \end{cases} \quad \begin{cases} y(t_m) = -H \\ \dot{y}(t_m) = 0 \\ \ddot{y}(t_m) = 0 \end{cases} \tag{10.59}$$

Where t_m denotes the maneuver duration and H represents the maximum lateral displacement during the lane-change maneuver.

The coordinate axes X, Y, and Z point toward the direction of the road, normal to the direction of the road and outward to the road curve, and normal to the road surface and upward, respectively. By applying the boundary conditions (10.59) to (10.58), the final trajectory equation results in the form of Eq. (10.60).

$$y(t) = \left(-\frac{6H}{{t_m}^5}\right) t^5 + \left(\frac{15H}{{t_m}^4}\right) t^4 + \left(\frac{-10H}{{t_m}^3}\right) t^3 \tag{10.60}$$

This equation is used as the main lane-change equation for determining the time constraints and extracting the safe path for the tractor semitrailer [22].

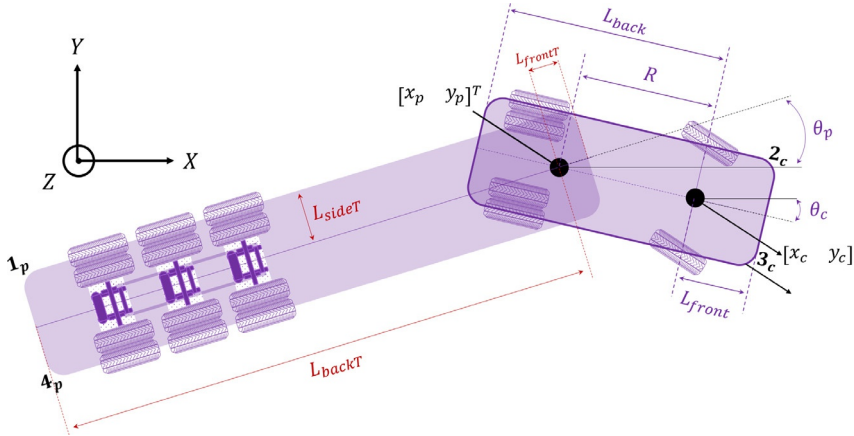

Fig. 10.11 Characteristics of a tractor semitrailer.

10.5.2 Derivation of the kinematic characteristics of the tractor semitrailer

Given that various points of the articulated vehicle are required in the equations henceforth, this vehicle is introduced in Fig. 10.11.

The coordinates, the longitudinal and lateral velocities, and the lateral acceleration of the mass center of the tractor (x_c, y_c) are presented in Eqs. (10.61)–(10.65), respectively, and the longitudinal velocity of the tractor ($\overline{V}_{xc}$) is assumed to be constant during the maneuver. Eq. (10.66) represents the angle between the tractor axis and the X axis of the reference frame.

$$x_c(t) = \overline{V}_{xc}t + x_{0c} \tag{10.61}$$

$$y_c(t) = \left(\frac{-6H}{t_m^5}\right)t^5 + \left(\frac{15H}{t_m^4}\right)t^4 + \left(\frac{-10H}{t_m^3}\right)t^3 + y_{0c} \tag{10.62}$$

$$\dot{x}_c(t) = \overline{V}_{xc} \tag{10.63}$$

$$\dot{y}_c = \left(\frac{-30H}{t_m^5}\right)t^4 + \left(\frac{60H}{t_m^4}\right)t^3 + \left(\frac{-30H}{t_m^3}\right)t^2 \tag{10.64}$$

$$\ddot{y}_c = \left(\frac{-120H}{t_m^5}\right)t^3 + \left(\frac{180H}{t_m^4}\right)t^2 + \left(\frac{-60H}{t_m^3}\right)t \tag{10.65}$$

$$\theta_c = \arctan\left(\frac{\dot{y}_c}{\dot{x}_c}\right) \tag{10.66}$$

In the following, the coordinates of the tractor corners are presented in Eqs. (10.67)–(10.70) in the form used in the equations. Moreover, the surrounding vehicles are named as shown in Eqs. (10.67)–(10.70), as mentioned in the following.

$$\begin{Bmatrix} x_{1_c} \\ y_{1_c} \end{Bmatrix} \simeq \begin{Bmatrix} -L_{back} \\ +L_{side} \end{Bmatrix} \rightarrow \begin{cases} x_{1_c} = -L_{back}(\cos\theta_c) - L_{side}(\sin\theta_c) + x_c \\ y_{1_c} = -L_{back}(\sin\theta_c) + L_{side}(\cos\theta_c) + y_c \end{cases} \tag{10.67}$$

$$\begin{Bmatrix} x_{2_c} \\ y_{2_c} \end{Bmatrix} \simeq \begin{Bmatrix} L_{front} \\ L_{side} \end{Bmatrix} \rightarrow \begin{cases} x_{2_c} = L_{front}(\cos\theta_c) - L_{side}(\sin\theta_c) + x_c \\ y_{2_c} = L_{front}(\sin\theta_c) + L_{side}(\cos\theta_c) + y_c \end{cases} \tag{10.68}$$

$$\begin{Bmatrix} x_{3_c} \\ y_{3_c} \end{Bmatrix} \simeq \begin{Bmatrix} L_{front} \\ -L_{side} \end{Bmatrix} \rightarrow \begin{cases} x_{3_c} = L_{front}(\cos\theta_c) + L_{side}(\sin\theta_c) + x_c \\ y_{3_c} = -L_{front}(\sin\theta_c) - L_{side}(\cos\theta_c) + y_c \end{cases} \tag{10.69}$$

$$\begin{Bmatrix} x_{4_c} \\ y_{4_c} \end{Bmatrix} \simeq \begin{Bmatrix} -L_{back} \\ -L_{side} \end{Bmatrix} \rightarrow \begin{cases} x_{4_c} = -L_{back}(\cos\theta_c) + L_{side}(\sin\theta_c) + x_c \\ y_{4_c} = -L_{back}(\sin\theta_c) - L_{side}(\cos\theta_c) + y_c \end{cases} \tag{10.70}$$

Because the edges of the tractor semitrailer are curved, the sign $\simeq$ is used instead of $=$ in Eqs. (10.67)–(10.70). According to Fig. 10.11, the joint between the tractor and the semitrailer (x_p, y_p) is apart from the local coordinates of the tractor, the center of which coincides with the mass center of the tractor, by -R in the x-direction. The coordinates of the joint in the reference frame are presented in Eq. (10.71).

$$\begin{Bmatrix} x_p \\ y_p \end{Bmatrix} \simeq \begin{Bmatrix} -R \\ 0 \end{Bmatrix} \rightarrow \begin{cases} x_p = -R(\cos\theta_c) + x_c \\ y_p = -R(\sin\theta_c) + y_c \end{cases} \tag{10.71}$$

By substituting Eqs. (10.61), (10.62), and (10.66) into Eqs. (10.72) and (10.73) and by using Eqs. (10.84) and (10.85), the longitudinal and lateral velocities of the joint connecting the tractor and the semitrailer (x_p, y_p) are calculated as follows, assuming constant velocity.

$$x_p = \overline{V}_{xc}t + x_0 - R\cos\theta_c \tag{10.72}$$

$$y_p = \left(\frac{-6H}{{t_m}^5}\right)t^5 + \left(\frac{15H}{{t_m}^4}\right)t^4 + \left(\frac{-10H}{{t_m}^3}\right)t^3 - R\sin\theta_c + y_0 \tag{10.73}$$

$$g(t)=\frac{\dot{y}_c}{\dot{x}_c} \tag{10.74}$$

$$\cos\left(\arctan\left(g(t)\right)\right)=\frac{1}{\sqrt{1+g(t)^2}}=f_1(g(t)) \tag{10.75}$$

$$\sin\left(\arctan\left(g(t)\right)\right)=\frac{g(t)}{\sqrt{1+g(t)^2}}=f_2(g(t)) \tag{10.76}$$

$$\begin{aligned}\dot{f}_1(g(t))&=\dot{f}(g(t))\cdot\dot{g}(t)=\frac{-g(t)}{\left(1+g(t)^2\right)^{\frac{3}{2}}}\times\dot{g}(t)\\&=\frac{-g(t)}{\left(1+g(t)^2\right)^{\frac{3}{2}}}\times\left(\frac{\ddot{y}_c\dot{x}_c}{\dot{x}_c^2}-\frac{\ddot{x}_c\dot{y}_c}{\dot{x}_c^2}\right)=\frac{-g(t)\cdot\ddot{y}_c}{\dot{x}_c\left(1+g(t)^2\right)^{\frac{3}{2}}}\end{aligned} \tag{10.77}$$

$$\begin{aligned}\dot{f}_2(g(t))&=\dot{f}_2(g(t))\cdot\dot{g}(t)=\frac{+1}{\left(1+g(t)^2\right)^{\frac{3}{2}}}\times\dot{g}(t)\\&=\frac{1}{\left(1+g(t)^2\right)^{\frac{3}{2}}}\times\left(\frac{\ddot{y}_c\dot{x}_c}{\dot{x}_c^2}-\frac{\ddot{x}_c\dot{y}_c}{\dot{x}_c^2}\right)=\frac{+\ddot{y}_c}{\dot{x}_c\left(1+g(t)^2\right)^{\frac{3}{2}}}\end{aligned} \tag{10.78}$$

$$\dot{x}_p=\overline{V}_{xc}+\frac{R\left(\frac{\dot{y}_c}{\dot{x}_c}\right)\ddot{y}_c}{\dot{x}_c\left(1+\left(\frac{\dot{y}_c}{\dot{x}_c}\right)^2\right)^{\frac{3}{2}}} \tag{10.79}$$

$$\dot{y}_p=\left(\frac{-30H}{{t_m}^5}\right)t^4+\left(\frac{60H}{{t_m}^4}\right)t^3+\left(\frac{30H}{{t_m}^3}\right)t^2-R\frac{\ddot{y}_c}{\dot{x}_c\left(1+\left(\frac{\dot{y}_c}{\dot{x}_c}\right)^2\right)^{\frac{3}{2}}} \tag{10.80}$$

$$\theta_p=\arctan\left(\frac{\dot{y}_p}{\dot{x}_p}\right) \tag{10.81}$$

$$\cos\theta_p=\frac{1}{\sqrt{1+\left(\frac{\dot{y}_p}{\dot{x}_p}\right)^2}} \tag{10.82}$$

$$\sin\theta_p=\frac{\left(\frac{\dot{y}_c}{\dot{x}_c}\right)}{\sqrt{1+\left(\frac{\dot{y}_c}{\dot{x}_c}\right)^2}} \tag{10.83}$$

$$\dot{x}_p = \overline{V}_{xc} + \frac{R\left(\frac{\dot{y}_c}{\dot{x}_c}\right)\ddot{y}_c}{\dot{x}_c\left(1+\left(\frac{\dot{y}_c}{\dot{x}_c}\right)^2\right)^{\frac{3}{2}}} \tag{10.84}$$

$$\dot{y}_p = \left(\frac{-30H}{{t_m}^5}\right)t^4 + \left(\frac{60H}{{t_m}^4}\right)t^3 + \left(\frac{30H}{{t_m}^3}\right)t^2 - R\frac{\ddot{y}_c}{\dot{x}_c\left(1+\left(\frac{\dot{y}_c}{\dot{x}_c}\right)^2\right)^{\frac{3}{2}}} \tag{10.85}$$

After computing the longitudinal and lateral velocities of the joint between the tractor and the semitrailer $(\dot{x}_p, \dot{y}_p)$, one can compute the angle between the semitrailer axis and the X axis in the form of Eq. (10.86).

$$\theta_p = \arctan\left(\frac{\dot{y}_p}{\dot{x}_p}\right) \tag{10.86}$$

By substituting Eqs. (10.72), (10.73), and (10.81), the corner points of the semitrailer, as shown in Fig. 10.11, can be computed by Eqs. (10.87)–(10.90).

$$\begin{Bmatrix} x_{1_p} \\ y_{1_p} \end{Bmatrix} \simeq \begin{Bmatrix} -L_{backT} \\ -L_{sideT} \end{Bmatrix}$$
$$\rightarrow \begin{cases} x_{1_p} = -L_{backT}(\cos\theta_p) - L_{sideT}(\sin\theta_p) + x_p \\ y_{1_p} = -L_{backT}(\sin\theta_p) + L_{sideT}(\cos\theta_p) + y_p \end{cases} \tag{10.87}$$

$$\begin{Bmatrix} x_{2_p} \\ y_{2_p} \end{Bmatrix} \simeq \begin{Bmatrix} L_{frontT} \\ L_{sideT} \end{Bmatrix}$$
$$\rightarrow \begin{cases} x_{2_p} = L_{frontT}(\cos\theta_p) - L_{sideT}(\sin\theta_p) + x_p \\ y_{2_p} = L_{frontT}(\sin\theta_p) + L_{sideT}(\cos\theta_p) + y_p \end{cases} \tag{10.88}$$

$$\begin{Bmatrix} x_{3_p} \\ y_{3_p} \end{Bmatrix} \simeq \begin{Bmatrix} L_{frontT} \\ -L_{sideT} \end{Bmatrix}$$
$$\rightarrow \begin{cases} x_{3_p} = L_{frontT}(\cos\theta_p) + L_{sideT}(\sin\theta_p) + x_p \\ y_{3_p} = L_{frontT}(\sin\theta_p) - L_{sideT}(\cos\theta_p) + y_p \end{cases} \tag{10.89}$$

$$\begin{Bmatrix} x_{4_p} \\ y_{4_p} \end{Bmatrix} \simeq \begin{Bmatrix} -L_{backT} \\ -L_{sideT} \end{Bmatrix}$$
$$\rightarrow \begin{cases} x_{4_p} = -L_{backT}(\cos\theta_p) + L_{sideT}(\sin\theta_p) + x_p \\ y_{4_p} = -L_{backT}(\sin\theta_p) - L_{sideT}(\sin\theta_p) + y_p \end{cases} \tag{10.90}$$

10.5.3 Determination of time constraints

To estimate the safe interval for the lane-change maneuver by the tractor semitrailer, four main situations that can occur for the articulated vehicle during this maneuver are considered, as explained in the following. The output of each situation will be specific time t_1, t_2, t_3, or t_4. Furthermore, the decision-making algorithm of the lane-change maneuver is derived by considering the minimum maneuver time t_m.

10.5.3.1 Situation 1: The articulated vehicle and the front vehicle lie on the same line

As shown in Fig. 10.12A, to be able to consider a general safe distance for the tractor semitrailer so that the lane-change can be adjusted, c_1 must first be considered as the safe distance between point 2c of the tractor and point 4A of the front vehicle that lies on the same line as the tractor.

Three maneuvers are shown in Fig. 10.12a–c. In these maneuvers, the safe distances C_1, C_1', and C_1'' are, respectively, the safe distances between points 2c, 2p, and 1p of the tractor semitrailer and point 4A of the front vehicle. Eqs. (10.91)–(10.93) represent the equations within the longitudinal and lateral directions at the instant of coincidence between the mentioned points from the tractor semitrailer and the front vehicle.

$$\begin{cases} y_{4_A} - y_{2_C} = C_1 \\ x_{4_A} = x_{2_c} \end{cases} \tag{10.91}$$

$$\begin{cases} y_{4_A} - y_{2_p} = C_1' \\ x_{4_A} = x_{2_p} \end{cases} \tag{10.92}$$

$$\begin{cases} y_{4_A} - y_{1_p} = C_1'' \\ x_{4_A} = x_{1_p} \end{cases} \tag{10.93}$$

Numerous simulations were performed for the first situation using various velocities and initial distances, with the results indicating that C_1 must be considered as the general safe distance. The following presents the simulation results for lane-change maneuvers in situation 1 with a tractor

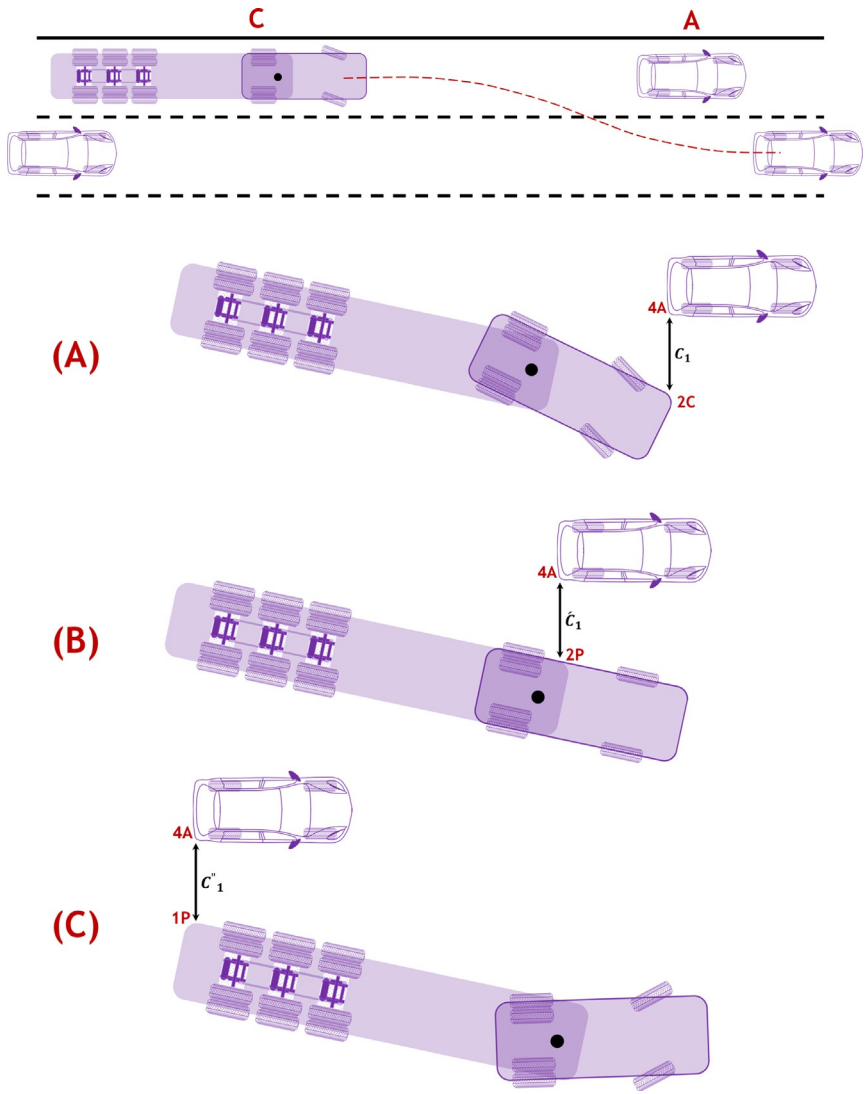

Fig. 10.12 Situation 1: The tractor semitrailer and the front vehicle lie on the same line.

semitrailer velocity of 100 km/h and an initial distance of 35 m between the tractor and the front vehicle, which moves at a velocity of 60 km/h. The maneuver duration and the alignment time between points 2c, 2p, and 1p and the point 4A for each maneuver duration have been computed and are presented in Table 10.2 for each of the safe distances C_1, C_1', and

Table 10.2 Longitudinal coincidence time of the respective point pair based on maneuver time.

Constraints with the conditions $Vcar_C = 100\,km/h$ $Vcar_A = 60\,km/h$ Distance = 35 m	Maneuver duration (T_m)	Time of 2c coinciding with 4A	Time of 2p coinciding with 4A	Time of 1p coinciding with 4A	Unit
Based on the constraint C_1	4.0814	2.8488	3.1014	3.8245	s
Based on the constraint C_1'	4.2942	2.8485	3.1009	3.8239	s
Based on the constraint C_1''	4.9459	2.8483	3.1003	3.8220	s

C_1'', according to Fig. 10.12. For instance, when the constraint C_1, the safe distance between the points 2c and 4A is considered as the general constraint, the maneuver time is obtained to be 4.0814 s, and the times for the points 2c, 2p, and 1p to reach the point 4A are obtained to be 2.8488 s, 3.1014 s, and 3.8245 s.

Table 10.3 displays the lateral distance between the points 2c, 2p, and 1p of the tractor semitrailer and point 4A of the front vehicle for the mentioned example when each of the points from the tractor semitrailer reaches point 4A along the longitudinal direction. As shown in the figure, only when the maneuver duration is considered based on the constraint C_1 are the lateral distances between points 2c, 2p, and 1p of the tractor semitrailer and point

Table 10.3 The lateral distance between points 2c, 2p, and 1p and point 4A at longitudinal coincidence times for situation 1.

Constraints	Point 2c	Point 2p	Point 1p	Unit
Lateral distance from point 4A based on the constraint C_1	1.000	1.1624	1.4983	m
Lateral distance from point 4A based on the constraint C_1'	0.8207	1.000	1.4106	m
Lateral distance from point 4A based on the constraint C_1''	0.2799	0.4774	1.000	m

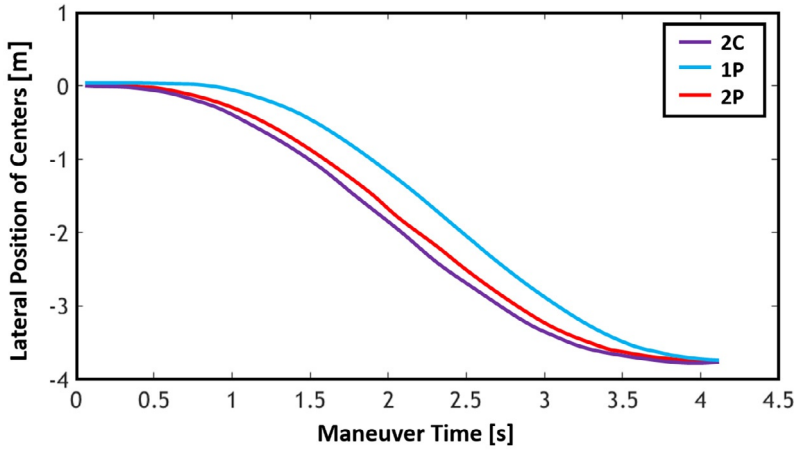

Fig. 10.13 The trajectory of the lane-change maneuver for points 2c, 2p, and 1p considering point 2c and constraint c_1.

4A of the front vehicle equal to larger than the safe lateral distance ($C_1 = 1$ m). Given that the results of all simulations for the first situation are similar, it can be concluded that point 2c of the tractor semitrailer and the constraint C_1 should be considered as the point of constraint application and the general constraint, respectively, and as the basis for path planning in situation 1.

The trajectory during the lane-change maneuver for points 2c, 2p, and 1p has been drawn in Fig. 10.13, considering point 2c of the tractor semitrailer as the constraint application point and constraint C_1 as the general constraint. The oblique line intersecting all three curves shows the locations of points 2c, 2p, and 1p at the instant they reach point 4A. It is clear that points 2p and 1p are at longer lateral distances than the safe distance C_1 at the critical moment of longitudinal coincidence with point 4A.

10.5.3.2 Situation 2: A vehicle is present on the target lane in front of the articulated vehicle

In this situation, it is assumed that the velocity of the front vehicle becomes zero due to a sudden halt [23]. Eq. (10.94) can be used to determine the safe distance C_2 as shown in Fig. 10.14d, and the maneuver duration, known as t_2 in this situation, can be determined accordingly.

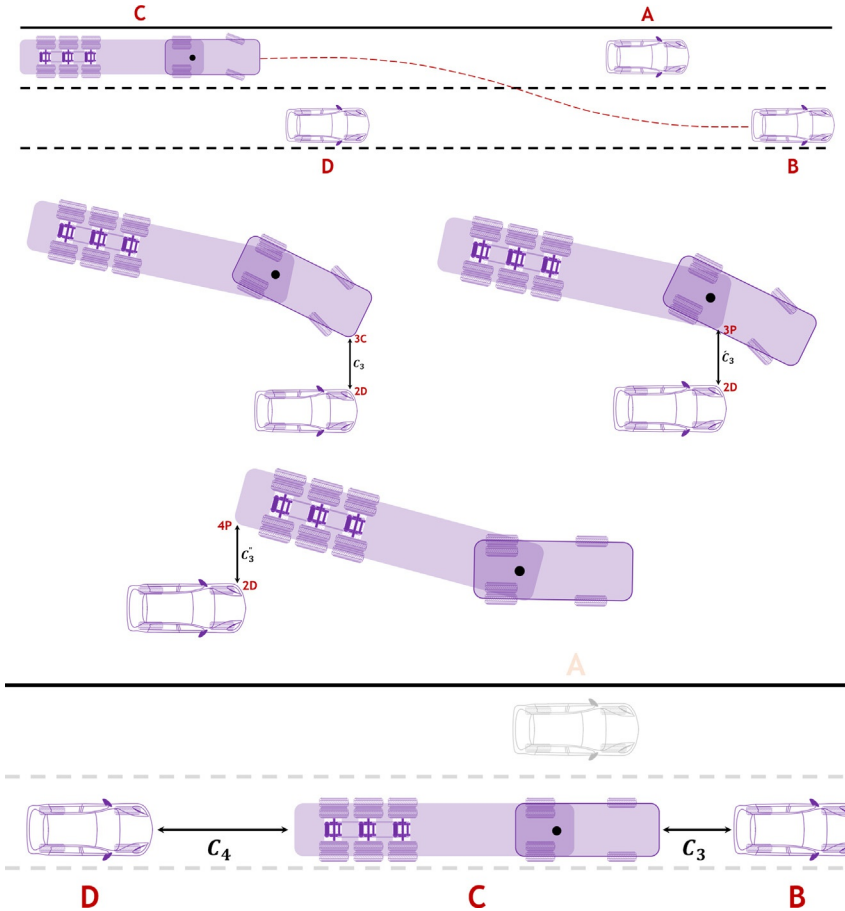

Fig. 10.14 Tractor semitrailer and the other vehicles in the second, third, and fourth situations.

$$\begin{cases} (X_B - X_C) = s_0 + v_{cx}t_d + \dfrac{{v_{cx}}^2}{2a_{cb}} + L_{back\,B} + L_{frontc} \\ y_B = y_c \\ c_2 = s_0 + v_{cx}t_d + \dfrac{{v_{cx}}^2}{2a_{cb}} \end{cases} \tag{10.94}$$

Where s_0 is the safe stopping distance, v_{cx} is the longitudinal velocity of the tractor semitrailer at the end of the maneuver, a_{cb} is the maximum braking deceleration of the tractor semitrailer, and t_d is the reaction time of the driver, which is between 0.67 s and 1.11 s [24].

Accordingly, all trajectories in which the longitudinal position of the rear end of the front vehicle is further than c_2 from the front end of the tractor semitrailer can be accepted as safe trajectories.

10.5.3.3 Situation 3: A side vehicle is on the target lane

Similar to the previous situation, a general constraint must first be defined for the tractor semitrailer performing a lane-change maneuver.

For this purpose, point 3c of the tractor and 3p and 4p of the trailer are considered with the lateral distance constraints C_3, C_3', and C_3'' relative to point 2D of the side vehicle present on the target lane, as shown in Fig. 10.14a, B, and c. The relationships are written down based on these constraints, similar to the first situation. The relevant equations are summarized in Eqs. (10.95)–(10.97).

$$\begin{cases} y_{3C} - y_{2D} = C_3 \\ x_{3_c} = x_{2D} \end{cases} \tag{10.95}$$

$$\begin{cases} y_{3_p} - y_{2D} = C_3' \\ x_{3_p} = x_{2D} \end{cases} \tag{10.96}$$

$$\begin{cases} y_{4_p} - y_{2D} = C_3'' \\ x_{4_p} = x_{2D} \end{cases} \tag{10.97}$$

Similar to the first situation, numerous simulations were performed for the third situation using various velocities and initial distances with the results indicating that C_3'' must be considered as the general safe distance. The following presents the simulation results for a lane-change maneuver in situation 1 with a tractor semitrailer velocity of 100 km/h and an initial distance of 30 m between the tractor and the side vehicle, which moves at a velocity of 35 km/h and is on the target lane, as shown in Tables 10.4 and 10.5 and Fig. 10.15. The maneuver duration and the critical longitudinal coincidence time when each of the points 3c, 3p, and 4p reach point 2D along the longitudinal direction are calculated and displayed in Table 10.4 for each of the safe distances C_3, C_3', and C_3'' according to Fig. 10.14.

The lateral distance upon longitudinal coincidence is calculated similar to situation 1 and displayed in Table 10.5. Only when the maneuver duration is considered according to the constraint C_3'' and point 4p do the lateral distances for points 3c and 3p exceed the safe lateral distance ($C_3'' = 1$ m). Hence, it can be concluded that point 4p and the constraint C_3'' should be the basis for path planning in situation 3.

Table 10.4

Constraints with the conditions: $Vcar_C = 100\,km/h$ $Vcar_D = 35\,km/h$ Distance = 30 m	Maneuver duration (Tm)	Time of 3c coinciding with 2D	Time of 3p coinciding with 2D	Time of 4p coinciding with 2D	Unit
Based on the constraint C_3	5.9841	1.6632	1.8184	2.2616	s
Based on the constraint C_3'	6.1723	1.6631	1.8182	2.2615	s
Based on the constraint C_3''	6.6412	1.6629	1.8180	2.2613	s

Table 10.5

Constraints	Point 3c	Point 3p	Point 4p	Unit
Lateral distance from point 2D based on the constraint C_3	1.000	0.9565	0.8385	m
Lateral distance from point 2D based on the constraint C_3'	1.0406	1.000	0.8904	m
Lateral distance from point 2D based on the constraint C_3''	1.1262	1.0917	1.000	m

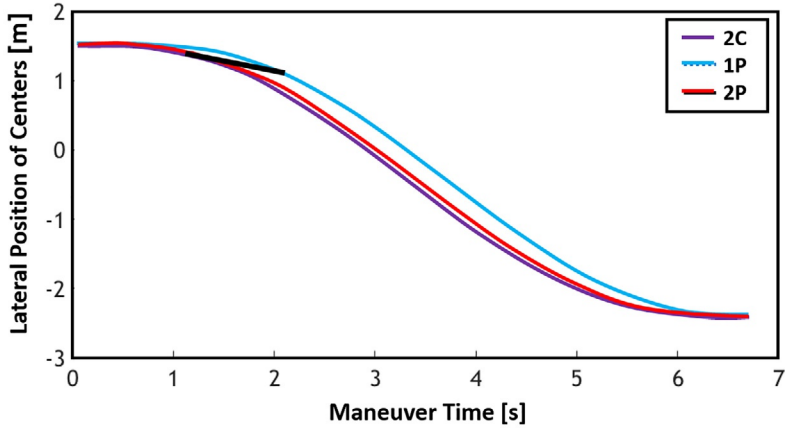

Fig. 10.15 The trajectory of the lane-change maneuver for points 2c, 3p, and 4p considering point 4P and constraint C_3''.

The trajectory during the lane-change maneuver for points 3c, 3p, and 4p has been drawn in Fig. 10.15, considering point 4P of the tractor semitrailer as the constraint application point and constraint C_3'' as the general constraint. The oblique line intersecting all three curves shows the locations of points 3c, 3p, and 4p at the instant they reach point 2D. It is clear that points 3p and 3c are at longer lateral distances than the safe distance C_3'' at the critical moment of longitudinal coincidence with point 2D.

10.5.3.4 Situation 4: Lane change of the articulated vehicle to the target lane and safe distance from the rear vehicle

This situation is displayed in Fig. 10.14d. A safe distance $C_4 = C_2$ similar to the second situation is defined, and the maneuver duration (t_4) is obtained using Eq. (10.98). It is clear that all the trajectories in which the longitudinal distance between the rear end of the trailer and the front end of the rear vehicle is larger than C_4 can be accepted as safe trajectories.

$$(X_C - X_D) = C_4 + L_{frontD} + L_{backC} + L_{trailer} \tag{10.98}$$

10.5.3.5 Situation 5: The most critical lane-change maneuver

One of the most important points that be considered in designing lane-change trajectories is the navigability of the trajectory. This means that the dynamic constraints governing the tractor semitrailer must be satisfied in addition to the kinematic constraints. To guarantee the stability of the tractor semitrailer during a lane-change maneuver, the lateral acceleration created must be attainable given the friction between the tire and the road. To this end, the duration for the most severe lane change maneuver is calculated and considered as the minimum time for any lane-change maneuver. Accordingly, the path must be planned in such a way that its navigation duration does not exceed this time.

The shortest possible lane change time $(t_m)_{min}$ depends on various factors, such as the velocity and acceleration of the vehicle, the tire material and quality, the road conditions, and some kinematic properties of the vehicle, such as its weight and the distance of its front and rear axles from its center of mass [25]. In the present work, the minimum lane change duration as a function of longitudinal velocity, weight, and friction has been studied, and a surface consisting of these three parameters has been formulated.

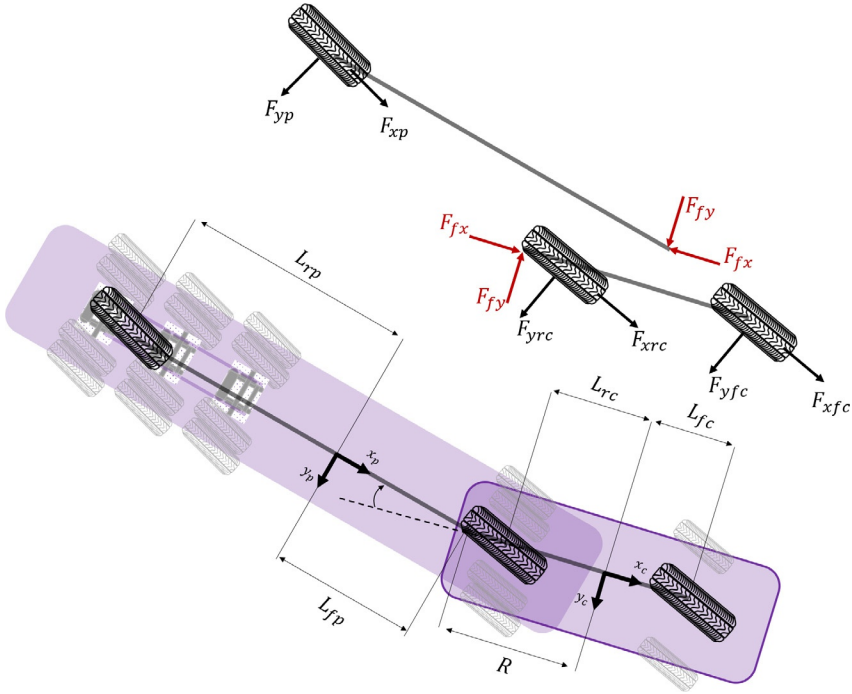

Fig. 10.16 Bicycle dynamic model of the tractor semitrailer.

10.5.4 Test method and minimum time acceptance criterion

To obtain the minimum lane change time given the dynamic constraints, a 4-DOF dynamic model including the longitudinal, lateral, and yaw motion of the tractor semitrailer and the angle between the tractor and the semitrailer is used according to the bicycle model shown in Fig. 10.16.

Eqs. (10.99) and (10.102) respectively represent the dynamic equations governing the longitudinal motion of the tractor and the trailer, Eqs. (10.100) and (10.103) represent the dynamic equations governing the lateral motion of the tractor and the trailer, and Eqs. (10.101) and (10.104) respectively represent the dynamic equation governing the rotational motion of the tractor and the trailer.

$$m_c\left(\dot{u}_c - v_c\dot{\psi}_c\right) = F_{xfc} + F_{xrc} - F_{fx} \tag{10.99}$$

$$m_c\left(\dot{v}_c + u_c\dot{\psi}_c\right) = F_{yfc} + F_{yrc} - F_{fy} \tag{10.100}$$

$$I_{zz_c}\ddot{\psi}_c = F_{fy}R + F_{yfc}L_{fc} - F_{yrc}L_{rc} \tag{10.101}$$

$$m_p\left(\dot{u}_c - v_c\dot{\psi}_c\right) = F_{xp} + F_{fx} \tag{10.102}$$

$$m_p\left(\dot{v}_c + u_c\dot{\psi}_c - \left(R + L_{fp}\right)\ddot{\psi}_c - L_{fp}\ddot{\theta}_p\right) = F_{yrp} + F_{fy} \tag{10.103}$$

$$I_{zzp}\left(\ddot{\psi}_c + \ddot{\theta}_p\right) = F_{fy}L_{fp} - F_{yrp}L_{rp} \tag{10.104}$$

10.5.5 Validation of the dynamic model

TruckSim software is used to validate the proposed dynamic model. To this end, the physical characteristics of the developed model are considered to be the same as those of the test vehicle (Table 10.6). The steering angle of the double lane change is shown in Fig. 10.17, and the validation results of double lane change maneuvers are displayed in Figs. 10.18 and 10.19.

Table 10.6 Tractor semitrailer vehicle parameters used in computer simulations.

Tractor semitrailer parameters	Value	Unit
The height of the gravity center of the tractor (semitrailer) sprung mass from the roll axis	0.438 (1.8)	m
The distance of the mass center of the tractor (semitrailer) from the ground	1.05 (1.9)	
The height of the fifth wheel from the ground	1.22	
The distance between the tractor mass center and the front axle of the tractor (the rear axle of the tractor)	1.115 m (2.583)	
The distance between the semitrailer mass center and the fifth wheel	5.653, 2.047	
The distance between the tractor mass center and the fifth wheel	1.959	
The distance between the central axle of the semitrailer and it's front (rear) axle	1.31	
The distance between the fifth wheel and the semitrailer end	9 m	
The wheel radius	0.4	
The tractor (semitrailer) width	2.04 (2)	
The yaw moment of inertia for the tractor (semitrailer) unit about the perpendicular axle passing through the gravity center of the unit	20,679 (238,898)	kgm^2
The roll moment of inertia the tractor (semitrailer) around the passing roll axle	3335 (120,024)	
The cross moment of inertia the sprung mass of the tractor (semitrailer)	602 (5756)	
The wheel moment of inertia	11.63	
The torsional stiffness of the front axle (the rear axle) suspension system of the tractor unit	380	kNm/rad
The torsional stiffness of the suspension system of the semitrailer	800	
Coupling torsional stiffness between the tractor unit and the semitrailer	30,000	
The whole mass (the sprung mass) of the tractor	6525 (4819)	kg
The whole mass (the sprung mass) of the semitrailer	33,221 (30,821)	

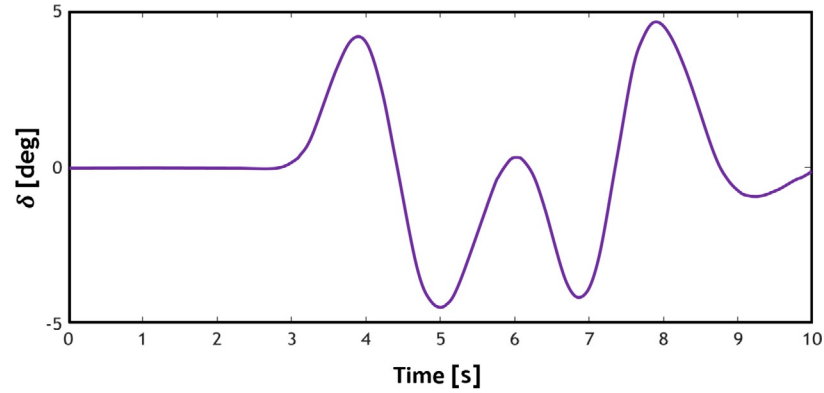

Fig. 10.17 The steering angle of the tractor semitrailer during a double lane-change maneuver.

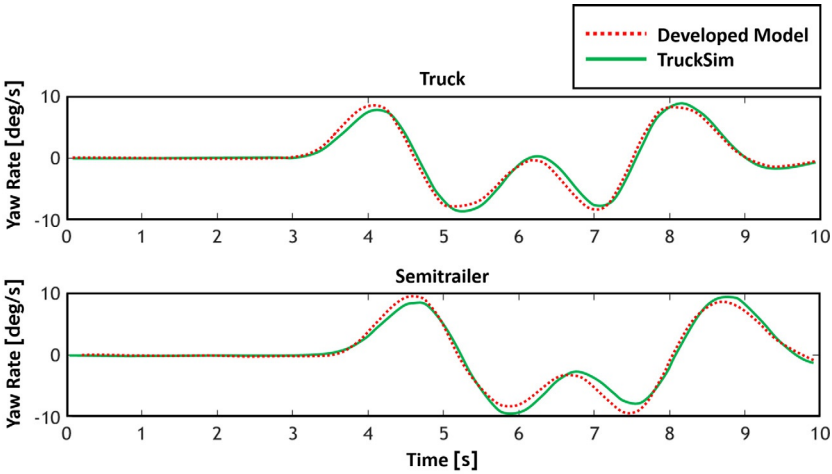

Fig. 10.18 Yaw velocity of the dynamic model and the TruckSim model of the tractor semitrailer during a double lane-change maneuver.

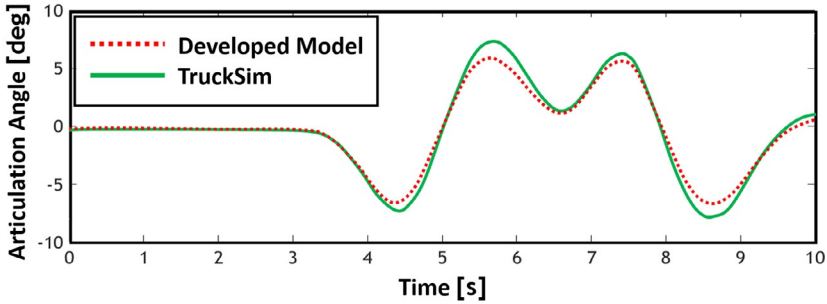

Fig. 10.19 The tractor semitrailer joint angle of the dynamic model and the TruckSim model during a double lane-change maneuver.

Fig. 10.18 shows the angular velocities of the tractor and semitrailer, respectively. As seen in the figures, the simulation results and experimental results in the TruckSim software are acceptable. Fig. 10.19 displays the joint angle during the double lane change maneuver. It can be seen that the discrepancy between the dynamics model and the TruckSim experimental results is negligible.

In the simulations, the tractor semitrailer is moving at a constant velocity along the highway. At a specific point along the path, an input, as shown in Fig. 10.20A, is applied to the steering wheel of the vehicle.

In the simulations, the 4-DOF tractor semitrailer is moving at a constant velocity along the highway. At a specific point along the path, an input, as shown in Fig. 10.20A, is applied to the steering wheel of the vehicle. Based on the lateral position of the tractor semitrailer, the maximum steering angle, denoted by θ in the figure, is determined as equivalent to lateral motion as much as the width of a single lane, that is, 3.75 m. Subsequently, the maneuver duration t_m is reduced in 0.05 s increments up to the instability threshold of the vehicle. The obtained time represents the minimum possible time for a lane change, given the surroundings and the vehicle conditions. This time

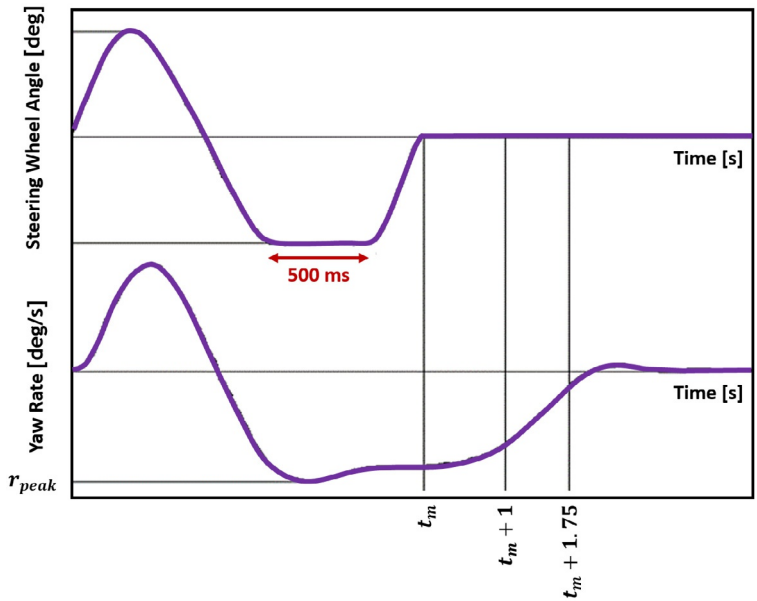

Fig. 10.20 Vehicle stability condition according to the electronic stability control (ESC) standard [26].

is recorded as $(t_m)_{min}$. This scenario has been repeated for velocities from 60 km/h up to 120 km/h with 20 km/h increments. For every specific velocity, the friction coefficient has been considered in the range of 0.1–1 between the tire and the road, varying in 0.1 increments. All the above tests have been repeated for unloaded and loaded states of the tractor semitrailer, with a total of 100 simulations. The stability of the vehicle has been examined according to the ESC standard [26, 27]. According to this standard, a given ESC system has an acceptable performance if by changing the steering wheels, as shown in Fig. 10.20A, the yaw rate does not exceed 35% and 25% of the maximum yaw rate, respectively 1 s and 1.75 s, after the end of the maneuver (Fig. 10.20B). In this figure, r_{peak} represents the maximum yaw rate during the maneuver.

Fig. 10.21 displays the results obtained for variations in the yaw rate at a constant velocity of 80 km/h separately for the tractor and the trailer. Because the variations of the yaw rate are much larger in the tractor than in the semitrailer, the tractor has been considered as the measurement criterion, according to Fig. 10.21A.

Fig. 10.22 displays the combined three-dimensional surface of the minimum maneuver duration, considering weight, vehicle velocity, and friction between the tire and the road. The surface shown in Fig. 10.22 divides the

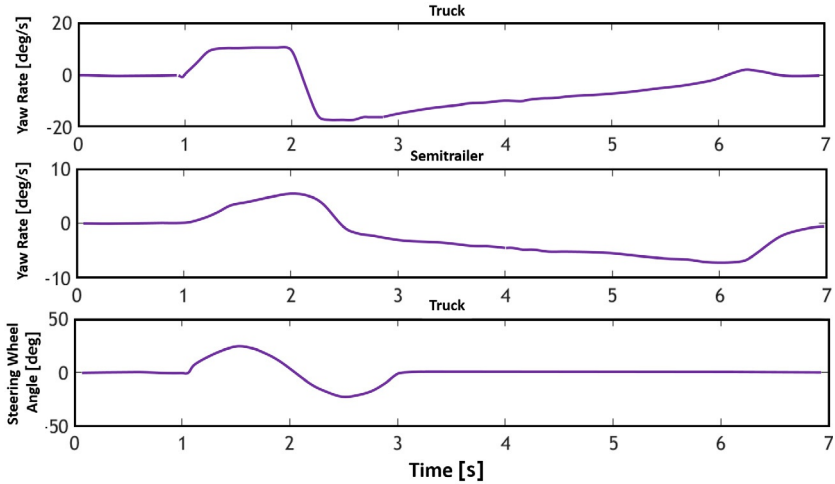

Fig. 10.21 Variations in the yaw rate in the tractor and the semitrailer for a specific steering angle.

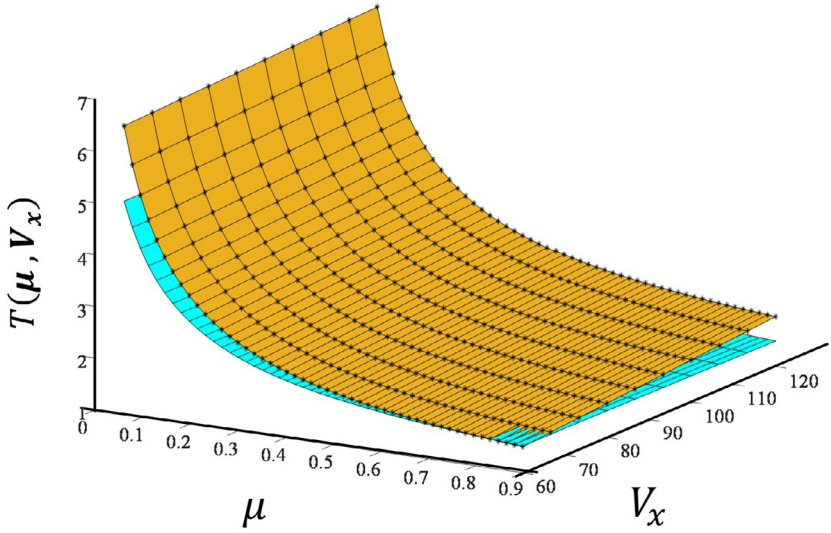

Fig. 10.22 The modified three-dimensional surface of the maneuver duration, considering weight, vehicle velocity, and friction between the tire and the road [28].

space into the points above the surface, representing the times appropriate for minimum maneuver duration, and those below the surface, representing the inappropriate times in terms of vehicle stability according to the mentioned criterion. A safety factor is considered to improve reliability. The lower surface in Fig. 10.22 is without a safety factor, and the upper surface has had a safety factor applied to it. This factor has been selected in such a way that the final surface has larger values at higher velocities and lower friction factors, where the instability of the tractor semitrailer is more probable. As such, the minimum time required for the tractor semitrailer to perform the lane change maneuver is obtained in an off-line manner considering the vehicle stability conditions. This time can be used for online simulations, which will result in a shorter computation time [28].

A reasonable estimate of this surface in the form of Eq. (10.105) has been made in MATLAB software. In this equation, the minimum time for the tractor semitrailer to perform the lane change maneuver has been expressed as a function of the road friction coefficient and the vehicle velocity.

$$T_m(\mu, V_x) = \frac{(31.42 + 12.53\mu + 0.35\mu V_x)}{(2.53 + 42.66\mu)} \tag{10.105}$$

10.6 Decision-making strategy for the lane change maneuver of the tractor semitrailer

In order to evaluate the decision-making algorithm, the times t_1 to t_4 and t_m are first calculated according to the conditions considered in the example of Fig. 10.23 and based on the values specified in Table 10.7.

By comparing the obtained times, the created state is considered equivalent to the 14th state in Table 10.8, that is, $t_2 > t_1 > t_3 > t_m > t_4$ [28].

As shown in Fig. 10.23, two lane-change maneuver trajectories based on t_1 and t_3 are drawn. The curves drawn between these two curves are the acceptable curves based on the decision-making strategy; however, Fig. 10.24 is used to obtain a more accurate trajectory in terms of comfort and safety.

As shown in Fig. 10.24C, the lateral acceleration decreases toward the trajectory obtained from t_1 (longest time) based on the determined trajectories, indicating better comfort in case this trajectory is selected. The final choice of the inappropriate path can be made based on various criteria, such as minimizing the maneuver time or providing maximum comfort, which is beyond the scope of this research.

An essential point relevant to the decision-making unit is its implementation for the tractor semitrailer vehicle and data collection and processing.

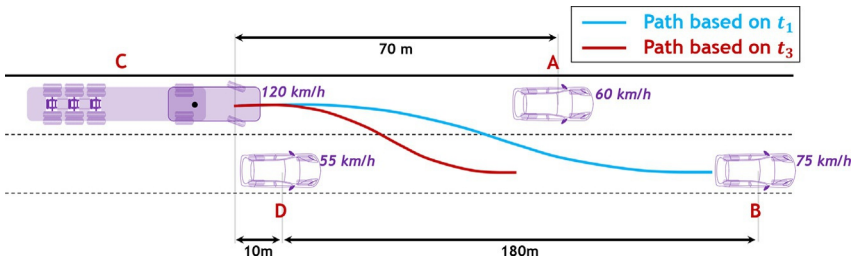

Fig. 10.23 Example of traffic conditions created based on state 14 of Table 10.8.

Table 10.7 Simulation parameters of the tractor semitrailer.

Parameter	Value	Parameter	Value
C_3	1 (m)	W_A	1.65 (m)
W_C	2.2 (m)	ab_D	9.81 μ (m/s^2)
ab_C	9.81 μ (m/s^2)	W_D	1.65 (m)
t_d	0.7 (s)	C_1	1 (m)
R	1.959 (m)	L_{front}	1.6 (m)
L_{backT}	7.5 (m)	L_{frontT}	1.115 (m)

Table 10.8 Different possible maneuver states for the tractor semitrailer and the proposed time [28].

No.	State	Acceptable time
1	$t_1 > t_2 > t_4 > t_3 > t_m$	$[t_4 \quad t_2]$
2	$t_1 > t_2 > t_4 > t_m > t_3$	$[t_4 \quad t_2]$
3	$t_1 > t_2 = t_4 > t_m > t_3$	t_4
4	$t_1 > t_2 > t_3 > t_4 > t_m$	$[t_3 \quad t_2]$
5	$t_1 > t_2 > t_3 > t_m > t_4$	$[t_3 \quad t_2]$
6	$t_1 > t_2 = t_3 > t_m > t_4$	t_3
7	$t_1 > t_2 > t_m > t_3 > t_4$	$[t_m \quad t_2]$
8	$t_1 > t_2 > t_m > t_4 > t_3$	$[t_m \quad t_2]$
9	$t_1 > t_2 = t_m > t_4 > t_3$	t_m
10	$t_2 > t_1 > t_4 > t_3 > t_m$	$[t_4 \quad t_1]$
11	$t_2 > t_1 > t_4 > t_m > t_3$	$[t_4 \quad t_1]$
12	$t_2 > t_1 = t_4 > t_m > t_3$	t_1
13	$t_2 > t_1 > t_3 > t_4 > t_m$	$[t_3 \quad t_1]$
14	$t_2 > t_1 > t_3 > t_m > t_4$	$[t_3 \quad t_1]$
15	$t_2 > t_1 = t_3 > t_m > t_4$	t_3
16	$t_2 > t_1 > t_m > t_3 > t_4$	$[t_m \quad t_1]$
17	$t_2 > t_1 > t_m > t_4 > t_3$	$[t_m \quad t_1]$
18	$t_2 > t_1 = t_m > t_4 > t_3$	t_m

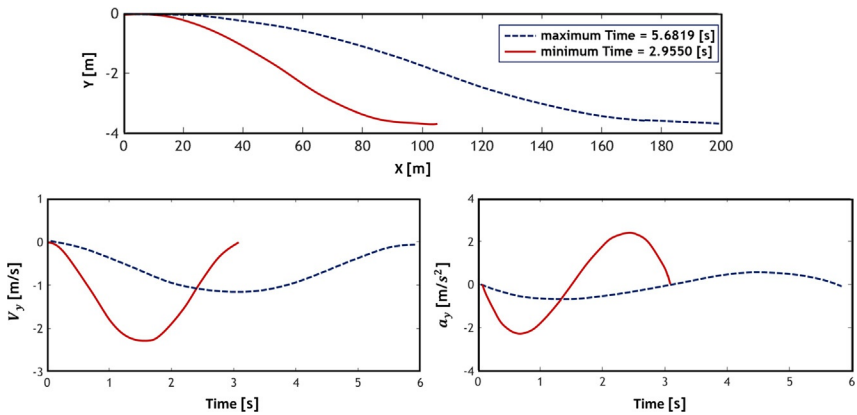

Fig. 10.24 Moving path, velocity, and lateral acceleration based on the acceptable time period.

Accordingly, three main parts are required for application and extracting the needed data. The first part is the sensors for the longitudinal and lateral acceleration, rotation, and position of the vehicle, which determine the state of the tractor semitrailer. Another part is the sensors used to determine the surrounding conditions and environmental data, including radars, ultrasonic sensors, and cameras. The final part is the actuators, and the use

of steer-by-wire is recommended in this regard. Instead of mechanically connecting the steering wheel to the vehicle wheels, this system uses steering angle and torque sensors to apply the required angle to the vehicle wheels.

10.7 Conclusion

The decision about whether to change lanes is made by comparing the times t_1, t_2, t_3, and t_4 and by considering $(t_m)_{min} = t_5$. A total of 120 possible states without considering equal times can be predicted based on the above conditions. The simulation results indicate that the time t_1, which is the time of collision of the tractor semitrailer with vehicle A (the front vehicle on the initial line), is the maximum time in this state; therefore, times shorter than this time are accepted as safe. Moreover, when vehicle B is on the target lane, time t_2 is the maximum acceptable time, and longer times are considered unsafe. When the tractor semitrailer is passing vehicle D (the side vehicle) through changing lanes from the initial lane to the target lane, any time smaller than t_3 disturbs safe conditions. Similarly, t_4 is the minimum safe time when the rear end of the semitrailer must be at a safe distance from the front end of the rear vehicle on the target lane at the end of the maneuver.

Given the simulation results, the number of these states can be considerably reduced. Therefore, once assuming the maneuver's time, between $(t_m)_{min}$ and t_1 and again between $(t_m)_{min}$ and t_2, many nonphysical states are identified and thus eliminated. After eliminating the impractical states, the acceptable time interval for different possible states of the lane-change maneuver while avoiding obstacles are presented in Table 10.8 [28].

It is important to note that the control system is prevented from performing the lane change maneuver only when the time comparison is not according to any of the states in Table 10.8. In this case, the vehicle is maintained in the current lane until the conditions for lane change are satisfied. Obviously, if any of the other vehicles are not on the path, the decision-making strategy will not change, and only the time relating to that particular vehicle is not taken into account in the computations.

In this example, the minimum time for a two-piece articulated vehicle to perform a lane change maneuver under real dynamic conditions (with changing surrounding conditions) was calculated by extending the path planning of the passenger car to tractor semitrailers. Furthermore, the equation for the minimum time for a lane change was derived using an off-line dynamic method for a tractor semitrailer. Based on the above, a decision-making unit for lane change maneuvers under real dynamic conditions was designed for tractor semitrailers using a comprehensive decision-making algorithm.

Appendix

$$\alpha_0 = x_A$$

$$\alpha_1 = \eta_1 \cos\theta_A$$

$$\alpha_2 = \frac{1}{2}\eta_3 \cos\theta_A - \frac{1}{2}\eta_1^2 k_A \sin\theta_A$$

$$\alpha_3 = -\left(\frac{1}{2}\eta_1\eta_3 k_A + \frac{1}{6}\eta_1^3 \dot{k}_A\right)\sin\theta_A + \frac{1}{6}\eta_5 \cos\theta_A$$

$$\alpha_4 = -\left(\frac{1}{6}\eta_1\eta_5 k_A + \frac{1}{4}\eta_1^2\eta_3 \dot{k}_A + \frac{1}{8}\eta_1^4 k_A^3 + \frac{1}{24}\eta_1^4 \ddot{k}_A\right)\sin\theta_A - \frac{1}{8}\eta_3^2 k_A \sin\theta_A + \frac{1}{24}\eta_7 \cos\theta_A$$

$$\begin{aligned}\alpha_5 = {} & 126(x_B - x_A) - \left(70\eta_1 + \frac{35}{2}\eta_3 + \frac{5}{2}\eta_5 + \frac{5}{24}\eta_7\right)\cos\theta_A + \left(\frac{35}{2}\eta_1^2 k_A + \frac{5}{8}\eta_1^4 k_A^3 + \frac{5}{2}\eta_1^3 \dot{k}_A + \frac{5}{24}\eta_1^4 \ddot{k}_A\right)\sin\theta_A \\ & + \left(\frac{15}{2}\eta_1\eta_3 k_A + \frac{5}{6}\eta_1\eta_5 k_A + \frac{5}{4}\eta_1^2\eta_3 \dot{k}_A + \frac{5}{8}\eta_3^2 k_A\right)\sin\theta_A - \left(56\eta_2 - \frac{21}{2}\eta_4 + \eta_6 - \frac{1}{24}\eta_8\right)\cos\theta_B \\ & - \left(\frac{21}{2}\eta_2^2 k_B + \frac{1}{8}\eta_2^4 k_B^3 - \eta_2^3 \dot{k}_B + \frac{1}{24}\eta_2^4 \ddot{k}_B\right)\sin\theta_B \\ & + \left(3\eta_2\eta_4 k_B - \frac{1}{6}\eta_2\eta_6 k_B - \frac{1}{4}\eta_2^2\eta_4 \dot{k}_A - \frac{1}{8}\eta_4^2 k_B\right)\sin\theta_B\end{aligned}$$

$$\begin{aligned}\alpha_6 = {} & 420(x_B - x_A) + \left(224\eta_1 + \frac{105}{2}\eta_3 + \frac{20}{3}\eta_5 + \frac{5}{12}\eta_7\right)\cos\theta_A \\ & - \left(\frac{105}{2}\eta_1^2 k_A + \frac{5}{4}\eta_1^4 k_A^3 + \frac{20}{3}\eta_1^3 \dot{k}_A + \frac{5}{12}\eta_1^4 \ddot{k}_A\right)\sin\theta_A \\ & - \left(\frac{105}{2}\eta_1^2 k_A + \frac{5}{4}\eta_1^4 k_B^3 + \frac{20}{3}\eta_1^3 \dot{k}_A + \frac{5}{12}\eta_1^4 \ddot{k}_A\right)\sin\theta_A \\ & - \left(20\eta_1\eta_3 k_A + \frac{5}{3}\eta_1\eta_5 k_A + \frac{5}{2}\eta_1^2\eta_3 \dot{k}_A + \frac{5}{4}\eta_3^2 k_A\right)\sin\theta_A \\ & + \left(196\eta_2 - \frac{77}{2}\eta_4 + \frac{23}{6}\eta_6 - \frac{1}{6}\eta_8\right)\cos\theta_B - \left(\frac{77}{2}\eta_2^2 k_B + \frac{1}{2}\eta_2^4 k_B^3 - \frac{23}{6}\eta_2^3 \dot{k}_B + \frac{1}{6}\eta_2^4 \ddot{k}_B\right)\sin\theta_B \\ & - \left(\frac{23}{2}\eta_2\eta_4 k_B - \frac{2}{3}\eta_2\eta_6 k_B - \eta_2^2\eta_4 \dot{k}_A - \frac{1}{2}\eta_4^2 k_B\right)\sin\theta_B\end{aligned}$$

$$\begin{aligned}\alpha_7 = {} & 540(x_B - x_A) - \left(280\eta_1 + 63\eta_3 + \frac{15}{2}\eta_5 + \frac{5}{12}\eta_7\right)\cos\theta_A + \left(63\eta_1^2 k_A + \frac{5}{4}\eta_1^4 k_A^3 + \frac{15}{2}\eta_1^3 \dot{k}_A + \frac{5}{12}\eta_1^4 \ddot{k}_A\right)\sin\theta_A \\ & + \left(\frac{45}{2}\eta_1\eta_3 k_A + \frac{5}{3}\eta_1\eta_5 k_A + \frac{5}{2}\eta_1^2\eta_3 \dot{k}_A + \frac{5}{4}\eta_3^2 k_A\right)\sin\theta_A \\ & - \left(260\eta_2 - 53\eta_4 + \frac{11}{2}\eta_6 - \frac{1}{4}\eta_8\right)\cos\theta_B - \left(53\eta_2^2 k_B + \frac{3}{5}\eta_2^4 k_B^3 - \frac{11}{2}\eta_2^3 \dot{k}_B + \frac{1}{4}\eta_2^4 \ddot{k}_B\right)\sin\theta_B \\ & - \left(\frac{23}{2}\eta_2\eta_4 k_B - \eta_2\eta_6 k_B - \frac{3}{2}\eta_2^2\eta_4 \dot{k}_A - \frac{3}{4}\eta_4^2 k_B\right)\sin\theta_B\end{aligned}$$

$$\begin{aligned}\alpha_8 = {} & 315(x_B - x_A) + \left(160\eta_1 + 35\eta_3 + 4\eta_5 + \frac{5}{24}\eta_7\right)\cos\theta_A - \left(35\eta_1^2 k_A + \frac{5}{8}\eta_1^4 k_A^3 + 4\eta_1^3 \dot{k}_A + \frac{5}{24}\eta_1^4 \ddot{k}_A\right)\sin\theta_A \\ & - \left(12\eta_1\eta_3 k_A + \frac{5}{6}\eta_1\eta_5 k_A + \frac{5}{4}\eta_1^2\eta_3 \dot{k}_A + \frac{5}{8}\eta_3^2 k_A\right)\sin\theta_A \\ & + \left(155\eta_2 - \frac{65}{2}\eta_4 + \frac{7}{2}\eta_6 - \frac{1}{6}\eta_8\right)\cos\theta_B + \left(\frac{65}{2}\eta_2^2 k_B + \frac{1}{2}\eta_2^4 k_B^3 - \frac{7}{2}\eta_2^3 \dot{k}_B + \frac{1}{6}\eta_2^4 \ddot{k}_B\right)\sin\theta_B \\ & - \left(\frac{21}{2}\eta_2\eta_4 k_B - \frac{2}{3}\eta_2\eta_6 k_B - \eta_2^2\eta_4 \dot{k}_A - \frac{1}{2}\eta_4^2 k_B\right)\sin\theta_B\end{aligned}$$

$$\alpha_9 = 70(x_B - x_A) - \left(35\eta_1 + \frac{15}{2}\eta_3 + \frac{5}{6}\eta_5 + \frac{1}{24}\eta_7\right)\cos\theta_A + \left(\frac{15}{2}\eta_1^2 k_A + \frac{1}{8}\eta_1^4 k_A^3 + \frac{5}{6}\eta_1^3 \dot{k}_A + \frac{5}{12}\eta_1^4 \ddot{k}_A\right)\sin\theta_A$$
$$+ \left(\frac{5}{2}\eta_1\eta_3 k_A + \frac{1}{6}\eta_1\eta_5 k_A + \frac{1}{4}\eta_1^2\eta_3 \dot{k}_A + \frac{1}{8}\eta_3^2 k_A\right)\sin\theta_A - \left(35\eta_2 - \frac{15}{2}\eta_4 + \frac{5}{6}\eta_6 - \frac{1}{24}\eta_8\right)\cos\theta_B$$
$$- \left(\frac{15}{2}\eta_2^2 k_B + \frac{1}{8}\eta_2^4 k_B^3 - \frac{5}{6}\eta_2^3 \dot{k}_B + \frac{1}{24}\eta_2^4 \ddot{k}_B\right)\sin\theta_B \left(\frac{5}{2}\eta_2\eta_4 k_B - \frac{1}{6}\eta_2\eta_6 k_B - \frac{1}{4}\eta_2^2\eta_4 \dot{k}_A - \frac{1}{8}\eta_4^2 k_B\right)\sin\theta_B$$

$$\beta_0 = \gamma_A$$

$$\beta_1 = \eta_1 \sin\theta_A$$

$$\beta_2 = \frac{1}{2}\eta_3 \sin\theta_A - \frac{1}{2}\eta_1^2 k_A \cos\theta_A$$

$$\beta_3 = -\left(\frac{1}{2}\eta_1\eta_3 k_A + \frac{1}{6}\eta_1^3 \dot{k}_A\right)\cos\theta_A + \frac{1}{6}\eta_5 \sin\theta_A$$

$$\beta_4 = \left(\frac{1}{6}\eta_1\eta_5 k_A + \frac{1}{4}\eta_1^2\eta_3 \dot{k}_A + \frac{1}{8}\eta_1^4 k_A^3 + \frac{1}{24}\eta_1^4 \ddot{k}_A\right)\cos\theta_A + \frac{1}{8}\eta_3^2 k_A \cos\theta_A + \frac{1}{24}\eta_7 \sin\theta_A$$

$$\beta_5 = 126(y_B - y_A) - \left(70\eta_1 + \frac{35}{3}\eta_3 + \frac{5}{2}\eta_5 + \frac{5}{24}\eta_7\right)\sin\theta_A - \left(\frac{35}{2}\eta_1^2 k_A + \frac{5}{8}\eta_1^4 k_A^3 + \frac{5}{2}\eta_1^3 \dot{k}_A + \frac{5}{24}\eta_1^5 \ddot{k}_A\right)\cos\theta_A$$
$$- \left(\frac{15}{2}\eta_1\eta_3 k_A + \frac{5}{6}\eta_1\eta_5 k_A + \frac{5}{4}\eta_1^2\eta_3 \dot{k}_A + \frac{5}{8}\eta_3^2 k_A\right)\cos\theta_A - \left(56\eta_2 - \frac{21}{2}\eta_4 + \eta_6 - \frac{1}{24}\eta_8\right)\sin\theta_B$$
$$+ \left(\frac{21}{2}\eta_2^2 k_B + \frac{1}{8}\eta_2^4 k_B^3 - \eta_2^3 \dot{k}_B + \frac{1}{24}\eta_2^4 \ddot{k}_B\right)\cos\theta_B$$
$$- \left(3\eta_2\eta_4 k_B - \frac{1}{6}\eta_2\eta_6 k_B - \frac{1}{4}\eta_2^2\eta_4 \dot{k}_B - \frac{1}{8}\eta_4^2 k_B\right)\cos\theta_B$$

$$\beta_6 = -420(y_B - y_A) + \left(224\eta_1 + \frac{105}{2}\eta_3 + \frac{20}{3}\eta_5 + \frac{5}{12}\eta_7\right)\sin\theta_A$$
$$+ \left(\frac{105}{2}\eta_1^2 k_A + \frac{5}{4}\eta_1^4 k_A^3 + \frac{20}{3}\eta_1^3 \dot{k}_A + \frac{5}{12}\eta_1^4 \ddot{k}_A\right)\cos\theta_A$$
$$+ \left(20\eta_1\eta_3 k_A + \frac{5}{3}\eta_1\eta_5 k_A + \frac{5}{2}\eta_1^2\eta_3 \dot{k}_A + \frac{5}{4}\eta_3^2 k_A\right)\cos\theta_A$$
$$+ \left(196\eta_2 - \frac{77}{2}\eta_4 + \frac{23}{6}\eta_6 - \frac{1}{6}\eta_8\right)\sin\theta_B - \left(\frac{77}{2}\eta_2^2 k_B + \frac{1}{2}\eta_2^4 k_B^3 - \frac{23}{6}\eta_2^3 \dot{k}_B + \frac{1}{6}\eta_2^4 \ddot{k}_B\right)\cos\theta_B$$
$$+ \left(\frac{23}{2}\eta_2\eta_4 k_B - \frac{2}{3}\eta_2\eta_6 k_B - \eta_2^2\eta_4 \dot{k}_4 - \frac{1}{2}\eta_4^2 k_B\right)\cos\theta_B$$

$$\beta_7 = 540(y_B - y_A) - \left(280\eta_1 + 63\eta_3 + \frac{15}{2}\eta_5 + \frac{5}{12}\eta_7\right)\sin\theta_A$$
$$- \left(63\eta_1^2 k_A + \frac{5}{4}\eta_1^4 k_A^3 + \frac{15}{2}\eta_1^3 \dot{k}_A + \frac{5}{12}\eta_1^4 \ddot{k}_A\right)\cos\theta_A$$
$$- \left(\frac{45}{2}\eta_1\eta_3 k_A + \frac{5}{3}\eta_1\eta_5 k_A + \frac{5}{2}\eta_1^2\eta_3 \dot{k}_A + \frac{5}{4}\eta_3^2 k_A\right)\cos\theta_A$$
$$- \left(260\eta_2 - 53\eta_4 + \frac{11}{2}\eta_6 - \frac{1}{4}\eta_8\right)\sin\theta_B + \left(53\eta_2^2 k_B + \frac{3}{4}\eta_2^4 k_B^3 - \frac{11}{2}\eta_2^3 \dot{k}_B + \frac{1}{4}\eta_2^4 \ddot{k}_B\right)\cos\theta_B$$
$$- \left(\frac{33}{2}\eta_2\eta_4 k_B - \eta_2\eta_6 k_B - \frac{3}{2}\eta_2^2\eta_4 \dot{k}_A - \frac{3}{4}\eta_4^2 k_B\right)\cos\theta_B$$

$$\beta_8 = -315(y_B - y_A) + \left(160\eta_1 + 35\eta_3 + 4\eta_5 + \frac{5}{24}\eta_7\right)\sin\theta_A + \left(35\eta_1^2 k_A + \frac{5}{8}\eta_1^4 k_A^3 + 4\eta_1^3 \dot{k}_A + \frac{5}{24}\eta_1^4 \ddot{k}_A\right)\cos\theta_A$$
$$+ \left(12\eta_1\eta_3 k_A + \frac{5}{6}\eta_1\eta_5 k_A + \frac{5}{4}\eta_1^2\eta_3 \dot{k}_A + \frac{5}{8}\eta_3^2 k_A\right)\cos\theta_A$$
$$+ \left(155\eta_2 - \frac{65}{2}\eta_4 + \frac{7}{2}\eta_6 - \frac{1}{6}\eta_8\right)\sin\theta_B - \left(\frac{65}{2}\eta_2^2 k_B + \frac{1}{2}\eta_2^4 k_B^3 - \frac{7}{2}\eta_2^3 \dot{k}_B + \frac{1}{6}\eta_2^4 \ddot{k}_B\right)\cos\theta_B$$
$$+ \left(\frac{21}{2}\eta_2\eta_4 k_B - \frac{2}{3}\eta_2\eta_6 k_B - \eta_2^2\eta_4 \dot{k}_A - \frac{1}{2}\eta_4^3 k_B\right)\cos\theta_B$$

$$\beta_9 = 70(y_B - y_A) - \left(35\eta_1 + \frac{15}{2}\eta_3 + \frac{5}{6}\eta_5 + \frac{1}{24}\eta_7\right)\sin\theta_A - \left(\frac{15}{2}\eta_1^2 k_A + \frac{1}{8}\eta_1^4 k_A^3 + \frac{5}{6}\eta_1^3 \dot{k}_A + \frac{5}{12}\eta_1^4 \ddot{k}_A\right)\cos\theta_A$$
$$- \left(\frac{5}{2}\eta_1\eta_3 k_A + \frac{1}{6}\eta_1\eta_5 k_A + \frac{1}{4}\eta_1^2\eta_3 \dot{k}_A + \frac{1}{8}\eta_3^2 k_A\right)\cos\theta_A - \left(35\eta_2 - \frac{15}{2}\eta_4 + \frac{5}{6}\eta_6 - \frac{1}{24}\eta_8\right)\sin\theta_B$$
$$+ \left(\frac{15}{2}\eta_2^2 k_B + \frac{1}{8}\eta_2^4 k_B^3 - \frac{5}{6}\eta_2^3 \dot{k}_B + \frac{1}{24}\eta_2^4 \ddot{k}_B\right)\cos\theta_B \quad - \left(\frac{5}{2}\eta_2\eta_4 k_B - \frac{1}{6}\eta_2\eta_6 k_B - \frac{1}{4}\eta_2^2\eta_4 \dot{k}_4 - \frac{1}{8}\eta_4^3 k_B\right)\cos\theta_B$$

References

[1] National Transportation Safety Board, Fatigue, Alcohol, Other Drugs, and Medical Factors in Fatal-to-the-Driver Heavy Truck Crashes, vol. 1, 1990. Washington, DC, (Safety Report NTSB SS–90/01).

[2] Factors That Affect Fatigue in Heavy Truck Accidents, National Transportation Safety Board, Washington, DC, 1995 (Safety Report NTSB SS–95/01).

[3] Evaluation of U.S. Department of Transportation Efforts in the 1990s to Address Operator Fatigue, National Transportation Safety Board, Washington, DC, 1999 (Safety report NTSB/SR–99/01) http://www.ntsb.gov/publictn/1999/SR9901.pdf. (Accessed 17 November 2003).

[4] N. McDonald (Ed.), The Role of Driver Fatigue in Commercial Road Transport Crashes, European Transport Safety Council, Brussels, 2001.

[5] Y. Sklyarenko, F. Schreiber, W. Schumacher, Maneuvering assistant for truck and trailer combinations with arbitrary trailer hitching, in: IEEE International Conference on Mechatronics (ICM), 2013.

[6] M.M. Michałek, Lining-up control strategies for N-trailer vehicles, J. Intell. Robot. Syst. 75 (1) (2014) 29–52.

[7] C. Keller, T. Dang, H. Fritz, A. Joos, C. Rabe, D.M. Gavrila, Active Pedestrian Safety by Automatic Braking and Evasive Steering, University of Heidelberg and Daimler R&D, Germany, 2010.

[8] T. Nayl, G. Nikolakopoulos, T. Gustafsson, Real-time bug-like dynamic path planning for an articulated vehicle, in: Informatics in Control, Automation and Robotics, Springer, 2015, pp. 201–215.

[9] J. Ng, T. Bräunl, Performance comparison of bug navigation algorithms, J. Intell. Robot. Syst. 50 (1) (2007) 73–84.

[10] I. Kamon, E. Rimon, E. Rivlin, Tangentbug: a range-sensor-based navigation algorithm, Int. J. Robot. Res. 17 (9) (1998) 934–953.

[11] I. Kamon, E. Rivlin, Sensory-based motion planning with global proofs, IEEE Trans. Robot. Autom. 13 (6) (1997) 814–822.

[12] V. Lumelsky, T. Skewis, Incorporating range sensing in the robot navigation function, IEEE Trans. Syst. Man Cybern. 20 (5) (1990) 1058–1069.

[13] L. Biagiotti, C. Melchiorri, Trajectory Planning for Automatic Machines and Robots, Springer-Verlag, Berlin Heidelberg, 2008, p. 52.

[14] R.H. Bartels, J.C. Beatty, B.A. Barsky, An Introduction to Splines for Use in Computer Graphics and Geometric Modeling, Morgan Kaufmann, Palo Alto, CA, 1995.

[15] A. Piazzi, C.G.L. Bianco, M. Bertozzi, A. Fascioli, A. Broggi, Quintic G2 - splines for the iterative steering of vision-based autonomous vehicles, IEEE Trans. Intell. Transp. Syst. 3 (1) (2002) 27–36.

[16] C.G.L. Bianco, A. Piazzi, Optimal trajectory planning with quintic G2 -splines, in: Proceedings of the IEEE Intelligent Vehicles Symposium, Dearborn, MI, USA, Oct. 2000, 2000, pp. 620–625.

[17] C.G.L. Bianco, O. Gerelli, Generation of paths with minimum curvature derivative with η 3 -splines, IEEE Trans. Autom. Sci. Eng. 7 (2) (2010) 249–256.

[18] A. Piazzi, C.G.L. Bianco, M. Romano, η 3 -splines for the smooth path generation of wheeled mobile robots, IEEE Trans. Robot. 23 (5) (2007) 1089–1095.

[19] G. Lini, A. Piazzi, L. Consolini, Multi-optimization of η 3 –splines for autonomous parking, in: Proc. 50th IEEE Conference on Decision and Control/European Control Conference, Orlando, FL, USA, Dec. 2011, 2011, pp. 6367–6372.

[20] F. Ghilardelli, G. Lini, A. Piazzi, Path Planning for a Truck and Trailer Vehicle Using η 4 - Splines, Dip. di Ingegneria dell'Informazione, Univ. di Parma, Italy, Tech. Rep. TSC01–11, 2011.

[21] F. Ghilardelli, G. Lini, A. Piazzi, Path generation using η^4-splines for a truck and trailer vehicle, IEEE Trans. Autom. Sci. Eng. 11 (1) (2013) 187–203.
[22] S. Samiee, S. Azadi, R. Kazemi, A. Eichberger, Towards a decision-making algorithm for automatic lane change manoeuvre considering traffic dynamics, PROMET Traffic Transp. 28 (2) (2016) 91–103.
[23] Y. Wu, J. Xie, L. Du, Z. Hou, Analysis on traffic safety distance of considering the deceleration of the current vehicle, in: Proceedings of The Second International Conference on Intelligent Computation Technology and Automation, Zhangjiajie, China, October 10-11, 2009, 2009.
[24] Y.L. Chen, S.C. Wang, C.A. Wang, Study on vehicle safety distance warning system, in: Proceedings of The 2008 IEEE International Conference on Industrial Engineering and Engineering Management (IEEM), Singapore, Singapore, Dec 08–11, 2008, 2008.
[25] S. Samiee, The Design of Vehicle Control System With Drowsy Driver Based on Vehicle-Driver Interaction (Doctor of Philosophy thesis), Faculty of Mechanical Engineering, K. N. Toosi University of Technology, 2016 (in Persian).
[26] Anonymous, The New Car Assessment Program Electronic Stability Control System Testing, U.S. Department of Transportation, National Highway Traffic Safety Administration, 2013.
[27] Anonymous, Electronic stability control and brake assist system, Off. J. Eur. Union 230 (2010) 61–73. 53.
[28] S. Shojaei, A. Rahmani Hanzaki, S. Azadi, M.A. Saeedi, Design of lane change decision-making algorithm of truck-semitrailer in real dynamic environment, Modares Mech. Eng. 17 (9) (2017) 351–360 (in Persian).

Index

Note: Page numbers followed by *f* indicate figures and *t* indicate tables.

A

ABS. *See* Antilock braking system (ABS)
ACC. *See* Adaptive cruise control (ACC)
Active braking system
  active steering systems, 81
  adaptive and robust controllers, 96
  controller structure, 103, 103*f*
  control logic, 97–98, 98*f*
  corrective yaw moment, 97–98, 97*t*
  lower layer control, 102–103
  methods, 95
  semiactive suspension systems, 82
  strategy, 96–98
  two-layer control system, 96
  upper layer control, 98–102
  vehicle dynamics control, 95–96
  yaw rate, 95
Active chassis subsystems
  active braking system, 95–103
  semiactive suspension system, 103–106
Active control system, 82
Active front steering (AFS), 78, 320
Active roll control (ARC), 78
  semitrailer unit, 289–290
  tractor unit, 288–289
Active roll system parameter estimation
  semitrailer unit, 305–306
  tractor unit, 305
Active steering system (ASS), 2, 81
  articulation angle, 290
  block diagram, 352, 352*f*
  linear optimal control method, 347–348
  modification, 294–295
  parameter estimation, 306–309
  simplified model, 291–293
  sliding mode control method, 290, 348–352
  stability analysis, 293–294
Active suspension (AS), 10, 78
ADAMS/CONTROL module
  advantages, 42
  dynamics model *vs.* controller
    control software, 46–48
    loading, 45, 46*f*
    plant export process, 46, 47*f*
  mechanical model preparation
    input functions, 43, 43*f*
    input state variables, 42–43, 43*f*
    model inputs and outputs, 45, 45*f*
    output state variables and functions, 44–45, 44*f*
  MSC ADAMS software, 39–40
  online communication, 39–40, 42*f*
ADAMS software, 31–33
ADAMS-sub block diagram, 47, 48*f*
Adaptive control, 3, 96
Adaptive cruise control (ACC), 117–118, 167, 430
Adaptive fuzzy controllers, 81
Adaptive neuro-fuzzy inference system (ANFIS), 387
  firing rule and layered structure, 396*f*
  layers, 392
  network structure, 390–393
  primary parameters, 392
  two inputs and single output, 395*f*
Adaptive neuro-fuzzy schemes, 382
Adaptive robust control system
  hybrid diagram, 308–309, 308*f*
  performance evaluation
    active roll system, 312–314
    active steering system, 312
    fishhook maneuver, 309–314, 310*f*
  sensors, 308–309, 309*t*
Adaptive sliding mode control (ASMC), 114
  active roll system parameter estimation, 304–306
  active steering system parameter estimation, 306–309
  advantages, 301–302
  liquid-carrying articulated vehicle, 299, 302*f*

Adaptive sliding mode control (ASMC) *(Continued)*
robust control system, 302–303 (*see also* Adaptive robust control system)
standard least-squares method, 303–304
system's uncertain parameters, 300
Advanced driver assistance system (ADAS), 117–118, 381, 385*f*, 433
AEB. *See* Autonomous emergency braking (AEB)
AFP. *See* Artificial potential field (AFP)
AFS. *See* Active front steering (AFS)
AHS. *See* Automated highway system (AHS)
ANFIS. *See* Adaptive neuro-fuzzy inference system (ANFIS)
Antilock braking system (ABS), 2, 9–10, 10*t*, 78, 117–118, 215
braking coefficient with slip, 52, 52*f*
control torque, 51–52
longitudinal and lateral friction coefficients *vs.* longitudinal and lateral slip, 54, 54*f*
road surface, 52, 53*f*
shortest braking distance, 51
tire pressure and normal tire load, 52, 54*f*
velocity, 52, 53*f*
wheel free-body diagram, 51–52, 51*f*
APS. *See* Automated parking systems (APS)
ARC. *See* Active roll control (ARC)
Articulated heavy vehicles (AHVs)
active steering controller, 346–352
bottom-up integration, 321
braking and steering integrated control subsystems, 358–373
classes, 320
commercial vehicle, 319, 319*f*
control variables, 337–346
differential braking method, 320–321
dynamics and constraint equations, 329–330
instability, 319–320
layouts and parameters, 319–320
mechatronic units, 319–320
modeling
applied coordinate systems, 322–323
longitudinal and lateral dynamics motion equations, 325–327, 325–326*f*
roll and yaw motion equations, 327–329, 327*f*
velocity and acceleration, 323–325, 323–324*f*
parameters, 335, 336*t*
payloads, 319
simplified dynamics model, 333–336, 334*f*
simulation *vs.* performance, 352–357
sixteen degree-of-freedom model, 321–322, 321*f*
tire normal forces, 330–333
wheel rotational equations of motion, 330
Articulated vehicle carrying fluid
baffle plates, 248–258
effects of viscosity, 236–237
fill percentage effects, 234–236, 235*f*
fixed input–steady steer, 229–234, 229*f*
holder plates effects, 242–248
lane-change maneuvers, 229
tanker's geometrical shape on roll response, 238–242, 238–239*f*, 239*t*
transient response, 236–237, 237*f*, 240, 240–241*f*
Articulated vehicles, 214–215. *See also* Articulated vehicle carrying fluid
components, 379
dynamic system, 269
minimum-path parallel parking, 380
Articulation angle, 341–346, 342–343*f*, 346*f*
Artificial neural networks, 389–390
Artificial potential field (AFP), 381
AS. *See* Active suspension (AS)
ASIRT. *See* Association for Safe International Road Travel (ASIRT)
ASMC. *See* Adaptive sliding mode control (ASMC)
ASS. *See* Active steering system (ASS)
Association for Safe International Road Travel (ASIRT), 429
Asymmetric braking method, 354
Automated driving, 117–118

Automated highway system (AHS)
benefits, 153–154
traffic flow, 153
Automated parking systems (APS), 117–118
articulated vehicle, 379
challenging tasks, 377
control system, 386–415
control theories, 380
decomposition technique, 380
design and implementation, mechanical equipment, 416–423, 418*t*, 421*f*
electrical and electronic equipment, 416, 419–420*t*
environmental constraints, 377
feedback-based scheme, 381
garage, 377, 379*f*
geometric and nongeometric constraints, 380–381
kinematics of motion
extracting optimal steering angle, 384–386
instantaneous velocity-position, 383, 390*f*
no-slip motion, 382–383
nonholonomic constraints, 377–378
parallel, 377, 378*f*
pushing and pulling control problem, 381, 388*f*
Autonomous emergency braking (AEB), 433–434

B

Baffle plates
improved design A, 249–251, 250–251*f*
optimum shape
cases A and C combination, 252–254, 253–256*f*
cases B and C combination, 255–258, 257–258*f*
Bicycle model, 120, 121*f*
Biologic neural system, 389
Bioneuron, 389, 394*f*
Body in white (BIW), 37
Brake torque, 52, 55–58
Braking system. *See also* Antilock braking system (ABS)
active
active steering systems, 81
adaptive and robust controllers, 96
controller structure, 103, 103*f*
control logic, 97–98, 98*f*
corrective yaw moment, 97–98, 97*t*
lower layer control, 102–103
methods, 95
semiactive suspension systems, 82
strategy, 96–98
two-layer control system, 96
upper layer control, 98–102
vehicle dynamics control, 95–96
yaw rate, 95
asymmetric braking method, 354
autonomous emergency braking (AEB), 433–434
differential braking mechanism, 97
strategy, 7–9, 9*f*, 9*t*
Bryson method, 57–58
Bug algorithms, 435–436

C

CAS. *See* Collision avoidance system (CAS)
Center of oscillation, 122
Chassis control systems, 1
Chassis subsystems, active
active braking system, 95–103
semiactive suspension system, 103–106
Chattering phenomenon, 350–351
Circuit card assembly (CCA), 416
Classical control theory, 159
Closed-loop control system
adaptive neuro-fuzzy inference system (ANFIS), 403–404
automatic parking of articulated vehicle, 403, 407*f*
computer simulation, 393, 394*t*, 398*f*
desired paths, 395–396, 400–401*f*
distance error relative, 410*f*
error calculation, 404–408
expert driver's behavior, 394–402, 399*f*, 403*f*
fuzzy rules, 402, 402*t*
inputs and desired outputs, 396*t*
neuro-fuzzy controller, 413–415, 418*f*
yaw angle error relative, 411*f*

Cluster treatment of characteristic roots (CTCR), 164, 172–177, 186–187, 192–193, 203
Collaborative/centralized control systems, 158–160
Collision avoidance system (CAS), 117–118, 126–132, 431–434
Communication delay, 177, 179–180, 182, 184
Communication networks, 159, 160*f*
Communication structure, 159
Computational intelligence tools, 387
Computer-assisted simulated neural network, 389
Constant headways segmentation policy
  bidirectional structure, 179–182
  unidirectional structure, 178–179
Constant spacing policy, 156–157
Constant spacing segmentation policy
  bidirectional structure, 166–177
  unidirectional structure, 164–166
Controlled state variables
  angular velocity of tractor unit, 285–286
  articulation angle, 285–287
  lateral velocity of tractor unit, 286
  liquid sloshing, 283–285
Control systems. *See also specific control system*
  active roll, 288–290
  active steering, 290–295
  active suspension system design, 10
  adaptive neuro-fuzzy inference system (ANFIS), 390–393
  antilock braking system (ABS), 9–10
  artificial neural networks, 389–390
  closed-loop, 393–408
  computational intelligence tools, 387
  critical maneuvers, 287
  dynamic roll responses, 287
  electronic stability program (ESP), 4–9
  fuzzy control, 387–388
  hierarchical strategy, 2, 3*f*
  integration algorithm, 2–3
  inverse kinematic equations, 408–415
  uncertainties, 387
Control variables
  articulation angle and desired value, 341–346, 342–343*f*, 346*f*
  lateral velocity and desired value, 341
  performance standards/characteristics, 338
  steady-state yaw velocity gain, 338–340, 339*f*
  tractor yaw velocity and desired value, 338–340
Coordinate systems, 322–323
CTCR. *See* Cluster treatment of characteristic roots (CTCR)
Cubic polynomial trajectory, 439, 440*f*

D

Decentralized control systems, 158–160
Decision-making strategy, 472–474
Degrees of freedom (DOFs), 29
16-Degrees of freedom (DOFs) dynamic model
  lateral slip angle of tire, 275
  longitudinal and lateral dynamics
    semitrailer unit, 274, 274*f*
    tractor unit, 272–273, 273*f*
  problem kinematics, 270–272, 270*f*
  system dynamic equations, 270
  tire dynamics, 276
  tractor unit and semitrailer unit, 271, 272*f*
  wheel dynamics, 275
Differential braking mechanism, 97
Directional dynamics, 354–357
Direct yaw moment control (DYMC), 65–67, 80
DistBug algorithm, 436–437
Double lane-change maneuver, 281, 281–282*f*, 468*f*
  lateral acceleration, 110–113, 111*f*
  lateral-load transfer ratio, 112*f*, 113
  lateral slip angle, 111*f*, 113
  path, 111*f*, 113
  roll angle, 112*f*, 113
  steering angle input, 109, 110*f*
  yaw rate, 110–113, 110*f*
Driver assistance systems, 117–118
  advanced driver assistance system (ADAS), 117–118, 381, 385*f*, 433
Driving, automated, 117–118
Dugoff tire model, 276

DYMC. *See* Direct yaw moment control (DYMC)
Dynamic load factor (DLF), 235–237, 236–237*f*
Dynamics modeling
  coordinate systems, 226, 226*f*
  fluid
    degrees of freedom, 220
    FLUENT software, 220–222
    gravity, forces and moments, 222–224
    hexahedral mesh, 224, 224*f*
    mesh types and number of cells, 224, 224*f*
    motion model and vehicle dynamics, 224–227, 227*f*
    pressure correction, 221–222
    pressure-velocity coupling technique, 221–222
    rigid sections, 220
    transient flow, 221–222
    two-phase flow, 221
  integrated longitudinal-lateral guidance system
    equations of motion for vehicle, 120–122
    equations of motion for wheel, 122–123
    tire dynamics, 123–125
  integrated vehicle dynamics control (IVDC)
    full vehicle model with 14 degrees of freedom (DOFs), 82–86, 83*f*
    MR damper modeling, 90–92
    random road input modeling, 88–90
    roughness value, 88–90, 90*t*
    tire modeling, 86–88
  liquid-carrying articulated vehicle
    acceleration of liquid mass center, 276, 277*f*, 279
    assumptions and simplifications, 269–270
    controlled state variables, 283–287
    16-DOF dynamic model, 270–276
    dynamic equations, 279–280, 280*t*
    potential function model, 277, 278*f*
    validation, 281–283
    meshes with hexahedral cells, 227, 228*f*
    sensitivity to number of cells, 227–228
    tractor semitrailers, 467–471

E

Electric power steering (EPS), 78
Electronic stability control (ESC), 117–118, 469–470, 469*f*
Electronic stability program (ESP), 77–78, 320–321
  braking strategy, 7–9, 9*t*
  lateral force estimator, 4–6
  longitudinal velocity estimation, 6
  self-tuning adaptive control strategy, 3
  yaw moment determination, 6–7
Equivalent mechanical model, 219–220, 219*f*
Eulerian method, 218

F

Feasibility analysis, 126–127, 132–134
Finite element (FE) model, 30, 38
Fishhook maneuver, 297–299, 297*f*, 309–314, 310*f*
Fixed input–steady steer
  accelerations of center of gravity, 233, 233*f*
  displacement of center of gravity, 230–232, 231*f*
  dynamic load factor and load transfer ratio, 234, 234*f*
  free surface of fluid, 229–230, 230*f*
  lane change, 229, 229*f*
  rigid load, 230
  tanker's body, 232–233, 232*f*
  transient response, tractor and trailer, 229–230, 231*f*
  vehicle rollover behavior, 233–234
Fluid-carrying vehicles. *See also* Fluid motion
  articulated vehicles, 214–215
  dynamics modeling, 215–228
Fluid dynamics
  dynamics methods, 218–219
  equivalent mechanical model, 219–220, 219*f*
  quasistatic methods, 216–217, 216*f*

Fluid motion
  dynamics methods, 218–219
  fluid-carrying vehicle, 213
  vehicle dynamics, 213
  vehicle instability, 214
Four-wheel drive (FWD), 79
Free-body diagram, 122, 123*f*
Full SEDAN vehicle model
  with flexible body, 37–38, 38*f*, 39*t*
  with rigid body
    body, 36, 37*f*
    brake system set, 35
    characteristic curve of front damper, 34, 34*f*
    characteristic curve of rear damper, 35, 36*f*
    characteristic curve of rear spring, 34–35, 35*f*
    front suspension system set, 33, 33*f*
    rear suspension system set, 34, 35*f*
    steering system set, 35, 36*f*
    stiffness coefficient, 33, 34*f*
    tires, 36
    transmission system set, 36
  sixth natural frequency of sixth body, 38, 40*f*
  10th natural frequency, 38, 40–41*f*
Full vehicle dynamics model
  ADAMS software, 31–33
  finite element (FE) model, 30
  modules, 32, 32*t*
Fully assembled model of SEDAN vehicle, 38–39, 41*f*, 41*t*
Fuzzy control, 387–388
Fuzzy logic, 80
FWD. *See* Four-wheel drive (FWD)

G

G4 polynomial interpolation problem, 443, 443*f*
Geo-reconstruct method, 221–222
Global planning methods, 435

H

Hard line swap maneuvers, 354, 355*f*
Hazardous behavior modes
  lateral instability, liquid-carrying vehicles, 266–267
  liquid-carrying heavy vehicles, 267–269
Heavy vehicles. *See also* Articulated heavy vehicles (AHVs)
  liquid-carrying
    approaches, 267
    literature, 268–269
Hierarchical control, 2
High-degree polynomials, 439–441
Holder plates
  baffle plates, 243, 243*f*
  fluid motion in tanker with baffle plates, 244–245, 246*f*
  fluid motion in tanker without baffle plates, 245, 246*f*
  lane change maneuver, 243
  limitations, 242–243
  roll angle of trailer at 75% fill percentage, 247–248, 249*f*
  vehicle dynamics and fluid, 50% fill percentage, 244–248, 244–245*f*, 247–248*f*
Hybrid control system
  active roll control system, 296
  active steering control system, 296
  diagram, 296, 296*f*
  performance evaluation
    adaptive sliding mode controller, 300–314
    control inputs, 297–299, 301*f*
    fishhook maneuver, 297–299, 297*f*
    roll angles, 297–299, 300*f*
    tractor unit yaw rate, 297–299, 298–299*f*
  tractor unit's lateral acceleration, 296
Hybrid *vs.* integrated controller responses, 366*f*

I

I-DEAS finite element software, 34–35
Integrated control systems, 365*f*
  computation procedure, 358
  limiting wheel slip ratio, 360–362, 360*f*, 364*f*
  performance
    braking yaw torques, 364, 367*f*

controlled *vs.* uncontrolled vehicles, vehicle path, 364, 368*f*
lane change maneuver, 362–368
slalom maneuver on semislippery road, 369, 369–372*f*
vehicle response with and without control, 364, 368*f*
weight coefficient variations, 364, 367*f*
pseudocode, 359–360
robustness against error and noise, 369–373, 373*f*
steering actuators, 358
Integrated longitudinal and lateral vehicle guidance algorithm
approximate and real coefficient, friction front tires, 142, 143*f*
approximate and real coefficient, friction rear tires, 142, 143*f*
front and rear wheels, 143–144, 145*f*
infeasible trajectory, 148, 149*f*
lane-changing maneuver, 143, 144*f*
lateral acceleration, 147–148, 148*f*
lateral direction angle and lateral slip angle, 147–148, 149*f*
lateral position, 140–142, 140*f*, 142*f*, 145–146, 146–147*f*
longitudinal position, 140–142, 140–141*f*, 144–145, 146*f*
longitudinal velocity, 143–144, 144–145*f*
maneuver assumptions, 137, 138*t*
overview and evaluation trajectories, 137–139, 138*t*
simulation results
integrated control, 143–149
trajectory planning, 137–142
steering angle, lane-changing maneuver, 145–146, 147–148*f*
Integrated longitudinal-lateral control
high computational cost, 134
kinematic model, 134
lateral control, 136–137
longitudinal control, 135–136
Lyapunov function, 134
Integrated longitudinal-lateral guidance system
applied rules and assumptions, 125–126
driver assistance systems, 117–118
dynamic model
equations of motion for vehicle, 120–122
equations of motion for wheel, 122–123
tire dynamics, 123–125
features, 149–150
layout, 118
summary, 118–120, 119*f*
trajectory planning, 126–134
Integrated vehicle dynamics control (IVDC). *See also* Control systems
advantages, 78–79
double lane-change maneuver
lateral acceleration, 110–113, 111*f*
lateral-load transfer ratio, 112*f*, 113
lateral slip angle, 111*f*, 113
path, 111*f*, 113
roll angle, 112*f*, 113
steering angle input, 109, 110*f*
yaw rate, 110–113, 110*f*
dynamic model
full vehicle model with 14 degrees of freedom (DOFs), 82–86, 83*f*
MR damper modeling, 90–92
random road input modeling, 88–90
roughness value, 88–90, 90*t*
tire modeling, 86–88
front-right wheel, 113, 114*f*
hierarchical control methods, 78–79
lateral and yaw stabilities, 106
operational task, 106–107, 107*t*
parameters, 2
parts, 81
reasons, 2
simulation
body vertical velocity, 11–13, 15*f*
14-degrees of freedom (DOFs) vehicle model, 108, 109*t*
handling and stability analyses, 109–113
handling control of vehicle, 11, 12*f*
lateral acceleration, 11, 13*f*, 19–20, 21*f*
lateral slip angle, 21, 22*f*
lateral velocity, 11, 13*f*, 21, 22*f*
longitudinal slip ratio, 16–18, 18–20*f*, 24, 24–25*f*
longitudinal velocity, 17–18, 21*f*

Integrated vehicle dynamics control (IVDC) *(Continued)*
motion path, 11, 14*f*
path traveled, 23–24, 23*f*
pitch angle, 11–13, 16*f*
pitch velocity, 11–13, 17*f*
quantities, 11, 12*t*
ride comfort analysis, 108–109
road input *vs.* displacement, 15–18, 18–19*f*
road irregularities, 11–15, 14*f*, 17*f*
roll angle, 11–13, 15*f*
roll rate, 11–13, 16*f*
sum of lateral forces, 24–26, 25–26*f*
suspension system and vehicle dynamics, 19–26
suspension system control, 11–18
vertical acceleration, 108–109, 109*f*
vertical displacement, 11–13, 14*f*, 21–23, 23*f*
yaw rate, 21, 22*f*
single central algorithm, 1
standard deviation of vertical forces, 113, 113*t*
structure, 106–108
vehicles, 1
Integration strategy, 11
Intervehicle spacing control policy, 156–157
Inverse kinematic equations
closed-loop control system, 413–415, 414*t*, 418*f*
fuzzy rules levels and outputs, 411–412, 417*f*
input membership functions and outputs, 411–412, 415*f*
training, desired data-fed adaptive neuro-fuzzy inference system (ANFIS), 410–412, 411*t*, 413–414*f*
verification, computer simulations, 408–410, 412*f*
IVDC. *See* Integrated vehicle dynamics control (IVDC)

K

Kalman filter, unscented, 92–96
Kinematics motion
extracting optimal steering angle, 384–386
instantaneous velocity-position, 383, 390*f*
no-slip motion, 382–383
Kronecker multiplication, 176

L

Lagrangian method, 218
Lane-change assistant (LCA), 117–118
Lane-change maneuver, 118, 119*f*
Lane departure warning systems (LDWS), 117–118
Lane-keeping assistant (LKA), 117–118, 433–434
Lateral control, 136–137
Lateral force estimator, 4–6
Lateral-load transfer ratio (LTR), 107, 245–247
Least-squares algorithm, 308–309
Linearized model, 162, 162*f*
Linear method, 218
Linear optimal control method, 347–348
Linear parameter varying (LPV), 80
Linear quadratic Gaussian (LQG), 81
Linear–quadratic regulator (LQR), 6
Linear time-invariant system, 172
Liquid-carrying articulated vehicle
advantages, 262–263
control system design, 287–295
dynamic modeling
acceleration of liquid mass center, 276, 277*f*, 279
assumptions and simplifications, 269–270
controlled state variables, 283–287
16-DOF dynamic model, 270–276
dynamic equations, 279–280, 280*t*
potential function model, 277, 278*f*
validation, 281–283
financial saving, 261
hazardous behavior modes, 266–267
hybrid control system, 296–314
off-tracking reduction, 261–262, 262*f*
performance-based standards (PBS)
handling quality, 263
lateral stability during braking, 263–264

rearward amplification, 265
static rollover threshold, 265
steady-state off-tracking, 264
transient off-tracking, 264–265
research, 314–316
tractor unit, 261
trailer units' acceleration, 262
Liquid-carrying heavy vehicles
approaches, 267
literature, 268–269
Liquid dynamic system, 270
Liquid motion, 266–267
Liquid sloshing, 266, 283–285
Liquid-solid interaction, 266
LKA. *See* Lane-keeping assistant (LKA)
Load transfer ratio (LTR), 235–236, 236*f*
Local planning methods, 435
Longitudinal control, 135–136
Longitudinal vehicle dynamics model, 161–163, 161*f*
Longitudinal velocity estimation, 6
LPV. *See* Linear parameter varying (LPV)
LQG. *See* Linear quadratic Gaussian (LQG)
LQR. *See* Linear–quadratic regulator (LQR)
Lyapunov function, 100–102, 134, 349–350
Lyapunov-Razumikhin methods, 164

M

MacPherson suspension system, 33
Mamdani fuzzy inference system, 104–105
Mass-spring-damper systems, 167
Mechanical-fluid methods, 213
Model-neutral format (MNF), 34–35, 37
Modified Bouc-Wen model, 90–92
Modified LuGre model, 90–92, 91*f*, 92*t*
MR damper modeling
force *vs.* velocity, 90–92, 92*f*
parameters, LuGre model, 90–92, 92*t*
parametric and nonparametric, 90–92
Multiinput-multioutput nonlinear system, 348–349
Multivariable control, 2

N

Navier-Stokes equations, 218–222, 268–269, 279–280
Neuro-fuzzy controller, 413–415
Neuro-fuzzy networks, 390
Neurons, 389
Neutral steering, 8
Nonlinear method, 218
Nonlinear tire model, 120
N-trailers, 431

O

ODE. *See* Ordinary differential equation (ODE)
Off-axle hitching, 431, 432*f*
On-axle hitching, 431, 432*f*
Online nonlinear optimization, 79
Optimal control systems, 3
adhesion threshold, 48
brake torque, 55–58
braking forces distribution, 59–62, 60–61*f*
control torque, 64–65, 64*f*
designing, antilock braking system (ABS), 51–55
desired vehicle path determination, 58–59
handling vehicle dynamics analysis, 63–65
lateral velocity, 64–65, 65*f*
longitudinal velocity, 64–65, 65*f*
operation principles, 49, 49*f*
safety requirements, 49
SEDAN vehicle parameters, 63, 63*t*
vehicle dynamics control system set, 62, 62*f*
vehicle manufacturers, 49
yaw rate, 64–65, 64*f*
yaw rate *vs.* slip angle, 50–51, 50*f*
Optimal control theory, 381
Ordinary differential equation (ODE), 167
Oversteered *vs.* understeered vehicles, 8, 8*f*
Oversteering, 7–8

P

Pacejka/Magic formula (MF), 124
Pacejka tire model
modified, 80–81
nonlinear, 81
parameters, 88, 89*t*
Parking system. *See also* Automated parking systems (APS)
automatic parking of articulated vehicle, 403, 407*f*
minimum-path parallel parking, 380

Partners for Advanced Transit and Highway (PATH), 153–154
Performance-based standard (PBS), 338
Plant export process, 46, 47*f*
Power spectral density (PSD), 88–90
Printed circuit assembly (PCA), 416
Printed circuit board assembly (PCBA), 416

Q

Quasistatic methods, 216–217, 216*f*

R

Random road input modeling, 88–90
Rearward amplification, 265
Recursive least squares (RLS), 3–4
Reference time path, 437–438
Ride comfort analysis, 108–109
Road friction coefficient, 88, 89*f*
Robust control system, adaptive
  hybrid diagram, 308–309, 308*f*
  parameters, 290, 290*t*
  performance evaluation
    active roll system, 312–314
    active steering system, 312
    fishhook maneuver, 309–314, 310*f*
  sensors, 308–309, 309*t*
Roll instability, 214
Rollover Index (RI), 107
Rollover stability, 265, 268–269, 287
Rollover threshold, 215, 266–267
Routh-Hurwitz stability criteria, 177, 182–183

S

Self-aligning torque (SAT), 79
Self-tuning regulator (STR), 3–4, 4*f*
Semiactive suspension (SAS), 78, 82
  characteristics, 103–104
  components, 103–104
  damping ratio, 104
  groups, 103–104
  SAS1 system, 104–105, 105*t*
  SAS2 system, 105–106, 106*t*
Siding mode controller (SMC), 98
Simple line swap maneuvers, 352–354, 353*f*
Simplified dynamics model, 333–336
Simplified vehicle model, 290, 291*f*
Simulation *vs.* performance, 352–357
SIMULINK environment, 46–47, 47*f*
Single lane change analysis
  control torque, 65–67, 66–67*f*
  lateral acceleration, 67, 69*f*
  lateral velocity, 65–67, 67–68*f*
  longitudinal velocity, 65–67, 66*f*, 68*f*
  path, 67, 69*f*
  roll angle, 67, 69*f*
  yaw rate, 65–67, 66*f*, 68*f*
Sliding mode control method, 348–352. *See also* Adaptive sliding mode control (ASMC)
SMC. *See* Siding mode controller (SMC)
Smooth open-loop control, 442–450
Snaking, 338
Sport utility vehicles (SUVs), 77–78
Stability
  bidirectional structure
    controlling parameters, 192, 192*t*
    differential equations with partial derivatives, 191–192
  cluster treatment of characteristic roots (CTCR), 172–177, 192–193
  constant headways segmentation policy, 177–182
  constant spacing segmentation policy, 164–177, 190–193
  constant time headways policy
    bidirectional structure, 197
    unidirectional structure, 193–196
  differential equations with partial derivatives, 167–172
  string (*see* String stability)
  time-variable communication delay, 190–191, 191*f*
  unidirectional structure, 190–191
Stability control method, 49, 159–160
Standard least-squares method, 303–304
Steady-state gains, 356–357, 357*f*
Steady-state off-tracking, 264
Steady-state turning test, 264, 264*f*
Steering. *See also* Active steering system (ASS)
  active front steering (AFS), 78, 320
  electric power steering (EPS), 78
  neutral steering, 8
  oversteering, 7–8
  understeering, 7–8

Steering angle (four-wheel steering), 320
Steering wheel angle, 64, 64*f*
Step steer analysis
  control torque, 70, 70*f*, 72, 72*f*
  lateral acceleration, 72, 74*f*
  lateral velocity, 70, 71*f*, 72, 73*f*
  longitudinal velocity, 70, 71*f*, 72, 73*f*
  path, 72, 74*f*
  roll angle, 72, 73*f*
  steering angle, 70, 70*f*
  yaw rate, 70, 71–72*f*, 72
STR. *See* Self-tuning regulator (STR)
String stability
  automated highway systems, 157–158
  bidirectional structure, 199–203
  cluster treatment of characteristic roots (CTCR), 186–187, 203
  constant headways policy
    bidirectional structure, 188–189
    one-sided structure, 187–188
  constant spacing policy
    bidirectional structure, 184–187
    unidirectional structure, 183–184, 199
  constant time headways policy
    bidirectional structure, 208–210
    unidirectional structure, 203–207
  definition, 158
  distributed position/speed error, 157–158
  longitudinal controller of vehicle, 163–164
  longitudinal vehicle dynamics model, 161–163, 161*f*
  system parameters, 199, 199*t*
  transfer functions, 183
Suspension system control, 11–18
SUVs. *See* Sport utility vehicles (SUVs)

T

Takagi-Sugeno-Kang (TSK) inference system, 388
Tangent Bug algorithm, 436–437
Tire modeling, 86–88
TISO. *See* Two-input single-output (TISO)
Tractor semitrailers, 227*f*
  automatic cautionary actions, 429–430
  characteristics, 454, 454*f*
  collision avoidance, 431–434
  decision-making strategy, 472–474
  double lane-change maneuver, 468*f*
  driver drowsiness, 429
  economic gap, 429
  introduction, 431
  motion planning, 430
  moving path, velocity and lateral acceleration, 473*f*
  operational speeds, 430
  path planning, 434–437, 435–436*f*, 437*t*
  schematic, 442, 442*f*
  simulation parameters, 467*t*
  smooth open-loop control, 442–450
  trajectory generation, 437–441, 450–471
  validation, dynamic model, 467–471
  yaw velocity, 468*f*
Traffic congestion, 153, 154*f*
Traffic flow stability, 154
Trailer swing, 264–265
Training dataset, 396–399
Trajectory equation, 453
Trajectory generation
  bicycle dynamic model, 466, 466*f*
  critical (coincidence) time, 463, 464*t*
  critical lane-change maneuver, 465
  cubic polynomial trajectory, 439, 440*f*
  high-degree polynomials, 439–441
  kinematic characteristics, 454–458
  lane change, 450–471, 464*f*
  lateral distance, 463, 464*t*
  methods, 438–441
  one-dimensional and multidimensional groups, 438
  path planning algorithm, 437–438
  target lane and safe distance, 465
  test method and minimum time acceptance criterion, 466
  time constraints
    front vehicle lie on same line, 458–461, 459*f*
    side vehicle on target lane, 463–465
    target lane in front, 461–463
  trajectory equation, 453
Trajectory planning
  collision avoidance, 126–132
  feasibility, 126–127, 132–134
  limitations, 126–127
  maximum longitudinal/lateral acceleration, 126–127
  online procedure, 126–127
Transient off-tracking, 264–265

Transportation systems, 266–267
Trial-and-error methods, 99
TruckSim software, 467, 469
Two-input single-output (TISO), 161

U

Understeering, 7–8
Unscented Kalman filter, 92–96

V

Variable spacing policy
  constant time headway policy, 157
  variable time headway policy, 157
Vehicle active safety systems, 78
Vehicle bicycle model, 4–5, 5*f*
Vehicle dynamics control (VDC)
  ADAMS/CONTROL module, 39–48
  advantages, 30
  defined, 29, 49
  dynamics handling analyses, SEDAN vehicle
    single lane change analysis, 65–69
    step steer analysis, 70–73
  full SEDAN vehicle model, 33–38
  full vehicle dynamics model, 30–39
  fully assembled model of SEDAN vehicle, 38–39, 41*f*, 41*t*
  optimal control, 48–65
  sensors, 29–30
Vehicle platoon control
  centralized and decentralized control, 158–160
  constant spacing policy, 156–157
  definitions, 155–160
  dense and dense traffic flow, 155
  infrastructure, 153–154
  intervehicle distance, 154
  intervehicle spacing control policy, 156–157
  issues, 155
  one-dimensional model, 155–156, 156*f*
  plans, 153
  string stability, 157–158
  traffic congestion, 153, 154*f*
  traffic flow stability, 154
  unidirectional and bidirectional communication structures, 210–211
  validation, simulation, 189–210
  variable spacing policy, 157
Vehicle rollovers
  behavior, 233–234
  threshold, 107
  tripped, 77–78
  untripped, 77–78
Vehicle stability, 77, 341
VisBug algorithm, 436–437
Volume of fluid (VOF), 218

W

Wheel and tire system, 269–270
Wheel dynamic model, 85, 85*f*
Wheel free-body diagram, 51–52, 51*f*
World Health Organization (WHO), 117–118, 429